1-1-2013

Structural Design Issues For Integral Abutment Bridges

Navid Nikravan
Ryerson University

STRUCTURAL DESIGN ISSUES FOR INTEGRAL ABUTMENT BRIDGES

By

Navid Nikravan
M.Eng., Ryerson University, Canada, 2009
B.Sc., K.N. Toosi Univesrsity, Iran, 2007

A dissertation
presented to Ryerson University
in partial fulfillment of the
requirements for the Degree of
Doctor of Philosophy
in the Program of
Civil Engineering

Toronto, Ontario, Canada, 2013

AUTHOR'S DECLARATION

I hereby declare that I am the sole author of this dissertation. This is a true copy of the dissertation, including any required final revisions, as accepted by my examiners.

I authorize Ryerson University to lend this dissertation to other institutions or individuals for the purpose of scholarly research.

I further authorize Ryerson University to reproduce this dissertation by photocopying or by other means, in total or in part, at the request of other institutions or individuals for the purpose of scholarly research.

I understand that my dissertation may be made electronically available to the public.

STRUCTURAL DESIGN ISSUES FOR INTEGRAL ABUTMENT BRIDGES

Navid Nikravan, Doctor of Philosophy, 2013

Department of Civil Engineering, Ryerson University

ABSTRACT

In recent years, integral abutment bridges have been increasingly used in Canada due to their low maintenance costs. Whereas a rational guideline to determine the maximum length and skew angle limits for integral bridges due to temperature variations do not exist in bridge codes. As such, structural behavior of integral bridges subjected to temperature variation was investigated through a numerical modeling. First, detailed 3D finite-element models were developed. The accuracy of finite-element models was validated against data collected from filed testing available in the literature on integral bridges subjected to the seasonal temperature variations and truck loading. Then, a parametric study was carried out to study the effects of key parameters on the performance of integral bridges when subjected to temperature variations. The numerical results indicated that number of design lanes, bridge length, abutment height, abutment-pile connection, pile size and skew angle had a significant impact on the behavior of integral bridges. Based on the data generated from the parametric study, new limits for the maximum length and skew angle of integral bridges based on displacement-ductility limit state of piles were established.

Literature review revealed that live load distribution among girders in integral bridges due to truck loading conditions is as yet unavailable. This study is extended to develop new equations to estimate girder live load distribution factors for integral bridges. First, 2D and 3D finite-element models (FEMs) of integral bridges were developed. Then, a parametric study was performed to study the effects of parameters such as abutment height, abutment thickness, wingwall length, wingwall orientation, number of design lanes, span length, girder spacing and number of intermediate diaphragms. The results indicated that the live load distribution factors obtained from the FEMs were lower than those obtained from current CHBDC equations. Consequently, sets of empirical expressions were developed in the form of reduction factors that can be applied

to CHBDC live load distribution factors to accurately calculate the girder distribution factors. Also, other set of equations for the live load distribution factors were developed in a similar form as that specified in CHBDC for possible inclusion in the bridge code.

ACKNOWLEGEMENTS

The author wishes to express his deep appreciation to his advisor Dr. Khaled Sennah, for his constant support and valuable supervision during the development of this research. Dr. Sennah devoted his time and effort to make this study a success. His most helpful guidance is greatly appreciated.

The author is very grateful to his father, mother and sister for their great support, understanding and encouragement during the course of study.

The financial supports from NSERC Discovery Grant and the Highway Infrastructure Innovation Funding Program of Ontario Ministry of Transportation (MTO-HIIFP), as well as Ryerson University, are greatly appreciated.

DEDICATION

To

My Family

for their endless love and support in every step of my life

TABLE OF CONTENTS

LIST OF TABLES

LIST OF FIGURES

LIST OF APPENDICES

LIST OF SYMBOLS

b	Bridge width
C_e	Correction factor for vehicle edge distance obtained from tables in CHBDC
C_f	Correction factor in % obtained from tables in CHBDC
C_u	Undrained shear strength of the clay
dL	Change in the length in longitudinal direction
dt	Change in the length in transverse direction
d_P	Pile width
E	Young's modulus
F	Width dimension that characterizes load distribution for a bridge as per CHBDC
F_m	Amplification factor for the transverse variation in maximum longitudinal moment intensity as per CHBDC
$F_{m\ int}$	Moment distribution factor of interior girder
$F_{m\ ext}$	Moment distribution factor of exterior girder
F_v	Amplification factor for the transverse variation in maximum longitudinal vertical shear intensity as per CHBDC
$F_{v\ int}$	Shear distribution factor of interior girder
$F_{v\ ext}$	Shear distribution factor of exterior girder
G	Shear modulus
I_G	Flexural moment of inertia of the girder section
J_G	Torsional moment of inertia of the girder section
k_a	Active earth pressure coefficients
k_o	At-rest earth pressure coefficients
K_s	Spring stiffness for clay for elastic portion

L	Span length between the fixed support and the movable joint or bearing
M_a	Moment that is induced by the active-soil pressure
M_f	Moment that is induced by the soil-friction force
M_g	Longitudinal bending moment per girder per CHBDC
M_{gavg}	Average moment per girder per CHBDC
M_T	Maximum moment per design lane per CHBDC
n	Number of design lanes as per CHBDC
N	Number of girders as per CHBDC
P_a	Total active backfill soil force
P_u	Soil resistance per unit length of pile
q	Surcharge pressure
R_L	Modification factor for multilane loading as per CHBDC
R_f	Reduction factor for distribution factors
S	Girder spacing
t	Concrete slab thickness
T_{AvgMax}	Maximum average temperature
T_{AvgMin}	Minimum average temperature
$T_{Install}$	Installation temperature
V_{ext}	Maximum shear force resulting from bridge analysis of exterior girders
V_g	Longitudinal vertical shear per girder per CHBDC
V_{gavg}	Average vertical shear per girder per CHBDC
V_{int}	Maximum shear force resulting from bridge analysis interior girders
V_o	Shear forces for the corresponding single girder resulting from 2D integral bridge analysis due to single truck
V_T	Maximum vertical shear per design lane per CHBDC

W_e	Width of a design lane
Δ_x	Total displacements components in the x-axis
Δ_y	Total displacements components in the x-axis
Δ_{cx}	Displacement capacity of pile in longitudinal direction
Δ_{cy}	Displacement capacity of pile in transverse direction
ΔT	Difference between extreme design temperatures and installation temperature
ΔT_{Fall}	Temperature fall
ΔT_{Rise}	Temperature rise
Θ	Skew angle of the integral abutment bridge
α	Coefficient of thermal expansion properties
γ	Unit Weight of soil
δ	Surface-friction angle of soil and abutment
ε	Skew parameter
ε_{50}	Soil strain at 50% of ultimate soil resistance
ϕ	Angle of internal friction of the soil
v	Poisson's ratio
σ_b	Average flexure stress at the bottom surface of bottom flange
σ_{ext}	Maximum flexure stress resulting from bridge analysis at the bottom surface of the bottom flange of exterior girders
σ_{int}	Maximum average flexure stress resulting from bridge analysis at the bottom surface of the bottom flange of the interior girder.
σ_o	Longitudinal stresses for the corresponding single girder resulting from 2D integral bridge analysis due to a single truck

CHAPTER 1: INTRODUCTION

1.1 BACKGROUND

Traditional bridge structures use expansion joint systems to accommodate the change in the bridge length that is induced by changes in the temperature of the bridge superstructure. An example of a bridge with expansion joints is shown in Figure 1.1.

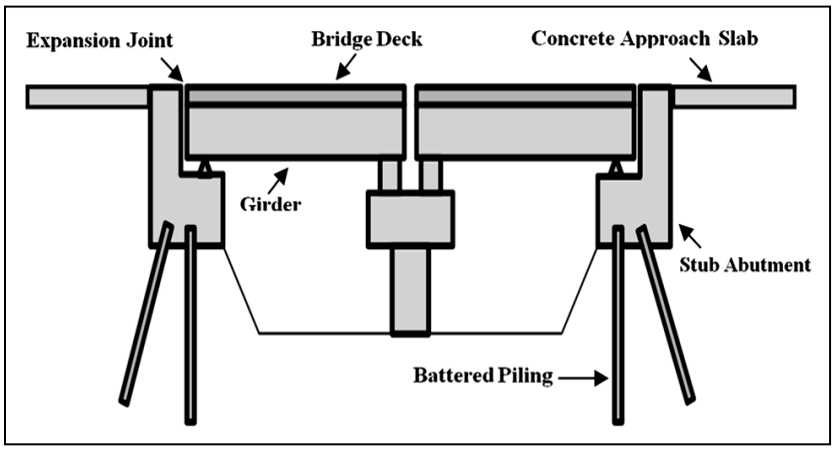

Figure 1.1: Typical two-span traditional bridge.

Performance deficiency of many expansion joints and other structural release mechanism systems in traditional bridges is a big issue. These joints fail in one or more important aspects, notably water-tigthness when they subject to traffic and bridge movement. They often leak and allow water contaminated with salt and debris which spilled onto substructure and underside of the deck. Example of damaged expansion joints in traditional bridges and their effect on the substructure is illustrated in Figure 1.2. The concept of integral abutment bridge was developed in an attempt to eliminate joints in these locations.

(a) (b) (c)

Figure 1.2: Typical problems in traditional bridges (a) Damaged expansion joint, (b) Corroded steel beam, (c) Damaged bridge seat [57].

Integral abutment bridges (Jointless bridges) have not joints between their superstructure and substructure. Integral abutment bridges are single or multi-span structures with flexible foundations in which the girders are integrated with the abutments. Expansion joints and moveable bearing at the end of the deck are replaced with cycle control joints at the end of approach slab where joint leakage will not adversely affect the structure. Such bridges have no bearings between the girders and abutments, therefore the abutments are usually referred to as integral. Maintenance cost of integral abutment bridges is less than equivalent bridge with expansion joint. Elimination of the joints reduces corrosion damage in the girders, bearing and underlying substructure due to leaking run-off water that often contains corrosive de-icing salts and pollutants from the deck to the supporting members. Initial cost of integral bridges construction is also less than traditional bridges due to the presence of fewer piles, elimination of bearings, lack of expansion joints and diaphragms at the abutments, and utilization of non-battered piles. In addition to reduced maintenance costs and reduced initial cost, advantages of integral bridges include improved structural integrity, reliability, redundancy, improved seismic performance, improved riding surface, and enhanced aesthetics. Figure 1.3 depicts a schematic diagram of a typical two-span integral bridge.

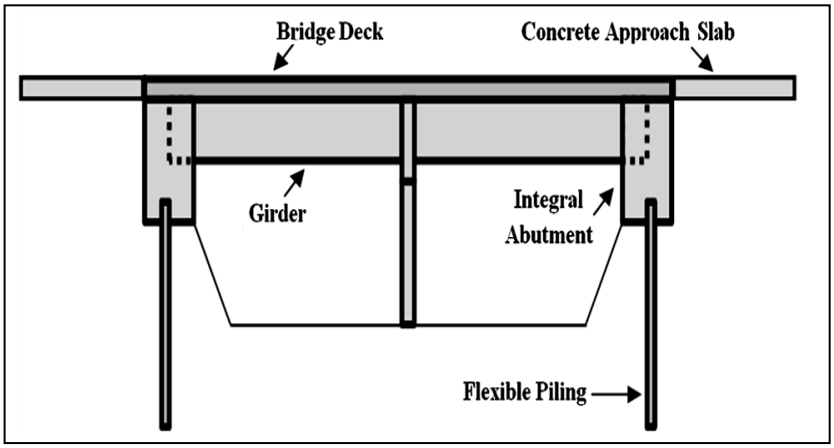

Figure 1.3: Typical two-span integral abutment bridge.

1.2 STATEMENT OF THE PROBLEM

Whereas the positive aspects outweigh the negative aspects of integral bridges, there are still problems to be addressed. The problems which has been taken into consideration is that a

rational guidelines to determine the maximum length and skew angle limits for integral bridges do not exist at present in the superseded Ontario Highway Bridge Design Code (OHBDC) [44, 45], Canadian Highway Bridge Design code (CHBDC) [13, 14] and American Association State Highway Transportation Officials (AASHTO) [3, 4, 5, 6]. Generally, Departments of Transportation use in-house specifications that provide length and skew angle limits for integral bridges. Ontario Ministry of Transportation (MTO) also impose the length and skew angle limits for integral bridges. These length and skew angle limitations specified by MTO and different Departments of Transportation in United States seem to be conservative [36, 52, 53]. Therefore, the maximum length and skew angle limitation of steel and concrete integral bridges in Ontario design guideline [35] for small and large skew angle should be re-evaluated and a rational guideline to determine the maximum length and skew angle limitations for integral bridges should be developed.

The other problem is that although many integral abutment bridges have been built in North America, there is no nationally accepted guideline on girder live load distribution factors (LLDFs) for integral abutment bridges in current bridge codes (AASHTO, AASHTO LRFD, and CHBDC). While numerous studies have been conducted on live load distribution among the girders of jointed or simple supported bridges (SSBs), similar research on integral abutment bridges is scarce. Due to lack of research on live load distribution in integral abutment bridges, bridge design codes do not possess live load distribution factors (LLDFs) for integral abutment bridge girders. Hence, design engineers do not have practical tools to estimate live load effects in integral abutment bridge girders efficiently. Many practicing engineers use the provisions for regular jointed bridges in current bridge design specifications to design integral abutment bridges. This also includes using such provisions for the design of integral abutment bridge girders under live load effects. The live load distribution equations in current bridge design specifications were basically developed for jointed bridges where superstructure is separated from abutments via expansion joints. However, in the case of integral abutment bridges, the monolithic construction of the superstructure abutment joint forces with the superstructure and the abutments to act together under live load effects. The continuity of the superstructure-abutment joint in integral abutment bridges is found to improve the distribution of live load moment among the girders especially for short spans [20, 66]. Accordingly, the bridge design

codes live load distribution factors (LLDFs) for the design of integral abutment bridge girders may result in incorrect estimates of live load effects [54].

1.3 RESEARCH OBJECTIVES

The aim of this research was to contribute to the efficient design of integral bridges by developing experimentally calibrated analytical models capable of predicting accurately their response when subjected to construction, service and ultimate loading conditions. The proposed research was intended to fill the gaps found in bridge codes. This research expected to develop a simplified method and guidelines to design integral bridges more reliably and economically, converting to less spending of tax payer's money. The proposed method would be used by code writers, practicing engineers and bridge researchers. Specific research objectives were as follows:

- Develop limitations of total bridge span and skew angle for integral abutment bridges of different bridge configurations (i.e. slab-on-girder bridges and box-girder bridges) to accommodate temperature variations over the year.
- Develop simplified method of analysis of girder moments and shears of integral abutment bridges made of slab on concrete or steel I-girders subjected to CHBDC truck loading conditions [14] at ultimate limit state (ULS), serviceability limit state (SLS) and fatigue limit state (FLS).

1.4 REASERCH METHODOLOGY

To achieve the objectives outlined earlier in this research study, the following tasks have been performed.

Task 1. A literature review has been conducted to reveal previous experimental and analytical attempts regarding the length limitations and live load distribution factors on integral bridges. Also, the national and international state-of-the-art and state-of-practice pertained to integral bridges have been reviewed. Moreover, the current integral bridge construction practice and design guidelines followed in Ontario have been compared with those employed by other provinces in Canada and Department of Transportation in United States.

Task 2. Detailed 2-D and 3-D finite-element models (FEM) have been built for both superstructure and substructure to determine length limitations and live load distribution factors

for integral bridges. Numerical models have been validated using data collected from newly-constructed integral abutment bridges subjected to temperature changes and truck loading.

Task 3. A sensitivity study on the effect of temperature variation on expansion and contraction of integral abutment bridges was performed. The key parameters in the sensitivity study were pile size, pile orientation, abutment height, abutment thickness, girder type, girder depth, girder spacing, number of design lanes, connection of abutment pile cap to pile, soil stiffness, wingwall orientation and wingwall length. The effects of different FEA models have been compared to find the critical parameters which led to the maximum pile deformations due to expansion and contraction. In this study, critical parameters (which produce more than 10% difference in pile displacement) have been identified as: abutment height, piles size, number of design lanes and connection of abutment pile cap.

Task 4. Maximum length and skew limitations for integral abutment bridge have been developed based on displacement-ductility limit state of the pile. The limitations were a function of bridge span, skew angle and bridge width. Also the effect of bridge cross-section configurations (i.e. slab-on-girder bridges and box-girder bridges) on bridge span and skew angle limitation was considered in this study.

Task 5. A parametric study also has been performed to evaluate live load distribution factors for integral abutment bridges subjected to CHBDC truck loading conditions. Based on data generated from parametric studies, influential parameters have been distinguished as: number of design lanes, bridge span length and girder spacing. This parametric study is limited to integral abutment bridges made of slab-on-girders and single spans.

Task 6. Using regression analysis techniques, empirical expressions to evaluate moment and shear distribution factors for integral abutment bridge have been developed. These proposed equations have been presented in Tables 6.24 to 6.35.

1.5 DISSERTATION ORGANIZATION

Following this introductory chapter, chapter 2 describes the literature review which is a thorough explanation of integral bridge length and skew angle limitations imposed by various agencies. In chapter 2 different methodologies on distribution factors of traditional bridges which are used to

determine live load distribution factors are also explained. Chapter 3 discusses structural model developed for analysis of different integral bridge prototypes using the finite element method. Chapter 4 presents the observed behaviour of 8 instrumented integral abutment bridges which were continuously monitored. In this chapter, the detailed numerical models are validated against the results of those instrumented bridges. Chapter 5 and 6 include the results of sensitivity study and parametric study conducted on various integral abutment bridges. In chapter 5, proposed graphs to determine maximum length and skew angle based on pile displacement capacity are given. In chapter 6, sets of live load distribution equations (LLDEs) in the form of correction factors to be multiplied by live load distribution factors obtained from CHBDC to accurately estimate the live load moments and shears are developed. In addition, results from FEA modelling are used to develop set of live load distribution factors in the same format specified in CHBDC. Chapter 7 contains brief summary of the research study, conclusions of research and suggestions for future research involving integral abutment bridges.

CHAPTER 2: REVIEW OF THE LITERATURE

2.1 GENERAL

Traditional bridge design makes use of expansion joints in conjunction with expansion bearings to accommodate superstructure movements. However, leaking expansion joints and frozen bearings are the major issues related to maintenance. As a result, considerable interest in integral abutment (jointless) bridges has been increased in the past few decades in Canada and United States. Integral bridge superstructure is constructed to work integrally with the abutments to accommodate movements due to temperature changes by using flexible piling and relief joints at the end of the approach slabs. In addition to reduced maintenance costs, advantages of integral bridges include improved structural integrity, reliability and redundancy, improved long-term serviceability, improved seismic performance, improved riding surface, reduced initial cost, and enhanced aesthetics. In addition to building new bridges with integral construction, integral bridges can be used to retrofit existing bridges by eliminating the abutment joints in an effort to reduce maintenance costs.

Integral bridge superstructures built in Ontario were constructed of concrete deck-over (i) steel I-girders; (ii) prestressed concrete I-girders; (iii) multiple-box steel girders; and (vi) precast/prestressed box girder [35]. The abutment consists of an abutment wall, wingwall and supporting piles along a line under the abutment. Most of the recently published research on integral bridges has been focused on studying the geotechnical considerations, creep effects and seismic effects on the bridge substructure. A literature search indicates that there are very limited research studies on the design and evaluation of the superstructure of integral bridges. Further, there are no nationally accepted and economical guidelines in the current bridge codes [5, 14] on how to compute the girder dead and live load distribution factors, the dominant flexural frequency and dynamic load allowance for such bridges as opposed to those for conventional girder bridges. Each bridge Department relies on the experience of its engineers and on the results of limited research recently conducted in the development of design criteria. This shortcoming has led contractors to submit bid prices for construction cost higher than necessary.

The most recent state-of-the-art and state-of-practice survey on the use of integral bridges was conducted by Hassiotis and Roman [33]. They summarized the cumulative gain in knowledge through research and experience in integral abutment, the pile supporting the abutment, the connection of the abutment to the superstructure, the soil behind the abutment and the approach slab. They also stated limitations on the use of integral bridges include the uncertainty of flexural stresses in loaded piles and the imposed limits on the span length of the superstructure. However, PCI Subcommittee on Integral Bridges [56] reported future research needs in this area, including (i) establishing design criteria for the superstructure and substructure for the effects of temperature; (ii) identifying span length limitations for integral bridges taking into account the combined effects of actual rotation, translations, skews and horizontal curvature; (iii) determining how these structures should be designed to resist earthquake and determine how they will actually perform during earthquakes (i.e. seismic considerations may require increased abutment stiffness whereas the thermal movements require the abutment to be flexible); and (vi) determining the best type of wingwall to use, how it should be designed and the effect of its length on force distribution and general behaviour. Albendroth et al. [2] emphasized on future research on (i) effect of superstructure skew angle on live load distribution coefficients, as compared to those for the traditional straight girder bridges supported on end isolated bearings; (ii) the effect of superstructure-to-abutment continuity on dynamic load allowance for live load analysis; and (iii) the prediction of the ultimate load-carrying capacity of the entire bridge superstructure under truck loading conditions which is still unavailable.

2.1.1. INTEGRAL BRIDGES AT CONSTRUCTION PHASE

Construction of integral bridges starts with abutments and wingwalls up to bearing seat elevations. Girders are then placed on supports that allow rotation and deflection of girders due to self-weight and dead weight of the deck. The deck and the portion of the abutment above bearings seat elevation are then cast integrally with the girders, producing fixation between the superstructure and the abutment. Finally, backfill is placed simultaneously behind both abutments. The Canadian Highway Bridge Design Code [14] Clause A5.1.14 states that the change in nature of the structural system that occurs during the construction sequence shall be taken into consideration. While Clause 5.5.5.2 states that integral bridges shall meet the requirements for slab-on-girder bridges for the use of the simplified method of structural analysis specified in Chapter 5. For dead load analysis, CHBDC Table 5.12 specifies the simplified method of analysis in Clause 5.6.1.2 for slab-on-girder

bridges with shored construction provided that the skew parameter, $\varepsilon = S \tan \Theta / L$, does not exceed 1/18, where S is the centre-to-centre spacing of longitudinal girders, Θ is the skew angle and L is the bridge span. However, for slab-on-girder bridges built with unshored construction, Clause 5.6.1.1 specifies no limitation on the value of the skew parameter, ε. This clause may not be true in case of braced steel girders in skew alignment. As such, further research is needed to examine the applicability to integral bridges and to develop moment and shear distribution factors for skew non-composite braced steel girders at construction phase before concrete hardening, as well as similar factors for dead load analysis of these girders after achieving the composite action to check for deflection control due to sequence of construction at serviceability limit state (SLS). Few researchers have dealt with the effect of construction sequence on the structural response of traditional girder bridges.

2.1.2 DYNAMIC RESPONSE OF INTEGRAL BRIDGES

CHBDC specifies a unified dynamic load allowance (DLA) for all bridge types. However, it is expected that the DLA will be lower in case of integral bridges. Few researchers dealt with the free-vibration response of skewed bridges (among them: Maleki [46]; Meng and Lui [47]). These studies need to be extended to integral bridges. Siddique et al. [64] conducted 3D finite element modeling for both the superstructure and substructure of an existing integral bridge to simulate the dynamic response of the bridge. The extracted natural frequencies and mode shapes derived from analysis were then used to evaluate the ability of proposed vibration-based damage detection conditions to detect and locate the damage on the bridge. In the conventional design approach (i.e. 2D frame analysis of both the superstructure and substructure), the effect of seismic forces is usually neglected assuming that integral bridges are not prone to such forces because of their continuity. However, earthquake excitations may cause remarkable rotations and settlements at the abutment foundations due to the flexible nature of single-row pile arrangement. Therefore, rigorous analysis may be required to assess the capacity of the structure to resist seismic forces. As such, Dicleli [19] proposed a 3D finite-element modeling for seismic analysis of integral bridge. In this model, 3D beam elements were utilized to model the bridge superstructure, the abutment and each pile in a 3D fashion. Both AASHTO and CHBDC [6, 14] specify general guidelines with respect to structural analysis and design of traditional bridges for earthquake loading but with no explicit guidance with respect to soil-structure interaction for integral bridges. As such, research should be conducted to proportion integral bridges to limit displacement to a certain value

to minimize damage due to earthquake. Hassiotis and Roman [33] recommended further research to develop simplified methods to take into account soil-structure interaction for earthquake loading calculations.

2.2 EXTENDING THE LENGTH LIMIT OF INTEGRAL BRIDGES

In section 2.2.1 the maximum length limits for integral abutment bridges imposed by various transportation agencies are presented and compared. It can be concluded from this section that length limits imposed by Ontario Ministry of Transportation (MTO) for integral abutment bridges are really conservative. Then in section 2.2.2, the method of pile displacement capacity which can be employed to determine the maximum length limitations for non-skewed and skewed integral bridges is explained. In section 2.2.3, due to the fact that the value of horizontal pile and abutment displacements of integral abutment bridge depends on the value of seasonal temperature variation, the pathways to define the temperature variation (maximum and minimum temperature) based on AASHTO, AASHTO LRFD and CHBDC are fully described. Finally, in section 2.2.4, a literature review focusing on past numerical models and field studies regarding temperature effect on integral abutment bridges is presented.

2.2.1 MAXIMUM LENGTH LIMITS IMPOSED BY VARIOUS AGENCIES

At this time, MTO allows integral abutment for a total bridge length less than 150 *m* for both steel and concrete girders with skew angle limitation of 30^o [35]. Nevertheless, as illustrated in Table 2.1, most of Departments of Transportations in United States impose the length limits more than 150 *m* with skew limitation of either 20^o or 30^o. For instance, Tennessee Department of Transportation (DOT) allows concrete integral bridges for a total length less than 358 *m* and the New York department of transportation (DOT) allows steel integral bridges for a total length less than 200 *m* with skew angle limitation of 30^o. Certainly, it is derived that integral abutment length limitations (especially for concrete bridges) imposed by MTO with respect to the length limitations imposed by these transportation agencies are too conservative and rational length limitation for integral bridge with small skew angle is urgently needed.

The maximum length limits of integral abutment bridges with skew angle limitation of 30^o imposed by various transportation agencies in the United States are listed in Table 2.1 for comparison purposes [56].

Table 2.1: Integral abutment bridge length limitation for small skew angles.

State or Province	Steel bridges	Concrete bridges	Skew Angle
Alberta [19]	90 *m* (295 *ft*)	120 *m* (394 *ft*)	20
Colorado [18]	195 *m* (640 *ft*)	241 *m* (790 *ft*)	30
Iowa [45]	122 *m* (400 *ft*)	175 *m* (575 *ft*)	30
Missouri [45]	130 *m* (425 *ft*)	183 *m* (600 *ft*)	30
New York [68]	**200 *m* (650 *ft*)**	200 *m* (650 *ft*)	30
Ontario [35]	150 *m* (492 *ft*)	150 *m* (492 *ft*)	20
South Dakota [45]	107 *m* (350 *ft*)	214 *m* (700 *ft*)	30
Tennessee [18]	152 *m* (500 *ft*)	**358 *m* (800 *ft*)**	30
Vermont [45]	119 *m* (395 *ft*)	210 *m* (695 *ft*)	20

In addition, according to the Table 2.2, Ontario ministry of transportation, MTO, specifies that integral abutment with a skew exceeding 30^{o} should not be considered for integral abutment due to lack of research results for such bridges with large skews [35]. However, as indicated in Table 2.2, many states in United States allow integral abutment bridge to be built with skew angle exceeding 30^{o} and it seems that the existing skew angle limitation in MTO guideline is also conservative. As a result, to improve this deficiency in MTO guideline, research is required to identify the length limitation for integral abutment bridge. Table 2.2 presents some length limitations imposed by different states of United States which allow the engineers to design and build the integral abutment bridges with skew angles exceeding 30^{o}.

Table 2.2: Integral abutment bridge length limitation for large skew angles.

State or Province	Steel bridges	Concrete bridges	Skew Angle
Georgia [45]	79 *m* (259 *ft*)	79 *m* (259 *ft*)	**30-40**
Missouri [45]	130 *m* (425 *ft*)	183 *m* (600 *ft*)	**30-45**
New York [68]	200 *m* (650 *ft*)	200 *m* (650 *ft*)	**30-45**
Ontario [35]	Not Allowed	Not Allowed	**30-45**
South Dakota [45]	107 *m* (350 *ft*)	214 *m* (700 *ft*)	**30-35**
Tennessee [18]	152 *m* (500 *ft*)	358 *m* (800 *ft*)	**30-45**

2.2.2 PILE DISPLACEMENT CAPACITY

Similar to the conventional bridge, an integral bridge experiences length changes due to seasonal temperature variations. Length changes in both bridges type, ΔL, are computed as follow:

$$\Delta L = \alpha L \Delta T \qquad (2.1)$$

Where, α is the coefficient of thermal expansion properties; L is the length between the fixed support and the movable joint or bearing; and ΔT is the difference between the extreme design temperatures and the installation temperature.

Whereas conventional and integral bridges experience similar length changes, they accommodate this length change differently. A conventional bridge has a thermally active bridge superstructure and thermally inactive substructure, while an integral bridge connects this thermally active superstructure to the substructure. Due to thermal variations throughout the integral bridge service life, the abutment-backfill system and the piles supporting the abutments may be subjected to horizontal displacements. When integral bridges expand in length, thermal induced horizontal displacements in the bridge components and the surrounding soil become larger so that steel H-Piles experience larger lateral deformations. This may lead to a reduction in the bridge service life due to reduction of load-carrying capacity of piles affected by lateral displacement. The maximum allowable horizontal displacement of pile without any detrimental effects is referred as the steel H-Piles displacement capacity. In sections 2.2.2.1 and 2.2.2.2 methods of estimation piles displacement capacity for non-skewed and skewed integral bridges have been described in details.

2.2.2.1 NON-SKEWED INTEGRAL BRIDGE

The criterion which is taken into consideration to limit the maximum length is the pile displacement capacity. The seasonal and daily temperature changes result in imposition of horizontal displacements on the continuous bridge deck of integral bridges and on the steel H-piles and prestressed pile supporting the abutments. The magnitude of the temperature-induced displacements in steel H-Piles is a function of the temperature differences and the length of the structure. As the length of integral bridges becomes longer, piles may experience horizontal deformations beyond their elastic limit which may induce the reduction of the integral bridge

service life. The design criteria used by the majority of Departments of Transportation for pile displacement in the United States [4] limit the horizontal movement of a pile with fixed abutment-pile connection at the ground surface to 38 *mm* in each direction. Further, the value of 38 *mm* is suggested by Deatherage et al. [17] as a reasonable allowable horizontal movement of piles with fixed abutment-pile connection based on lateral tests on H-Piles and prestressed piles. The hinged abutment-pile connection compared to fixed abutment-pile connection dramatically increases the displacement capacity of the pile by eliminating damage of the concrete surrounding the pile-head. It was found that the pile's displacement capacity for the hinged case is about 1.2 times of that for the fixed case. Hence, the value of 46 *mm* is recommended for pile displacement capacity with hinged abutment-pile connection. The pile horizontal displacement capacity is demonstrated in Figure 2.1 as y_t.

.

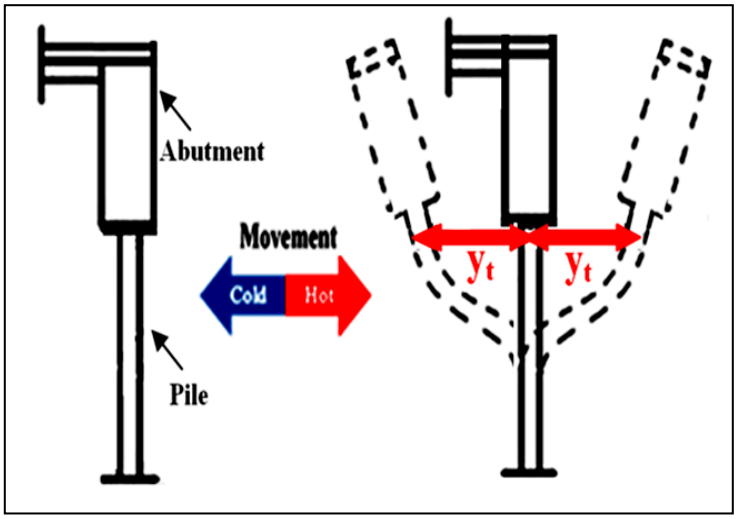

Figure 2.1: H-Pile displacement capacity.

2.2.2.2 SKEWD INTEGRAL BRIDGE

Besides longitudinal displacement under temperature rise and fall, in skewed integral bridge transverse displacement can occur due to horizontal rotation of the slab. Figure 2.2 shows that the active soil pressures exerts a normal forces, P_a, on the back of each abutment due to bridge contraction. These forces induce a counter-clockwise moment, M_a, about Point C. This moment is expressed as:

$$M_a = P_a.tan\Theta.L.cos\Theta = P_a.\mathrm{L}.\sin\Theta \qquad (2.2)$$

Where, Θ is the skew angle of the integral abutment bridge; P_a is the total active backfill soil force acting against the abutment and L is the total bridge length in the direction of traffic.

Also, Figure 2.2 displays that the static friction force between the abutment and the backfill forms a force couple, M_f, about point C to resist the rotation of the slab, which is expressed as:

$$M_f = F_{af}.L.cos\Theta = P_a.tan\delta.L.cos\Theta \quad (2.3)$$

Where, δ is the surface-friction angle of soil and abutment with the value of 22^o to 26^o based on the NCHRP Report No. 343, Manual for the Design of Bridge Foundations [8].

For the plan view of the skewed bridge shown in Figure 2.2, the sum of these moments about the "point-of-fixity" (Point C) of the bridge gives:

$$\Sigma M_c = M_a - M_f = P_a.L.\sin\Theta - P_a.tan\delta.L.cos\Theta \quad (2.4)$$

The bridge rotates when the moment M_a that is induced by the active-soil pressure is larger than the moment M_f that is provided by the soil-frictional force. By setting Equation (2.4) equal to zero, it can be concluded that rotation of skewed integral bridge is occurred when the skew angle, Θ, exceeds surface-friction angle, δ. Using the above mentioned range for the angle δ, transverse displacements of an integral abutment (bridge rotation) need to be considered when the skew angle for an integral-abutment bridge is equal to or greater than 20^o.

.

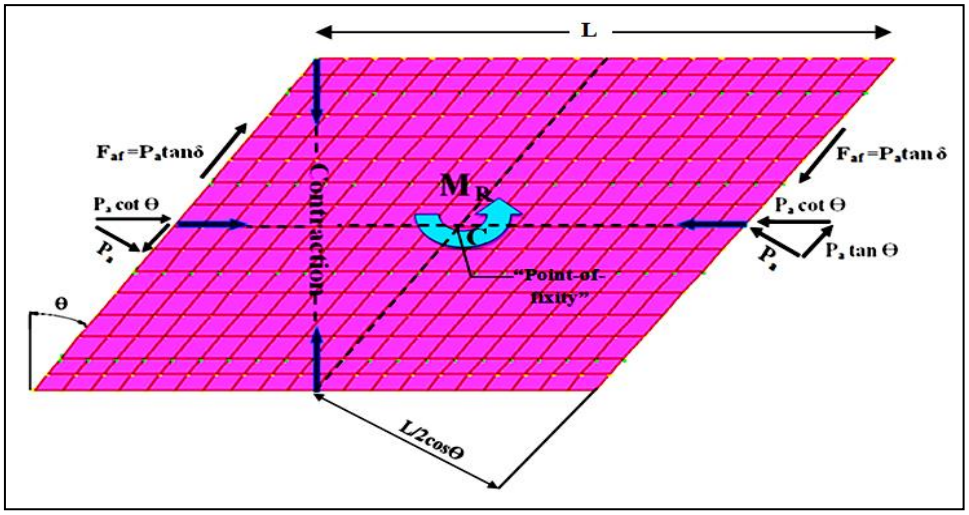

Figure 2.2: Horizontal rotation of the slab during the temperature changes in a skewed bridge.

The criterion to limit the maximum length for skewed integral bridge is the ductility capacity of the abutment piles. Accordingly, the values of pile longitudinal and transverse displacement pile are acceptable when a pile ductility-limit state is satisfied. The displacement-ductility limit state for biaxial bending of an integral abutment pile that was presented by Greimann et al. [28] is re-written here as Equation (2.5):

$$\left(\frac{\Delta_x}{\Delta_{cx}}\right) + \left(\frac{\Delta_y}{\Delta_{cy}}\right) \leq 1 \tag{2.5}$$

With,

$$\Delta_x = (dl)\, sin\Theta - (dt) cos\Theta \tag{2.6}$$

$$\Delta_y = (dl)\, cos\Theta + (dt) sin\Theta \tag{2.7}$$

Where, dl and dt are the distances of Point A to Point A' along the longitudinal and transverse directions which has been shown in Figure 2.3; Δ_x and Δ_y are total displacements components in the x-axis and y-axis directions for a pile and Θ is the skew angle of the integral abutment bridge. The Δ_{cx} and Δ_{cy} are the displacement capacities of fixed and hinge piles which as it explained before are considered 38 and 46 *mm*, respectively.

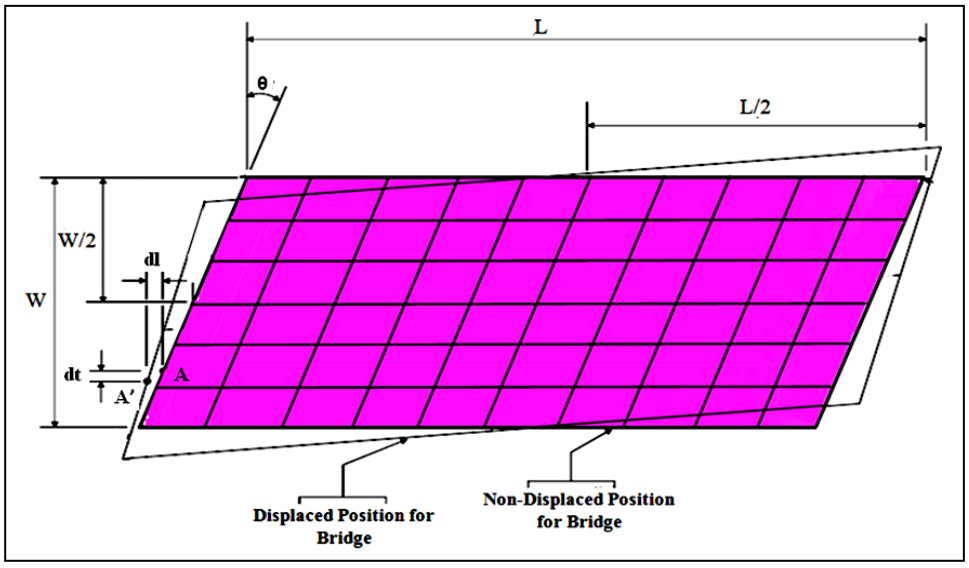

Figure 2.3: Longitudinal displacement and transverse displacement of a skewed integral bridge.

It is important to mention that steel's thermal coefficient ($\alpha_{Steel} = 1.17\times10^{-5}\ 1/^{o}C$) is larger than concrete's thermal coefficient ($\alpha_{Concrete} = 0.99\times10^{-5}\ 1/^{o}C$) and larger thermal coefficient based on Equation (2.1) causes larger length change and pile displacement in steel bridge compared to concrete bridge. As a result, with consideration of horizontal pile displacement capacity for integral abutment bridges, shorter length limit for steel bridges is expected in comparison with concrete bridges.

2.2.3 TEMPERATURE VARIATION IN INTEGRAL BRIDGES

As denoted previously, the maximum allowable length for integral bridge is based on horizontal displacement of piles. The magnitude of these horizontal displacements based on Equation (2.1) is a function of the level and values of thermal variation [1]. There are two temperature effects that cause forces in an integral abutment bridge namely: a uniform temperature range applied to the entire structure and temperature gradient in the girder [22, 43, 50, 51, 55, 59, 60]. A change in the average bridge temperature (uniform temperature) induces a change in the length of a bridge. Also, the bridge will experience a curvature in the vertical plane when the temperature through the depth of a bridge superstructure is not constant (temperature gradient). In sections 2.2.3.1 and 2.2.3.2, average bridge temperature and vertical-temperature based on AASHTO, AASHTO LRFD and CHDBC are completely described and compared.

2.2.3.1 AVERAGE (EFFECTIVE) BRIDGE TEMPERATURE

In United States, AASHTO and AASHTO LRFD state that provisions should be made for stresses or movements resulting from variations in temperature. The rise and fall in temperature shall be fixed for the locality in which the structure is constructed and shall be computed from an assumed temperature at the time of erection. The rise and fall in temperature are given by the following equations:

$$\Delta T_{Rise} = T_{AvgMax} - T_{Install} \quad (2.8)$$

$$\Delta T_{Fall} = T_{AvgMin} - T_{Install} \quad (2.9)$$

Where, $T_{Install}$ is the installation temperature; and T_{AvgMax} and T_{AvgMin} are the maximum and minimum extreme average bridge temperatures expected in the life of the bridge [59]. AASHTO

and AASHTO LRFD [5, 6] Clause 3.12.2 divide the United States into cold and mild climate zones and guidance is provided as to which regions fall into these zones. Table 2.3 listed the maximum and minimum temperature defined for bridges in AASHTO and AASHTO LRFD.

Table 2.3: Maximum and minimum effective temperature [5, 6].

Girder Type	**Steel**		**Concrete**	
	Mild	Cold	Mild	Cold
Minimum Temperature	-18°*C* (0°*F*)	-34°*C* (30°*F*)	-12°*C* (10°*F*)	-18°*C* (0°*F*)
Maximum Temperature	49°*C* (120°*F*)	49°*C* (120°*F*)	27°*C* (80°F)	27°*C*(80°F)

In Canada, CHBDC [14] specifies that different temperature variation shall be considered for different types of superstructures. Minimum average temperatures used for steel and concrete bridges are considered as of 10°*C* (18°*F*) and 5°*C* (9°*F*), respectively below the minimum daily mean temperature. On the other hand, maximum average temperature for steel and concrete are considered as 20°*C* (36°*F*) and 10°*C* (18°*F*) above the maximum daily mean temperature, respectively. In the absence of site specific data, an effective construction temperature of 15°*C* (27°*F*) is specified for steel and concrete bridges. The maximum and minimum daily mean temperatures are taken from the given maps in CHBDC Clause A3.1.1. Table 2.4 shows maximum and minimum temperature design of four large cities in Canada adapted from CHBDC [14].

Table 2.4: Maximum and minimum effective temperature for big cities in Canada [14].

City	**Minimum Temperature**		**Maximum Temperature**	
	Steel	Concrete	Steel	Concrete
Toronto	-33°*C* (-27°*F*)	-23°*C* (-9°*F*)	50°*C* (122°*F*)	40°*C* (104°*F*)
Vancouver	-19°*C* (-2°*F*)	-14°*C* (7°*F*)	44°*C* (111°*F*)	34°*C* (93°*F*)
Ottawa	-39°*C* (-38°*F*)	-24°*C* (-11°*F*)	51°*C* (124°*F*)	41°*C* (106°*F*)
Montreal	-39°*C* (-38°*F*)	-24°*C* (-11°*F*)	50°*C* (122°*F*)	40°*C* (104°*F*)

2.2.3.2 VERTICAL TEMPERATURE GRADIENT

In addition to uniform temperature, the bridge experiences temperature gradient through the depth of the superstructure. The upper elements and the exterior beams vary in temperature depending upon the amount of solar radiation received, the wind and the amount and type of perception. The bottom elements of a bridge ordinarily have the same temperature as that of the air. Accordingly, the top of the deck slab has higher temperature than the bottom of the bridge when the sun shines on the exposed decks and the top will cool faster than the girders when exposed to rain or snow. A vertical-temperature gradient within an integral bridge can induce bending stresses in the bridge members and abutment rotations in a vertical plane that is parallel to the length of the bridge. In this study, to achieve a precise modeling of temperature loading, the effect of temperature gradient on integral bridge is brought into consideration.

In United States, AASHTO LRFD [5] recommended positive temperature gradient through the depth of the concrete deck slab and girder. AASHTO LRFD temperature gradient is based on a model proposed in NCHRP Report 276, which was based on work initially done by Potgieter and Gamble [55]. Negative temperature gradients are obtained by multiplying the positive gradient by -0.3 for a concrete wearing surface. The standard temperature gradient from Figure 3.12.3-2 in the AASHTO LRFD is shown in Figure 2.4(a). In Canada, CHBDC Clause 3.9.4.4 [13] suggested positive linear temperature differential of 15°*C* (27°*F*), through the concrete deck slab, ignoring that for the girder. The temperature shall be assumed to remain constant throughout the girder below the slab. CHBDC [14] ignores negative temperature gradient. The CHBDC standard temperature gradient through the girder is illustrated in Figure 2.4(b).

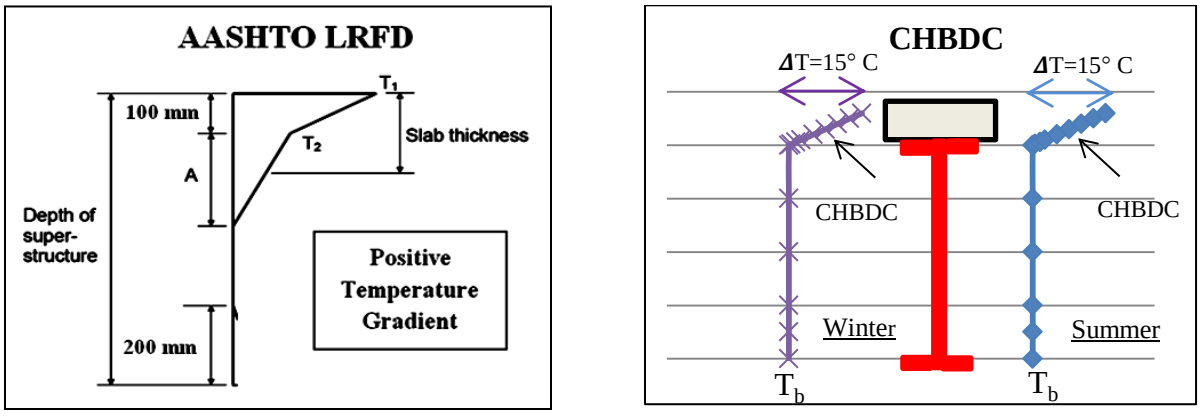

(a) (b)

Figure 2.4: Code vertical temperature gradients (a) AASHTO LRFD [5], (b) CHBDC [14].

2.2.4 PREVIOUS ANALYTICAL AND EXPERIMENTAL STUDIES PERTAINED TO INTEGRAL BRIDGE LENGTH LIMITATIONS

Previous experimental and analytical studies investigated many aspects of integral bridges. Due to the fact that integral bridge length limitations are based on temperature variation, recent publications discussing about temperature effects on integral bridges have been more elaborated.

2.2.4.1 REVIEW OF PREVIOUS ANAYLITICAL STUDIES

Regarding numerical modeling of integral abutment structures, different models have been developed to explore bridge behaviour. Jorgenson [38] proposed a 2D linear frame model. The soil was simulated as linear springs; the soil-structure interaction between backfill and abutment was neglected. Girton, et al. [27] improved the 2D frame model of Jorgenson. The refined model was developed to predict the longitudinal displacements of pile that are induced by longitudinal movements of an abutment. Faraji et al. [24] built a 3D model using beam-column and shell elements to model the girders, deck, abutments and piles. In this 3D model, the abutment backfill interaction was represented by resistance-displacement curves. Hassiotis and Khodair [32] studied the soil-structure interaction of the soil-pile system of the integral abutment bridge to determine thermal stresses in the piles due to temperature. A displacement and rotation boundary condition was imposed as a load case by applying a displacement of 23 *mm*. This displacement corresponded to a temperature increase of 59°C.

2.2.4.2 REVIEW OF PREVIOUS EXPERIMENTAL STUDIES

Over the past 30 years, several integral abutment bridges have been instrumented and monitored. Bonczar et al. [10] conducted a field study in Massachussets on the 82.3 *m* three-span straight integral bridge with steel plate girders to investigate changes in bridge length and abutment movement. The change in total pile deformation from readings in the month of August to the readings in the month of March was reported as 14 *mm*. The south and north abutment moved inward 12.8 and 9.1 *mm*, respectively. Girton et al. [27] instrumented the integral bridge in Iowa several years after its construction to measure air and bridge temperature, bridge longitudinal movement and abutment pile strains. The integral bridge spanned 99 *m* with four spans of prestressed girders at a skew of 45^{o}. Girton et al. [27] reported that predrilling abutment pile holes and orienting abutment piles were valuable to ensure a flexible substructure.

Frosch et al. [25] investigated abutment-pile interaction of integral abutment and jointless bridges by instrumenting four bridges in Indiana. By means of strain gauges, tiltmeters and convergence meters, they concluded that the field translation is slightly smaller than theoretically computed, but the computed value can be used as a conservative estimate.

Laman and Kim [44] instrumented a four-span, 128 *m* long integral abutment bridge in Pennsylvania to investigate the effects of seasonal expansion and contraction. The bridge was monitored with strain gauges, joint meters, tiltmeters, earth pressure cells and temperature gauges. Measured translations along the centerline agreed with calculated translations, but unexpected abutment rotation also occurred.

Abendroth and Greimann [1] instrumented and monitored an integral abutment bridge in Iowa. The bridge was 97-*m* long with a 30^{o} skew, and the abutments were supported by a single row of piles oriented with their webs parallel to the abutment face. They reported maximum longitudinal displacements of about 30 *mm* after two years of monitoring. During the two year monitoring period, maximum rotations of about 0.1^{o} (corresponding to maximum longitudinal expansion in the month July) was recorded.

2.2.4.3 SUMMARY COMMENTS

In the above mentioned research, progress has been made in several areas. First, advanced nonlinear modeling, considering soil-structure interaction, has been developed for numerical simulation. Second, the monitoring of integral abutment bridges has led to a deeper understanding of the bridge behaviour, especially regarding the effects of thermal changes on bridge length, pile strains, skew effects and backfill soil pressure. Third, advances have been made in design, which have been used by some states, including plastic methods of design for piles under lateral loads and specifying the use of predrilled holes around piles. However, effects of some key design variables (i.e., Abutment height and thickness; bridge length and depth; pile type and orientation; number of design lanes and skew angle) are still not fully understood. To minimize those uncertainties, a deeper understanding of bridge behaviour is needed. Therefore, in this study, the numerical modeling and parametric study were conducted to expand the results to general cases under different variables and to develop a rational basis for expanding the length limitations of integral abutment bridges in Ontario.

2.3 DEVELOPING LOAD DISTRIBUTION FACTORS FOR GIRDERS

In section 2.3.1, the concept of live load distribution factor is completely explained. From this section, it can be concluded that the design moments obtained from simplified two-dimensional (2D) bridge models are required to be multiplied by the live load distribution factor in order to consider the accurate structural response of the bridge. In section 2.3.2, different methodologies which are implemented in practice to arrive at the live load distribution factors are compared. The live load distribution equations (LLDEs) defined in different methodologies and bridge design codes are only valid for conventional bridges. Accordingly, using the LLDEs in bridge design codes for the design of integral abutment bridge girders result in incorrect estimates of live load effects. In section 2.3.3, previous research work pertained to live load distribution in integral bridges are described. In this section, it is noticed that there are very limited research studies available on determination of live load distribution in integral abutment bridge. As a result, a comprehensive research is necessary to be performed on this topic as well.

2.3.1 CONCEPT OF LATERAL LOAD DISTRIBUTION FACTOR

In the analysis and design of a bridge, the calculation of structural response of a bridge to live loads is complicated and lengthy. The design values for bending moment and shear force for I-girders depend on the location and the number of moving trucks on the bridge, boundary conditions and the cross-section properties of the bridge components. These values vary with the change in girder span, width of bridge, number of girders and load cases.

In order to calculate the live load carried by each girder in case of a straight bridge, lateral load distribution factor is a key element and important in analyzing existing bridges and designing new ones. To simplify the design process, North American bridge codes, such as CAN/CSA-S6-06 [14], AASHTO-LRFD bridge design specifications [3, 4, 5] and the superseded AASHTO standard specifications [6], treat the longitudinal and transverse effects of wheel loads as uncoupled phenomena. Based on these codes, to obtain the design moment and shear force, first the maximum moment and shear force caused by a single truck live load using a single interior girder are calculated. Then, those values are multiplied by a magnification factor, which is usually referred as live load distribution factor. Since one girder may carry truck load more than

average load per girders, this is attributed to the different position of locating trucks in design lanes of bridge cross-section.

2.3.2 REVIEW OF DIFFERENT METHODOLOGIES ON DISTRIBUTION FACTORS

A number of methods with different degree of sophistication such as orthotropic plate analogy, grid work model, lever rule, hinged joint, fixed joint, AASHTO standard, AASHTO LRFD and CHBDC simplified method have been used over the years to achieve the live load distribution factors for conventional bridges. In section 2.3.2, these commonly known methodologies on live load distribution factors are presented. It should be mentioned that these different methodologies were developed for traditional bridges where superstructure is separated from substructure. However, in the case of integral bridges, the monolithic construction of the superstructure and substructure causes that superstructure and substructure act together under live load effects. The continuity of the superstructure-substructure in integral abutment bridges is found to improve the distribution of live load shear and moment among the girders.

2.3.2.1 ORTHOTROPIC PLATE ANALOGY

In 1979, Bakht et al. [7] used the concept of orthotropic plane to develop a simplified method for calculating the design live load longitudinal moments as illustrated in Figure 2.5.

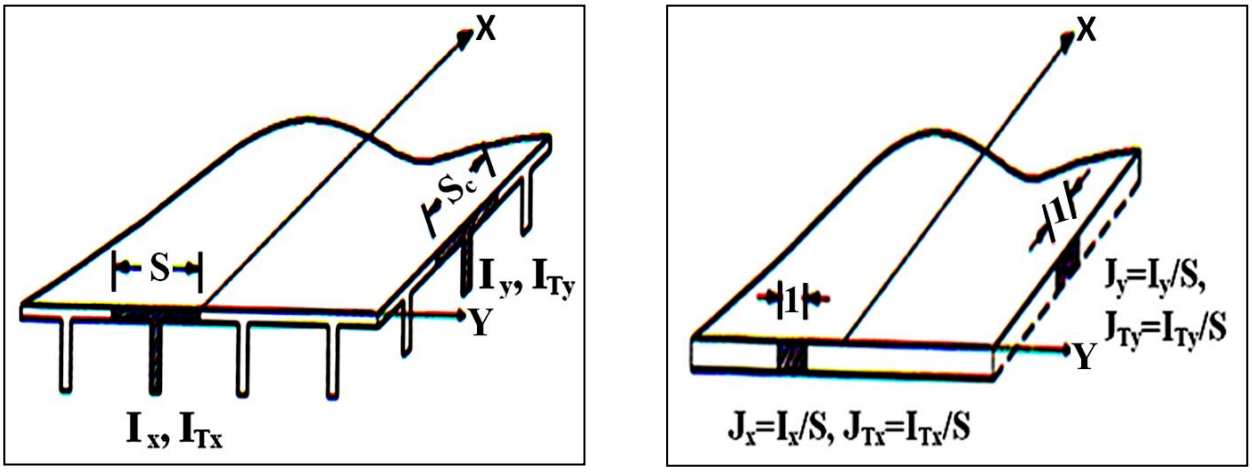

(a) (b)

Figure 2.5: Real structure and orthotropic plate analogy (a) Real Structure, (b) Equivalent Orthotropic Plate.

In their research, extensive parametric studies have been conducted which led them to find out that distribution factors of bridges are related to a torsional parameter, $\alpha_{torsional}$, and a flexural parameter, $\theta_{flexural}$, which are functions of geometry and material properties of the bridge. These parameters are given by following equations:

$$\alpha_{torsional} = \frac{D_{xy} + D_{yx} + D_1 + D_2}{2(D_x D_y)^{0.5}} \tag{2.10}$$

$$\theta_{flexural} = \frac{b}{2L}\left(\frac{D_x}{D_y}\right)^{0.25} \tag{2.11}$$

Where b is the bridge width, L is the span length of the bridge and the various rigidities are given by:

$$D_x = \frac{E_G I_G}{S} + \frac{E_c t^3}{12} \tag{2.12}$$

$$D_y = \frac{E_c t^3}{12(1 - v_c{}^2)} \tag{2.13}$$

$$D_{xy} = \frac{G_G J_G}{S} + \frac{G_c t^3}{6} \tag{2.14}$$

$$D_{yx} = \frac{G_c t^3}{6} \tag{2.15}$$

$$D_1 = D_2 = v_c D_y \tag{2.16}$$

Where E_c is the Young's modulus, G_c is the shear modulus, v_c is the Poisson's ratio, t is the slab thickness, S is the girder spacing, I_G is the flexural moment of inertia and J_G is torsional moment of inertia of the girder section. The subscript G refers to girder and c refers to the concrete slab. This method gives better results than AAAHTO recommendations that assume the girder spacing S is the only parameter that affects load distribution in slab-on-girder bridges. This method formed the basis of the 1991 version of the OHBDC as well as the CHBDC provisions.

2.3.2.2 GRID WORK MODEL

This method is opposite to orthotropic plate analogy in the sense that in this case the deck structure is represented by a grid work of longitudinal and transverse members rigidly interconnected at the intersection points, see Figure 2.6.

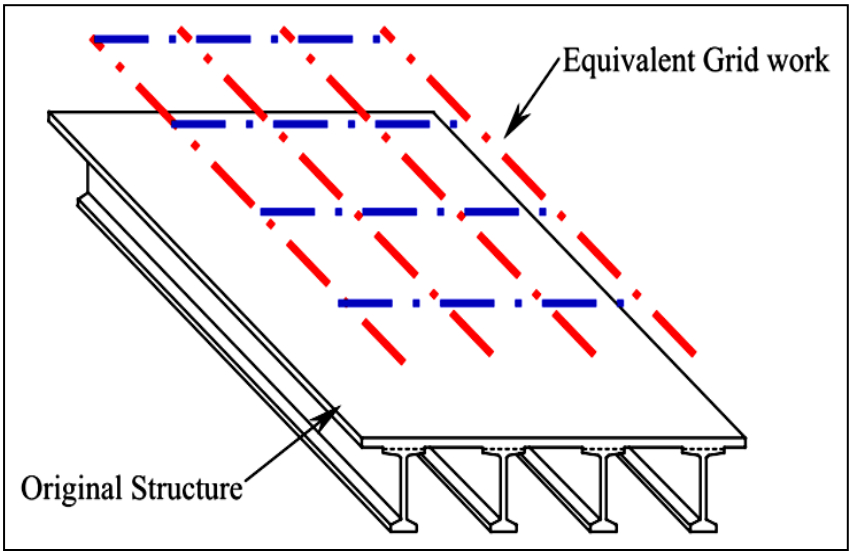

Figure 2.6: Grid work model of bridge deck system [41].

The section properties of the grid members are approximate equivalent of the girders and transverse beams and deck slab by assuming imaginary cuts in the deck slab between the girders and the transverse beams. Numbers of analytical methods as well as computer-based tools are available to analyze such grid work.

In 1982, Jaeger and Bakht [37] used the grillage analogy method for the idealization of slab and beam bridges. In grillage analogy method, the longitudinal members were positioned to coincide with the actual girder centerlines and were given the properties of the composite section. The transverse members were considered as beams replacing the strips of the top slab. The moment of inertia, I_y, of the transverse beam is considered as follows:

$$I_y = \frac{L_x t^3}{12} I_x \tag{2.17}$$

And the torsional inertia, J_x, is given by the relationship:

$$J_x = \frac{E_c}{G_c} I_y = \left(\frac{E_c}{G_c}\right)\left(\frac{L_x t^3}{12}\right) \tag{2.18}$$

Where, L_x is the length of the strip in the longitudinal direction, t is the thickness of the strip, E_c is the Young's modulus and G_c is the concrete shear modulus.

2.3.2.3 LEVER RULE METHOD

The lever rule is one of the most frequently used methods for calculation of distribution factors. In this method the deck between the girders is assumed to acts as a simply supported beam or cantilever beam, as shown in Figure 2.7.

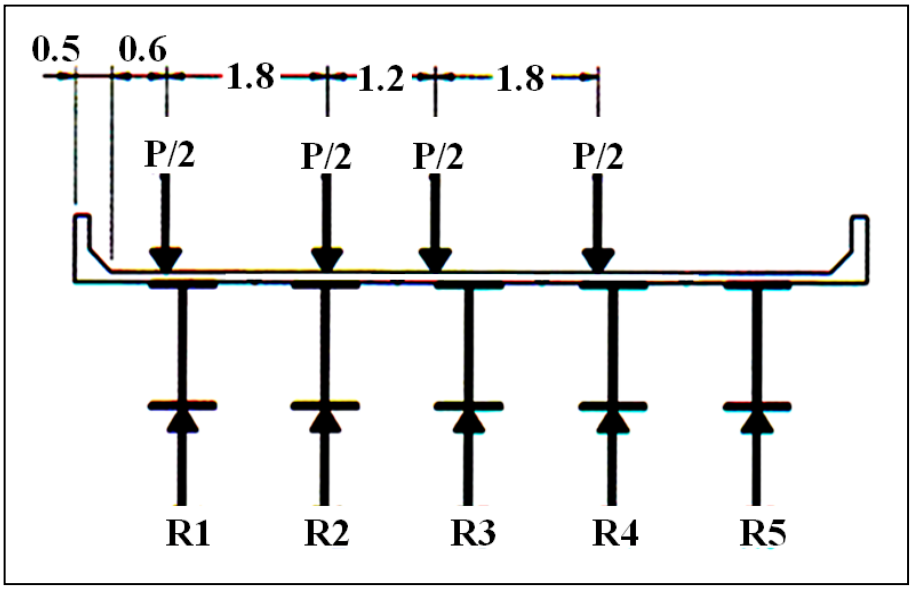

Figure 2.7: Free body diagram of lever rule method.

In this case, the load on each girder shall be taken as the reaction of the wheel loads. Lever rule is very accurate for two girder bridges. Lever rule can also be used for shear distribution near support, since the load would pass to the pier or abutment mostly through the adjacent two girders. Lever rule can also give very good results when the bridge transverse stiffness is relatively flexible. However, the results usually would be slightly conservative for interior girders and unconservative for exterior girders.

2.3.2.4 HINGED JOINT METHOD

The hinged joint method also can be used for small span concrete girder bridges without intermediate diaphragms. Figure 2.8 demonstrates the free body diagram of unit length section at bridge middle span of the hinged girder bridge under unit sinusoidal load.

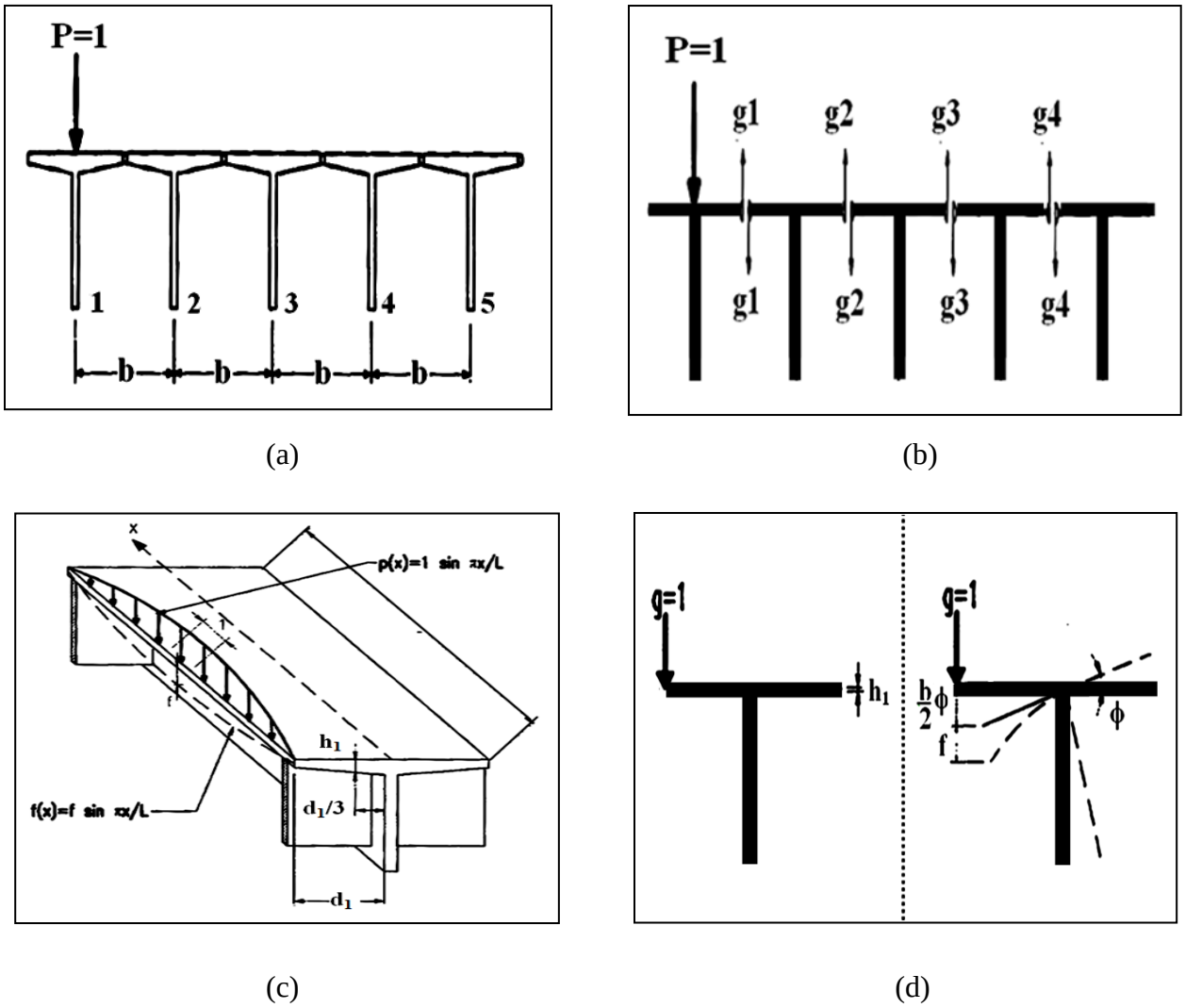

Figure 2.8: Free body diagram for hinged girder bridge.

When the cantilever length is within 0.8 *m* and the span length is greater than 10 *m*, the tables for calculating transverse influence line values for hinged slab bridges can also be used for hinged girder bridges. For better accuracy, detailed calculation is required for bridges beyond this range.

2.3.2.5 FIXED JOINT GIRDER METHOD

In case when the lateral connection between girders is stiffer, the joint can be considered as a fixed joint. In addition to shear force at the joint, moment also must be considered, as shown in Figure 2.9.

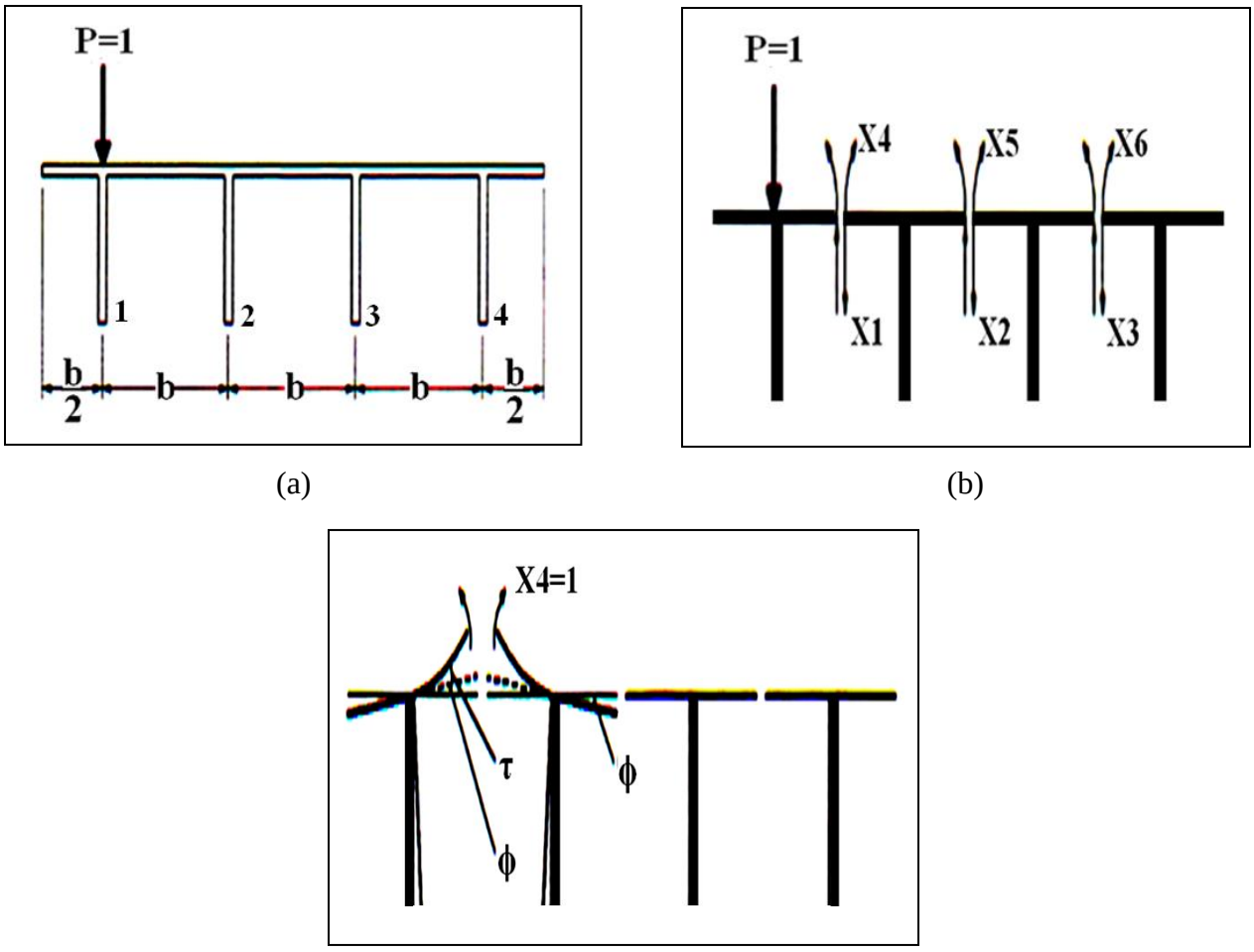

Figure 2.9: Free body diagram of fixed joint girder bridge [39].

For *n*-girder bridge, a 2(*n*-1) order of intermediate problem is to be solved to obtain the shear and moment at each joint. However, only shearing force g_i is known, the same procedure as in

hinged joint method can be followed to obtain the transverse influence line as well as the distribution factors.

2.3.2.6 AASHTO STANDARD METHOD

In United States, AASHTO standard specifications for highway bridges contain live load distribution factors for traditional bridge since 1931. The early values were based on the work done by Newmark [51], but the factors were modified as new research results became available. The superseded AASHTO standard specifications [6] adopted the simplified formulas for distribution factors based on the work done by Newmark. For a bridge constructed with a concrete deck on girders which carries two or more lanes of traffic, the AASHTO distribution factor was *S*/5.5 or in the format of (S/D), where *S* is the girder spacing in feet and D is constant based on the bridge type to obtain the moment in an individual girder. This factor, multiplied by the moment on a single girder, caused by one line of wheels, gives the girder design moment [9]. It was proved that formula would be accurate when girder spacing is near 1.8 *m* (6 *ft*) and span length is approximately 18 *m* (60 *ft*). For relatively medium or long bridges, these formulas would lose accuracy [69].

2.3.2.7 AASHTO LRFD METHOD

AASHTO LRFD (Load and Resistance Factor Design) specifications [3, 4, 5] introduced other formulas to calculate load distribution factors under the National Cooperation Highway Research Program (NCHRP) 12-26. This guide recommends the use of simplified formulas, simplified computer analysis and detailed finite element analysis (FEA) in calculating the actual distribution of loads in highway bridges. It was noted that those formulas were generally more complicated than those recommended by Standard Specifications for Highway Bridge [6], but their use is associated with a greater degree of accuracy. For example the lateral load distribution factor for bending moment in interior girders of concrete slab-on-steel girder bridge superstructure is:

$$g = 0.15 + (\frac{S}{3})^{0.6} + (\frac{S}{L})^{0.2}(\frac{K_g}{12Lt_s{}^{0.1}})^{0.1} \quad (2.19)$$

Where g is the wheel load distribution factor, S is the girder spacing in feet (3.5 *ft* ≤ S ≤ 16 *ft*), L is the span length of the beam in feet (20 *ft* ≤ L ≤ 200 *ft*), t_s is the concrete slab thickness in inches (4.5 *in.* ≤ t ≤ 8 *in.*), K_g is the longitudinal stiffness parameter = $n(I + Ae_g^2)$, where n is modular ratio between beam and deck material, I is the moment inertia of beam ($in.^4$), A is the cross-sectional area of beam ($in.^4$) and e_g is the distance between the center of gravity of the basic beam and deck (*in.*).

AASHTO LRFD specifications have become highly attractive for bridge engineers because of its permitting the better and more economical use of material. More parameters, such as girder spacing, bridge length, slab thickness, girder longitudinal stiffness and skew effect are considered in the developed formulas which earned them second accuracy. The AASHTO-LRFD formulas were evaluated by Shahawy and Huang [63]. Their evaluation showed a good agreement with test results for bridges with two or more loaded design lanes, provided that girder spacing and overhang deck did not exceed 2.4 *m* and 0.9 *m*, respectively. Outside of these ranges, the error could be as up to 30%. For one loaded design lane, the relative error was less than 10% for interior girders and could be as high as 100% and as low as -30% for exterior girders. Shahawy and Huang presented modification factors for the AASHTO LRFD formulas and the results of the modified formulas showed good agreement with their test.

2.3.2.8 CANADIAN HIGHWAY BRIDGE DESIGN CODE

In Canada, CHBDC [14] specifies equations for the simplified method of analysis to define the longitudinal bending moments and vertical shear in slab-on-girder bridges due to live load for ultimate, serviceability and fatigue limit states (ULS, SLS and FLS) using load distribution factors. The Simplified Method of Analysis specified in Clause 5.7.1 of the current CHBDC allows a bridge to be treated as a beam for live load analysis. Live load analysis requires determining the longitudinal bending moments as well as the longitudinal vertical shears due to live loads, as specified in Clause 5.7.1.2 and 5.7.1.4. This methods, requires determining the applicable loadings on the structure. CHBDC Clause 3.8 specifies live loading as the CL-W loading (truck loading) and lane loading. The CHBDC distribution factor equations for slab-on-girders are defined as follows:

The longitudinal bending moment per girder, M_g, can be defined for ultimate and serviceability limit states as:

$$M_g = F_m M_{gavg} \tag{2.20}$$

Where, M_{gavg} is the average moment per girder, and F_m is an amplification factor for the transverse variation in maximum longitudinal moment intensity (Distribution Factor).

$$M_{gavg} = \frac{nM_T R_L}{N} \tag{2.21}$$

$$F_m = \frac{SN}{F(1 + \frac{\mu c_f}{100})} \geq 1.05 \tag{2.22}$$

$$\mu = \frac{W_e - 3.3}{o.6} \; but \leq 1.0 \tag{2.23}$$

While the longitudinal bending moment per girder at fatigue limit state can be obtained by Equation (2.20), average moment per girder and amplification factor for fatigue limit state should be calculated by the following equations:

$$M_{gavg} = \frac{M_T}{N} \tag{2.24}$$

$$F_m = \frac{SN}{F(1 + \frac{\mu c_f}{100} + \frac{C_e}{100})} \geq 1.05 \tag{2.25}$$

Where, M_T is the maximum moment per design lane, n is the number of design lanes, R_L is modification, S is center-to-center girder spacing in meters, N is the number of girders, F is a width dimension that characterizes load distribution for a bridge, W_e is the width of a design lane in meter, C_f is a correction factor in %; obtained from tables in CHBDC and C_e is a correction factor for vehicle edge distance obtained from tables.

The governing live load shears for ULS and SLS are determined by the method outlined in Clause 5.7.1.4.1.2. For the longitudinal vertical shear per girder, V_g, for ultimate, serviceability and fatigue limit states can be defined as:

$$V_g = F_v V_{gavg} \tag{2.26}$$

Where, V_{gavg} is the average shear per girder and F_v is an amplification factor for the transverse variation in maximum longitudinal vertical shear intensity (distribution factor).

$$V_{gavg} = \frac{nV_T R_L}{N} \tag{2.27}$$

$$F_v = \frac{SN}{F} \geq 1.05 \tag{2.28}$$

Where, V_T is the maximum shear per design lane, n is the number of design lanes, R_L is modification, *S* is center-to-center girder spacing in meters, *N* is the number of girders and *F* is a width dimension that characterizes load distribution for a bridge and can be obtained from tables in CHBDC.

CHBDC Clause 5.5.5.2 states that integral bridges shall meet the requirements for the traditional girder bridges. However, as integral bridges eliminate the expansion joints at the abutments, the effect of structural continuity needs to be taken into account. Also, for live load analysis, CHBDC Clause 5.7.1 specifies the simplified method of live load analysis in Chapter 5 for slab-on-girder bridges for the calculating longitudinal moment and shears. However, CHBDC Clause A5.1.3.1.2.2 states that for integral abutment bridges, the simplified method of analysis for longitudinal moment may be used in the absence of a more refined method so it recommends the designer to consider a more rigorous analysis to account the skew effects. All the above CHBDC clauses need to be revised for integral bridges, given the level of fixity between the superstructure and the abutments.

2.3.3 PREVIOUS ANALYTICAL AND EXPERIMENTAL STUDIES PERTAINED TO LIVE LOAD DISTRIBUTION FACTORS

2.3.3.1 REVIEW OF PREVIOUS ANAYLITICAL STUDIES

The first attempt to estimate the shear and negative moment distribution of two selected single-span composite concrete and steel I-girder integral bridges subjected to AASHTO truck loading using the 3-D finite element modeling was conducted by Tabsh and Mourad [66]. The results showed that AASHTO girder distribution factors for flexure and shear were much higher than those obtained from the finite-element analysis. The comparison of the analyses results revealed that live load distribution factors (LLDFs) for girder moments and exterior girder shear of integral abutment bridges are generally smaller than those calculated for simply supported bridges (SSBs) using AASHTO formulas especially for short spans [21]. Along with previous research study, Knickerbocker and Basu [41] conducted the 3-D FE analysis of a two-span jointless high performance concrete (HPC) bridge built in United States with precast bulb-tee girders to study live load distribution factors under AASHTO truck loading. It was found that the load distribution factors calculated using AASHTO specifications as well as the lever-rule method were not consistent with the values obtained by actual load tests and the finite element analysis.

2.3.3.2 REVIEW OF PREVIOUS EXPERIMENTAL STUDIES

The first static live load tests with trucks on integral bridges were conducted by Huang et al. [34]. The live-load tests were conducted with Minnesota Department of Transportation sand trucks placed at 23 different positions across the bridge #55555 in Rochester, MN. The bridge was 66 *m* long with three spans of four MnDOT Type 45M prestressed concrete bridge girders spaced at 3.4 *m* on center across the width of the bridge. The bridge was instrumented with sets of three concrete embedment gauges and three convergence meters gauges placed through the girder depth to measure the moments. The live-load tests were conducted statically because the vibrating wire gauges, used to instrument the bridge, required a few seconds to stabilize. It took a total of 4 hours for the loads to be positioned at the various locations across the bridge. Data from the static live load tests indicated that the bridge behaved as a series of individual spans. The center span behavior was very similar to a simple span. The end span behaviour fell between

a simple span model and a fixed-pinned model indicating the abutment substructure provided some rotational restraint to the end-span girders.

Hartt et al. [31] conducted a live load testing on Nash Stream Bridge, ME. The two fully loaded Maine Department of Transportation (MaineDOT) dump trucks were used for live loading. Thirteen loading positions were chosen to magnify the difference in integral bridge responses. Each position was held for nine minutes, allowing for three sets of data to be taken for each loading. The maximum stress in a pile from the live load test was -41.2 *MPa* (-6.0 *ksi*) that was 28% of the dead load stress. This stress occurred when the total live load of 572 *kN* (128 *kips*) was at an obtuse corner. In addition, it was found that skew of the abutments affected the distribution of axial loadings to the piles as a result of the difference in tributary area of deck for a given pile.

A short-span integral abutment bridge located in New York State was instrumented by Gangone et al. [26] with a wireless sensor system measuring acceleration and strain to monitor the behaviour of the structure under various loading conditions including ambient, environmental and traffic loading. Acceleration measurements were used to extract the superstructure's first five natural frequencies and corresponding mode shapes. Experimental results were compared to a developed finite element method (FEM) model based on the bridge as built drawings.

2.3.3.3 SUMMARY COMMENTS

All over again, it can be denoted from the above-mentioned researches that analytical study on the effect of live load on integral abutment bridge is scarce and limited to maximum two or three studies. It is also noticeable that experimental study on load distribution is yet unavailable. The sensitivity of girder distribution factors to change in superstructure and substructure geometry (i.e., girder spacing, abutment height, bridge length pile size, pile orientation, wingwall length and wingwall orientation) has not been evaluated. In addition, finite element analysis results of girder distribution factors for integral bridges with those obtained for traditional bridges supported on bearing have not been compared. Thus, a parametric study was needed to be performed to achieve the results of the numerical models under different variables and to develop new empirical equations for girder distributions of integral bridges.

CHAPTER 3: FINITE ELEMENT MODELING

This chapter discusses the 3-D and 2-D finite-element models that were developed for different bridge prototypes using the SAP2000 computer software [61]. The finite element model consisted of the superstructure and the substructure. The superstructure included girders, deck and diaphragms, while the substructure included the piles, abutments and wingwalls.

3.1 GENERAL

The finite element method is considered as the most powerful and versatile method of analysis available nowadays. Because of the recent development in finite element method and the large capacities of high speed computers, it is possible to model a bridge in a very realistic manner and to provide a full description of its structural response due to different loading. The finite element analysis software SAP2000 was used throughout this study to determine the structural behaviour of integral bridges. This software is a structural analysis program that uses the finite element method and has a range of capabilities depending on the version used. Widespread use across many countries during 1980s and 1990s made this software a popular choice for finite element analysis. It is capable of analyzing structures in static and dynamic modes using the different type of elements that are available in the program:

- Frame element: The frame element is a two-node three-dimensional element, which includes the effect of biaxial bending, tension, axial deformation and biaxial shear deformation.

- Shell element: The shell element is a four-node dimensional element, which combines separate membrane and plate behaviour. The four-node shell element has six degrees of freedom at each node that are three displacements (U_1, U_2, U_3) and three rotations (ϕ_1 ϕ_2 ϕ_3). A detailed diagram of the shell element is presented in Figure 3.1. The membrane behaviour includes translational in-plane stiffness components and rotational stiffness component in the direction normal to plane of the element. The plate bending behaviour includes two-way, out of plane, plate rotational stiffness component in the direction normal to the plane of the element. The program allows using pure membrane, pure plate or full shell behaviour.

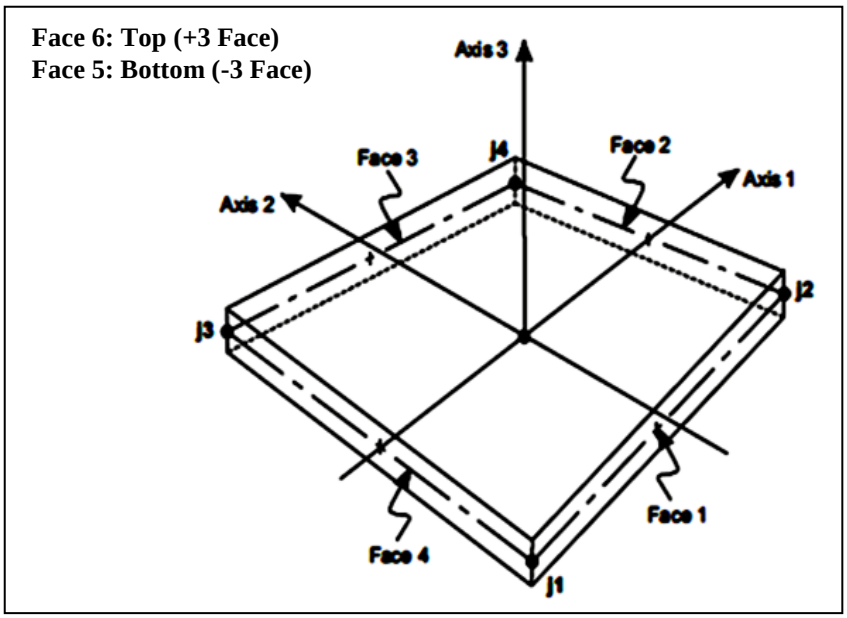

(a)

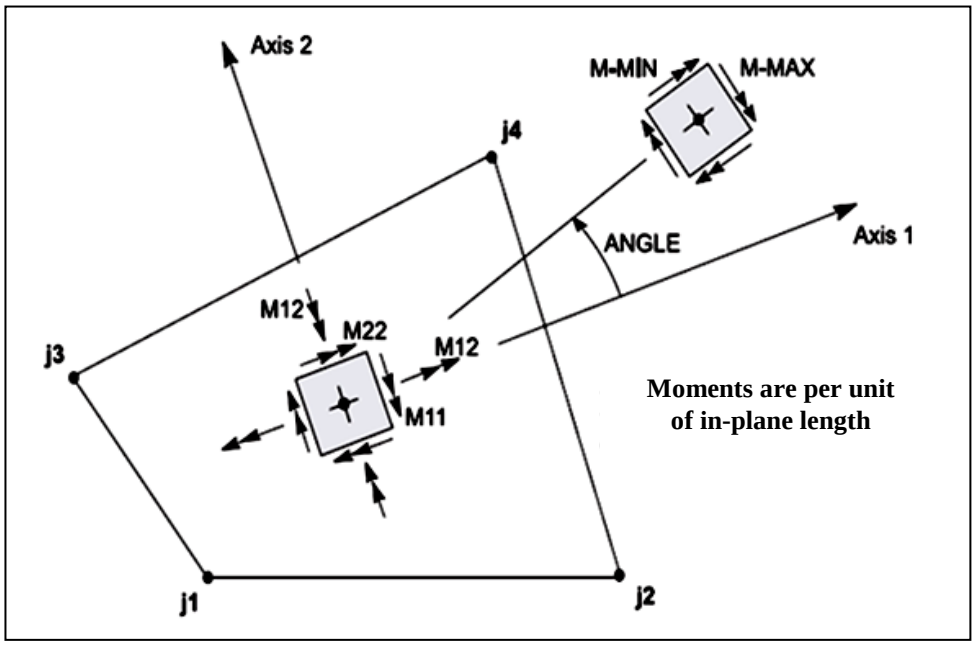

(b)

Figure 3.1: Shell elements used in the analysis (SAP2000) (a) Four node shell element, (b) Plate bending moments.

- Solid element: The solid element is an eight-node three-dimensional element which includes nine optional incompatible bending modes. The solid element contributes stiffness in all three translational stiffness in all three translational degrees of freedom at each of its connected joints.

- Nlink element: A NlLink element is an element with structural nonlinearities. A NlLink element may be either a one-joint grounded spring or a two-joint link and is assumed to be composed of six separate springs, one for each degree of deformational degrees of freedom including axial, shear, torsion and pure bending. Non-linear behaviour is exhibited during nonlinear time-history analyses or nonlinear static analyses.

3.2 3-D FINITE ELEMENT MODEL OF THE SUPERSTRUCTURE

Three dimensional (3-D) finite-element models of integral abutment bridge, as illustrated in Figure 3.2, were built using "SAP2000" software [61].

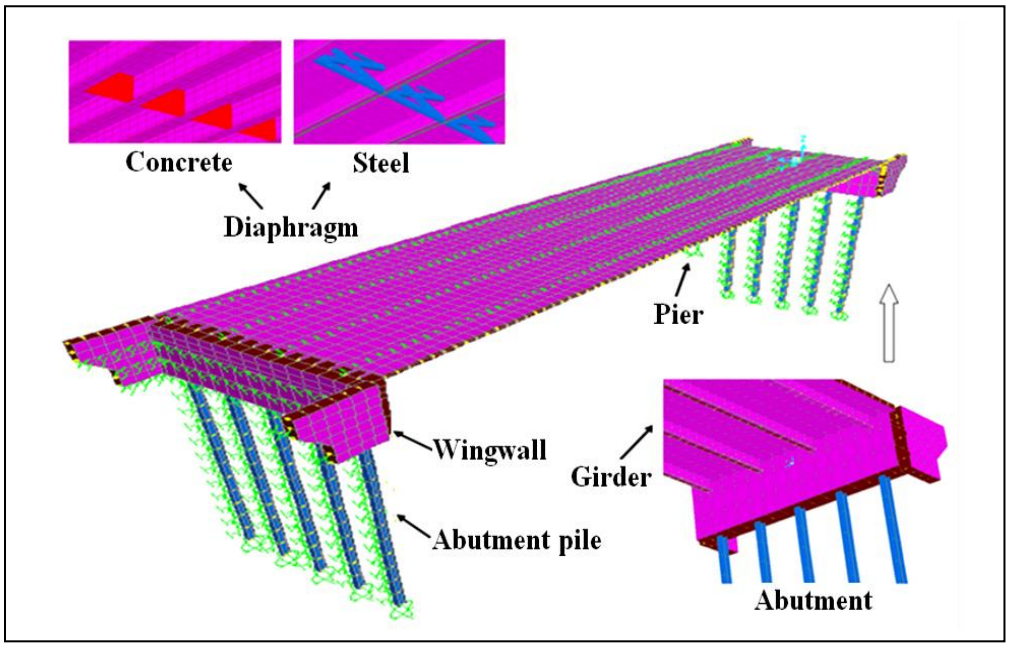

Figure 3.2: 3-D finite element model for integral abutment bridges.

Shell elements were used to model the concrete deck, abutments, concrete and steel I-girders. The thicknesses of each layer of shell elements corresponded to the widths of the cross-section fibers. For example, shell elements modeling the web had a thickness the same as that of the girder web. In order to improve the computation accuracy, the shape factor (length-width ratio) of the shell elements was limited be less than 4. The superstructure cross section of bridge as shown in Figure 3.3 was composed of a 250 *mm* thick concrete slab on four steel or concrete girders with girder spacing of 2.75 *m*.

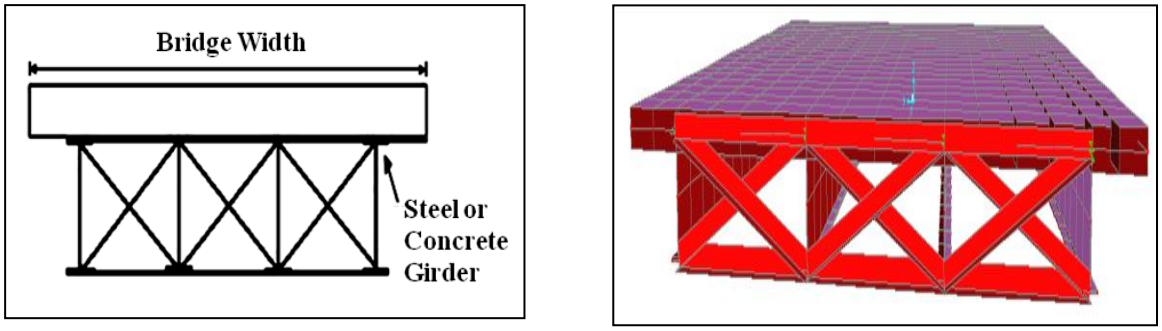

(a) (b)

Figure 3.3: View of bridge cross section (a) Two-dimensional (2-D), (b) Three-dimensional (3-D).

X-type steel bracing was modeled using frame elements. The cross bracings consisted of L150×150×25 *mm* were spaced at the middle of each span with no diaphragm at abutment. Bearing at the pier locations were also modeled to provide only vertical support, while released in all horizontal directions. Full-composite action was provided between the slab and girders. Rigid links, as displayed in Figure 3.4, were placed between the centroids of all top flange shell elements and the centroids of the deck slab shell elements above them in order to satisfy the compatibility of the composite behaviour.

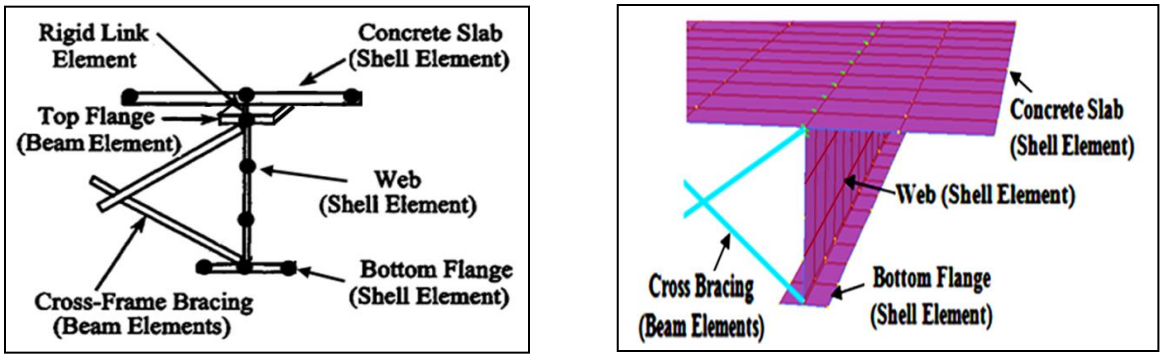

(a) (b)

Figure 3.4: Details of finite element modeling (a) Two-dimensional (2-D), (b) Three-dimensional (3-D).

3.3 3-D FINITE ELEMENT MODEL OF THE SUBSTRUCTURE

For the substructure of the finite element model, the abutments and wingwalls were modeled with shell elements, while piles were modeled with frame elements. Full-moment continuity was modeled between the steel H-piles and the abutments. The abutment walls for integral bridge were 10.25 *m* long, 1 *m* thick and 3 *m* height. Five HP 310×110 steel piles at spacing of 2 *m* were used to support the substructures of bridges. Each wingwall was 4 *m* long; 0.5 *m* thick with non

prismatic depth varying between 2 to 3 *m*. Figure 3.5 illustrates dimensions and views of wingwalls and abutments.

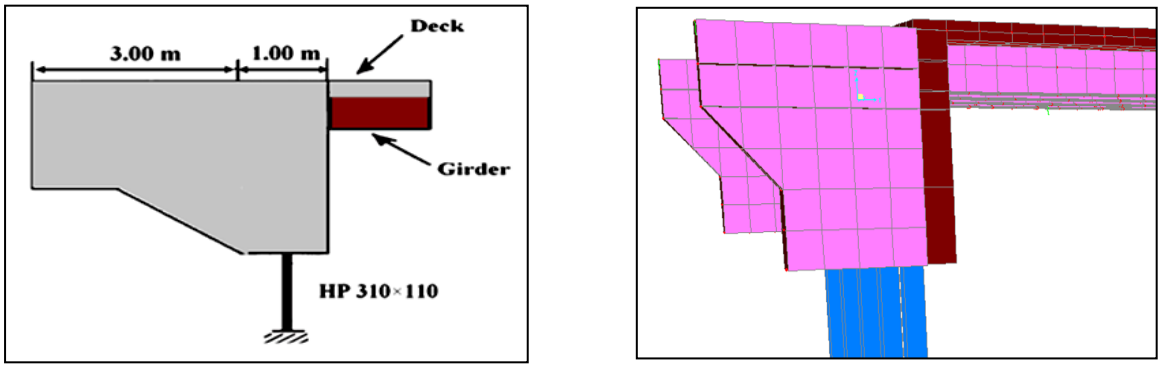

(a) (b)

Figure 3.5: Dimension of wingwalls and abutments (a) Two-dimensional, (b) Three-dimensional.

The soil-pile and soil-abutment interaction models were based on the subgrade reaction approach, developed by Reese and Impe [58]. This approach was based on the winkler foundation, where the foundation was assumed to be elastic and the soil was modeled as continuous springs as shown in Figure 3.6. In the developed finite element model, soil springs had nonlinear resistance displacement relationships represented by two types of interaction curves, namely: soil-abutment interaction curves and soil-pile interaction curves.

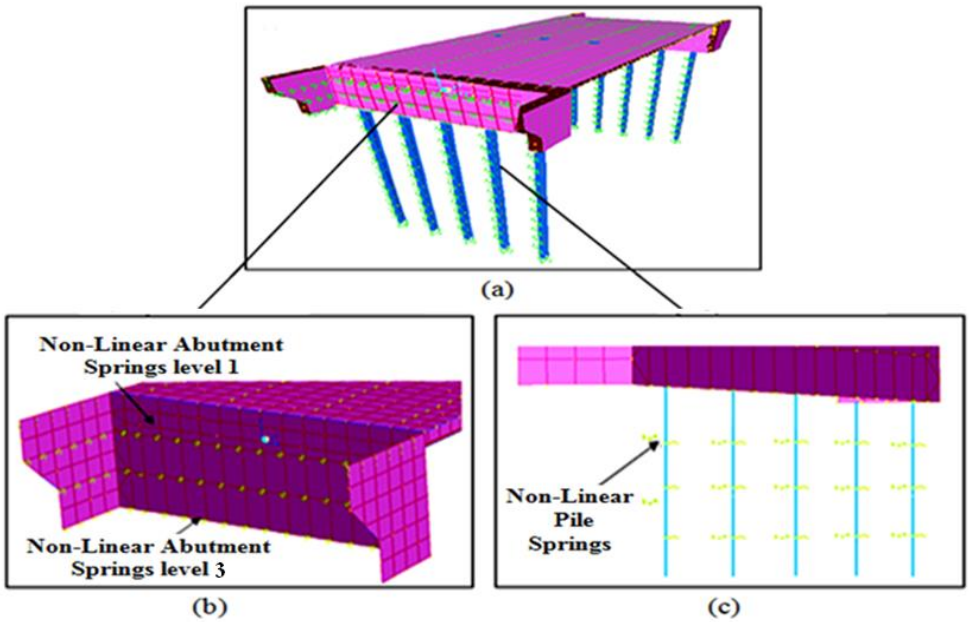

Figure 3.6: Finite element model of bridge prototypes (a) Full model, (b) Non-linear springs modeling the soil-abutment interaction, (c) Non-linear springs modeling the soil-pile interaction.

3.3.1 SOIL-ABUTMENT INTERACTION MODELING

Since the abutment backfills were considered as critical part in the entire structural system of integral abutment bridges, soil structure interaction became crucial to ensure results well–representative of actual structural behaviour. For this reason, soil was modeled by multi-linear spring. Multi-linear soil spring approximation of force-displacement curve was represented using link element in SAP2000. Spring coefficients shown in Figure 3.7(b) were based on the curve represented by Canadian guidelines mentioned elsewhere [12, 16, 35] as a function of the ratio of the abutment movement to the abutment height. Different spring values for different heights adopted in this study are illustrated in Figure 3.7(a). Horizontal spring elements were attached to each node along the abutment wall and perpendicular to the walls. Granular uncompacted material with ϕ= 30^{o} and unit weight of soil γ= 20 kN/m^3, which is typically used in integral bridge construction [35], was assumed for the backfill.

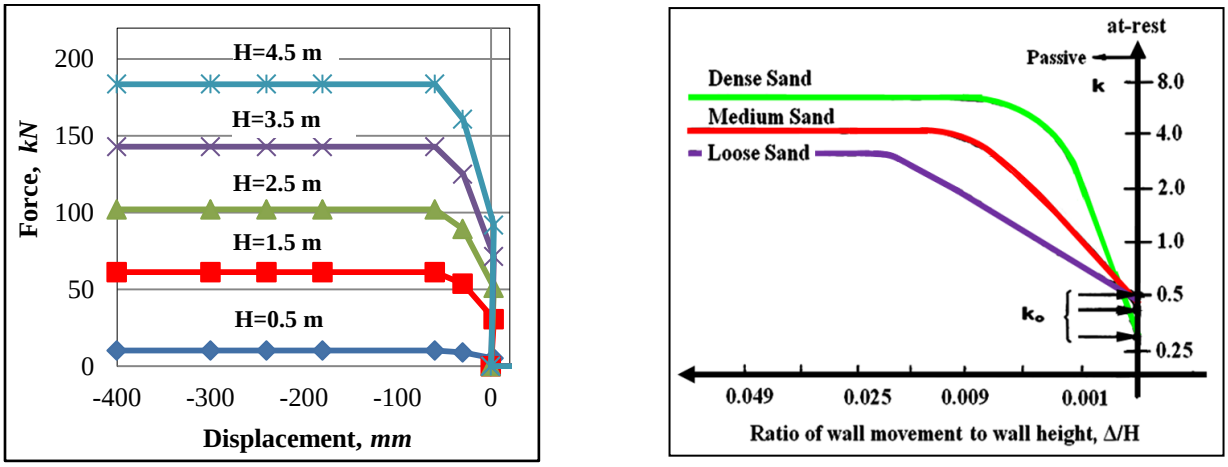

(a) (b)

Figure 3.7: Backfill interaction modeling (a) Typical P-Δ curve for backfill, (b) Soil horizontal-stiffness design curves [35].

It should be noted that for skewed bridges, in addition to the normal pressure acting against the surface of the abutments, the friction between the abutment and backfill becomes very important. To simulate the friction force, a series of multi-linear springs were placed in the direction parallel to the abutment. The stiffnesses of those springs were obtained by multiplying the stiffness of the

normal soil springs with the friction coefficient between the abutment concrete and the backfill, which was expressed as:

$$Friction\ Coefficient = tan\delta \simeq 0.4 \quad (3.1)$$

Where, δ is the surface-friction angle of soil and abutment.

3.3.2 SOIL-PILE INTERACTION MODELING

Horizontal multi-linear springs were also used to model the soil pile interaction. The soil–pile interaction for a particular point along the pile was defined by a nonlinear load (P)-deformation (Y) curve or P–Y curve, where P was the lateral soil resistance per unit length of pile and Y was the lateral deflection. The computation of the lateral-force–displacement response of a pile involved the construction of a full set of P–Y curves along the pile to model the force deformation response of the soil. A typical P-Y curve for soil subjected to lateral movement of a pile is shown with a solid line in Figure 3.8(b). This non-linear behaviour may be simplified using an elasto-plastic curve displayed on the same figure with a dashed line. It should be indicated that two types of soil (sand and Clay) have been considered in this research. The method of modeling clay and sand are presented respectively.

For piles driven in clay the soil resistance per unit length of pile, P_u, is expressed as [30]:

$$P_u = 9C_u d_P \quad (3.2)$$

Where, C_u is the undrained shear strength of the clay, and d_P is the pile width. Based on the method proposed by Skempton [65], the spring stiffness for clay for elastic portion (K_s) with consideration of 1 m spring spacing is obtained as:

$$K_s = \frac{9C_u}{5\varepsilon_{50}} \quad (3.3)$$

Where, ε_{50} is the soil strain at 50% of ultimate soil resistance. For soft, medium and stiff clay, corresponding values of C_u=20, 60 and 120 kPa respectively, and ε_{50}=0.02, 0.008 and 0.005,

respectively, are used in the parametric study. Different spring force-displacement values for different clay types (soft to stiff) adopted in this study has been shown in Figure 3.8(a).

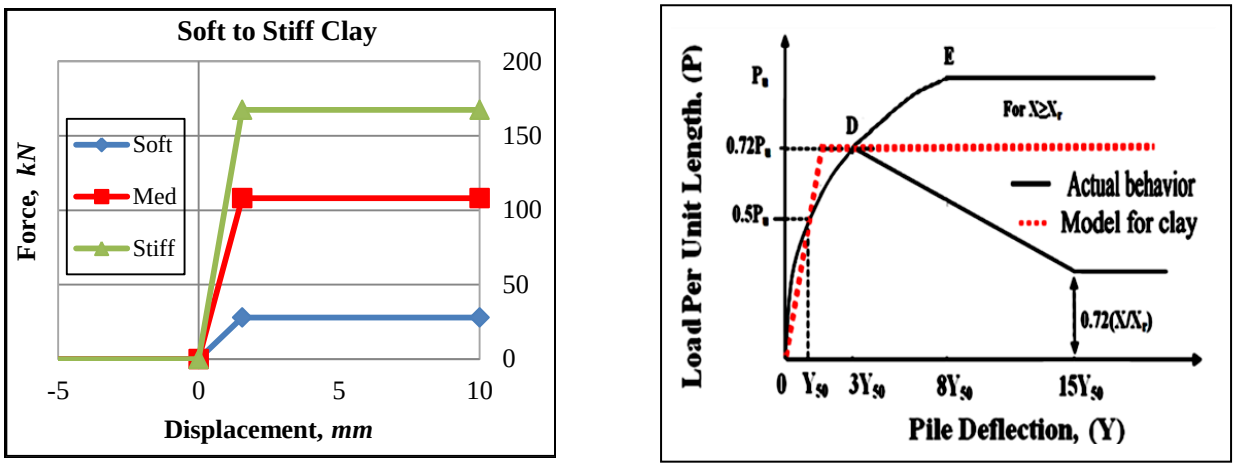

(a) (b)

Figure 3.8: Soil–H-pile interaction modeling (a) Typical force-displacement curve, (b) Actual and modeled P–Y curve for clay.

For piles driven in sand, the soil resistance per unit length of pile, P_u, is expressed as [30]:

$$P_u = k_a d_P(\gamma x + q)(tan^8\beta - 1) + k_o d_P(\gamma x + q)tan^4\beta tan\phi \quad (3.4)$$

Where, k_a and k_o are the active and at-rest earth pressure coefficients; γ and ϕ are, the unit weight of soil and the angle of internal friction of the soil in degrees, respectively, x is the depth below the ground surface, q is the surcharge pressure and β is expressed as:

$$\beta = \left(45 + \frac{\phi}{2}\right) \quad (3.5)$$

For sand, spring stiffness for elastic portion (K_s) with consideration of 1 m spring spacing is assumed to increase linearly with depth from the ground surface and expressed as [30]:

$$K_s = K'x \quad (3.6)$$

Where, K' is the subgrade constant of the soil. For loose, medium and dense sand, corresponding

values of K' are considered 2000, 6000 and 12000 kN/m^3, corresponding value of γ are considered 16, 18 and 20 kN/m^3 and corresponding value of ϕ are taken 30^o, 35^o and 40^o in the parametric study [11]. Different spring force-displacement values for different sand types (loose to dense) adopted in this study have been displayed in Figure 3.9.

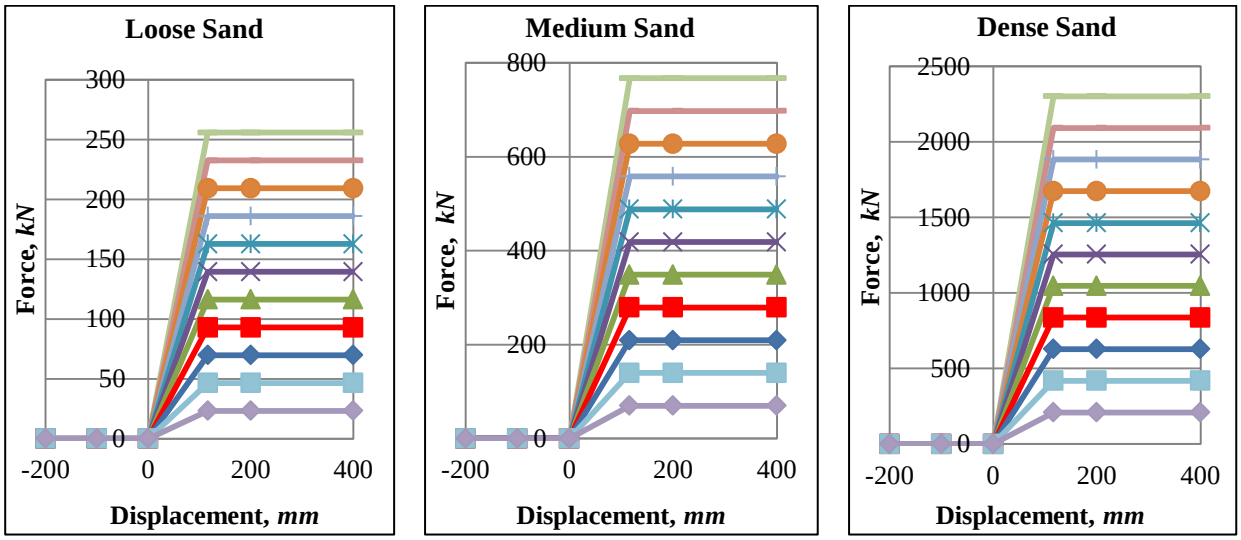

(a) (b) (c)

Figure 3.9: Soil–H-pile interaction modeling for Sand (a) K'=2000 kN/m^3, (b) K'=6000 kN/m^3, (c) K'=12000 kN/m^3.

3.3.3 SENSITIVITY STUDY ON DISTRIBUTION OF NONLINEAR SOIL SPRINGS

In the developed model, discrete multi-linear springs were placed surrounding the piles to approximate the continuous winkler springs. Multi-linear springs surrounding the piles were placed in two directions: longitudinal and lateral. In order to determine a reasonable spacing of the soil springs, a sensitivity analysis was conducted. Figure 3.10 demonstrates that the number of soil springs in finite element model (FEM) was very important to have sufficient accuracy. When the number of soil springs in the FEM was more than 10 (corresponding to a spring spacing of 1 m), the computation errors were less than 1.5%. Figure 3.10(a) and 3.10(b) show the computed deflections and moments along the pile depths, respectively. Large errors occurred when the number of soil springs was less than 10. To keep the accuracy of the solution, it was necessary to limit the spacing of the soil springs on the depth below the top soil surface to less than 1 m.

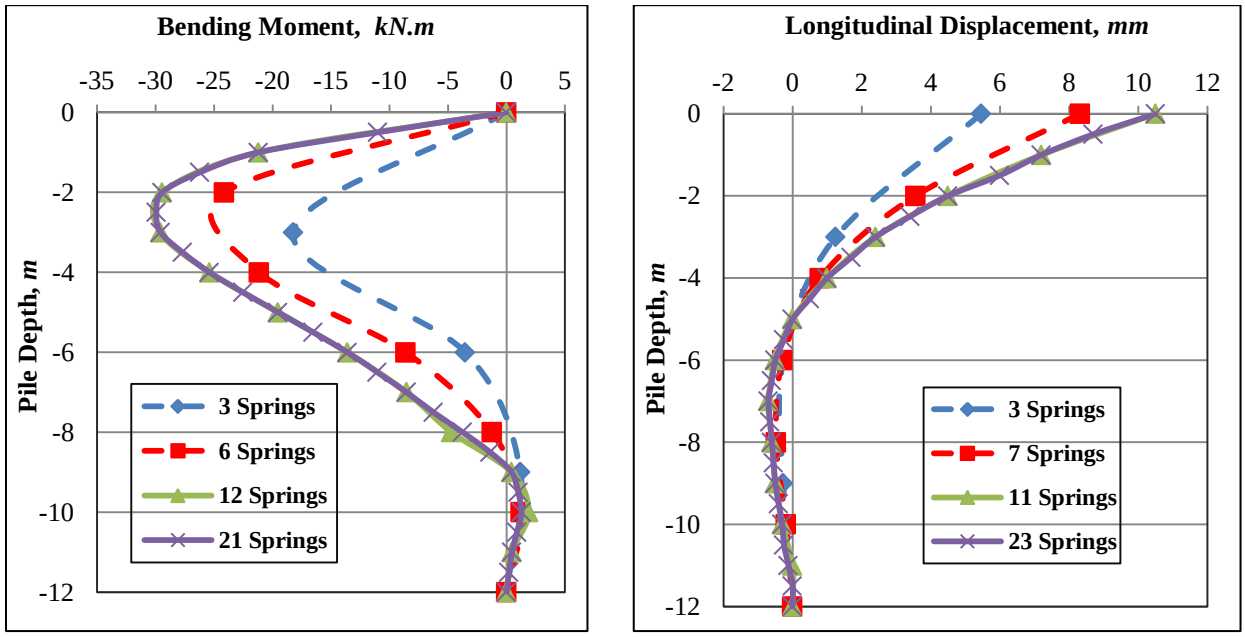

(a) (b)

Figure 3.10: Results for H-pile with different spring numbers (a) Longitudinal deflection, (b) Bending moment.

Behind the abutment, three layers of soil springs were positioned against the abutment as depicted in Figure 3.6(b). In the transverse direction, the spacing of the nonlinear springs was approximately 0.5 *m*. Fourteen multi-linear springs were placed against each wingwall as depicted in Figure 3.6(b). The interaction curves used for the springs behind the wingwalls were obtained using the same method as for the interaction curves of the springs behind the abutment.

3.4 2-D FINITE ELEMENT MODEL OF INTEGRAL BRIDGES

In order to achieve live load distribution factors (LLDFs) for integral abutment girders, 2-D finite element models of different integral bridges were required to be built and analyzed. A two-dimensional 2-D frame version was built for each 3-D structural model of the integral abutment bridges to enable the calculation of LLDFs. The 2-D structural models of a typical integral abutment bridge used in the analyses are shown in Figure 3.11. The model was built using 2-D elastic beam elements considering a single girder. In the structural model, the tributary width of the slab and abutments was set equal to the spacing of the girders. For the deck, full composite action between the slab and the girders was assumed. The stiffness properties of the composite slab-on-girder deck were expressed in terms of the properties of the slab using the transformed

area method. The stiffness properties of the pile element in the 2-D model were calculated as the stiffness properties of a single pile multiplied by the number of piles per girder. The soil–structure interaction modeling for the 2-D model was similar to that of the 3-D model, except the spring constants are calculated using a tributary area equal to the girder spacing times the vertical spacing between the nodes.

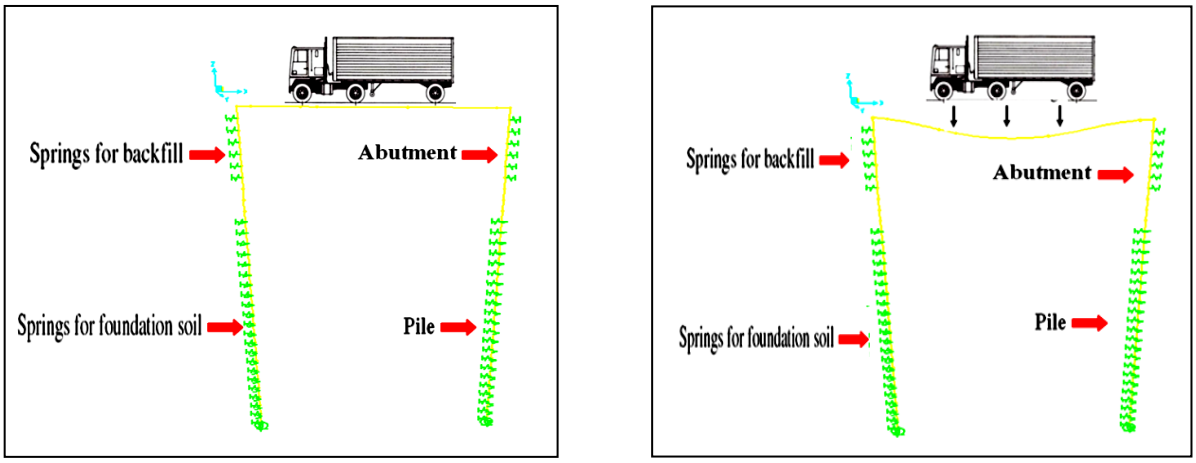

(a) (b)

Figure 3.11: Views of 2-D finite-element models (a) IAB with no truck loading, (b) Deformed IAB under truck loading.

3.5 INPUT MATERIAL PROPERTIES

3.5.1 MATERIAL PROPERTIES OF STRUCTURAL COMPONENTS

The specified 28-day compressive strength of concrete in deck slab and concrete girder was 25 *MPa*. The modulus of elasticity of the girder and deck concrete was 24 *GPa*. The modulus of elasticity of steel in the beams, intermediate cross frames and H-pile was taken equal to 200 *GPa*. The Poisson's ratios of the concrete and steel were assumed to be 0.2 and 0.3, respectively. The material properties of the concrete intermediate diaphragms and abutments were assumed to be the same as those of the deck. Concrete and steel were assumed to be homogeneous and linear elastic. Cracking of the structural concrete was not considered. The reason for assuming linear elastic properties of the concrete and steel was that the stresses due to temperature changes was not high as suggested by CHBDC. Thus, it was not necessary to consider the material nonlinearity. The coefficient of thermal expansion of concrete and steel were assumed to be $\alpha_{Concrete} = 0.99\times10^{-5}\ 1/^{o}C$ and $\alpha_{Steel} = 1.17\times10^{-5}\ 1/^{o}C$, respectively.

3.5.2 MATERIAL PROPERTIES OF SOILS

3.5.2.1 INITIAL SUBGRADE LATERAL STIFFNESS, k_s

Initial subgrade lateral stiffness for sand recommended by different researchers shows significant variance. Reese and Impe [58] recommended values for different types of sand as shown in Table 3.1. Terzaghi [67] gave the range of k_s for each type of sand (Table 3.1), which were much smaller than those recommended by Reese et al. It can be observed that the lower bound and upper bound of 2,000 kN/m^3 and 12,000 kN/m^3 reported by Bowles [11] were close to the recommended lower bound and upper bound, by Terzaghi. For the finite element model of integral bridges, the recommendation of Bowles was used to determine the initial subgrade lateral stiffness for different layers of soil under the abutment.

Table 3.1: Properties of different types of soils.

Soil Type	Reese et al. [58]			Terzaghi [67]			Bowles [11]		
	Soil Modulus (kN/m^2)	Density (kN/m^3)	Friction angle (ϕ)	Subgrade Modulus (kN/m^3)	Density (kN/m^3)	Friction angle (ϕ)	Subgrade Modulus (kN/m^3)	Density (kN/m^3)	Friction angle (ϕ)
Loose sand	5430	17	30	1930	17	30	2000	16	30
Medium sand	16300	18	35	6790	18	35	6000	18	35
Dense sand	33900	20.3	40	13850	20.3	40	12000	20	40

3.5.2.2 INTERNAL FRICTION ANGLE OF SAND, (ϕ)

The internal friction angles of sand are shown in Table 3.1. The internal friction angles of loose, medium and dense sand were assumed to be 30^o, 35^o and 40^o in the FEA models, respectively.

3.5.2.3 COHESION OF CLAY C_u AND THE 50% STRAIN, ε_{50}

In finite element models, suggestions of Skempton [65], with corresponding values of C_u=20, 60 and 120 kPa and ε_{50}=0.02, 0.008 and 0.005 for soft, medium and stiff clay have been used.

3.6 FINITE ELEMENT MODELING OF LOADS

In finite element analysis, two different loading conditions have been considered. To predict the length limits, the performance of integral bridges subjected to temperature variations has been considered. To evaluate live load distributions, the behaviour of integral bridges under CHBDC truck loading has been investigated. Temperature loading cases and live loading cases are explained in section 3.6.1 and 3.6.2.

3.6.1 TEMPERAUTURE LOADING CASES

Temperature variations considered in finite element analysis were based on CHBDC for province of Ontario. The maximum and minimum daily mean temperature has been selected from CHBDC maps. The minimum and maximum adopted temperature values for steel bridges were $-33^{o}C$ and $+50^{o}C$. The minimum and maximum temperature amplitude of $-23^{o}C$ and $40^{o}C$ were used for concrete bridges. According to CHBDC, $15^{o}C$ positive temperature gradient in the deck was considered as well. Therefore, maximum temperatures based on Moorty and Roeder [50] equations for steel and concrete bridges were equal to $55^{o}C$ and $45^{o}C$. Assuming a construction temperature of $15^{o}C$, and using the uniform temperature and temperature gradient specified by CHBDC, the average positive and negative ranges for steel integral bridges were considered as $-48^{o}C$ and $+40^{o}C$. Those ranges for concrete bridges were specified as $-38^{o}C$ and $+30^{o}C$. Figure 3.12 displays nodal temperatures for the steel bridges during temperature decrease and increase.

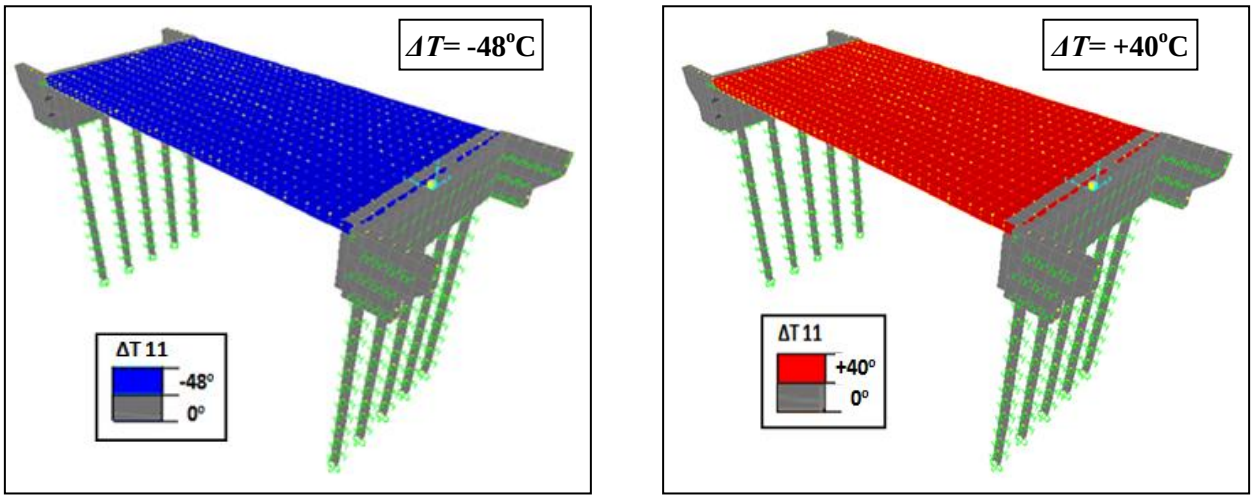

(a) (b)

Figure 3.12: Temperature loading (a) Temperature decrease (ΔT= -48 °C), (b) Temperature increase (ΔT= +40 °C).

3.6.2 MODELING OF LIVE LOAD

The live load, specified in the CHBDC, consists of CL-W truck and CL-W lane loading. The CL-W truck consists of idealized five axles with total load of 625 *kN* as shown in Figure 3.13. The CL-W lane loading consists of CL-W truck loading with each axle load reduced to 80% of its original value and superimposed within uniformly distributed load of 9 *kN/m* over 3 *m* width.

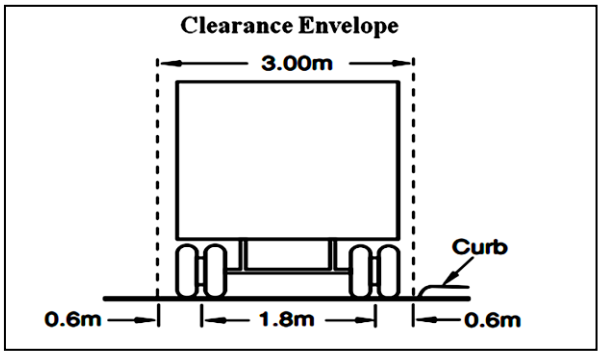

(a)

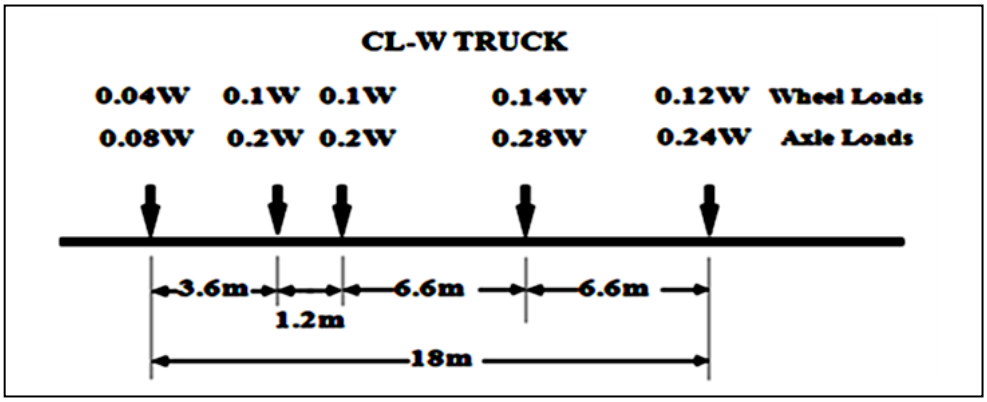

(b)

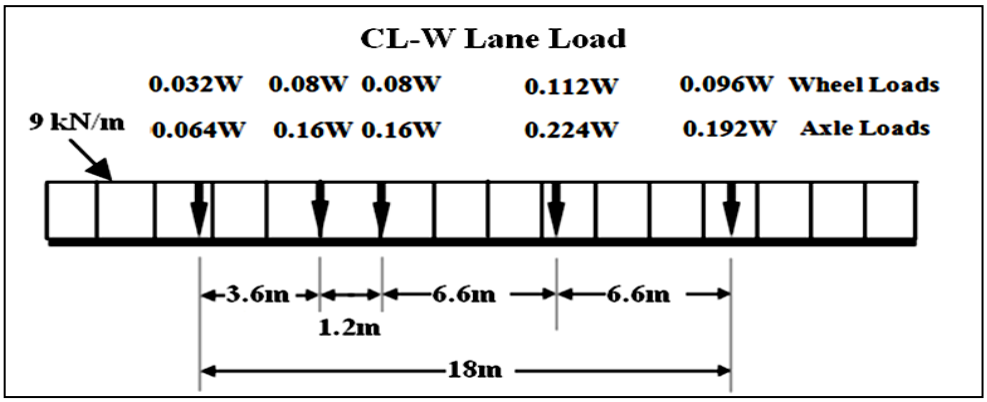

(c)

Figure 3.13: CHBDC truck loading: (a) CL-W truck, (b) CL-W truck loading, (c) Lane loading.

The selection between two different CHBDC types of live loads (CL-W truck and CL-W lane) depends on whichever gives the greatest design values. A sensitivity study which was carried out in this regard showed that the CL-W truck loading is governs the extreme design values. Accordingly, the CL-W truck loading was utilized as a live loading in finite element modeling.

SAP2000 software has the ability to run a moving load along a bridge. For moving load analysis, lanes, vehicle and vehicle class were modeled and defined. The line or the area where the traffic load acted upon the bridge superstructure was first identified. The lane width was specified in the program as well as the distance between the vehicle and the lane edge. Multiple lanes were defined per the actual traffic pattern on the bridge. Truck was represented in the program by number of concentrated forces. Each truck axes were represented by single or double loads with defined axle width. The minimum or the maximum distances between each axe was specified in the program. Vehicle class was used to combine several vehicles together to run on the bridge at the same time. It was used to define the dynamic amplification factor for the truck loading used in the analysis. In the moving load analysis, vehicles were automatically located at each possible location along the lanes and within the width of the lanes to produce the maximum and minimum response quantities throughout the structure.

CHAPTER 4: VALIDATION OF PROPOSED FINITE ELEMENT MODEL WITH THE EFFECT OF TEMPERATURE AND LIVE LOAD

The detailed finite element model provided a numerical tool to predict bridge performance under different load conditions. The finite element models explained in chapter 3 were verified by the results obtained from field testing on integral bridges. In section 4.1, finite element models were validated for the effect of temperature against long term monitoring results of Bridge 109, Wendell Depot Bridge, Bridge 203, Iowa Highway 60 Bypass of Sheldon, Boone River Bridge and Guthrie County Bridge [40, 10, 44, 29, 27, 1]. In section 4.2, finite element models were verified for live load test result of Bridge #55555 and Coplin Plantation Bridge [34, 31].

4.1 VALIDATION FOR THE EFFECT OF TEMPERATURE

The finite element models for the effect of seasonal and daily temperature changes were verified against the results of non-skewed and skewed integral bridges. First in section 4.1.1, field test results of non-skewed integral bridges, including Bridge 109, Wendell Depot Bridge and Bridge 203, were used to validate finite element models. Then, in section 4.1.2, results of field testing of skewed integral bridges namely: Iowa Highway 60 Bypass, Boone River Bridge and Guthrie County Bridge, were used to verify the finite element model. The validation of the accuracy of the finite element analysis required a comparison with the field data, whereby the field data was interpreted for thermal loads only so as to have the consistency in the response comparison.

4.1.1 NON-SKEWED INTEGRAL BRIDGES

In this part, finite element modeling was validated based on observed structural behaviour of non-skewed integral bridges. Observed behaviour was on the basis of field monitoring conducted at Bridge 109, Wendell Depot Bridge and Bridge 203. Integral bridges data were continuously collected and complied, processed and evaluated over the time. Based on the comparison between the observed behaviour and those obtained by numerical modeling, it was concluded that the model used for this research was sufficiently verified and validated.

4.1.1.1 BRIDGE 109

4.1.1.1.1 FIELD TESTING OF BRIDGE 109

4.1.1.1.1.1 BRIDGE DESCRIPTION

Bridge 109 is located 3.2 *km* west of Port Matilda, PA [40, 44]. The bridge is a four-span, composite structure with four prestressed concrete I-girders bearing on reinforced concrete piers and abutments with end and interior spans of 26.8 and 37.2 *m*, respectively. The total length of the bridge is 128 *m* (see Figure 4.1). The four AASHTO Type I-Beam 28/78 prestressed concrete girders are spaced at 3.5 *m* and cast integrally with both abutments (see Figure 4.2).

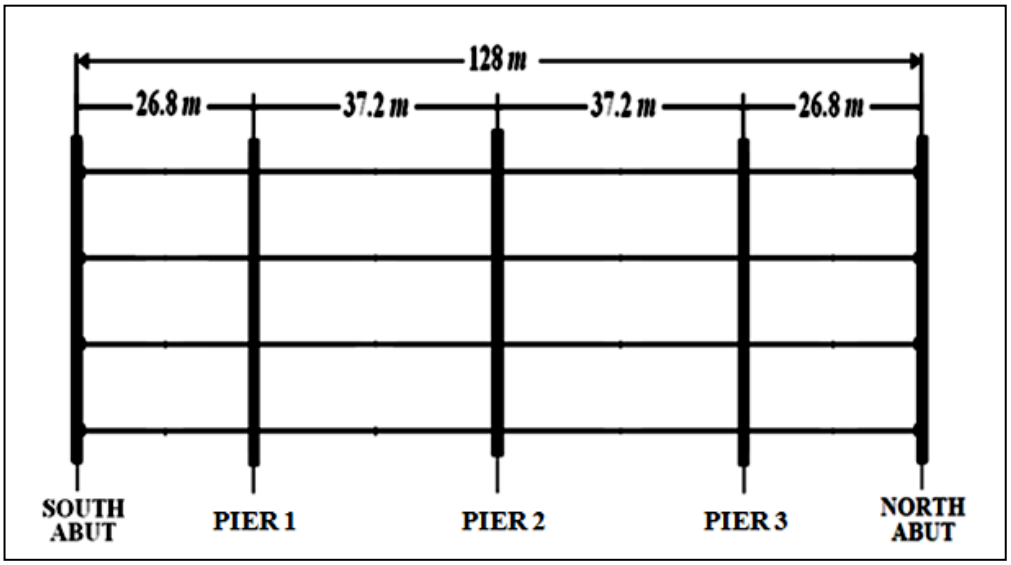

Figure 4.1: Plan view of bridge [40].

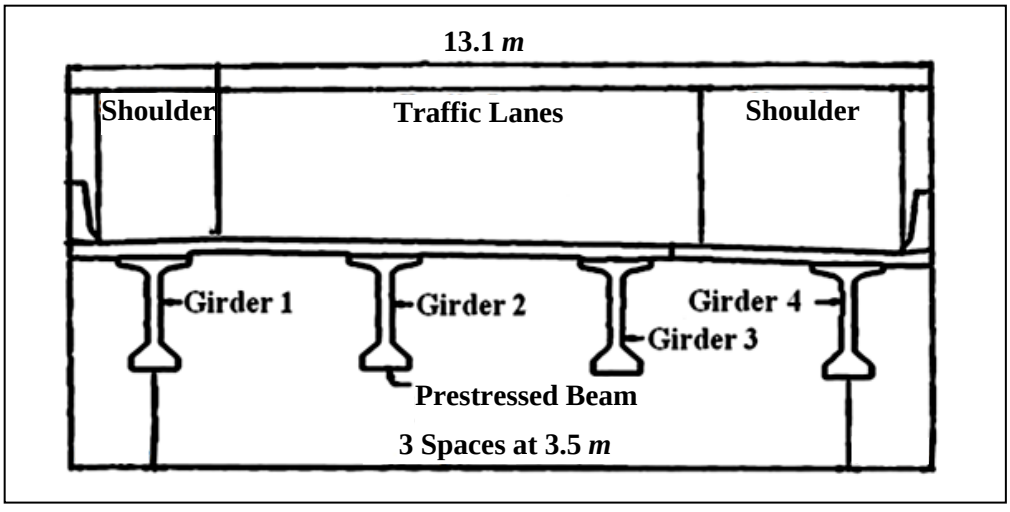

Figure 4.2: Transverse section of bridge [40].

The total abutment height is approximately 3.5 *m.* Both abutments are integral with a single row of twelve HP 310×110 steel piles bending about the weak axis in response. Details of soil strata properties of both north and south abutments are presented in report prepared by Laman and Kim [44]. As an example, soil strata properties at north abutment are shown in Figure 4.3. The piers are designed as semi-rigid, self-supporting substructures with 80 *mm* elastomeric bearing pads that allow movement between the pier and superstructure. The deck is 230 *mm* thick including integral wearing surface.

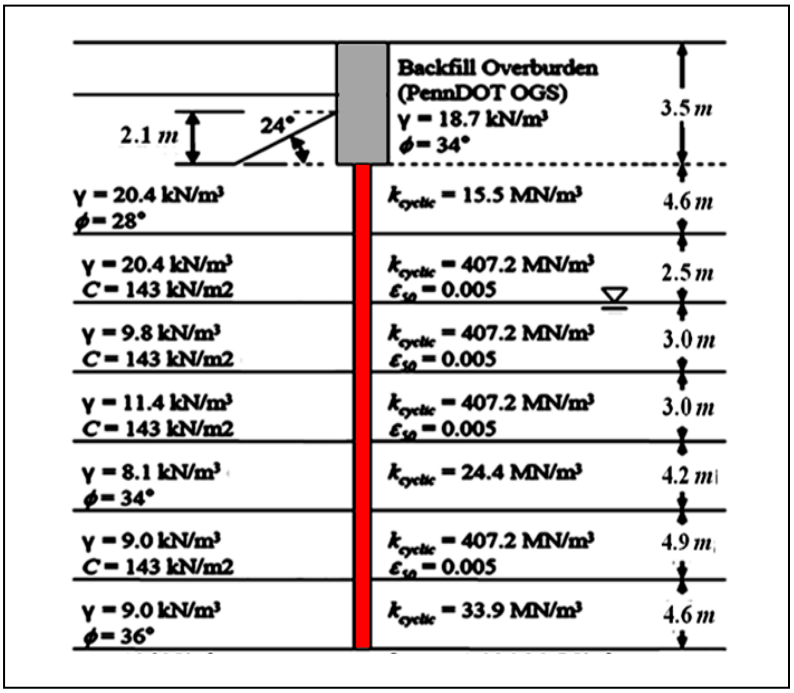

Figure 4.3: Soil properties under north abutment [44].

4.1.1.1.1.2 BRIDGE INSTRUMENTATION PLAN

Monitoring of bridge commenced in September 2005 and has continued uninterrupted to January 2009. Figure 4.4 and 4.5 present the instrumentation plan for the bridge. Vibrating wire based instruments were installed on the bridge consisting of surface-mounted strain gages, extensometers and tiltmeters. Strain gages mounted on each pile include three sets of three gages to measure bending and axial strain and six single gages to measure axial strain only. The gages placed in sets of three were located just below the abutment, between the abutment and predicted point of maximum moment and at the predicted point of maximum moment. The remaining individual gages were attached to the center of gravity at even intervals between the estimated point of fixity for the pile and the pile tip. Borehole extensometers were placed to monitor

abutment longitudinal translation and indirectly abutment rigid body rotation about a transverse horizontal axis and a vertical axis. North abutment longitudinal movement and three axis of rotation were monitored. Tiltmeters were installed on the north abutment to verify rotations calculated from extensometer readings and north span girders. Additional tiltmeters were mounted to the web of each girder at the north abutment to observe the rotational restraint of the diaphragm by comparing rotations between girders and abutment [40].

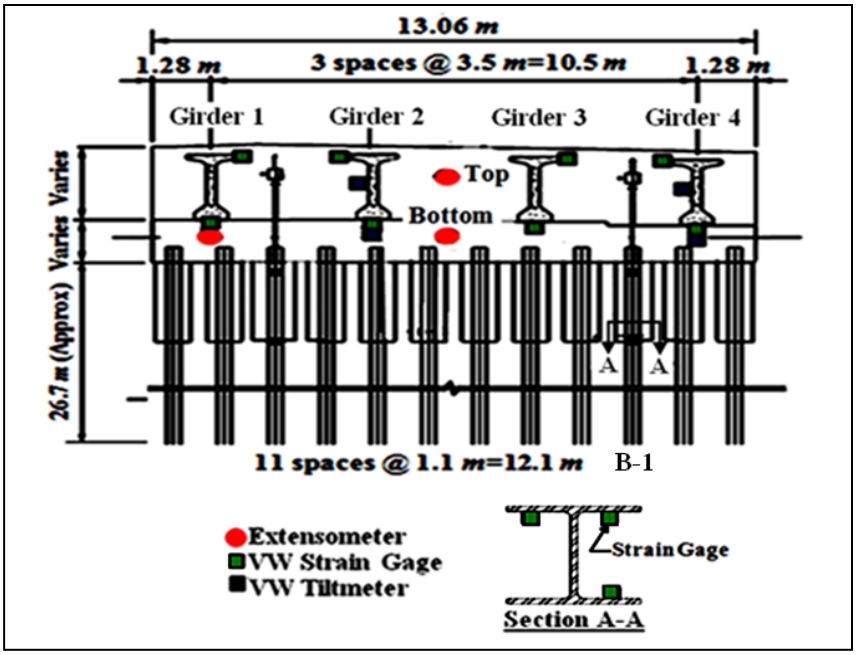

Figure 4.4: Instrumentation plan of north abutment elevation view [40].

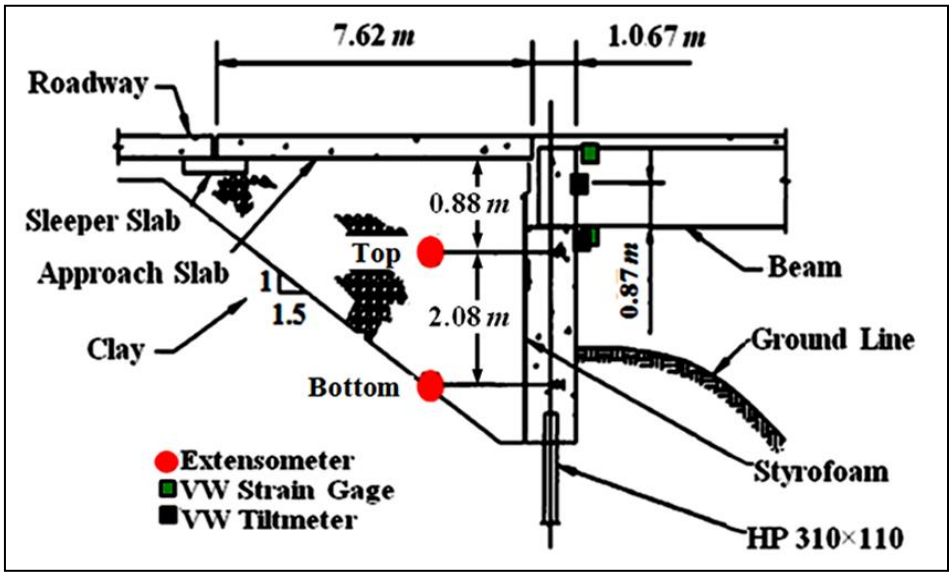

Figure 4.5: Bridge abutment section and instrument location [44].

4.1.1.1.1.3 BRIDGE MONITORING RESULTS

The primary component of the structure thermal loading as shown in Figure 4.6 was ambient air temperature. On the basis of a bridge construction temperature of +20°*C*, the extreme temperature range was approximately -42°*C* fall and +15°*C* rise.

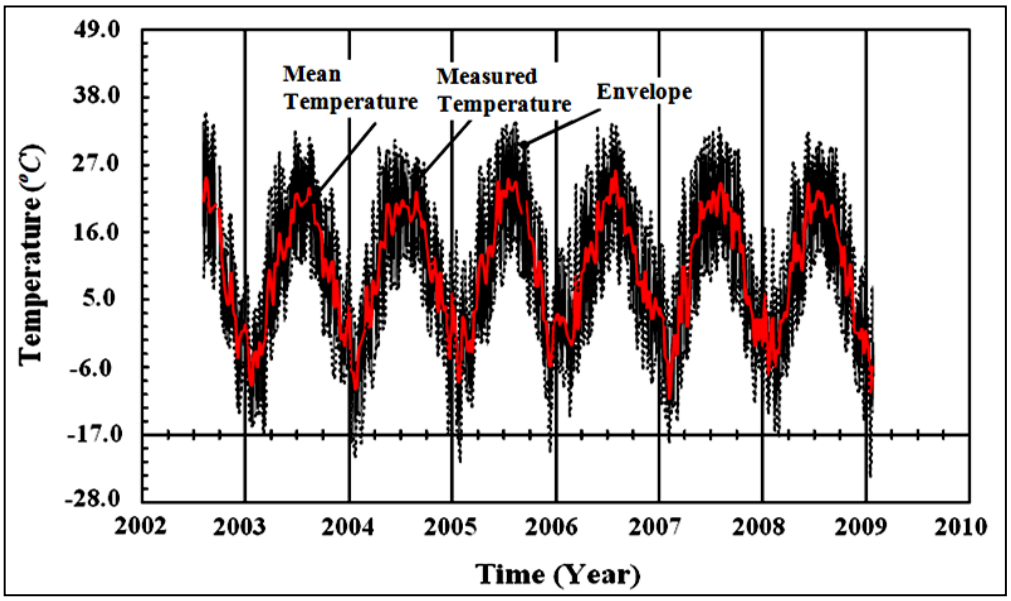

Figure 4.6: Ambient temperature [44].

Collected data from extensometers at south and north abutments are presented in Figure 4.7 and 4.8. The extensometers measured abutment movement as a result of superstructure expansion and contraction.

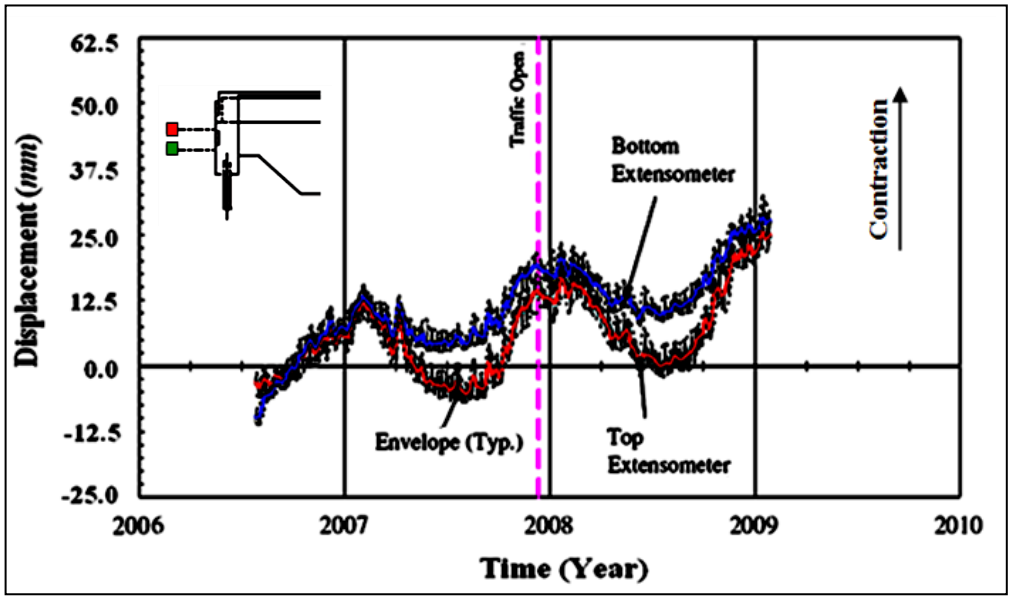

Figure 4.7: South abutment top and bottom displacement [40].

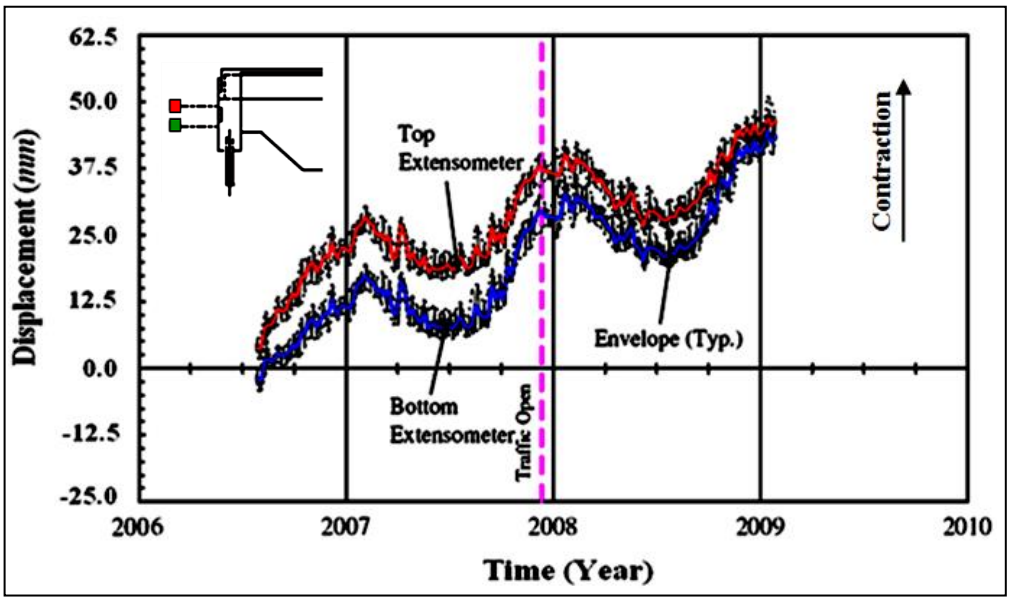

Figure 4.8: North abutment top and bottom displacement [40].

By inspecting the measured displacements in Figures 4.7 and 4.8, it is apparent that both abutments were experiencing an annual net inward movement. It is commonly believed that as the bridge cycles through seasonal movements, soil pressures will continue to build behind the abutments. This phenomenon, known as ratcheting, causes the abutments to creep inward resulting in a shortening of the bridge. Abutment rotation on north abutment is illustrated in Figure 4.9. Tiltmeters were mounted on each abutment under centerline of girders 1 and 3.

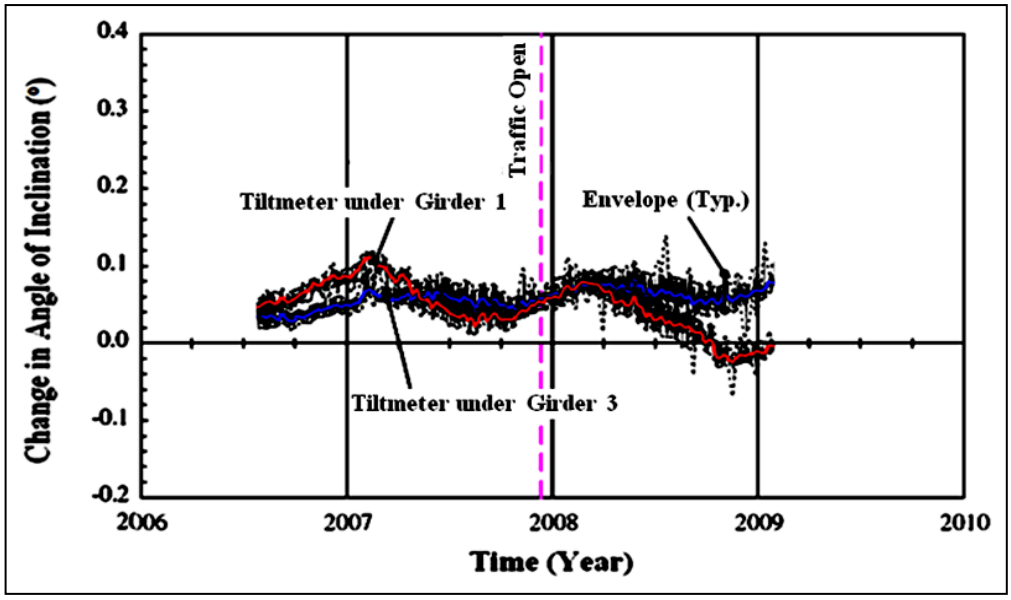

Figure 4.9: Abutment rotations by tiltmeters on north abutment of bridge [40].

The second interior pile (B-1) bending moments about weak axis derived from strain measurements is shown in Figure 4.10. It is observed that pile moments were much less than the section bending capacity. The pile yielding resisting moment was 172 $kN.m$ (Based on F_y =345 MPa) [40].

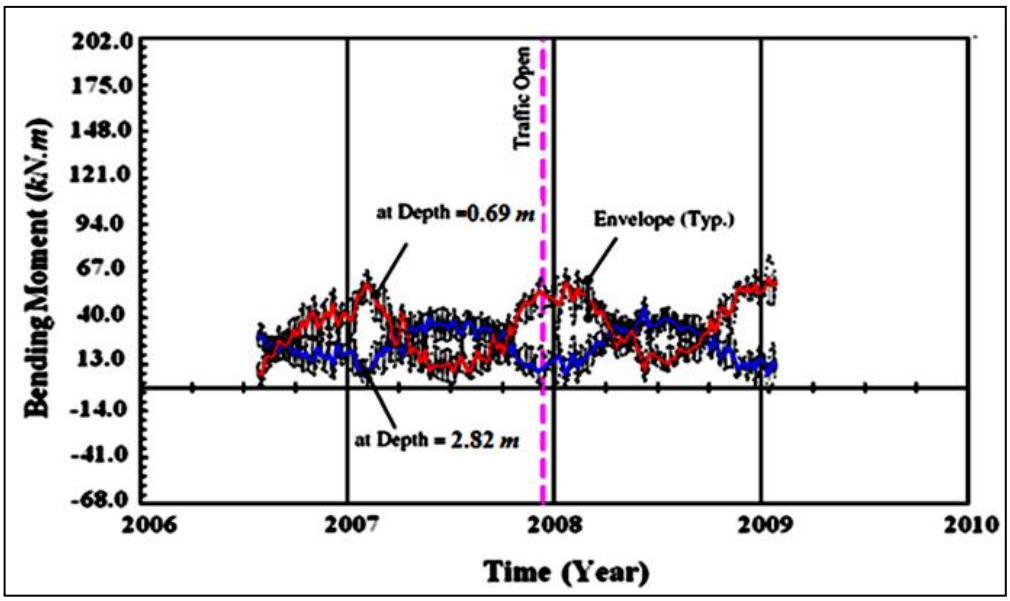

Figure 4.10: Pile moments under north abutment [40].

4.1.1.1.2 BRIDGE 109 NUMERICAL MODELING

As illustrated in Figure 4.11, a 3-D finite element model of Bridge 109 was developed. Figure 4.12 shows finite element model view of bridge superstructure.

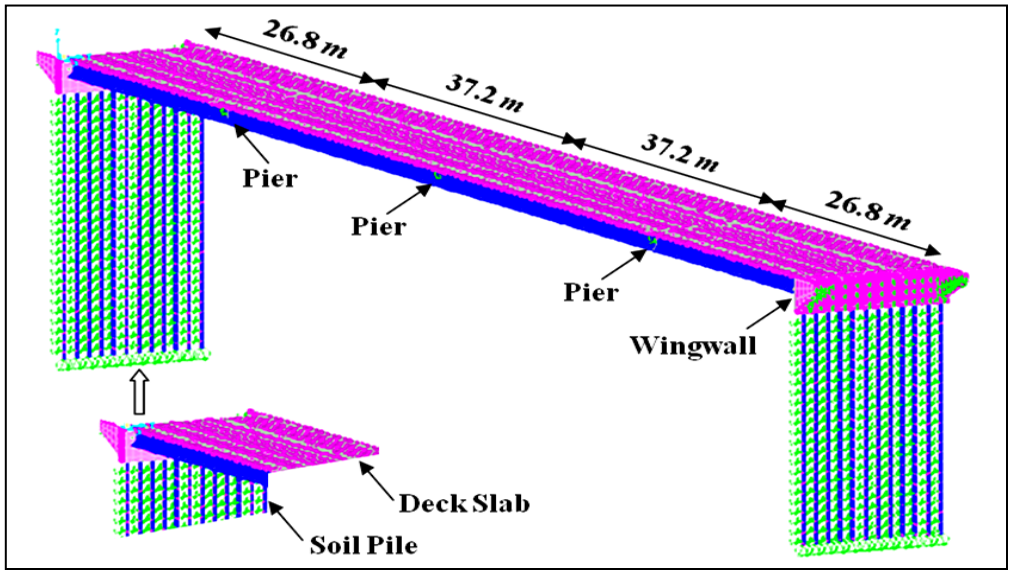

Figure 4.11: 3D finite element model view of Bridge 109.

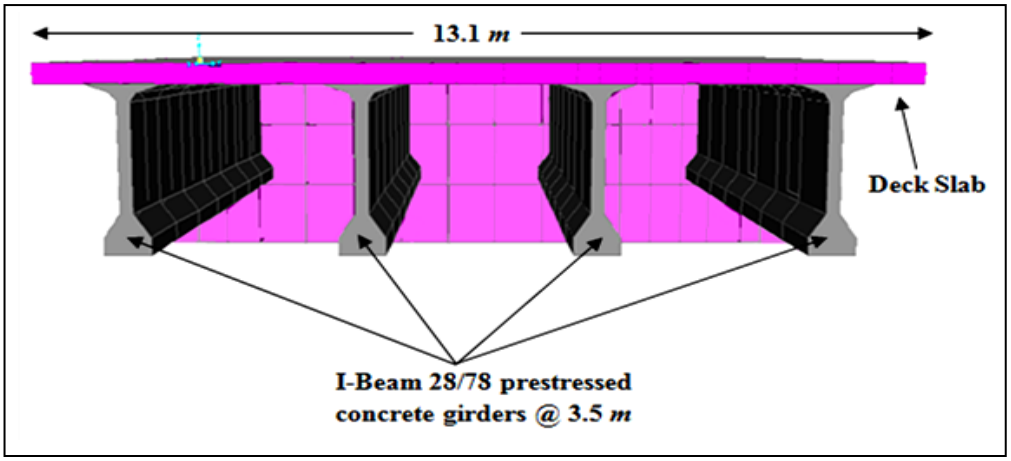

Figure 4.12: 3D finite element model view of bridge superstructure.

Prestressed girders, deck, diaphragms and abutments were modeled using shell elements. Piles were modeled with beam elements. Multi-linear springs were used to simulate soil behind abutments and surrounding piles. Element material properties are presented in Table 4.1.

Table 4.1: Bridge 109 material properties [44].

Material	Strength ($f_c^{'}$or F_y) (*MPa*)	Young's Modulus (*MPa*)	Poisson's Ratio	Thermal Expansion Coefficient (*mm/mm/*^{o}C)
Concrete (Prestressed Girder)	55	35,535	0.2	9×10^{-6}
Concrete (Deck)	27.5	25,124	0.2	9×10^{-6}
Concrete (Diaphragm)	24	23,504	0.2	9×10^{-6}
Concrete (Abutment)	20.5	21,760	0.2	9×10^{-6}
Steel (H-Piles)	350	199,948	0.3	11.7×10^{-6}

4.1.1.1.3 COMPARISON OF ANALYTICALLY-PREDICTED AND EXPERIMENTALLY-MEASURED RESULTS OF BRIDGE 109

This section presents the abutment displacement, abutment rotation and pile bending moment obtained from finite element analysis due to effect of temperature change. Comparisons between these analytically-predicted and experimentally-measured results are also discussed.

Changes in the bridge length induced by temperature changes were investigated using finite element models. In order to compare the results, temperature variations implemented in the finite element modeling were the same as the measured temperature variation from the field testing. The two temperature ranges considered were included extreme seasonal cycles between summer and winter temperatures. Different temperature variations for finite element modeling were -42°*C* and +15°*C*. Figures 4.13 and 4.14 display maximum nodal temperature decrease and increase for the bridge.

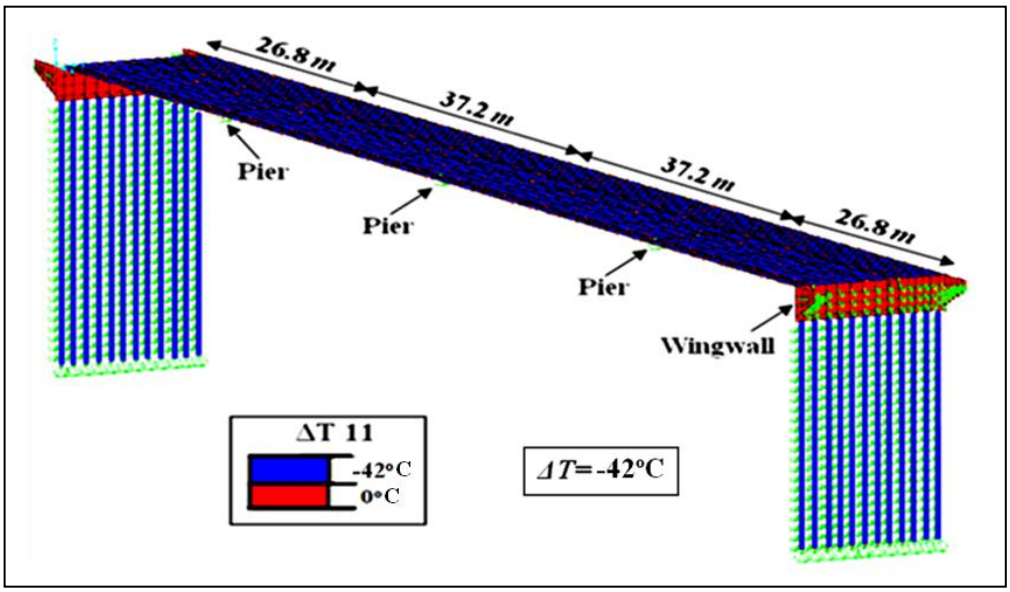

Figure 4.13: View of 3D FE model corresponded to temperature loading of -42°C.

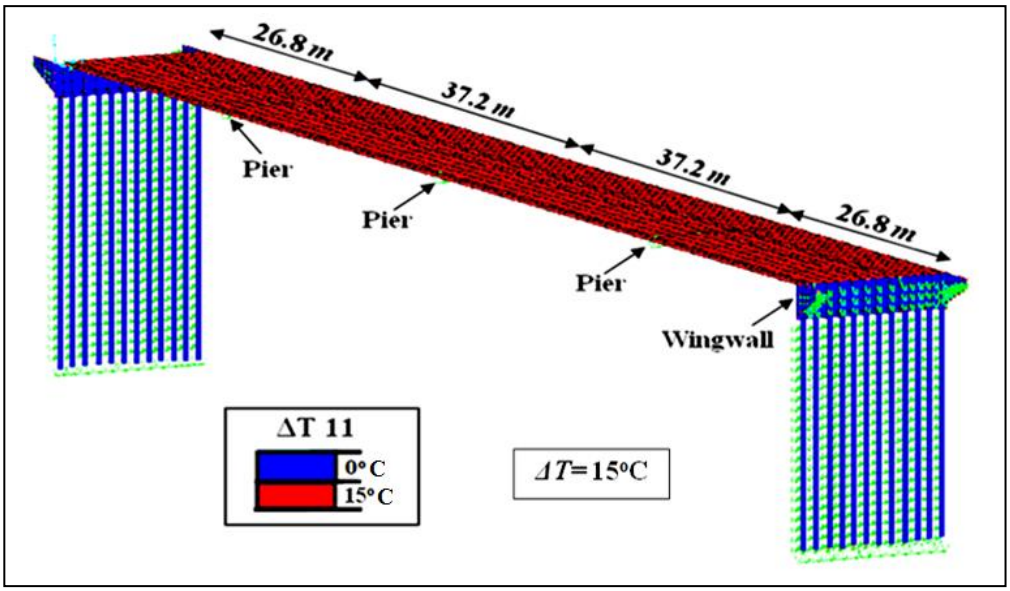

Figure 4.14: View of 3D FE model corresponded to temperature loading of +15°C.

Longitudinal displacements due to temperature change have been computed from numerical models. Figures 4.15 and 4.16 show the 3D FE views of longitudinal displacements (U_1) for the bridge corresponding to maximum temperature changes.

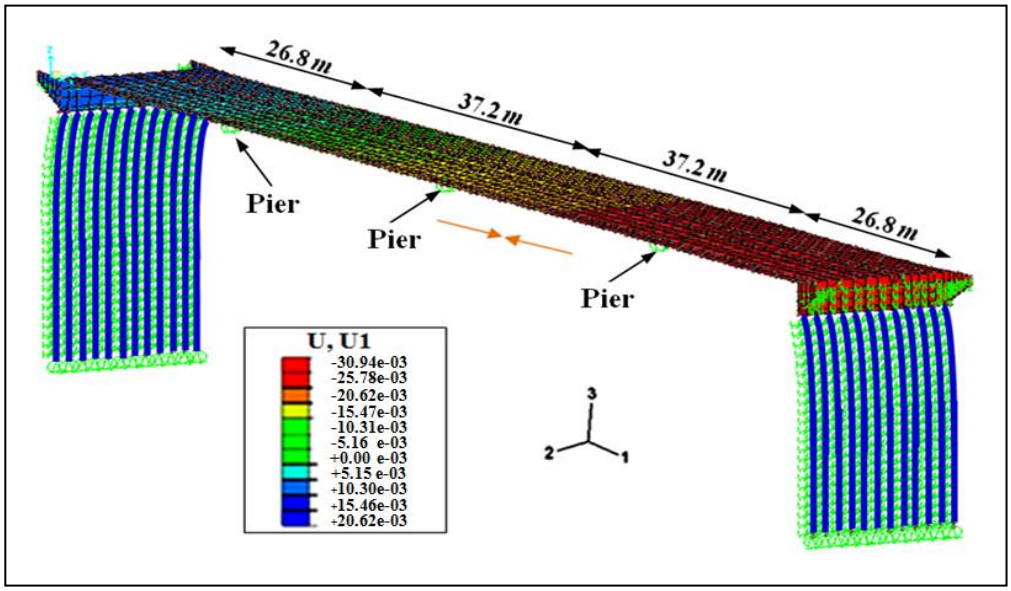

Figure 4.15: Bridge contraction due to temperature decrease of -42 ^{o}C.

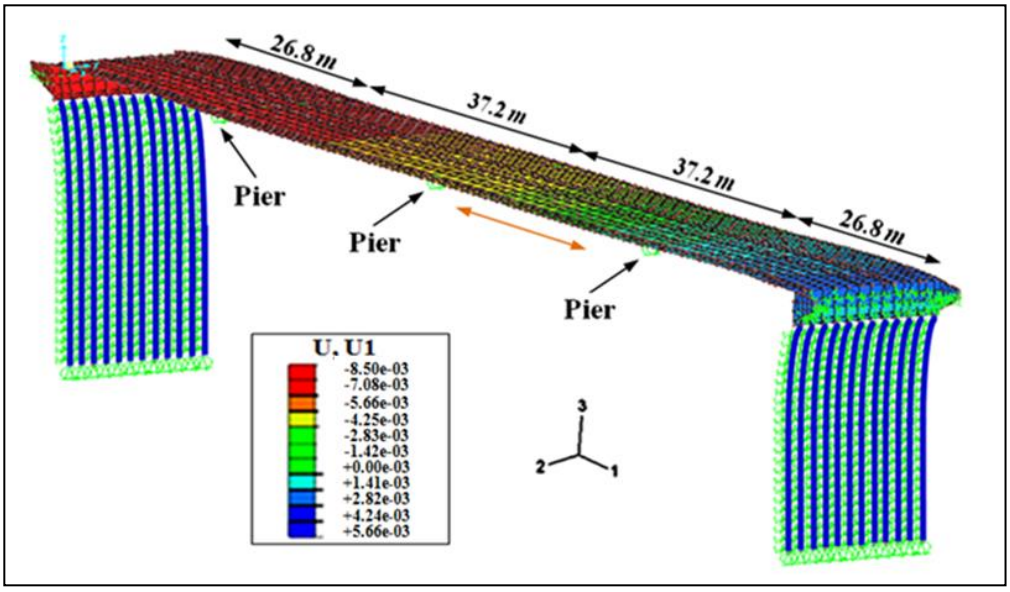

Figure 4.16: Bridge expansion due to temperature increase of +15^{o}C.

In order to determine the accuracy of finite element models for predicting bridge responses, predicted and measured abutment displacement ranges due to temperature change of [ΔT=+15°*C*-(-42°*C*) = +67°*C*] at extensometer locations were compared as shown in Table 4.2.

Table 4.2: Comparison between predicted and measured abutment displacements.

Abutment	Transducer Position	Abutment Displacement Range, (*mm*)			Difference between Field Data and FE Model, (%)	Difference between Field Data and Eq.(4.1), (%)
		Field Data [44]	FE Model	ΔL Eq. (4.1)		
South	Top	35.2	39.4	38.6	11	8
	Bottom	37.2	38.7	38.6	4	4
North	Top	49.1	54.0	38.6	10	27
	Bottom	51.5	52.5	38.6	2	34

Finite element results obtained during the validation process were close to those reported in field tests. For instance, predicted finite element model and field measured displacement ranges at bottom of south abutment due to temperature change were 38.7 and 37.2 *mm*, respectively, (an overestimation of only 4%).

Equation (4.1) was also used to determine the lateral displacement for the piles. For instance, when the superstructure was being loaded by a temperature differential of approximately $+67^{o}C$, pile displacement at each abutment was calculated as follow:

$$\Delta L = \alpha_{concrete} \frac{L}{2} \Delta T = (9 \times 10^{-6}) \left(\frac{128}{2}\ m\right) (67^{o}C) = 0.0386\ m = 38.6\ mm \qquad (4.1)$$

While Equation (4.1) predicted longitudinal displacement at south abutment within 8% error compared to the experimentally-measured displacements, it significantly underestimated longitudinal displacement at north abutment by about 34%. The difference between results obtained from equation and actual results was attributed to different properties of soil strata at south and north abutment. In calculating the displacement based on equation, the effect of soil resistance behind abutment and surrounding pile was neglected.

In addition to abutment displacement, Table 4.3 presents the measured and predicted FEA abutment rotation ranges on north abutment due temperature change of $+67°C$. The predicted FEA and measured field results for girder 1 were in good agreement (difference of around 5%), while abutment rotations derived from field data differed significantly from numerical model results for girder 3 (difference of about 37%).

Table 4.3: Comparison between predicted and measured abutment rotations.

Tiltmeter Locations	Abutment Rotation Range, (Degree)		Difference between FE Model and Field Data (%)
	Field Data [44]	FE Model	
Under Girder 1	0.12	0.11	9
Under Girder 3	0.07	0.11	37

Pile bending moments due to temperature change were also determined. Figures 4.17 and 4.18 show 3D FE views of pile moments corresponded to extreme temperature changes.

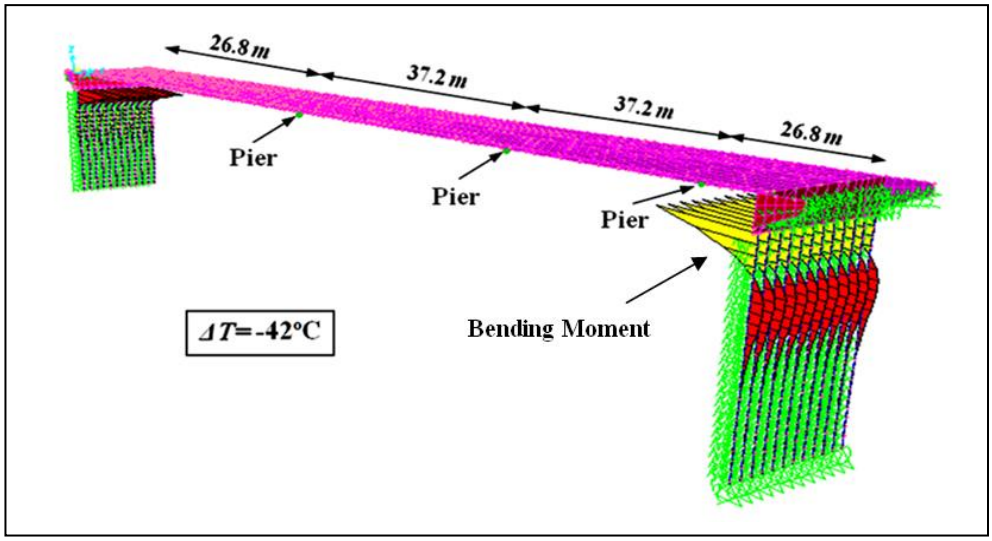

Figure 4.17: 3D FE views of pile bending moment under temperature decrease of -42°C.

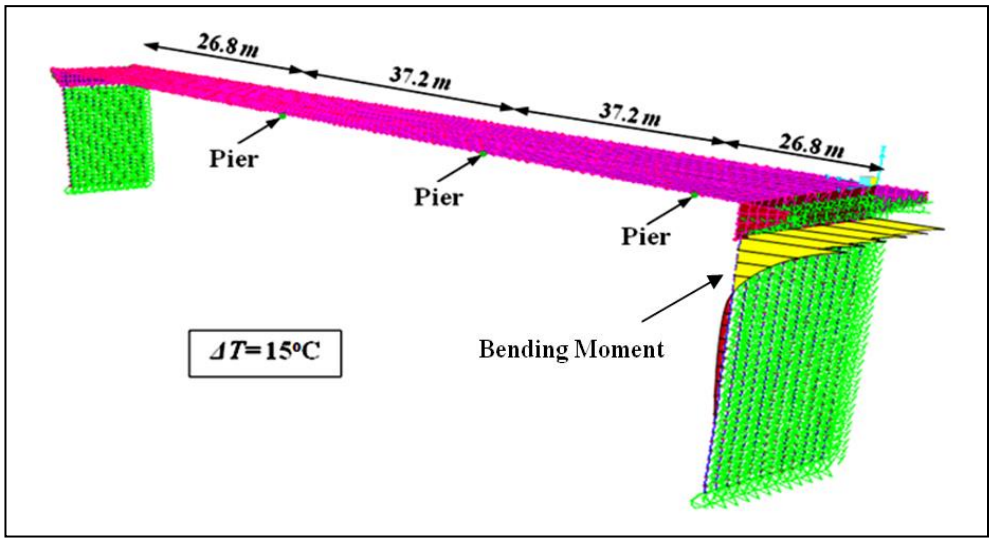

Figure 4.18: 3D FE views of pile bending moment under temperature increase of +15°C.

Figure 4.19 displays bending moments for the first 15 *m* of pile (B-1) under abutment obtained from finite element analysis due to different temperature loading. As shown in Table 4.4, comparison of the pile bending moments showed close agreement between experimental and computational results. For instance, it can be observed that the maximum pile bending moment value subjected to temperature change of $-42^{o}C$ at depth of 0.69 *m* from bottom of abutment obtained from finite element analysis was 68.62 *kN.m* and this value obtained from field testing was 64 *kN.m*, representing only 7% difference.

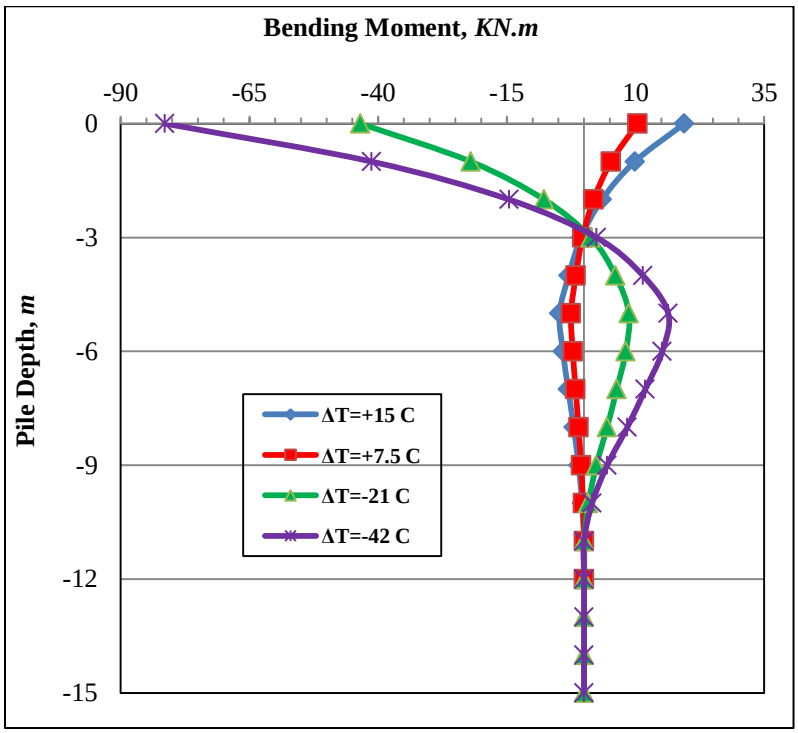

Figure 4.19: Pile bending moment obtained from FEM for bridge.

Table 4.4: Comparison between predicted and measured pile bending moments.

Depth Below Abutment, (*m*)	Pile Bending Moment, (*kN.m*)		Difference between FE Model and Field Data (%)
	Field Data [44]	FE Model	
0.69	64	68.62	7
2.82	15	16.55	10

4.1.1.2 WENDELL DEPOT BRIDGE

4.1.1.2.1 FIELD TESTING OF WENDELL DEPOT BRIDGE

4.1.1.2.1.1 BRIDGE DESCRIPTION

The integral abutment bridge is located on Wendell Depot Road in Massachusetts. The three-span bridge has a total length of 82.3 *m* and width of 9.8 *m*. As shown in Figure 4.20, the exterior spans are 24.4 *m* long and the interior span is 33.5 *m* long.

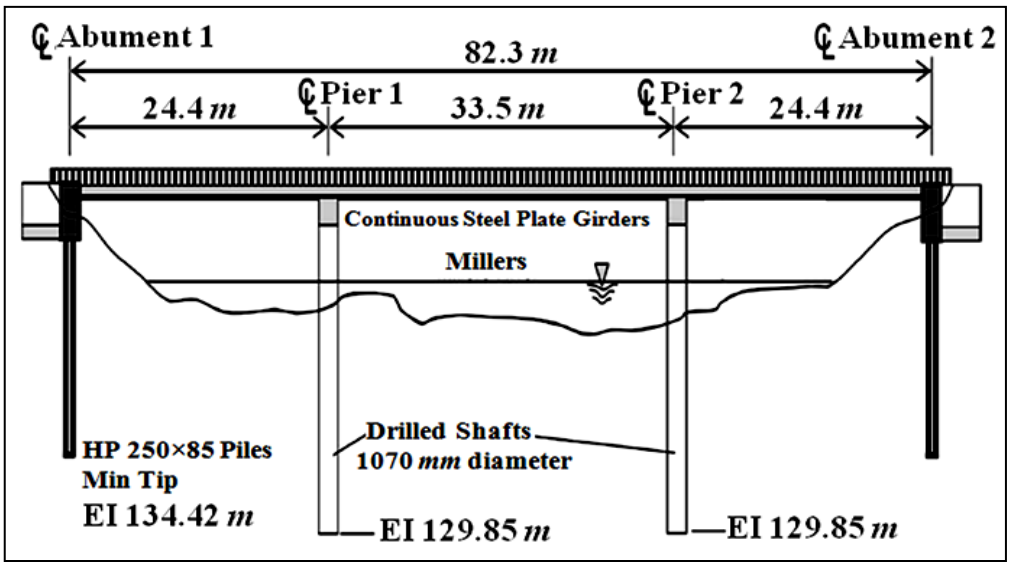

Figure 4.20: Bridge elevation [10].

The structure includes a 200 *mm* concrete deck supported on four 1220 m*m* steel plate girders. The girders are spaced every 2.64 *m* across the bridge starting at 0.91 *m* from each deck edge. A 1.62-*m* sidewalk is provided along the east side of the bridge deck. The steel girders are embedded into the abutment walls at both ends of the bridge and supported on elastomeric bearing pads on the two interior concrete bents. The bents consist of a bent cap 1.22 *m* wide by 1.07-*m* deep supported on three 1.07-*m* diameter concrete piers that extend approximately 13.7 *m* into the riverbed. Each abutment wall is supported on eight HP 250×85 steel piles equally spaced every 1.25 *m*. The piles are embedded 0.6 *m* into the bottom of the abutment and driven 18.3 *m* into the ground. Piles were driven in 3.0 *m* augered holes that were backfilled with uncrushed gravel after pile driving. Piles are oriented with their weak axis parallel to the transverse bridge axis to offer the least resistance to bending. That was done to provide maximum deformation

capacity to accommodate thermal displacements of the bridge. Approach slab detail is shown in Figure 4.21. Wing walls are perpendicular to the abutment and separated by an expansion joint.

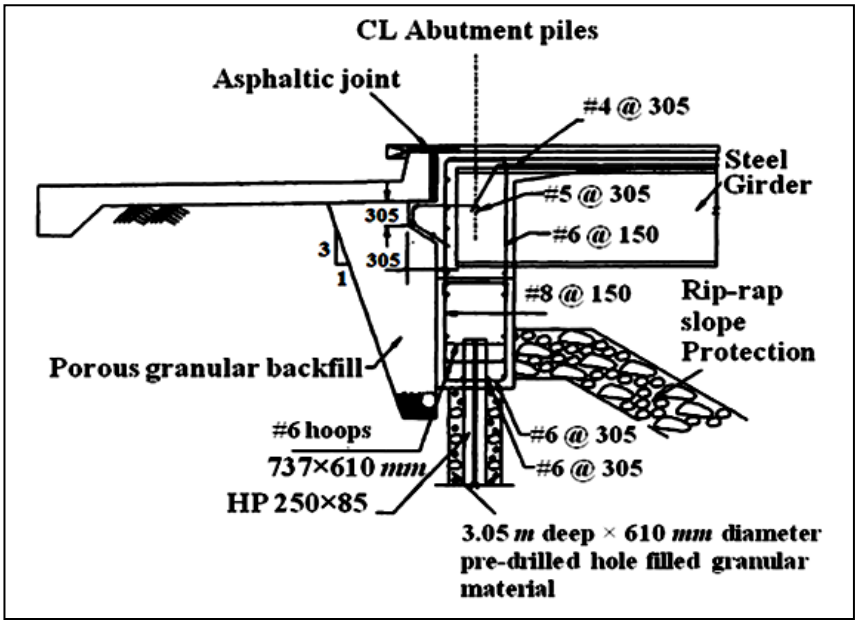

Figure 4.21: Abutment and approach slab details [10].

4.1.1.2.1.2 BRIDGE INSTRUMENTATION PLAN

Different types of gauges such as tiltmeters, temperature gauges, strain gauges and thermistors were installed in this bridge. Most instrumentation was concentrated near the abutment components (walls or piles) as shown in Figure 4.22 [10].

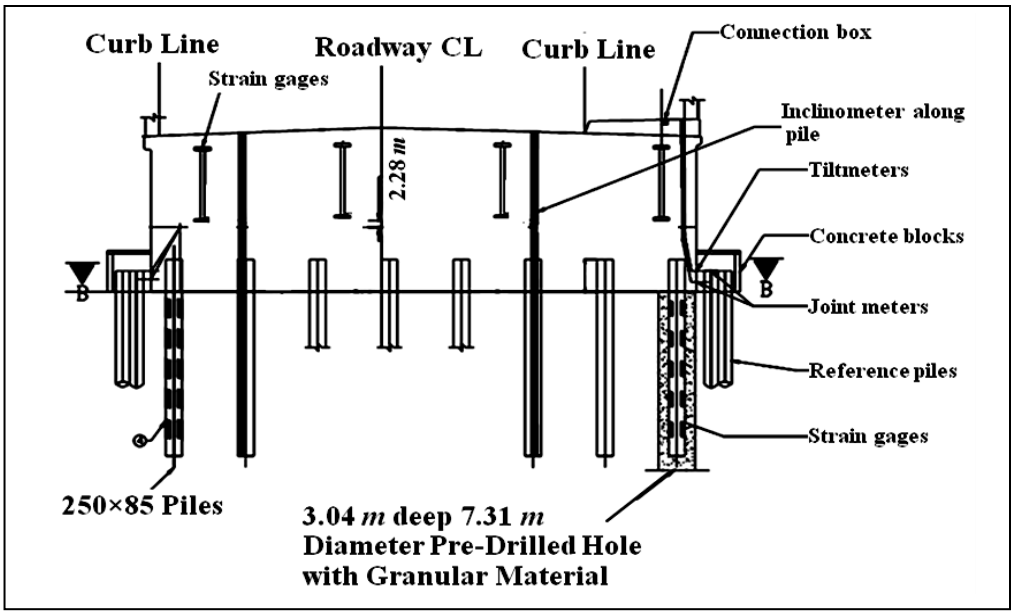

Figure 4.22: Abutment construction and instrumentation details [10].

Longitudinal (parallel to the traffic) displacements of the bridge were measured using joint meters on the east and west sides of each abutment. These instruments measured the displacement of abutment walls relative to reference piles located on each side of the bridge. Reference piles were offset laterally from the abutment to be negligibly influenced by abutment displacements. One tiltmeter was positioned at each end of both abutment walls to monitor rotation near the base of the walls. Vibrating wire strain gauges were attached to each flange of the two exterior H-piles supporting each abutment (Figure 4.22). These instruments were positioned in the upper portion of the piles at depths equal to 0.15, 0.76, 1.37, 1.98 and 2.59 *m* measured from the bottom of the abutments. Temperature gauges were located on the underside of the bridge deck at 3.0 *m* from the face of the abutments. These instruments provided readings of the temperatures occurring at each edge of the bridge deck.

4.1.1.2.1.3 BRIDGE MONITORING RESULTS

The response of the bridge was monitored for a period of three years, from January 2002 through December 2004. Bridge construction finished in late 2000 and initial instrument readings were taken at an average reference temperature of 19.1°*C* near the end of construction. Ambient temperature measured during the three years monitoring period was averaged from four temperature gauges located under the deck near the ends of the bridge (Figure 4.23). The average ambient temperature ranged between −23°*C* and +35°*C*.

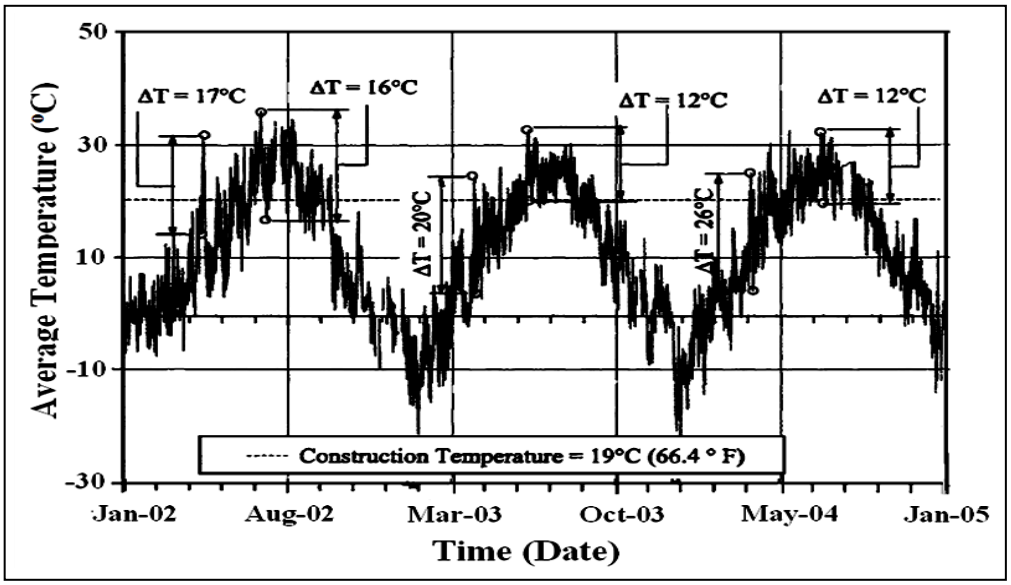

Figure 4.23: Measured temperature changes of Orange–Wendell (OW) Bridge [10].

Displacements of the bridge abutments were determined using joint meters and tiltmeters located at 0.30 and 0.61 *m* from the bottom of the abutment. Negative displacements and rotations correspond to bridge contraction induced by a temperature decrease. Joint meter data measured at the north and south abutments are plotted as a function of temperature change in Figure 4.24 and 4.25, respectively.

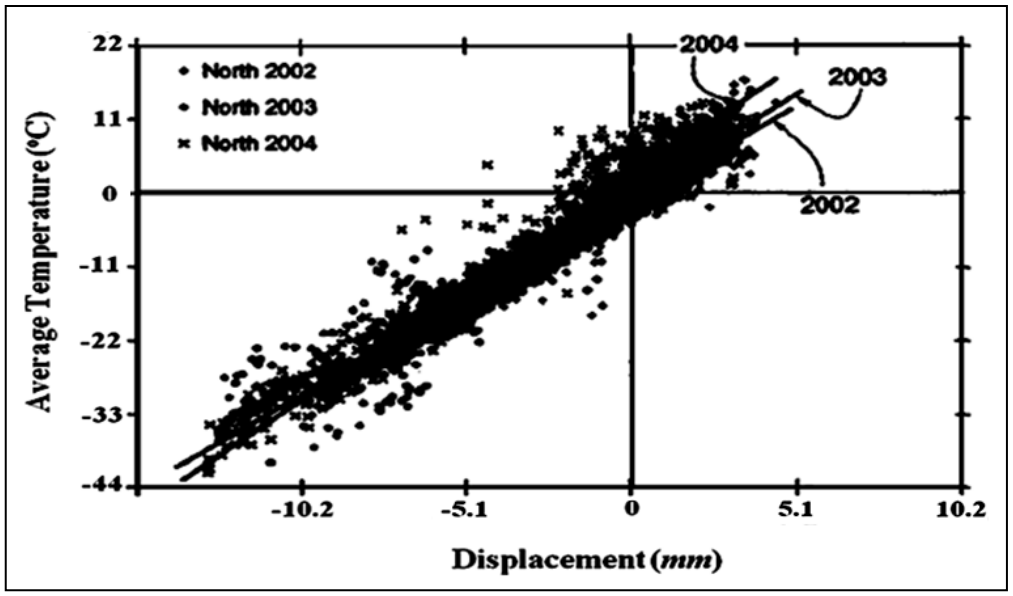

Figure 4.24: Measured displacements at joint meters in north abutments [10].

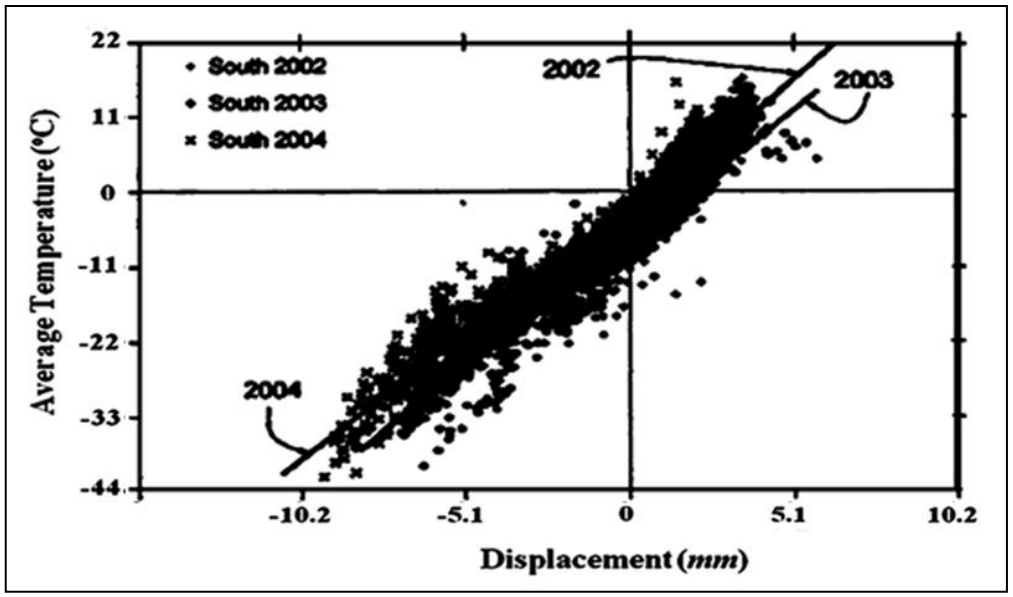

Figure 4.25: Measured displacements at joint meters in south abutments [10].

Tiltmeter data measuring abutment rotation at the north abutment from 2002 to 2004 is shown in Figure 4.26. For abutment rotation, the data trends did not exhibit marked changes in slope from year to year. Similar behaviour was observed from tiltmeter data in the south abutment.

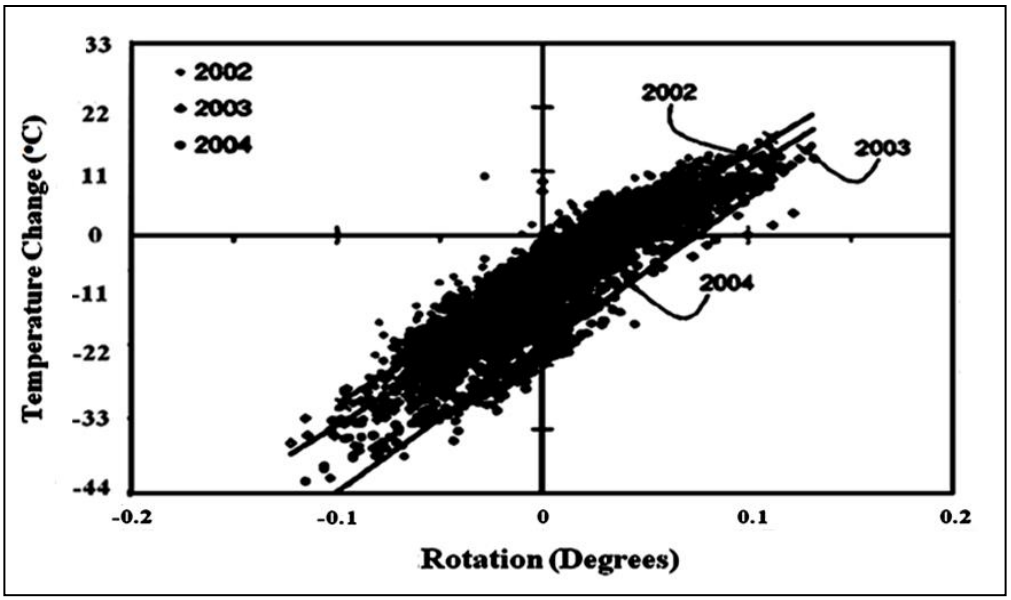

Figure 4.26: Measured rotation at north abutment [10].

Inclinometer casings were installed along the third interior pile from each side in each abutment as indicated in Figure 4.27. Inclinometer readings were taken on a biweekly basis for one year starting in summer 2003. Inclinometer readings taken at the northeast and southeast locations at selected dates are shown in Figures 4.27 and 4.28, respectively.

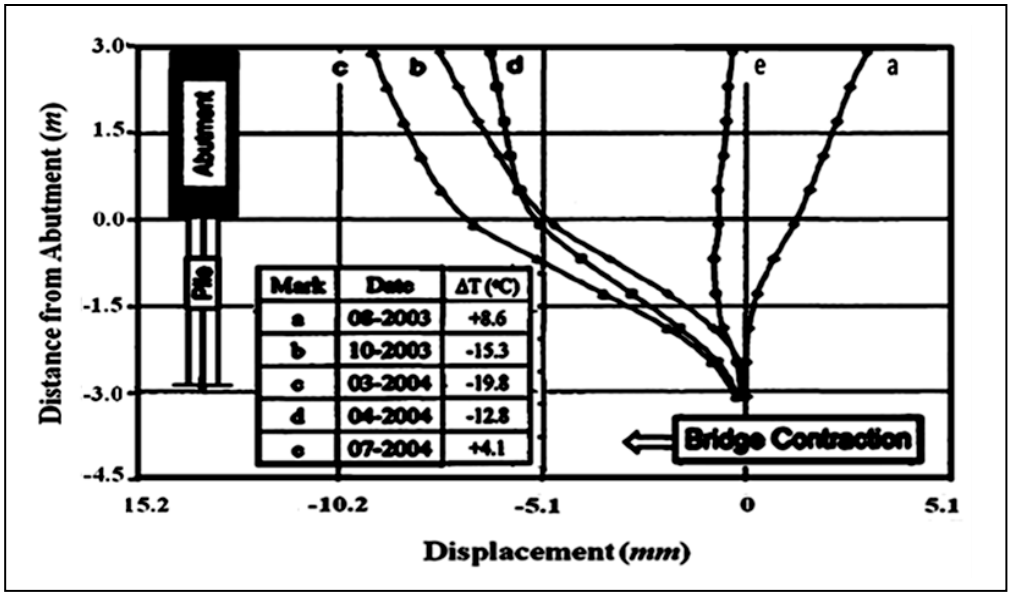

Figure 4.27: Inclinometer readings at northeast [10].

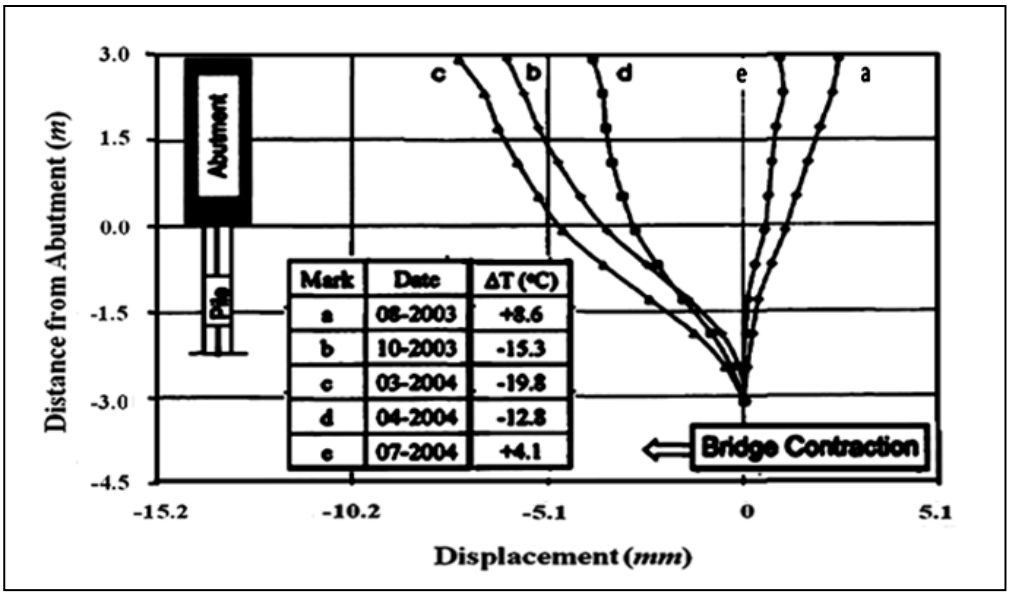

Figure 4.28: Inclinometer readings at southeast [10].

It was observed that H-piles exhibit double curvature deformation in their top region with a point of zero displacement approximately 3.1 *m* below the base of the abutments. Maximum bridge expansion was measured in August in both abutments at a temperature increase of +8.6°*C* and maximum contraction was measured in March at a temperature decrease of -19.8°*C*.

4.1.1.2.2 WENDELL DEPOT BRIDGE NUMERICAL MODELING

The refined 3D finite model of Wendell Depot Bridge consists of four spans was built as shown in Figure 4.29 and 4.30.

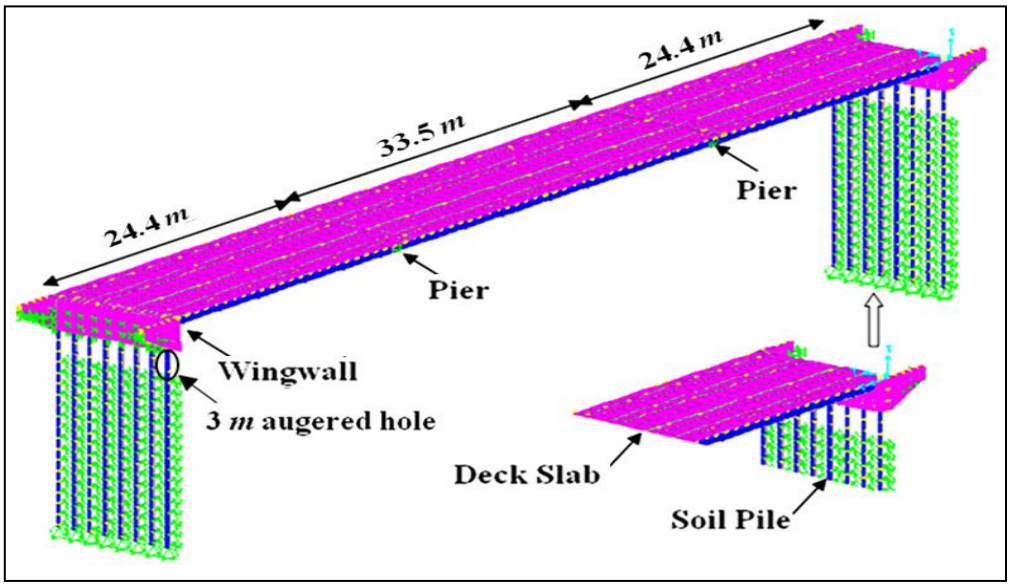

Figure 4.29: 3D finite element model view of Wendell Depot Bridge.

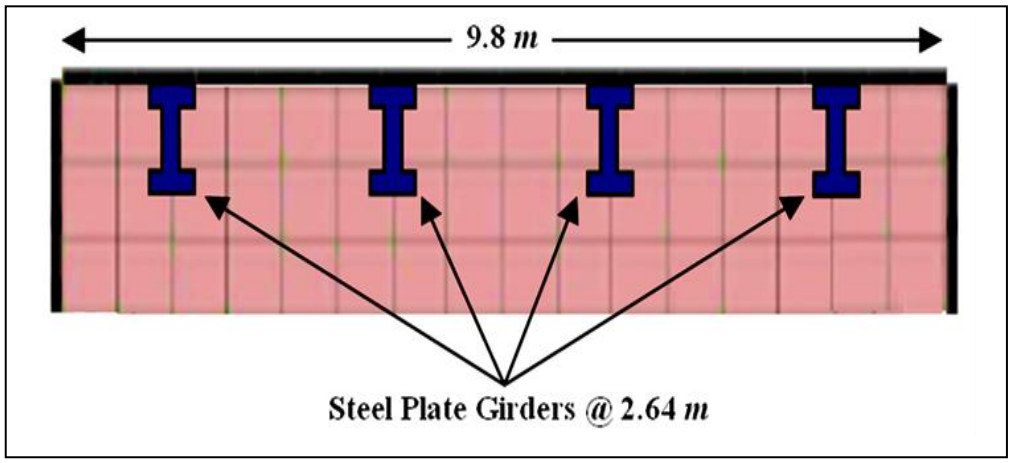

Figure 4.30: 3D finite element model view of bridge superstructure.

Shell elements were used to model steel girders, deck and abutments. Beam elements were used to simulate cross bracings and piles. Soil behind abutments and surrounding piles were modeled by multi-linear springs. Element material properties are presented in Table 4.5.

Table 4.5: Wendell Depot Bridge material properties [10].

Material	Young's Modulus (*MPa*)	Shear Modulus (*MPa*)	Poisson's Ratio	Thermal Expansion Coefficient ($mm/mm/^{o}C$)
Concrete	24,800	9,900	0.17	10.8×10^{-6}
Steel	200,000	75,800	0.3	11.7×10^{-6}

4.1.1.2.3 COMPARISON OF ANALYTICALLY-PREDICTED AND EXPERIMENTALLY-MEASURED RESULTS OF WENDELL DEPOT BRIDGE

In this section, results obtained from numerical modeling and field test were compared and discussed. For the purpose of accurate comparison, values of predicted and measured data were initialized with identical starting point established. This adjustment was required due to constraints on filed instrumentation imposed by construction sequences and schedules, which cannot be explicitly modeled.

Abutment movements that were caused by temperature changes were investigated using finite element models. Temperature variations considered for the bridge in the finite element modeling were identical to measured temperature variations from the field testing. Different temperature variations for finite element modeling were -44°*C*, -19.8°*C*, -11°*C*, +8.6°*C* and +22^{o}*C*. Figures

4.31 and 4.32 display nodal temperatures for the bridge during maximum temperature decrease and increase of -44°*C* and +22^{o}*C*. Longitudinal displacements due to temperature change were obtained from numerical models. Figures 4.33 and 4.34 show the longitudinal displacements for the bridge corresponding to highest temperature changes.

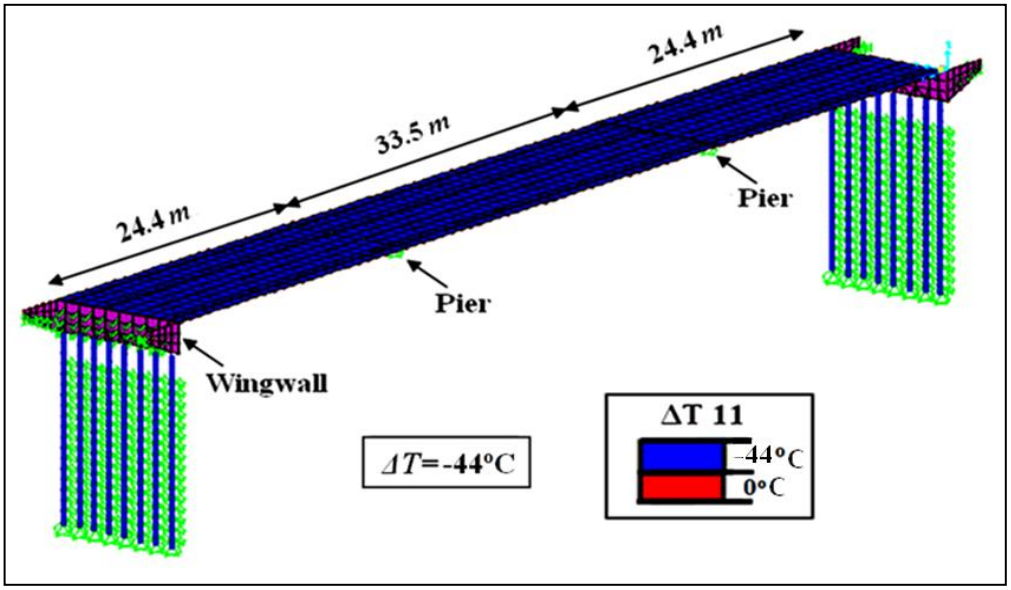

Figure 4.31: View of 3D FE model corresponded to temperature loading of -44^{o}C.

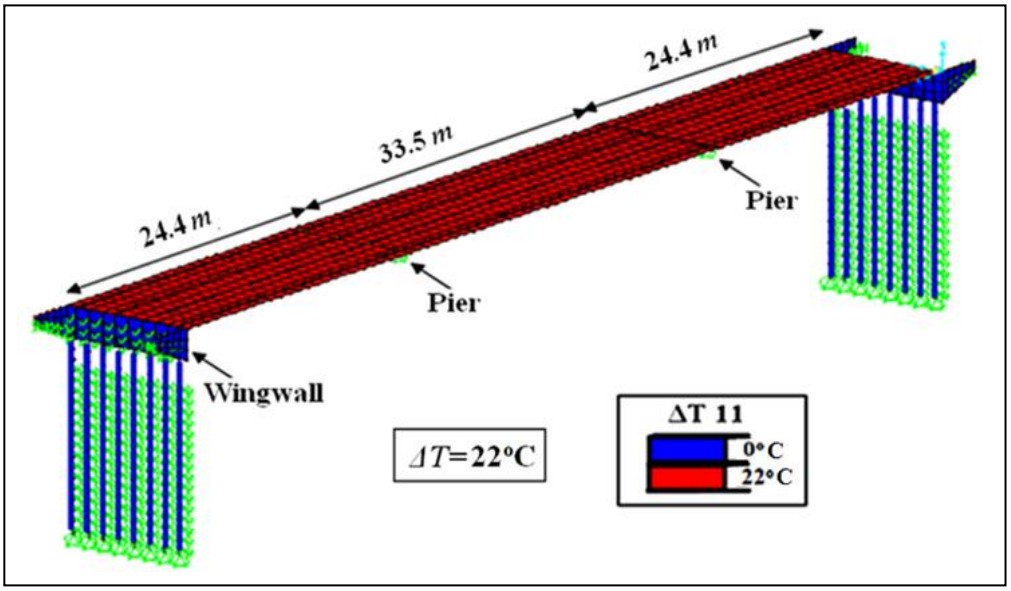

Figure 4.32: View of 3D FE model corresponded to temperature loading of +22^{o}C.

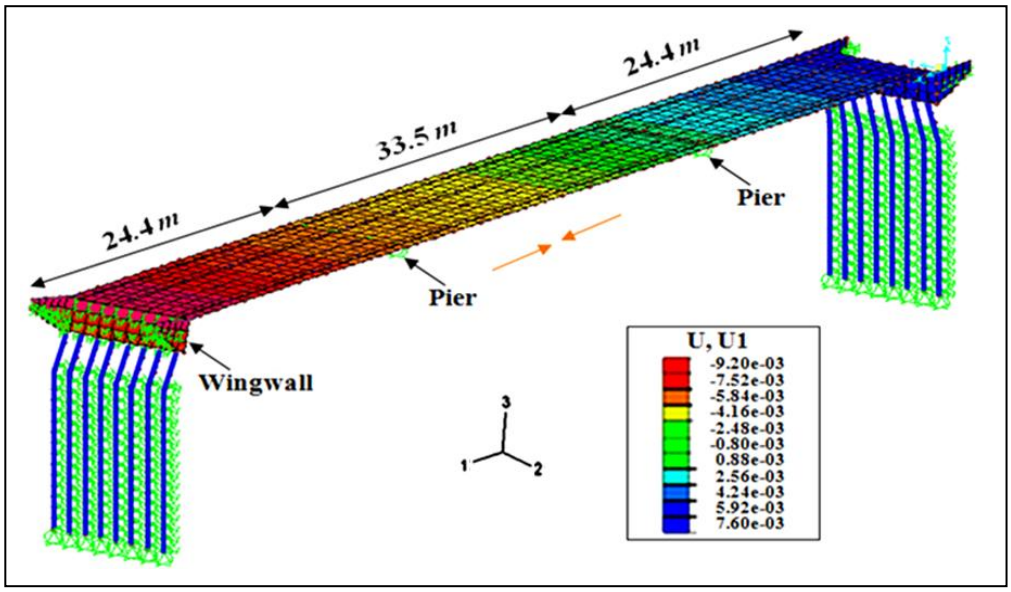

Figure 4.33: Bridge contraction due to temperature decrease of -44 °C.

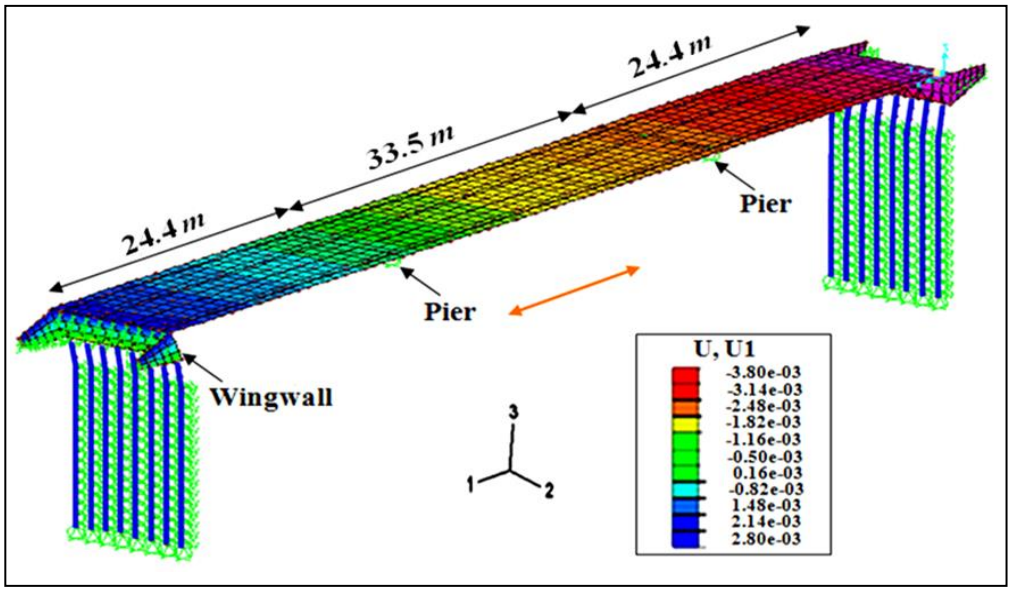

Figure 4.34: Bridge expansion due to temperature increase of +22 °C.

To examine the precision of the finite element models, as shown in Figure 4.35 and 4.36, predicted and measured longitudinal displacement at join meter of north and south abutments for different temperature variations were compared.

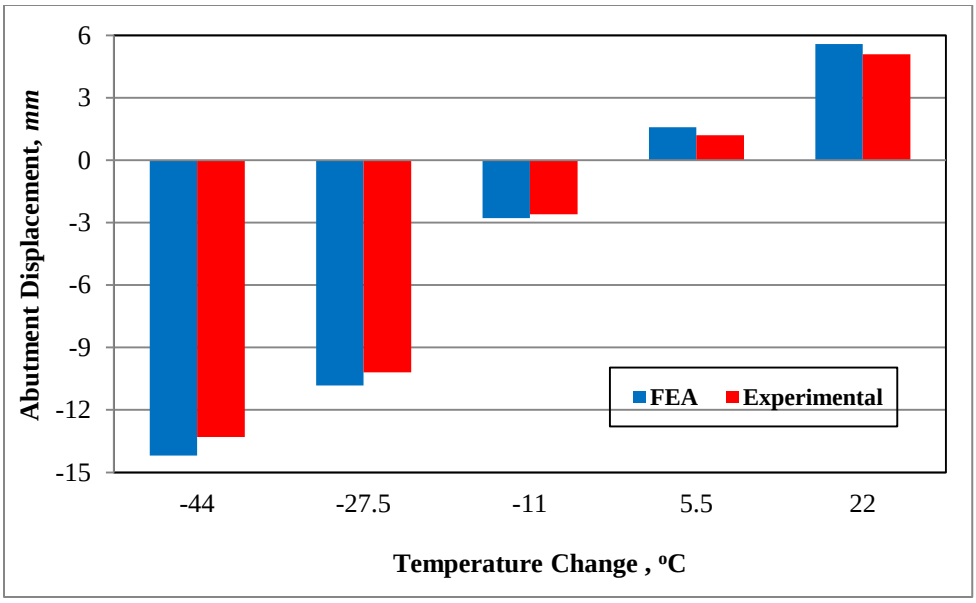

Figure 4.35: Measured and predicted displacement of north abutment.

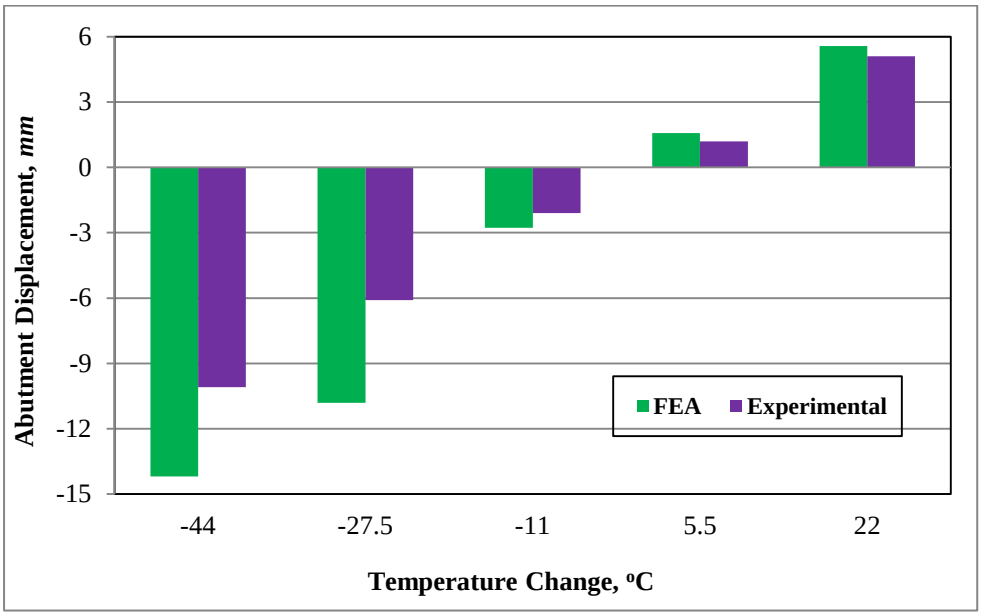

Figure 4.36: Measured and predicted displacement of south abutment.

Predicted FEA results for longitudinal abutment displacements showed a similar trend as field test results. The only observed difference was that the finite element model predicted symmetric response of the two abutments. However, significant difference was measured in experimental results for longitudinal displacements at north and south abutments. As an example, numerical model predicted the contraction of -14.2 *mm* for both abutments due to temperature change of -

44^oC whereas measured displacements in the field monitoring change for north and south abutments were -13.3 and -10.1 *mm* due to the same temperature. The observed differences as reported elsewhere Bonczar et al. [10], may be attributed to unequal backfill conditions, possibly compounded by thermal differences due to unequal solar heating at abutments.

In addition to abutment displacement, predicted and measured results of abutment rotation versus temperature change are depicted in Figure 4.37. It can be observed that the numerical model predicted well the abutment rotation during temperature increase and decrease. It is also observed that abutment rotations for the same temperature change were significantly higher during temperature increase compared to temperature decrease. For instance, the abutment rotations were -0.05 and 0.1 degrees for temperature change of $-20°C$ and $+20^oC$.

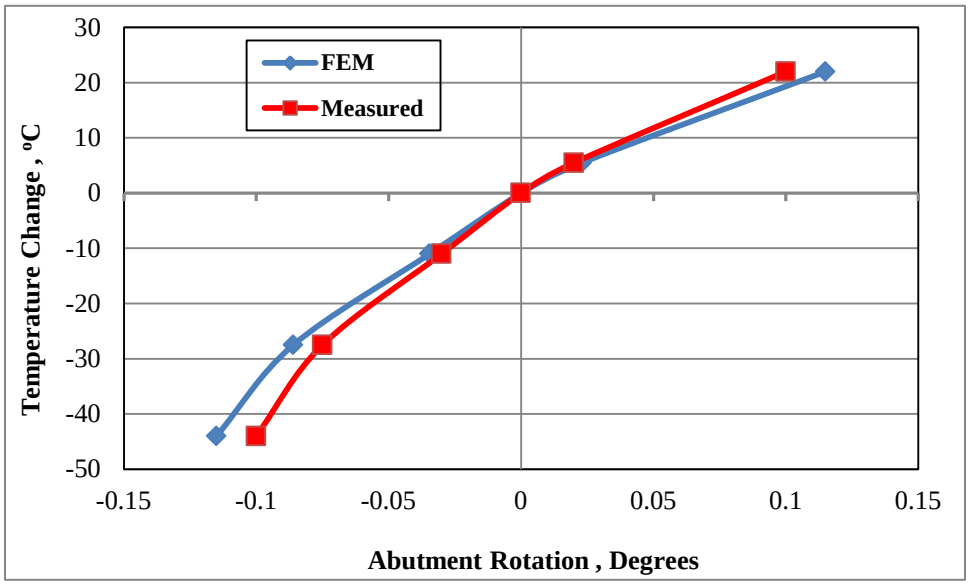

Figure 4.37: Measured and predicted north abutment rotation versus temperature.

Figure 4.38 and 4.39 include north and south abutment/pile deformations results obtained from FEA model for specific temperature changes. Those figures also include inclinometer field data for selected temperature differentials. As shown in Figure 4.38, FEA results for northeast abutment/pile deformation were consistent with experimental results. It is noted that when bridge expansion and contraction occurred the differences between predicted FEA and experimental results for northeast abutment were limited to 10%.

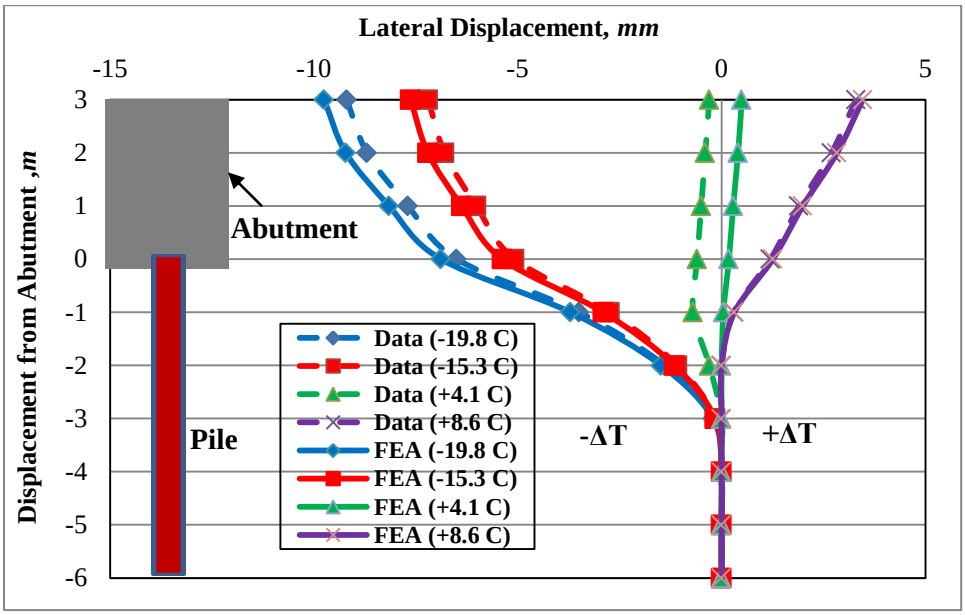

Figure 4.38: Comparison of FEM and measured deformation of northeast abutment/pile.

Figure 4.39 depicts that southeast abutment/pile deformations were overestimated by finite element model. This observation was especially true during temperature decrease. For example, predicted and measured displacements for temperature decrease of -19.8^{o}C were -9.7 and -6.8 *mm* (an overestimation of 42%).

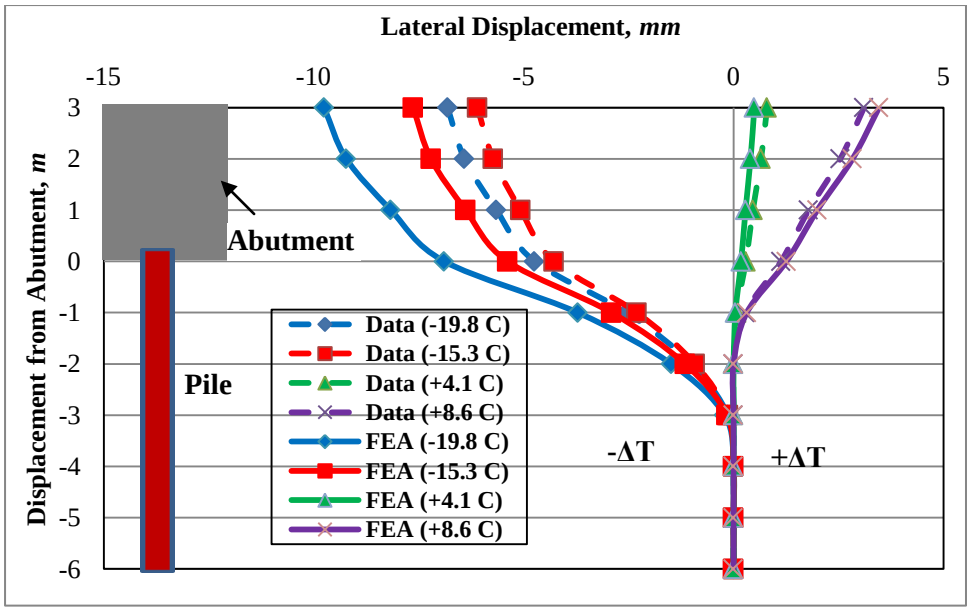

Figure 4.39: Comparison of FEM and measured deformation of southeast abutment/pile.

4.1.1.3 BRIDGE 203

4.1.1.3.1 FIELD TESTING OF BRIDGE 203

4.1.1.3.1.1 BRIDGE DESCRIPTION

The monitored integral abutment bridge is a three-span, composite structure with four AASHTO Type I-Beam with bearing on reinforced concrete piers and abutments with spans of 14.3, 26.8 and 11.3 *m* (see Figures 4.40). The girders were cast during March 2002 and are spaced at 3.59 *m*, cast integrally with abutments and supported a 230-*mm* concrete deck [44].

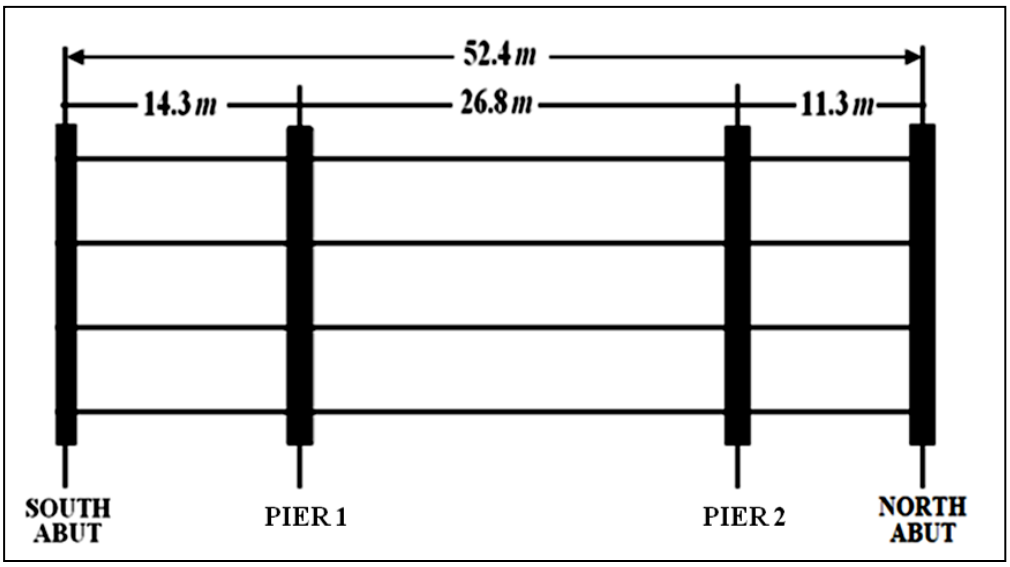

Figure 4.40: Plan view of bridge [44].

Piers are designed as semi-rigid self-supporting, substructures with 70-*mm* elastomeric bearing pads that allow longitudinal movement of the superstructure. The south abutment and south girder ends are fixed against translation and rotation (no expansion joint) and the abutment bears directly on rock. The north abutment is a standard Pennsylvania Department of Transportation (PennDOT) integral abutment, 4.4 *m* average height from bottom of abutment to bottom of girder. The abutment is supported by a single row of eight HP 310×110 piles with weak axis orientation, embedded 0.61 *m* into the abutment, and driven to refusal as shown in the cross sections of Figure 4.41. Reinforced concrete approach slabs, 7.62 *m* long by 0.46 *m* thick, are constructed at both ends of the bridge. A 0.05 *m* thick extruded polystyrene insulation sheet separates the abutment from the wing walls to isolate component movements.

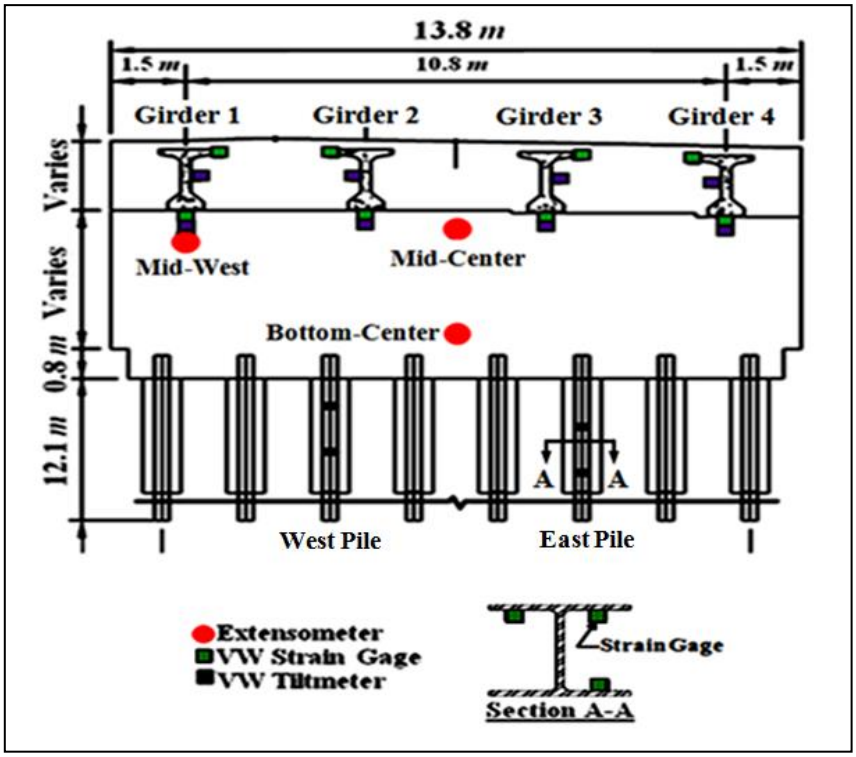

Figure 4.41: Instrumentation plan of north abutment elevation view [44].

The integral abutments of the bridge is backed with 25 *mm* foam board and are supported by a single row of weak axis oriented steel piles as shown in the cross section of Figure 4.42.

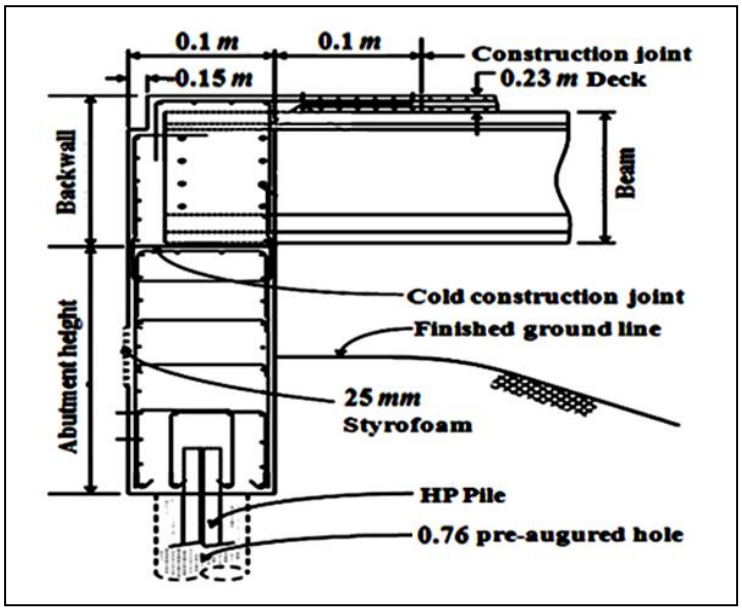

Figure 4.42: Typical abutment section for bridge [44].

North abutment piles were driven in a 3.05 *m* deep predrilled hole. Loose sand was placed in each predrilled hole prior to driving, however, the sand was compacted significantly during pile driving. The top 1.2 to 1.5 *m* of the predrilled hole was filled with loose sand at each location at the completion of pile driving. Derived engineering properties of soil strata around supporting piles at north abutment appear in Figure 4.43.

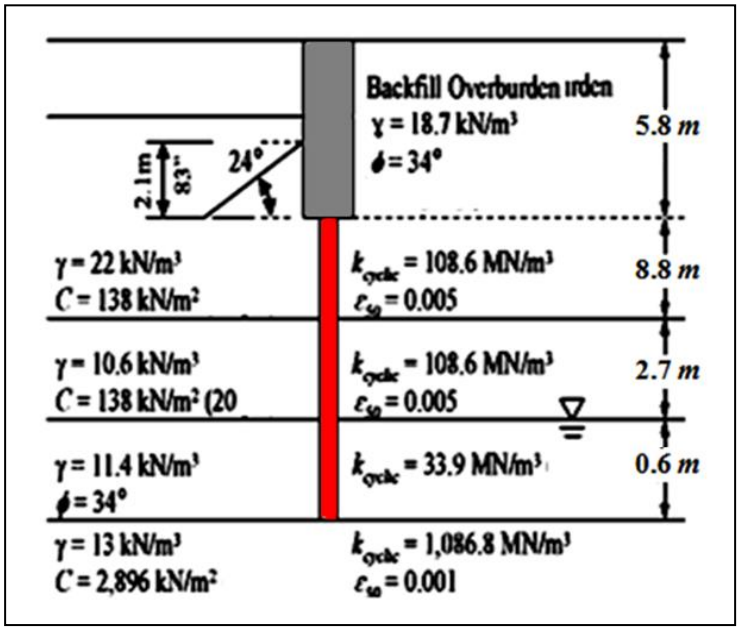

Figure 4.43: Soil properties under north abutment [44].

4.1.1.3.1.2 BRIDGE INSTRUMENTATION PLAN

A weather station was constructed to monitor environmental conditions. Instrumentation plan of Bridge 203 was similar to Bridge 109. Electronic transducers were attached to the bridge to monitor strains, displacements and relative tilting angles. Vibrating wire-based instruments consisted of extensometers, strain gauges and tiltmeters.

4.1.1.3.1.3 BRIDGE MONITORING RESULTS

Ambient air temperature for Bridge 203 was similar to Bridge 109 (see Figure 4.6). Abutment displacement measurements at the bridge are presented in Figure 4.44. Traffic open date of bridge is also presented in the figure. The top extensometers measured a wide displacement range as compared with the bottom extensometers.

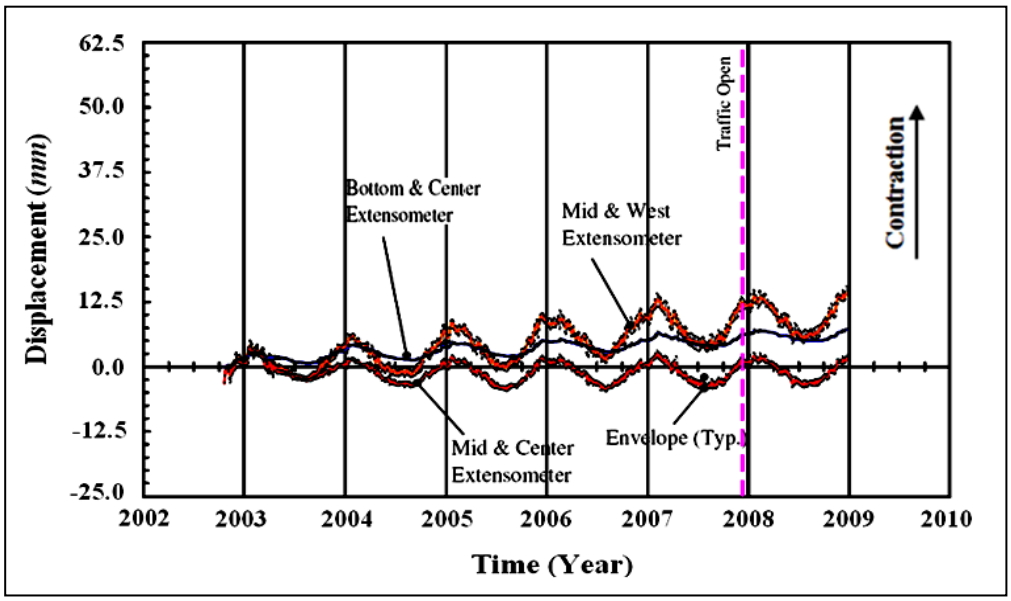

Figure 4.44: North abutment top and bottom displacement [44].

Measured abutment and girder rotations are illustrated in Figure 4.45 and 4.46, respectively. The rotation at interior girders or the abutment is consistent with rotations calculated from displacement measurements. However, exterior girder tiltmeter rotation tends to vary within a narrow range. This result is dependent on bridge geometry and boundary conditions. Generally, abutment rotations were less than girder rotations. Relatively short abutments of Bridge 109 compared with tall abutment of Bridge 203 caused smaller abutment rotations.

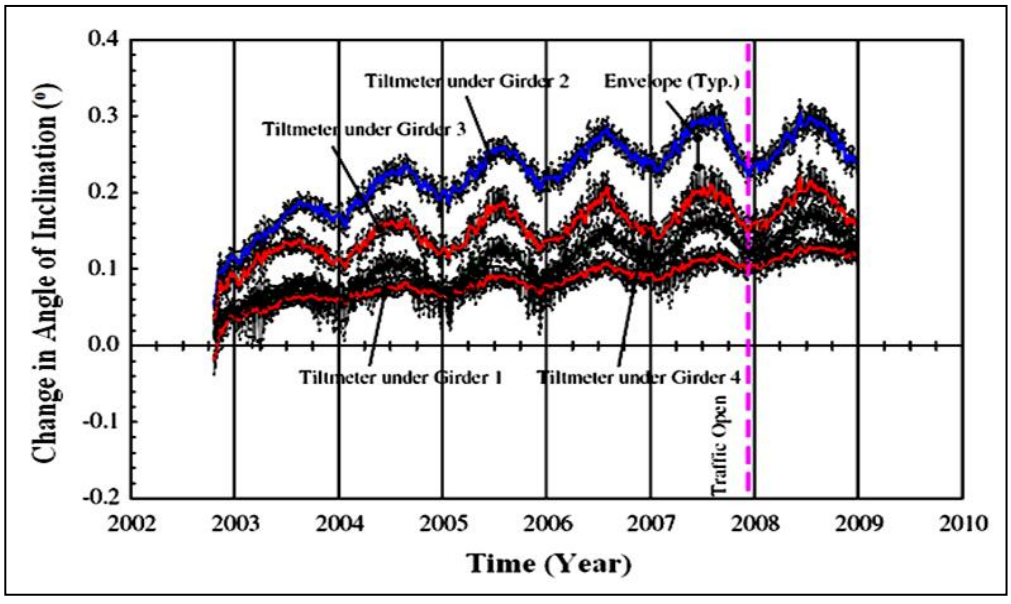

Figure 4.45: Abutment rotations by tiltmeters on north abutment [44].

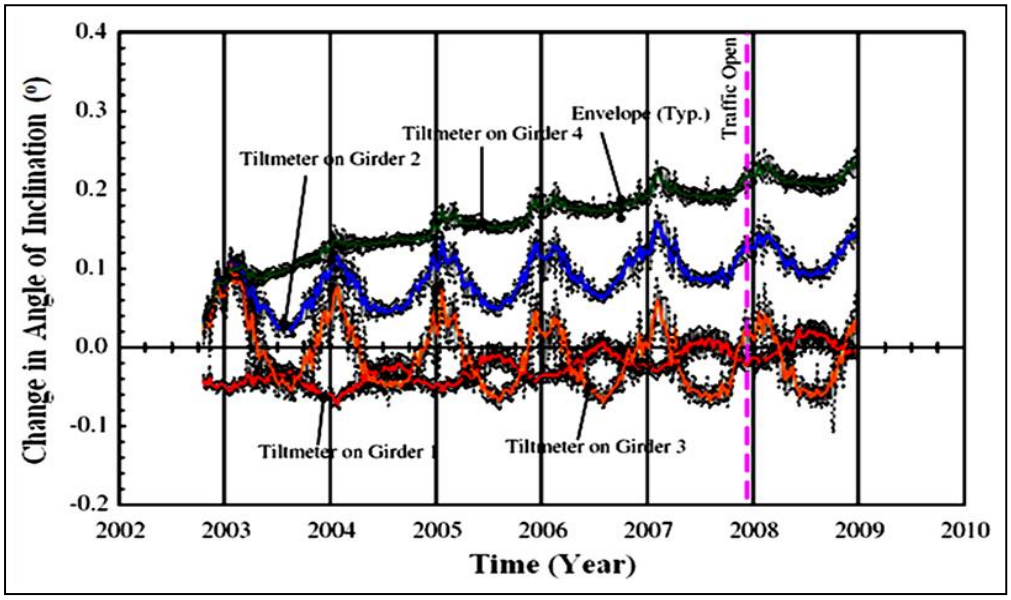

Figure 4.46: Girder rotations by tiltmeters near north abutment [44].

Bending moments for east and west piles derived from strain measurements are presented in Figure 4.47. Pile moments are generally below the section bending capacity. Moments at the bottom strain gauges are generally smaller attributable to proximity to the point of fixity.

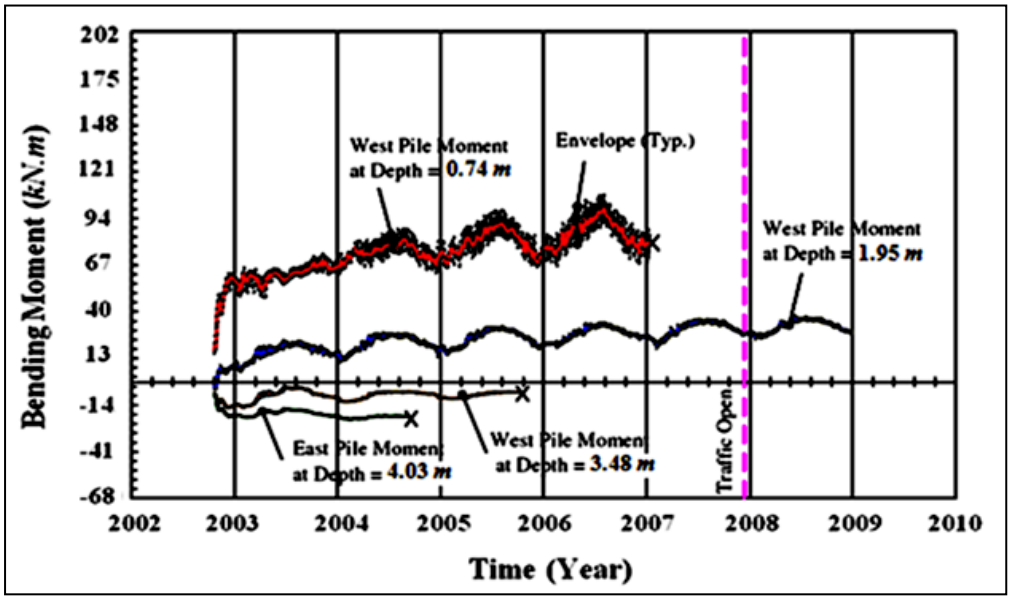

Figure 4.47: Pile moments under north abutment [44].

4.1.1.3.2 BRIDGE 203 NUMERICAL MODELING

The numerical model developed for Bridge 203 (see Figure 4.48) follows the same element scheme as Bridge 109. Detail of bridge superstructure modeling is shown in Figure 4.48. Bridge 203 is unique among bridges in that south abutment is supported on rock and north abutment is supported on piles. Reflecting the actual construction, south abutment foundation element boundary conditions consist of restrained translation, effectively fixing the abutment bottom against all rotations and translations. North abutment is modeled in the same manner as the abutments for Bridge 109.

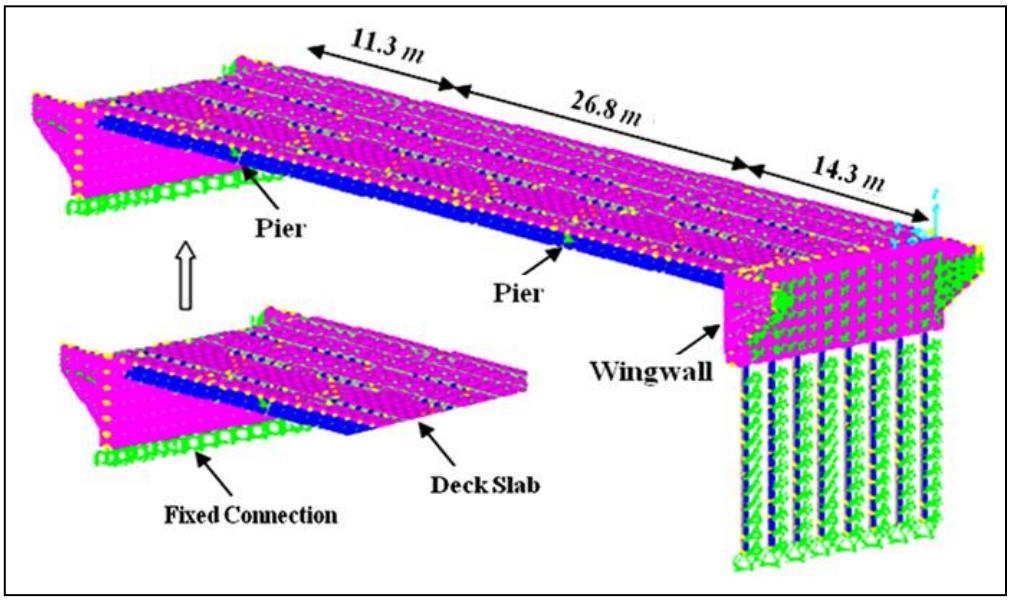

Figure 4.48: 3D finite element model view of Bridge 203.

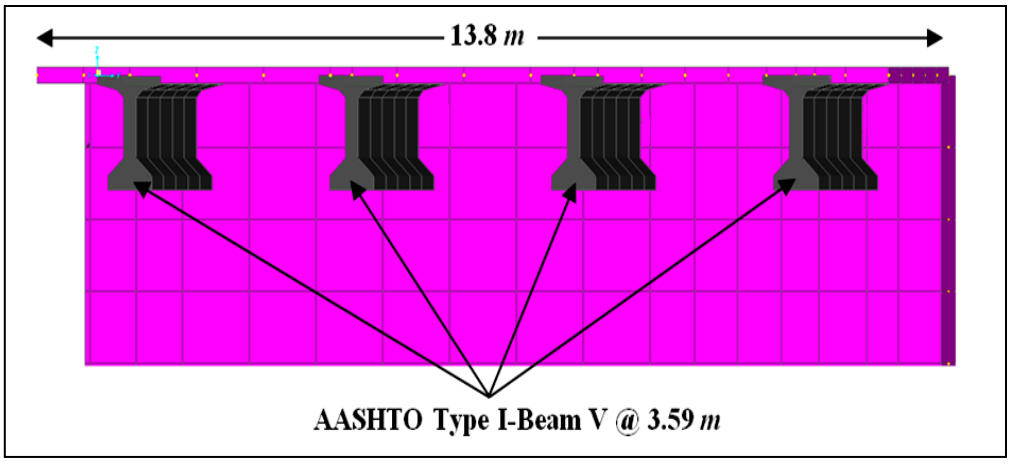

Figure 4.49: 3D finite element model view of bridge superstructure.

4.1.1.3.3 COMPARISON OF ANALYTICALLY-PREDICTED AND EXPERIMENTALLY-MEASURED RESULTS OF BRIDGE 203

Two different temperature variations considered for finite element modeling were -42°*C* and +15°*C*. Figures 4.50 and 4.51 display nodal temperatures for the bridge during maximum temperature decrease and increase, respectively. Figures 4.52 and 4.53 show the longitudinal displacements corresponding to those temperature changes.

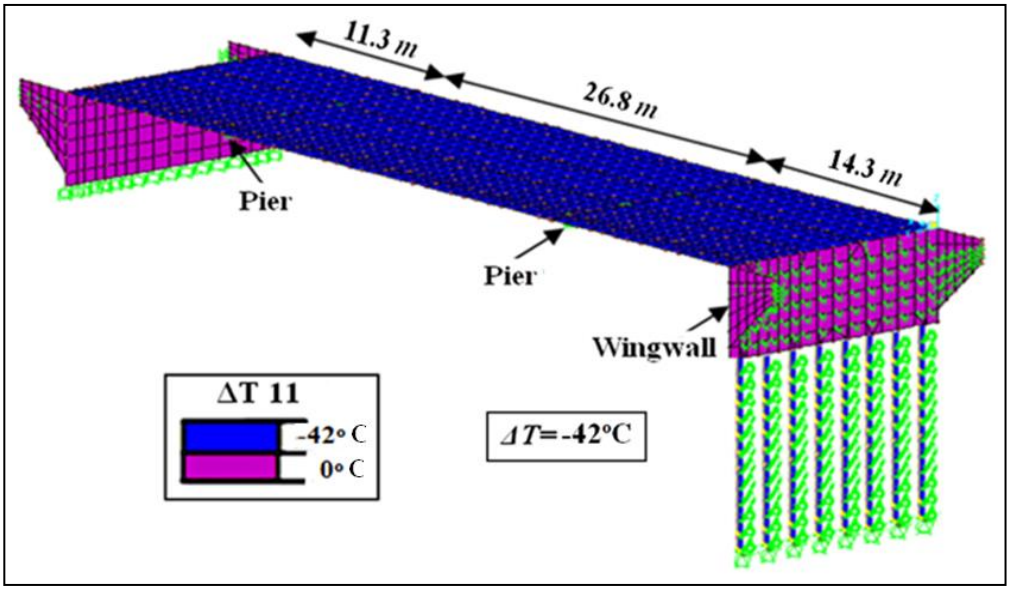

Figure 4.50: View of 3D FE model corresponded to temperature loading of -42°C.

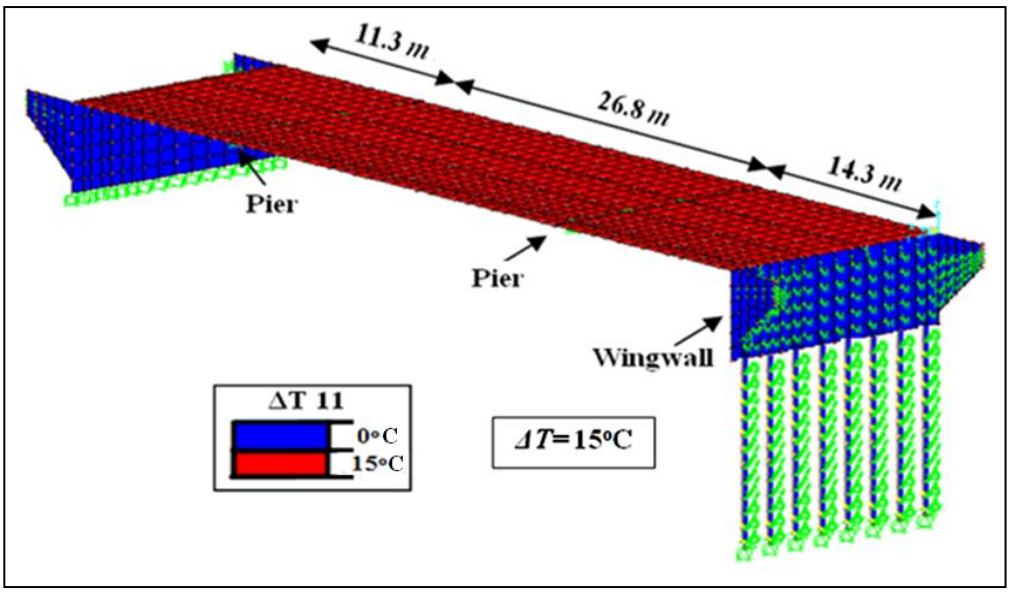

Figure 4.51: View of 3D FE model corresponded to temperature loading of +15°C.

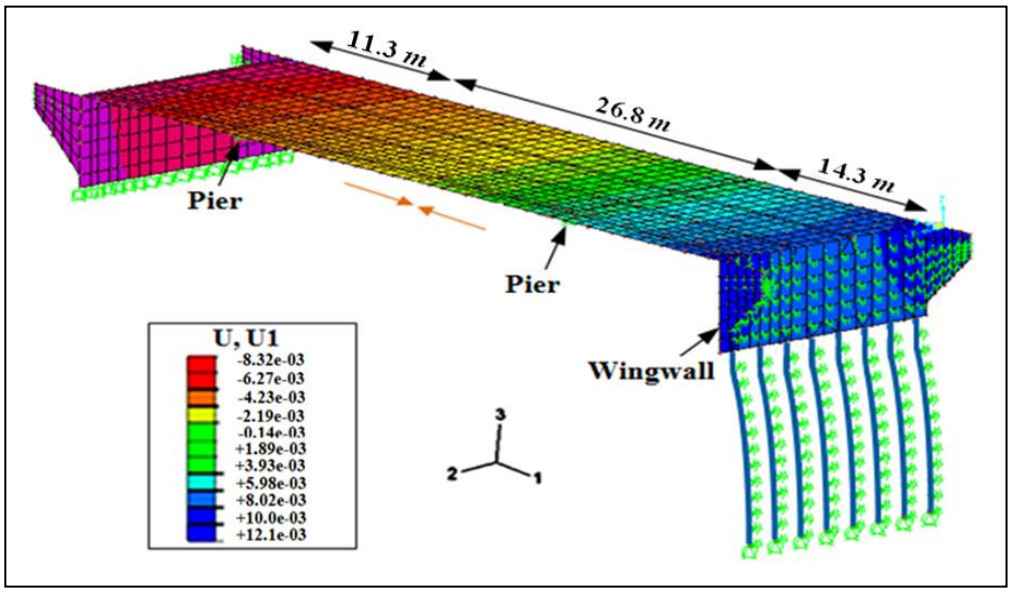

Figure 4.52: Bridge contraction due to temperature decrease of -42 ^{o}C.

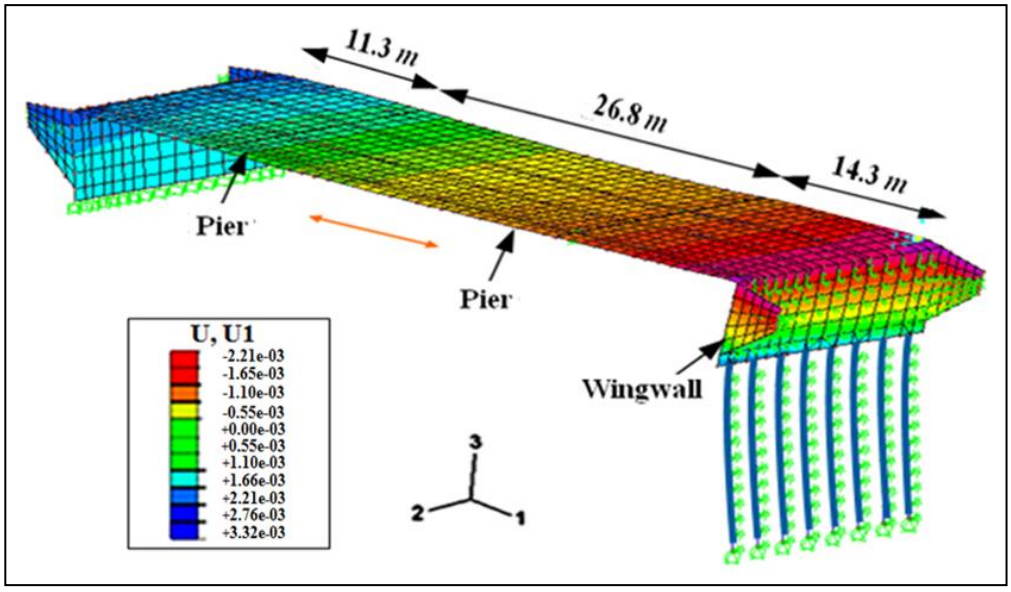

Figure 4.53: Bridge expansion due to temperature increase of +15 ^{o}C.

The displacement ranges obtained from numerical models and measured field responses due to temperature change of 67^{o}C at equivalent location of extensometers are shown in Table 4.6. The numerical model predicted displacements very well at mid-west and bottom-center locations (Overestimation of around 11 and 17%, respectively). Contrary to mid-west and bottom-center locations, large discrepancy was observed between numerical results and field test at mid-center location (Overestimation of around 122%). This difference may be attributed to the limited field

data and the necessity to extrapolate field data to the maximum and minimum design temperature ranges. Table 4.6 also demonstrates that finite element modeling predicted the abutment displacement range of 13.3 *mm* at the mid-west location, while Equation (4.1) predicted 15.8 *mm* at the same location (an overestimation of around 11 and 31% compared to measured displacement). This indicates that the 3D finite element modeling provided more accurate and reliable results for abutment displacement compared to predicted displacement obtained from equations.

Table 4.6: Comparison between predicted and measured abutment displacements.

Transducer Position	**Abutment Displacement Range, (*mm*)**			**Difference between Field Data and FE Model, (%)**	**Difference between Field Data and Eq.(4.1) (%)**
	Field Data [44]	**FE Model**	**ΔL Eq. (4.1)**		
Mid-Center	6	13.3	15.8	122	163
Mid-West	12	13.3	15.8	11	31
Bottom-Center	8	9.4	15.8	17	97

Table 4.7 presents predicted FE and measured abutment and girder rotations of the bridge. The numerical model predictions seemed to exhibit almost similar girder and abutment rotations. The predicted girder and abutment rotations at girder 2 and 3 of the north abutment were within 12% of the experimentally-measured rotations at those locations.

Table 4.7: Comparison between predicted and measured rotations on north abutment.

Segment	**Tiltmeter Location**	**Rotation Range, (Degree)**		**Difference between FE Model and Field Data (%)**
		Field Data [44]	**FE Model**	
Abutment	**Under Girder 2**	0.2	0.18	11
	Under Girder 3	0.16	0.18	12
Girder	**On Girder 2**	0.16	0.16	0
	On Girder 3	0.15	0.16	6

Bending moment for west pile subjected to temperature variations was determined using the finite element method (FEM). Figures 4.54 shows the pile bending moments obtained from FEM for specific temperature changes. It is clear from Table 4.8 that a good agreement was achieved between computational and experimental results for bending moments of west pile. As an example, predicted pile bending moment value subjected to temperature decrease of $-42^{o}C$ at depth of 1.95 *m* from the bottom of abutment was 8.3 *kN.m* while the measured pile bending moment value at the same location was 8 *kN.m* (only 3% difference).

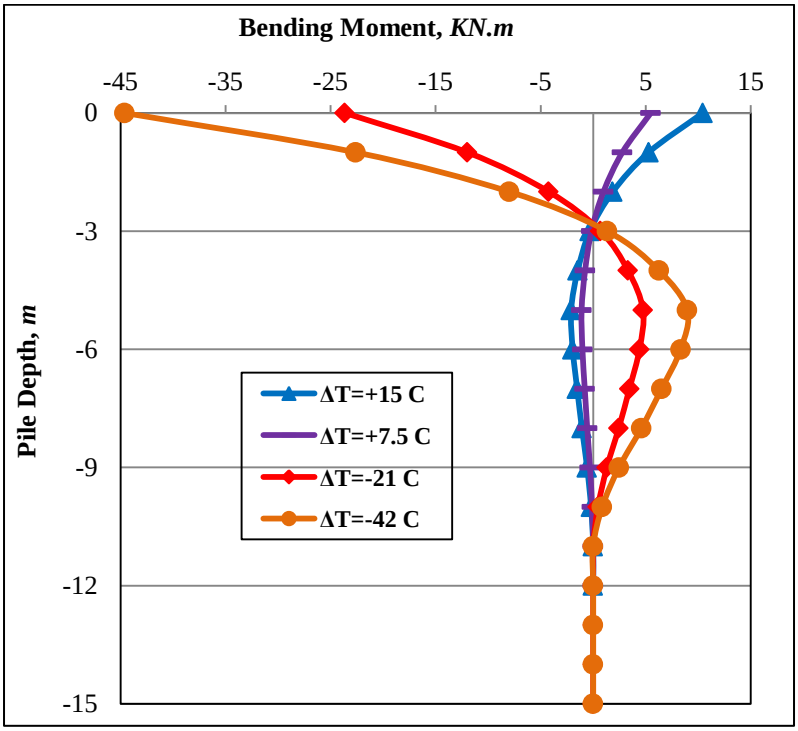

Figure 4.54: Pile bending moment obtained from FEM for bridge.

Table 4.8: Comparison between predicted and measured bending moments of west pile.

Depth Below Abutment, (*m*)	Pile Bending Moment, (*kN.m*)		Difference between FE Model and Field Test (%)
	Field Data [44]	FE Model	
0.74	26	28.1	8
1.95	8	8.3	3

4.1.2 SKEWED INTEGRAL BRIDGES

The method of analysis described in Chapter 3 was also validated and verified against the experimental results obtained from skewed bridges namely: Iowa Highway 60 Bypass of Sheldon, Boone River Bridge and Guthrie County Bridge. The finite element modeling results obtained during the validation processes were observed to be close to field monitoring ones.

4.1.2.1 IOWA HIGHWAY 60 BYPASS OF SHELDON

4.1.2.1.1 FIELD TESTING OF IOWA HIGHWAY 60 BYPASS

4.1.2.1.1.1 BRIDGE DESCRIPTION

The bridge is located on the newly constructed Iowa highway 60 bypass, northeast of Sheldon Iowa, at the crossing of the Floyd River [29]. The bridge is three-span-continuous prestressed concrete girder bridge, 92.32 *m* total length and 12.2 *m* width normal to traffic, with a right-hand-ahead 30^o skew angle. The end spans are 27.66 *m* and the interior span is 37 *m*. The bridge is inclined with a change in elevation from the south abutment to the north abutment of 0.37 *m*. A general plan view of the global geometry of bridge is shown in Figure 4.55.

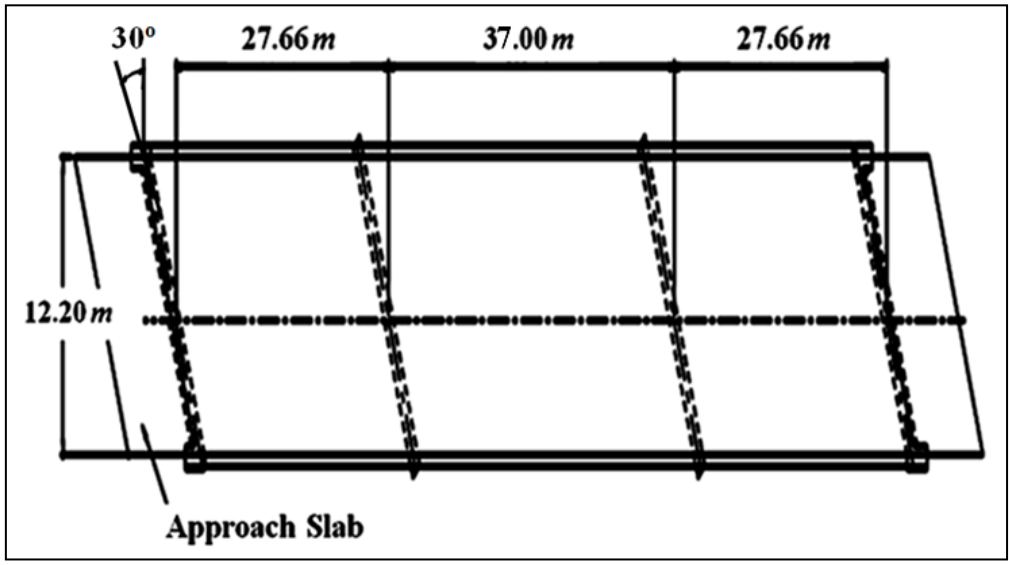

Figure 4.55: Plan view of Iowa highway 60 bypass [29].

The superstructure consists of a 200 *mm* thick cast-in-place deck that acts compositely with seven prestressed concrete girders. The girders are standard Iowa DOT LXD90 and LXD120 shapes depending on the span length. The girders measure 1.37 *m* deep with 0.56 *m* wide bottom flanges and 0.51-*m* wide top flanges. Spacing of the girders is 1.88 *m* center to center. The

girders are integrally cast at abutments and piers. The bridge abutments are founded on a single row of nine 21.33 *m* long HP250×85 piles with an additional HP250×85 pile under each wing wall (see Figure 4.56).

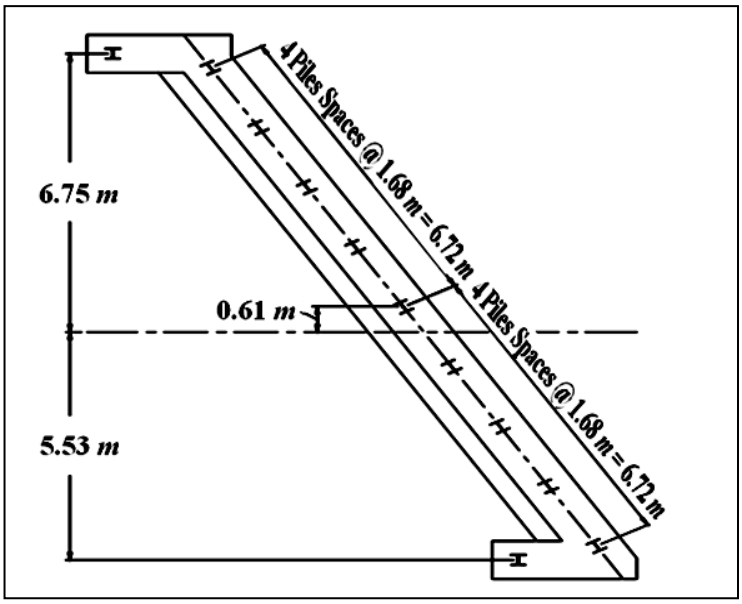

Figure 4.56: Plan view of a typical abutment [29].

The piles are aligned with the web parallel to the face of the abutment and wing walls. The piles were driven the entire 21.33 *m* length, with the top 4.57 *m* predrilled. The piers consist of pile caps, 1.01×1.01 *m* at the lowest step, founded atop a line of seventeen HP250×85 piles with 22.86 *m* long. The exterior piles are battered transversely at a ratio of 1:12 horizontal to vertical.

4.1.2.1.1.2 BRIDGE INSTRUMENTATION PLAN

Ambient temperature at selected locations in the bridge was recorded by thermistors encapsulated in the coil of sensors. Ambient temperature data were also collected from archives of the National Climate Data Center (NCDC) and the Weather Channel website for the local community of Sheldon, IA. Long range displacement meters were used to measure longitudinal and transverse movements of bridge abutments. Displacement meters were installed at each end of the south abutment to measure the longitudinal displacement and a single transducer was installed on each south abutment to measure transverse displacement. A cable was extended from the displacement meter and attached to a reference post that is assumed not to move (see Figure 4.57). As the abutment displaces in relation to the post, rotation of the drum is converted into linear motion that is recorded by a vibrating wire transducer.

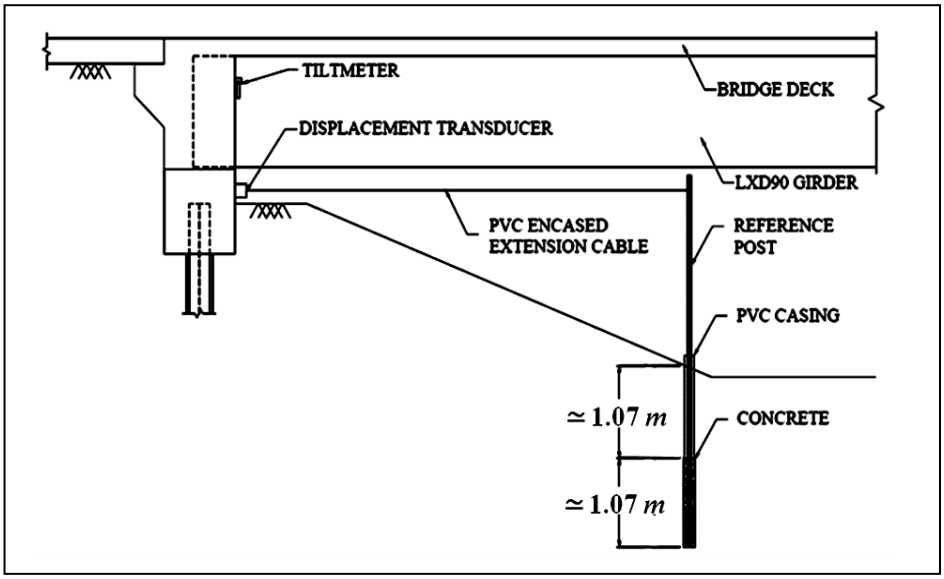

Figure 4.57: Typical displacement meter installation [29].

The reference posts, 0.06 *m* diameter steel pipes, were installed 2.13 to 2.44 *m* into the ground. The bottoms 0.91 to 1.22 *m* of the holes were filled with concrete. In the top of the holes a 0.15 *m* diameter PVC pipe was used as casing to isolate the reference post from the soil. The cable running from the displacement meter to the reference post was enclosed in a PVC pipe to protect it from build up of snow ice and animals. In addition to the displacement meters, tiltmeters were attached to the front abutment face to measure rotation. Spot-weldable vibrating wire strain gauges were epoxied to the flanges of piles beneath the bridge abutments. Four sensors as illustrated in Figure 4.58 were installed per pile, 25 *mm* from the flange tips; and 305 *mm* below the bottom of the abutment.

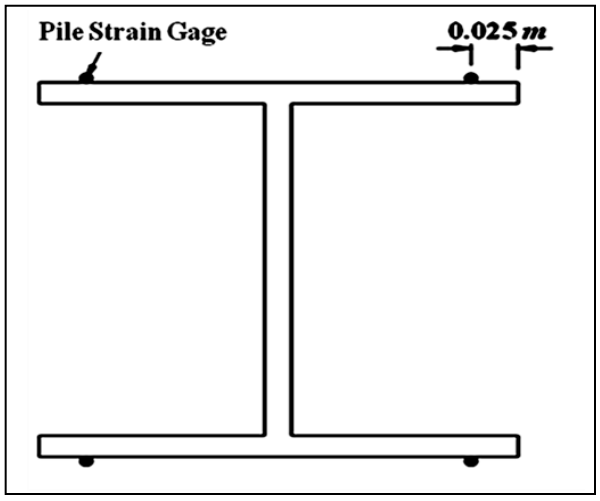

Figure 4.58: Pile strain gauge layout of an instrumented pile.

4.1.2.1.1.3 BRIDGE EXPERIMENTAL RESULTS

The average bridge temperature was compared to the observed Sheldon, IA ambient air temperature (referred to herein as the "air temperature") daily highs and lows gathered from the Weather Channel website for Sheldon, IA. The resulting comparison is shown in Figure 4.59. Longitudinal displacement (Δ_{abut}) and rotational displacement (Δ_{θ}) were measured by transducer and tiltmeter. Displacements due to both sources are shown in Figure 4.60.

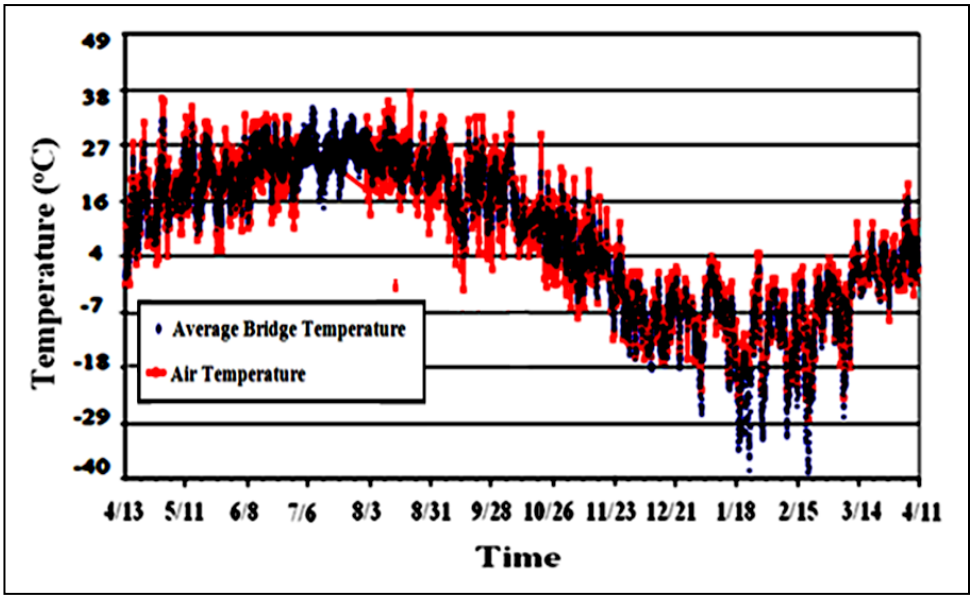

Figure 4.59: Average bridge air temperatures over time [29].

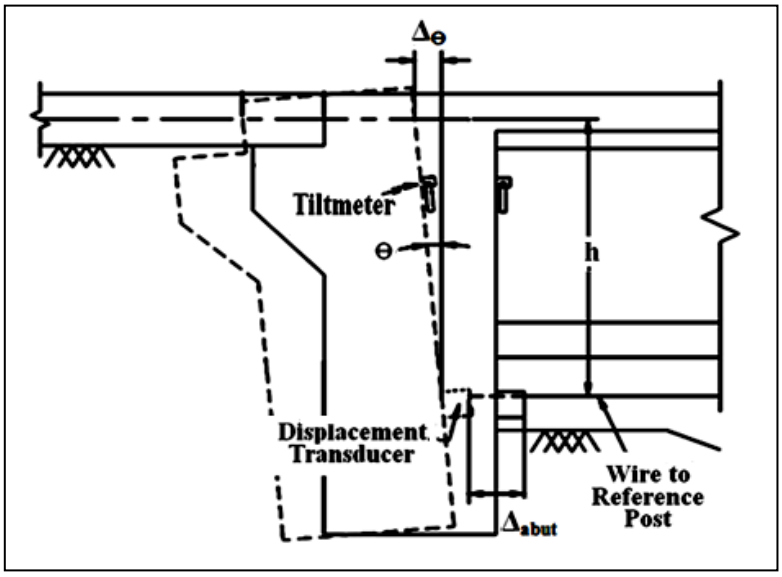

Figure 4.60: Drawing showing displacement of a typical abutment [29].

A representative plot of the corrected actual longitudinal abutment displacement relative to initial readings taken in April 13, 2007 versus time is shown in Figure 4.61. As can be seen, the typical displacement range is approximately -0.013 to 0.09 *m* for a total movement of 0.022 *m*. A displacement transducer was placed at the west end of the abutment to measure transverse displacement. Transverse abutment displacement over time is shown in Figure 4.62.

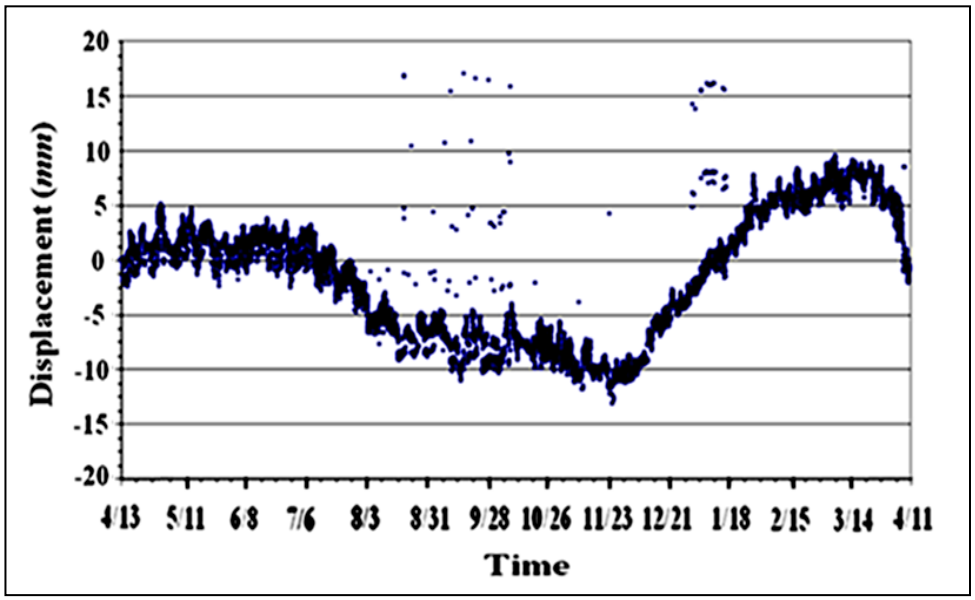

Figure 4.61: Typical bridge longitudinal abutment displacement (Δ_{abut}) over time [29].

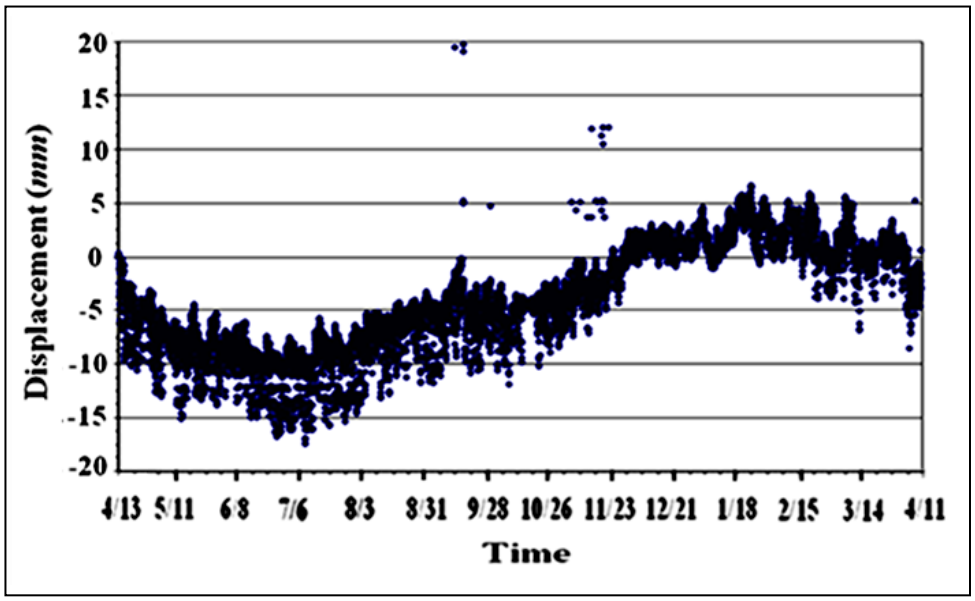

Figure 4.62: Abutment transverse displacement over time [29].

Typical displacement at approach slab mid-depth due to abutment rotation alone is shown in Figure 4.63. The abutments rotate very little, only about 0.05 degrees on average.

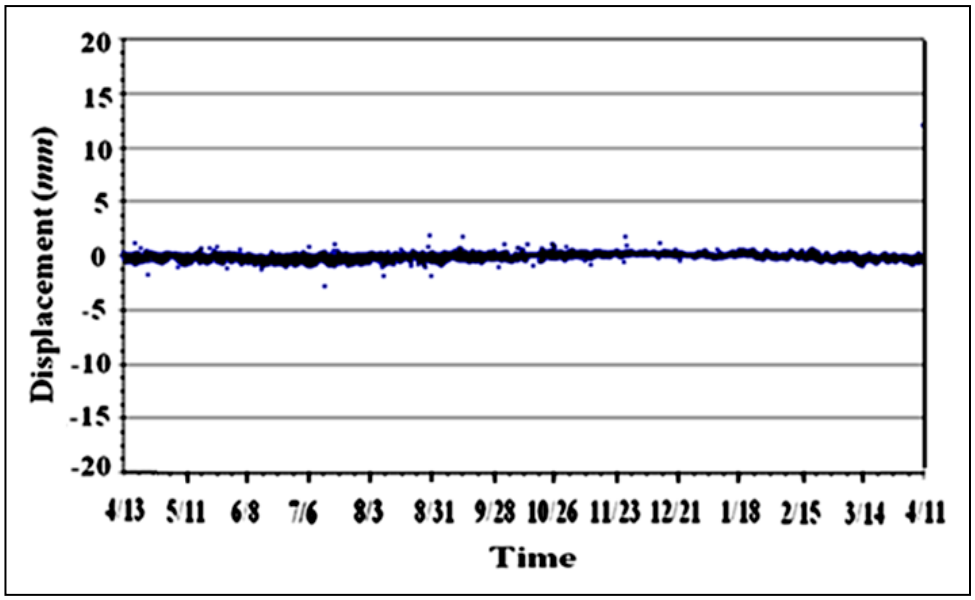

Figure 4.63: Typical displacement of the abutment due to rotation over time [29].

Three HP 250×85 piles located in the south abutment were monitored with four strain gauges located on each pile. The location of the strain gauges and positive local axis orientation of the piles is shown in Figure 4.64(a). The pile orientation and location with respect to the abutment is shown in Figure 4.64(b).

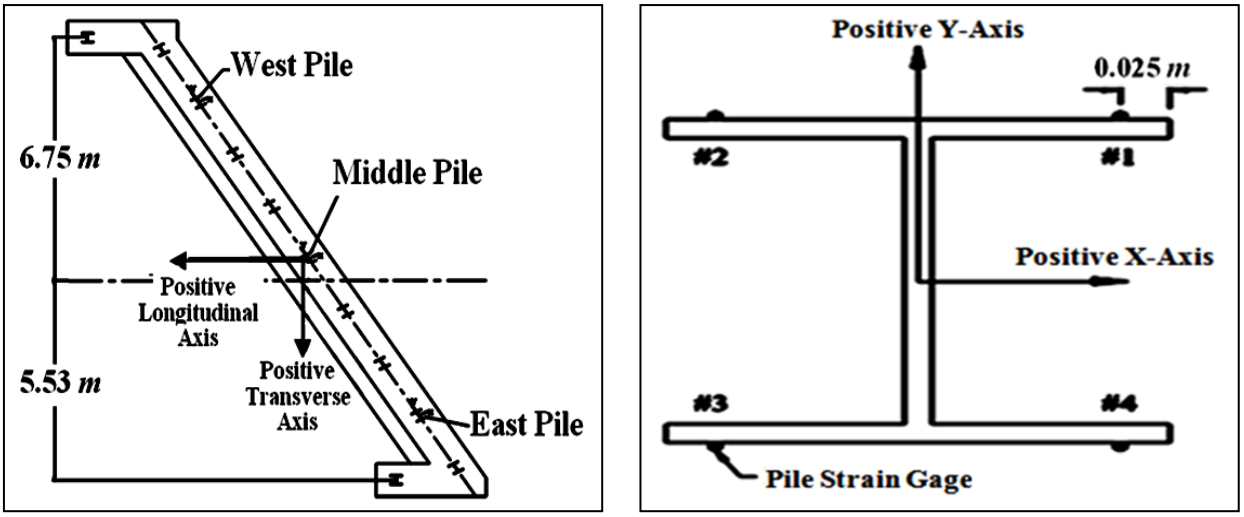

(a) (b)

Figure 4.64: (a) Pile location and global axis orientation, (b) Gauge location and orientation of local axis [29].

The axial x-axis bending and y-axis bending strains obtained for the west and middle piles are shown in Figure 4.65 and 4.66. It was observed that the west and middle pile showed very different responses during the testing period.

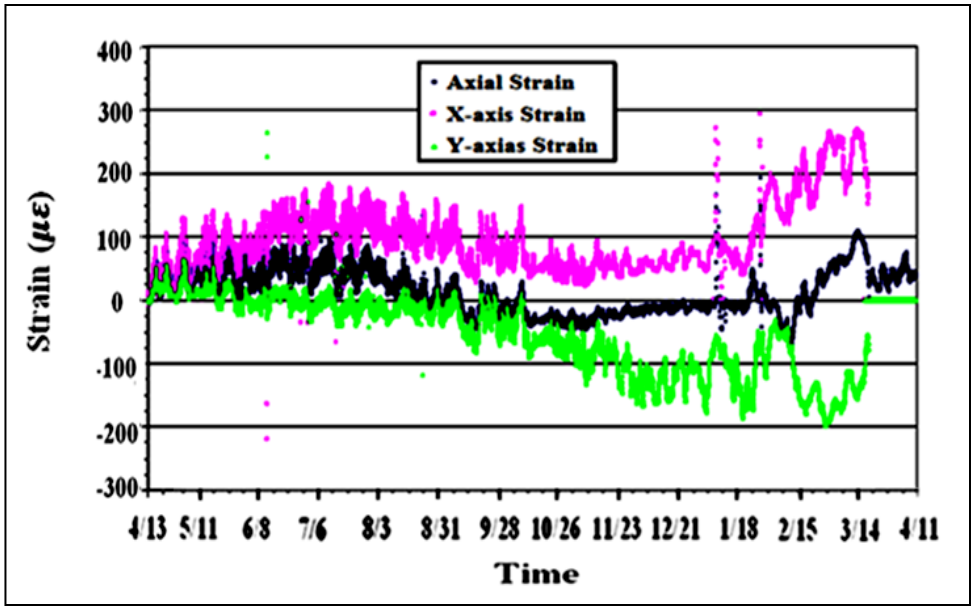

Figure 4.65: Bridge west pile axial and bending strains [29].

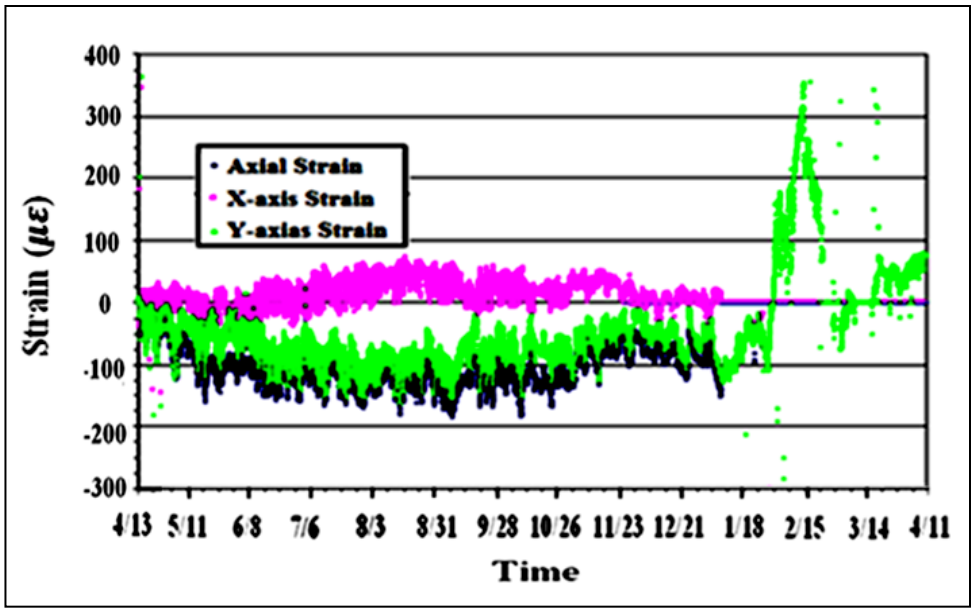

Figure 4.66: Bridge middle pile axial and bending strains [29].

4.1.2.1.2 IOWA HIGHWAY 60 BYPASS NUMERICAL MODELING

Finite element model for Iowa highway bypass consists of three spans was developed as shown in Figure 4.67 and 4.68. Numerical models were assembled using elements described in chapter 3. Coefficients of thermal expansion and modulus of elasticity of the concrete were considered to be 9×10^{-6} $1/^{o}C$ and 29000 *MPa*.

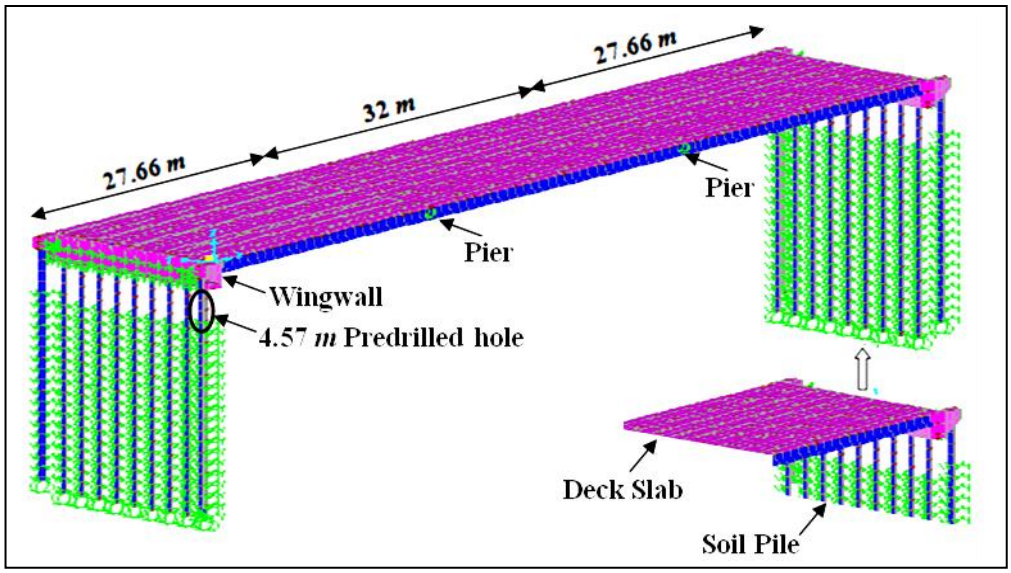

Figure 4.67: 3-D finite element model view of Iowa highway 60 bypass.

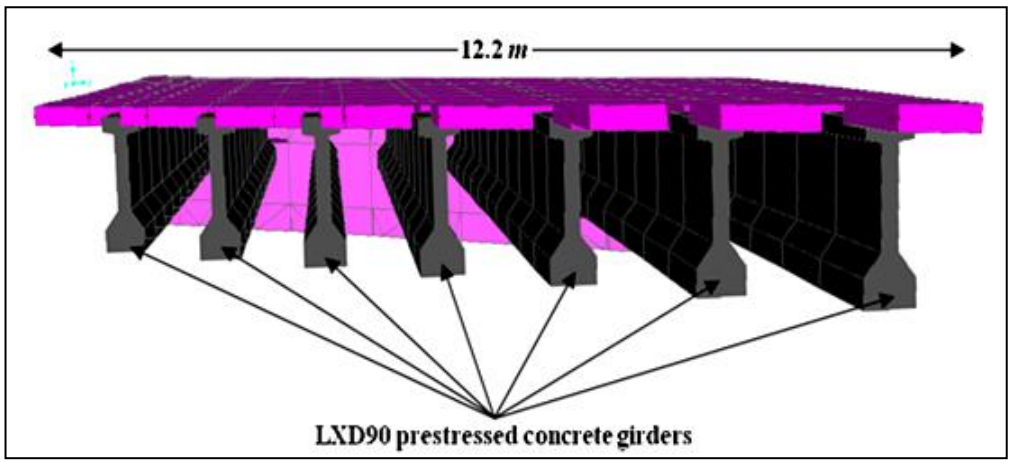

Figure 4.68: 3D finite element model view of bridge superstructure.

4.1.2.1.3 ANALYITICAL STUDY AND INTERPRETATION EXPERIMENTAL RESULTS FOR THE IOWA HIGHWAY 60 BYPASS

To assess the quality of the model, a comparison with experimental results were made in form of abutment displacements, abutment rotation and pile strains.

For numerical analyses, the temperature of superstructure exposed to the atmosphere was increased by an amount ΔT, while the temperature of the partial region of the substructure under the ground was held constant. Five different values for ΔT were used herein corresponding to -40°*C*, -25°*C*, -10°*C*, 5°*C* and +20°*C*. Figures 4.69 and 4.70 display the schematics of nodal temperatures for the bridge during maximum temperature decrease and increase, respectively.

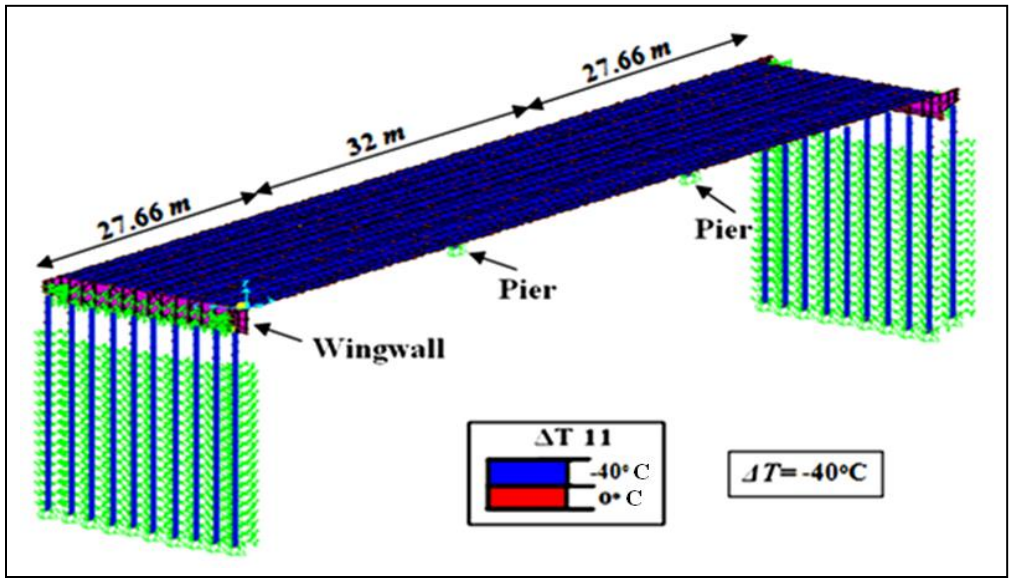

Figure 4.69: View of 3D FE model corresponded to temperature loading of -40°C.

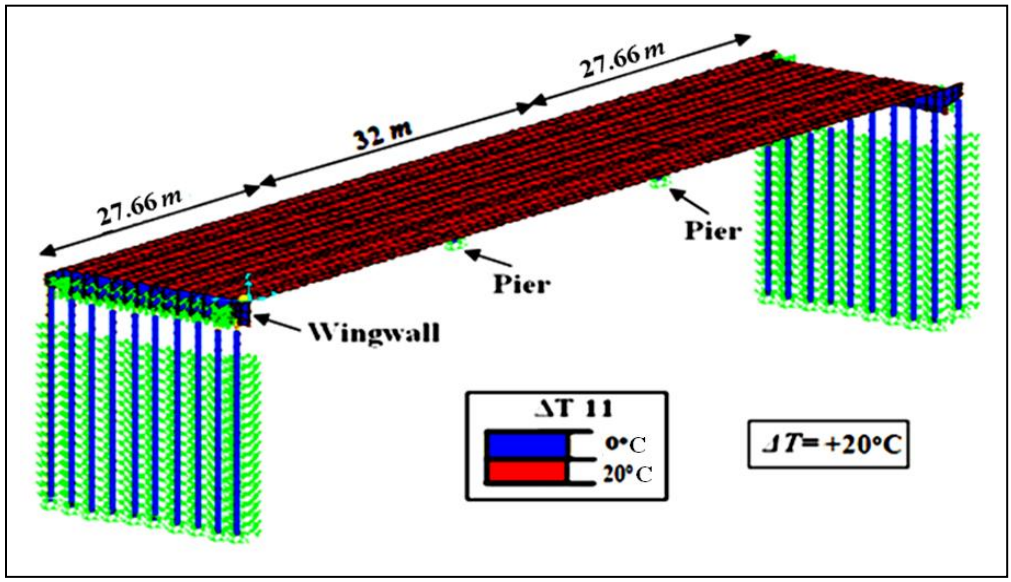

Figure 4.70: View of 3D FE model corresponded to temperature loading of +20°C.

The displacements obtained from numerical analysis in the longitudinal direction of the bridge at the ends of abutments are shown in Figure 4.71 and 4.72.

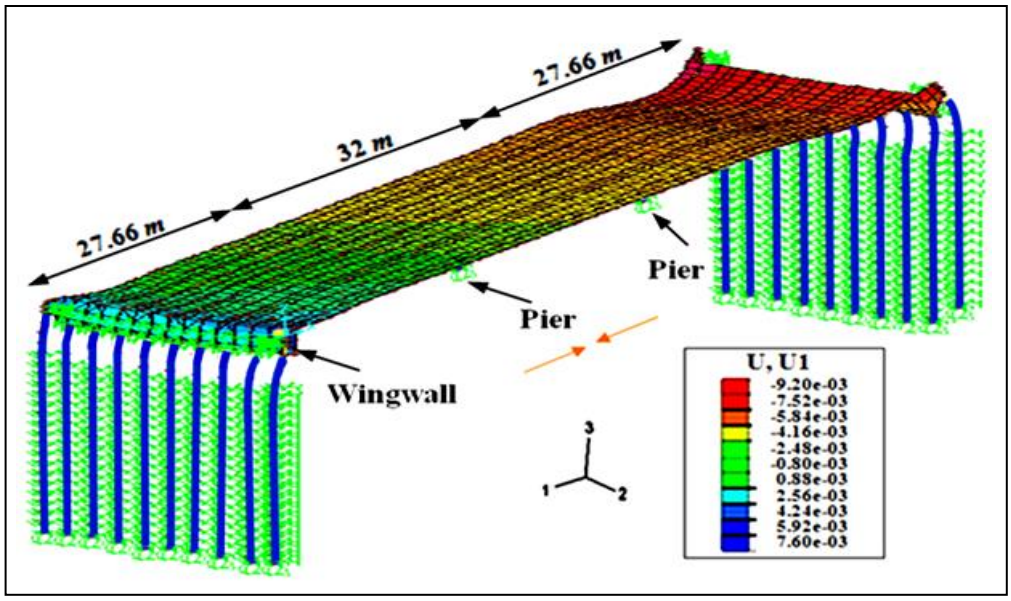

Figure 4.71: Bridge contraction due to temperature decrease of -40 ^{o}C.

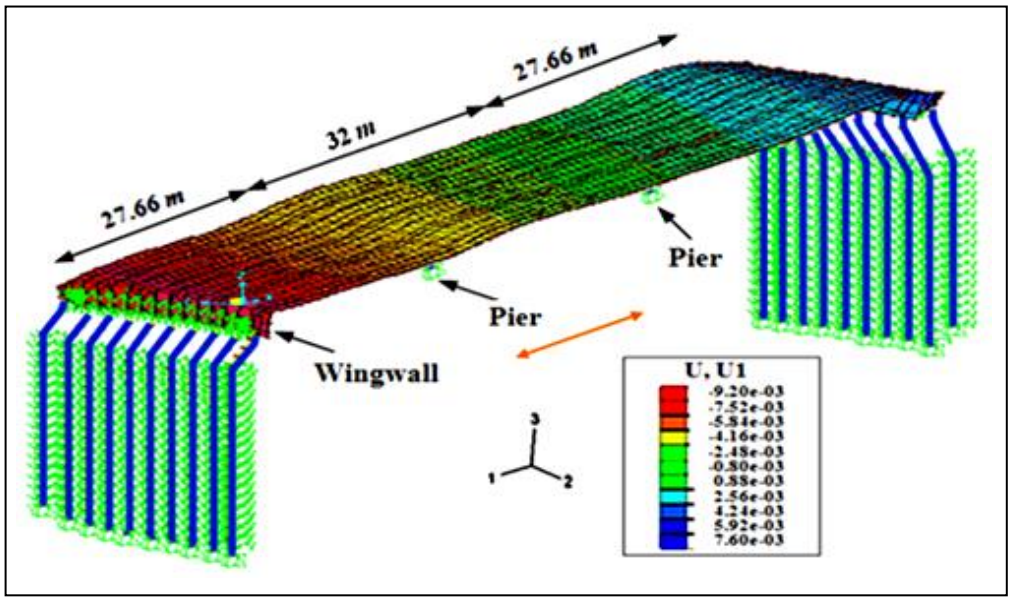

Figure 4.72: Bridge expansion due to temperature increase of +15 ^{o}C.

In structural modeling, the horizontal stiffness for the abutment backfill was adjusted until the analytically-predicted abutment displacements, which were in the longitudinal direction of the bridge at the ends of abutments, were within an acceptable degree of accuracy of these

experimentally-measured displacements. As illustrated in Figure 4.73, the analytical model predicted abutment displacements closely matched to the corresponding experimentally-measured displacements. It was observed that the analytical model had displacement errors of less than 12% for the longitudinal displacements.

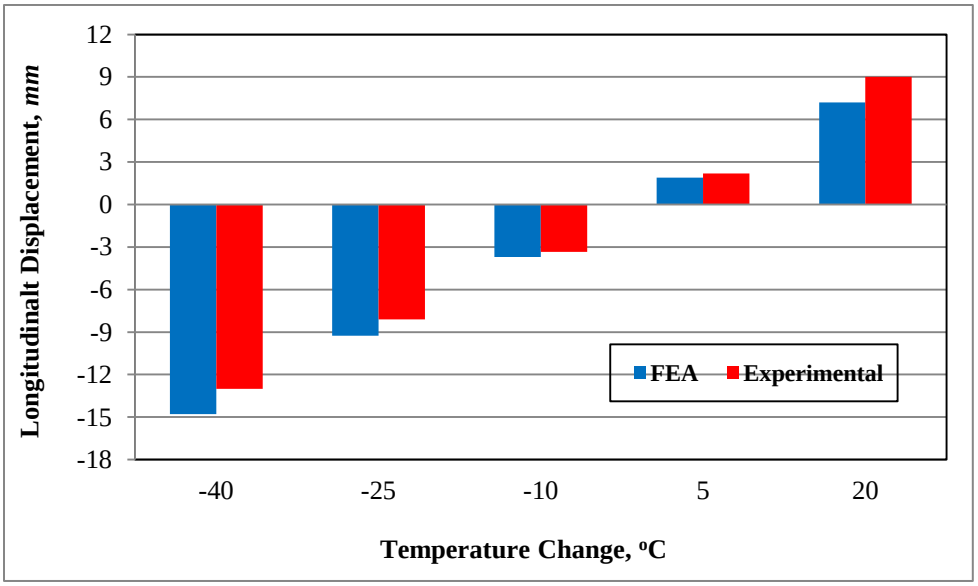

Figure 4.73: Measured and predicted longitudinal abutment displacement.

Abutment displacements in the transverse direction of a skewed bridge can occur since the passive-soil pressure acts normal to the abutment backwall. A component of this force acts perpendicular to the longitudinal axis of the bridge. If the skew angle is large enough, this soil-force component pushes the abutment in the transverse direction of the bridge and towards the acute-angle corner of the bridge deck. Thermal expansion of an abutment induces abutment displacements that are additive with the transverse displacement of the abutment at the acute-angle corner of the bridge deck that are induced by the passive-soil pressure behind the abutment.

In order to study the sensitivity of the transverse abutment displacements to the horizontal stiffness of the soil, models were analyzed with an upper-bound and a lower-bound. For the numerical model of the bridge, the stiffness of tangential soil-springs on the back face of an abutment was set equal to a percentage of the normal-spring stiffness for the backfill. Initially, the stiffness of tangential springs was assumed to be 40% (lower-bound) of that for the normal

springs as recommended by NCHRP Report No. 343 [8]. For this magnitude of tangential-spring stiffness, as illustrated in Table 4.9, analytically predicted transverse abutment displacements essentially matched experimentally-measured transverse abutment displacements (difference of about 5%). When the tangential-spring stiffness was set equal to the normal-spring stiffness (upper-bound), analytically predicted transverse displacements of the abutment were too small (difference of around 28%). Table 4.9 shows the analytically-predicted and experimentally measured ranges for the transverse displacements at the west corner of south abutment. These displacement ranges were in the transverse direction of the bridge and they were based on temperatures between the coldest and hottest day (temperature change of $+60^{o}C$).

Table 4.9: Comparison between predicted and measured abutment transverse displacement.

Type of Backfill	**Transverse Abutment Displacement, (mm)**		**Difference between Field Data and FE Model, (%)**
	Field Data [29]	**FE Model**	
Lower-Bound ($tan\delta \simeq 0.4$)	17	16.23	5
Upper Bound ($tan\delta \simeq 1$)	17	12.34	28

Besides abutment transverse displacement, predicted and measured abutment rotations results were analyzed. The experimental rotation for the south abutment was extremely small. The range for the rotation of this abutment was approximately 0.05 degree. The two, previously described, soil-stiffness-bound models (lower-bound and upper-bound backfill) were used to determine the minimum and maximum limits for the abutment rotations. A summary of abutment rotations are listed in Table 4.10. The prediction obtained from lower-bound model closely estimated actual abutment rotations. The lower-bound model overestimated the field-measured rotation of the abutment only by 13%. Therefore, the model predicted x-axis, y-axis and flexural-bending strains for the abutment piles with lower-bound soil stiffness were only slightly affected by the abutment rotation. The finite-element models with the upper-bound soil stiffness predicted the rotation of abutment with the range of 0.041 degree (underestimation of around 22%). These analytically-measured displacements were small compared to experimentally-measured ones.

Table 4.10: Comparison between predicted and measured abutment rotation.

Type of Soil	Vertical Abutment Rotation, (Degree)		Difference Between FEM and Field Data, (%)
	Field Data [29]	FE Model	
Lower Bound ($tan\delta \simeq 0.4$)	0.05	0.057	13
Upper Bound ($tan\delta \simeq 1$)	0.05	0.041	22

The numerical models predicted that the pile near the acute-angle corner of the bridge deck had the largest horizontal displacement along the longitudinal direction and the greatest y-axis flexural-bending strains compared to those displacements and strains for the other piles in the same abutment. The greatest x-axis flexural-bending strains were predicted to occur in the piles near the ends of the abutments, since at these locations, transverse abutment displacements were the largest. The x-axis and y-axis strain ranges from the finite element models are shown in Figure 4.74. In this Figure, the first letter in the pile notation refers to the pile location in the abutment (W for west, M for middle). The x-axis and y-axis flexural-bending pile strains had a good correlation with the experimental measurements in FEA models with lower-bound. A comparison of the analytical results indicates that soil stiffness had a noticeable effect on the flexural-bending strains. As expected, the largest difference in the magnitude of these predicted pile strains occurred with the upper-bound stiffness of the soil.

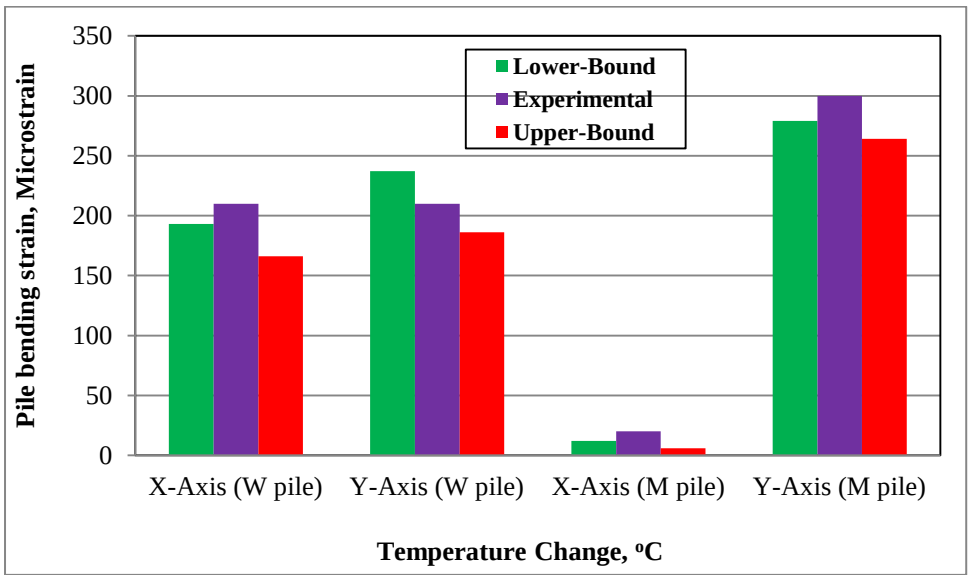

Figure 4.74: Measured and predicted X-axis and Y-axis bending pile strains.

4.1.2.2 BOONE RIVER BRIDGE

4.1.2.2.1 FIELD TESTING OF BOONE RIVER BRIDE

4.1.2.2.1.1 BRIDGE DESCRIPTION

The Boone River Bridge is made of concrete deck on prestressed girder, 99 *m* long and 12.2 *m* wide normal to traffic. Figures 4.75, 4.76 and 4.77 show a plan, cross-sectional and profile view of the bridge [27].

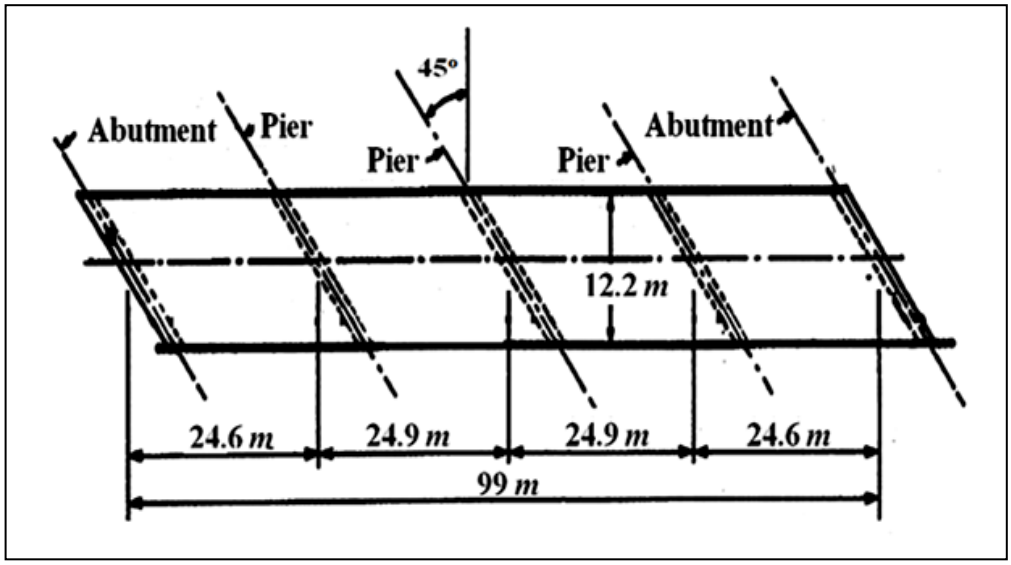

Figure 4.75: Plan view for the Boone River Bridge [27].

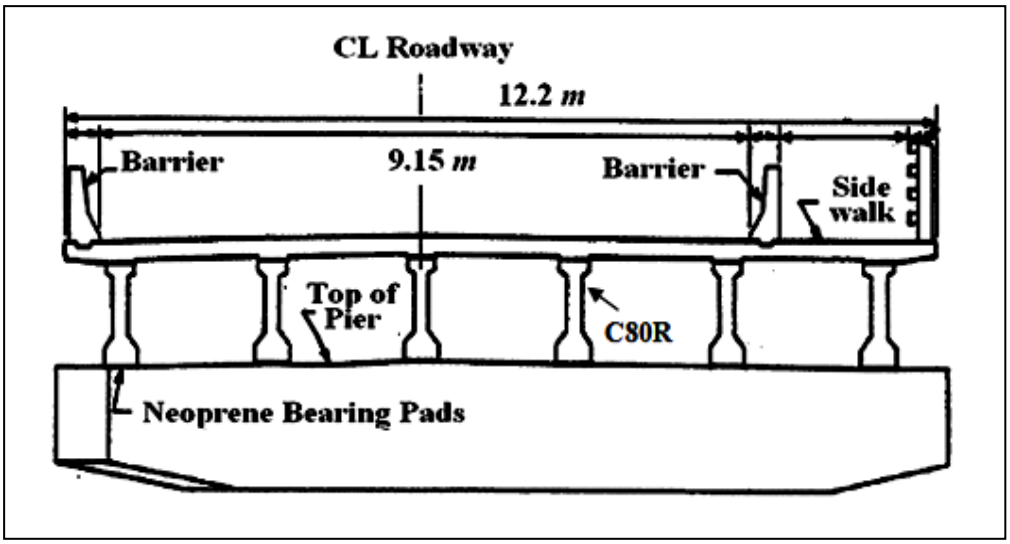

Figure 4.76: Cross-sectional view of bridge [27].

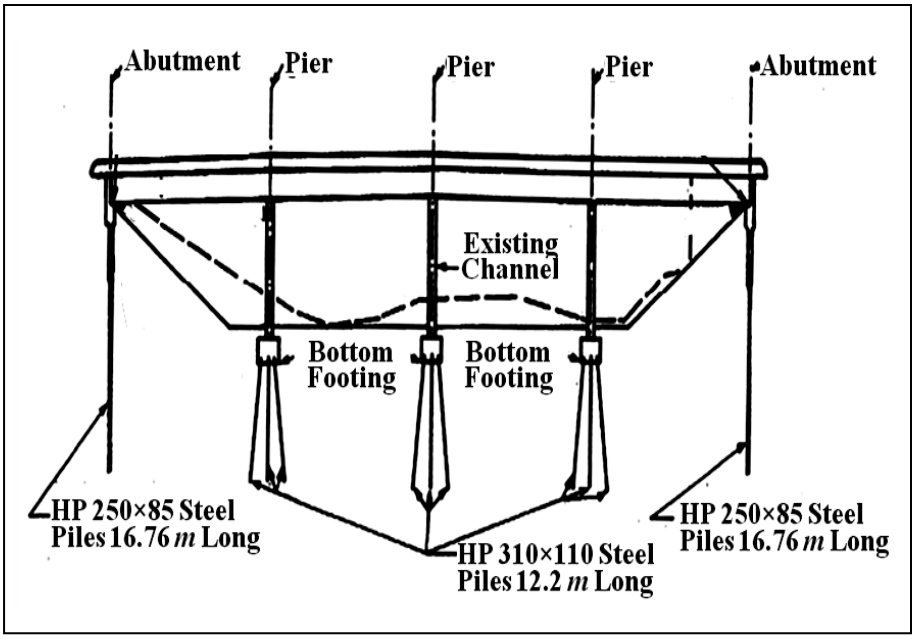

Figure 4.77: Longitudinal section along center line of the bridge [27].

The bridge is a continuous four-span bridge. Two of the piers are located 24.6 *m* from each abutment and the third pier is located in the center of the bridge. The prestressed girders are not integral with the piers but sit on neoprene pads around 25 *mm* thick. The rest of the structure is monolithically constructed. The skew angle of the bridge is 45^{o}. The 190 *mm* deck is of reinforced concrete with a compressive strength of 20.7 *MPa*. The prestressed concrete girders are C80R type with design strength of 34.5 *MPa*. The piles were driven in a predrilled hole approximately 2.74 *m* with the strong axis parallel to the longitudinal direction and battered at a slope of 4:l in the lateral direction only (see Figure 4.78).

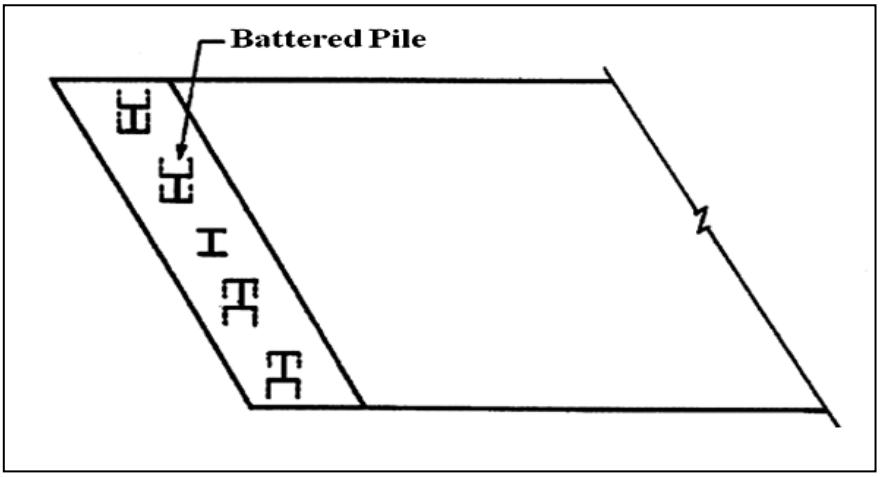

Figure 4.78: Typical pile orientation predominantly weak axis bending [27].

Soil conditions are summarized in Figure 4.79(a). Soil parameters, such as k_h, are very difficult to predict with any degree of certainty. The interaction of the loose sand in the predrilled hole with the surrounding material was certainly complicated to predict. In recognition of this, a range of parameters was considered. A range of stiffnesses versus depth are shown in Figure 4.79(b) for the bridge site. The sand in the predrilled hole and the surrounding in-situ soil was assumed to be bounded by loose sand and medium-loose sand (The stiffness for medium-loose sand is the average of the stiffnesses for medium and loose sand). Below the predrilled hole, the in-situ soil was estimated to be between medium and dense sand (The medium-dense stiffness is the average of the medium and dense sand).

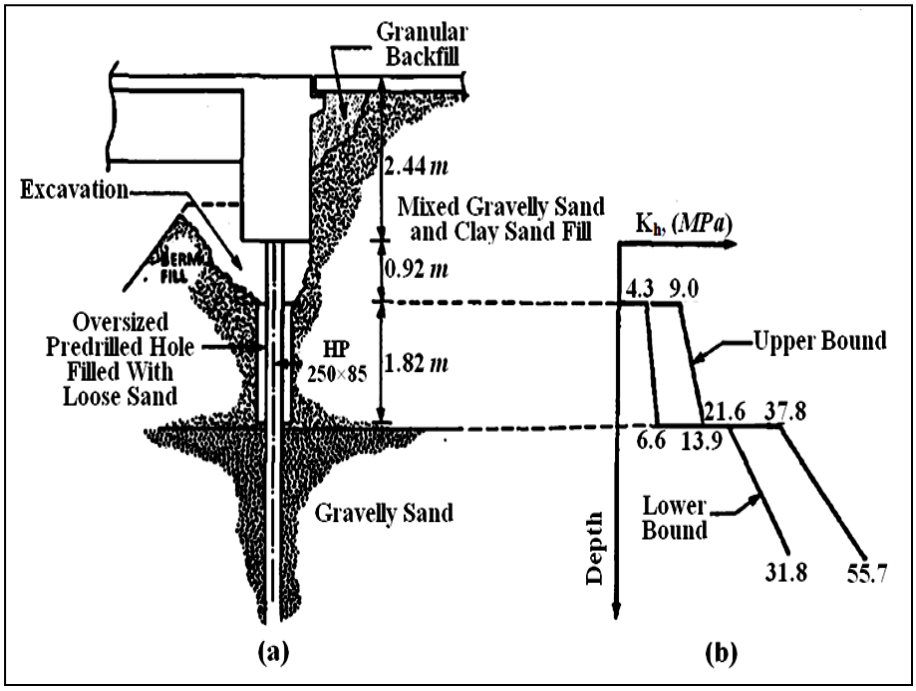

Figure 4.79: (a) Cross-section of abutment and pile; and (b) Initial Stiffness versus depth [27].

4.1.2.2.1.2 BRIDGE INSTRUMENTATION AND DATA RECORDING

To monitor air and superstructure temperatures, thermocouples were used at locations shown in Figure 4.80. Holes were drilled in precast girders. Thermocouple wires were then placed inside holes and sealed with grout.

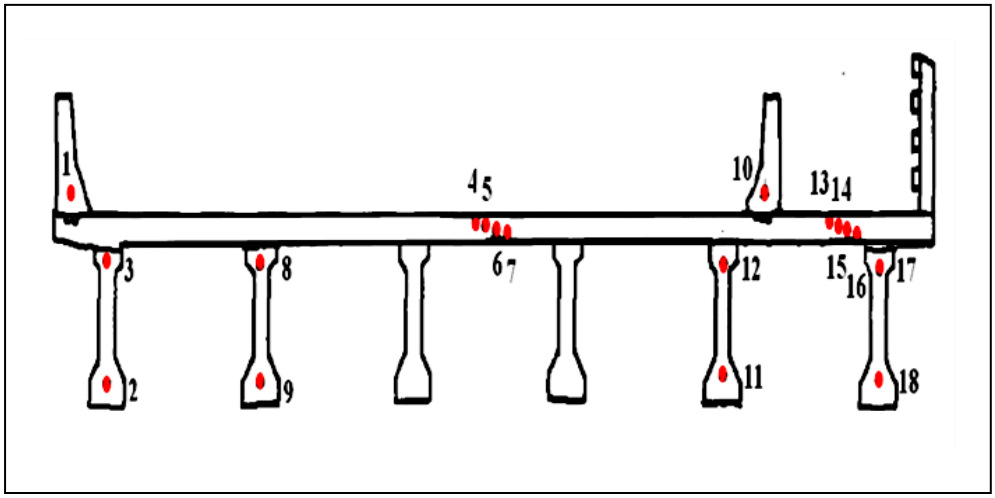

Figure 4.80: Typical thermocouple locations [27].

Data collection started on January 8, 1987 and ended on February 28, 1989. Readings were taken every 10 minutes, averaged for 1 hour and stored on computer for the 26-month period. Figure 4.81 illustrates that the actual air temperature at the bridge ranged from -32°*C* to +40°*C*.

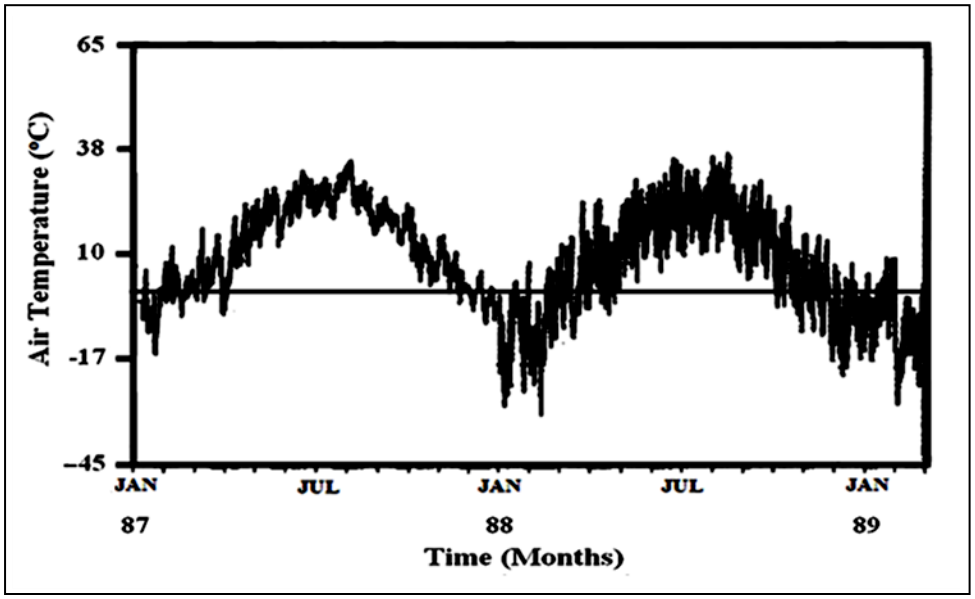

Figure 4.81: Air temperature versus time for bridge from January 1987 to February 1989 [27].

One linear variable differential transformer (LVDT) was also installed on the bridge to monitor the longitudinal expansion. The LVDT was placed at one end of each bridge under the overhang, in an electrical box. The LVDT was clamped inside a spring that was attached to a wire stretched across the length of the bridge. The nickel-iron wire (coefficient of thermal expansion equals 12.6×10^{-6} $1/°C$) was enclosed in lubricated conduit to reduce frictional effects. Figure 4.82 shows the longitudinal expansion versus time for the bridge. The expansions were obtained from the LVDT readings, taking into account the elongation of the wire due to changes in temperature and internal stress. The bridge had a displacement range of approximately 25 *mm* in winter time and 12.5 *mm* during summer time.

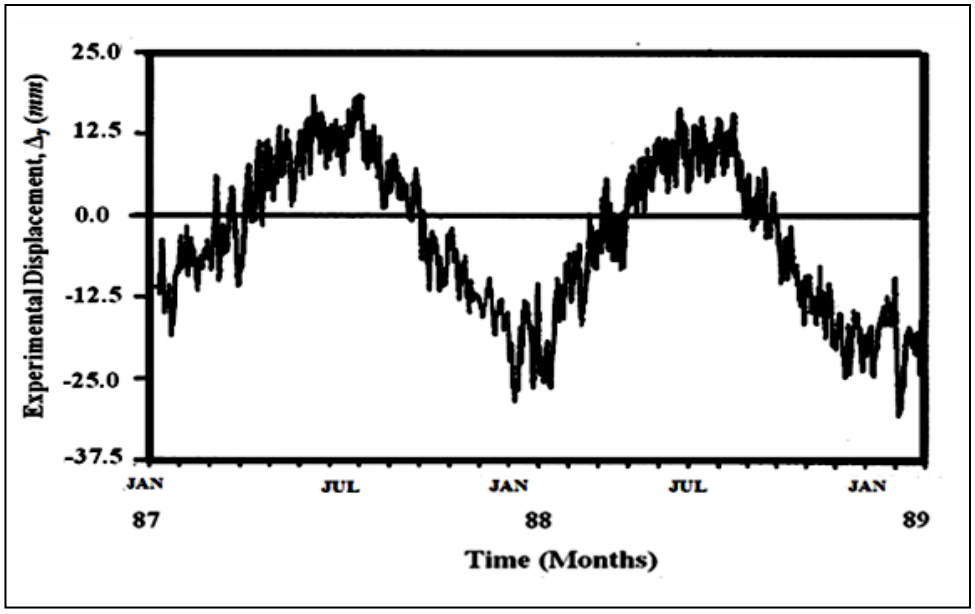

Figure 4.82: Experimental longitudinal bridge displacement versus time
for bridge from January 1987 to February 1989 [27].

Four electrical resistance strain gages were placed on the second battered pile from the west end of each abutment. Figure 4.83 shows the orientation and location of these gages. The strain gages were placed about 0.15 to 0.2 *m* below the bottom of the abutment. Excavation was required at the pile-abutment interface, where approximately 0.91 *m* of the pile was exposed for placement of strain gages. The excavated area was left unfilled for the duration of the testing.

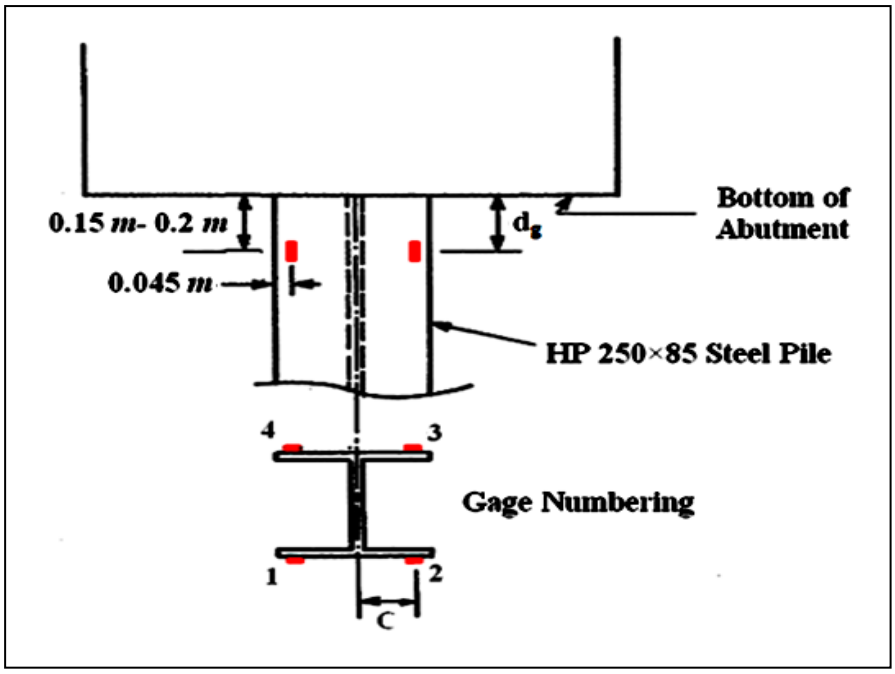

Figure 4.83: Typical strain gage locations and numbering scheme [27].

Figures 4.84 and 4.85 show experimental strain ranges due to temperature only. The strain ranges was approximately 700 and 250 μ *mm*/*mm* for ε_y and ε_x. Thermal strains will be greater than this at the flange tips (beyond the strain gages) and just below the abutment. Strains due to vertical and other loading are not included in the experimental values.

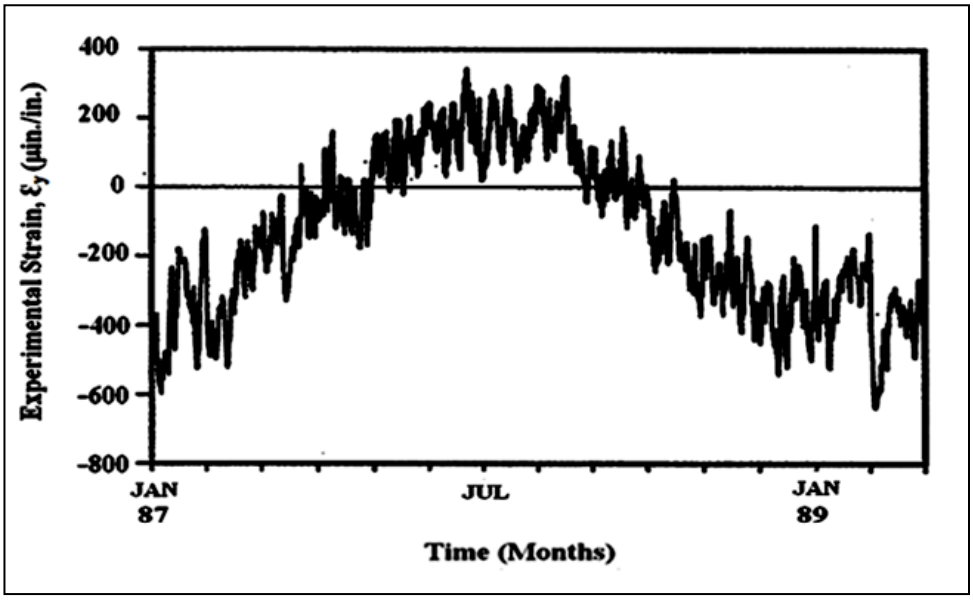

Figure 4.84: Experimental weak axis strains versus time from January 1988 to February 1989 [27].

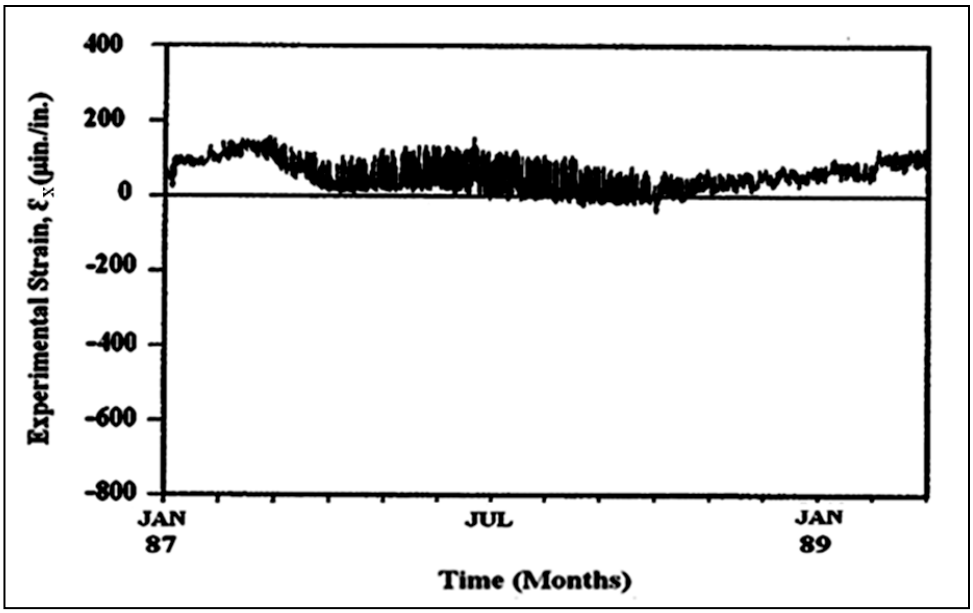

Figure 4.85: Experimental strong axis strains versus time from Jan. 1988 to Feb. 1989 [27].

4.1.2.2.2 BOONE RIVER BRIDGE NUMERICAL MODELING

The numerical model for Boone River Bridge consists of three spans was developed as shown in Figure 4.86 and 4.87. The modulus of elasticity for the model was considered as 21,525 *MPa* for the deck and 27,790 *MPa* for the prestressed girders. The coefficient of thermal expansion of concrete was taken 7.2×10^{-6} $1/^{o}C$.

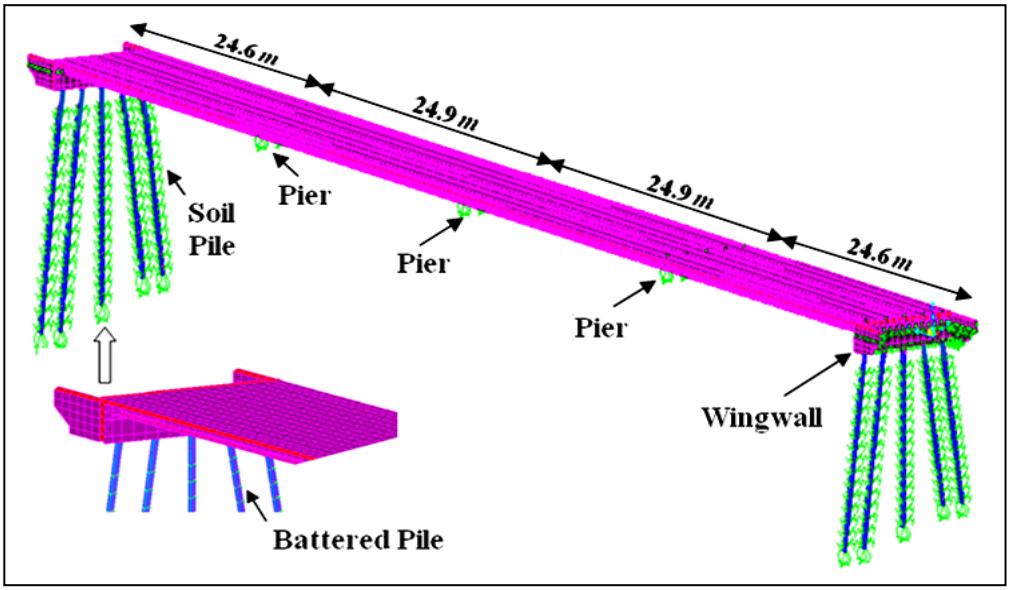

Figure 4.86: 3-D finite element model view of Boone River Bridge.

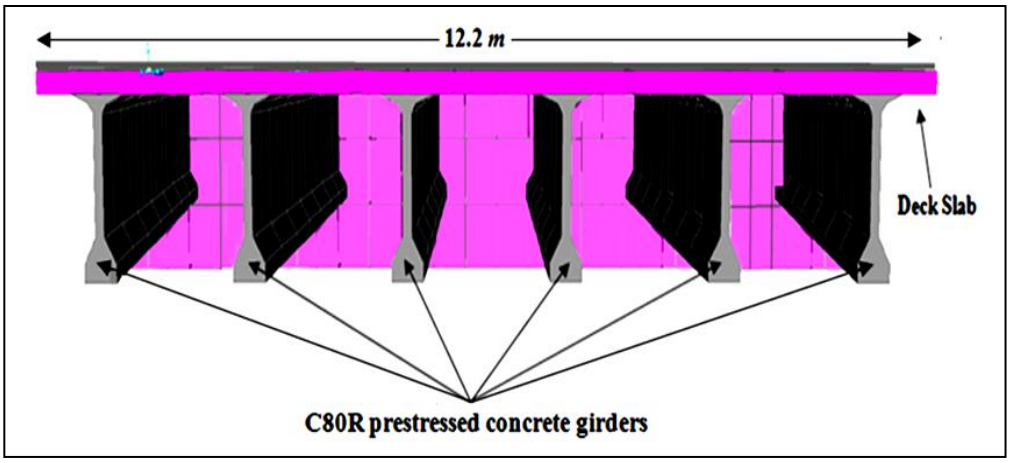

Figure 4.87: 3D finite element model view of bridge superstructure.

4.1.2.2.3 COMPARISON OF ANALYTICALLY-PREDICTED AND EXPERIMENTALLY-MEASURED OF BOONE RIVER BRIDGE RESPONSES

Since the main objective of the numerical modeling was to determine the influence of temperature changes on the response of the bridge, three different values of temperatures change ranges were selected. Assuming a construction temperature of $+15^{o}C$, different temperature ranges including $-40°C$, $-20°C$ and $+20^{o}C$ were applied to the analytical models. Figures 4.88 and 4.89 show temperature loading cases for the bridge corresponding to $-40°C$ and $+20^{o}C$.

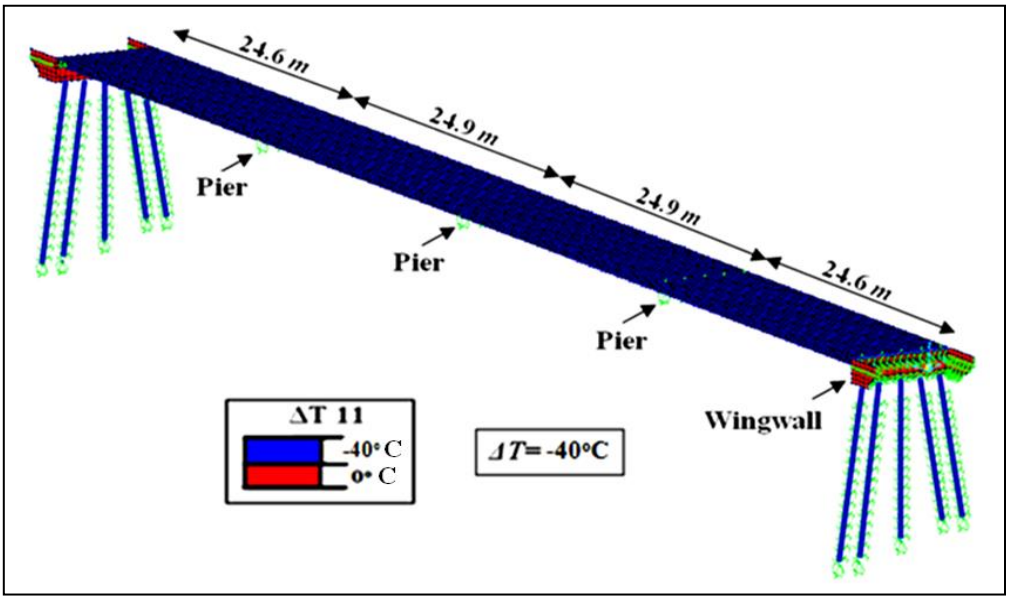

Figure 4.88: View of 3D FE model corresponded to temperature loading of $-40^{o}C$.

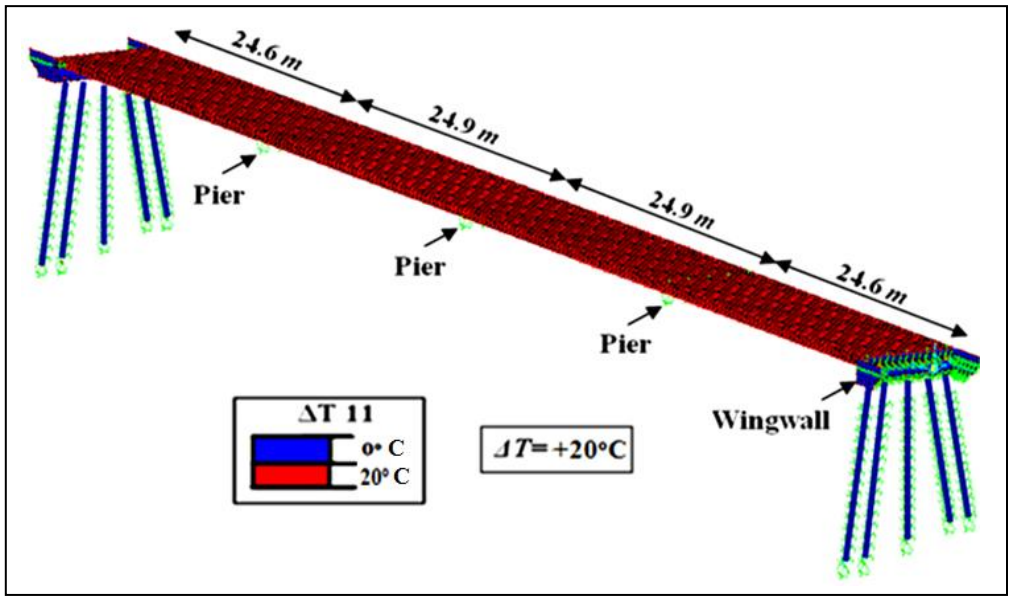

Figure 4.89: View of 3D FE model corresponded to temperature loading of +20°C.

Figures 4.90 and 4.91 show longitudinal displacements at the end of bridge abutments. The corresponding coordinate systems are also shown in figures.

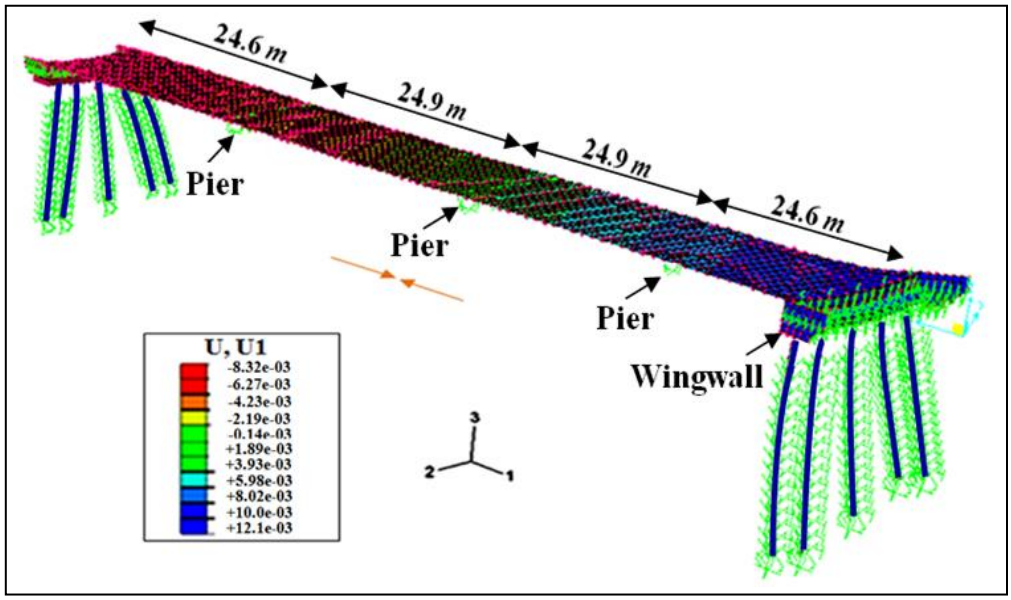

Figure 4.90: Bridge contraction due to temperature decrease of -40°C.

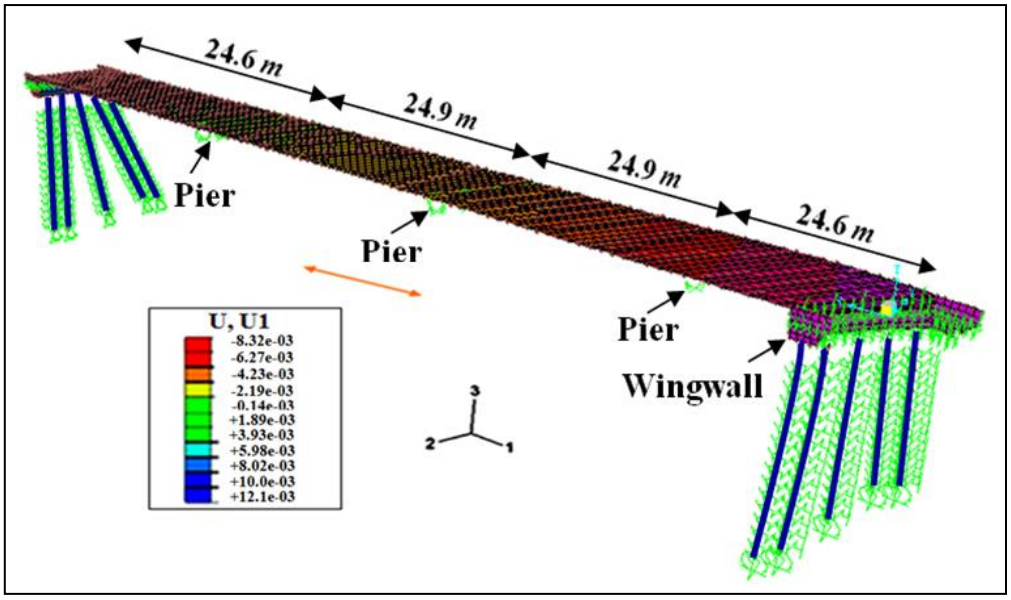

Figure 4.91: Bridge expansion due to temperature increase of +20°C.

The longitudinal displacements at the abutment were extracted from FEA and experimental results. Those displacements were plotted versus temperature changes in Figure 4.92. It can be observed that pile longitudinal displacement increase linearly with change in temperature. It can also depicted in figure that both FEA and experimental showed good correlation of longitudinal displacement for different temperature changes. As an example, abutment displacements for temperature change of -40^{o}C, were computed as -23.8 and -22.6 *mm* from experimental and numerical analysis, respectively.

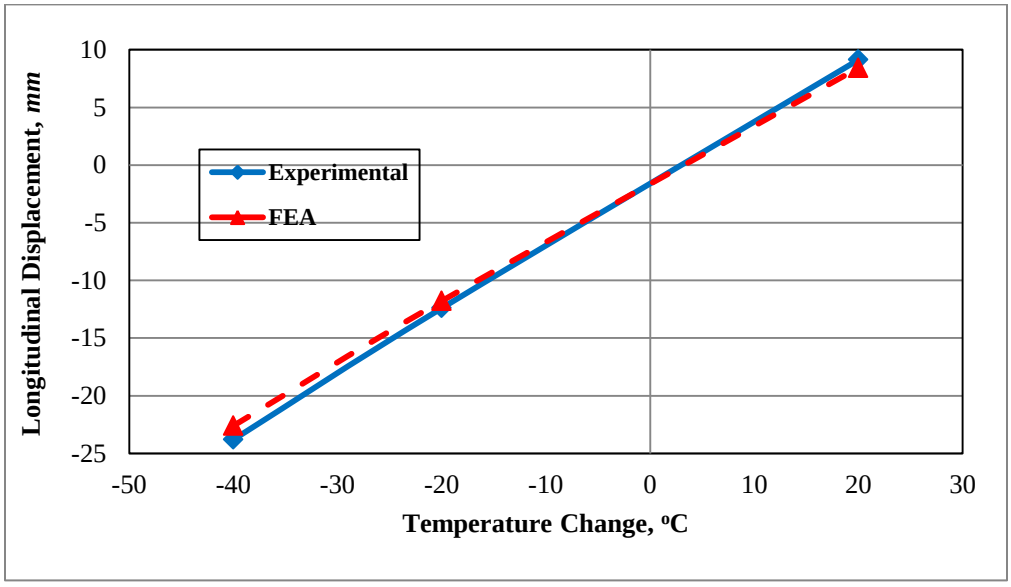

Figure 4.92: Displacement at the abutment vs. temperature change.

Figure 4.93 plots the comparison of FEA and experimental results obtained for weak axes strain, ε_y, of the second battered pile from west end of abutment. The results from finite element analysis showed similar trends as the experimental ones, but the computed strains were slightly smaller than the experimentally measured strains. As an example, the computed strain value from FEA in June 1987 was 183.8 μ *mm*/*mm* while this value from experimental test was 200 μ *mm*/*mm* (underestimation of around 8%).

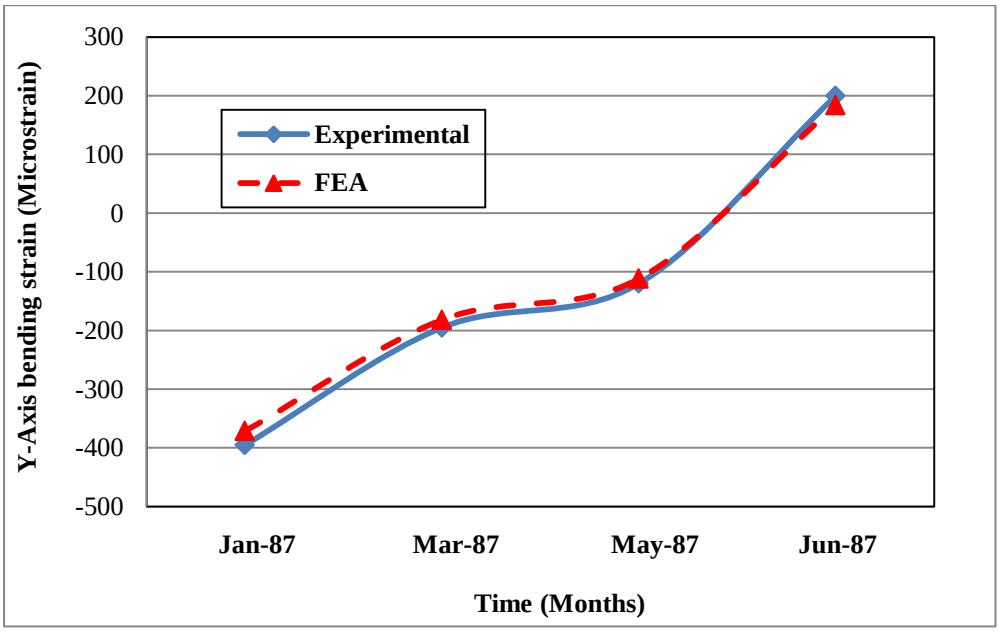

Figure 4.93: Y-axis flexural-bending strains predicted by the finite element analysis and experimentally measured at the bridge.

Analytically-predicted and experimentally-measured strong axes strains were also compared to determine the accuracy of the finite element models for predicting bridge responses to temperature changes. The strong axes strain ranges, ε_x, obtained from experimental results corresponding to temperature changes was approximately 250 μ *mm*/*mm* at the bridge (Figure 4.85). The strain range obtained from numerical modeling of the bridge was around 272.8 μ *mm*/*mm*. It can be observed that numerical results demonstrate close correlation to experiments with error in strain of about 9%.

4.1.2.3 GUTHRIE COUNTY BRIDGE

4.1.2.3.1 FIELD TESTING OF GUTHRIE COUNTY BRIDGE

4.1.2.3.1.1 BRIDGE DESCRIPTION

The Guthrie County Bridge is a prestressed concrete (PC) girder bridge, 97 *m* long and 9.75 *m* wide (see Figure 4.94). The concrete girders are Type-D, as specified by the Iowa Department of Transportation. The bridge has a skew angle of 30°. The bridge is a continuous three-span bridge with two piers located 32.25 *m* from each abutment [1].

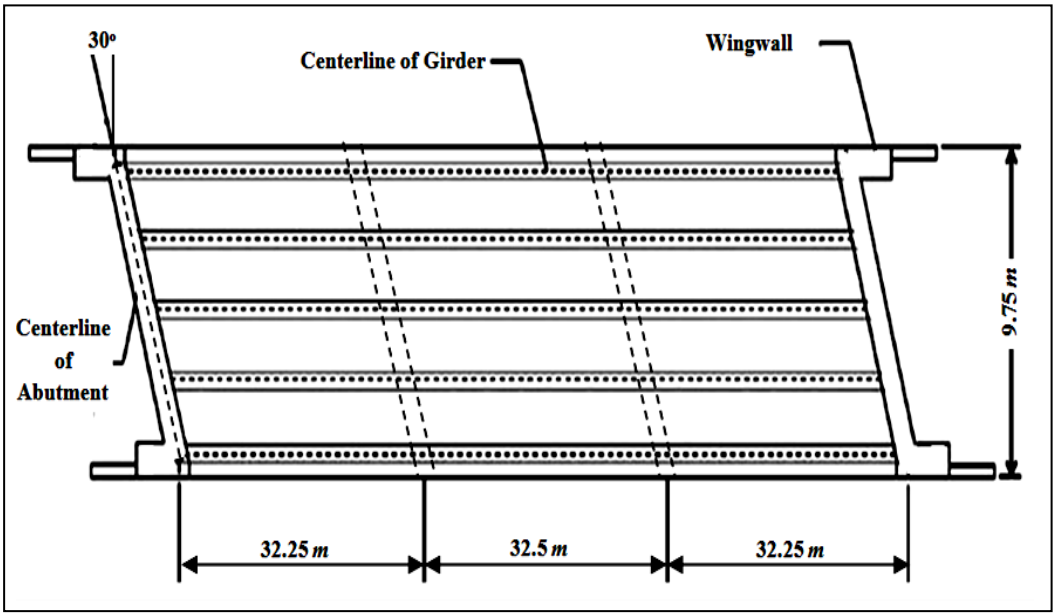

Figure 4.94: Plan view of Guthrie County Bridge [1].

This bridge has a U-shaped abutment with a single row of ten HP 250×85 steel piles under the reinforced-concrete (RC) backwall and an HP250×85 pile under each wingwall. The piles under the RC backwall are oriented with their webs parallel to the abutment face. The wingwall piles are oriented with the webs perpendicular to the longitudinal axis of the bridge. The piles were driven to a depth of at least 13.7 *m* into shale bedrock at the south abutment and to a depth of at least 12.2 *m* into shale bedrock at the north abutment. Pre-bored holes that were filled with bentonite slurry were specified for the piles at this bridge. The backfill soil behind the abutments of the bridge is a compacted granular soil. Soil parameters were based on the soil-boring data that is shown in Figure 4.95 for piles at north and south abutments.

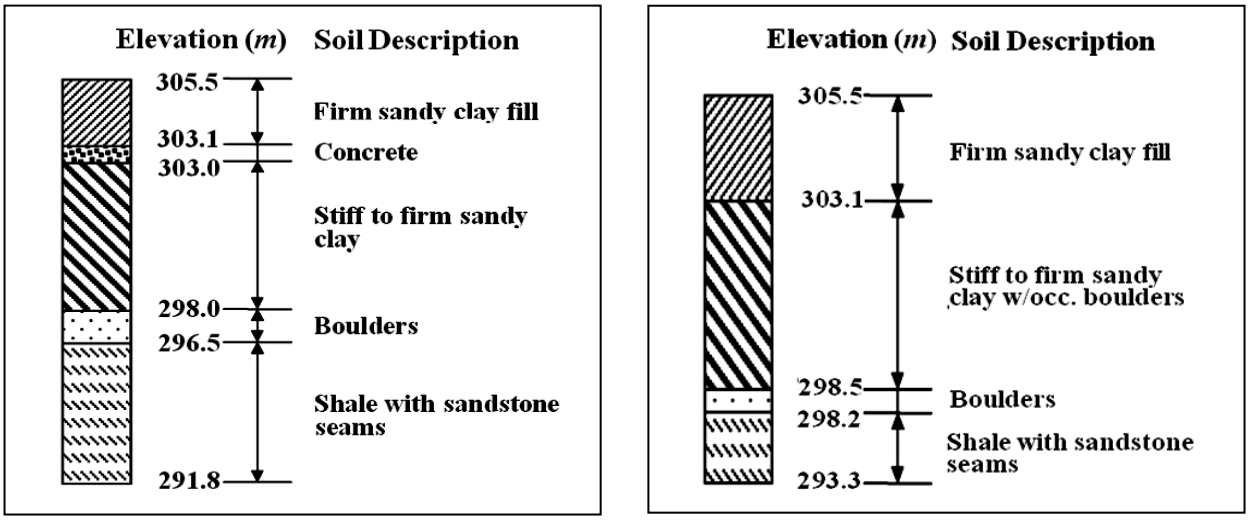

Figure 4.95: Soil borings at the bridge (a) Near the south abutment; and (b) Near the north abutment [1].

A spread footing that is keyed into the shale bedrock supports the each Tee-shaped pier. At the south pier, which is an expansion pier, the bridge girders bear on 95 *mm* thick steel reinforced, neoprene pads. At the north pier, which is a fixed, bridge girders bear on 25 *mm* thick neoprene pads at this pier.

4.1.2.3.1.2 BRIDGE INSTRUMENTATION PLAN

Bridge movements were measured with string potentiometers and displacement transducers. Figure 4.96 shows the location of these string potentiometers and transducers on the bridge.

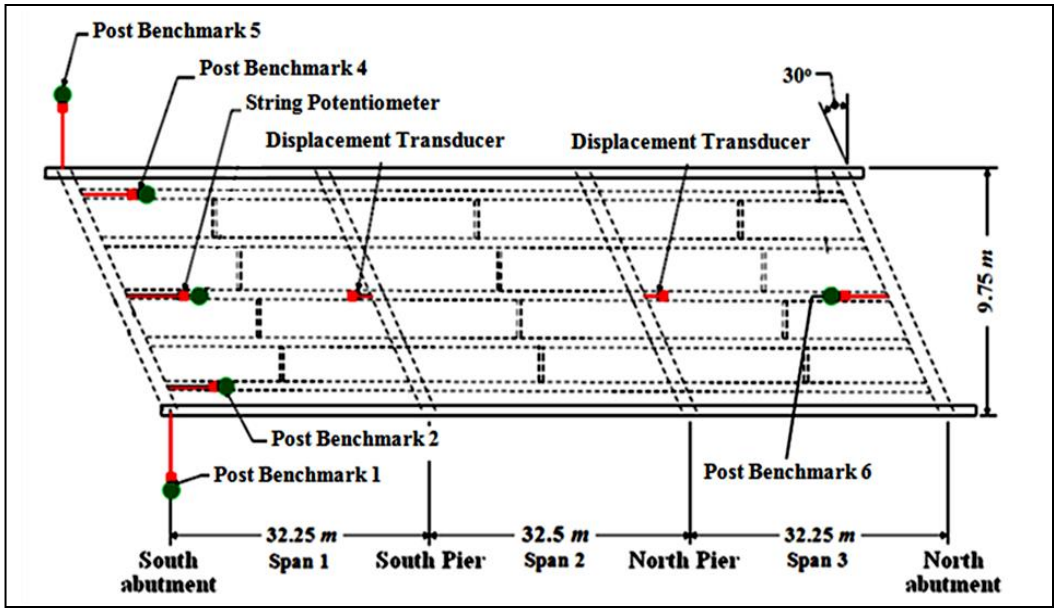

Figure 4.96: Post benchmarks and transducers locations at the bridge [1].

Seven string potentiometers were used to measure absolute displacements of abutments. These string potentiometers, as illustrated in Figure 4.97(a), were mounted on benchmark posts that were installed about 3 *m* from bridge abutments. Six displacement transducers were mounted on the bridge to record differential displacements between bridge elements. Displacement transducers that measured the relative longitudinal displacements between the pier cap and the center PC girder at the north pier were installed in July 1998. Figure 4.97(b) shows the location of transducers at abutment and pier locations in longitudinal view.

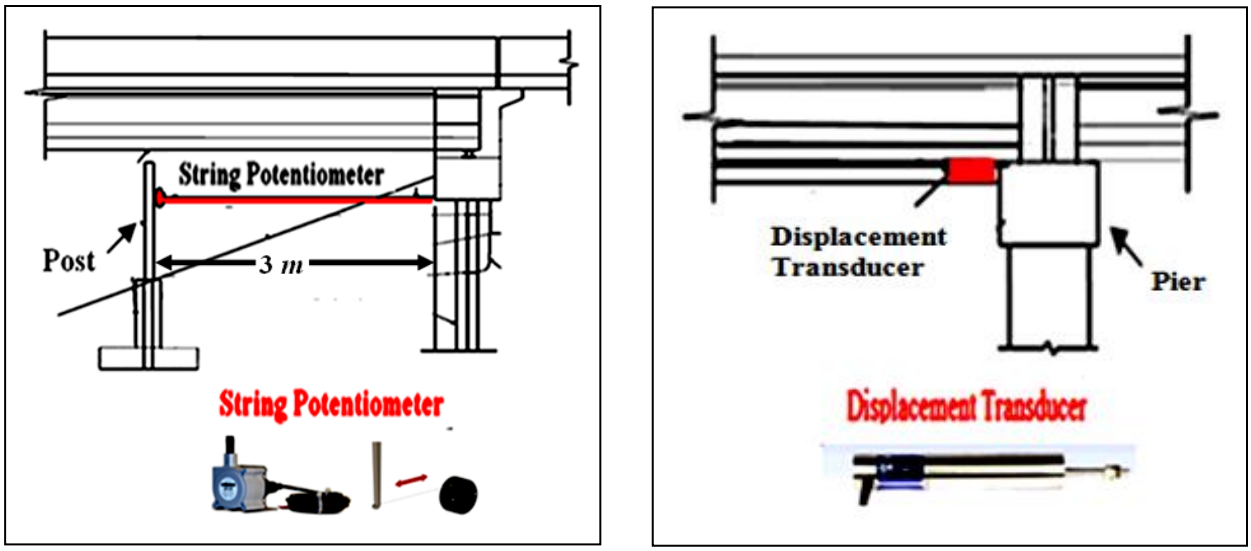

(a) (b)

Figure 4.97: (a) Benchmark-post installation, (b) Displacement transducer at a pier cap and abutment [1].

Besides measuring abutment movement and relative displacements as a primary objective, abutment rotation was determined as the second objective of field testing. Abutment rotations in the vertical plane that is parallel with the bridge length were calculated using the measured displacements from a pair of post-mounted displacement transducers at the mid-width of the south abutment. These transducers measured absolute longitudinal displacements at two points that were at a set distance apart and in vertical alignment on the pile cap. This abutment rotation was also measured by a tiltmeter. Figures 4.98(a) and 4.98(b) present tiltmeter locations for the bridge.

Environmental information including effective temperature at selected locations in the bridge was captured in the meanwhile of abutment movements and rotations by thermocouples. Thermocouples were installed along the length, across the width and through the depth of the

superstructure to determine the temperature of the superstructure. Figure 4.98(a) and 4.98(c) depict the locations for thermocouples through the girder depth.

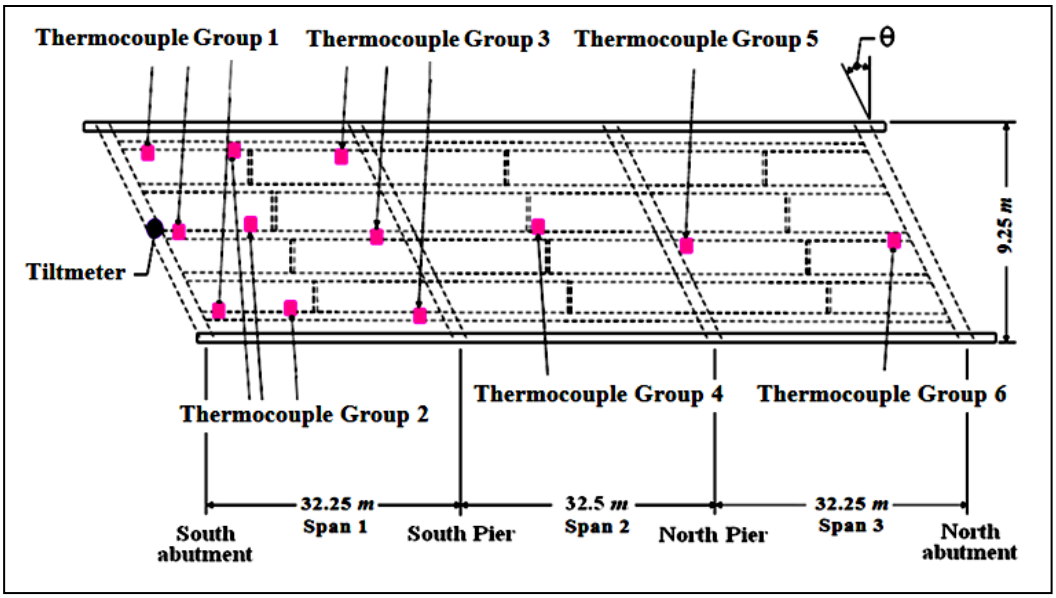

(a)

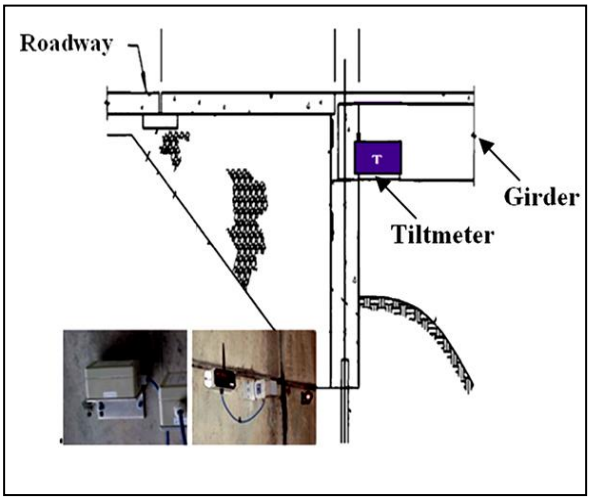

(b)

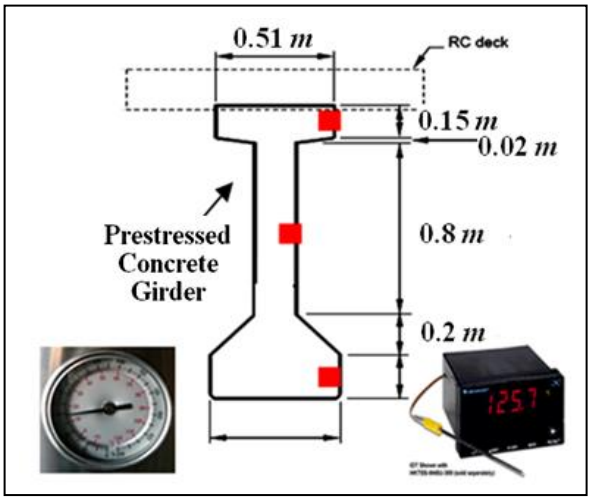

(c)

Figure 4.98: (a) Plan view of integral bridge including tiltmeters and thermocouples locations, (b) Locations for tiltmeters, (c) Locations for thermocouples [1].

At bridge, as shown in Figure 4.99(a), two displacement transducers that were clamped to a steel pile were used to measure relative displacements between the underside of abutment pile cap and a pile. The transducers were mounted to a pile near the mid-width of the south abutment. The horizontal separation between the two transducers allowed for the determination of the relative

rotation between the pile cross section, where the transducers were attached at 0.46 *m* below the bottom of the pile cap and the bottom of the pile cap. This relative rotation was in the vertical plane parallel to the longitudinal axis of the bridge.

Also, bondable electrical-resistance strain gages were applied to the flanges of abutment piles. In most instances, each abutment pile that was instrumented had a total of eight electrical-resistance strain gages that were applied to the outside faces of the flanges near the flange tips, as shown in Figure 4.99(b). An arrangement of four strain gages was used at two cross sections that were located at 0.23 and 0.84 *m* below the bottom of the pile cap. If four longitudinal strains are known at a monitored pile cross section, the x-axis bending, y-axis bending, axial and torsional-warpage strains can be computed from the measured strains. Strain gages were used at two pile cross sections to possibly permit the determination of the moment gradient along the pile length.

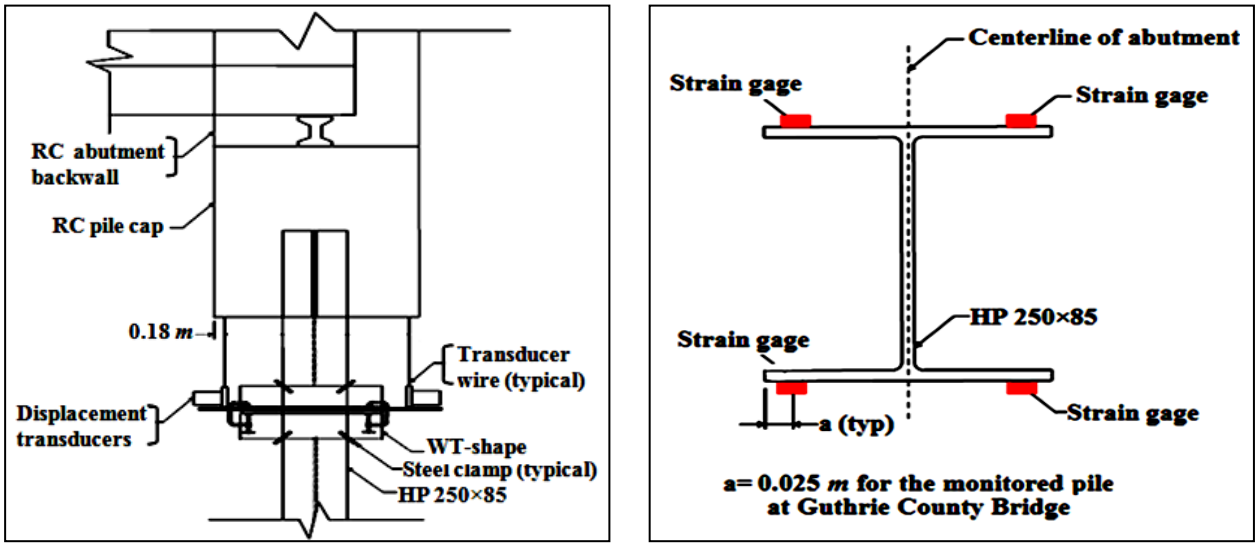

(a) (b)

Figure 4.99: (a) Displacement transducers at the bottom of an abutment-pile cap, (b) Strain gages on an HP-shaped pile [1].

4.1.2.3.1.3 BRIDGE MONITORNIG RSULTS

The bridge was monitored from December 17, 1997 until April 1, 2000. Since thermocouples measure absolute temperatures, the raw data was presented without modifications in most instances. Each thermocouple reading was plotted versus time to determine if the thermocouple was properly functioning. Figures 4.100 show graphs of temperature versus time that were measured by a thermocouple with reliable data over the entire monitoring period.

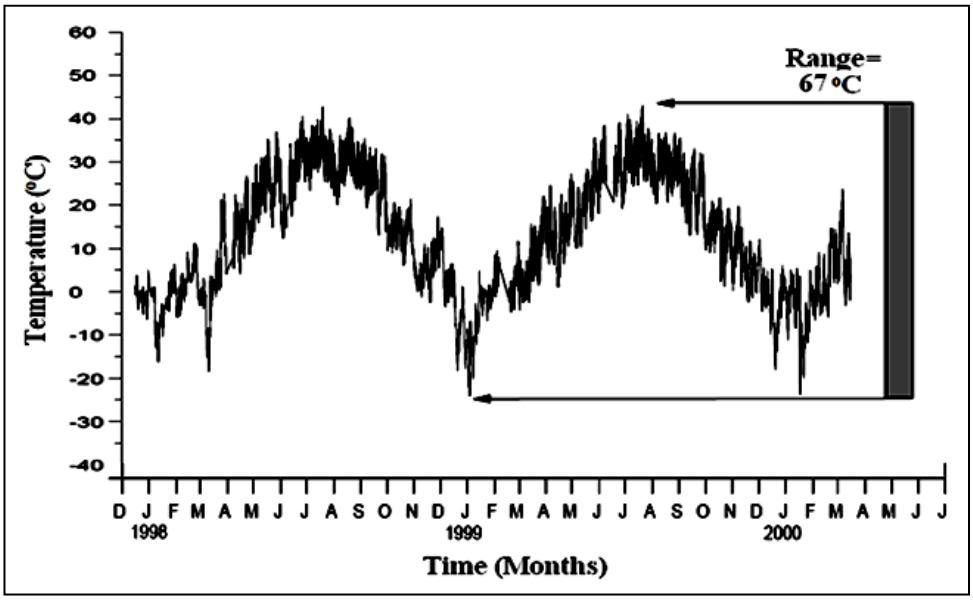

Figure 4.100: Typical thermocouple plots [1].

The change in bridge length was determined by summing the experimentally measured longitudinal displacements of abutments at the mid-width of the abutment pile cap at each end of the bridge. The experimentally-based range in the length of the bridge was 0.045 *mm*. The maximum change in average bridge temperature and thus the maximum change in the bridge length occurred during the time period between July 20, 1998 and January 5, 1999. Figure 4.101 shows the change in the bridge length versus the average bridge temperature for the monitored bridge.

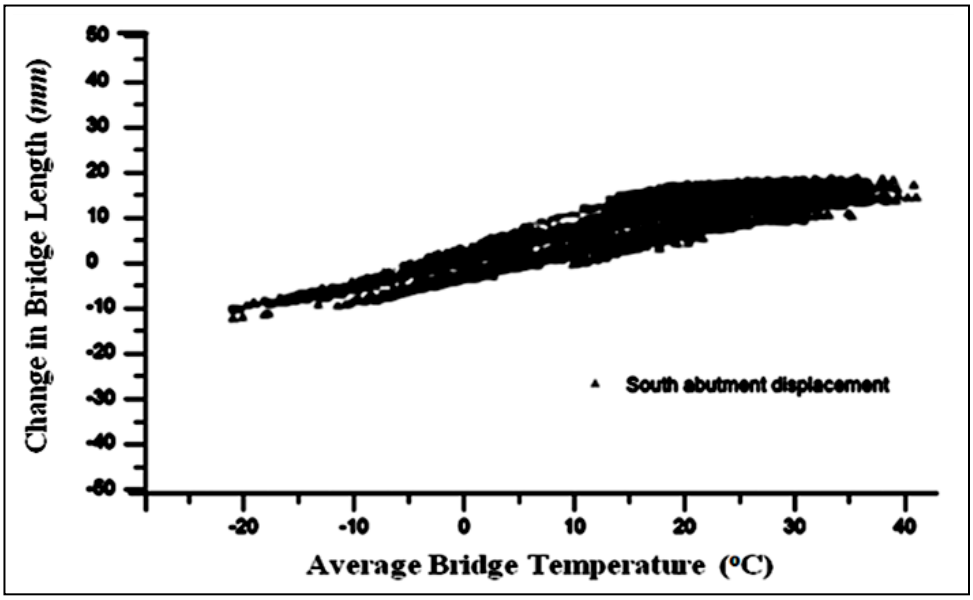

Figure 4.101: Change in the bridge length versus average bridge temperature [1].

Figure 4.102 shows the measured transverse displacements of the center of gravity of the south abutment pile cap for the bridge. Positive displacements indicate that the abutment translated towards the acute-angle corner of the bridge deck.

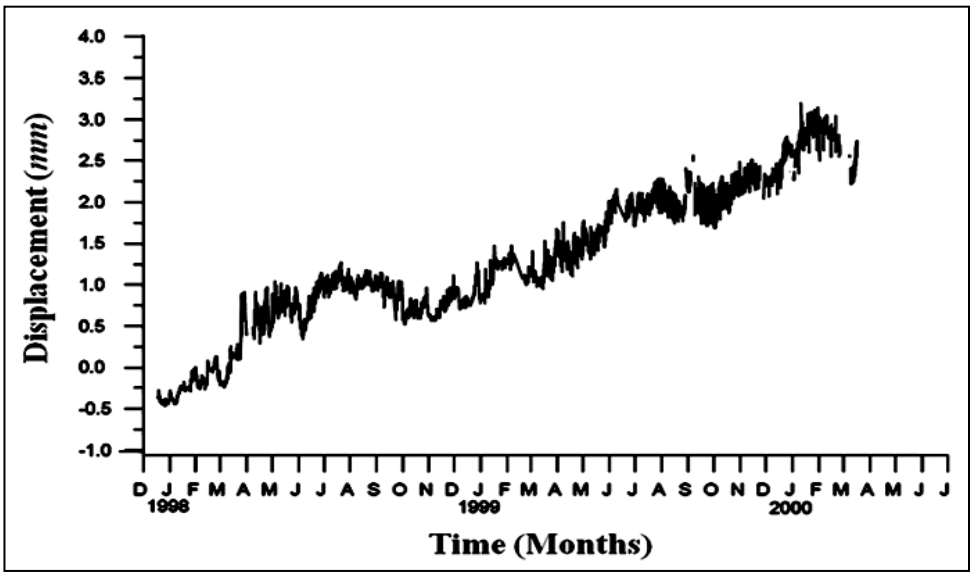

Figure 4.102: Transverse displacements of the south abutment [1].

Relative movement of the bridge superstructure over the pier caps were measured between the bottom of the center PC girder and top of the RC pier cap. The relative displacement at the north abutment of bridge is shown in Figure 4.103. The range in relative displacements of the superstructure over the north piers was around 1.8 *mm*.

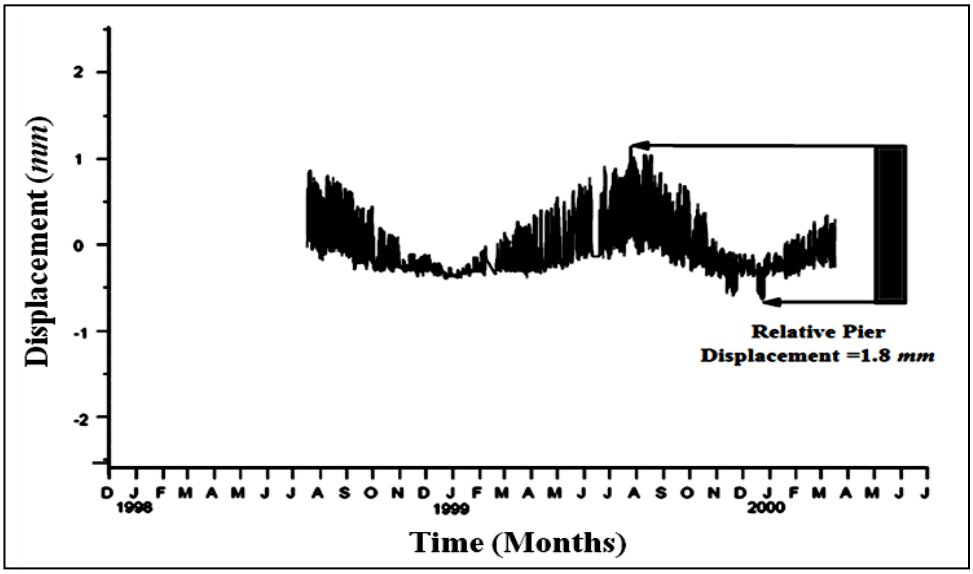

Figure 4.103: Relative displacements at north piers for the bridge [1].

Relative vertical displacements between the abutment pile near the mid-width of an abutment and its RC pile cap were measured at the bridge. Using these displacements, rotations were calculated by dividing the difference between the measured relative vertical displacements at the front and at the back of the pile cap by the horizontal distance between these displacement transducers. This relative rotation was the rotation between the bottom of the pile cap and a point that was 0.457 *m* below the pile cap, where the transducers were attached to the pile. Figure 4.104 shows these experimentally-based, relative rotations for the pile near the mid-width of the south and east abutments. A positive relative rotation for the top of an abutment pile is associated with a pile curvature that has its center of curvature on the side of the pile that is facing the span of the bridge. For the time period of reliable measurements for both displacement transducers that were used to compute the relative pile rotation at the bridge, a directional shift was not observed for that relative rotation.

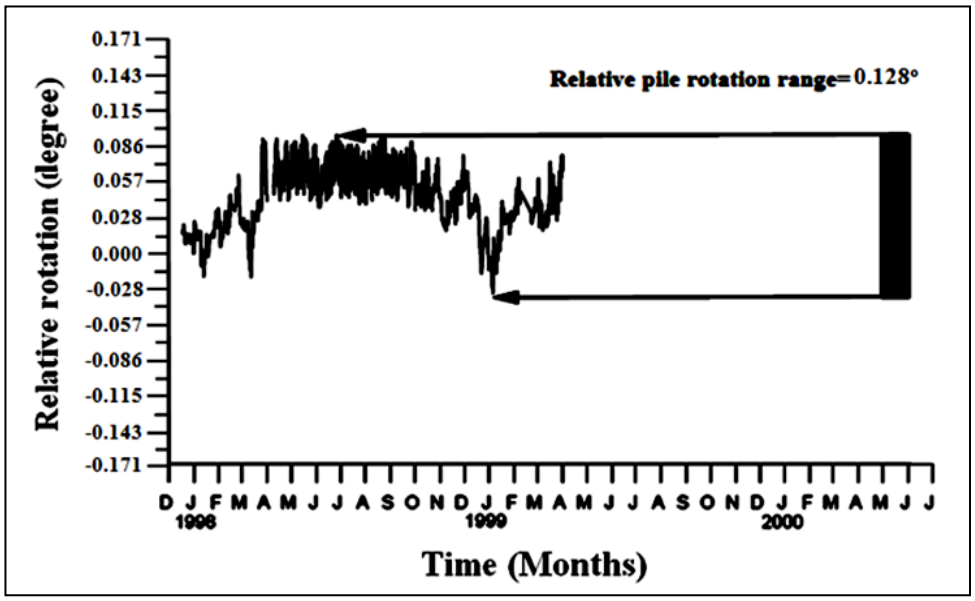

Figure 4.104: Relative rotation between a pile and a pile cap [1].

Since the bridge has a 30^{o} skew angle, the pile-head displacement in a horizontal plane will induce both x-axis and y-axis flexural-bending strains in the piles. Figure 4.105 and 4.106 shows the x-axis and y-axis flexural-bending strains at the monitored upper cross section of the pile near the mid-width of the north abutment. The upper cross section was located at 0.229 *m* below the bottom of the pile cap.

The range in the x-axis and y-axis flexural-bending strains were approximately 510 and 620 μ *mm*/*mm*. For structural steel with a yield stress of 248 *MPa*, the yield strain is equal to 1240 μ *mm*/*mm*.

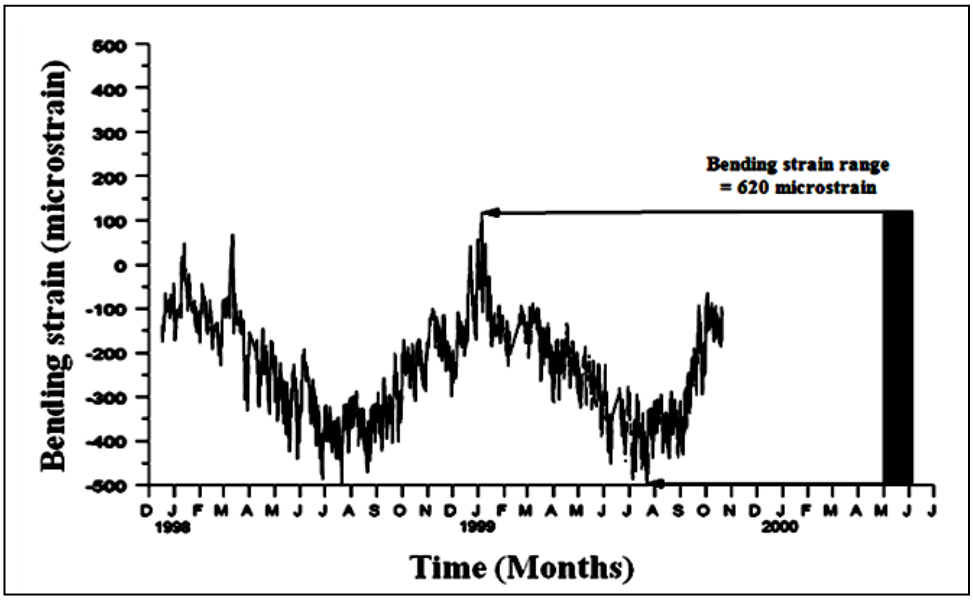

Figure 4.105: Biaxial, flexural Y-bending strains of north abutment [1].

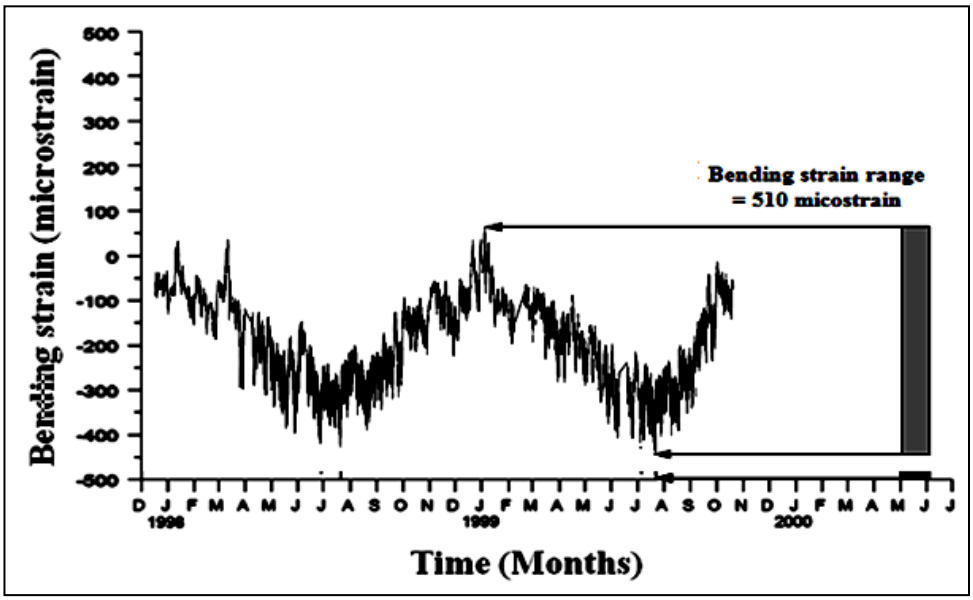

Figure 4.106: Biaxial, flexural X-bending strains of north abutment [1].

4.1.2.3.2 GUTHRIE COUNTY BRIDGE NUMERICAL MODELING

As shown in Figure 4.107, a four span integral bridge was considered for the purpose of numerical modelling of Guthrie County Bridge. Figure 4.108 shows the bridge superstructure cross section considered for the finite element model. The modulus of elasticity for the model was considered as 23,440 *MPa* for the cast-in-place concrete and 30,330 *MPa* for the prestressed girders. The thermal expansion coefficient value for cast-in-place concrete and prestressed concrete was $10.4\times10^{-6}\ 1/^{o}C$ and $7.7\times10^{-6}\ 1/^{o}C$, respectively.

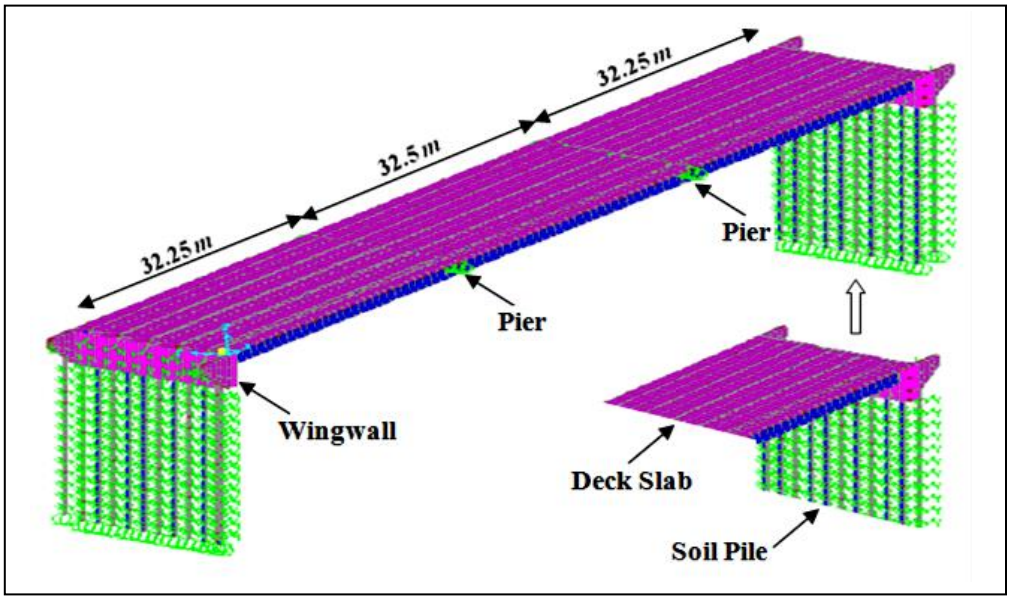

Figure 4.107: 3-D finite element model view of Guthrie County Bridge.

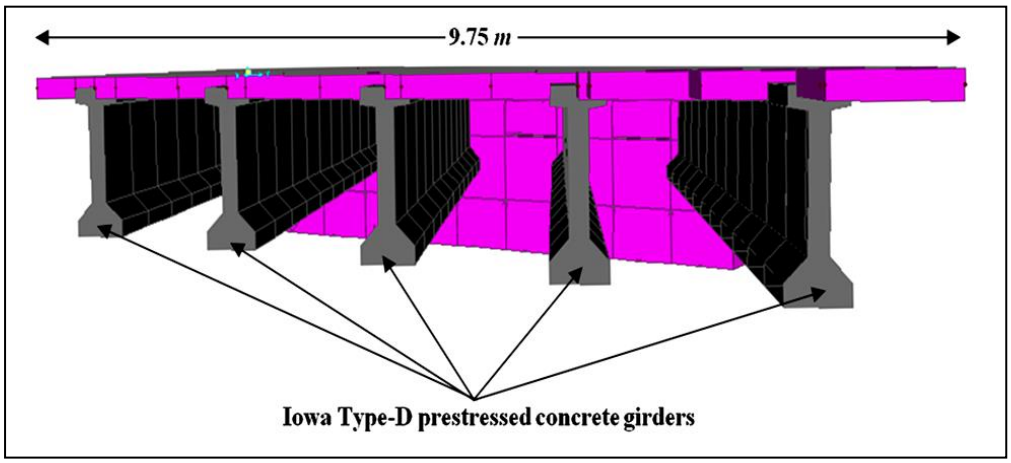

Figure 4.108: 3D finite element model view of bridge superstructure.

4.1.2.3.2 COMPARISON OF ANALYTICALLY-PREDICTED AND EXPERIMENTALLY-MEASURED OF GUTHRIE COUNTY BRIDGE

Different temperature variations (-26°*C* and +41^{o}*C*) were implemented in the finite element modeling with considering the results obtained from field testing. Figure 4.109 and 4.110 show 3D FE temperature loadings for a bridge corresponding to those temperature changes.

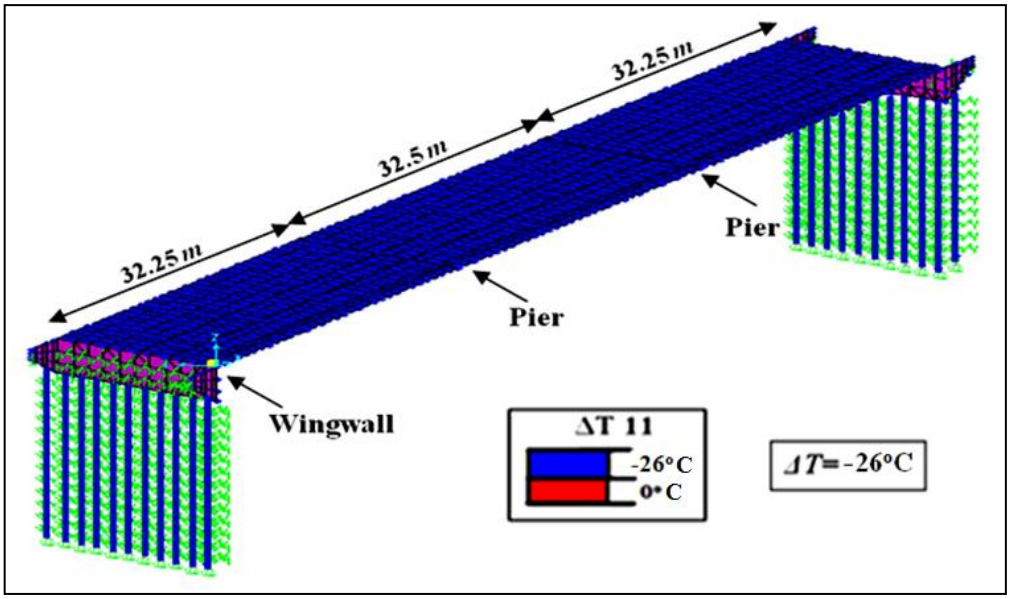

Figure 4.109: View of 3D FE model corresponded to temperature loading of -26^{o}C.

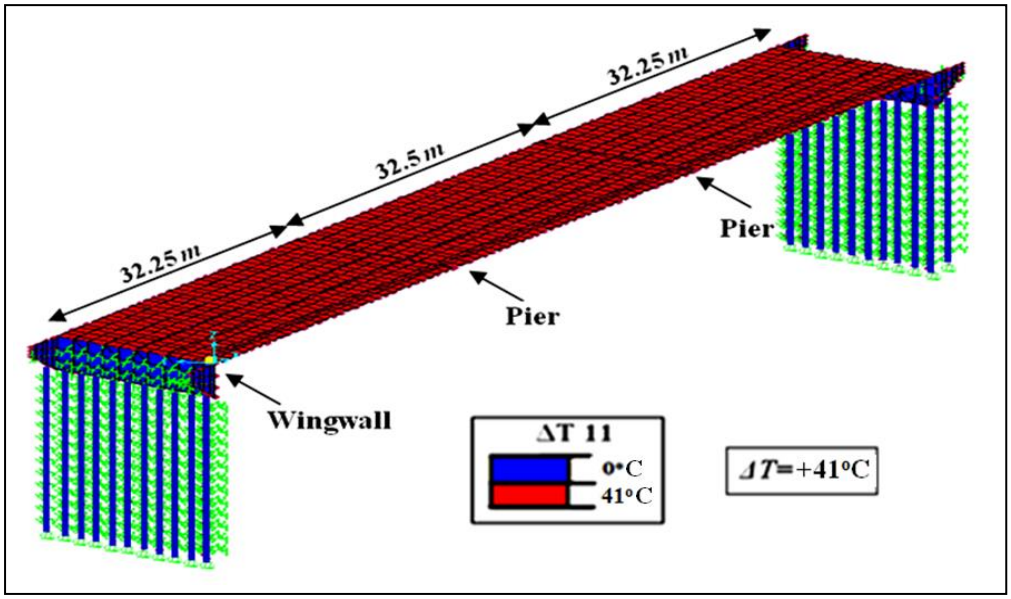

Figure 4.110: View of 3D FE model corresponded to temperature loading of +41^{o}C.

Skew of the bridge causes rotation and transverse movement of the structure. As a result, expansion and contraction of the bridge consist of longitudinal and transverse displacements. Figure 4.111 and 4.112 show longitudinal contraction and expansion for the bridge subjected to temperature decrease and increase, respectively.

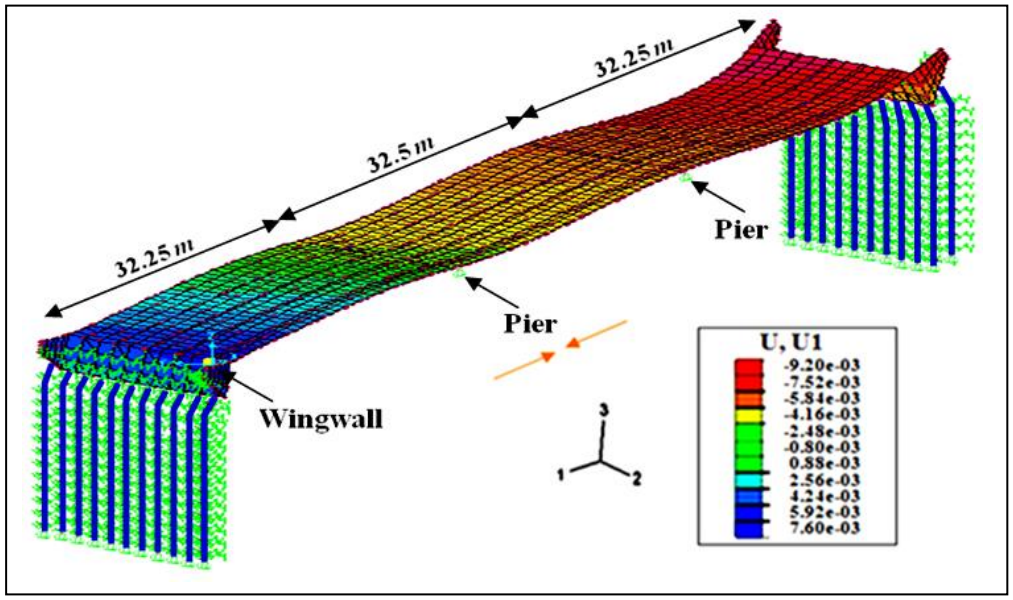

Figure 4.111: Bridge contraction due to temperature decrease of -26^{o}C.

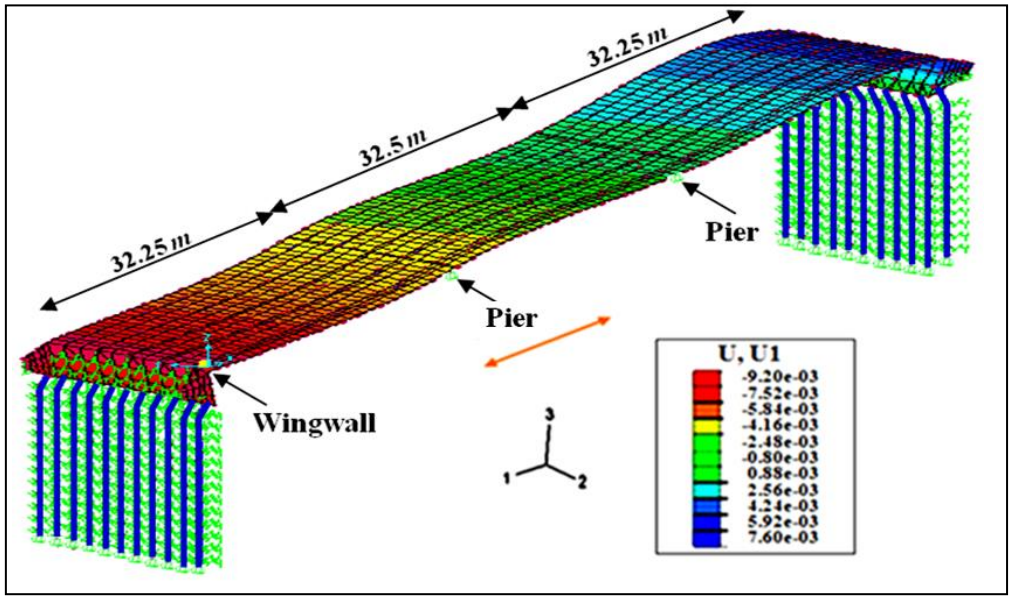

Figure 4.112: Bridge expansion due to temperature increase of +41^{o}C.

Table 4.11 shows the maximum longitudinal and transverse displacements obtained from numerical and experimental analysis. It was observed that finite element results agree well with experimental ones. For instance, longitudinal displacement value obtained from finite element analysis for south abutment pile cap due to temperature increase of $+41^{o}C$ was +17 *mm* and this value obtained from experimental was +18 *mm* (difference of around 5%).

Table 4.11: Comparison of predicted and measured south abutment displacement.

Temperature Variation, (ΔT), (^{o}C)	**Longitudinal Displacement, (*mm*)**		**Transverse Displacement (*mm*)**	
	Field Data [1]	**FE Model**	**Field Data [1]**	**FE Model**
-26	-10	-11	+0.75	+1.1
+41	+18	+17	+2.1	+1.6

Table 4.12 shows the comparison between predicted and measured relative displacements of superstructure and rotation between the pile and pile cap of the bridge. It can be observed that FEM predicted relative displacements very close to the experimentally-measured ones. For instance, relative displacements for bridge subjected to $-26^{o}C$ temperature decrease were computed as -0.86 and -0.8 *mm* by using FEA and field testing (less than 8% error). Similar trend were also witnessed between numerical and experimental results in case of relative rotation between the pile and the pile cap.

Table 4.12: Comparison of predicted and measured relative displacement of superstructure and rotation between pile and pile cap.

Temperature Variation, (ΔT), (^{o}C)	**Relative Displacement of Superstructure over the North Pier Caps, (*mm*)**		**Relative Rotation between a Pile and a Pile Cap, (*mm*)**	
	Field Data [1]	**FE Model**	**Field Data [1]**	**FE Model**
-26	-0.8	-0.86	-0.28	-0.3
+41	+1.0	+0.94	+0.1	+0.09

As shown in Figure 4.113, results for pile bending strains obtained from finite element analysis and experimental test were drawn against each other in graphical format. Results from finite element analysis showed same trends as experimental weak axes strain, ε_y, but the computed strains were slightly greater than the experimentally measured strains. For example, due to temperature decrease of -26^oC (from 0^oC to -26^oC), weak axes strain, ε_y, was increased by value of 133.2 and 120 μ *mm*/*mm* in numerical modeling and field testing, respectively. Similar trend was observed for pile strong axis strain, ε_x, and strains obtained from numerical analysis were just a little greater than field test.

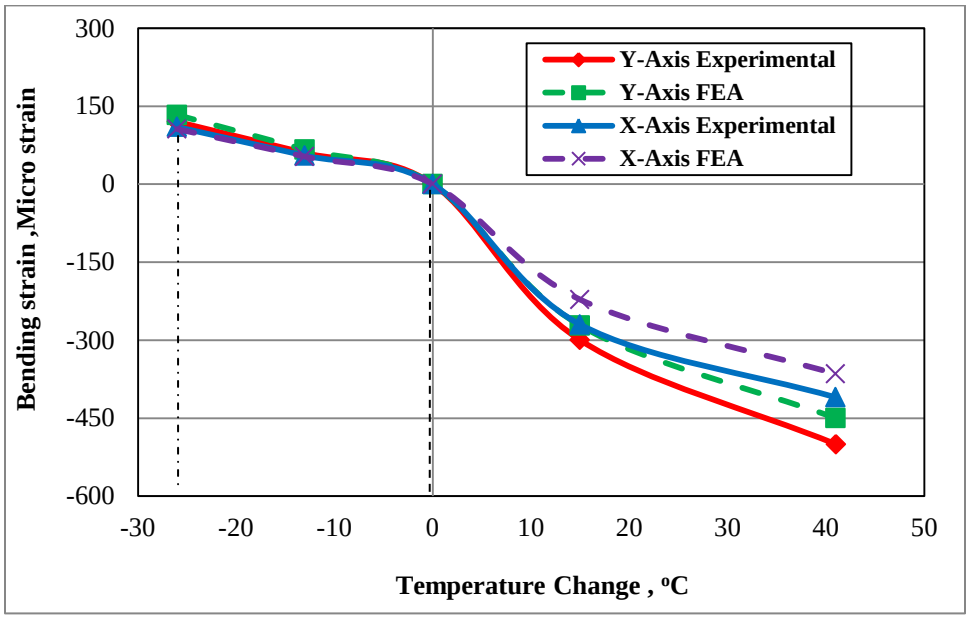

Figure 4.113: Comparison of finite element analysis and field test results for pile bending strains due to different temperature changes.

It is clear from above mentioned correlation that FEA results agreed well with experimental results for non-skewed and skewed integral abutment bridges subjected to temperature changes, indicating that finite element method was a powerful predictive tool that could be used in predicting integral abutment bridge behaviour.

4.2 VALIDATION FOR THE EFFECT OF LIVE LOAD

The numerical models for the effect of live loads were also verified against the results of field testing. The measured data of integral bridges, namely: Minnesota DOT Bridge #5555 and Coplin Plantation Bridge, were used to validate finite element models.

4.2.1 MINNESOTA DEPARTMENT OF TRANSPORTATION BRIDGE #55555

4.2.1.1 FIELD TESTING OF MINNESOTA DOT BRIDGE #5555

4.2.1.1.1 BRIDGE DESCRIPTION

Minnesota Department of Transportation (Mn/DOT) Bridge #55555 was constructed on CR 104, 2.6 *km* south of CSAH 25, Minnesota [34]. The bridge was a three-span prestressed concrete bridge with a total length of 66 *m*. Each span consisted of four type 45M prestressed girders with a center-to-center spacing of 3.35 *m*. The total bridge width was 12 *m*, including two Jersey barriers and one lane of shoulder in each direction. The bridge elevation is shown in Figure 4.114.

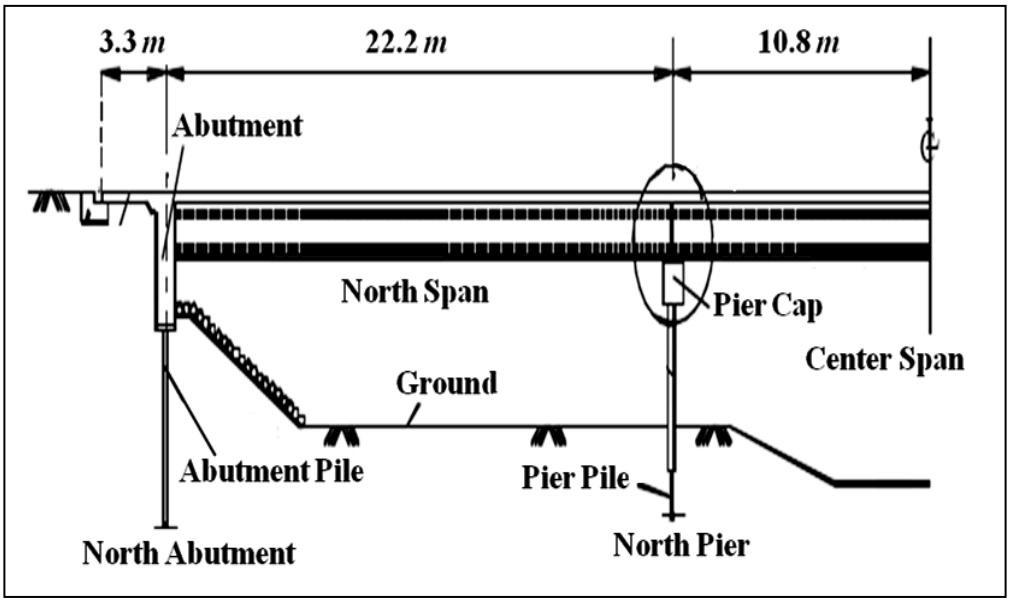

Figure 4.114: Bridge elevation [34].

At the piers, the girders were supported by a curved plate-bearing assembly to achieve a simple support. The continuity of the superstructure over the piers was provided by a 230 *mm* thick

reinforced concrete deck. A 20 *mm* V groove was set into the bottom of the deck over the centerline of the pier, and a saw cut was made at the top of the deck soon after the deck was poured. At abutments, ends of the side-span girders were cast into abutment diaphragm at the same time the deck was poured. The expansion and contraction of the bridge were compensated by the thermal expansion joint located between the sill and the approach slab which was keyed into the deck slab. The soil profile under the north abutment is shown in Figure 4.115. Details of soil profile of south abutment can be found in the report prepared by Huang et al. [34]. The properties of the filled soil were not clear. Under the fill, poorly graded loose sand and soft lean clay were two typical soils within a distance of 6.35 *m* from the bottom of the abutment. For the soils under the south abutment, a level of clayey sand, with a thickness of 0.76 *m*, existed between the fill and the lean clay. A single row of six piles was driven at each abutment of the bridge. Figure 4.116 shows an elevation of abutments with six HP 310×79 piles oriented in weak-axis bending to facilitate abutment movements when the superstructure expanded and contracted due to seasonal temperature. Wingwalls were oriented at 45^{o} to the abutment centerline. Six HP250×85 pier piles were oriented in strong axis bending and encased in a 0.4 *m* concrete-filled steel tube.

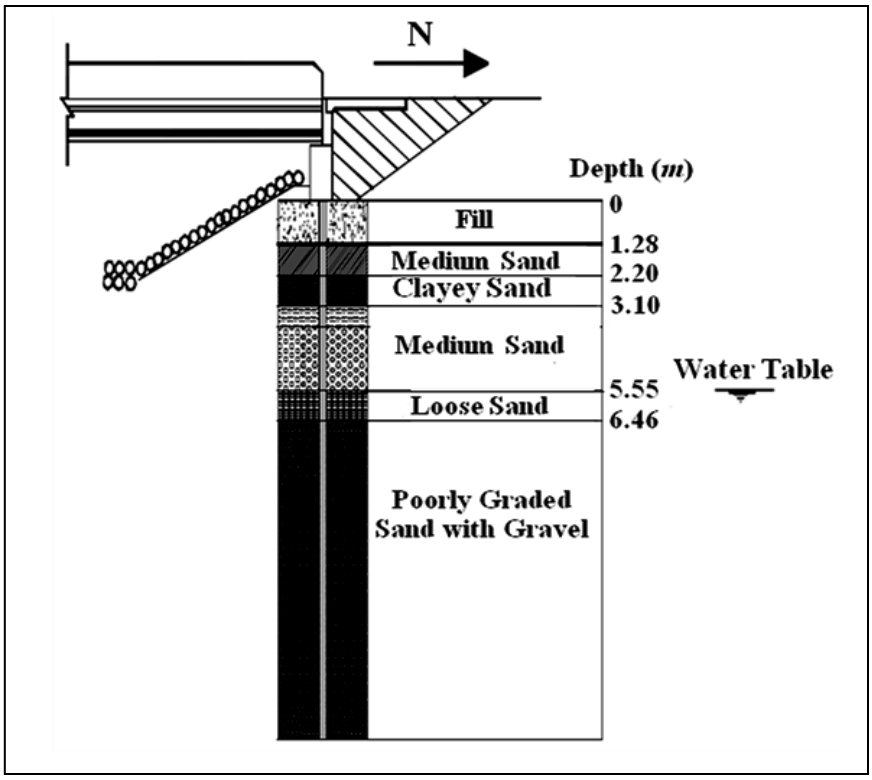

Figure 4.115: Soils under the north abutment [34].

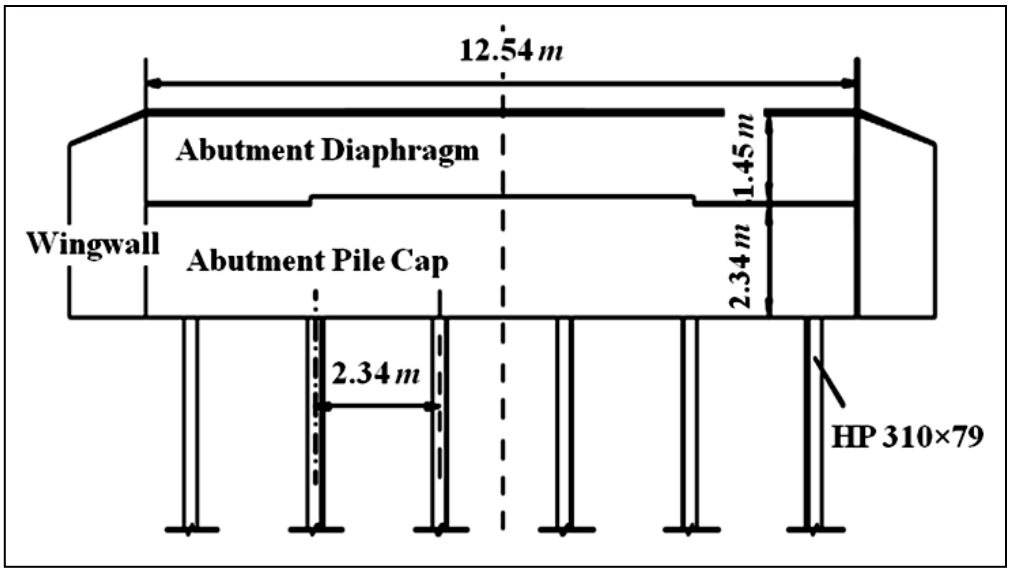

Figure 4.116: Elevation of abutment [34].

4.2.1.1.2 BRIDGE INSTRUMENTATION PLAN

The live load tests were undertaken with various combinations of longitudinal and transverse positions of the trucks to create worst effects in the girders at midspan, near pier and at the abutment. Two live load tests were conducted in 1997 and 1999 on the test bridge. In 1997, both one-truck and two-truck tests were conducted. The truck positions of the one-truck tests are shown in Figure 4.117.

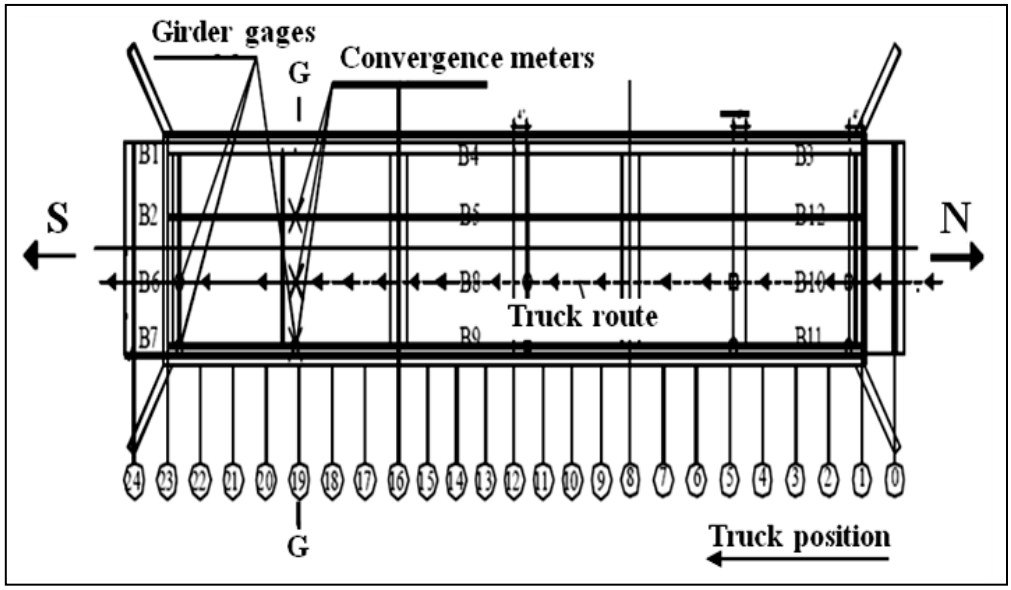

(a)

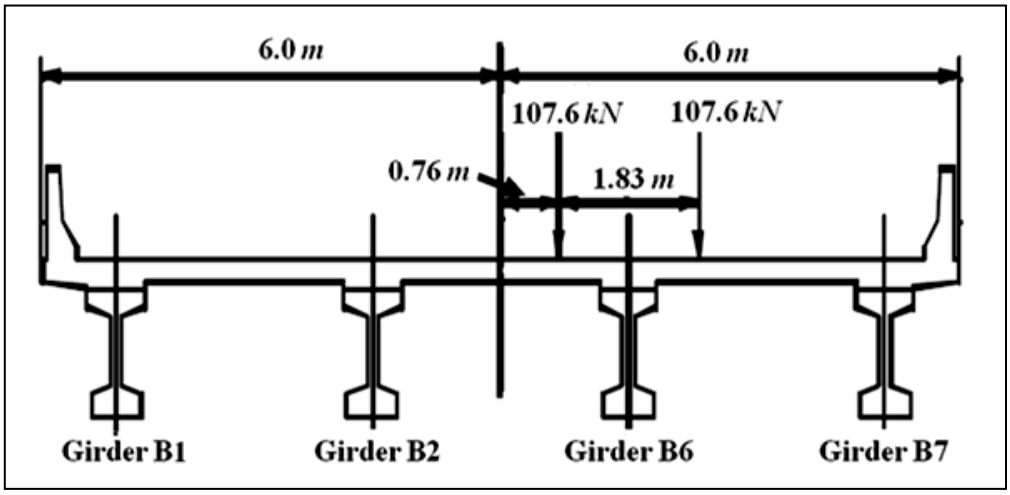

(b)

Figure 4.117: Layout of one-truck test in 1997, (a) Layout of truck test, (b) Section G-G [34].

The truck moved from the north abutment to the south abutment across 24 truck positions over the centerlines of girders B6, B8 and B10. Convergence meters were positioned near the midspan of girders B7, B6 and B2 to measure the girder deflections during the tests. The positions of the convergence meters are shown in Figures 4.117(a) and 4.118.

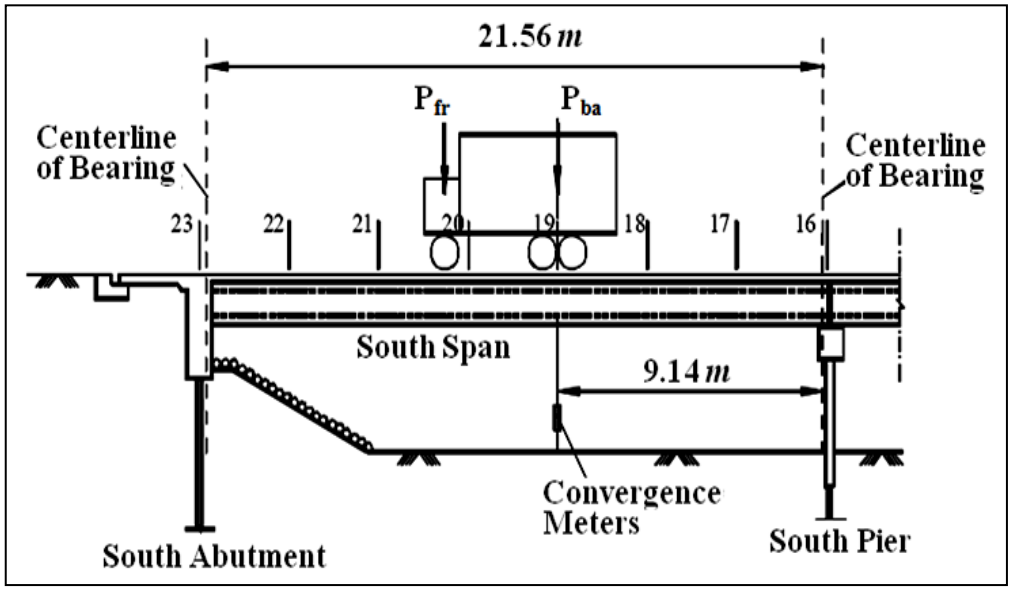

Figure 4.118: South span convergence meters measured girder deflection during load tests [34].

In 1999, one-truck and two-truck tests were conducted at 37 truck positions along the total bridge length and 26 truck positions in the south side span. The truck moved across 26 truck positions over the centerlines of the side-span girders. The types of gages and their locations used for data measurements were same as those of the live load tests in 1997. Comparing the truck positions of the one-truck load tests in 1997 and 1999, the positions 17, 18, 19 in the 1997 tests were close to the truck positions 12, 13, and 14 in the 1999 tests. Consequently, those three truck positions were picked to compare the finite element model with experimental findings. The sizes and axial wheel loads of the trucks used for the one truck tests in 1997 and 1999 are shown in Figure 4.119.

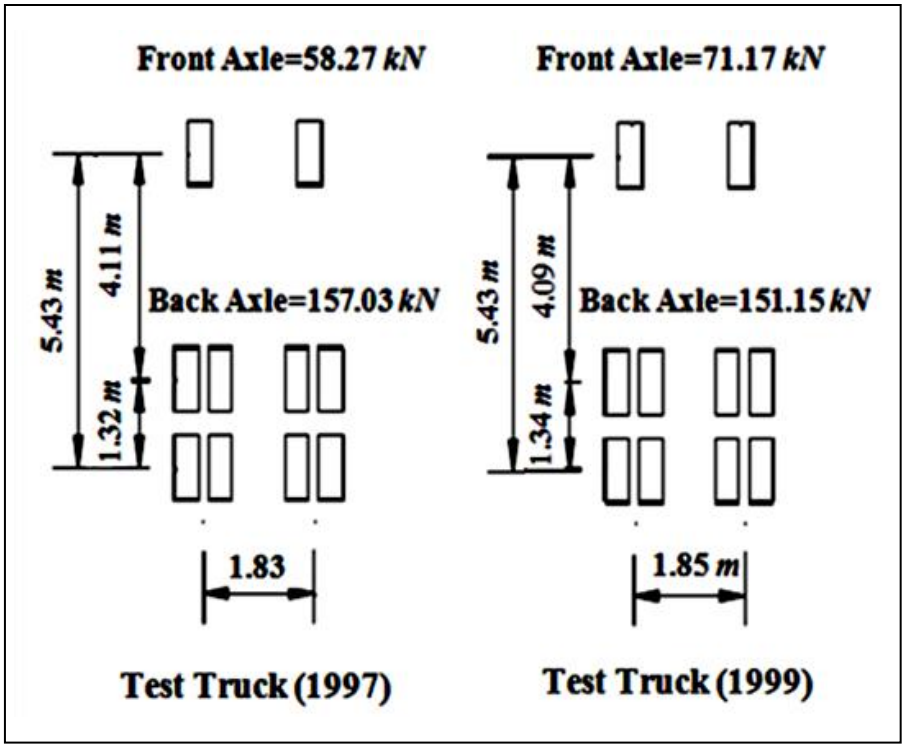

Figure 4.119: Trucks used in one-truck tests [34].

4.2.1.1.3 LIVE LOAD TESTING RESULTS

For Truck Positions 17, 18 and 19 (illustrated in Figure 4.117), the measured data obtained from live load testing for girder deformations are listed in Table 4.13.

Table 4.13: Girder deflections due to single truck [34].

Girder	Test	P-19(1997) or P-12(1999)	P-18(1997) or P-13(1999)	P-17(1997) orP-14(1999)
		Deformation (*mm*)	Deformation (*mm*)	Deformation (*mm*)
B7 (Mid)	1997	-0.92	-0.84	-0.58
	1999	-0.79	-0.61	-0.38
B6 (Mid)	1997	-1.44	-1.22	-0.78
	1999	-1.42	-1.00	-0.58
B2 (Mid)	1997	-0.81	-0.78	-0.53
	1999	-0.76	-0.61	-0.35

4.2.1.2 MINNESOTA DOT BRIDGE #5555 NUMERICAL MODELING

A 3D finite element model of Bridge #5555 was developed as illustrated in Figure 4.120. Numerical models were assembled using elements described in previous sections. The modulus of elasticity of the girder and deck concrete were considered 34,400 and 30,000 *MPa*.

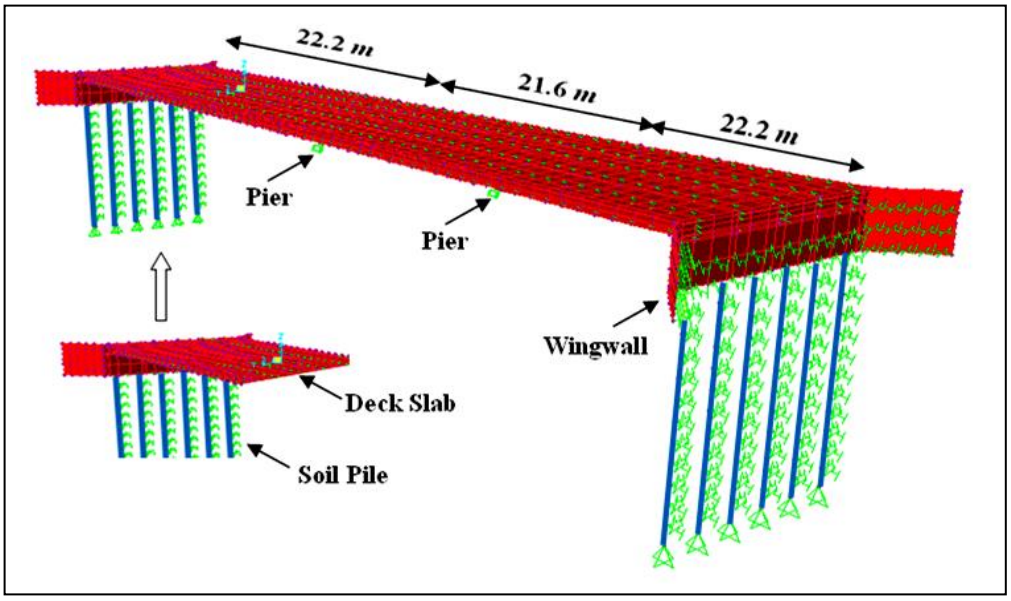

Figure 4.120: 3D Finite element model view of bridge #5555.

Truck Loadings were applied to the top joints of the shell elements using defined load cases and combinations of the trucks wheel loading. The weight of each wheel for either the test truck 1997 or 1999 was applied as a joint load in the negative Z direction. Different truck loads were placed

at different longitudinal positions down the entire length of the bridge deck for each load path. Figure 4.121 shows a partially loading assignment of the 1997 test truck on the bridge.

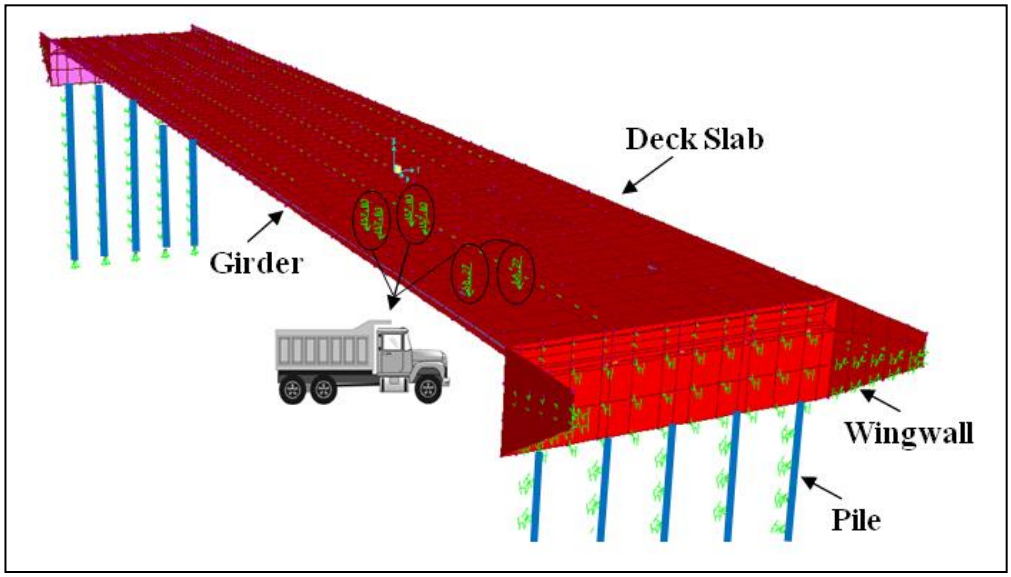

Figure 4.121: Truck load applied to shell element joints.

4.2.1.3 COMPARISON OF ANALYTICALLY-PREDICTED AND EXPERIMENTALLY-MEASURED TRUCK TEST DATA OF MINNESOTA DOT BRIDGE #5555

For Truck Positions 17, 18, and 19, B7, B6 and B2 girder deformations were calculated using FEA and compared to the field data as shown in Figure 4.122 to 4.124.

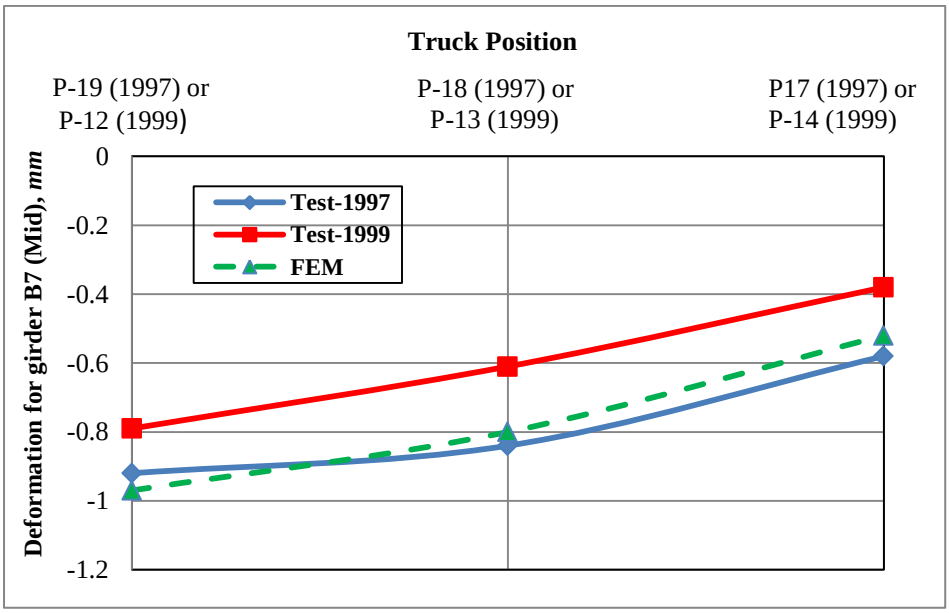

Figure 4.122: FEM and test results for girder B7 (Mid) deflection.

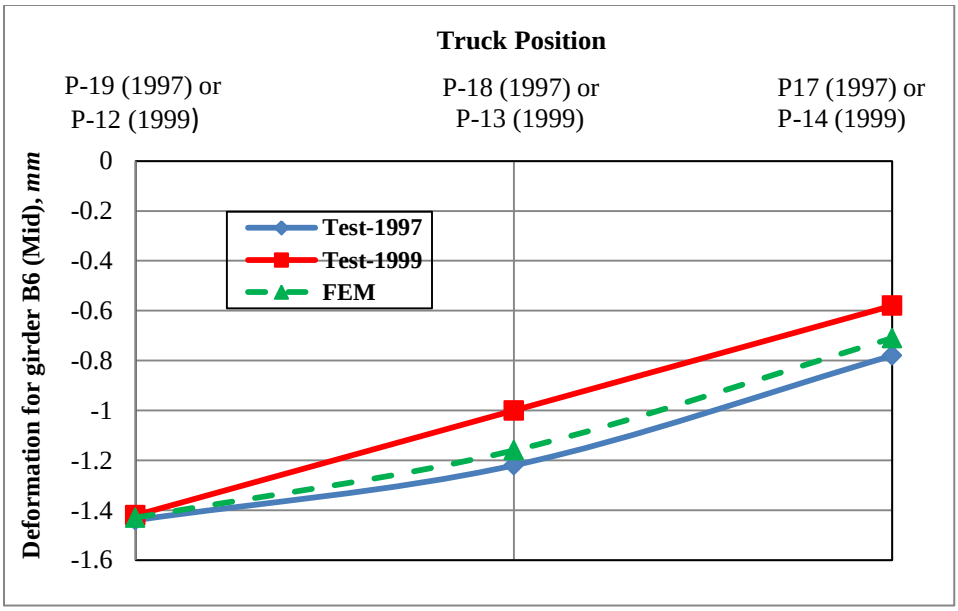

Figure 4.123: FEM and test results for girder B6 (Mid) deflection.

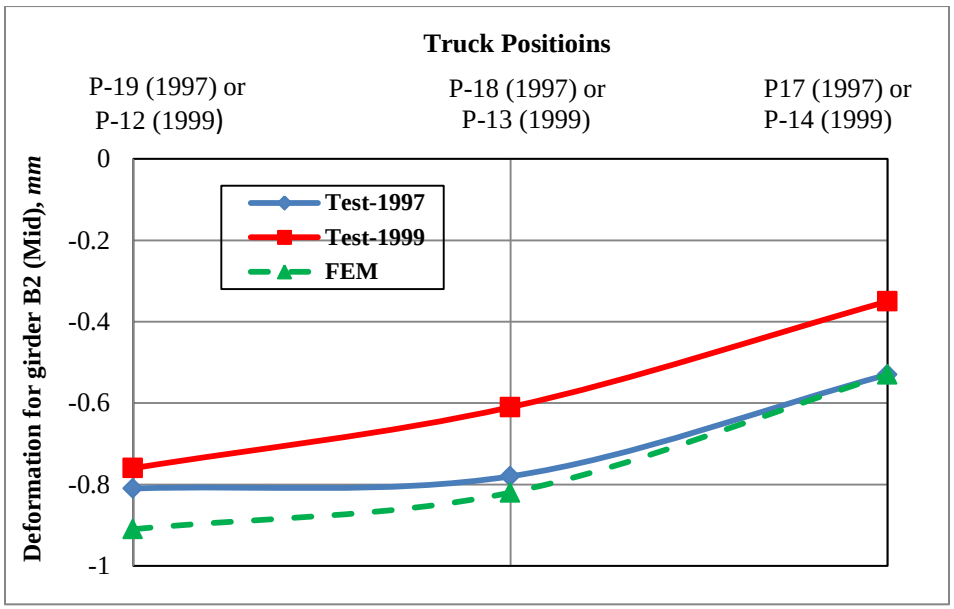

Figure 4.124: FEM and test results for girder B2 (Mid) deflection.

It can be observed that the finite element model provided a good representation of the measured data during truck load tests especially for 1997 test truck. For instance, as illustrated in Figure 4.123, deflection value obtained from field test at mid-span of girder B6 for truck loading (P-18, 1997) was -1.22 *mm* and this value obtained from finite element analysis was -1.16 *mm* (an overestimation of only 5%).

4.2.2 COPLIN PLANTATION BRIDGE

4.2.2.1 FIELD TESTING OF COPLIN PLANATATION BRIDGE

4.2.2.1.1 BRIDGE DESCRIPTION

A single-span, composite steel girder bridge over Nash Stream in Coplin Plantation, Maine was constructed in the summer and fall of 2004. The bridge replaced an existing through-truss steel structure, spans 30 *m* and is 10 *m* wide overall. Both abutments are skewed at 35° and measure 0.2785 *m* from the bottom of the abutment to the top of the concrete deck. The total abutment height is approximately 1.2 *m.* The abutment backwall thickness is 0.9 *m*, and full reinforcing extends through the single construction joint located approximately 0.3 *m* below the top of the piles. The superstructure consists of four, 1.005-*m* deep plate girders spaced at 2.735 *m* with a 0.2 *m* thick composite concrete deck. The abutments are supported by four HP 360×132 Grade 345 steel HPs oriented with their weak-axis perpendicular to the span direction and driven to refusal. Each pile rests directly under a girder and was welded to the bottom flange of the steel plate girder prior to the deck casting per MaineDOT standard design details. Figure 4.125 shows a plan view of the deck [31].

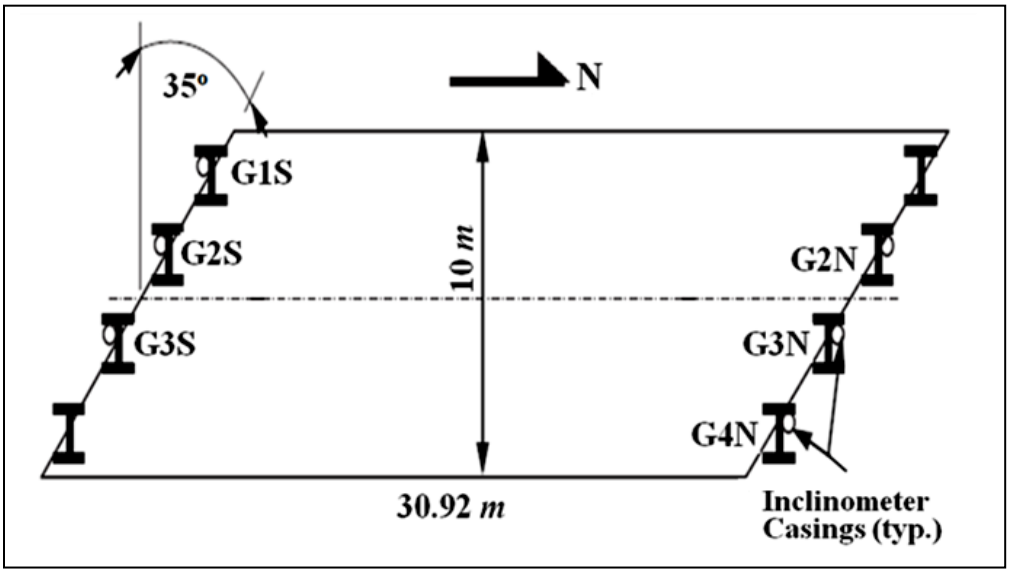

Figure 4.125: Plan view of bridge showing thermistors and instrumented piles [31].

Five borings were completed throughout the site, including a cased washboring behind each abutment location. Soil profile with depth to bedrock for north abutment is shown in Figure 4.126.

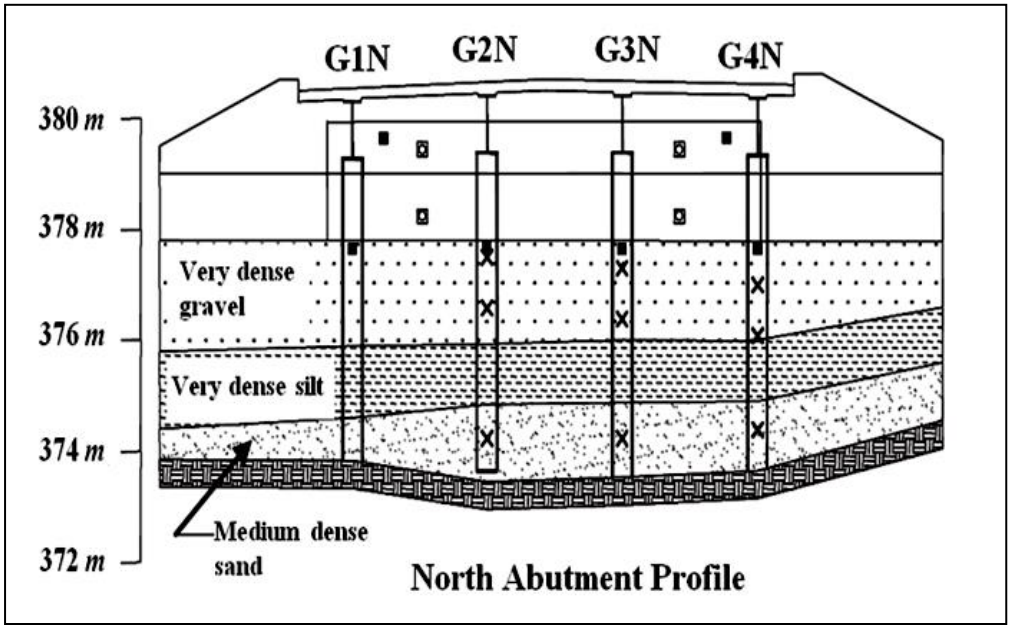

Figure 4.126: Profile view of north abutment of bridge [31].

The depth from the bottom of the abutment to bedrock at the south abutment varied from 6.22 to 8.67 *m* and piles were expected to develop rotational fixity at the south abutment. However, at the north abutment, pile depths varied from only 3.94 to 4.24 *m*. Thus, the bridge was well-suited for comparing the in situ behaviour of both moderately short (less than the equivalent depth of fixity of 4.5 *m*) and long (greater than the equivalent depth of fixity) HPs. The south abutment has a thick layer of medium dense to dense sand with traces of silt and gravel. This deposit is underlain by very dense silty sand with gravel, which is thought to be glacial till. The north abutment has a very dense gravel layer near the surface, likely fill material from the construction of the previous bridge. This layer is underlain by a very dense layer of silt, followed by a medium dense sand, which is likely glacial till. For a more complete description of the geotechnical and structural characteristics of the bridge, see Hartt et al. [31] and Sandford et al. [62]. The backfill was dense wellgraded sand with some gravel.

4.2.2.1.2 BRIDGE INSTRUMENTATION PLAN

Upon completion of bridge construction, live load testing was conducted on the bridge. The results of live load testing can provide a basis for predicting responses under other loadings. Thirteen cases were utilized to examine differences in responses between the long and short

piles, as well as the effects of the large skew. Live load testing was completed on the bridge on October 7, 2004. The two Maine Department of Transportation (MaineDOT) dump trucks used for live loading were fully loaded with gravel and weighed 297.8 *kN* and 273.6 *kN* each, for a total of 571.4 *kN*. The dimensions of each truck including the contact area of each tire, the length of the wheel base, and distance between wheels were taken (see Figure 4.127). The deck was loaded by the two trucks in thirteen different positions (see Figure 4.127). The two data acquisition systems were adjusted to read every three minutes at concurring intervals. Each loading position was held for at least nine minutes so that three complete sets of readings were taken for each position.

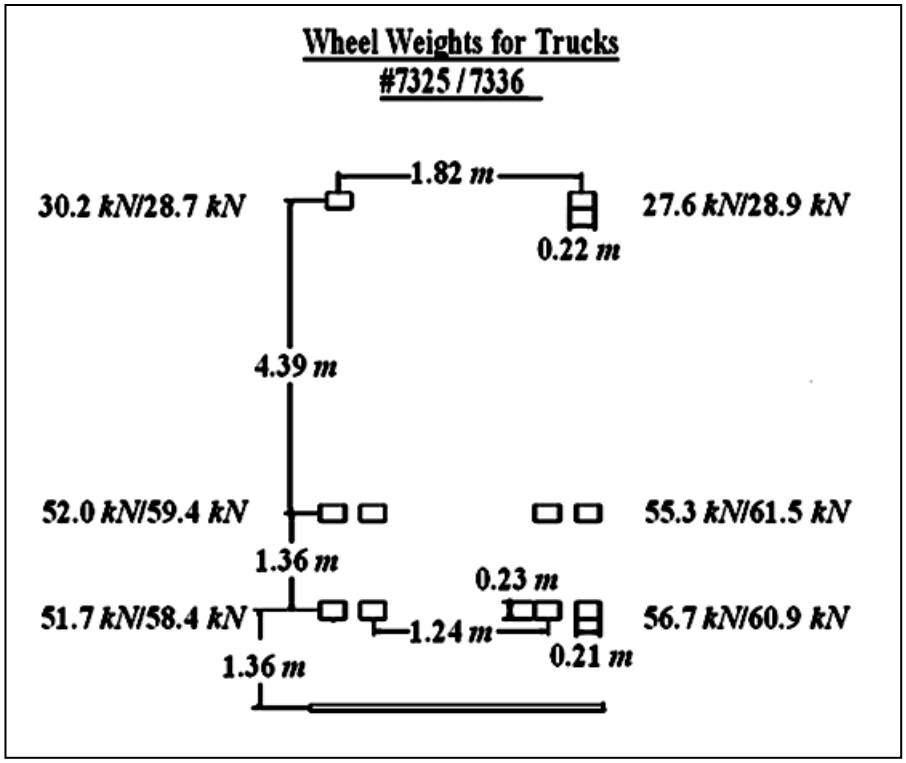

Figure 4.127: Truck dimensions and wheel weights [30].

Live loading positions were chosen to simulate and magnify the effects of traffic moving across the bridge. Several series of progressions were completed with each consisting of three positions at the one-quarter, one-half and three-quarter points along the length of the span. To create a worst case loading on a single pile, the two dump trucks were positioned facing opposite directions, with their rear bumpers touching (cases #4 and #9). In these worst load cases, the

weight of the rear axles is concentrated within an area of 12.8 m^2. The trucks were progressed down each curb line, with readings at the one-quarter, one-half and three-quarter points of the span length.

The trucks were also progressed down the length of the bridge, positioned side by side (cases #1, #2, #3 and #10). They were shifted towards the eastern curb line, which loaded girders #3 and #4. This distributed the load to two girders rather than concentrating the load on one girder as was done in the bumper to bumper loadings. The final series of positions consist of a truck centered in each lane with both facing southward and progressing together along the bridge (cases #11, #12 and #13). Figure 4.128(a) and 4.128(b) layout the loading positions which will be referenced often in the subsequent sections. The location of the truck with reference to the edge of the deck is given for each case. For side-by-side loadings, the dimension is to the center of the rear axle, while for bumper-to-bumper loadings, the dimension is to the touching bumpers. In Figure 4.128 truck # 7336 is denoted with a (*); the other truck is #7325.

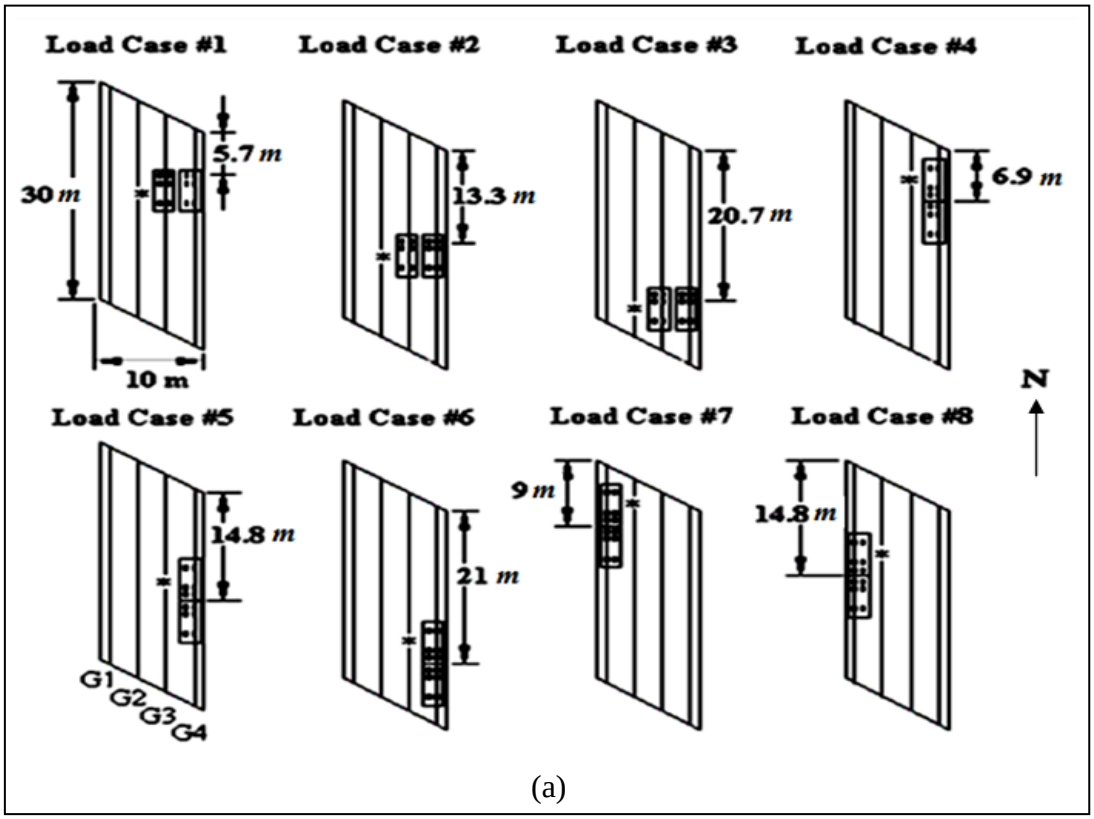

(a)

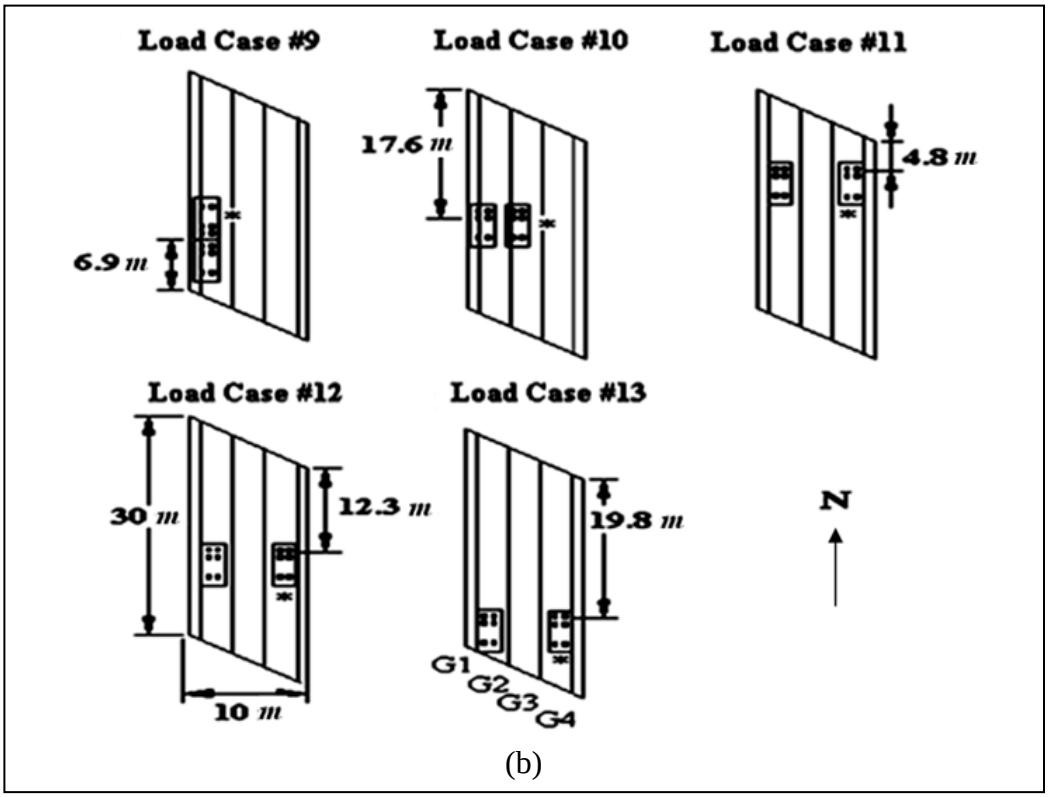

Figure 4.128: Live loading positions [31].

The bridge was instrumented during construction with twelve strain gages on six of the eight piles to track movement of the piles. Protection for the strain gages and their cables was provided by welding steel covers over them with a tapered protection block at the bottom (Figure 4.129).

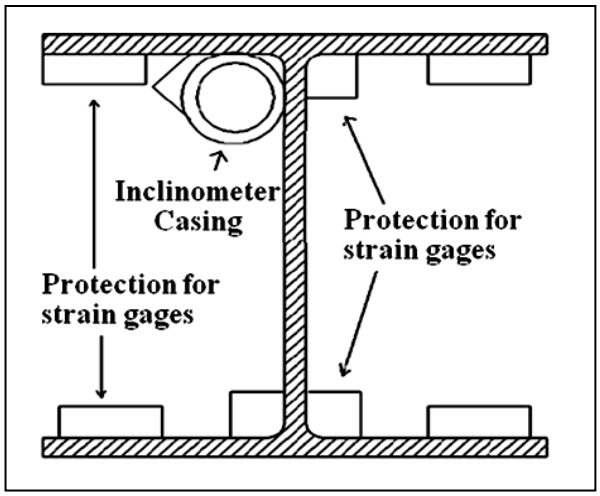

Figure 4.129: Strain gage and inclinometer layout on piles [31].

A summary of the elevations of strain gage sets for each pile is summarized in Table 4.14.

Table 4.14: Elevation of strain gage sets [31].

South Abutment - Elevation, *m*			
Pile	Bottom	Middle	Top
G1-S	370.30	376.93	377.84
G2-S	370.76	376.83	377.67
G3-S	371.89	376.36	377.27
North Abutment - Elevation, *m*			
Pile	Bottom	Middle	Top
G2-N	374.27	376.62	377.43
G3-N	374.26	376.37	377.20
G4-N	374.39	376.11	376.93

Inclinometers were used to measure shapes of the six instrumented piles. Every vibrating wire instrument (strain gages) was connected to a solar-powered automated data retrieval system that allows remote access to the data via modem. A manual readout unit was used to take initial readings as well as subsequent readings until the data acquisition systems were functional. A plan view of instrument locations is shown in Figure 4.130.

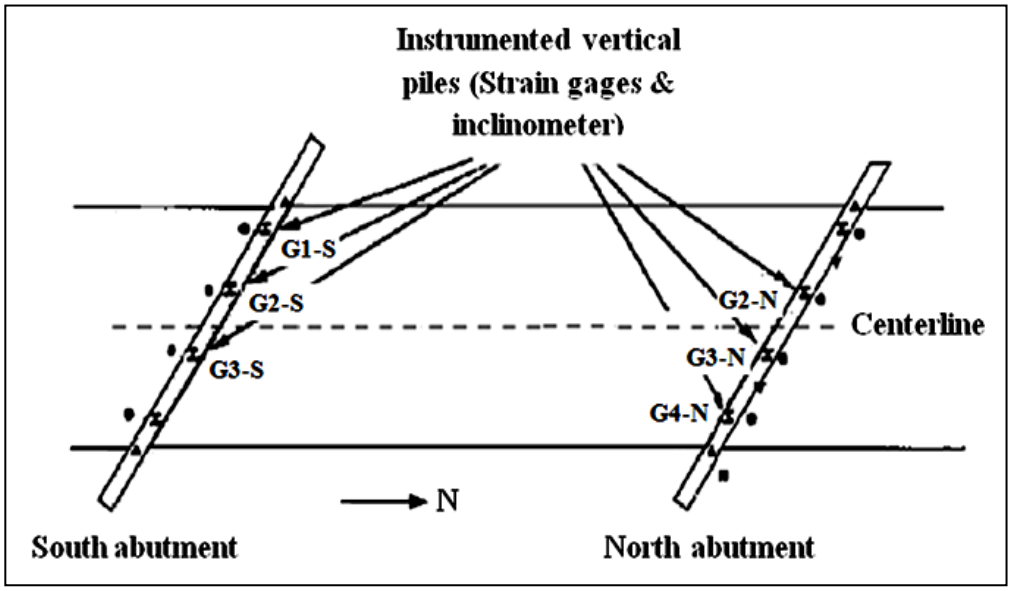

Figure 4.130: Plan view of instrumentation on bridge [31].

4.2.2.1.3 LIVE LOAD TESTING RESULTS

Tables 4.15 summarize measured axial load, weak axis and strong axis moment of pile due to the various cases of live loading. The distribution of live load to each pile is important in determining which load situation produces the largest bending moment in the piles. The different nature of pile support at each abutment and the skew angle affects the magnitude of bending moments of the piles.

Table 4.15: Pile axial loads and bending moments due to each live load case [31].

Case	Axial Pile Loads (*kN*)			Weak Axis Moment (*kN.m*)			Strong Axis Moment (*kN.m*)		
	G2-S	G3-S	G3-N	G2-S	G3-S	G3-N	G2-S	G3-S	G3-N
1	-8.3	-18.5	-63.7	0.31	2.72	-1.43	0.43	0.02	-0.02
4	0.6	-19.4	-59.0	1.29	1.57	-1.39	0.49	-1.28	0.1
7	-5.4	3.9	-63.7	-1.77	1.04	-1.47	-1.63	0.32	0.65
10	-59.7	-28.4	-64.4	-8.92	0.05	-2.99	-10.52	-3.62	0.37
13	-85.2	-70.7	-7.3	-8.02	-0.33	-1.27	-9.51	-5.14	0.26

Table 4.16 shows south and north pile movements directly below the abutment due to truck loading. The inclinometer readings, parallel to the centerline of the bridge, are positive when the movement is in the northerly direction and negative when the movement is in the southerly direction. For the south piles, negative displacement is consistent with deck expansion, while positive displacement for the north piles is consistent with deck expansion.

Table 4.16: South and north pile movements during live loading [31].

Case	Pile Movement (*mm*)						
	South Abutment				North Abutment		
	G1-S	G2-S	G3-S	G4-S	G1-N	G2-N	G4-N
1	0.33	0.33	0.25	0.14	0.19	0.20	0.19
4	0.35	0.27	0.15	0.05	0.29	0.26	-0.02
7	-0.11	0.16	0.17	0.14	-0.26	-0.06	0.14
10	-0.17	-0.12	0.04	-0.04	-0.27	-0.18	0.05
13	-0.1	--0.12	-0.05	-0.11	-0.12	-0.08	-0.04

4.2.2.2 COPLIN PLANATATION BRIDGE NUMERICAL MODELING

A numerical model of Coplin Planatation Bridge, as illustrated in Figure 4.131, was built and analyzed.

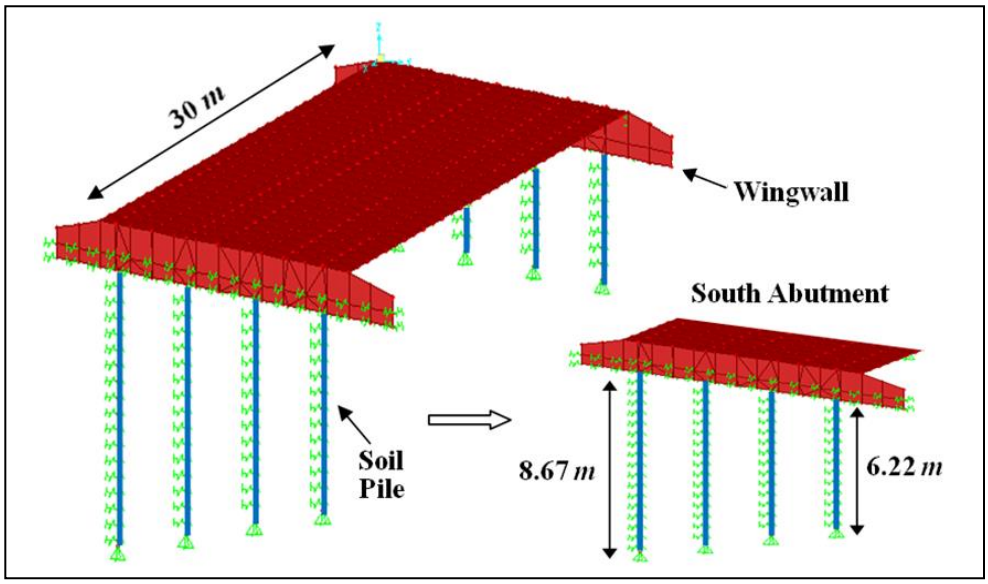

Figure 4.131: 3D Finite element model view of Coplin Planatation Bridge.

In order to evaluate the anticipated structural response to vehicle traffic, a number of truck loading conditions were considered. The FEA presents the deflected pile shape, pile axial load and pile bending moments resulting from truck #7336 and #7325 located at different location of the span. Figure 4.132 shows 3D FEA of live load case #13 on the bridge.

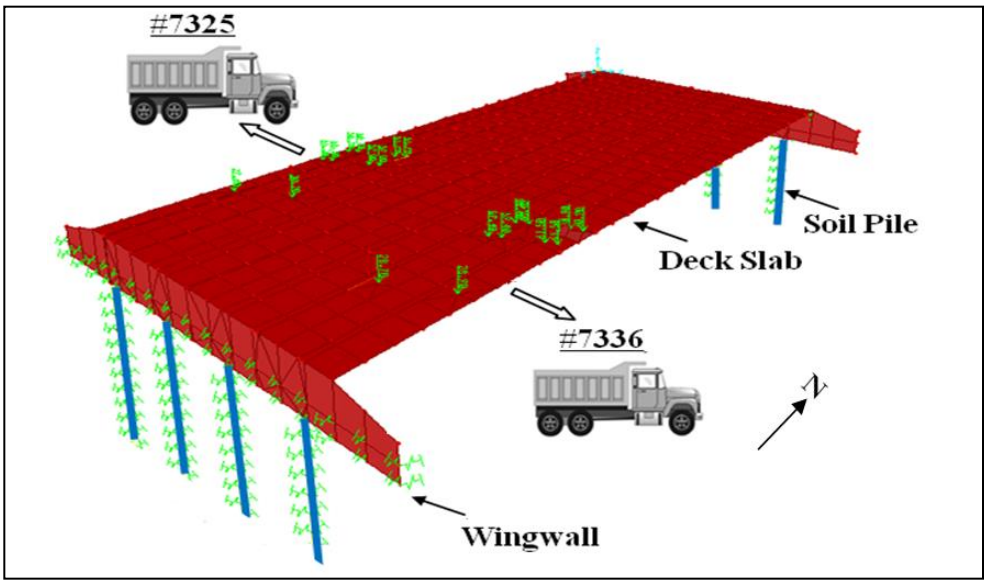

Figure 4.132: 3D Truck loading for bridge at load case #13 in FEA.

4.2.2.3 COMPARISON OF ANALYTICALLY-PREDICTED AND EXPERIMENTALLY MEASURED TRUCK TEST DATA OF COPLIN PLANATATION BRIDGE

Verification of the suitability of the finite element model and a check on the performance of the elements used in modeling the structure was done by comparing the FE with the field test. Among thirteen load cases, field test results of five load cases (#1, 4, 7, 10 and 13) were considered for comparison with the results obtained from the linear static finite element analysis. The pile load, moment and deflection that corresponded to these five locations were retrieved from live load tests to be compared to those obtained from the analytical investigation. As shown in Figure 4.133 to 4.135, finite element analysis yielded results that were in close agreement with the measured pile axial load for truck load cases # 1, 7, 10 and 13. For instance, Figure 4.133 shows that the pile axial load obtained from numerical analysis for Pile G3- N in load case #7 was -68.16 *kN* and this value obtained from field test as shown in Table 4.15 was -63.7 *kN* (only around 7% difference). In truck load case #4, pile axial loads obtained from finite element analyses showed some variation with those of the field test results. As an example, for pile G3-S in load case #4, the axial load obtained from FEM was -10.05 *kN* while this value obtained from live load test as shown in Table 4.15 was -19.4 *kN* (difference of 93%).

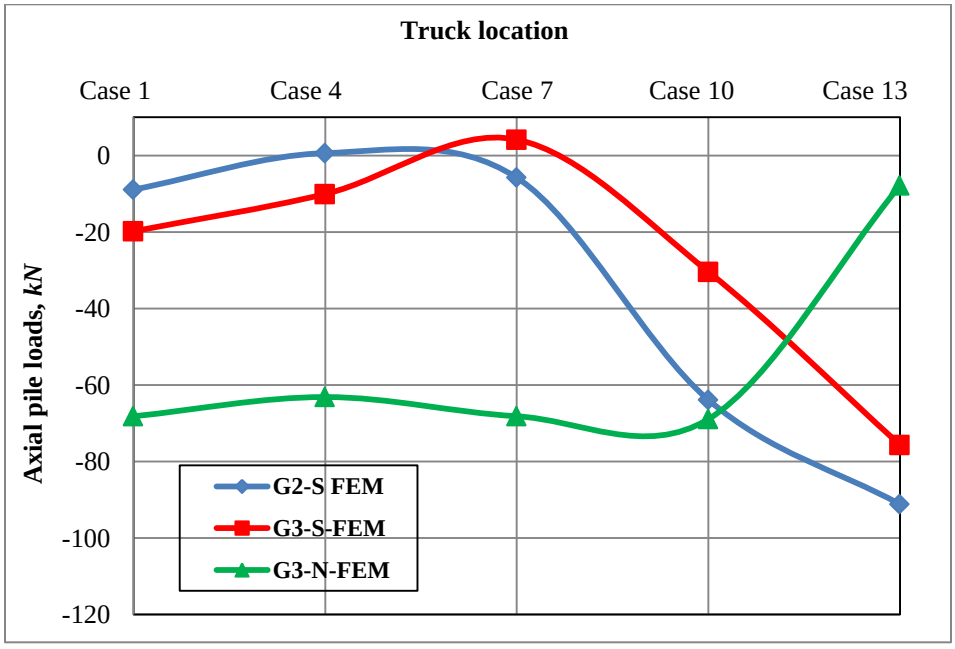

Figure 4.133: FEA results for pile axial loads due different live load cases.

Figures 4.134 and 4.135 demonstrate pile weak and strong axis moments obtained from numerical analysis for different truck load cases.

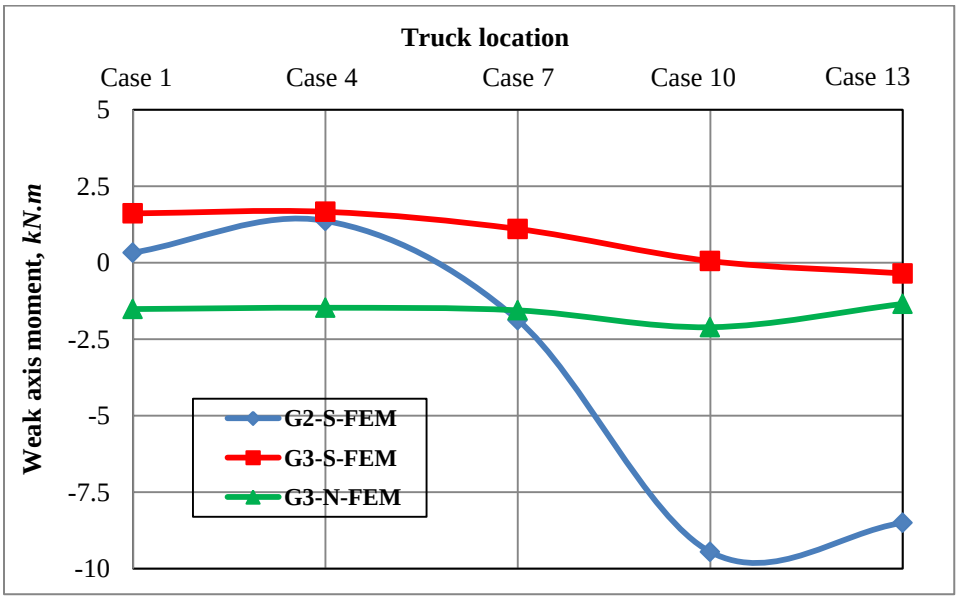

Figure 4.134: FEA results for pile weak axis moment due different live load cases.

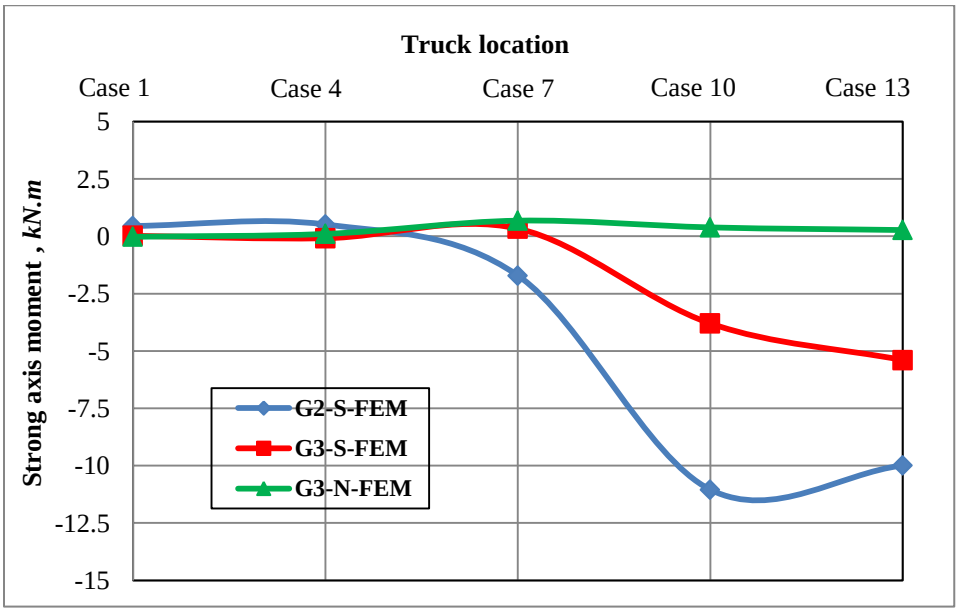

Figure 4.135: FEA results for pile strong axis moment due different live load cases.

By inspection of results, small differences were found between FEA and field test results. As displayed in Figure 4.135, strong axis moment for pile G3-S in load case #10 was predicted as -3.80 *kN.m* using numerical analysis. Table 4.15 shows that strong axis moment for the same pile

and loading condition was measured as -3.62 *kN.m* in live load testing (difference of only 5%). Figure 4.136 and 4.137 present numerical results of pile movement for north and south abutment directly below the abutment for different live loading conditions.

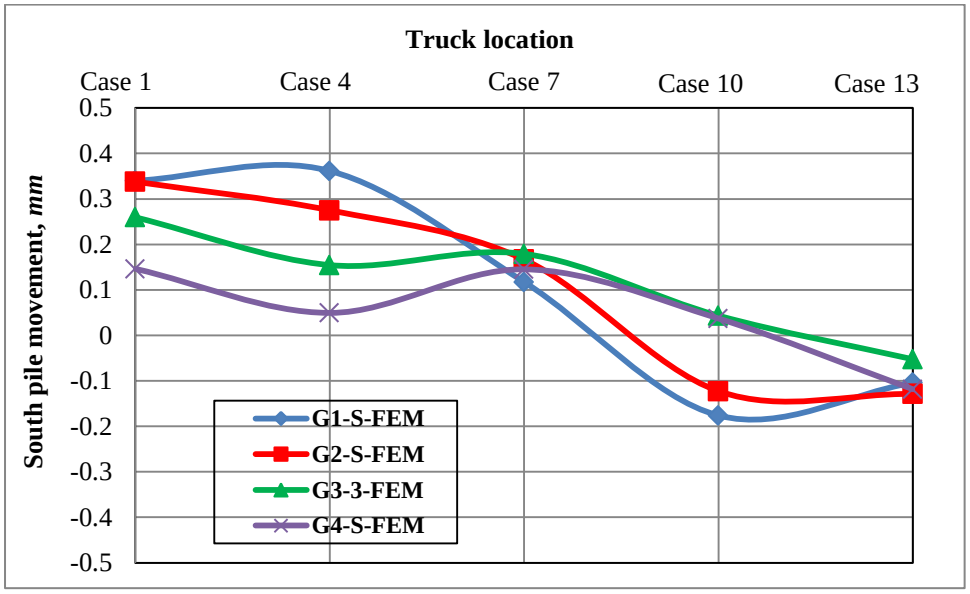

Figure 4.136: FEA results for south pile movements due to different live load cases.

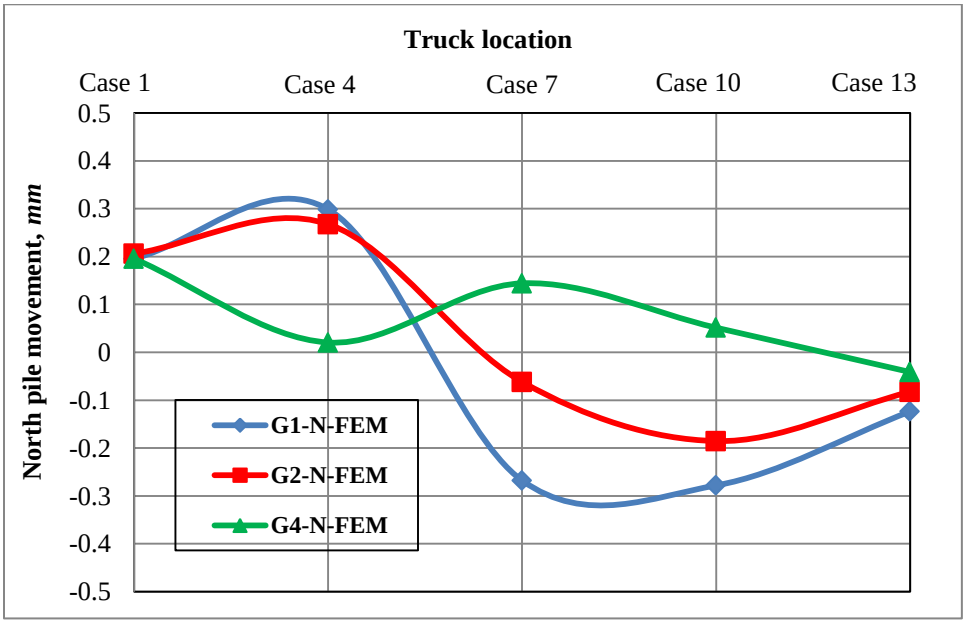

Figure 4.137: FEA results for north pile movements due to different live load cases.

By comparing finite element analysis and field test results, similar trend was observed for pile movements of north and south abutment due to different live loading. For example, Table 4.17

depicts that the pile displacement of south abutment for pile G1-S in live load test was increased from 0.33 to 0.35 *mm* and in finite element model from 0.34 to 0.36 *mm* by changing the live load case #1 to 4. In addition, Table 4.17 shows that the difference between measured and predicted pile movement were less than 3%. For example, measured movement for pile G1-S under truck load case#4 was 0.36 *mm* and predicted movement obtained from FEA was 0.35 *mm* (overestimation of only 2%).

Table 4.17: Comparison of FEA and measured results for G1-S pile movement.

Load Case	**Pile Movement, (*mm*)**		**Difference between FE Model and Field Data (%)**
	Field Data [31]	**FE Model**	
#1	0.33	0.34	3
#4	0.35	0.36	2

In general, as indicated in section 4.2.1.3 and 4.2.2.3, predicted results obtained from finite element analysis compared satisfactorily with results from the field test. Maximum 5% difference was observed between FEA and field test results. This means that finite element analysis could predict the behaviour of integral abutment bridges by almost 95% accuracy.

CHAPTER 5: DEVELOPMENT OF TOTAL LIMITING SPAN AND SKEW ANGLE FOR INTEGRAL ABUTMENT BRIDGES

5.1 EXTENDING THE LENGTH LIMIT OF INTEGRAL BRIDGES

A parametric study, using FEA modelling, was conducted to investigate the effects of different variables included pile size, pile orientation, abutment height, abutment thickness, girder type, girder depth, connection of abutment pile cap to pile, soil stiffness, number of design lanes, wingwall orientation and wingwall length on the performance of integral abutment bridges subjected to temperature variation.

In order to evaluate the effect of each variable, thermally induced pile longitudinal deformation, transverse deformation and bending moment were studied extensively. Figure 5.1 displays the three dimensional FE views of thermally induced pile displacement and bending moment.

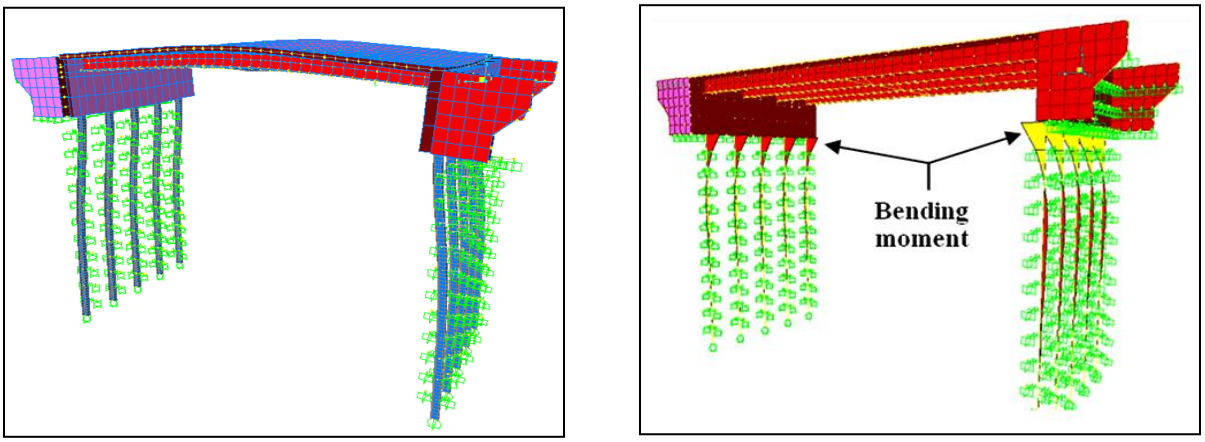

(a) (b)

Figure 5.1: Typical view of FEA results (a) Pile deformation, (b) Pile bending moment.

To make the parametric study more efficient, a two-step procedure was applied. In step 1, the finite element model of the integral bridge was extended to fourteen new models listed in Table 5.1 by varying the parameters of each variable individually. These new models were analyzed using SAP2000 software under temperature variations. Then, numerical results from fourteen models were compared to find the critical parameters of each variable which led to the maximum

pile deformations due to expansion and contraction. Based on data generated from parametric study, critical parameters (which induced more than 10% difference in pile displacement) were identified as: abutment height, number of design lanes, piles size, and connection of abutment pile cap. The parametric study of step 2 was performed based on critical parameters which was determined in previous step. New finite element models with different lengths and skew angles were set up by combining all of critical parameters. It was assumed that the general trend of an independent variable would remain consistent, i.e., the worst single variable for a type of behaviour would remain as the worst variable when combined with other variables. The new models in parametric study step 2 were used to specify allowable lengths and skew angles based on displacement-ductility limit state of pile.

5.1.1 ASSUMPTIONS FOR THE PARAMETRIC STUDY

Before the parametric study, the following assumptions were made:

(1) Two symmetrical integral bridges with different girder types (steel and concrete) were chosen as the base bridges such that the study covers a wide range of superstructure properties.

(2) The first bridge referred as the steel bridge in the parametric was composed of a 225 *mm* thick concrete slab supported on four steel I-girders (W 760×173) spaced at 2.75 *m*.

(3) The second bridge referred as the concrete bridge was consisted of a 225 *mm* thick concrete slab supported on four prestressed concrete I-girders (CPCI 900) spaced at 2.75 *m*.

(4) The average negative and positive temperature ranges for steel integral bridges were considered as $-48^{o}C$ and $+40^{o}C$, respectively.

(5) The average negative and positive temperature ranges for concrete integral bridges were specified as $-38^{o}C$ and $+30^{o}C$, respectively.

(6) The superstructures of base bridges were supported on elastomeric bearings (modeled as rollers) over the piers. Base bridges had 20 *m* long spans.

(7) The abutment walls for integral bridges (steel and concrete bridges) were 10.25 *m* long, 1 *m* thick and 3 *m* height. The type of backfill behind the abutments was assumed to be granular uncompacted material which is typically used in integral bridges.

(8) Five HP 310×110 steel piles at spacing of 2 *m* were used to support the substructures of steel and concrete bridges. H-piles were oriented in their weak axis bending in medium clay.

(9) Each wingwall was 2 *m* long; 0.5 *m* thick with non prismatic depth varying between 2 to 3 *m*. Wingwalls were oriented in parallel direction (i.e. direction of traffic).

(10) Coefficients of thermal expansion of steel and concrete were assumed to be 1.17×10^{-5} and 0.99×10^{-5} $1/^{o}C$, respectively, as specified in the CHBDC.

(11) Modulus of elasticity of the concrete and steel were assumed to be 24 and 200 *GPa*.

It is essential to remark that henceforth if the values of bridge parameters have not specified, above mentioned parameters (the same as those for the base cases) have been used.

5.1.2 PARAMETRIC STUDY OF STEP 1: SENSIVITY ANALYSIS

First in section 5.1.2.1, variables considered in the sensitivity analysis have been briefly introduced. Then in subsequent sections effects of those variables on behaviour of integral bridges have been thoroughly described.

5.1.2.1 VARIABLES CONSIDERED IN THE PARAMETRIC STUDY

Table 5.1 illustrates fourteen variables considered in the parametric study and the corresponding cases or runs to investigate the effects of these parameters on pile displacement.

Table 5.1: Variables considered in parametric study.

Variables	**Range of variables**	
	Number of cases	Description
Pile size	3	HP 200×53, HP 250×85 and HP 310×110
Pile Orientation	4	Strong axis (Local and global axis), Weak axis (Local and global axis)
Skew angle	5	15^{o}, 20^{o}, 30^{o},45^{o},60^{o}
Abutment height	2	3, 5 *m*
Abutment thickness	3	1, 1.25, 1.5 *m*
Bridge total length	3	20, 100, 180 *m*
Girder type	5	Steel box girder, Steel I-girder ,Concrete box girder, Concrete I-girder, Deck slab
Girder depth	3	CPCI 900, CPCI 1500, CPCI 2300
Abutment-pile connection	2	Fixed, Hinged
Soil stiffness	4	Soft clay, Stiff clay, Loose sand, Dense sand
Wingwall orientation	3	Perpendicular, Parallel, 45^{o} to traffic
Wingwall length	3	3, 4, 5 *m*
Number of design lanes	8	1, 2, 3, 4, 5, 6, 7, 8
Number of bracings or diaphragms	4	0, 1, 2, 3

5.1.2.1.1 EFFECT OF PILE SIZE

From the literature, a range of discussions have been presented regarding the type of piles designed for integral abutment bridges. A survey conducted by Kunin and Alampalli [42] reported that steel H or HP piles were most frequently used in the design of integral abutment bridges. In order to determine the effect of pile size, the behaviour of non-skewed steel I-girder bridges (W 760×173) with 100 *m* length and different steel H piles (HP 200×53, HP 250×85 and HP 310×110) were compared. The cross sections of these three piles are shown in Figure 5.2.

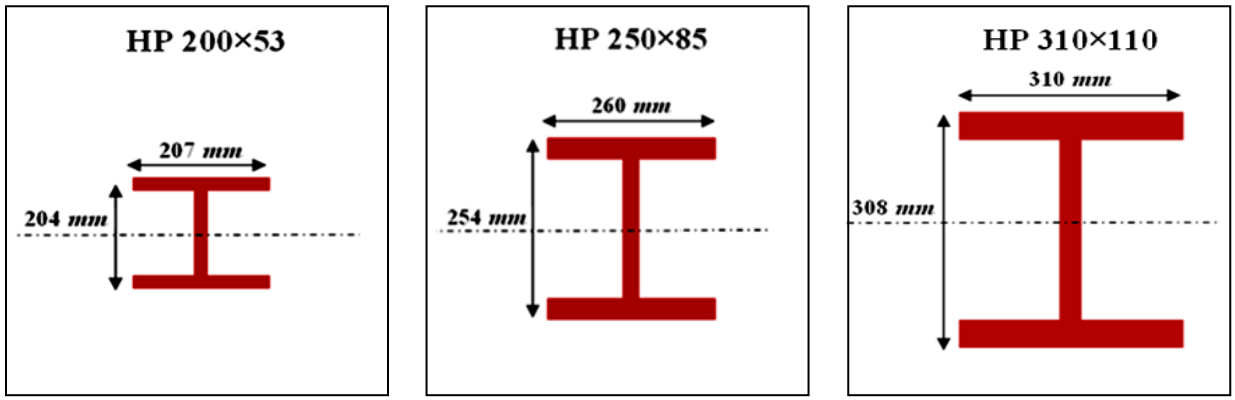

(a) (b) (c)

Figure 5.2: Different pile cross sections (a) HP 200×53, (b) HP 250×85, (c) HP 310×110.

Figure 5.3(a) illustrates that smaller pile-head displacement occurred for stiffer piles during both temperature rise and fall. For instance, pile-head displacement remarkably decreased by 18% from 22.4 to 26.4 *mm* when the pile size changed from HP 310×110 to HP 200×53. The reason of smaller pile displacement was attributed to that larger pile flexural stiffness brought larger constraints to the expansion and contraction of the superstructure. It should be pointed out that pile-head displacements were larger under contraction than under expansion. For HP 250×85, the pile displacement was equal to 23.96 *mm* during temperature fall and was equal to -12.65 *mm* during temperature rise.

The tendency for the pile bending moment as shown in Figure 5.3(b) was similar to that for the pile displacement. HP 310×110 had the largest pile bending moment and HP 200×53 had the smallest one. Hence, based on the finite element results it can be derived that pile displacement and bending moment changed considerably by changing the pile sizes.

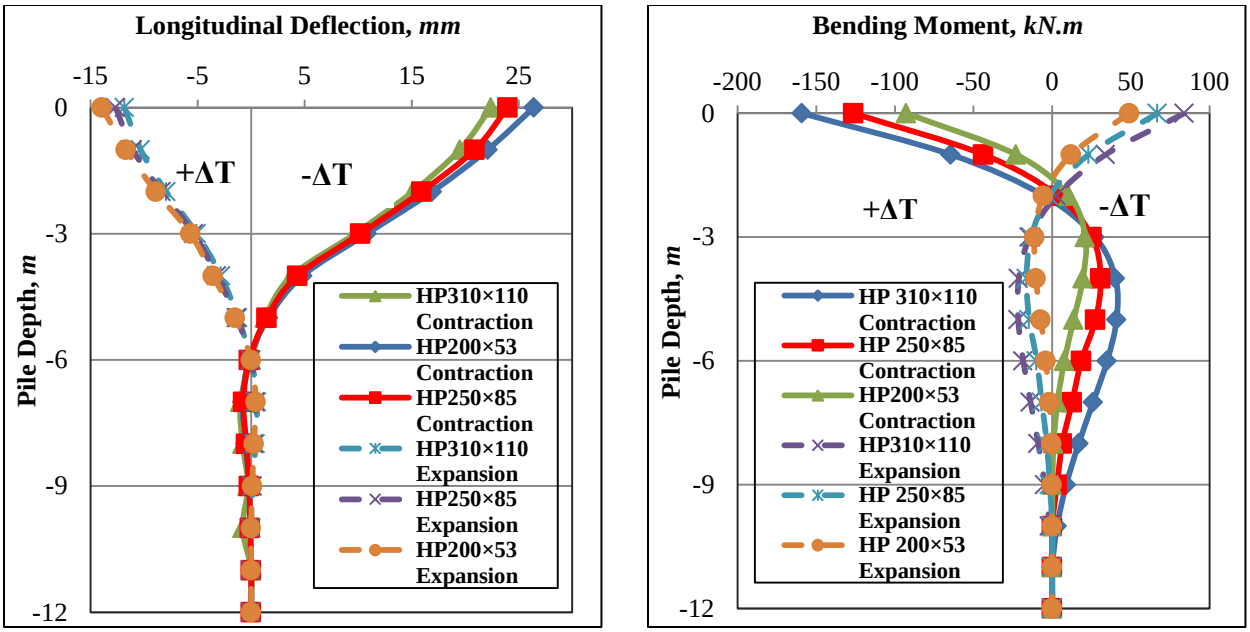

(a) (b)

Figure 5.3: Effect of different pile size on (a) Pile deformation, (b) Pile bending moment.

5.1.2.1.2 EFFECT OF PILE ORIENTATION

Figure 5.4 displays orientations for an H-pile in an integral abutment namely: Type-A that has the strong-axis of the pile perpendicular to the Y-axis of the bridge, Type-B that has the strong-axis of the pile parallel to Y-axis of the bridge, Type-C that has the strong-axis of the pile perpendicular to the bridge skew and Type-D that has the strong-axis of the pile parallel to the bridge skew.

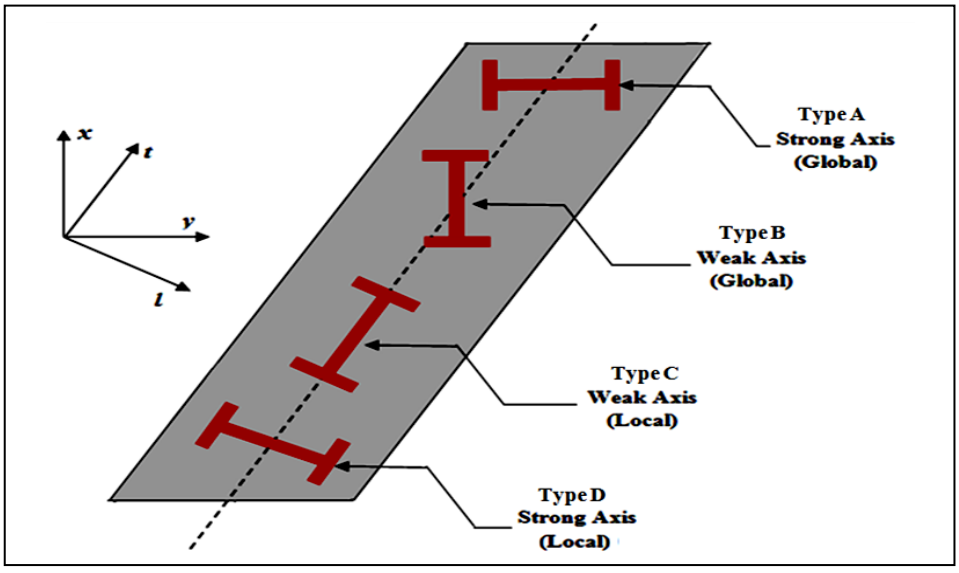

Figure 5.4: Pile orientations for integral abutments.

Concrete I-girder bridges (CPCI 900) with 160 *m* length, 10.25 *m* wide and 45^{o} skew angle with above mentioned pile orientations were considered to examine the influence of pile orientations. As presented in Figure 5.5, pile orientations have insignificant effect on pile-head displacement under either expansion or contraction. The magnitudes of the pile-head displacement were, however, larger for weak axis oriented piles than for strong axis oriented piles. Figure 5.5 shows that during the temperature rise and fall, the pile horizontal displacement for the weak axis was increased only by 3 to 4% compared to strong axis.

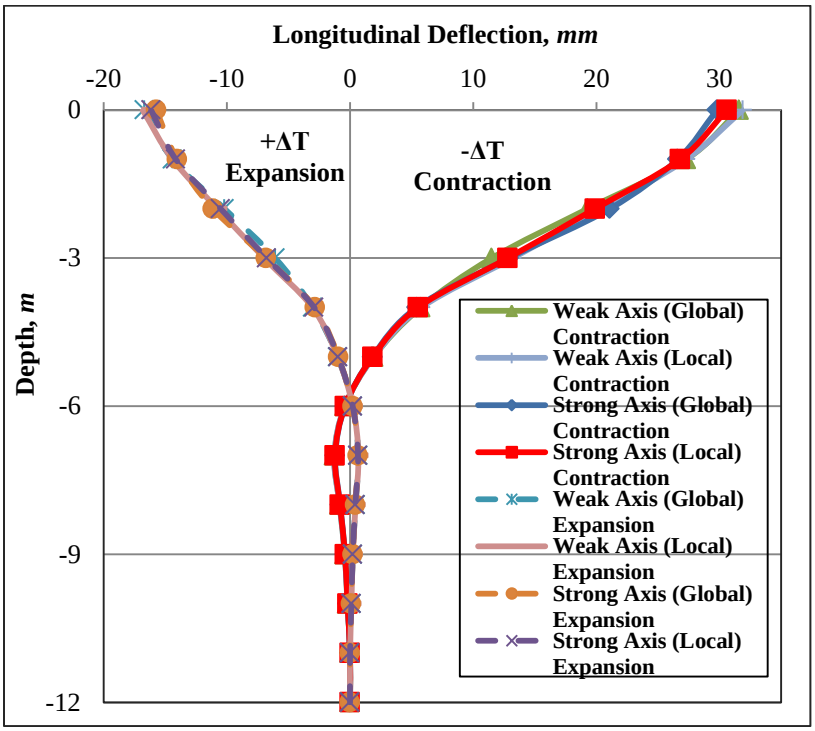

Figure 5.5: Influence of different pile orientation on pile longitudinal deflection.

It is noteworthy to remark that orientation of strong axis bending benefited pile displacement but caused to somewhat larger concrete stresses in the superstructure. In practice, pile orientation should be determined based on the specific condition of the bridge to be designed. For long integral bridges, pile horizontal displacement and bending moment may become critical and piles may be oriented in strong axis bending to benefit the pile behaviour. However, for short integral bridges, weak-axis bending would be more helpful to reduce the stresses in the superstructure.

5.1.2.1.3 EFFECT OF SKEW ANGLE

Skewed bridges are sometimes unavoidable due to road alignment at bridge site. Behaviour of skewed integral bridges is much more complicated than straight integral bridges due to the uncertainty of soil-structure interactions. With skewed bridges, the soil passive and active pressure developed in response to thermal elongation and contraction. Therefore, skewed bridges respond to temperature change with both longitudinal and transverse movements. Figure 5.6 demonstrates that the deformed shape of the skewed integral abutment bridge under temperature fall consisted of the longitudinal displacements (U_1) and the transverse displacements (U_2). The longitudinal direction is parallel to the traffic and the transverse direction is perpendicular to the traffic.

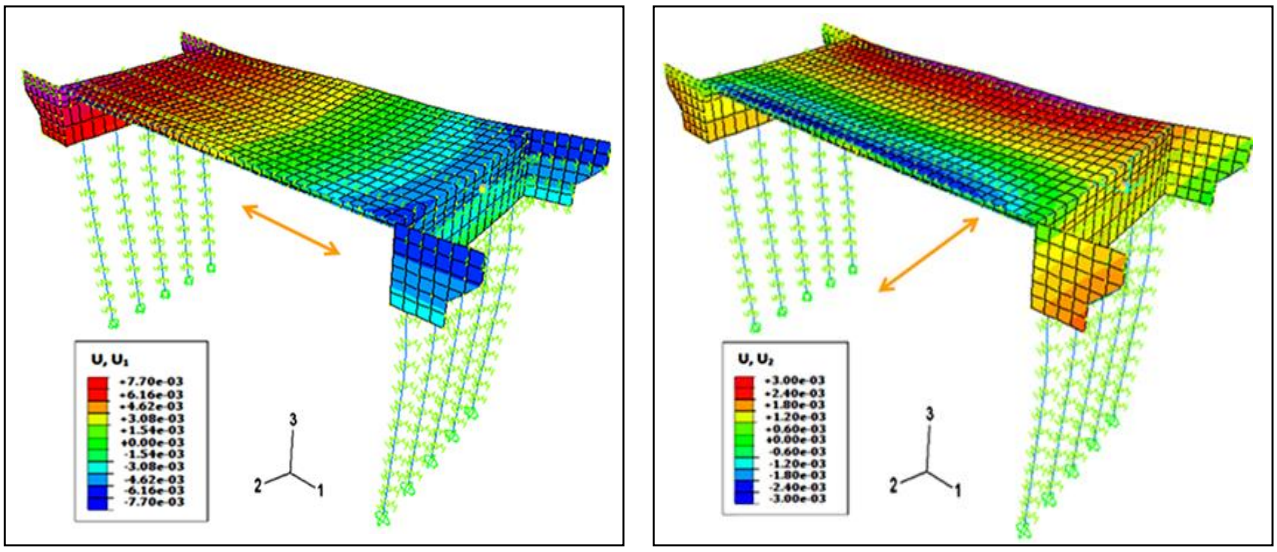

(a) (b)

Figure 5.6: Displacement types (a) Longitudinal (U_1), (b) Transverse (U_2).

In integral bridges corners 1 and corners 2, as illustrated in Figure 5.7, are defined as the acute-angle corners and obtuse-angle corners. Longitudinal and transverse displacements at these corners were not equal. Based on finite element results, longitudinal and transverse displacements of pile near the acute-angle corner of the bridge deck were greater than that for the obtuse-angle corner of the bridge deck.

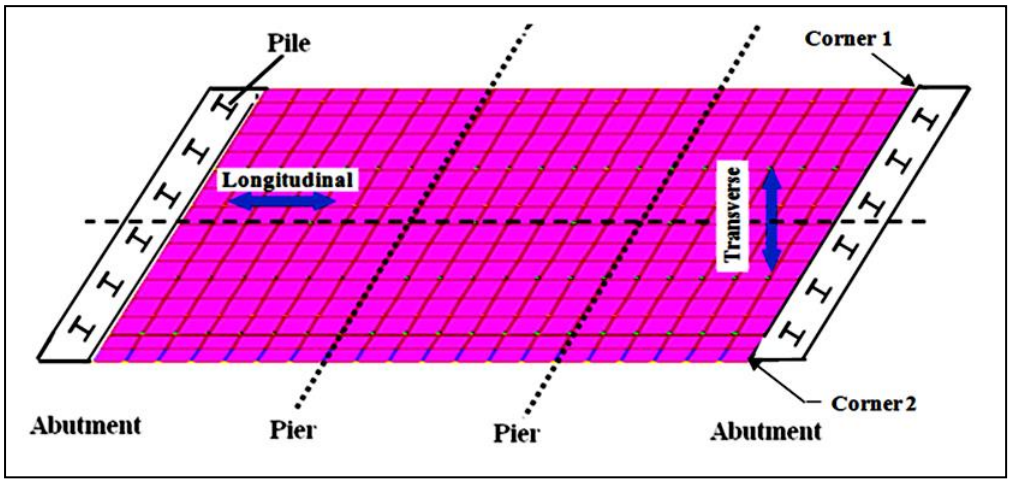

Figure 5.7: Deformed shape of integral abutment bridge during temperature rise.

Figure 5.8 displays the pile deflections at acute corner and obtuse corner of 45^{o} skewed concrete I-girder bridges made of CPCI 900 with different lengths (20 and 140 *m*). The longitudinal pile-head deflection at obtuse corner for bridge with 140 *m* length was 14.8 *mm*, while it was 24.9 *mm* at acute corner for a similar bridge (an increase of about 68%). A similar trend was observed in case of transverse pile displacement. Transverse pile-head deflection of bridge with 140 *m* length increased from 13.1 *mm* at obtuse corner to 18.6 *mm* at acute corner. Since maximum thermal longitudinal deformation and the transverse displacement was occurred at acute corner, all figures in this study for longitudinal and transverse pile displacements of skewed integral bridge represent pile deformations at this corner.

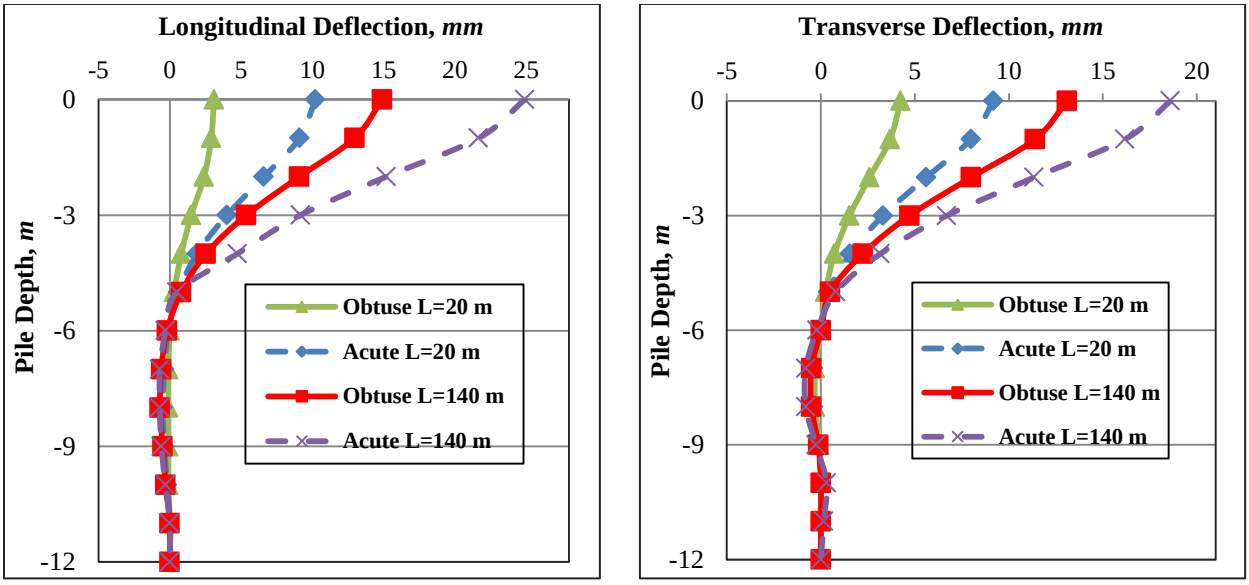

(a) (b)

Figure 5.8: Displacement at acute and obtuse corners (a) Longitudinal (U_1), (b) Transverse (U_2).

For the purpose of realizing the influence of skew angle, behaviour of steel I-girder bridges (W 760×173) with different skew angles ranging from 0° to 60° during temperature fall have been studied. Figure 5.9 presents plan views of the various skewed integral bridge models which have been examined.

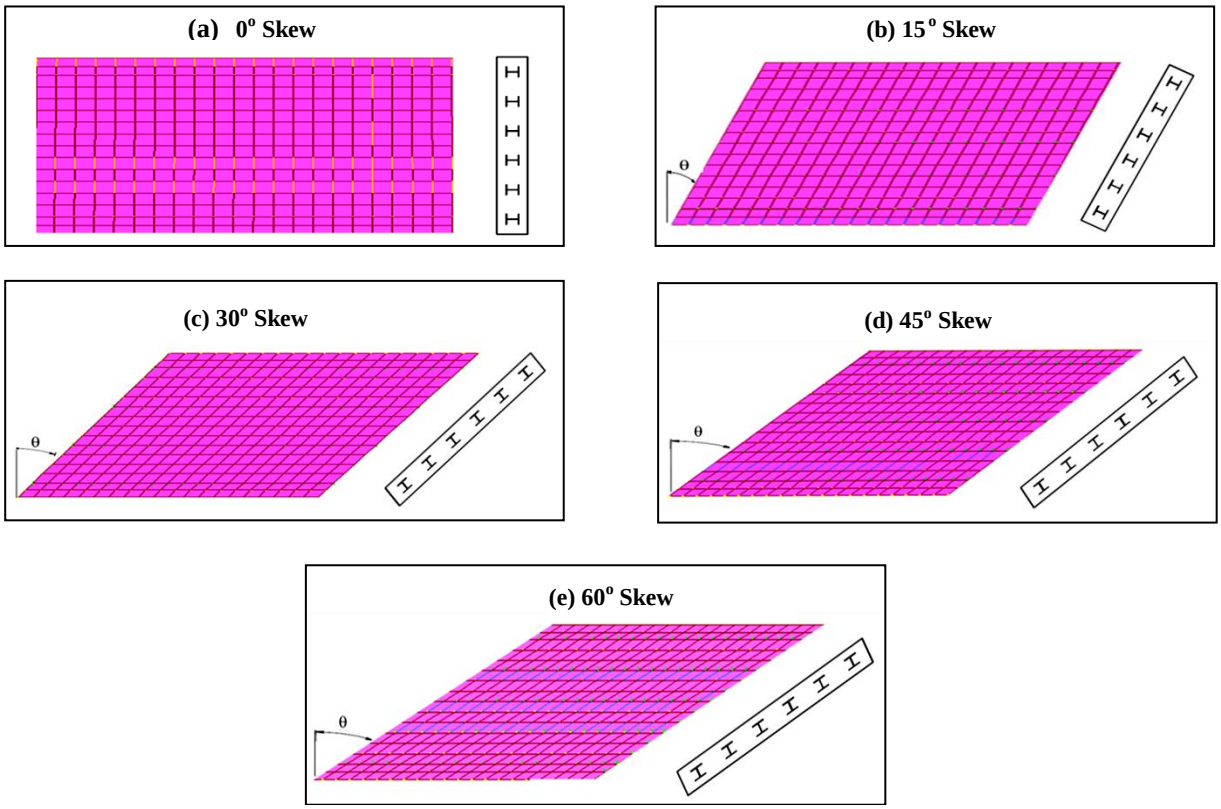

Figure 5.9: Plan view of 3-D FE models of bridges with different skew angles.

Figure 5.10(a) shows that skew increase from 0° to 60° caused greater longitudinal pile-head displacement and the largest longitudinal pile-head displacement occurred for the 60° skewed integral bridges with the value of 28.74 *mm*. Besides longitudinal displacement, it has been observed in Figure 5.10(b) that the skew angle of bridge had a remarkable effect on the temperature-induced transverse pile displacement. Maximum pile transverse displacement generally increased with increasing skew angle under both expansion and contraction. During temperature fall, for a 60° skewed integral bridge compared to 30° skewed integral bridge, pile transverse displacement increased by 71% (from 13.03 to 22.3 *mm*).

The fact worthy of attention is that in the case of integral abutment bridges with skew angles less than surface-friction angle between the abutment and the backfill ($\Theta \leq \delta = 20^o$), transverse pile displacements were equal to zero.

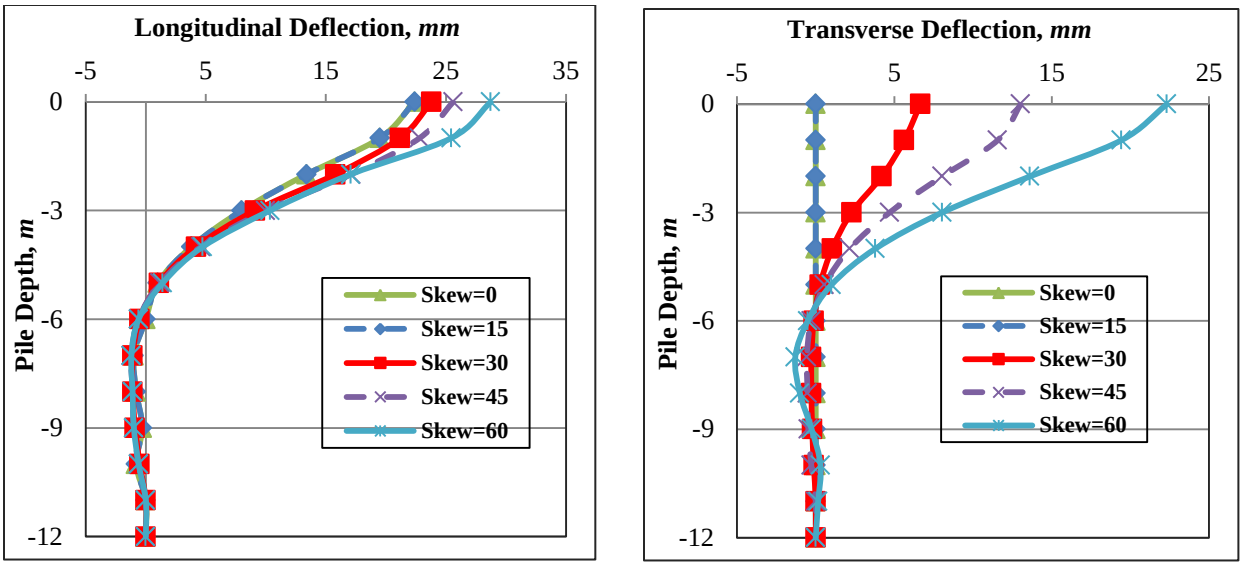

(a) (b)

Figure 5.10: Influence of different skew angles on pile (a) Longitudinal, (b) Transverse deformation.

As illustrated in Figure 5.11, similar observation can be found for pile moments with superstructure skewness ranging from 0° to 60°. Pile bending moment about an axis parallel to the strong axis of abutment pile (M_{11}) and pile bending moment about an axis parallel to its weak axis (M_{22}) markedly increased with increasing skew angle. During contraction, the strong axis pile moment (M_{11}) was increased by 10% (from 123.46 to 135.83 *kN.m*) with increasing skew angle from 30° to 60°. In the same sense, the weak axis pile moment (M_{22}) was increased almost three times from 12.16 to 37.54 *kN.m* with increasing skew angle from 30° to 60°.

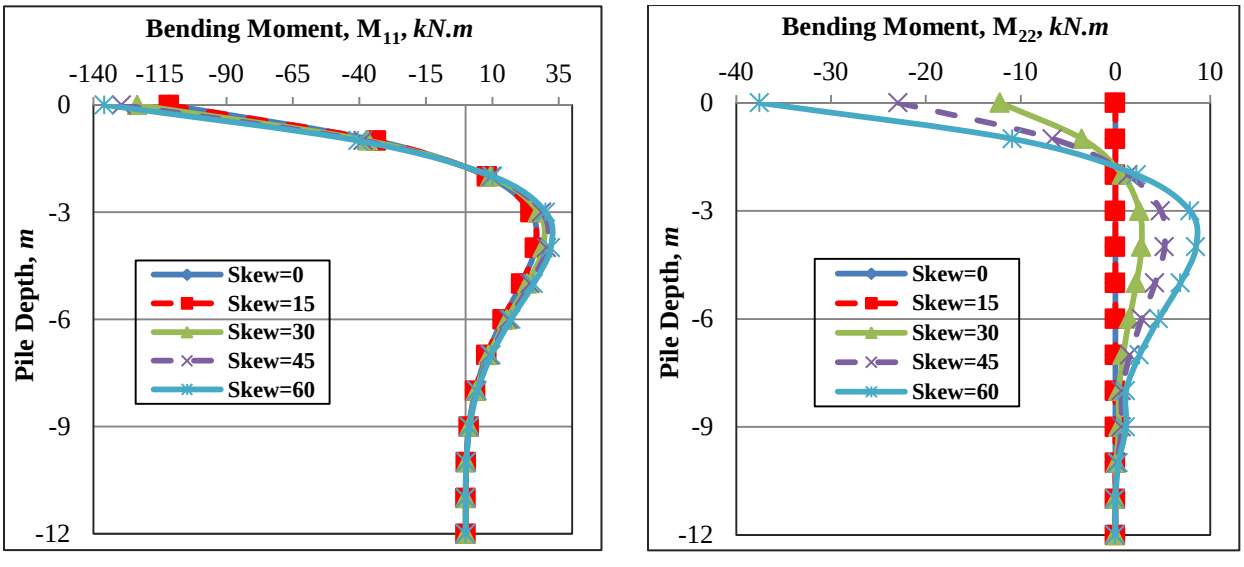

(a) (b)

Figure 5.11: Effect of different skew angles on pile bending moment about (a) Strong axis, (b) Weak axis.

5.1.2.1.4 EFFECT OF ABUTMENT HEIGHT

The abutment height is also anticipated to affect the pile displacement of integral bridges. Based on Ontario Ministry of Transportation (MTO) recommendations [35], bridges with abutment height more than 6 *m* should not be considered for integral abutment design. Accordingly, as shown in Figure 5.12, two different abutment heigths, 3 and 5 *m*, are considered.

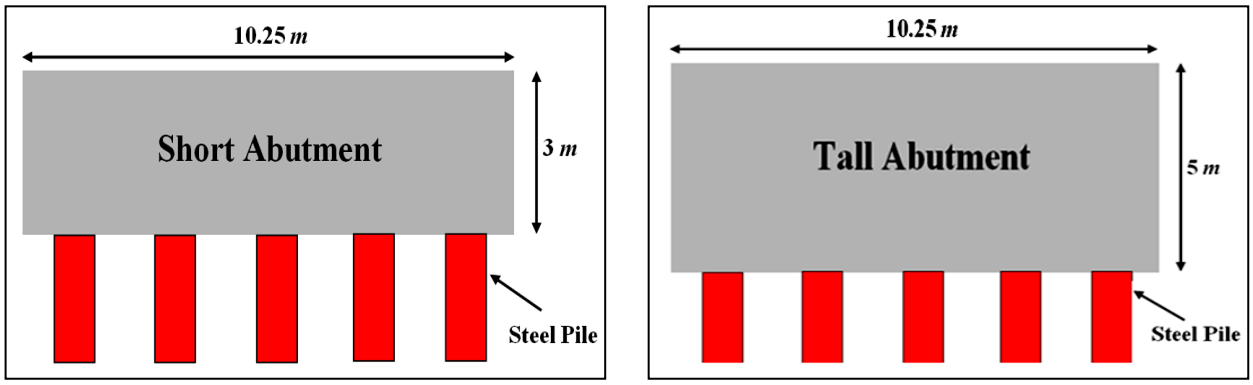

(a) (b)

Figure 5.12: Different abutment height: (a) Short abutment, H= 3 *m*, (b) Tall abutment, H=5 *m*.

Non-skewed steel I-girder bridges (W 760×173) with 160 *m* length and different abutment heights were chosen to investigate the effect of the abutment height. Figure 5.13 presents the relationship between the change in pile displacement and abutment heights for selected bridges.

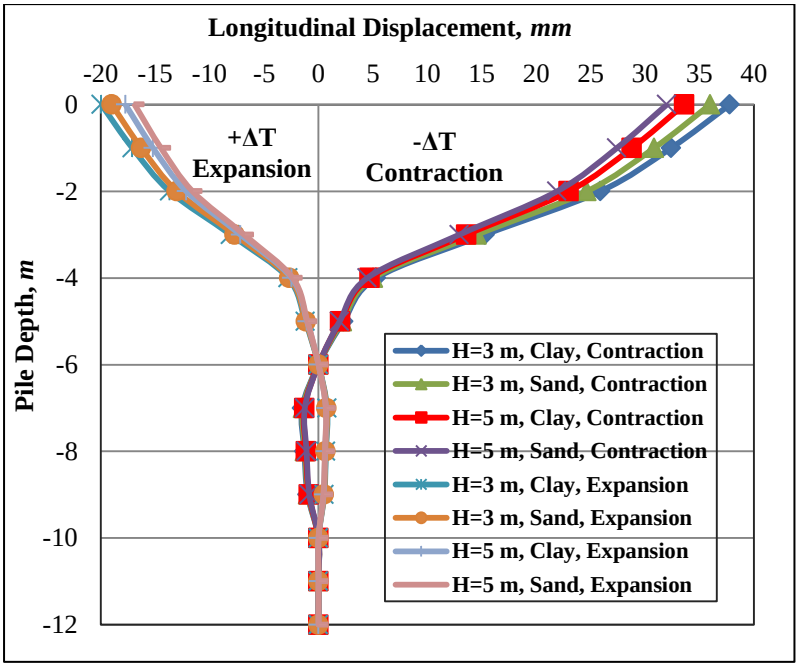

Figure 5.13: Effect of different abutment height (a) H= 3 *m*, (b) H=5 *m*.

It has been observed from Figure 5.13 that the horizontal pile displacement has been decreased notably with increasing the abutment height. As an example, pile displacement for clay during temperature decrease has been reduced around 13% (from 37.8 to 33.6 *mm)* by changing abutment heigth from 3 to 5 *m*. Hence, it can be stated that substantial variations in horizontal pile displacement are found depending on the abutment height.

5.1.2.1.5 EFFECT OF ABUTMENT THICKNESS

The abutment thickness of integral bridges is often limited to 1.5 *m*. Accordingly, for evaluating the influence of abutment thickness, performance of non-skewed steel I-girder bridges made of W760×173 and 180 *m* length and different abutment thicknesses (1, 1.25 and 1.5 *m*) during contraction were compared. Three different abutment thicknesses are shown in Figure 5.14.

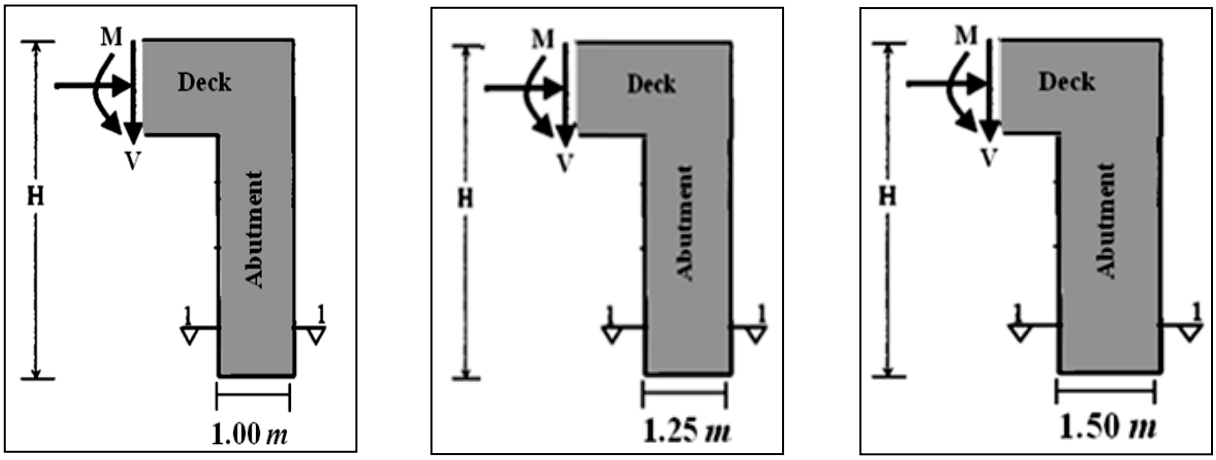

(a) (b) (c)

Figure 5.14: Different abutment thicknesses (a) t=1 *m*, (b) t=1.25 *m*, (c) t= 1.5 *m*.

The analysis results revealed that an increase in the abutment thickness within a practical range of dimensional limits had a negligible effect on the pile displacement. Figure 5.15 displays that the bottom of the abutment was restrained more effectively by the pile-soil system as the top of the abutment at the deck level was pulled toward the backfill because of the contraction of the deck under negative thermal variation. Much larger displacements were produced at the abutment top relative to the displacements at the abutment bottom for the abutment. However,

the rate of change of the abutment displacement was constant along the abutment height, regardless of the abutment thickness.

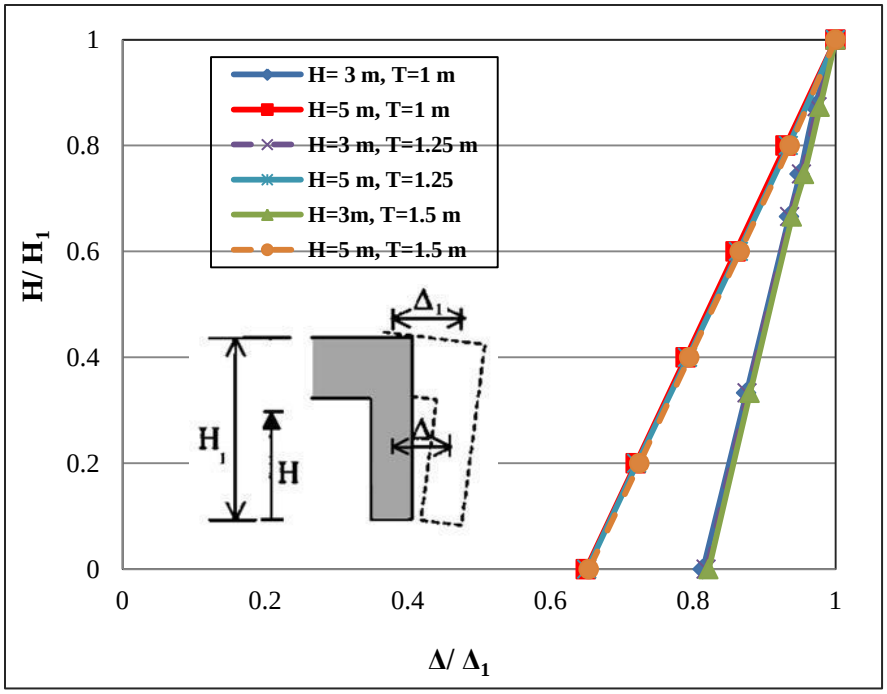

Figure 5.15: Relative displacement profile for 3 and 5 *m* tall abutment.

5.1.2.1.6 EFFECT OF BRIDGE LENGTH

Bridge length may influence the performance of integral bridge piles. Figure 5.16 illustrates three non-skewed steel I-girder bridges (W 760×173) with three different lengths (20, 100 and 180 *m*) that have been analyzed to evaluate the effect of increasing length on integral abutment bridge behaviour under thermal loading.

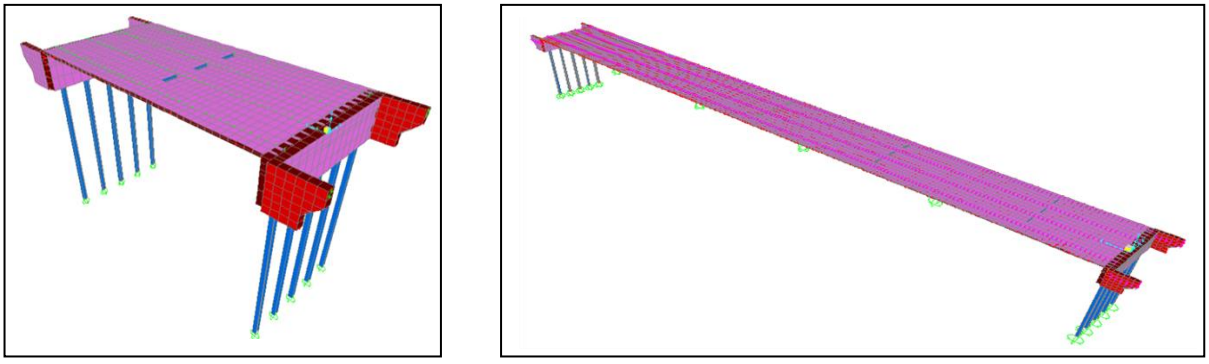

(a) (b)

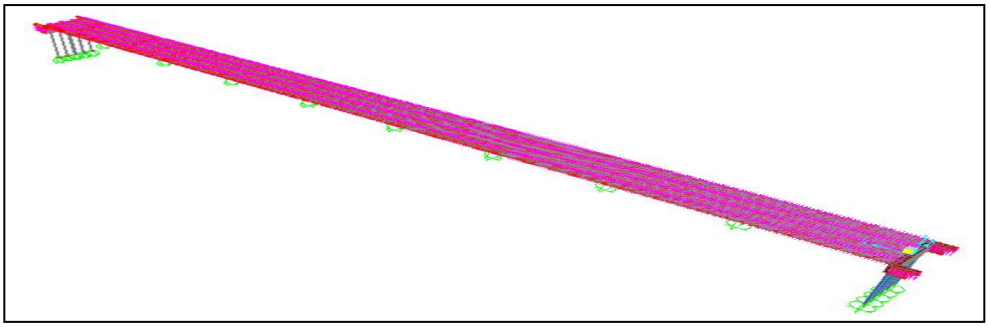

(c)

Figure 5.16: Finite element of an integral abutment bridge with three different lengths (a) L=20 *m*, (b) L=100 *m*, (c) L=180 *m*.

In this part along with displacement, pile bending moment and shear force values of integral bridges with different lengths have been obtained and compared. To understand the behaviour of piles under negative temperature variation, plots of maximum shear force and pile moment versus lateral head displacement were developed for piles with strong axis. Figure 5.17 provides sample results for a 310×110 H-Pile oriented for strong axis bending in medium clay. Figure 5.17(a) illustrates that the pile horizontal displacement of 7.3 *mm* for 20-*m* length integral bridge has been increased to 23.1 and 37.8 *mm* with increasing bridge length to 100 and 180 *m*, respectively. The pile bending moments in bridges with length of 100 and 180 *m* were approximately two to three times greater than that for the bridge with length of 20 *m* as depicted in Figure 5.17(b). The same trend also has been observed in the shear force in pile as depicted in Figure 5.17(c). Thus, it can be concluded that the bending moment, shear force and pile displacement of integral bridges increase considerably as the bridge becomes longer.

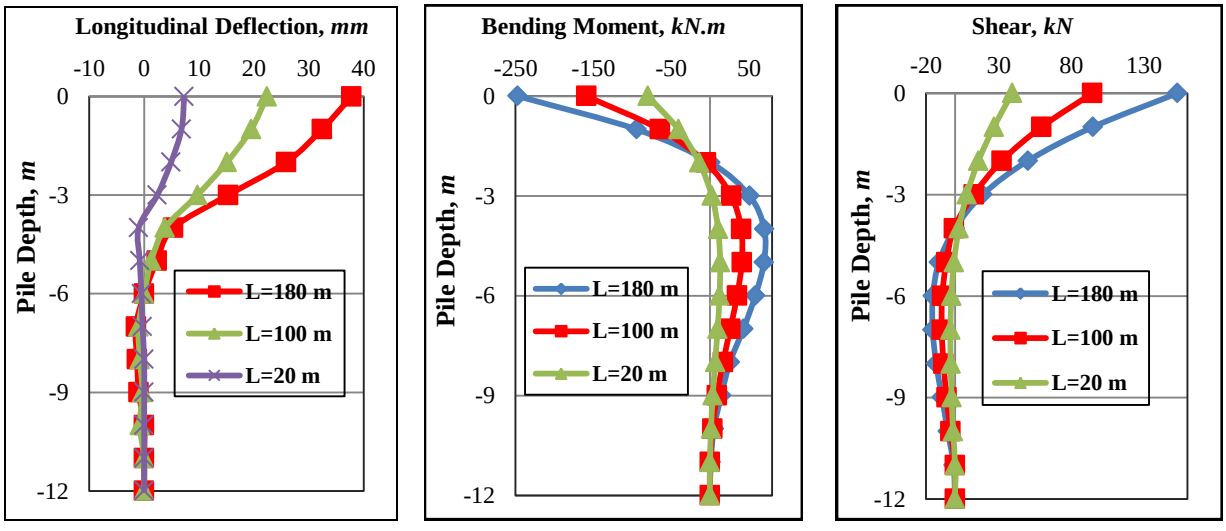

(a) (b) (c)

Figure 5.17: Results for 310×110 H-pile oriented for strong axis bending in soft clays (a) Longitudinal deflection, (b) Bending moment, (c) Shear force.

5.1.2.1.7 EFFECT OF CONNECTION OF ABUTMENT PILE CAP TO PILE

In practice, hinged connections may be designed to reduce the concrete stresses in the superstructure or pile stresses. To achieve a physical hinge, the following methods may be possible:

Method A: In this detail, the pile head is surrounded on all sides by a 50 *mm* layer of polystyrene as shown in Figure 5.18(a). This detail is intended to provide enough rotational capacity to allow the pile to be designed as hinge-headed.

Method B: This design method, as displayed in Figure 5.18(b), consists of strips of high durometer neoprene along either side of the dowels along the centerline of the integral abutment, through which vertical loads are transmitted to the footing.

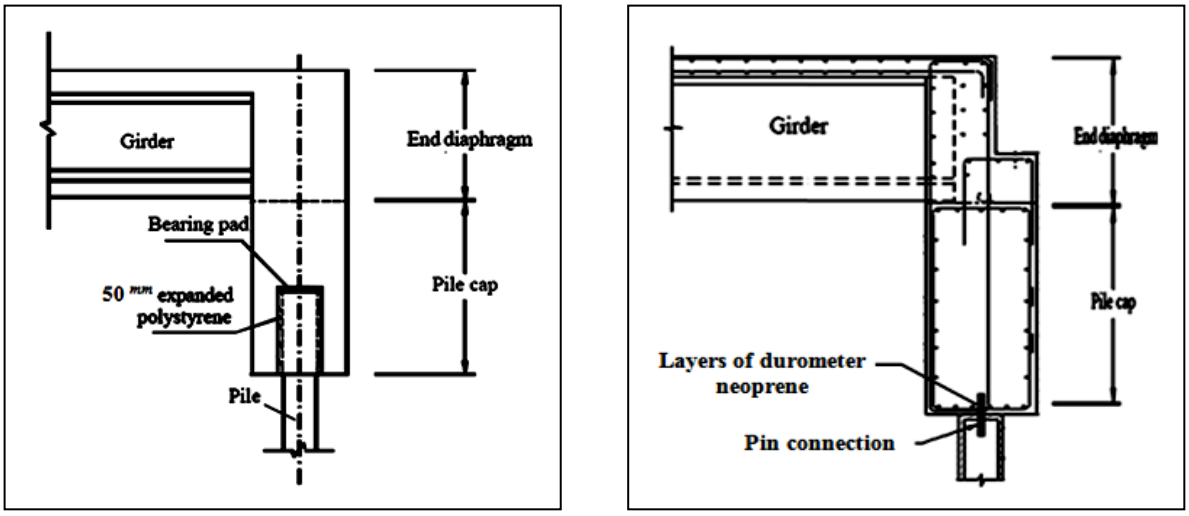

(a) (b)

Figure 5.18: Abutment/ pile hinged connections (a) Method A, (b) Method B.

The results of using a hinged connection between the abutment pile cap and the pile were compared to those of a fixed connection. For the hinged connection, relative rotation between the abutment pile cap and the pile was permitted while for the fixed connection the abutment pile cap and pile were connected rigidly. Figure 5.19 provides sample results for steel integral abutment bridges with different total lengths (20, 100 and 180 *m*) with fixed-head 310×110 H-piles oriented for weak axis bending through a medium clay soil embankment and foundation.

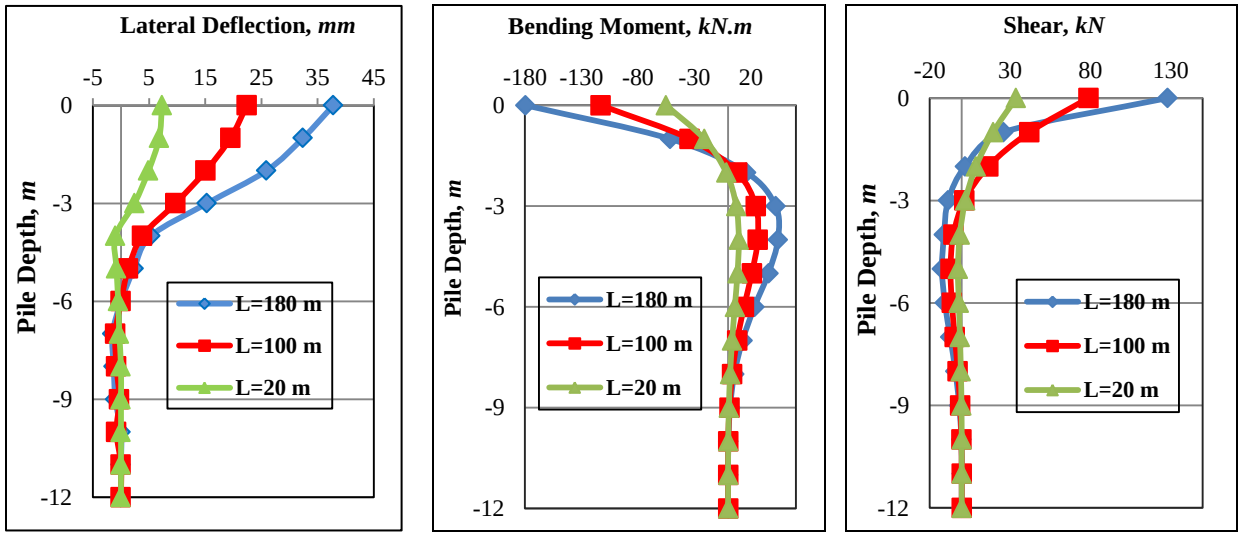

(a) (b) (c)

Figure 5.19: Results for fixed head 310×110 H-pile (a) Longitudinal deflection, (b) Bending moment, (c) Shear Force.

Figure 5.20 presents similar results for free-head conditions (hinged connection) with weak axis bending. As anticipated, Figure 5.20(b) shows that the maximum bending moments occurred below the pile head for free-head conditions, while these values reached their maximum at the pile head for fixed-head conditions. The maximum shear force in the pile occurred at the pile head for both fixed- and hinged-head conditions as depicted in Figure 5.19(c) and 5.20 (c).

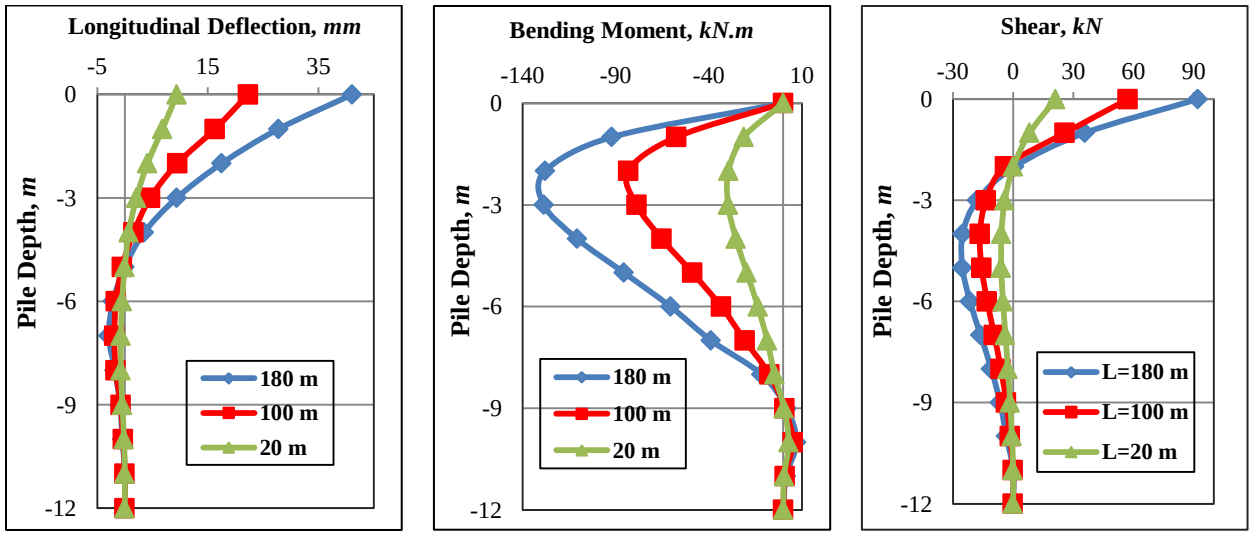

(a) (b) (c)

Figure 5.20: Results for free head 310×110 H-pile (a) Longitudinal deflection, (b) Bending moment, (c) Shear Force.

Figure 5.21 shows that maximum bending moments and shear force for hinged connection were noticeably less than that of for fixed connection. This means that the moment relief alternative (hinged connection) could significantly reduce the shear force and maximum bending moment of the piles by more or less 40 and 50% for straight bridge.

Certainly, to have a longer integral abutment bridge, hinged connection is recommended because (i) the moment and shear at the pile is smaller and (ii) the moment through the hinged connection can not be transferred to the superstructure.

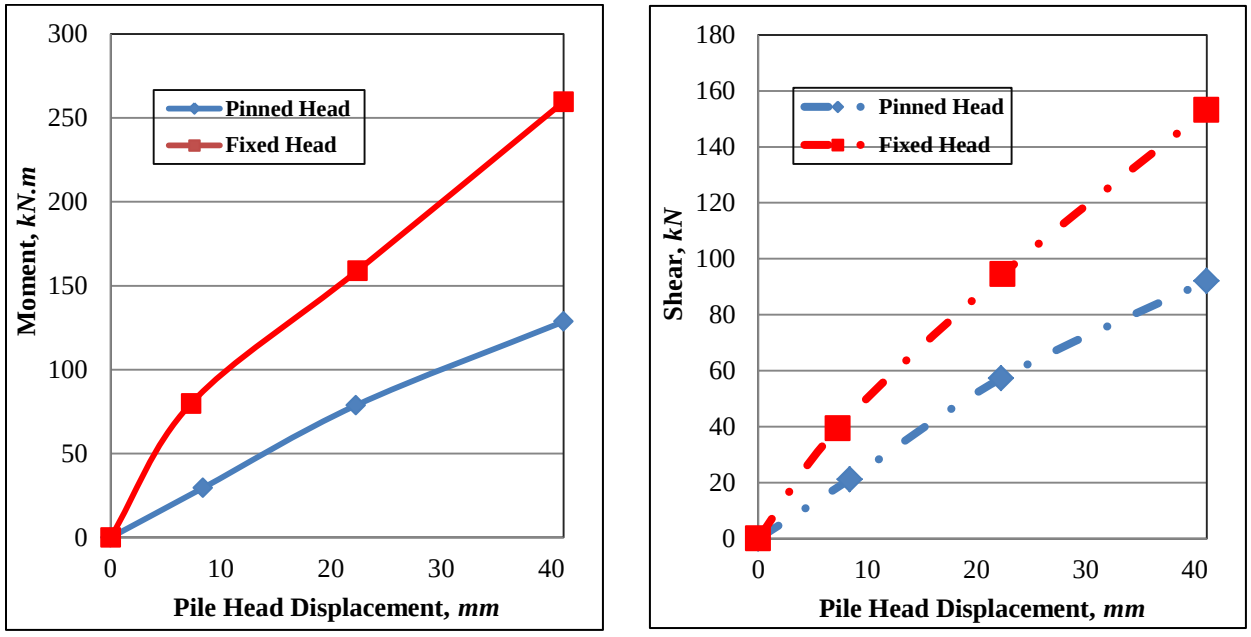

(a) (b)

Figure 5.21: Results for hinged and fixed 310×110 H-pile (a) Maximum bending moment versus imposed pile head displacement (b) Maximum shear versus imposed pile head displacement.

5.1.2.1.8 EFFECT OF GIRDER TYPES

Integral bridges superstructures built in Ontario are constructed of concrete deck-over (i) steel I-girders; (ii) multiple-box steel girders; (iii) prestressed concrete I-girders; (vi) precast/prestressed box girders [35]. For this reason, first in section 5.1.2.1.8.1 the effect of different steel girder types, such as steel I-girder and multiple-box steel girders, on integral bridge behaviour was studied. Then, in section 5.1.2.1.8.2, the influence of different concrete girders types including concrete I-girder, concrete box girder and voided deck slab on the integral bridge pile deformation was compared.

5.1.2.1.8.1 EFFECT OF DIFFERENT STEEL GIRDER TYPES

As our main interest is concentrated on the effect of different steel girder types (steel I-girder and steel box girder), all parameters were selected the same as the parameters in the base bridges and only steel girder cross-section has been changed. The cross-section of steel I-girder bridges was taken W 760×173 as previously explained. The prototypes of steel box-girder bridges used in the parametric study were based on an extensive survey of actual designed straight bridges. The steel box-girder bridges consisted of two box girders with spacing of 5.125 *m*. The box girders had the height of 800 *mm* and width of 2562.5 *mm*. The thickness of the steel top flanges, webs and bottom flanges of steel boxes were considered as 16, 10 and 15 *mm*, respectively. Figure 5.22 shows the cross-sectional dimension of steel I-girder and steel box-girders.

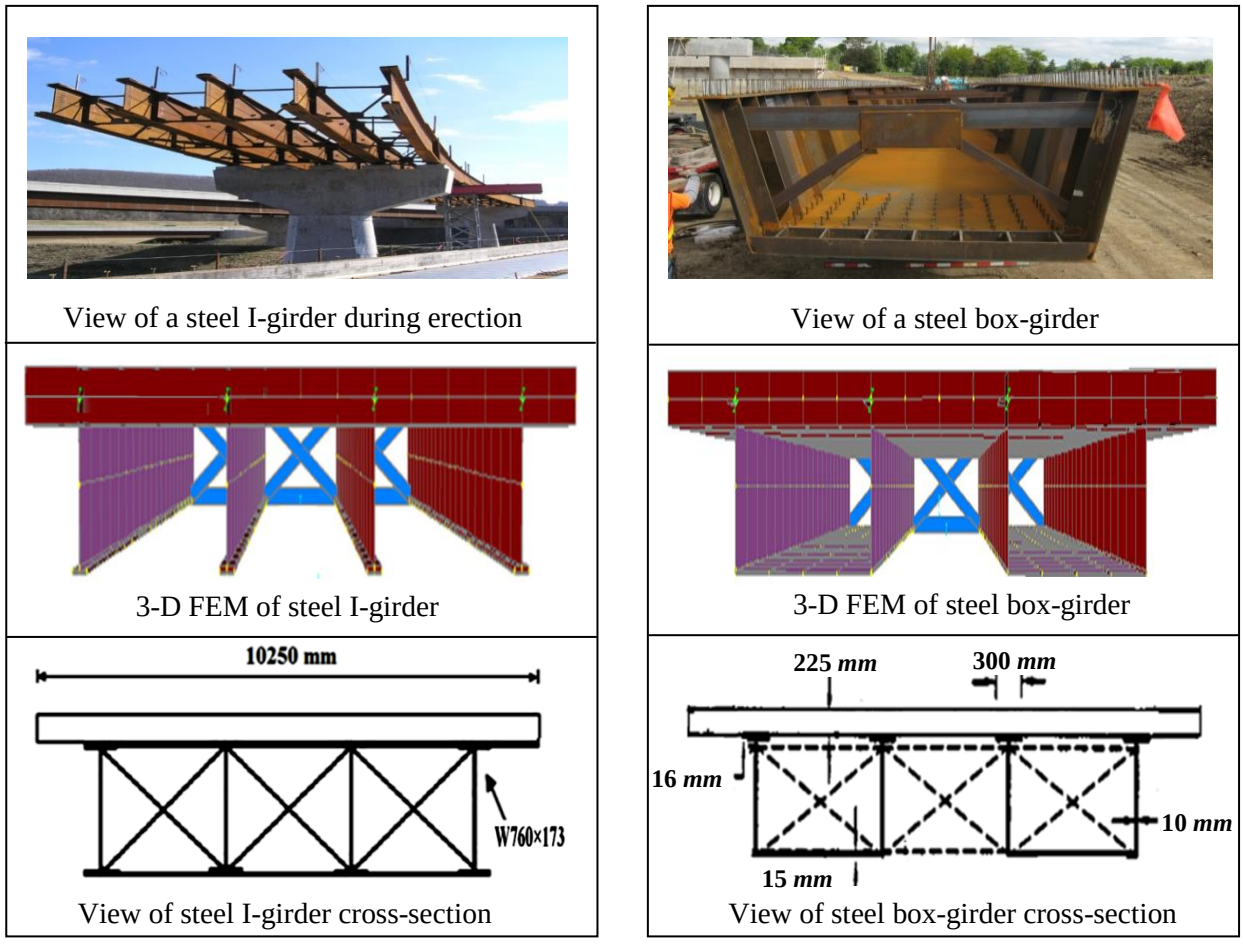

Figure 5.22: View of (a) Steel I-girder, (b) Steel box-girder.

Four different bridge total lengths (80, 120, 160 and 180 *m*) were considered to study the effect of bridge type. Table 5.2 illustrates the influence of simultaneous changes in girder types (steel I-girder or steel box-girder), bridge length and skew angle on the bending moment, shear force and displacement of pile. A change in girder type had a very smaller effect on the pile displacement than that for a change in bridge length and skew angle. For instance, the pile-head displacement, in non-skewed bridge with 180 *m* length, only increased from 40.1 to 40.9 *mm* when the girder changed from steel I-girder to steel-box girder, representing only a 2% increase in the pile displacement.

Table 5.2: Pile displacement, bending moment and shear force of bridges with different steel girder types.

Bridge #	Girder Type	Bridge Length (*m*)	Skew Angle	Moment (*KN.m*)		Shear (*KN*)		Displacement (*mm*)			
				Pile		Pile		Deck		Pile	
				Strong Axis	Weak Axis	Strong Axis	Weak Axis	Strong Axis	Weak Axis	Strong Axis	Weak Axis
				M11	M22	V11	V22				
A-1	Steel I-Girder	180	0	247.32	0	153.18	0	45.5	0	40.1	0
A-2	Steel Box-Girder	180	0	269.22	0	165.31	0	45.6	0	40.9	0
B-1	Steel I-Girder	160	30	131.86	8.17	104.74	8.56	35.2	10.9	29.3	8.02
B-2	Steel Box-Girder	160	30	141.72	8.8	108.52	8.83	35.9	11.23	30.8	8.23
C-1	Steel I-Girder	120	45	123.46	20.85	90.81	19.07	22.7	19.69	27.73	12.23
C-2	Steel Box-Girder	120	45	131.31	21.23	94.06	19.95	23.87	20.23	27.8	12.95
D-1	Steel I-Girder	80	60	111.51	32.56	76.34	22.37	26.78	20.64	23.95	17.84
D-2	Steel Box-Girder	80	60	117.02	34.41	80.66	23.32	28.12	21.67	25.38	18.72

5.1.2.1.8.2 EFFECT OF DIFFERENT CONCRETE GIRDER TYPES

In this part, the effect of different concrete girders types including concrete I-girder, box-girder and deck slab on pile displacement due to temperature variation was studied. The cross-section of concrete I-girder bridges was made of CPCI 900 was described earlier. The voided slab consisted of prestressed 600 *mm* concrete bridge deck which incorporates circular voids along its

length. The eleven circular voids in voided slab were comprised of 0.46 *m* diameter. The diameter to spacing ratio of the voids was approximately 0.88 and the maximum void to depth ratio was 0.76. The top and bottom cover were 40 *mm*. The concrete box-girder bridge consisted of three concrete box girders with spacing of 4.46 *m*. The overall depth of box girders was 0.91 *m* and edge to edge width of girders was 2.5 *m*. The thickness of the webs and bottom flanges of concrete boxes were considered as 0.17 and 0.15 *m*, respectively. The configurations of the bridge models for different concrete girder types are demonstrated in Figure 5.23.

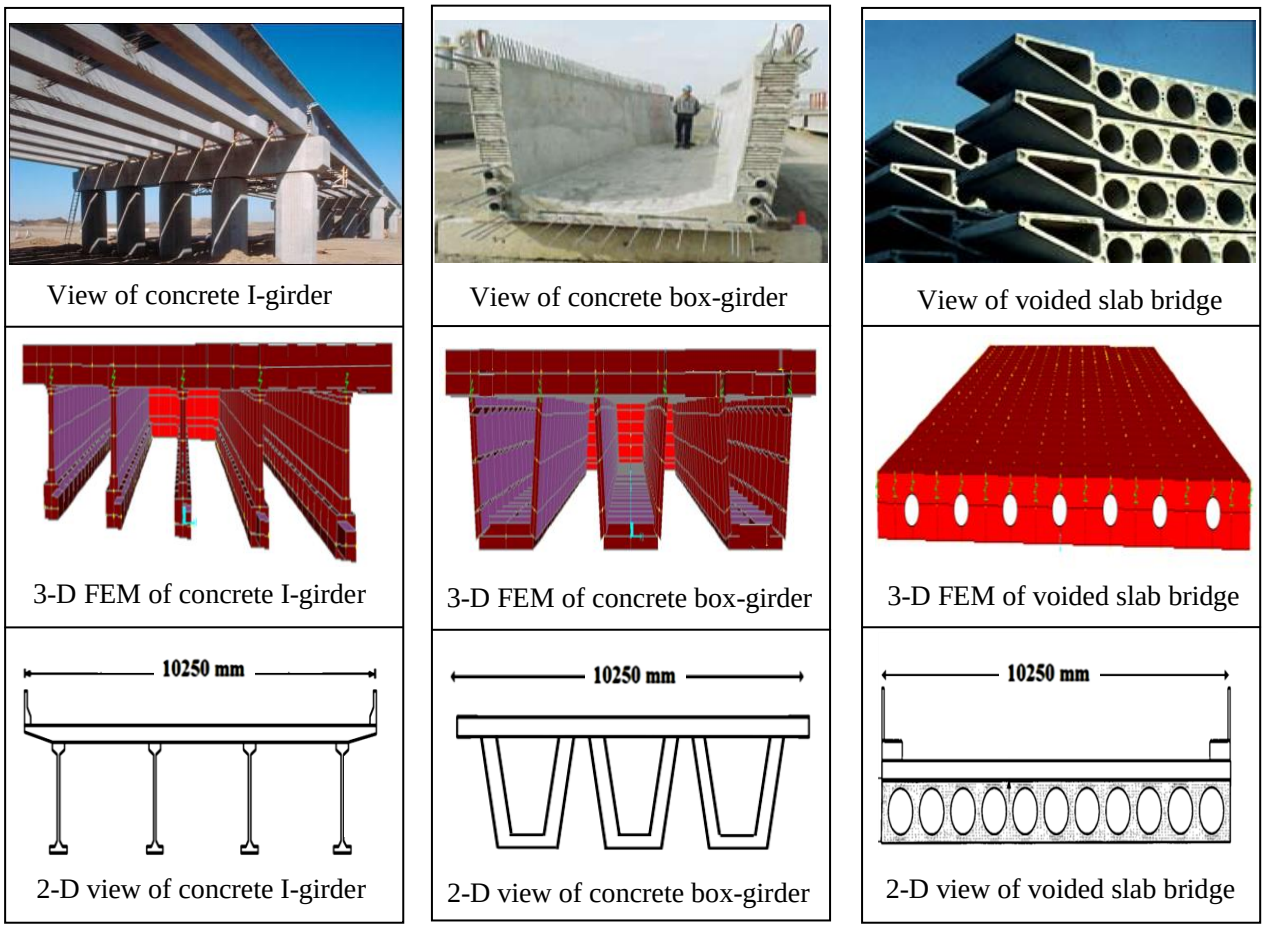

Figure 5.23: View of (a) Concrete I-girder, (b) Concrete box-girder, (c) Voided slab bridge.

Table 5.3 shows that differences between pile deformations of concrete-I girder and voided slab for various combinations of length and skew angles were just around 7%. In the same manner, it has been noticed that these differences for concrete I-girder bridges and voided slab bridges were approximately 5%. This reveals that the different concrete girder types (concrete I-girder,

concrete box-girder and deck slab) essentially have no major effect on the pile displacement for integral bridges.

Table 5.3: Pile displacement, bending moment and shear force of bridges with different concrete girder types.

Bridge #	Girder Type	Bridge Length (*m*)	Skew Angle	Bending Moment (*kN.m*)		Shear (*kN*)		Displacement (*mm*)			
				Pile		Pile		Deck		Pile	
				Strong Axis M11	Weak Axis M22	Strong Axis V11	Weak Axis V22	Strong Axis	Weak Axis	Strong Axis	Weak Axis
E-1	Voided Slab	240	0	213.38	0	108.26	0	37.86	0	34.02	0
E-2	Concrete I-Girder	240	0	222.84	0	113.31	0	39.3	0	35.3	0
E-3	Concrete Box-Girder	240	0	232.58	0	117.51	0	41.45	0	37.1	0
F-1	Voided Slab	200	30	114.5	6.71	79.85	9.88	32.61	8.05	28.74	6.73
F-2	Concrete I-Girder	200	30	123.21	7.27	85.64	10.63	34.7	8.65	29.87	7.26
F-3	Concrete Box-Girder	200	30	124.72	7.28	86.92	10.76	35.3	8.77	31.33	7.33
G-1	Voided Slab	160	45	107.88	17.98	70.07	14.56	27.36	12.38	24.92	10.82
G-2	Concrete I-Girder	160	45	115.23	19.37	75.67	15.83	29.43	13.32	26.81	11.53
G-3	Concrete Box-Girder	160	45	116.31	19.81	76.06	15.96	29.87	13.96	27.8	11.89
H-1	Voided Slab	140	45	95.27	27.66	58.06	17.71	23.57	18.04	20.78	15.52
H-2	Concrete I-Girder	140	60	102.53	29.63	63.41	18.57	25.08	19.37	22.36	16.73
H-3	Concrete Box-Girder	140	60	103.62	30.41	63.96	19.45	25.79	19.77	22.8	17.02

5.1.2.1.9 EFFECT OF GIRDER SPAN AND ASSOCIATED GIRDER DEPTH

Girder depth and bridge span length are often related. To achieve the total bridge length of a multi-span bridge, the bridge may consist of a series of short-span shallow girders or fewer long-span deep girders. Figure 5.24 presents three combinations that were investigated. In these three combinations, non-skewed concrete integral bridges had the same total length of 240 *m* and

different girder depths. The first bridge was continuous over twelve-equal spans of 20 *m*, while the second bridge was continuous over eight-equal spans of 30 *m*. The third bridge was over six spans with a span length of 40 *m*. The first, the second and the third girder types for 20, 30 and 40 *m* spans were made of CPCI 900, CPCI 1500 and CPCI 2300. As such, the girder depths were 900, 1500 and 2300 *mm* for bridge span 20, 30 and 40 *m*, respectively.

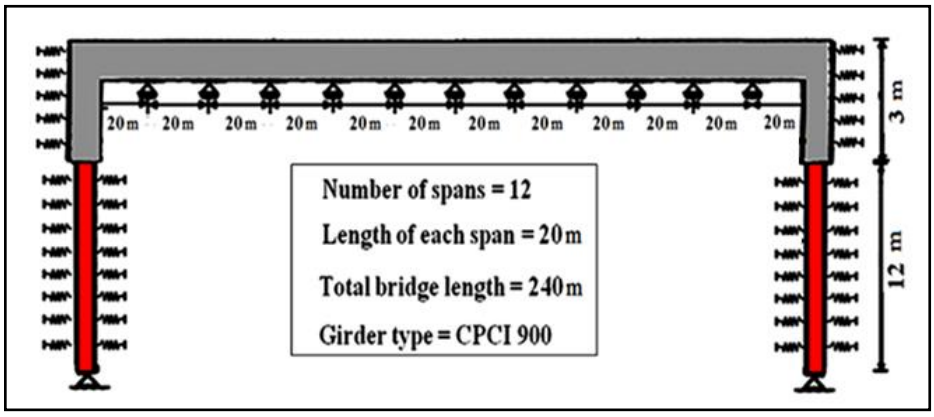

(a)

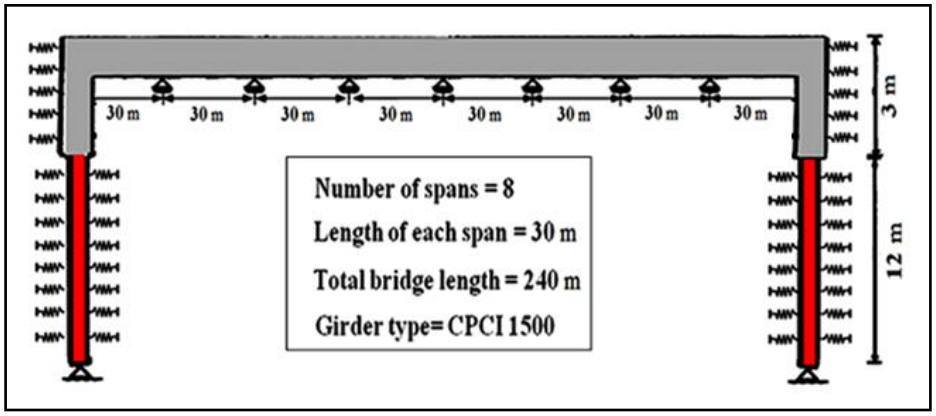

(b)

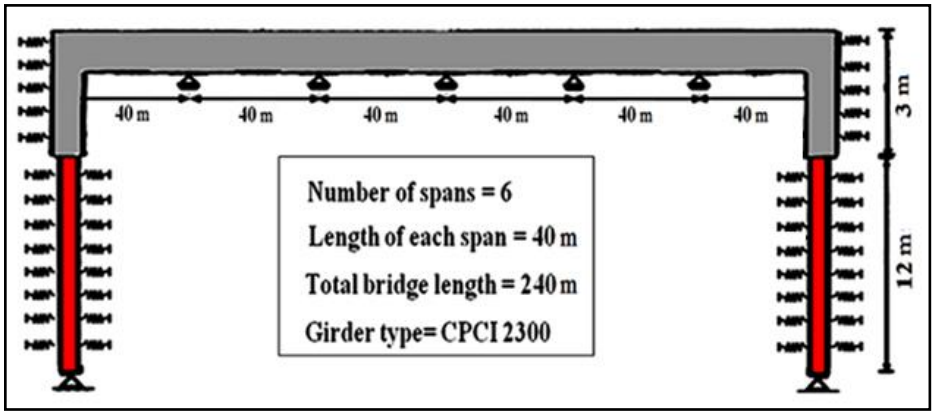

(c)

Figure 5.24: View of bridges with same total length and different span length (a) 20 *m*, (b) 30 *m*, (c) 40 *m*.

Table 5.4 shows that an increase in the girder depth had a little effect on the pile displacement than that for an increase in the bridge length. For example, an increase in the girder span from 20 to 30 *m* and accordingly girder depth from CPCI 900 to 1500 increased pile displacement from 35.3 *mm* to 36.88 *mm* (an increase of 4.5%). Also, increase in girder span from 30 to 40 *m* increased pile displacement by 4%. Similar observation was observed in case of pile bending moment and pile shear force. Pile moment and pile shear force was increased just about (2.7 to 5.8%) by increasing the girder span from 20 to 30 *m* or from 30 to 40 *m*.

Table 5.4: Pile displacement, bending moment and shear force of bridges with different girder depths.

Bridge #	Girder Type	Bridge Length (*m*)	Skew Angle	Moment (*kN.m*)		Shear(*kN*)		Displacement (*mm*)			
				Pile		Pile		Deck		Pile	
				Strong Axis	Weak Axis	Strong Axis	Weak Axis	Strong Axis	Weak Axis	Strong Axis	Weak Axis
				M11	M22	V11	V22				
M-1	CPCI 900	240	0	222.84	0	113.31	0	39.3	0	35.3	0
M-2	CPCI 1500	240	0	228.95	0	117.21	0	39.95	0	36.88	0
M-3	CPCI 2300	240	0	242.22	0	123.81	0	40.5	0	38.37	0

5.1.2.1.10 EFFECT OF SOIL TYPES SURRONDING PILES

Four different soil type, namely: soft clay, stiff clay, loose sand and dense sand, were considered to investigate the effect of soil types on pile deformation. Soil properties were given in section 3.5.2 of this dissertation. Integral bridges which were analyzed at this time were non-skewed steel I-girder bridges made of W 760×173 with different lengths and soil types. It can be observed from Figure 5.25 that displacement and bending moment of piles were nearly identical for different soil types. These results appeared to be independent of bridge length. It can be observed that bridges built with sandy soil around pile exhibit slightly larger pile displacement and pile bending moment that those for clayey soil. It is important to point out that generally in stiff soil conditions, predrilled oversize holes filled with loose sand are provided along the top portion of the pile to reduce the resistance of the surrounding stiff soil to lateral movements of the pile. For that reason, in the estimation of the length limits for integral bridges, the bridges can be conservatively assumed as built on medium clay.

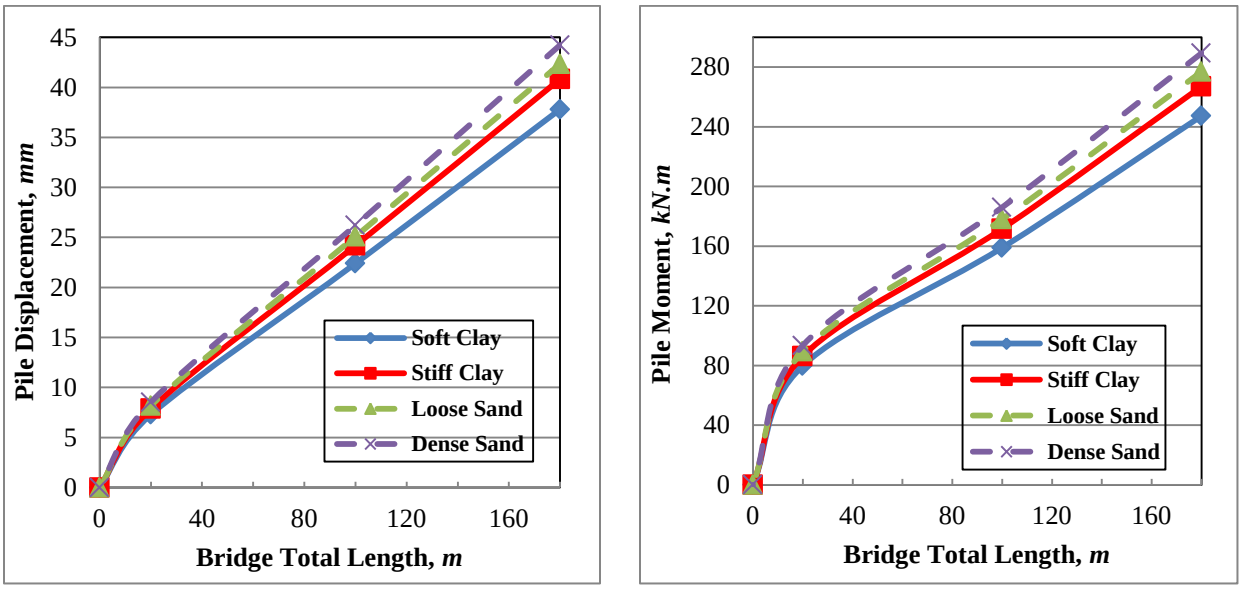

(a) (b)

Figure 5.25: Effect of different soil types surrounding piles on (a) pile deformation, (b) pile bending moment.

5.1.2.1.11 EFFECT OF WINGWALL ORIENTATION

Wingwalls are positioned at the ends of the bridge to support the backfill. The wingwall orientations considered in the parametric study are shown in Figure 5.26. Wingwalls were oriented in three directions to the roadway: perpendicular, parallel and 45°. All of the considered wingwalls had a thickness of 0.5 *m* and length of 3 *m*.

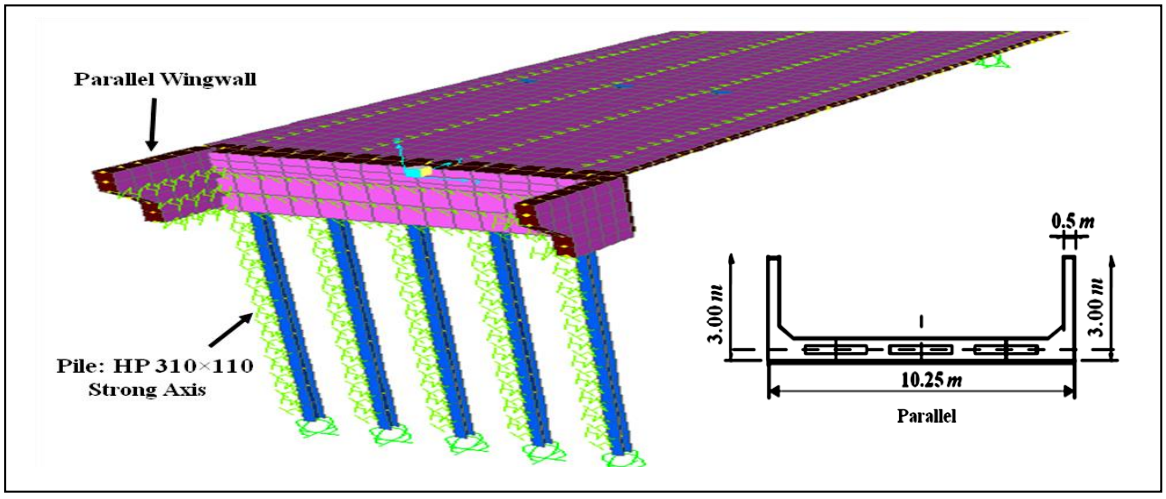

(a)

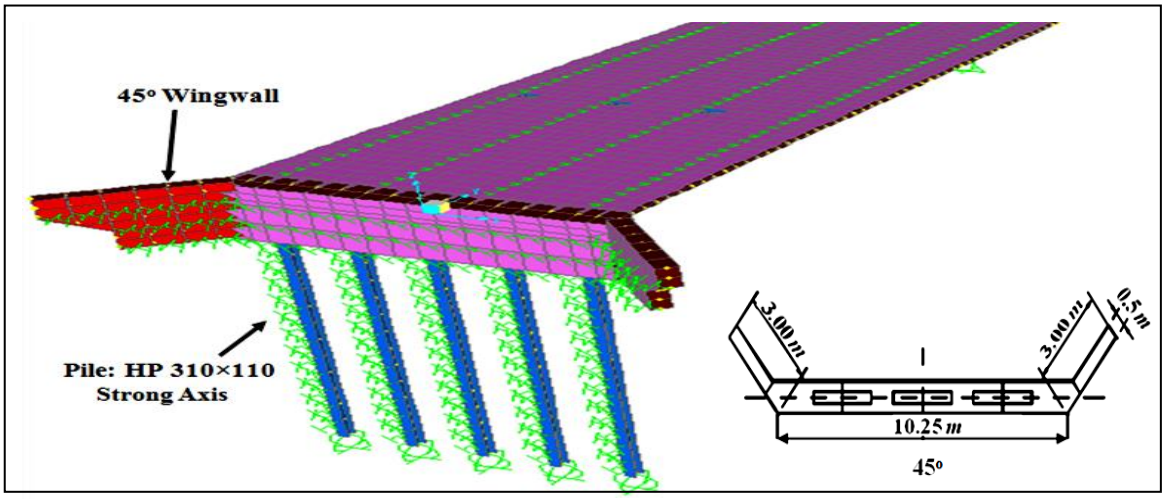

(b)

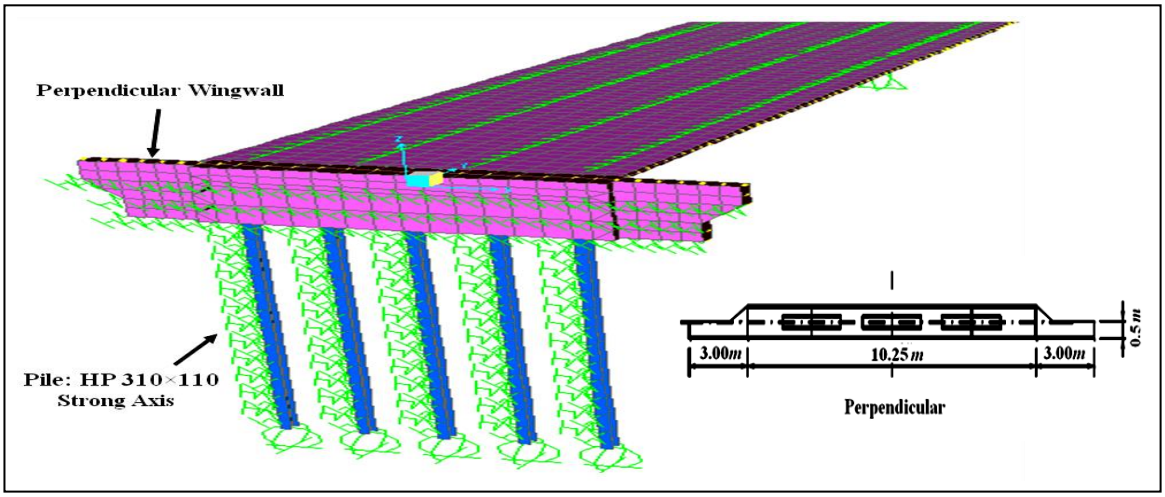

(c)

Figure 5.26: Finite element modeling of integral bridges with different wingwall orientations (a) Parallel wingwall, (b) 45^{o} wingwall, (c) Perpendicular wingwall.

Steel I-girder integral bridges made of W 760×173 with 180 *m* length and different wingwall orientations were chosen to examine the effect of wingwall orientations. By inspection of results, it was found that the influence of wingwall orientations on pile displacement was insignificant as depicted in Figure 5.27. For instance, by changing the wingwall orientation from perpendicular orientation to 45^{o} and parallel orientation the horizontal pile-head displacements have been decreased only around 1.5 and 3%. Thus, it can be concluded that wingwall orientation has insignificant effect on the pile response.

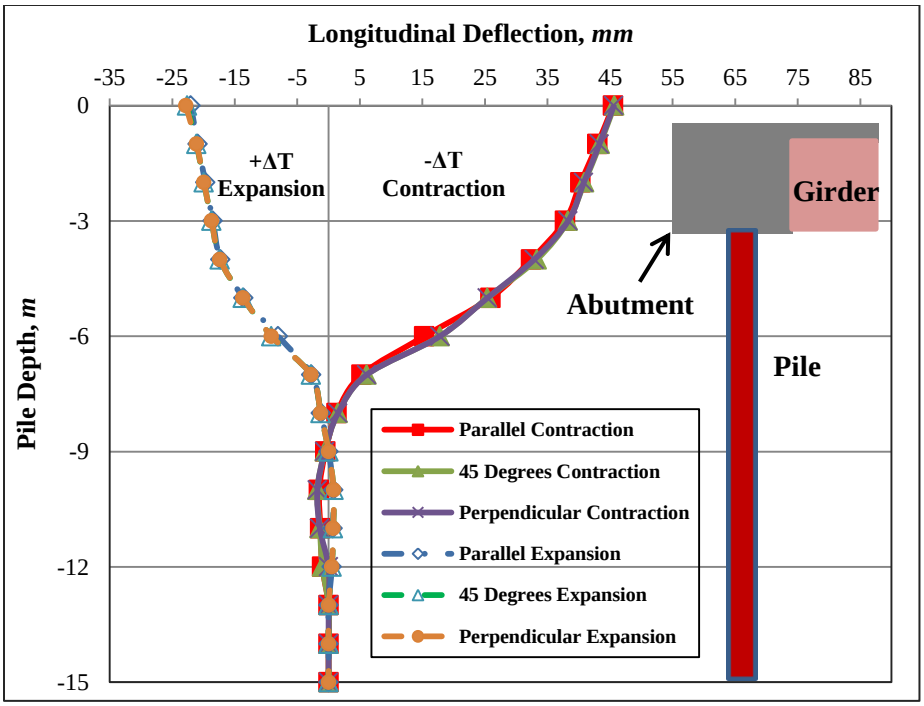

Figure 5.27: Effect of wingwall orientations on pile longitudinal deformation.

5.1.2.1.12 EFFECT OF WINGWALL LENGTH

Three different wingwall lengths (3, 4 and 5 *m*) are typically used in Ontario. To study the effect of wingwall length, as displayed in Figure 5.28, three non-skewed steel I-girder bridges made of W 760×173 with 180 *m* length and different wingwall lengths (3, 4 and 5 *m*) were analyzed.

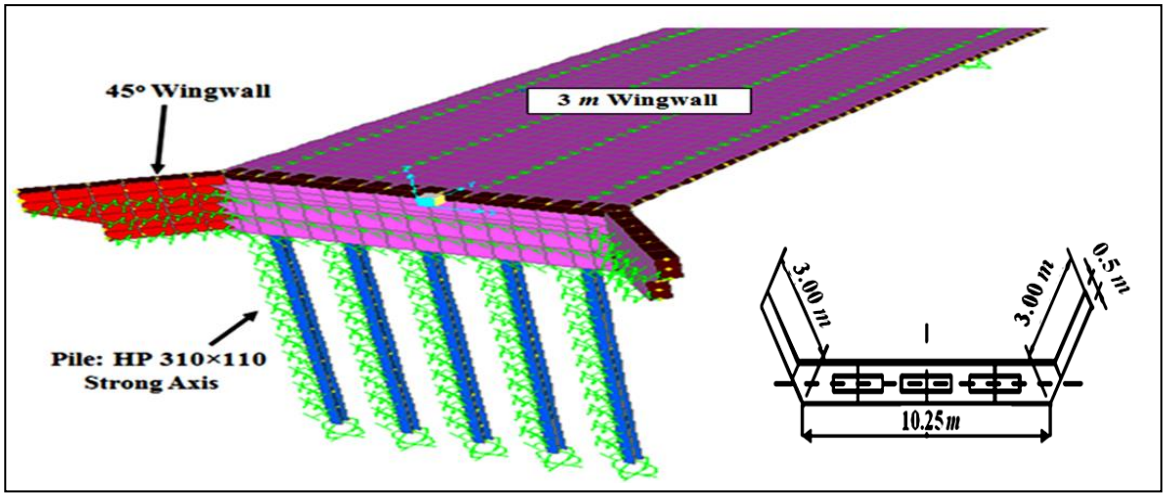

(a)

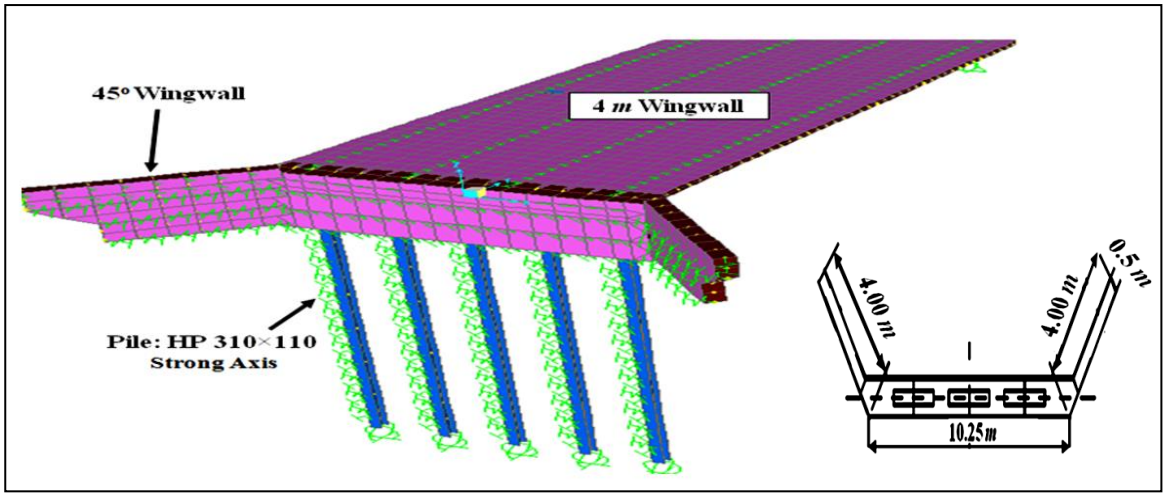

(b)

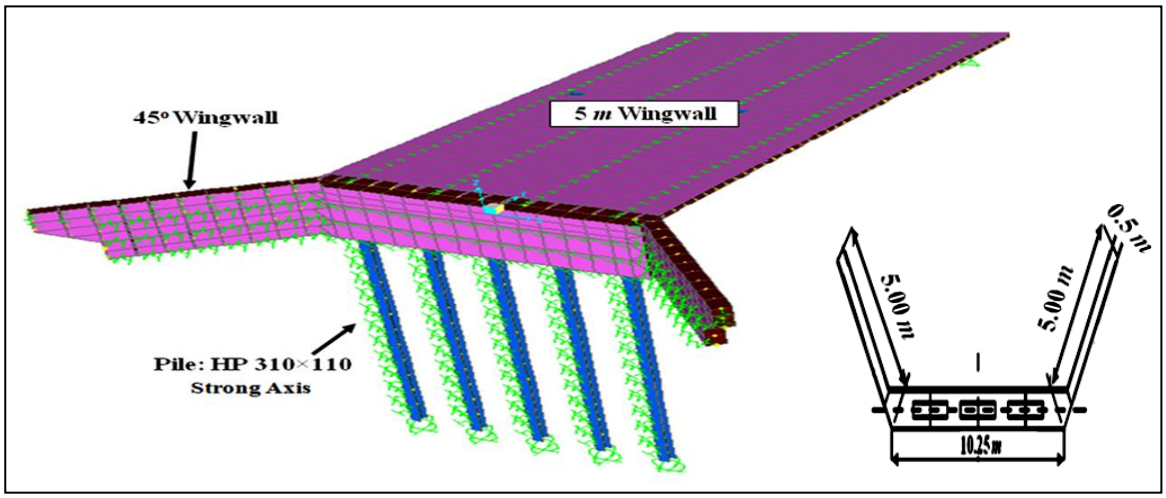

(c)

Figure 5.28: Finite element modeling of integral bridges with different wingwall lengths (a) L=3 *m*, (b) L=4 *m*, (c) L= 5 *m*.

Figure 5.29(a) and 5.29(b) illustrate that a change in the wingwall length has not considerably affected the magnitude of the bending moment and displacement of piles. For example, a decrease in the wingwall length from 5 to 3 *m* caused a small decrease in pile displacement from 34.6 to 33.3 *mm* during temperature fall. Similar behaviour with even less effect was witnessed in case of pile bending moment. Pile bending moment was reduced by more or less 2% from 270.48 to 264.14 *kN.m* during contraction by decreasing wingwall length from 5 to 3 *m*. As such, it can be concluded that wingwall length has insignificant effect on the pile displacement and moment.

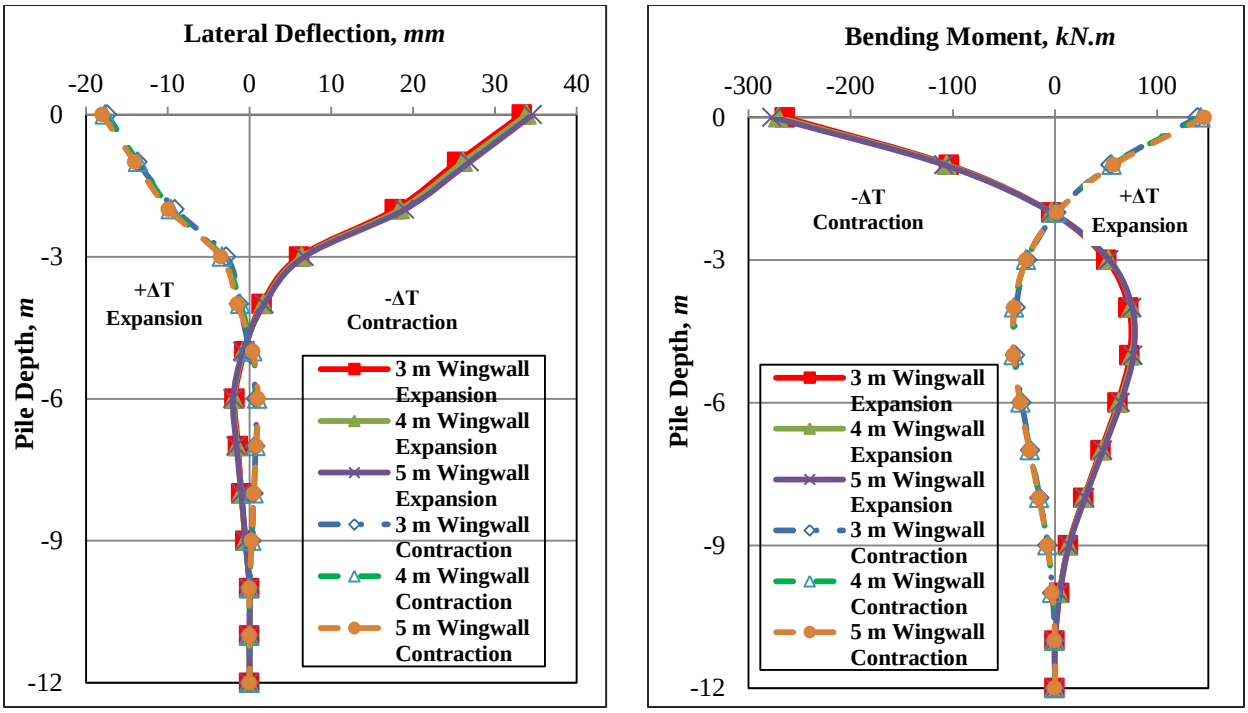

(a) (b)

Figure 5.29: Effect of wingwall length on (a) Pile longitudinal deformation, (b) Pile bending moment.

5.1.2.1.13 EFFECT OF NUMBER OF DESIGN LANES

To evaluate the influence of number of design lanes on pile response, steel integral bridges with 100 *m* length and different widths (7.00, 10.25, 13.5, 16.75, 20.00, 23.25, 26.5 and 29.75 *m* representing bridges with 1 to 8 design lanes), as shown in Figure 5.30, were analyzed.

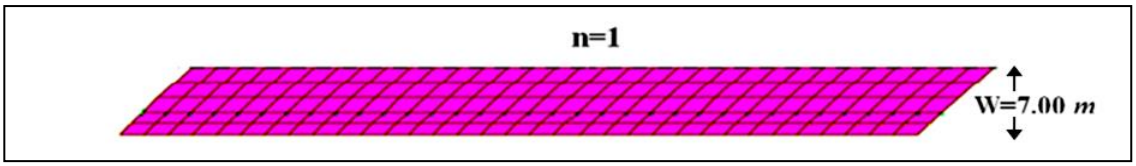

(a)

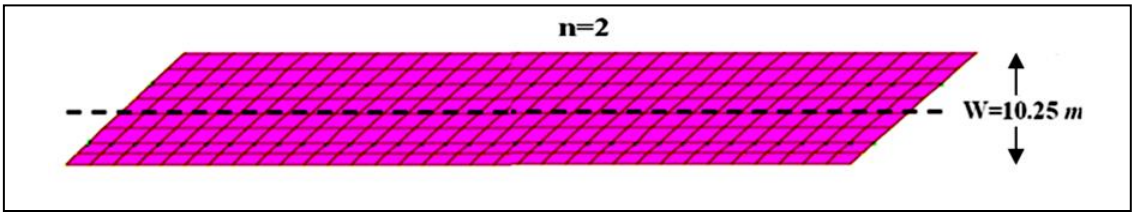

(b)

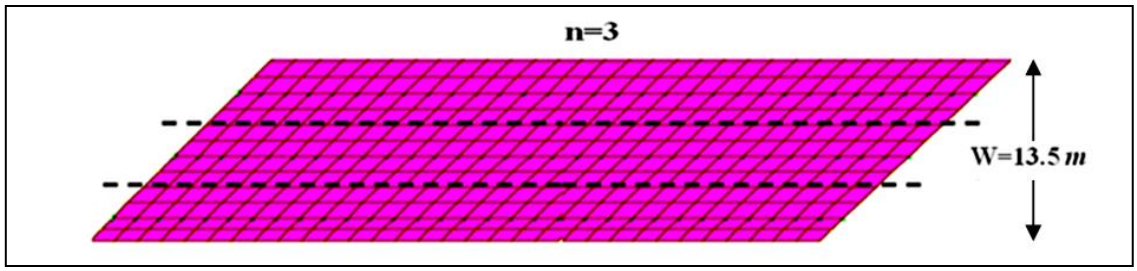

(c)

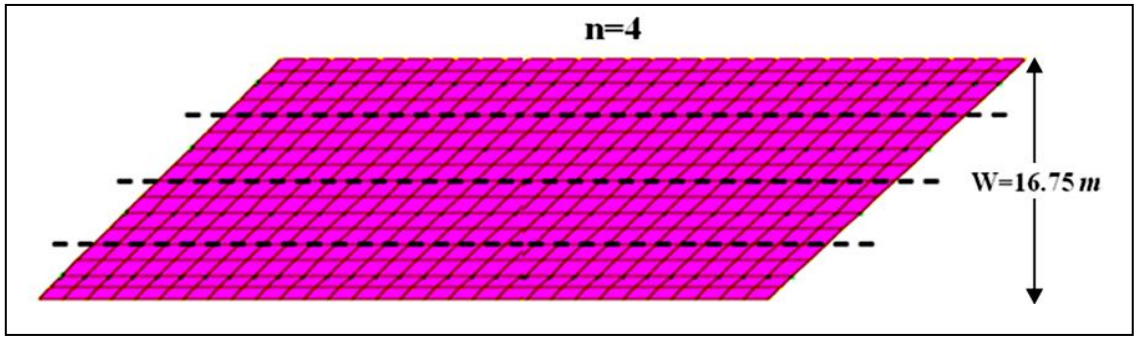

(d)

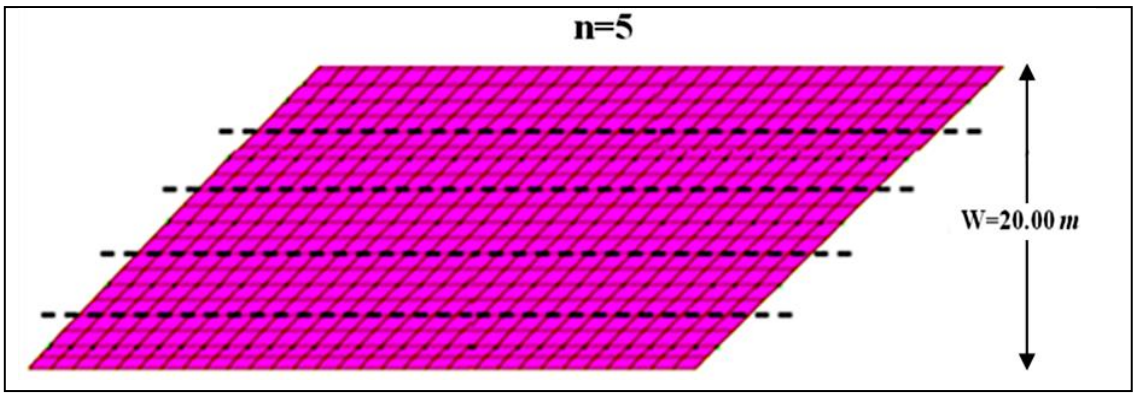

(e)

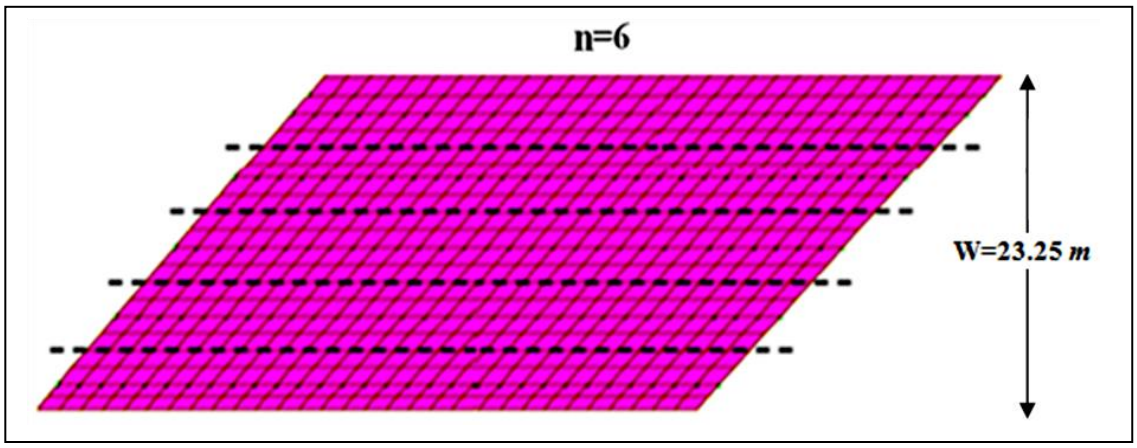

(f)

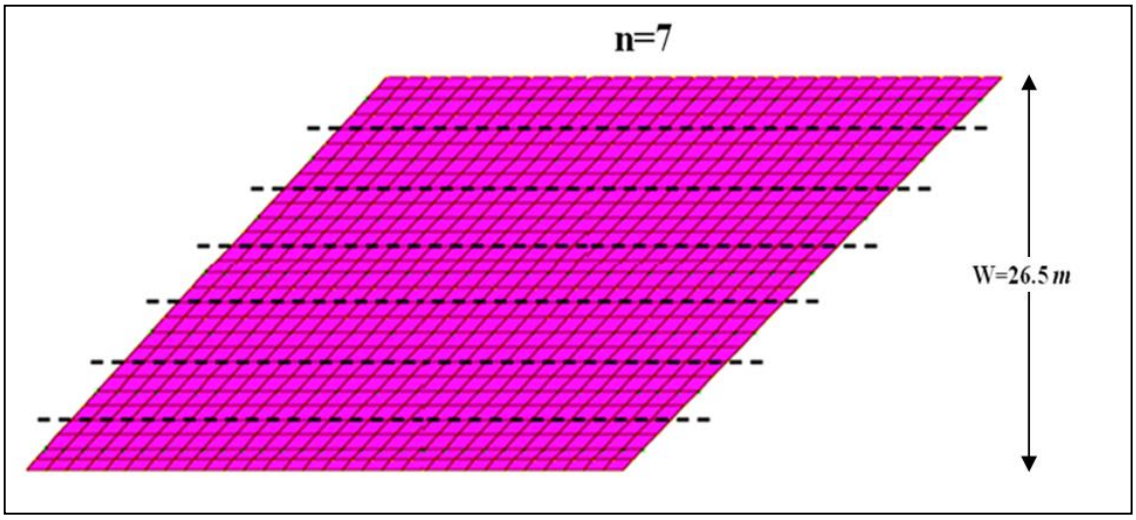

(g)

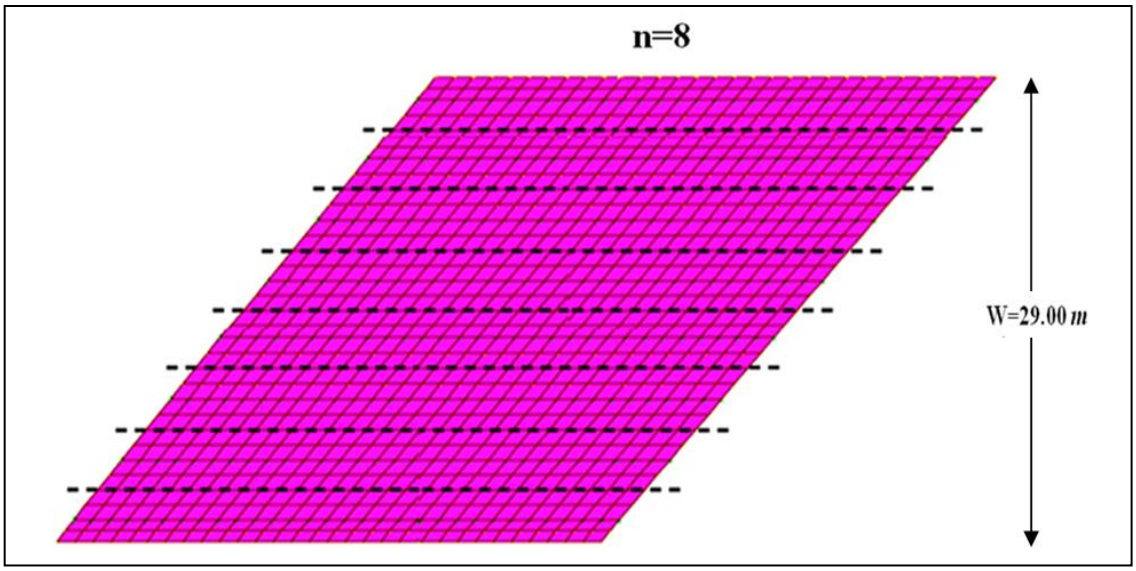

(h)

Figure 5.30: View of integral bridges with different widths (a) 7.00 *m*, (b) 10.25 *m*, (c) 13.5 *m*, (d) 16.75 *m*, (e) 20.00 *m*, (f) 23.25 *m*, (g) 26.5 *m*, (h) 29.00 *m*.

By inspection of finite element analysis results shown in Figure 5.31, it was found that a change in the number of design lanes significantly affected the transverse displacements of the pile when the bridge skew angle, θ, exceeds about 20^o. For angles θ larger than about 20^o, an increase in the number of design lanes, n, caused an increase in the transverse displacement. As an example, for one-design-lane steel integral bridge, the transverse pile displacement at a skew angle of 60° was approximately 20.15 *mm* while for eight design lanes integral bridge, the transverse displacement at a skew angle of 60^o was approximately 27.08 *mm*. This demonstrates the increase in restraint

resulting from the increase in resistance to lateral moment because of the larger ratio of wingwall length to abutment length. It is noteworthy to mention that integral bridges with the same length irrespective of different number of design lanes had the same value of longitudinal displacements.

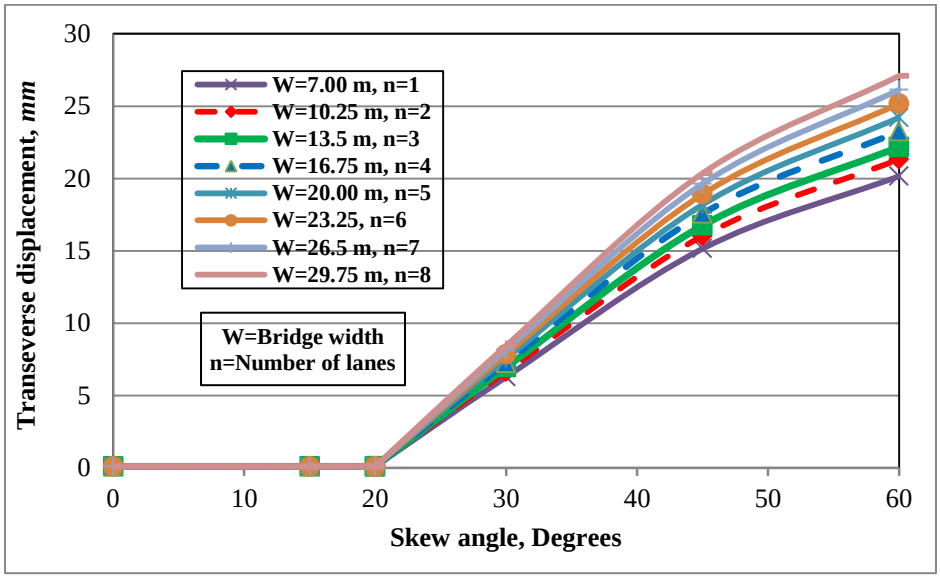

Figure 5.31: Influence of the bridge width on the transverse pile displacement.

5.1.2.1.14 EFFECT OF NUMBER OF INTERVAL CROSS-BRACINGS

A sensitivity study was conducted on 60 *m* steel integral bridges with skew angle of 30^{o} to examine the effect of different number and orientation of cross bracings on pile deformation.

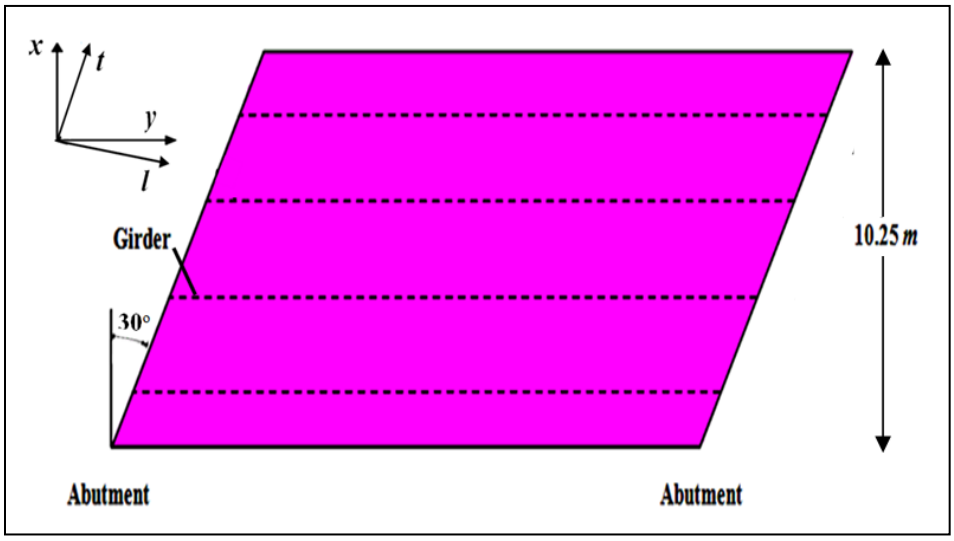

Figure 5.32: Integral bridge without cross bracing (N-1).

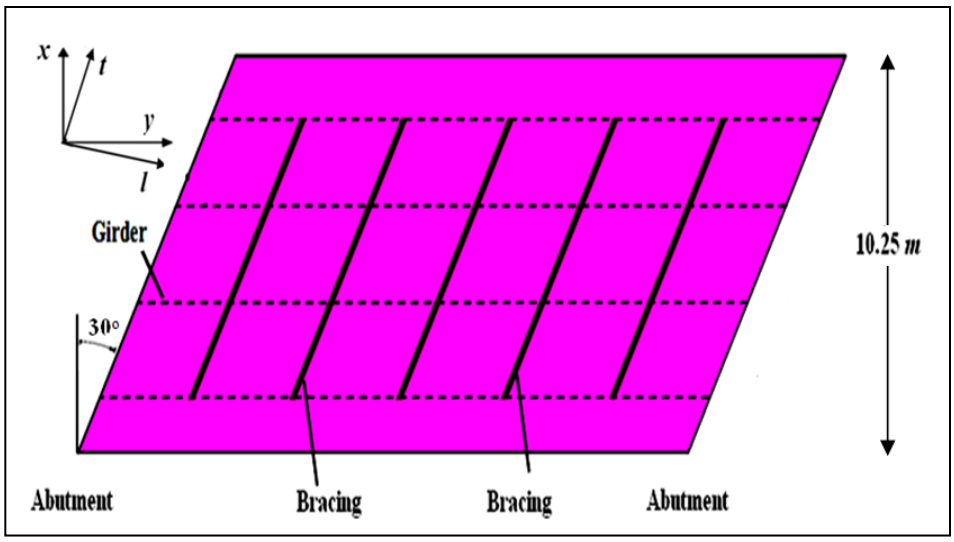

Figure 5.33: Integral bridge with cross bracing parallel to skew angle (N-2).

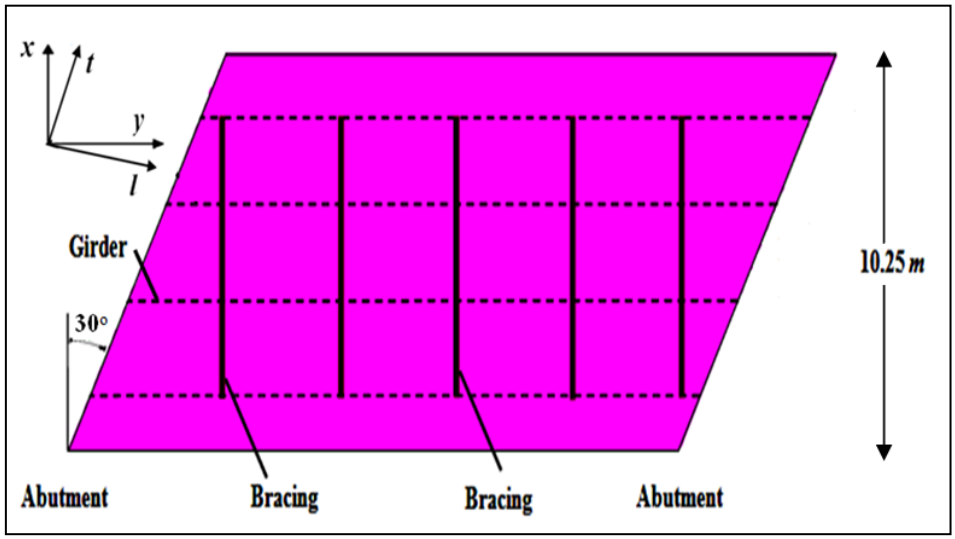

Figure 5.34: Integral bridge with cross bracing parallel to x-axis (N-3).

As shown in Figure 5.32 to 5.34, three different bridge prototypes (N-1, N-2 and N-3) were considered herein. The first bridge (N-1) had no X-type cross bracings (L150×150×25 *mm)*, while the second bridge (N-2) had 5 interval bracings parallel to skew angle, one each 10 *m*. The third bridge (N-3) had 5 bracing parallel to x-axis, one each 10 *m*.

It can be observed from Figure 5.35(a) that different number and orientation of cross bracings had an insignificant effect on the pile displacement. For example, pile longitudinal displacement

was increased from 29.8 to 31.6 *mm* during temperature fall when the bridge prototype changed from N-1 to N-3 (an increase of only 6%). As shown in Figure 5.35(b), similar trend was observed in case of pile transverse displacement.

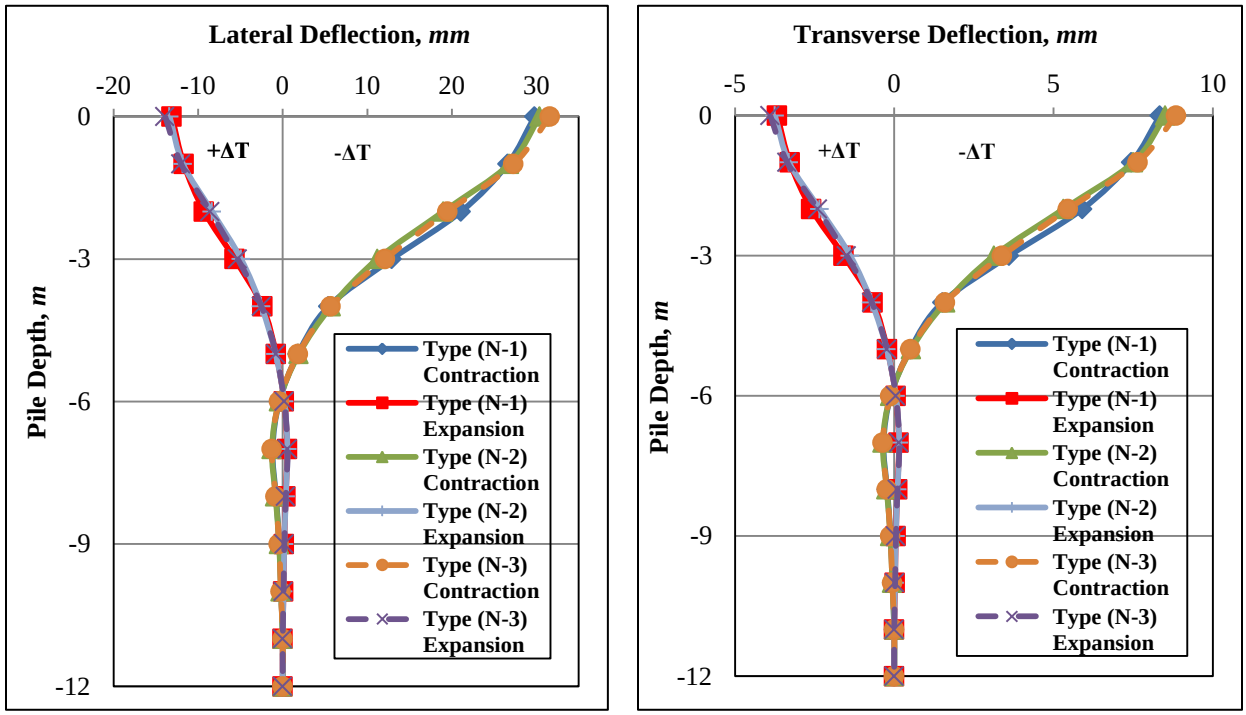

(a) (b)

Figure 5.35: Effect of number of bracing on (a) Pile longitudinal deformation, (b) Pile transverse deformation.

5.1.3 PARAMETRIC STUDY OF STEP 2: LIMIT ANALYSIS

Based on the results in section 5.2 (step 1), it can be stated that pile displacements of the integral bridges were qualitatively independent of the pile orientation, abutment thickness, girder types, girder depths, soil surrounding piles, wingwall orientations and wingwall lengths. On the contrary, results in section 5.2 clearly indicate that the pile displacements of integral bridges were qualitatively and quantitatively dependent on critical variables including the pile size, bridge skew angle, bridge length, number of design lanes and connection of pile cap to pile.

Parametric study of step 2 (Limit analysis) were conducted based on different combinations of critical variables to compute the critical pile longitudinal and transverse displacement. Subsequently, the critical pile displacements were used to determine length limits for non-skewed and skewed integral bridges. Maximum length for integral bridge was the longest length

in which the critical pile displacements obtained from step 2 in the bridge were less than the pile-displacement capacity demand.

5.1.3.1 MAXIMUM BRIDGE LENGTH

In order to understand in what way length limitations based on pile displacement capacity were determined, the following example is introduced. In this example, the maximum length limits for 45^{o} skewed steel integral bridge with the critical parameters such as 3 *m* abutment height, 310×110 H-pile and fixed abutment-pile connection was determined.

Using the finite element methods, dl and dt, distances of point A to point A' along the longitudinal and transverse directions of abutment piles (see section 2.2.2.2), have been specified for different lengths of 20, 40, 80, 120 and 160 *m*. By using Equations (2.6) and (2.7), Δ_x and Δ_y, total displacements components in the x-axis and y-axis directions for abutment pile, could be calculated. As it can be noticed in Table 5.5, the value of Δ_x and Δ_y, total displacements in x-axis and y-axis, were increased with increase in total bridge length. The maximum length for integral bridge was considered herein as the longest length in which the total pile displacements satisfied the pile displacement capacity demand which was presented by Equation (2.5). The longest steel integral bridge which satisfied the pile displacement demands had a length of 120 *m*. Thus, length limit of 120 *m* was chosen for 45^{o} skewed steel integral bridge with 3 *m* abutment height, 310×110 H-pile and fixed abutment-pile connection.

Table 5.5: Pile longitudinal and transverse displacements of bridges with different lengths.

Bridge Length (*m*)	**dl (*mm*)**	**dt (*mm*)**	**Δ_x (*mm*) Eq. (2.6)**	**Δ_y (*mm*) Eq. (2.7)**	**$\left(\frac{\Delta_x}{38}\right)+\left(\frac{\Delta_y}{38}\right)\leq 1$ Eq. (2.5)**
L=20	8.19	4.16	2.66	8.74	0.30
L=60	15.15	7.7	5.32	15.96	0.56
L=120	26.61	13.01	9.5	28.12	0.99
L=180	43.21	21.95	15.2	45.98	1.61

5.1.4 RECOMMENDED LENGTH AND SKEW ANGLLE LIMITS

Figure 5.36 through 5.39 graphically summarize the allowable lengths and skew angles for integral bridges with 2 design lanes and variables examined in this study. For practical purposes, a maximum skew for the plots of 60° was selected. Figures display that maximum bridge lengths

occur for bridge-skew angles less than 20^{o} because the transverse displacements do not occur for the integral abutments for either pile orientations. These figures also show that longer integral-abutment can be constructed with concrete girder compared to steel girder. The reason is that concrete bridges are less sensitive to temperature variations compared to steel bridges.

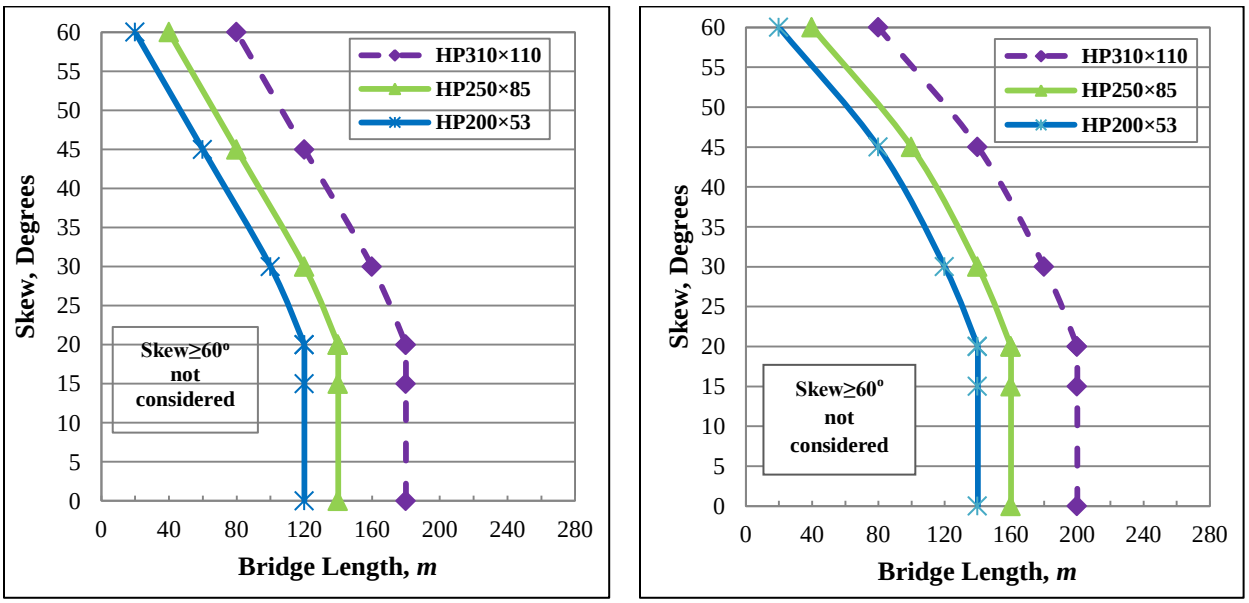

(a) (b)

Figure 5.36: Allowable steel IAB lengths and skews for various pile types with fixed abutment-pile connection: (a) Abutment height=3 *m*, (b) Abutment height=5 *m*.

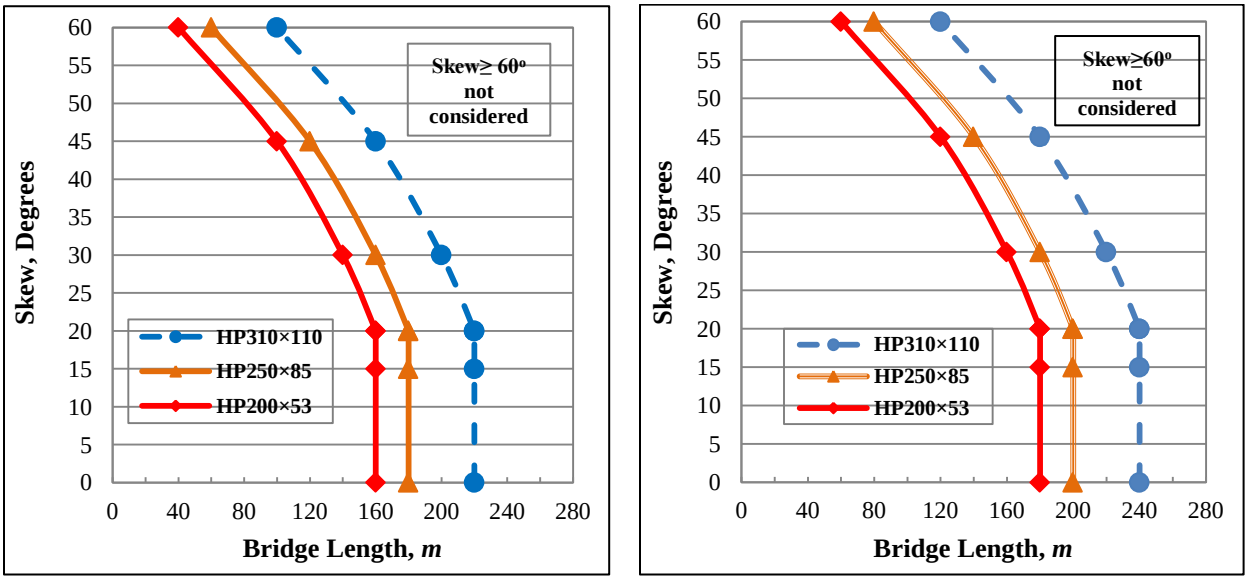

(a) (b)

Figure 5.37: Allowable steel IAB lengths and skews for various pile types with hinged abutment-pile connection: (a) Abutment height=3 *m*, (b) Abutment height=5 *m*.

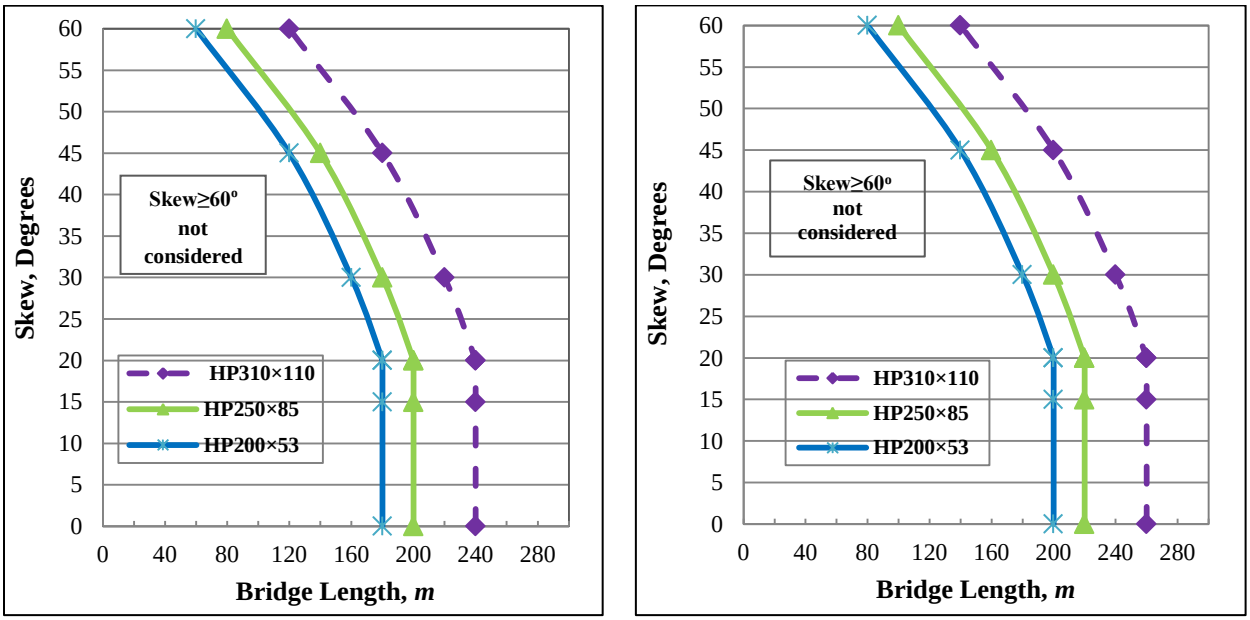

(a) (b)

Figure 5.38: Allowable concrete IAB lengths and skews for various pile types with fixed abutment-pile connection: (a) Abutment height=3 *m*, (b) Abutment height=5 *m*.

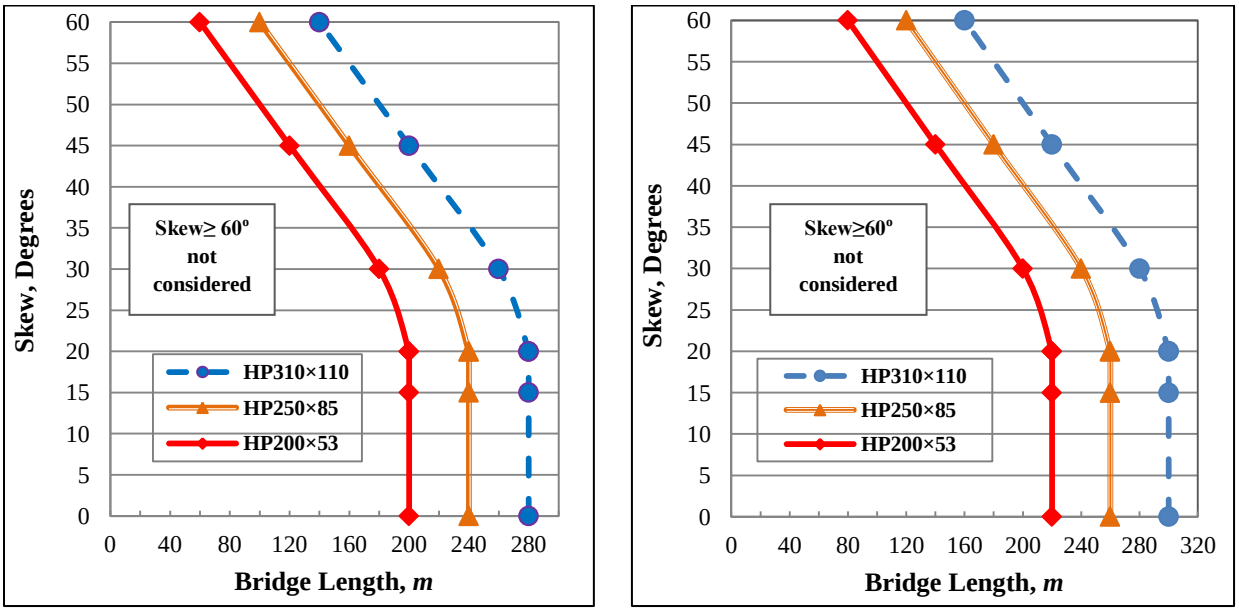

(a) (b)

Figure 5.39: Allowable concrete IAB lengths and skews for various pile types with hinged abutment-pile connection: (a) Abutment height=3 *m*, (b) Abutment height=5 *m*.

Figure 5.36 through 5.39 can be used to determine acceptable length and skew combinations for integral bridges with two design lanes. In those integral abutment bridges, induced deformations in the foundation piles were less than the pile displacement capacity. In order to include the effect of number of design lanes on allowable bridge length, different steel integral bridges with different bridge prototypes which have been already explained in section 5.1.2.13 have been analyzed.

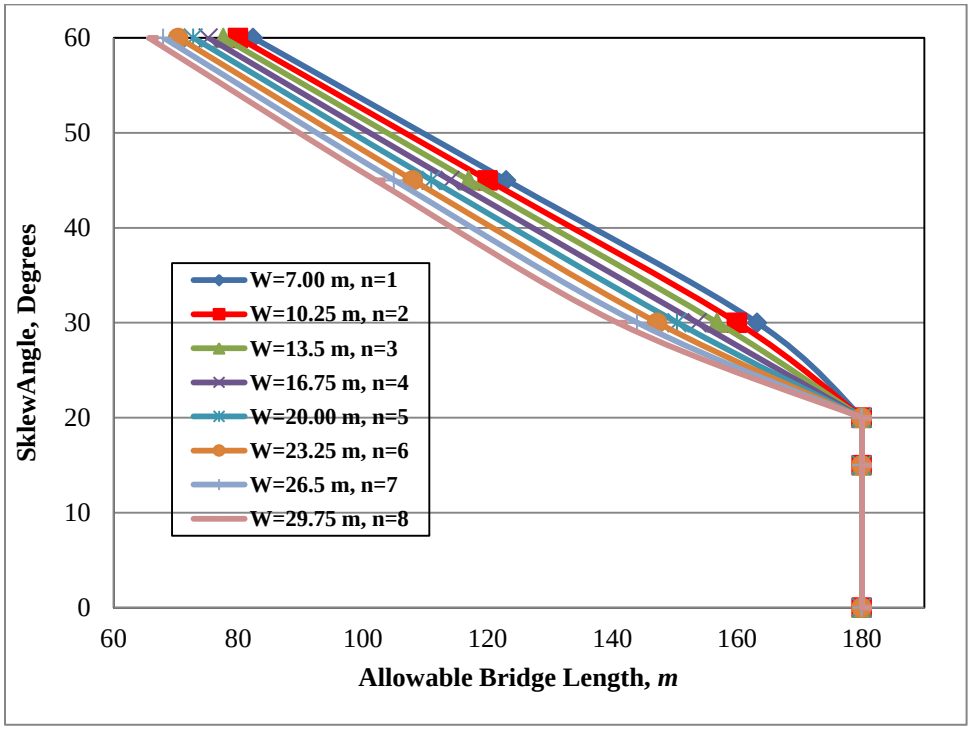

Figure 5.40: Allowable lengths and skew angles for steel bridges with different number of design lanes.

As it can be observed in Figure 5.40, allowable lengths of integral bridges were not affected by the change in the number of design lanes when the skew angle was smaller than 20^{o}. For skew angles larger than 20^{o}, the increase in the number of design lane caused decrease of approximately 3% in allowable length.

Additionally, Figure 5.36 through 5.39 can be used to determine the allowable length and skew combinations for integral bridges with two abutment heights (3, 5 *m*). To include the effect of different abutment heights on allowable integral bridge length, non-skewed steel bridges with six different abutment heights (1, 2, 3, 4, 5, 6 *m*) were selected.

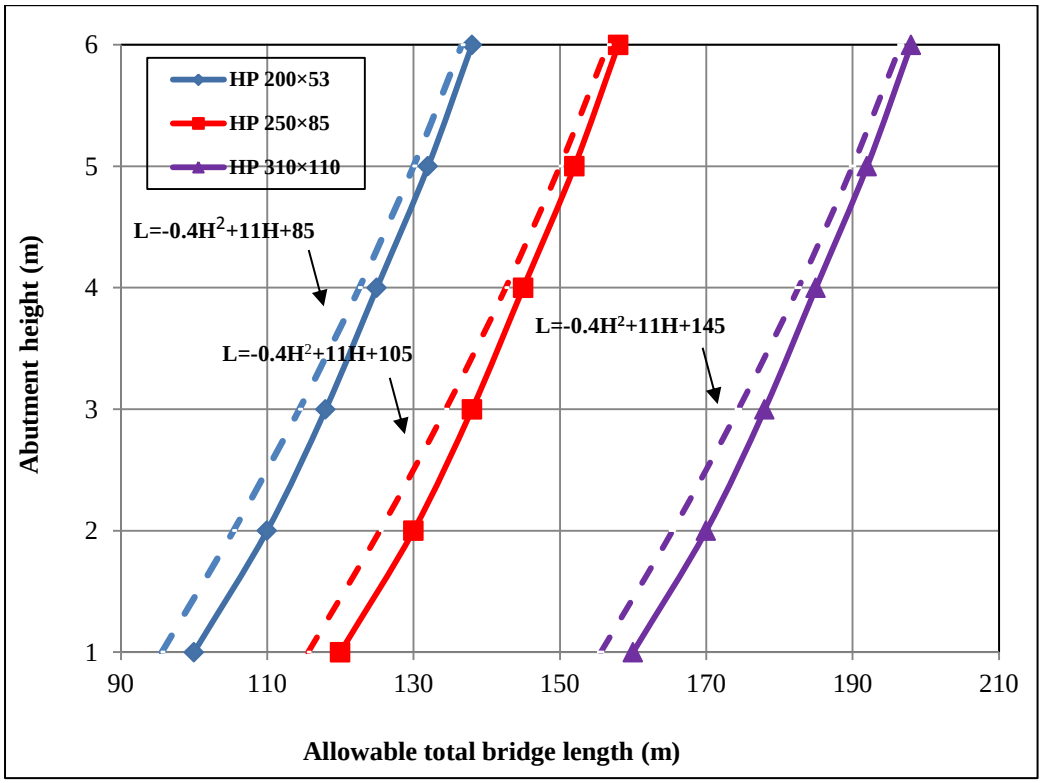

Figure 5.41: Allowable lengths for steel bridges with different abutment heights.

The change in bridge length limits by changing abutment height is shown in Figure 5.41 with solid curve (nonlinear) lines. It can be observed that allowable lengths of integral bridges were increased by increasing the abutment height. As an example, allowable lengths of integral bridges supported on HP 200×53 for abutment heights of 2 and 5 *m* were 110 and 132 *m*. The nonlinear relationship between abutment height and allowable bridge length was simplified using a quadratic curve displayed on the same figure with a dashed line. The use of quadratic curve made us to be in a safe side for design in a way that the values obtained from quadratic curve for allowable bridge lengths were smaller than nonlinear ones.

Alternatively, maximum length and skew combinations for bridges with different number of design lanes and different abutment heights outlined in Table 5.6 and 5.7 could be adopted. These values conservatively interpret the nonlinear trends presented in the Figure 5.36 through 5.39. Furthermore, we adopted a practical maximum skew value of 60° for the recommendations in the table.

Table 5.6: Allowable length and skew combinations for steel integral abutment bridges.

Abutment Pile Connection	**Skew Angle, Θ, (Degrees)**	**Maximum Length , L, (*m*)**		
		HP200 ×53	HP 250 ×85	HP 310 ×110
Fixed	**0≤Θ≤20**	$L=-0.4H^2+11H+85$	$L=-0.4H^2+11H+105$	$L=-0.4H^2+11H+145$
	20≤Θ≤60	$L=[(-0.01\Theta^2-1.675\Theta)+(-0.4H^2+11H+123)][1-0.03(n-2)]$	$L=[(-0.01\Theta^2-1.675\Theta)+(-0.4H^2+11H+138)][1-0.03(n-2)]$	$L=[(-0.01\Theta^2-1.675\Theta)+(-0.4H^2+11H+178)][1-0.03(n-2)]$
Hinged	**0≤Θ≤20**	$L=-0.4H^2+11H+125$	$L=-0.4H^2+11H+145$	$L=-0.4H^2+11H+185$
	20≤Θ≤60	$L=[(-0.037\Theta^2+0.008\Theta)+(-0.4H^2+11H+139.5)][1-0.03(n-2)]$	$L=[(-0.037\Theta^2+0.008\Theta)+(-0.4H^2+11H+159.5)][1-0.03(n-2)]$	$L=[(-0.037\Theta^2+0.008\Theta)+(-0.4H^2+11H+199.5)][1-0.03(n-2)]$

Note: n = number of design lanes, H = abutment height in meter (1 *m*≤ H ≤6 *m*).

Table 5.7: Allowable length and skew combinations for concrete integral abutment bridges.

Abutment Pile Connection	**Skew Angle, Θ, (Degrees)**	**Maximum Length , L, (*m*)**		
		HP200 ×53	HP 250 ×85	HP 310 ×110
Fixed	**0≤Θ≤20**	$L=-0.4H^2+11H+145$	$L=-0.4H^2+11H+165$	$L=-0.4H^2+11H+205$
	20≤Θ≤60	$L=[(-0.037\Theta^2+0.008\Theta)+(-0.4H^2+11H+159.5)][1-0.03(n-2)]$	$L=[(-0.037\Theta^2+0.008\Theta)+(-0.4H^2+11H+179.5)][1-0.03(n-2)]$	$L=[(-0.037\Theta^2+0.008\Theta)+(-0.4H^2+11H+219.5)][1-0.03(n-2)]$
Hinged	**0≤Θ≤20**	$L=-0.4H^2+11H+165$	$L=-0.4H^2+11H+205$	$L=-0.4H^2+11H+245$
	20≤Θ≤60	$L=[(-0.031\Theta^2-1.029\Theta)+(-0.4H^2+11H+199.3)][1-0.03(n-2)]$	$L=[-0.031\Theta^2-1.029\Theta+(-0.4H^2+11H+239.3)][1-0.03(n-2)]$	$L=[-0.031\Theta^2-1.029\Theta+(-0.4H^2+11H+289.3)][1-0.03(n-2)]$

Note: n = number of design lanes, H = abutment height in meter (1 *m*≤ H ≤6 *m*).

5.1.5 CORRELATION OF RECOMMENDED EQUATION FOR MAXIMUM LEMGTH LIMITS WITH FEA RESULTS

Figure 5.42 shows the correlation of imperial expressions with the corresponding values as obtained from the finite element analysis for maximum length limits. It can be observed that developed equations correlate very well with the FEA results. Maximum length limit values obtained from equations and FEA differed by less than 5%. As an example, maximum length limit for 2 design lane steel integral bridge with 3 *m* abutment height, 30^{o} skew angle, 310×110 H-piles and fixed abutment-pile connection were computed as 98.75 *m* and 100 *m* based on proposed equation and FEA results (around only 1% difference). It is noteworthy to mention that based on current Ontario ministry of transportation (MTO) guideline for length and skew angle limits (skew angle limitation of 20^{o}), the above mentioned steel bridge is not allowed to be constructed. As a result, imperial equations compared to existed integral bridge length limits in current guidelines provide more economical and reliable design for integral bridges.

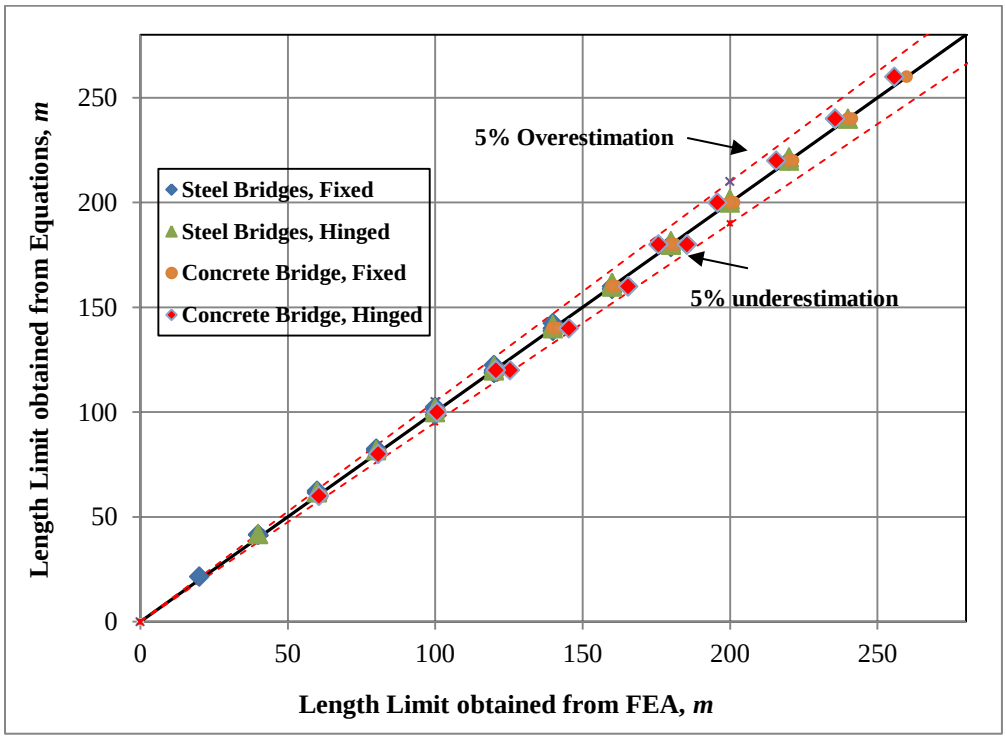

Figure 5.42: Correlation between FEA results and those from developed equations for maximum length limits.

CHAPTER 6: DEVELOPING LIVE LOAD DISTRIBUTION FACTORS FOR SINGLE-SPAN INTEGRAL ABUTMENT BRIDGES

6.1 GENERAL

First in section 6.1.1, it has been described that how load distribution factors were computed for longitudinal bending moments and shear force based on CHBDC equations and finite element method. Then, in section 6.1.2 practical-design-oriented parametric study pertained to live load distribution factor on single-span concrete and steel integral bridge prototypes was described. The integral bridges were analyzed to evaluate their responses when subjected to CL-W truck loading conditions. The parametric studies included the effect of substructure and superstructure on distribution factors for longitudinal bending moments and shear force at ultimate, serviceability and fatigue limit states. Variables considered in section 6.1.2 were foundation soil stiffness, pile size, pile orientation, abutment thickness, abutment height, span length, number of girders, girder spacing, number of intermediate diaphragms or bracings and number of design lanes. Next, in section 6.1.3, comparison between the results obtained from finite element modelling and the corresponding factors from the simplified method of analysis specified in the CHBDC for slab-on-girder bridges was conducted. Based on the results generated from parametric study, refined equations was proposed in section 6.1.4 to adjust the results obtained from the CHBDC simplified method of analysis for slab-on-girder so that can be applied to integral abutment bridges. Finally, live load distribution equations (LLDEs) derived for girder moments and shears are verified against available FEA results.

6.1.1 LOAD DISTRIBUTION FACTORS

6.1.1.1 LOAD DISTRIBUTION FACTOR BASED ON CHBDC EQUATIONS

Eliminating the joint at the end spans provides restraint against both rotation and translation. The rotational restraint creates a negative moment at the junction of superstructure-abutment and also reduces the positive moment at mid-span. The negative moment, positive moment and shear distribution factors based on CHBDC can be calculated using equations provided in section 2.3.2.8. To compute distribution factors based on CHBDC equations, the length parameters used

in those equations should be determined. For negative moment distribution factor, sum of the distances between points of contraflexure ($L_1 + L_2$) from a uniform load on the span was used as a length parameter. For positive moment distribution factor, length between two zero moments (L_3) in the superstructure was used as a length parameter. Finally for the shear force distribution factor, the bridge span length (L) was used as a length parameter. The length parameters to define distribution factors for shear and moment are summarized in the Figure 6.1.

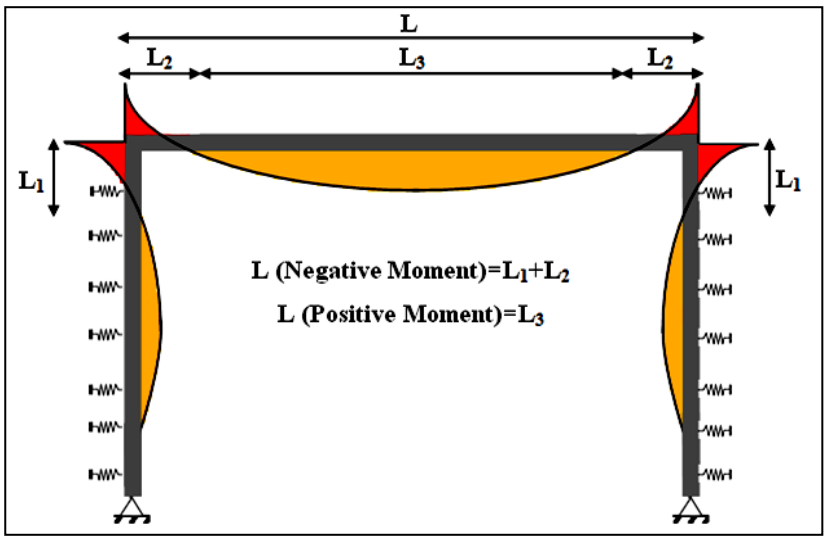

Figure 6.1: Bending moment of single-span integral bridge under uniform load.

6.1.1.2 LOAD DISTRIBUTION FACTOR BASED ON FINITE ELEMENT METHOD

6.1.1.2.1 LOAD DISTRIBUTION FACTOR FOR LONGITUDINAL MOMENT

Besides distribution factors derived from CHBDC equations, different 2D and 3D finite element analyses were conducted to determine positive and negative moment distribution factors.

6.1.1.2.1.1 LOAD DISTRIBUTION FACTOR FOR POSITIVE MOMENTS

To determine the load distribution factor for positive longitudinal bending moment (F_m) for exterior and interior girders, longitudinal stresses, as shown in Figure 6.2, in girder at the bottom surface of the bottom flange (σ) resulting from the 3D finite element analysis due to truck loading were identified. The maximum stress at the bottom surface of the bottom flange was identified from average stress results for elements adjacent to the chosen section. Thus, the girder moment can be calculated from obtained stresses using the following equation:

$$\sigma_b = M \times \frac{y_b}{I} \tag{6.1}$$

Where, σ_b is the average flexure stress at the bottom surface of bottom flange, M is the bending moment, y_b is the distance from neutral axis of the section to the bottom surface of the bottom flange and I is the moment of inertia of the section.

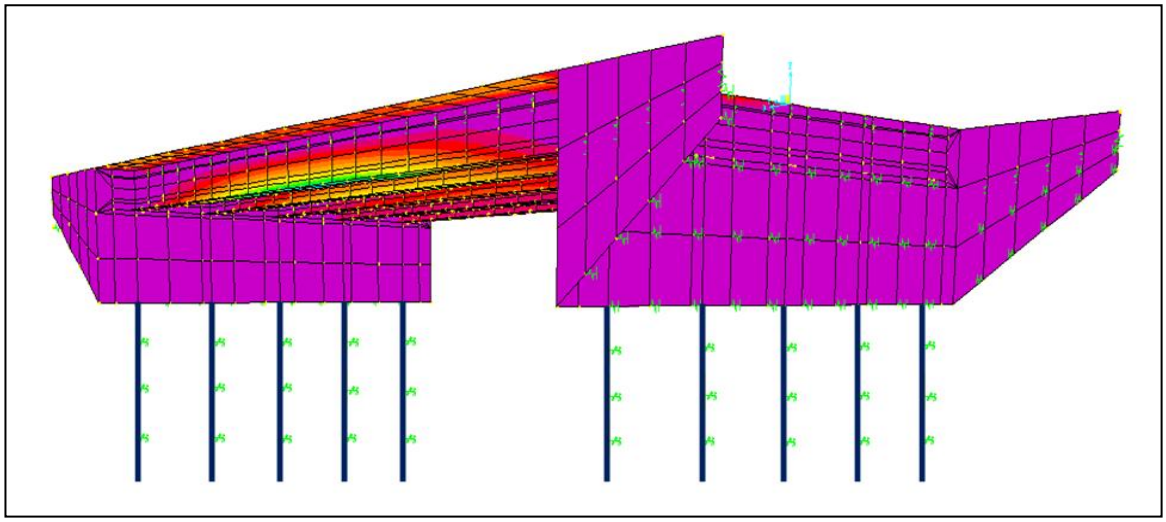

Figure 6.2: View of contour lines of normal stresses in integral abutment bridge due to truck loading for maximum positive moment condition.

Also, longitudinal stresses for the corresponding single girder (σ_o), resulting from 2D integral bridge analysis due to a single truck loading were identified.

Based on the concept shown in chapter 3, the distribution factors for the exterior and interior longitudinal bending moment (F_m) were calculated in accordance with CHBDC as follows:

For longitudinal bending moment at exterior girders ($F_{m\,ext}$):

$$F_{m\,ext} = \frac{N(\sigma_{ext})}{n\sigma_o R_L} \tag{6.2}$$

For longitudinal bending moment at interior girders ($F_{m\,int}$):

$$F_{m\,int} = \frac{N(\sigma_{int})}{n\sigma_o R_L} \tag{6.3}$$

Where, N is the number of girders, n is the number of design lanes, R_L is the modification factor multilane loading in accordance with CHBDC, σ_{ext} is the maximum flexure stress resulting from bridge analysis at the bottom surface of the bottom flange of exterior girders and σ_{int} is the maximum average flexure stress resulting from bridge analysis at the bottom surface of the bottom flange of the interior girder.

6.1.1.2.1.2 LOAD DISTRIBUTION FACTOR FOR NEGATIVE MOMENTS

In order to define the load distribution factor for negative longitudinal bending moment (F_m) for exterior and interior girders, the longitudinal stresses, as shown in Figure 6.3, at the top surface of the top flange (σ) at girder-abutment intersection resulting from the 3D integral bridge analysis due to truck loading were identified. The maximum stress was identified from average stress results for elements adjacent to the chosen section.

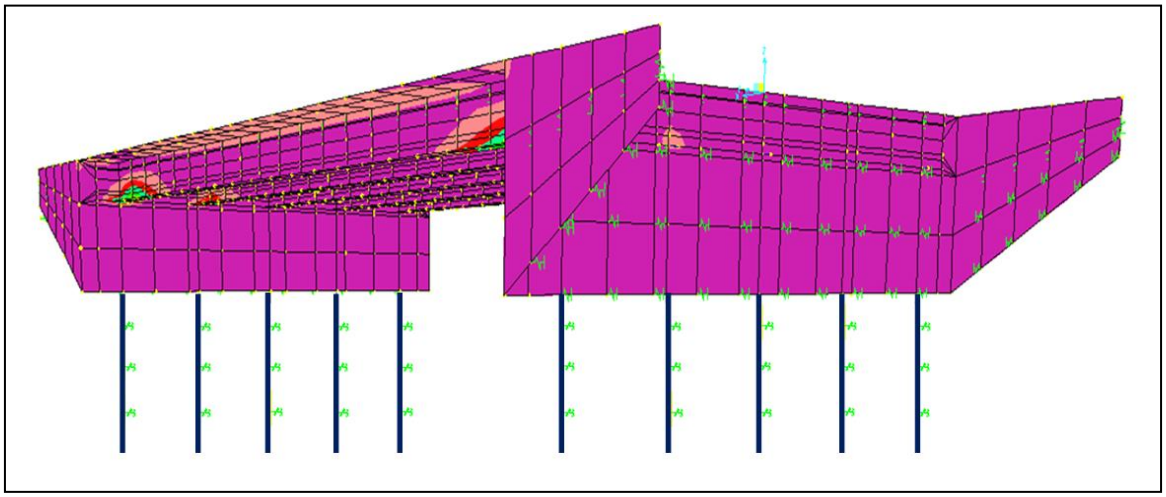

Figure 6.3: View of contour lines of normal stresses in integral abutment bridge due to truck loading for maximum negative moment condition.

Also, longitudinal stresses for the corresponding single girder (σ_o), resulting from 2D integral bridge analysis due to a single truck loading were identified.

Then, negative longitudinal bending moment distribution factors for the exterior and interior girders (F_m) were calculated based on Equations (6.2) and (6.3).

6.1.1.2.2 LOAD DISTRIBUTION FACTOR FOR VERTICAL SHEAR FORCE

To determine the load distribution factor for shear (F_v) for the exterior and interior girders, the maximum shear forces (V) at the girder-abutment joints resulting from 3D finite element analysis due to truck loading were identified. The maximum shear force, as shown in Figure 6.4, was identified from the total shearing force at the superstructure-substructure joint.

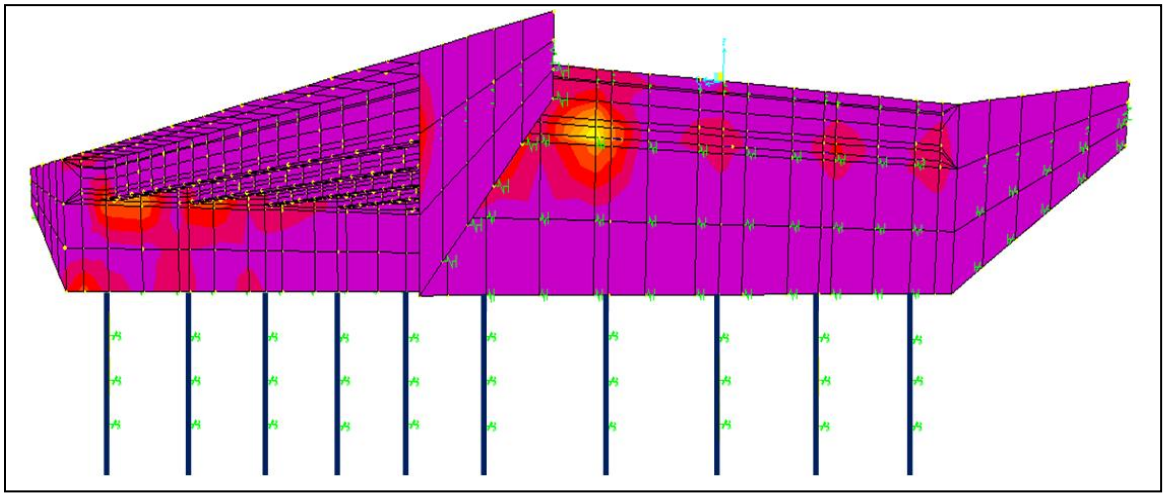

Figure 6.4: View of contour lines of shearing stresses in integral abutment bridge due to truck loading for maximum shear force condition.

Also, shear forces for the corresponding single girder (V_o), resulting from 2D finite element analysis due to single truck loading were identified.

The distribution factors for shear (F_v) were calculated in accordance with CHBDC as follows:

For longitudinal shear force at exterior girders ($F_{v\,ext}$):

$$F_{v\,ext} = \frac{N(V_{ext})}{nV_oR_L} \tag{6.4}$$

For longitudinal shear force at exterior girders ($F_{v\,int}$):

$$F_{v\,int} = \frac{N(V_{int})}{nV_oR_L} \tag{6.5}$$

Where, N is the number of girders, n is the number of design lanes, R_L is the modification factor multilane loading in accordance with CHBDC, V_{ext} is the maximum shear force resulting from bridge analysis of exterior girders and V_{int} is the maximum shear force resulting from bridge analysis interior girders.

6.1.2 EFFECT OF SUBSTRUCTURE AND SUPERSTRUCTURE ON DISTRIBUTION FACTOR

Table 6.1 illustrates eleven variables considered in the parametric study and the corresponding cases to examine the effects of these parameters on moment and shear distribution factors.

Table 6.1: Variables to be considered in parametric studies.

Variables		**Range of variables**	
		Number of cases	Description
Substructure	Pile size	2	HP 200×53, HP 310×110
	Soil stiffness	4	Soft clay, Stiff clay, Loose sand, Dense sand
	Backfill	2	With backfill, Neglecting backfill
	Abutment height	2	3, 5 *m*
	Abutment thickness	3	1, 1.5 *m*
	Wingwall orientation	3	Perpendicular, Parallel
	Wingwall length	2	3, 5 *m*
Superstructure	Span Length	5	10, 20, 25, 35, 45 *m*
	Number of design lanes	4	1, 2, 3, 4
	Girder Spacing	4	2, 2.4, 2.8, 3.2 *m*
	Number of bracings or diaphragms	4	0, 1, 2, 3

6.1.2.1 CHBDC TRUCK LOADING CONDITIONS

Based on CHBDC, the design of the bridge is characterized by three limit states, namely: ultimate limit state (ULS), serviceability limit state (SLS) and fatigue limit state (FLS). As such, live load conditions include truck-loading cases for those three limit states of design. For fatigue

analysis, only one truck CL-W truck is placed at the center of one travelling lane. The lane load is not considered for fatigue limit state (FLS). CHBDC states that for longitudinal moments at fatigue limit state and superstructure vibration, the vehicle edge distance (the distance from the centre of the outer wheel load to the edge of the bridge) shall not be greater than 3 *m*. Additionally, for ultimate limit state as shown in Figure 6.5 to 6.8, two different loading cases (full and partial CL-W truck loadings) were considered for each bridge prototype. In different loading cases, the wheel loads close to the curbs were applied at a distance of 0.6 *m* from the inside edge of the curb.

The numbers of lanes, n, were taken as 1, 2, 3 and 4. Integral bridges with different girder types (steel and concrete) were chosen such that the study covers a wide range of superstructure properties. The concrete bridge width was 4 *m* in the case of one lane, 8 *m* in the case of two lanes, 12 *m* in the case of three lanes and 16 *m* in case of four lanes. The concrete bridges had 2 *m* girder spacing. The steel bridge width was 4.8 *m* in the case of one lane, 9.6 *m* in the case of two lanes, 14.4 *m* in the case of three lanes and 19.2 *m* in case of four lanes. The steel bridges had 2.4 *m* girder spacing. Figures 6.5 to 6.8 schematically indicate all possible live load cases considered for both exterior and interior girders in one to four deign lanes integral abutment bridges. The exterior girder is the one closest to bridge barrier location while the interior girder is any girder between both exterior girders. It should be noted that when applying the truck loads on FEA modelling, the axial loads were multiplied by the factor for multi lane loading as 1, 0.9, 0.8 and 0.7 for the one, two, three and four loaded lanes.

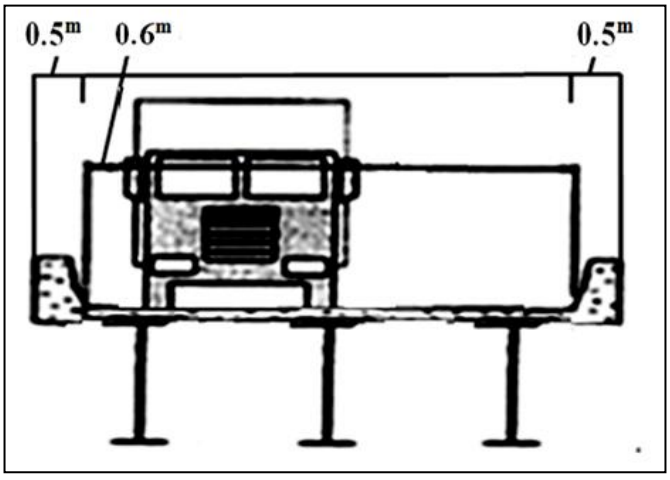

(a)

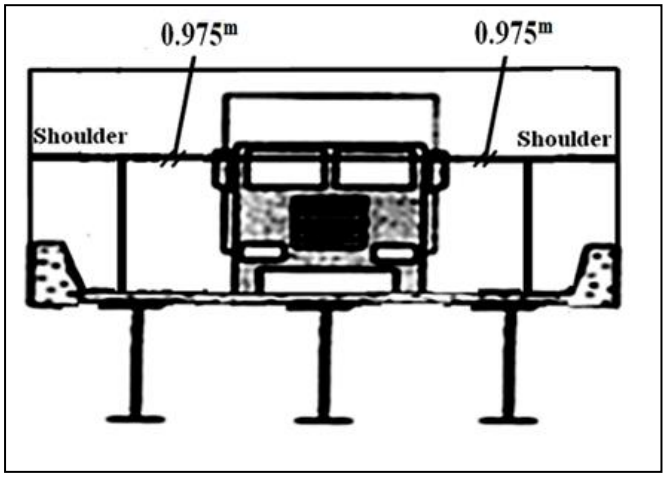

(b)

Figure 6.5: Live loading cases for one-lane integral abutment bridge
(a) Exterior and interior girder-partial load, (b) Fatigue load.

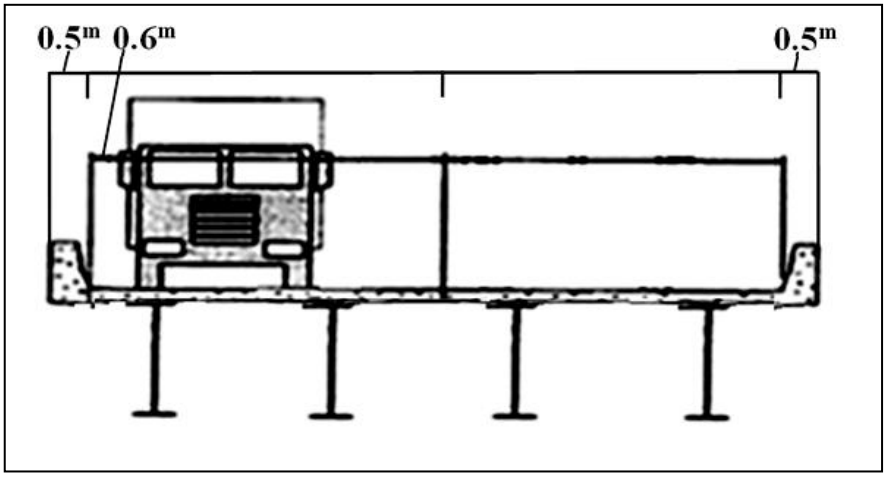

(a)

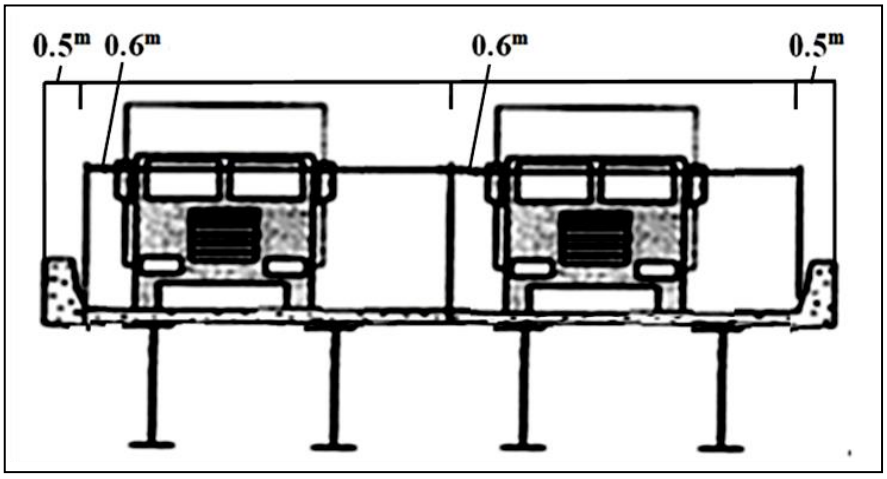

(b)

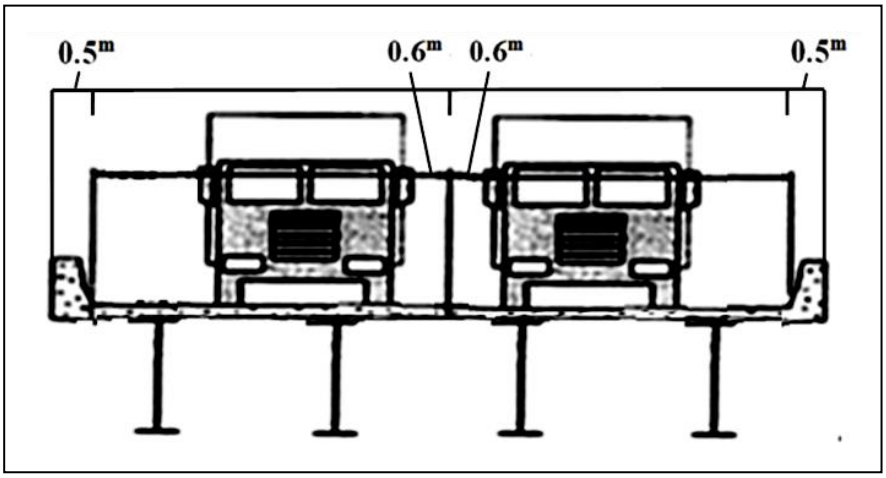

(c)

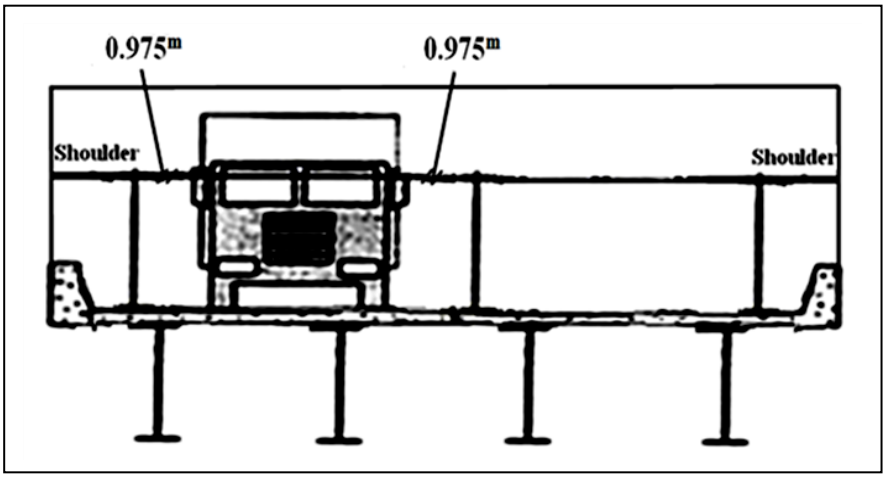

(d)

Figure 6.6: Live loading cases for two-lane integral abutment bridge
(a) Exterior girder-partial load, (b) Exterior girder-full load, (c) Interior girder-full load, (d) Fatigue load.

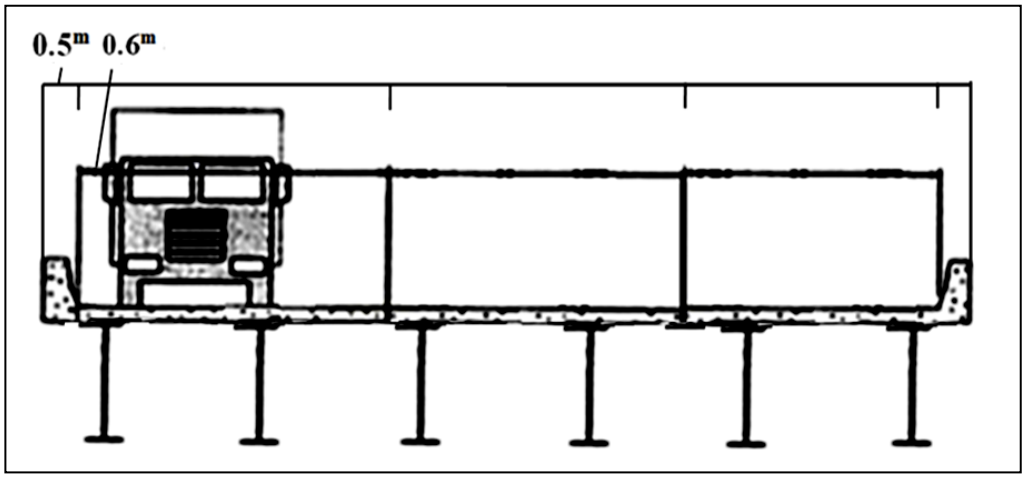

(a)

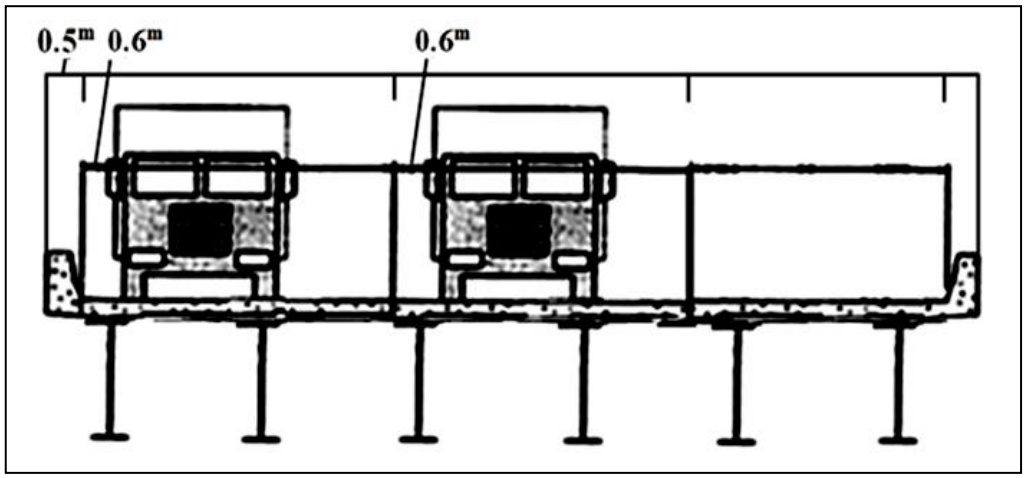

(b)

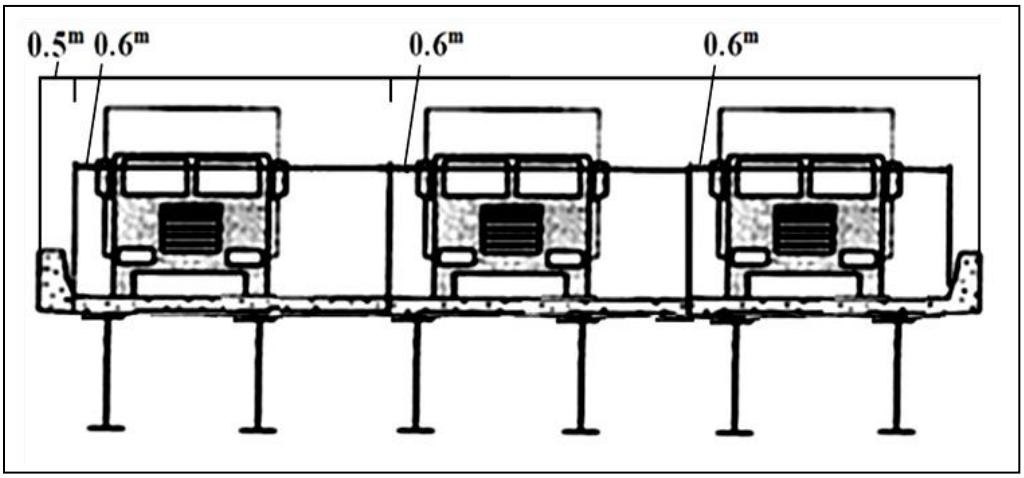

(c)

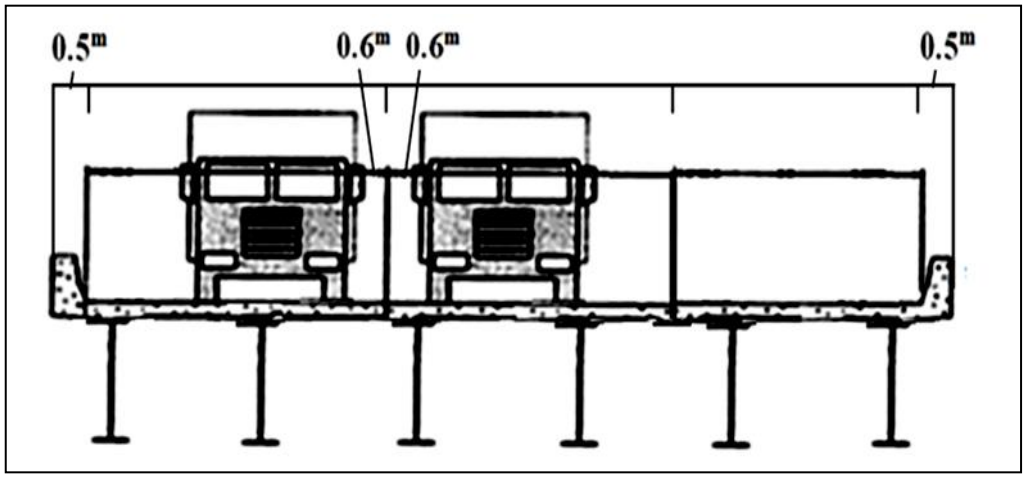

(d)

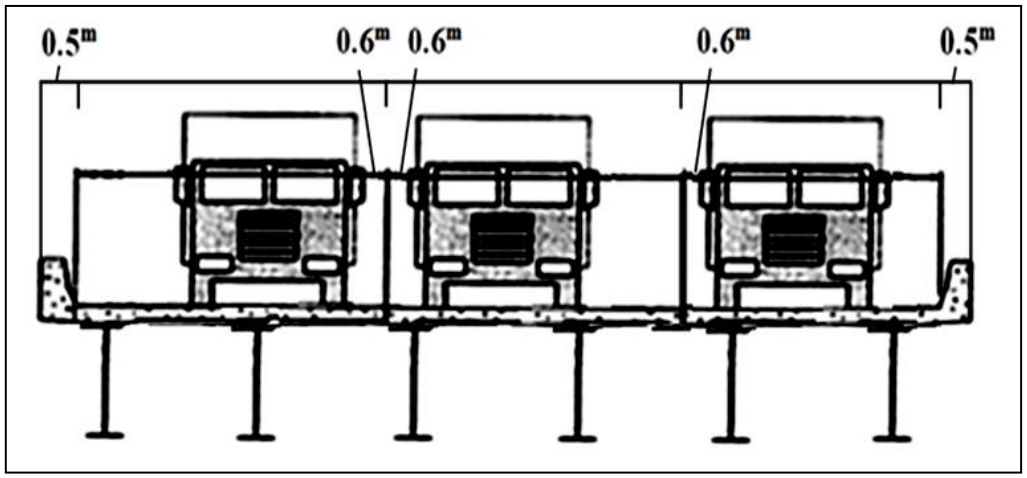

(e)

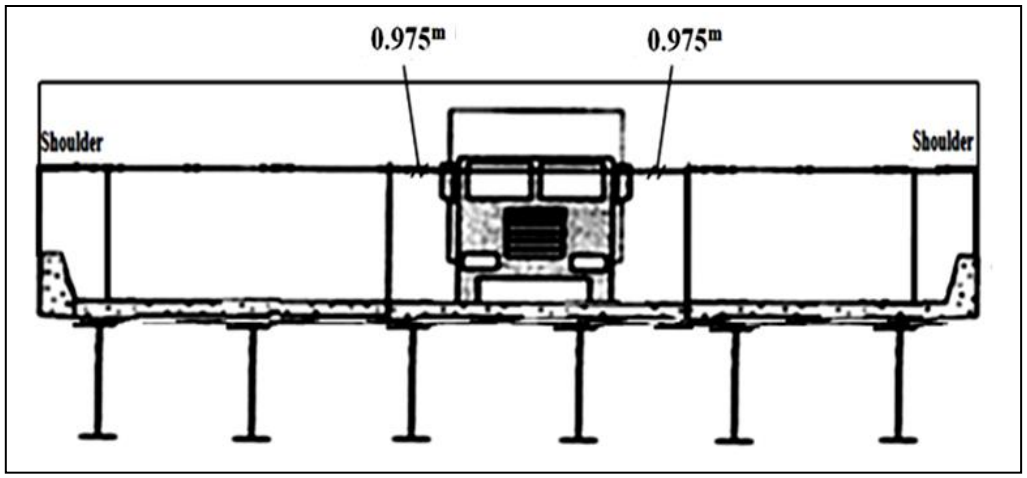

(f)

Figure 6.7: Live loading cases for three-lane integral abutment bridge
(a) Exterior girder-partial load, (b) Exterior girder-partial load, (c) Exterior girder-full load, (d) Interior girder-partial load, (e) Interior girder-full load, (f) Interior girder-fatigue load.

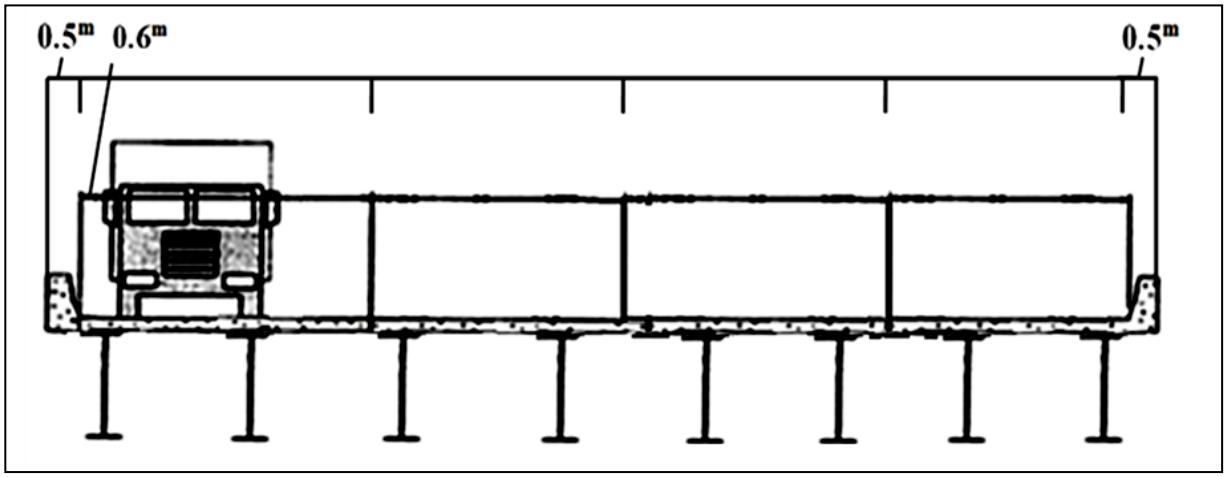

(a)

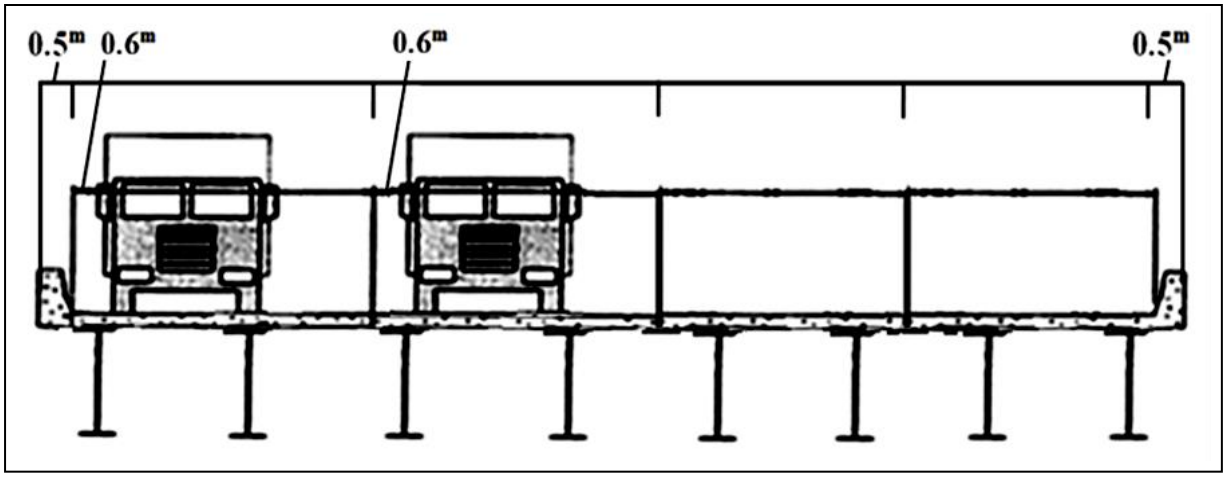

(b)

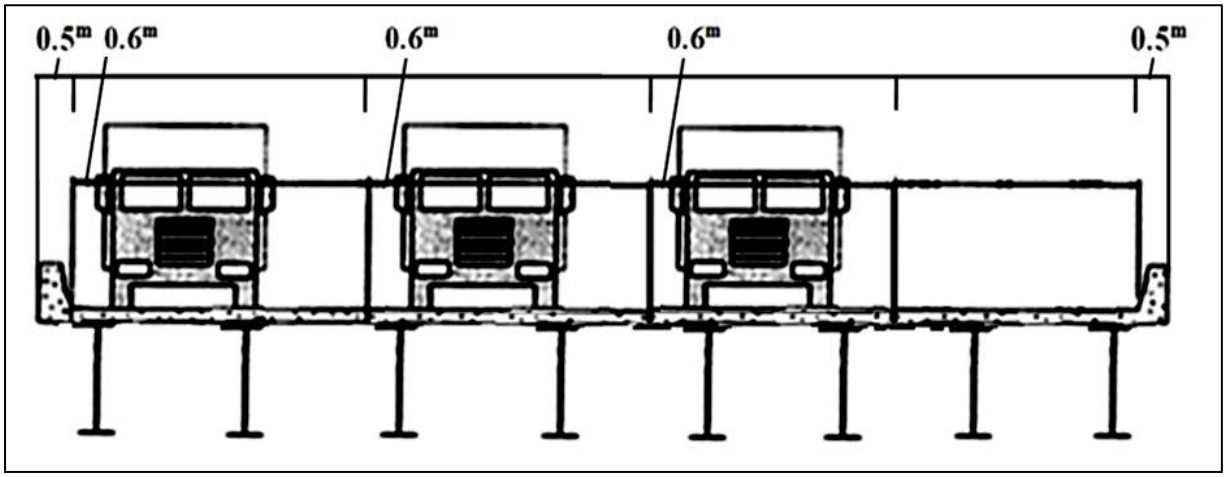

(c)

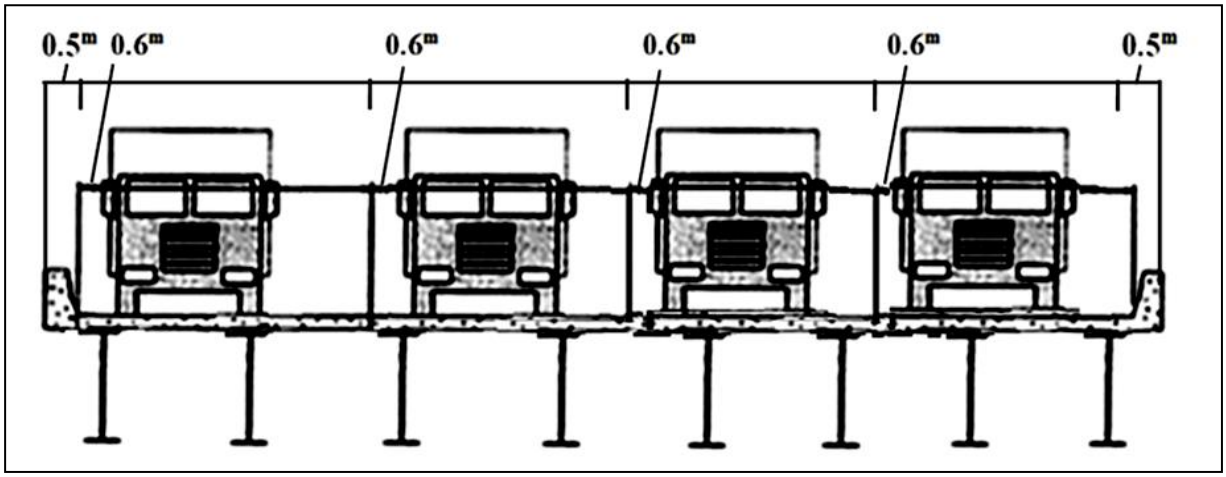

(d)

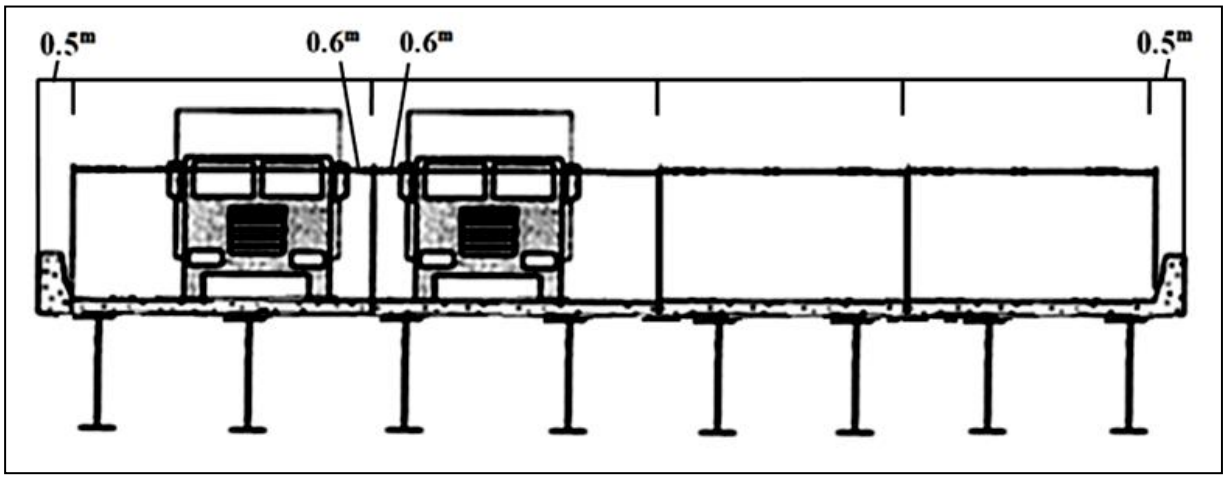

(e)

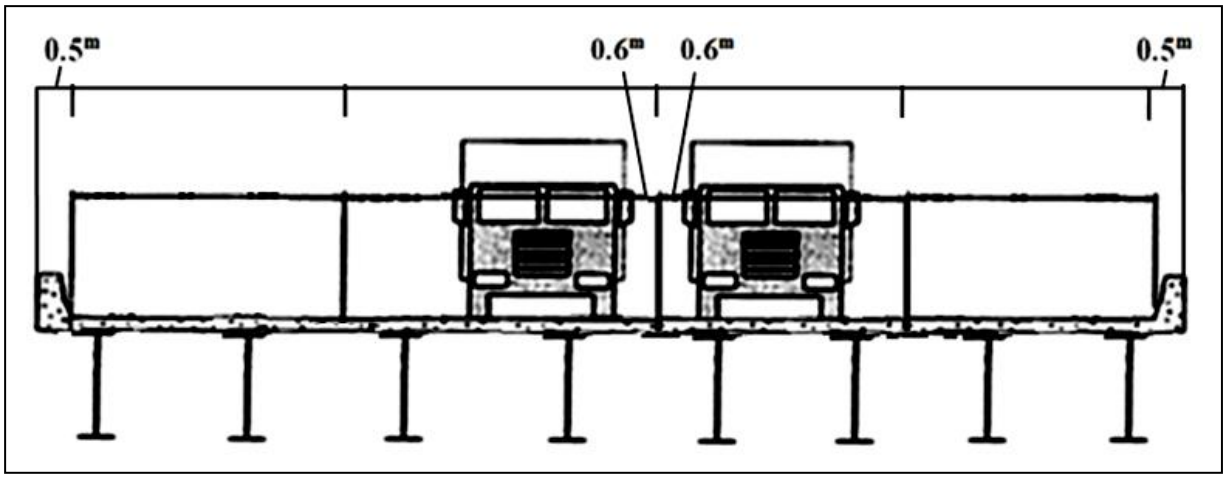

(f)

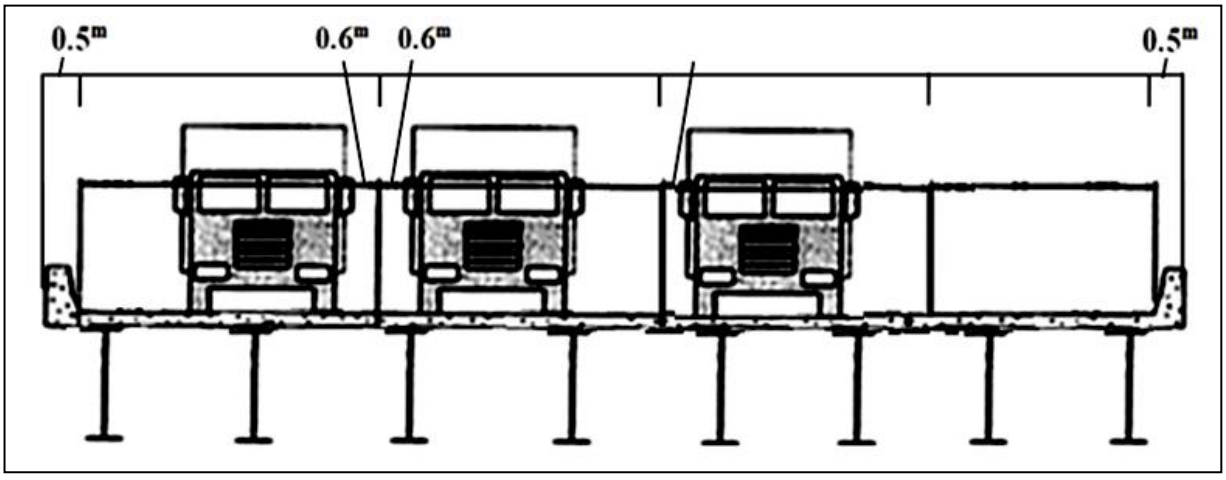

(g)

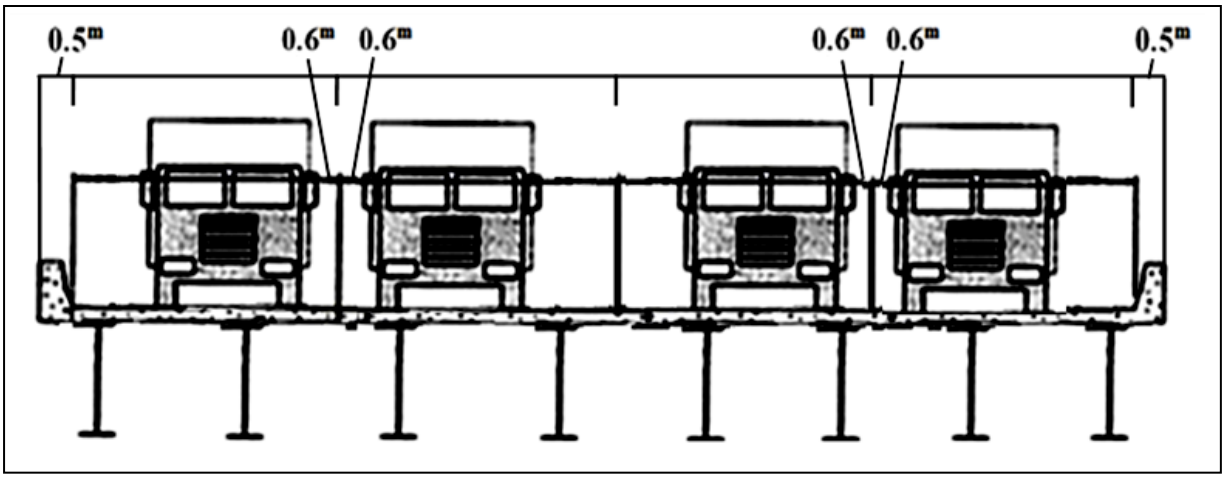
0.5m
0.6m
0.6m
0.6m
0.6m
0.5m

(h)

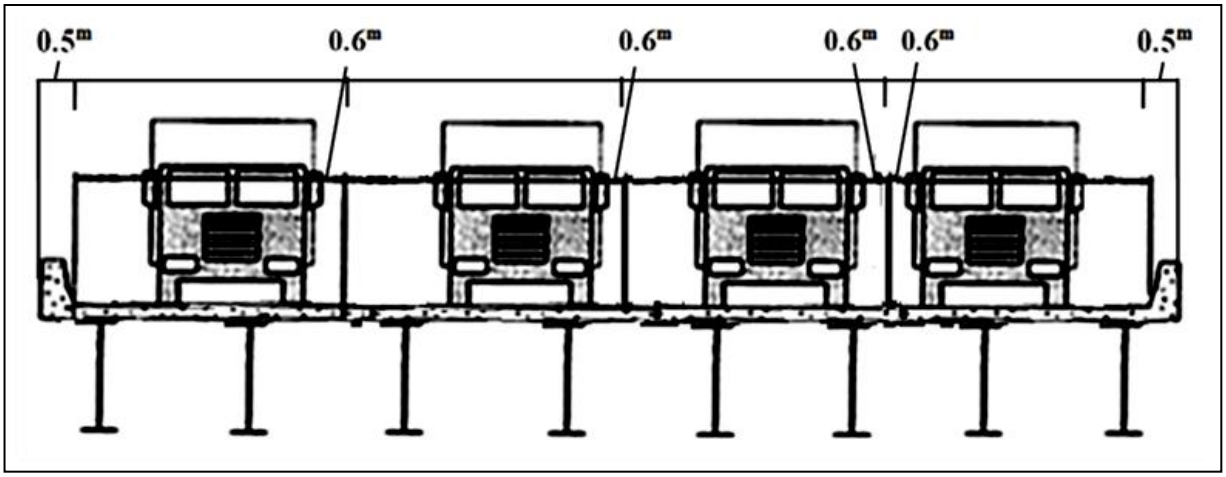
0.5m
0.6m
0.6m
0.6m
0.6m
0.5m

(i)

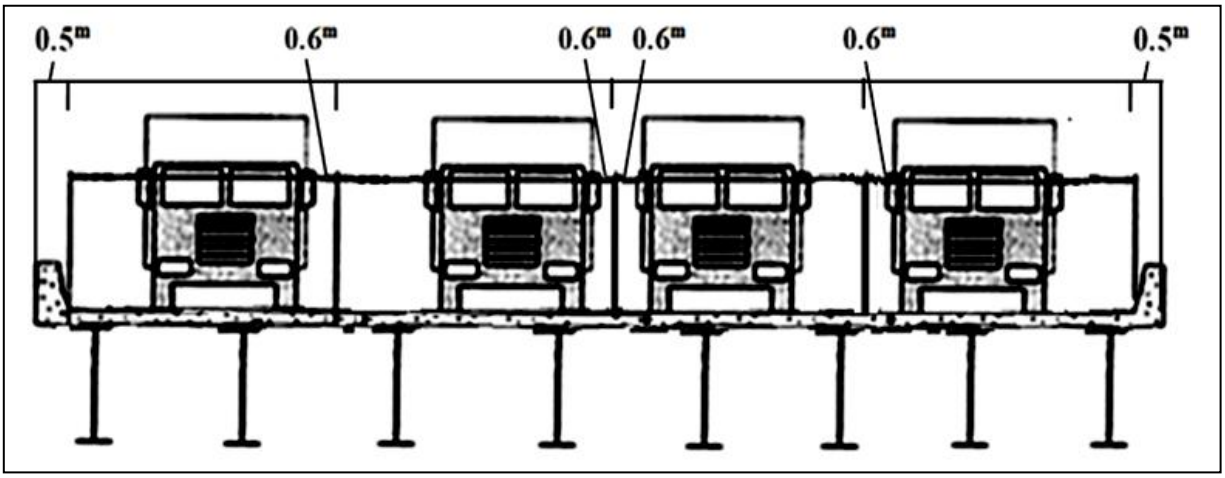
0.5m
0.6m
0.6m
0.6m
0.6m
0.5m

(j)

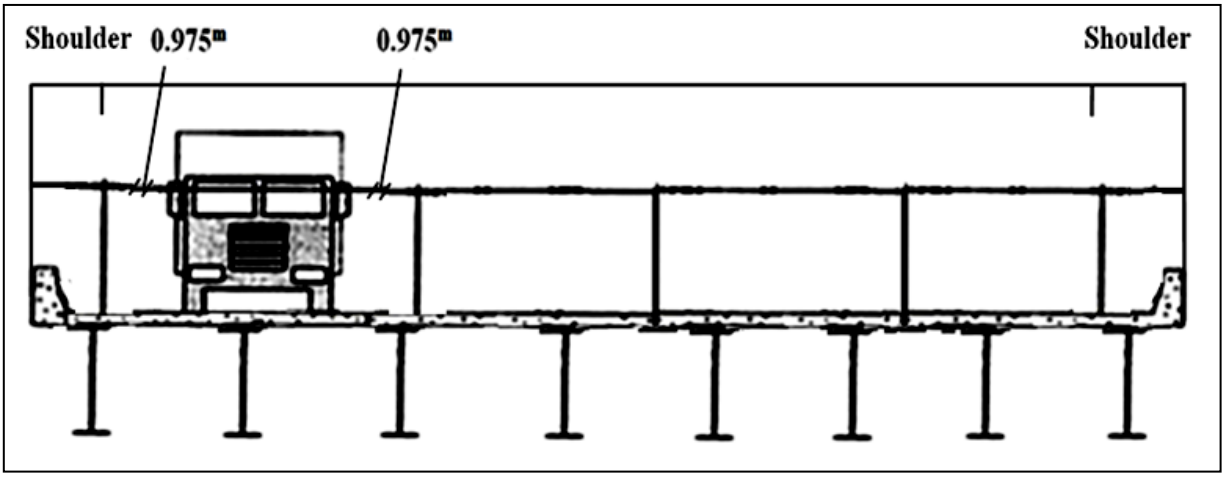

(k)

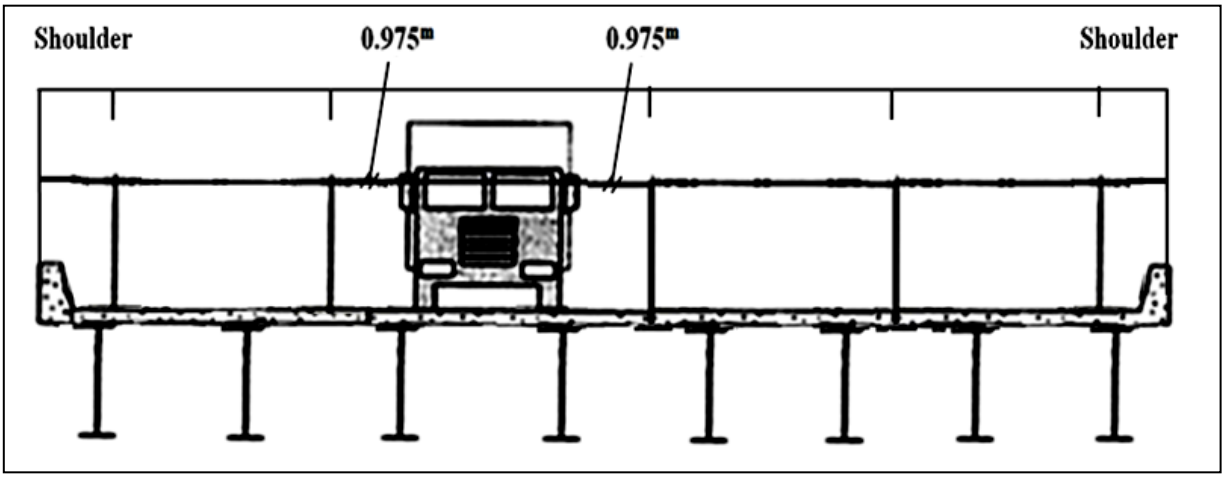

(L)

Figure 6.8: Live loading cases for four-lane integral abutment bridge
(a) Exterior girder-partial load, (b) Exterior girder-partial load, (c) Exterior girder-partial load, (d) Exterior girder-full load, (e) Interior girder-partial load, (f) Interior girder-partial load, (g) Interior girder-partial load, (h) Interior girder-full load, (i) Interior girder-full load (j) Interior girder-full load, (k) Exterior girder-fatigue load, (l) Interior girder-fatigue load.

6.1.2.2 EFFECT OF SUBSTRUCTURE PROPERTIES ON DISTRIBUTION FACTOR

Different integral abutment bridges have been considered to investigate the effect of soil–structure interaction and substructure properties on the live load distribution factors. For this purpose, numerous 3D and corresponding 2D structural models of typical integral abutment

bridges have been built and analyzed under CHBDC live-loading. The results from 3D and 2D analyses were then used to calculate the live-load distribution factors (LLDFs). In the analyses, effects of various geotechnical and substructure properties such as foundation soil stiffness, pile size, pile orientation, abutment thickness, abutment height, wingwall length and wingwall orientation have been considered.

Symmetrical 20-*m* span integral bridges with concrete girder types were chosen as base bridges to conduct sensitivity study for substructure variables. The superstructure of bridges as shown in Figure 6.9 were composed of a 225 *mm* thick concrete slab supported on five prestressed concrete I-girders (CPCI 900) spaced at 2.4 *m*.

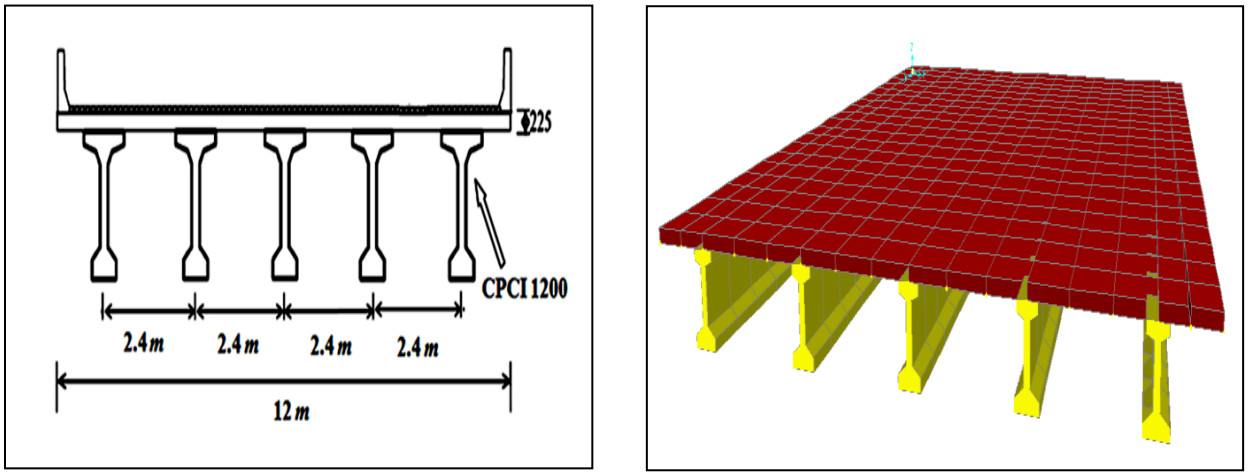

(a) (b)

Figure 6.9: Schematic diagram of the prestressed bridge cross-section (a) 2-D, (b) 3-D.

The abutment walls for integral bridges were 12 *m* long, 1 *m* thick and 3 *m* height. The type of backfill behind the abutments was assumed to be granular uncompacted material which is typically used in integral bridge. Five HP 310×110 steel piles at spacing of 2.4 *m* were used to support the substructures of integral bridges. H-piles were oriented in their weak axis bending in medium clay. Each wingwall was 2 *m* long; 0.5 *m* thick with non prismatic depth varying between 2 to 3 *m*. Wingwalls were oriented in parallel direction.

6.1.2.2.1 EFFECT OF ABUTMENT HEIGTH AND THICKNESS

For evaluation the effect of abutment height and thickness on distribution factors of base bridges, different abutment heights (3, 5 *m*) and different abutment thicknesses (1, 1.5 *m*) were selected for integral bridges. The effects of abutment height and thickness on moment and shear

distribution factors at ultimate limit state (ULS) for exterior girder are illustrated in Figure 6.10. The symbols (N, P) used in Figure 6.6 represent designations of the moment types considered: N stands for negative moment and P stands for positive moment. For example, P-Full Loading denotes the positive moment for integral bridges subjected to full loading.

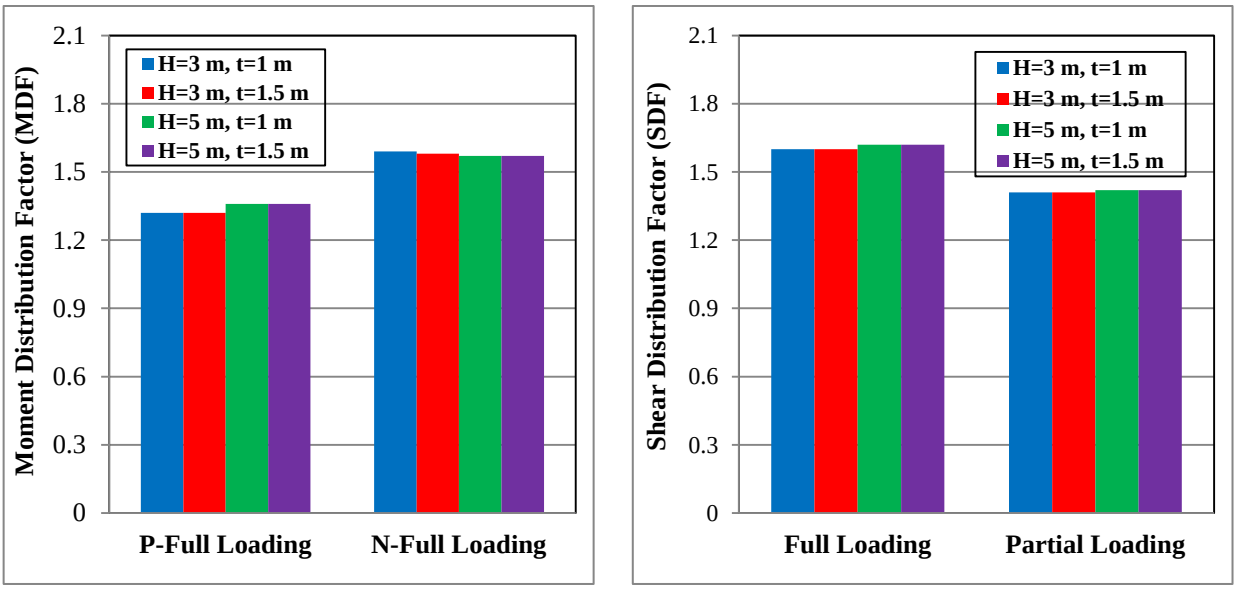

(a) (b)

Figure 6.10: Effect of various abutment heights and thicknesses versus different truck loading conditions on (a) Moment distribution factor, (b) Shear distribution factor.

The analyses results presented in Figure 6.10 reveal that the effect of the abutment height and abutment thickness on the LLDFs for the girder moment and shear was negligible. For instance, for integral bridges, positive moment distribution factors obtained from full loading (P-Full loading) for the girder moment were calculated as 1.32 and 1.36 for the 3 and 5 *m* tall abutments (a difference of 3%). Also, live load distribution factors for the girder shear were calculated as 1.6 and 1.62 for 3 and 5 *m* tall abutments (a difference of 1%). As such, it was decided to ignore the effect of abutment height and thickness when conducting parametric study.

6.1.2.2.2 EFFECT OF PILE SIZE AND ORIENTATION

In this part, effects of pile size and orientation on the distribution of live-load in integral abutment bridges have been studied. Figure 6.11 shows the live load distribution factors for various pile sizes [HP200×53 (SP) and HP310×110 (LP) piles] oriented to bend about their strong axes (SA) and weak axes (WA).

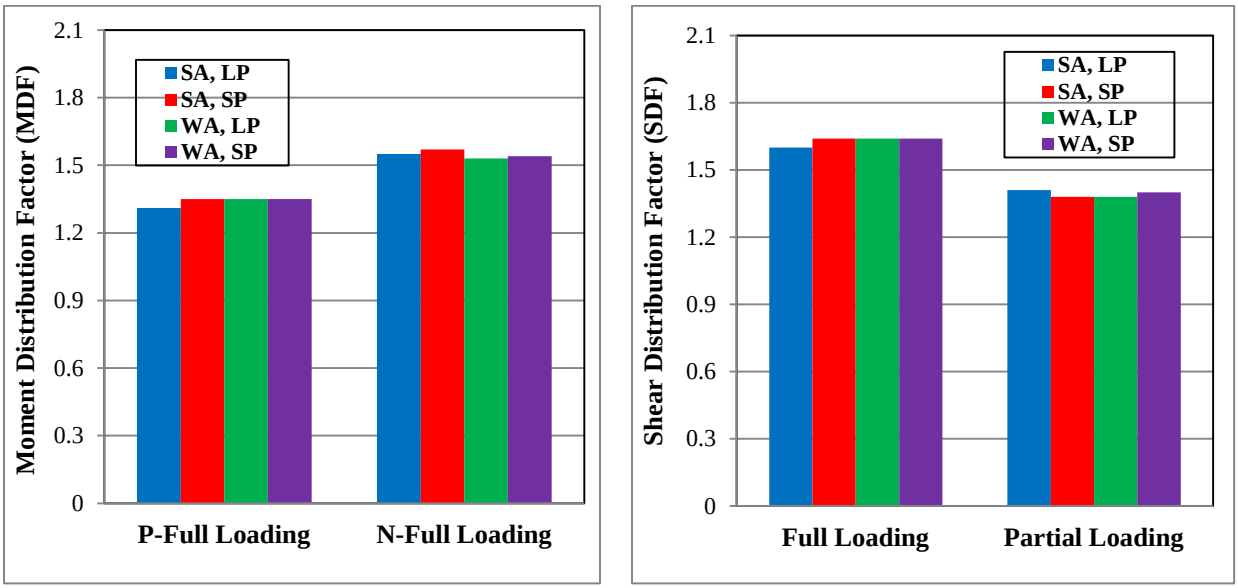

(a) (b)

Figure 6.11: Effect of pile size and orientation versus different truck loading conditions on (a) Moment distribution factor (b) Shear distribution factor.

Figure 6.11 demonstrates that the size and orientation of the piles had a minor effect on the girder moments and shears. For instance, in case of full loading and strong axis pile orientation (SA), distribution factors for the HP200×53 (SP) and HP310×110 (LP) were obtained as 1.35 and 1.31 for the positive girder moment and 1.64 and 1.6 for the girder shear. Similarly for integral bridges with the HP200×53 (SP), positive moment distribution factor for both strong axis (SA) and weak axis (WA) orientation of pile was obtained as 1.35. Therefore, it was decided to proceed with parametric study among one pile size and orientation.

6.1.2.2.3 EFFECT OF WINGWALL LENGTH AND ORIENTATION

In regular jointed bridges, the superstructure is separated from the substructure via joints and bearings. Therefore, wingwalls do not influence girder distribution factors. However, in the case of integral abutment bridges, due to the monolithic construction of the deck with abutments, wingwalls may influence girder distribution factors.

To study the influence of wingwall on distribution factors, 3D live-load analyses have been conducted on integral abutment bridges with different wingwall lengths and orientations. Wingwalls had different lengths of 3 and 5 *m* (SW and LW). In addition, wingwalls were oriented in two directions: perpendicular and parallel to the roadway. Figure 6.12 displays

moment and shear distribution factors for the exterior girder as a function of wingwall lengths and orientations.

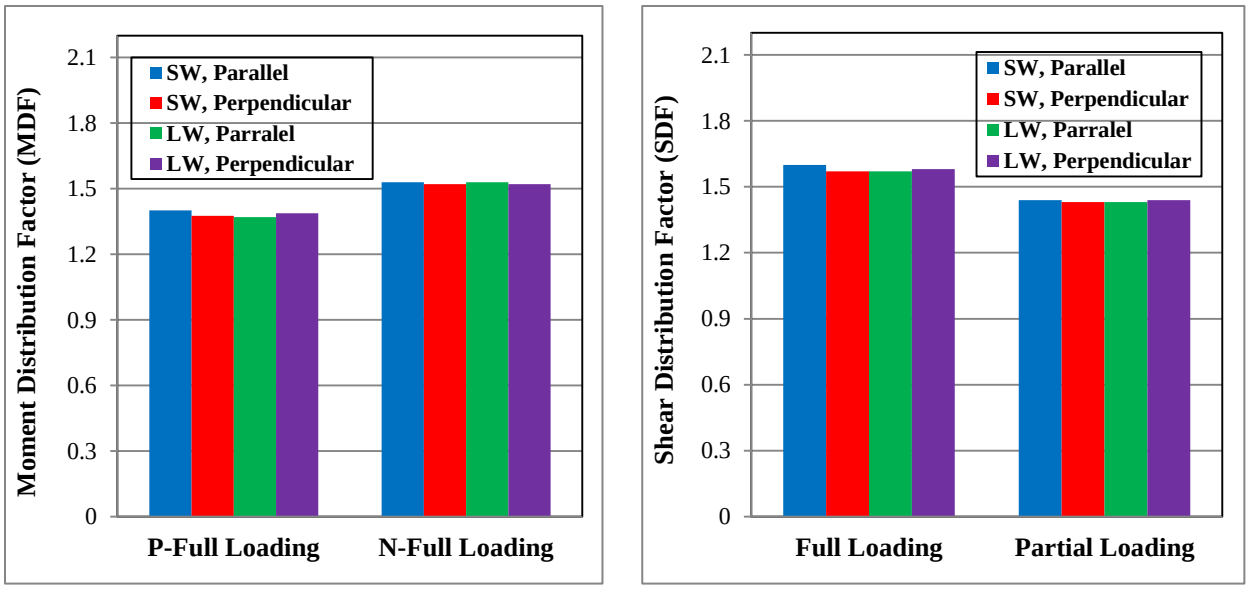

(a) (b)

Figure 6.12: Effect of wingwall length and orientation versus different truck loading conditions on (a) Moment distribution factor, (b) Shear distribution factor.

The live load distribution factors in case of full loading and perpendicular wingwall orientation for wingwall lengths of 3 and 5 *m* (SW and LW) were obtained as 1.37 and 1.36 for the positive girder moment and 1.57 and 1.58 for the girder shear. For the integral bridge with the wingwall length of 3 *m* (SW), live load distribution factors for parallel and perpendicular orientations of pile were obtained as 1.4 and 1.37 for the positive girder moment and 1.6 and 1.57 (a difference of 2%) for the girder shear. Accordingly, it is found that the effect of wingwalls on the moment and shear distribution factors was inconsiderable and the wingwalls need not be considered in estimating the live-load effects in girder distribution factors. As a result, it was decided to proceed with parametric study with wingwall orientation parallel to traffic.

6.1.2.2.4 EFFECT OF SOIL STIFFNESS AND BACKFILL

While the current state of design practice in North America normally neglects foundation soil stiffness and backfill–abutment interaction effects in live-load analyses of integral abutment bridges, the soil stiffness and backfill may affect the girder distribution factors. To evaluate the effect of the soil stiffness and backfill, two different soil conditions [soft clay (C_u=20 *kPa*), stiff

clay (C_u=120 *kPa*)] and two different backfill conditions [considering (WB) or neglecting backfill (NB)] have been considered.

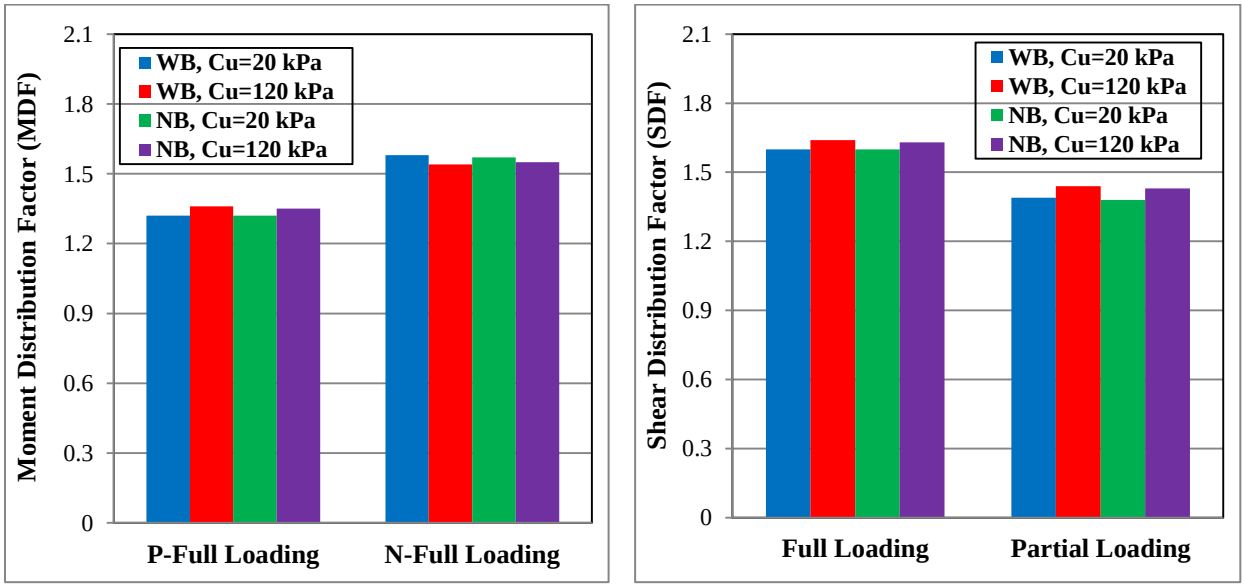

(a) (b)

Figure 6.13: Effect of soil stiffness and backfill versus different truck loading conditions on (a) Moment distribution factor, (b) Shear distribution factor.

As illustrated in Figure 6.13, finite element results revealed that soil stiffness and backfill had small effect on the live load distribution factors for girder moment and shear regardless of the bridge size, pile orientation and abutment thickness. For integral abutment bridges with stiff clay (C_u=120 *kPa*) and full tuck loading, the negative moment distribution factor (N-Full Loading) for the cases with considering backfill (WB) and neglecting backfill (NB) were calculated as 1.58 and 1.57 (a difference of about 0.5%). For the same integral abutment bridge with considering backfill (WB), shear distribution factors for soft clay (C_u=20 *kPa*) and stiff clay (C_u=120 *kPa*) for the girder shear were calculated as 1.6 and 1.64 (a difference of about 2.5%). Thus, it was decided to proceed with parametric study with backfill and soft clay.

Generally, it can be concluded from finite element results that live load distribution factors (LLDFs) for girders in integral abutment bridges are insensitive to substructure properties. Hence, the aforementioned substructure parameters are not required to be considered in the development of live load distribution equations (LLDEs) for girders of integral abutment bridges.

6.1.2.3 EFFECT OF SUPERSTRUCTURE PROPERTIES ON DISTRIBUTION FACTOR

Behaviour of different integral abutment bridges under live loading have been evaluated to examine the effect of various superstructure properties including span length, number of design lanes, girder spacing and number of bracing/diaphragm. The same assumptions for superstructure properties which were explained in section 6.1.2.2 have been used for both concrete and steel I-girder integral abutment bridge.

6.1.2.3.1 EFFECT OF NUMBER OF DESIGN LANES AND COMPARISON WITH CHBDC

6.1.2.3.1.1 EFFECT OF NUMBER OF DESIGN LANES ON MOMENT DISTRIBUTION FACTORS

In determining the effect of number of design lanes, bridge width increased by adding more girders at the same spacing of 2 *m* for concrete bridges and 2.4 *m* for steel bridges. This would maintain the same flexural stiffness of the girders per unit width of bridge cross-section.

Figure 6.14 to 6.17 show the effect of the number of design lanes on moment distribution factors for exterior and interior girder of base bridges. This includes positive moment distribution obtained from finite element analysis (P-FEA), positive moment distribution obtained from CHBDC (P-CHBDC), negative moment distribution factor obtained from finite element analysis (N-FEA) and negative moment distribution obtained from CHBDC (N-CHBDC) of 20 *m* concrete and steel bridges at ultimate limit state (ULS) design for the exterior and interior girders. In calculating positive and negative moment distribution factors using CHBDC equations for slab-on-girder bridges, the length in these equations was taken as L_3 for positive moment calculation and $L_1 + L_2$ for negative moment calculation based on dead load analysis of the 2-D integral abutment bridges as shown in Figure 6.1. It is observed that the moment distribution factor was markedly increased with increase in the number of design lanes. For example, as shown in Figure 6.14, the positive moment distribution factor for the exterior girder of a concrete bridge increased from 1.05 to 1.22 (an increase of 16%) with increase in number of design lanes from 1 to 4. Also Figure 6.14 shows that the negative moment distribution factor for the exterior girder of a concrete bridge increased from 1.08 to 1.36 (an increase of 26%) with increase in number of design lanes from 1 to 4. As an example of comparison of FEA results

with CHBDC values, Figure 6.17 depicts that positive moment and negative moment distribution factors obtained from finite element analysis (P-FEA and N-FEA) for steel exterior girders for 3-design-lane integral bridges with 2.4 *m* girder spacing were equal to 1.23 and 1.52, while those values obtained from CHBDC (P-CHBDC and N-CHBDC) were equal to 1.57 and 1.92. This means that for this specific case, CHBDC overestimate the positive and negative moment distribution factors by 28 and 26%, respectively.

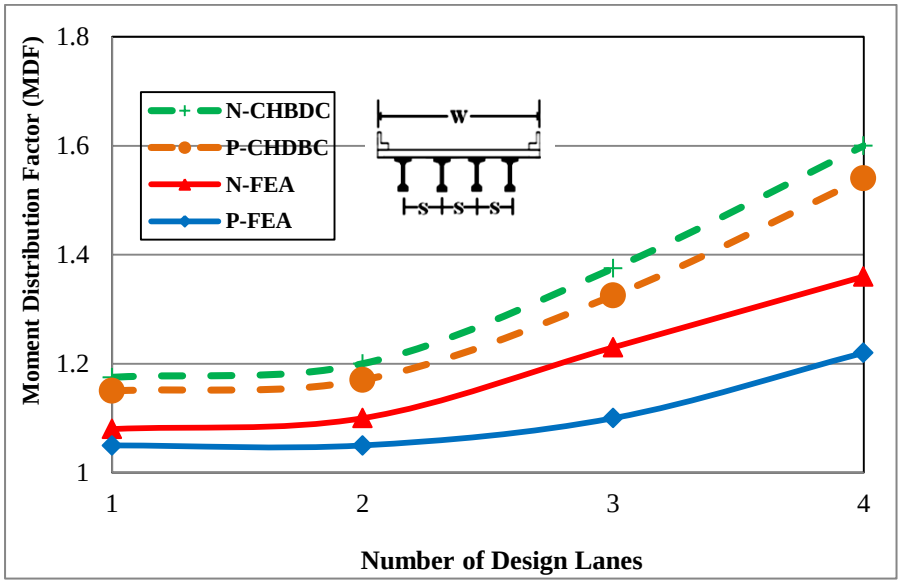

Figure 6.14: Effect of number of lanes on exterior girder MDF for ULS design of concrete bridges.

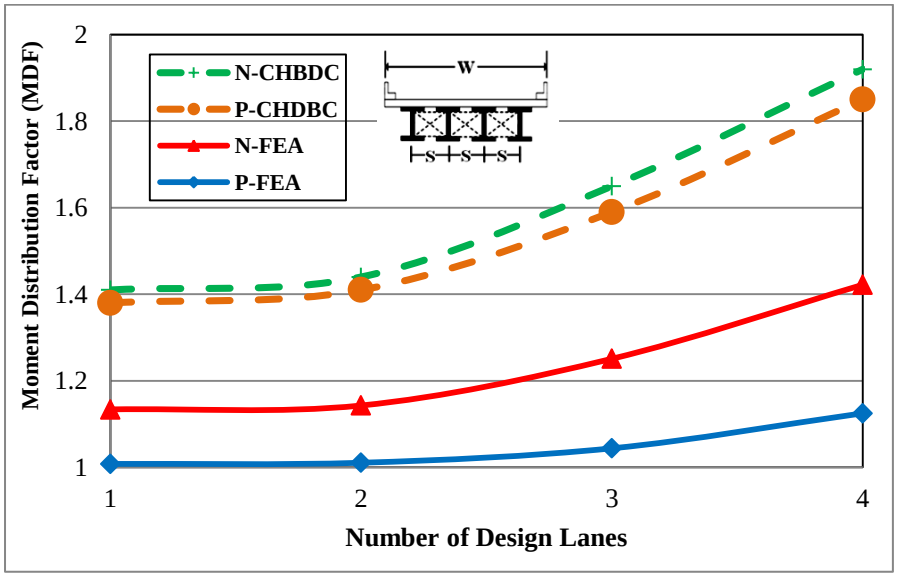

Figure 6.15: Effect of number of lanes on exterior girder MDF for ULS design of steel bridges.

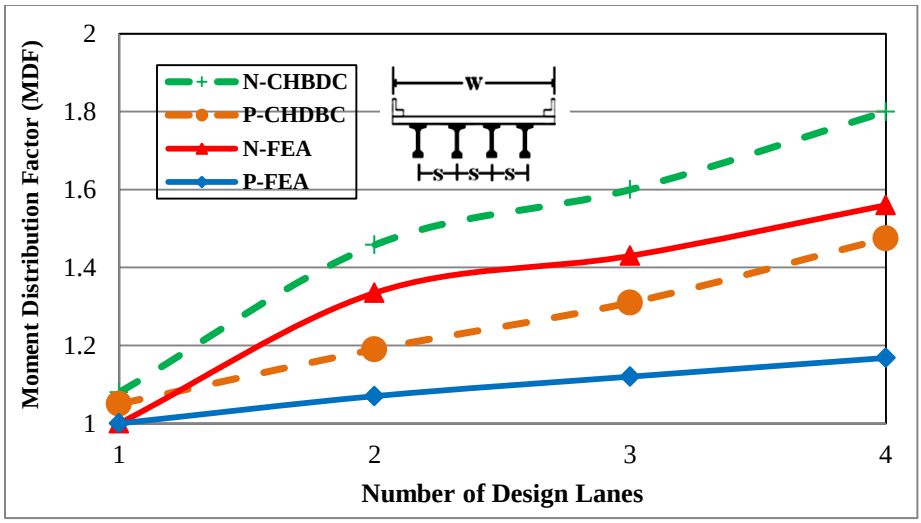

Figure 6.16: Effect of number of lanes on interior girder MDF for ULS design of concrete bridges.

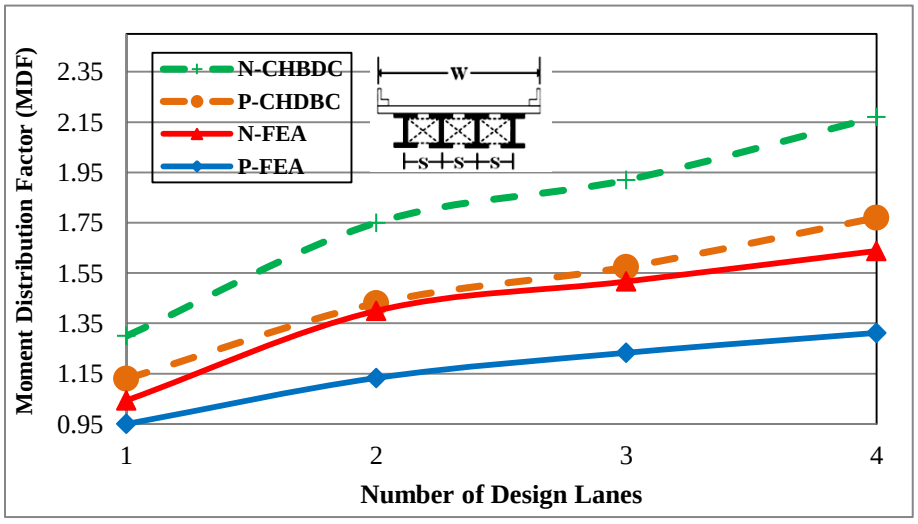

Figure 6.17: Effect of number of lanes on interior girder MDF for ULS design of steel bridges.

Figure 6.18 to 6.21 depict the change in moment distribution factor (MDF) with change in the number of design lanes at fatigue limit state (FLS) design for exterior and interior girder of integral bridges. As shown in Figure 6.19, positive moment and negative distribution factors obtained from finite element analysis (P-FEA and N-FEA) for steel exterior girders of four design lane integral bridges with 2.4 *m* girder spacing were equal to 2.03 and 2.52, while those values obtained from CHBDC (P-CHBDC and N-CHBDC) were equal to 3.35 and 3.41.

Therefore, it can be concluded that moment distribution factors obtained for the exterior girders at FLS design of integral bridges were generally lower than those calculated using CHBDC equations. Similar trend was observed for moment distribution factors of interior girders at FLS design. The data presented in figures also show that the difference between the finite element results for integral abutment bridges and CHBDC for both exterior and interior girders moment were more pronounced for bridges with greater number of design lanes.

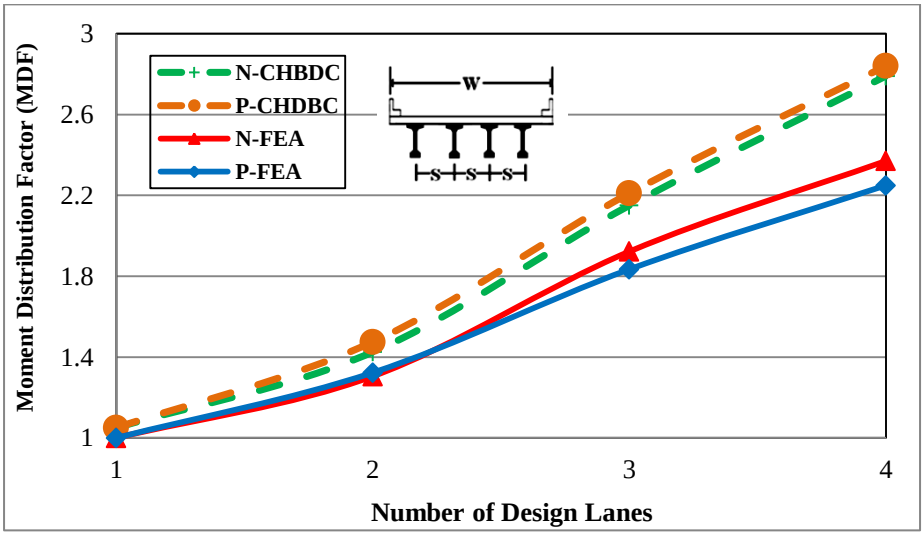

Figure 6.18: Effect of number of lanes on exterior girder MDF for FLS design of concrete bridges.

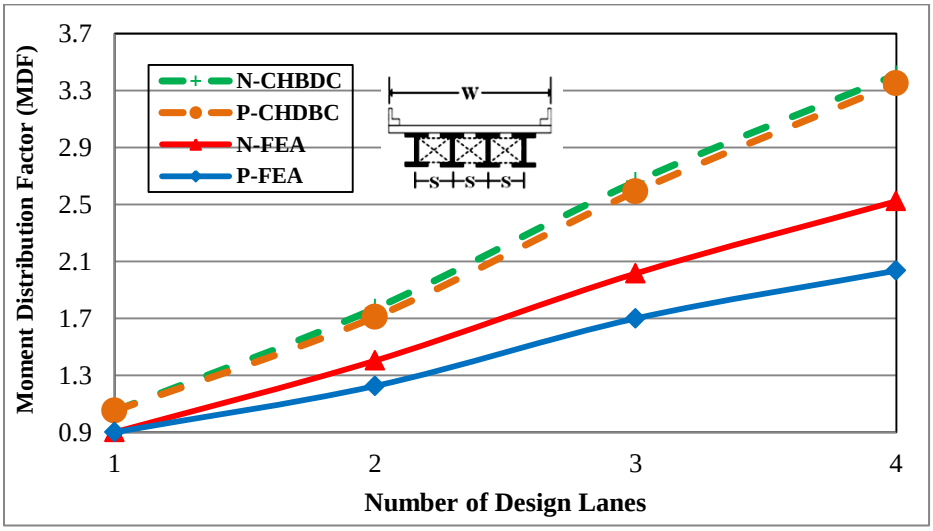

Figure 6.19: Effect of number of lanes on exterior girder MDF for FLS design of steel bridges.

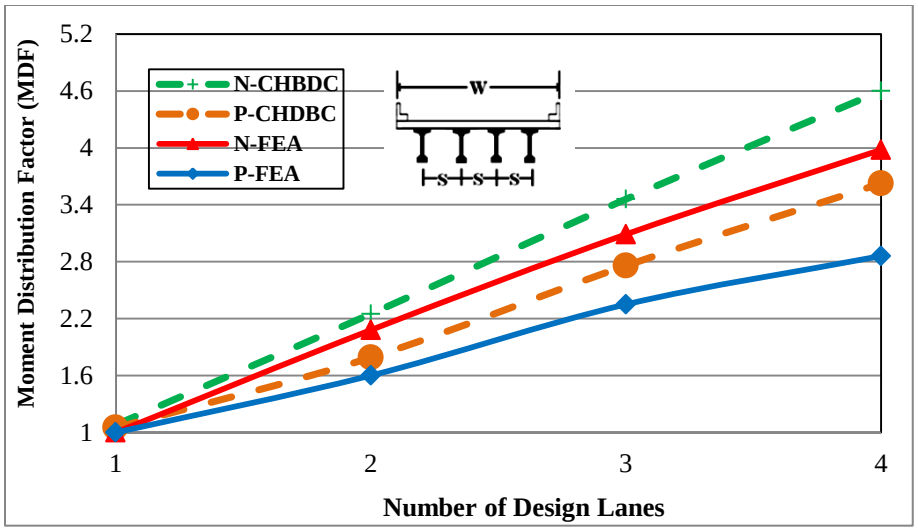

Figure 6.20: Effect of number of lanes on interior girder MDF for FLS design of concrete bridges.

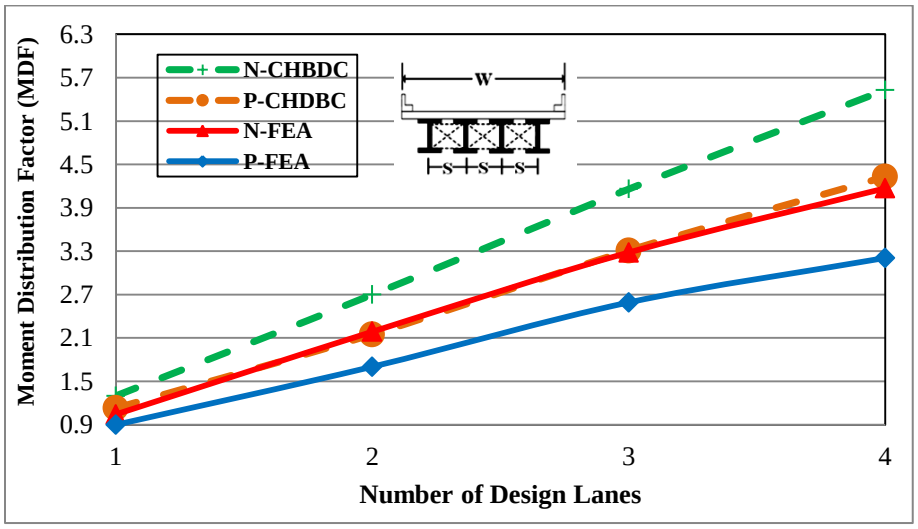

Figure 6.21: Effect of number of lanes on interior girder MDF for FLS design of steel bridges.

6.1.2.3.1.2 EFFECT OF NUMBER OF DESIGN LANES ON SHEAR DISTRIBUTION FACTORS

The relationship between the number of design lanes and shear distribution factor (SDF) of selected bridges for exterior and interior girders at ULS design are shown in Figure 6.22 and 6.23. The analysis showed that number of design lanes significantly affects the shear distribution factors. For example, it can be observed in Figure 6.23 that the shear distribution factor obtained

from finite element analysis (FEA) for steel integral bridge changed from 1.03 to 1.45 when the number of design lanes increased from one to four (an increase of 41%).

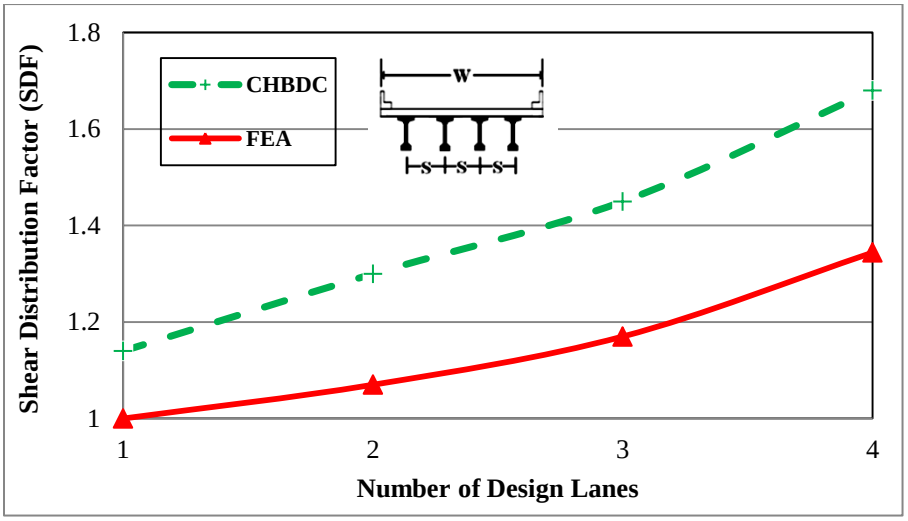

Figure 6.22: Effect of number of lanes on exterior girder SDF for ULS design of concrete bridges.

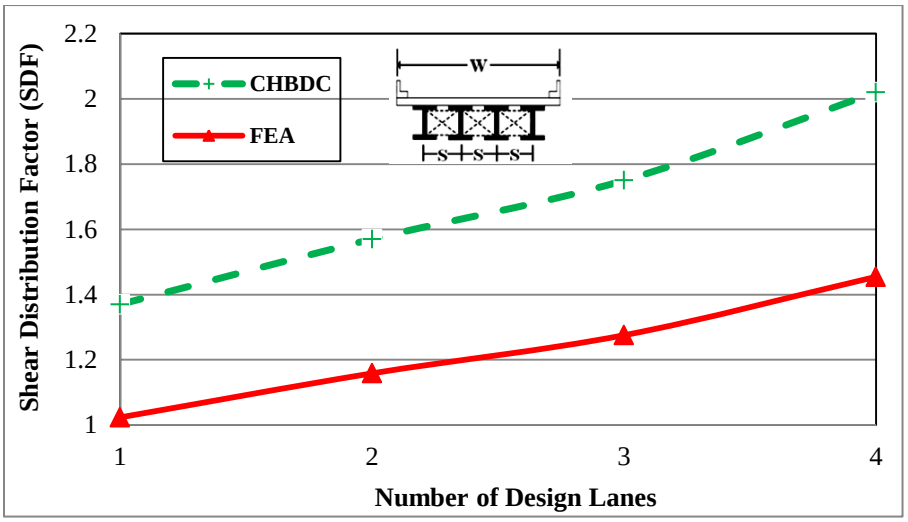

Figure 6.23: Effect of number of lanes on exterior girder SDF for ULS design of steel bridges.

Figure 6.24 and 6.25 shows similar graphs for interior girders. The analyses results indicate that the shear distribution factor (SDF) obtained for the interior girder of integral abutment bridges were generally in good agreement with those calculated using CHBDC live load distribution equations. As an example, Figure 6.24 shows that in case of one-design lane concrete integral

bridge, shear distribution as obtained from CHBDC was 1.15 and the corresponding value from finite element analysis was 1.11 (an overestimation of only %3).

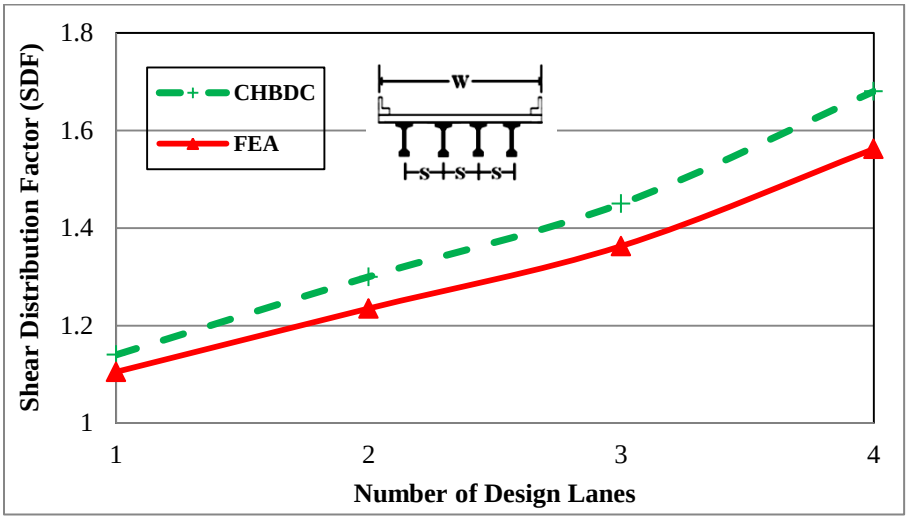

Figure 6.24: Effect of number of lanes on interior girder SDF for ULS design of concrete bridges.

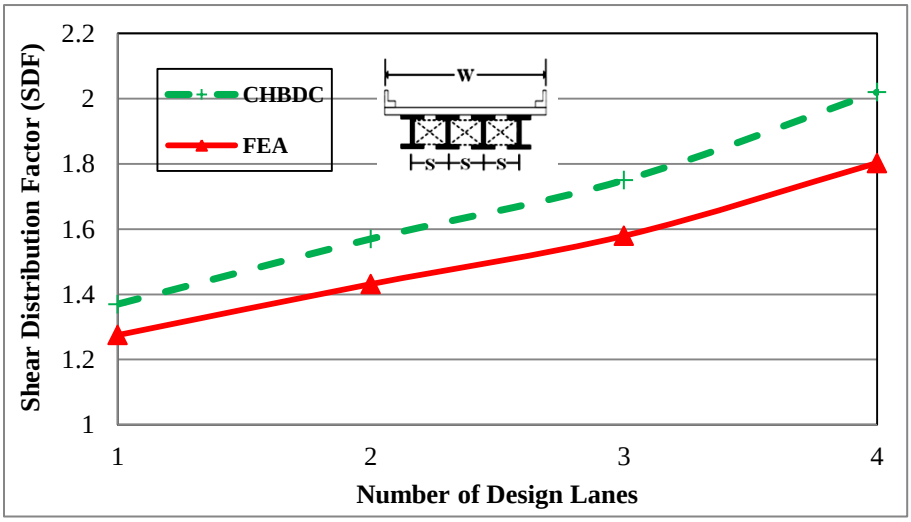

Figure 6.25: Effect of number of lanes on interior girder SDF for ULS design of steel bridges.

The influence of changes in the number of design lanes on the shear distribution factor (SDF) for exterior girders at FLS design are shown in Figure 6.26 and 6.27. The shear distribution factors were increased significantly with increase in the number of design lanes. Figure 6.27 depicts that shear distribution factor obtained from CHBDC was increased for steel integral bridge from 1.37

to 5.81, while shear distribution factor obtained from FEA was increased from 1.04 to 4.27 when the number of lanes increases from one to four. This means that CHBDC equation when applied to integral bridges will overestimate the shear distribution factor by 32% and 36% for one and four design lanes, respectively.

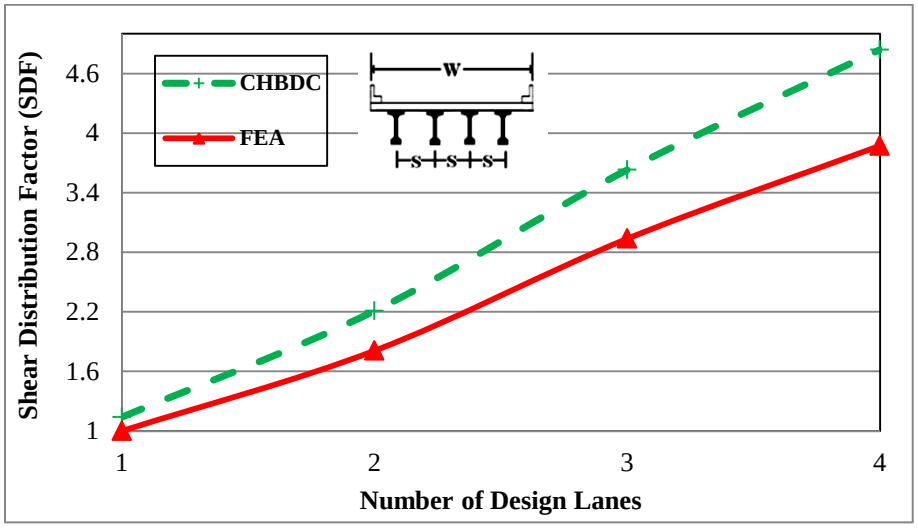

Figure 6.26: Effect of number of lanes on exterior girder SDF for FLS design of concrete bridges.

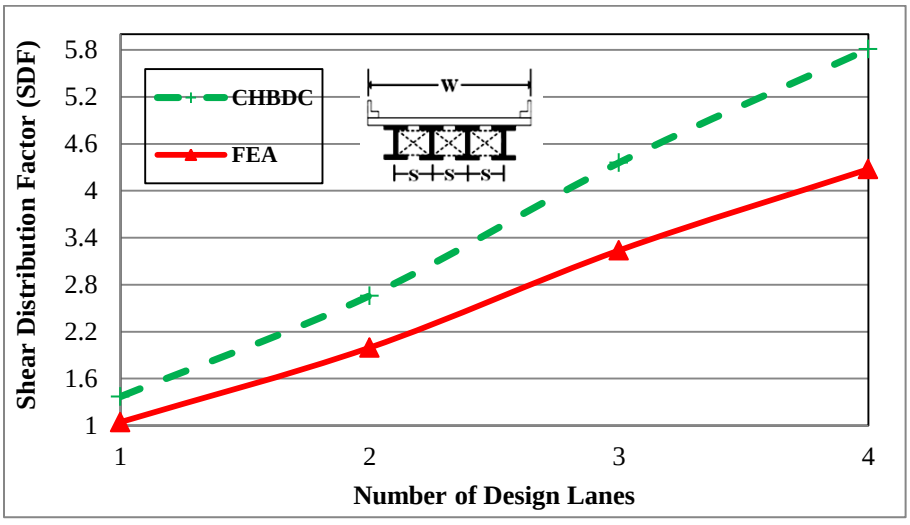

Figure 6.27: Effect of number of lanes on exterior girder SDF for FLS design of steel bridges.

Figure 6.28 and 6.29 illustrates the influence of number of design lanes on the shear distribution factor (SDF) for interior girders at FLS design. As illustrated in Figure 6.28, shear distribution

factor for interior girder of two design lanes concrete integral bridge as obtained from FEA was equal to 2.09 and as obtained from CHBDC was 2.21, representing only a 5% increase in shear distribution factors. The results also indicate that shear distribution factors at FLS design for interior girders were less sensitive to the number of design lane changes compared to shear distribution factors for exterior girders. This means that CHBDC expressions for slab-on-girders can be used only to determine the shear distribution factor at interior girders.

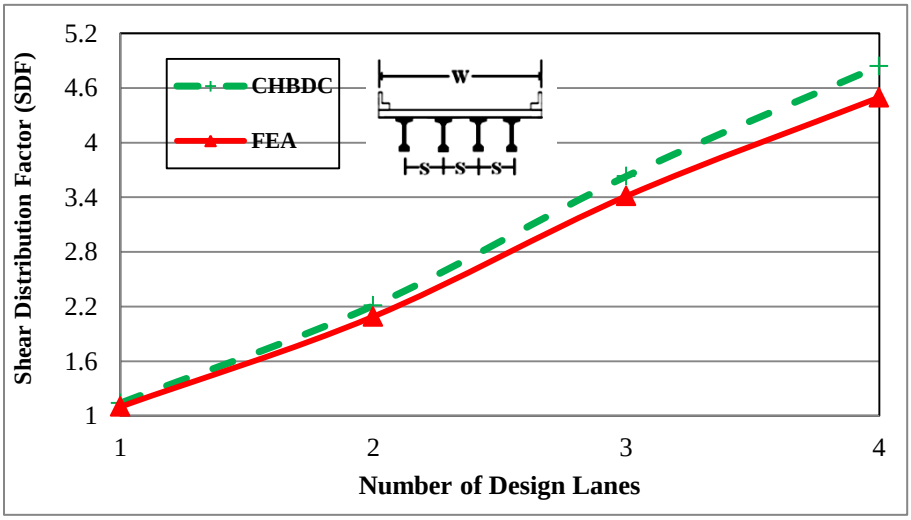

Figure 6.28: Effect of number of lanes on interior girder SDF for FLS design of concrete bridges.

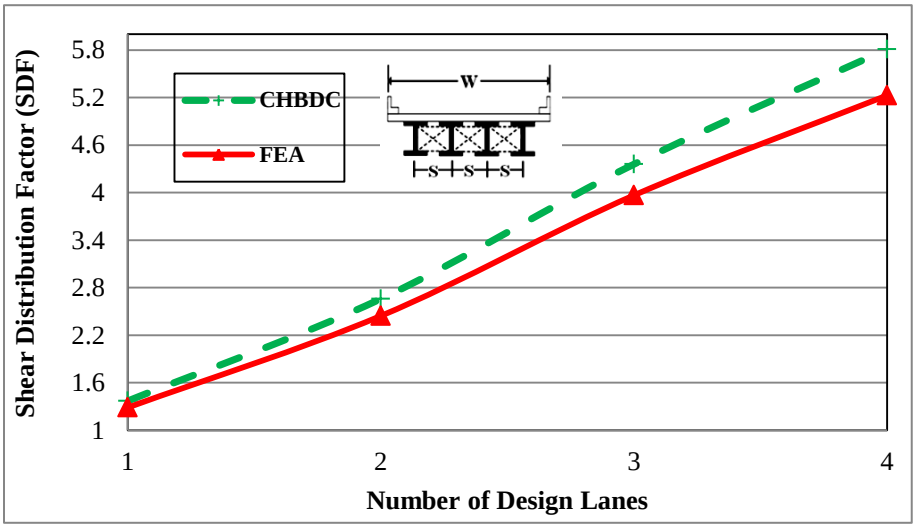

Figure 6.29: Effect of number of lanes on interior girder SDF for FLS design of steel bridges.

6.1.2.3.2 EFFECT OF SPAN LENGTH AND COMPARISON WITH CHBDC

In order to study the effect of span length, *L*, on the moment and shear distribution of integral abutment bridges, five different span lengths including 10, 20, 25, 35 and 45 *m* were considered. To maintain realistic bridge flexural stiffness with increase in the bridge span length, different girder sizes were used. For concrete integral bridges, three different concrete I-girders (CPCI 900 for 10 and 20 *m* spans, CPCI 1900 girder for 25 and 35 *m* spans and CPCI 2400 for 45 *m*) were studied in the finite element modeling. For steel bridges, the same girder types only with steel material have been used to model integral bridges. The loading on integral bridges were applied in such a way to produce maximum shearing force at abutments, maximum positive longitudinal stresses at midspan and maximum negative longitudinal stresses at abutment. Figure 6.30 presents a schematic diagram of truck locations to produce maximum positive bending moment on a single span integral bridge with different bridge lengths.

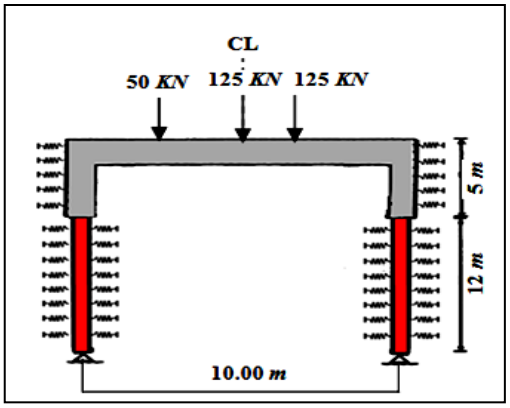

(a)

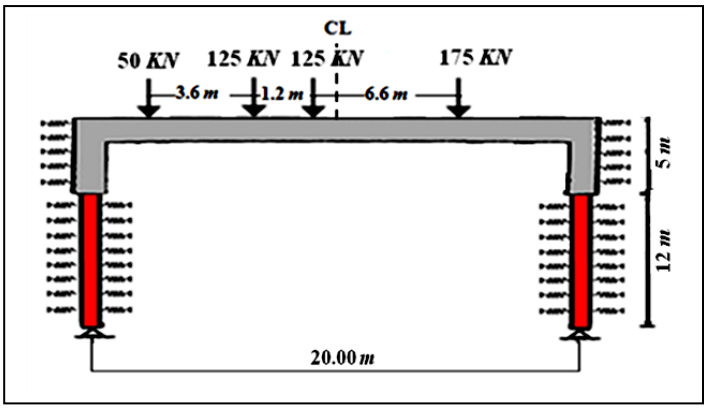

(b)

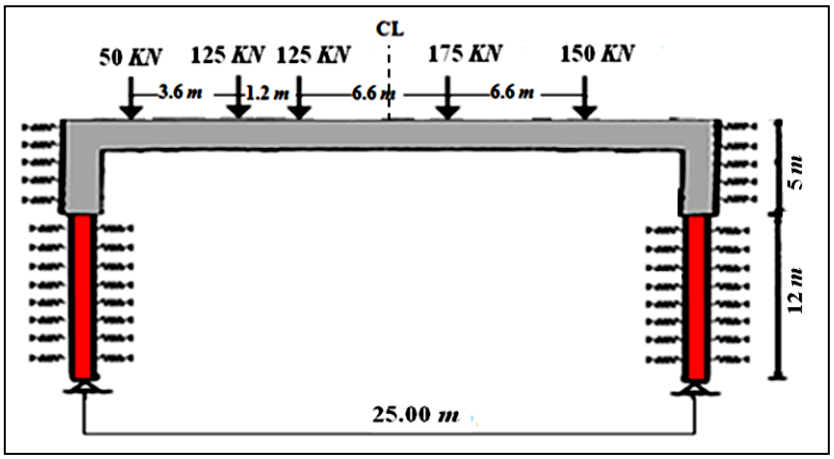

(c)

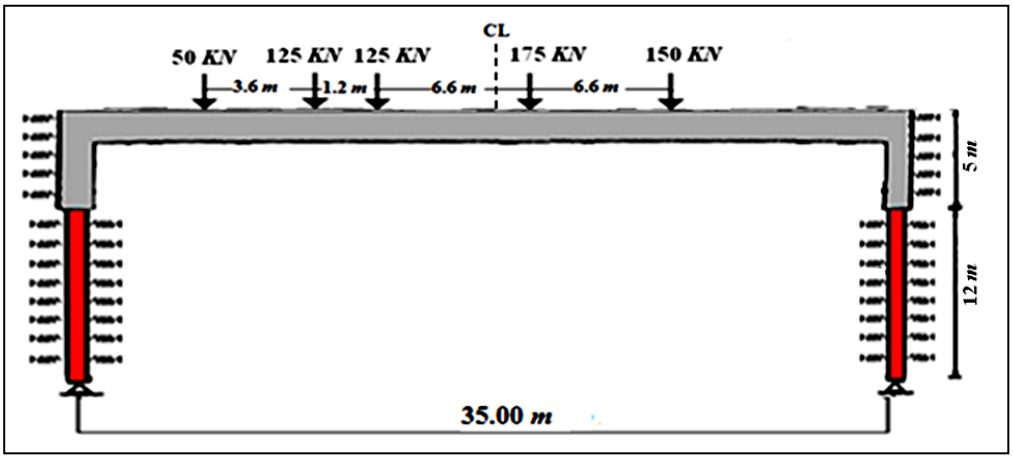

(d)

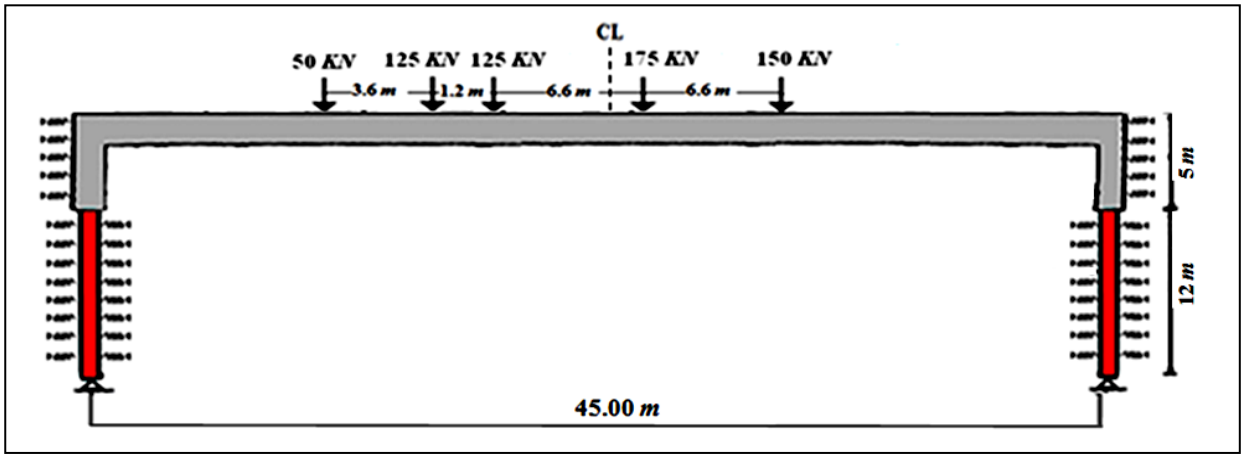

(e)

Figure 6.30: Location of wheel loads for maximum positive bending moment on various spans: (a) 10 *m*, (b) 20 *m*, (c) 25 *m*, (d) 35 *m*, (e) 45 *m*.

6.1.2.3.2.1 EFFECT OF SPAN LENGTH ON MOMENT DISTRIBUTION FACTORS

The relationship between the span length and the moment distribution factor (MDF) of concrete and steel bridges at ULS design for exterior and interior girders is shown in Figure 6.31 to 6.34 for base bridge configurations. It can be noticed that the moment distribution factor slightly decreased with increase in the span length. Moreover, on average moment distribution factors obtained for interior and exterior girders from finite element analysis (FEA) were approximately 20% less than those obtained from CHBDC equations.

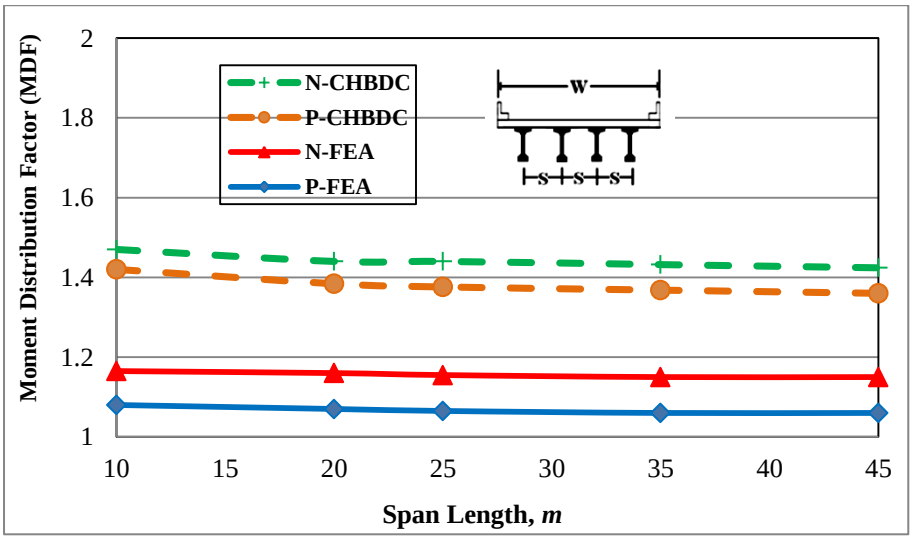

Figure 6.31: Effect of span length on exterior girder MDF for ULS design of concrete bridges with width (W) 9.6 *m* and girder spacing (S) 2.4 *m*.

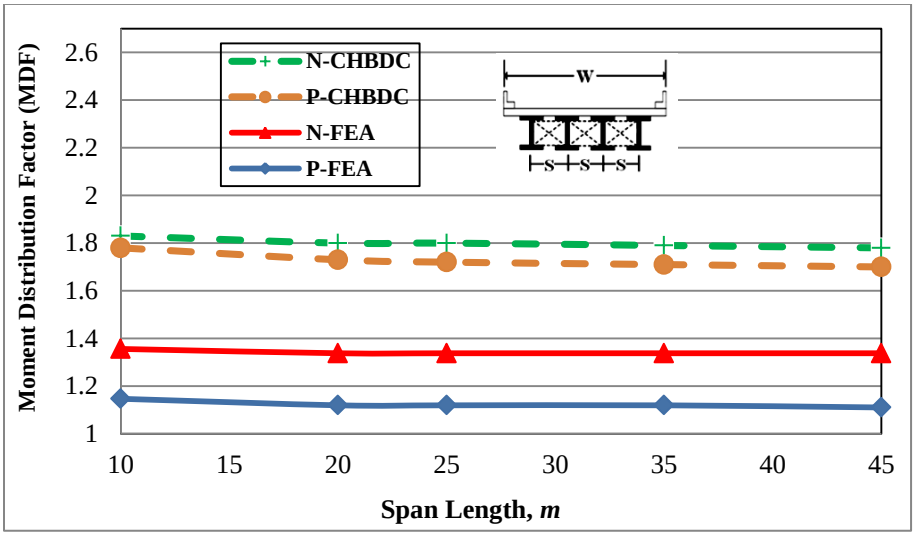

Figure 6.32: Effect of span length on exterior girder MDF for ULS design of steel bridges with width (W) 12 *m* and girder spacing (S) 2.4 *m*.

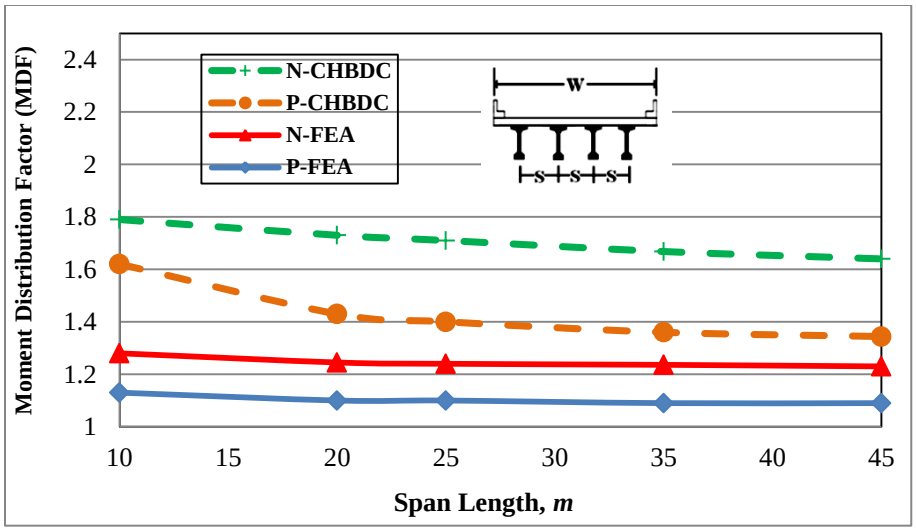

Figure 6.33: Effect of span length on interior girder MDF for ULS design of concrete bridges with width (W) 9.6 *m* and girder spacing (S) 2.4 *m*.

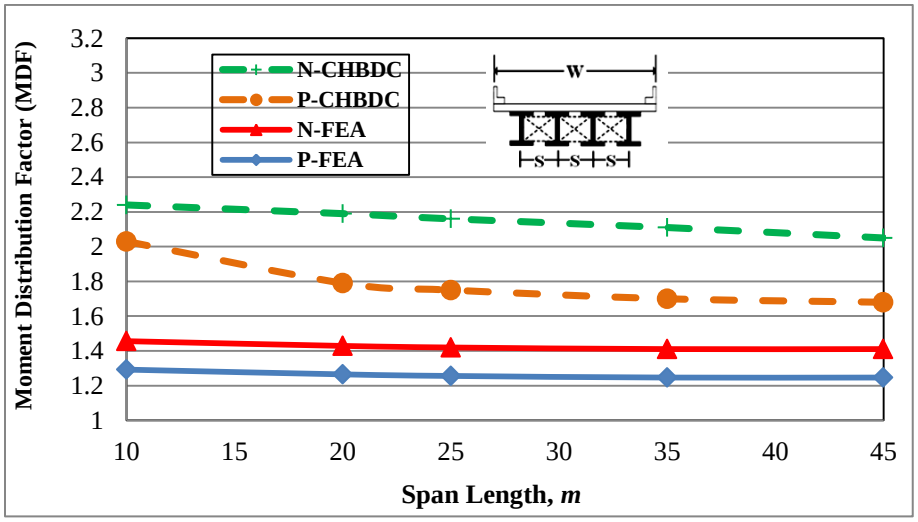

Figure 6.34: Effect of span length on interior girder MDF for ULS design of steel bridges with width (W) 12 *m* and girder spacing (S) 2.4 *m*.

Figure 6.35 to 6.38 show exterior and interior girder moment distribution factor (MDF) at FLS design for various bridge lengths. Figure 6.35 shows the change in moment distribution factor with increase in span length from 10 to 45 *m* in concrete integral bridges. It can observed that the negative moment distribution factor obtained from finite element analysis (N-FEA) decreased only from 1.43 to 1.40 by increasing the bridge span length from 10 to 45 *m*. Hence, it can be concluded that the moment distribution factors at FLS design were not noticeably affected by the changes in span length.

The moment distribution factors obtained from CHBDC were much greater than those obtained from FEA when span length was small. This difference was less in integral bridges with larger span length. In other words, moment distributions factors for interior and exterior girders obtained from CHBDC equations at FLS design were more conservative in small integral bridges compared to large integral bridges.

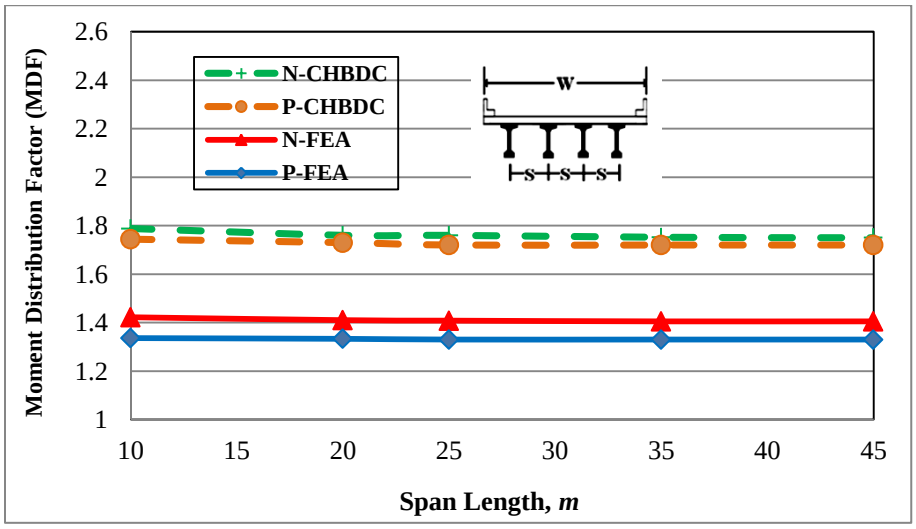

Figure 6.35: Effect of span length on exterior girder MDF for FLS design of concrete bridges with width (W) 9.6 *m* and girder spacing (S) 2.4 *m*.

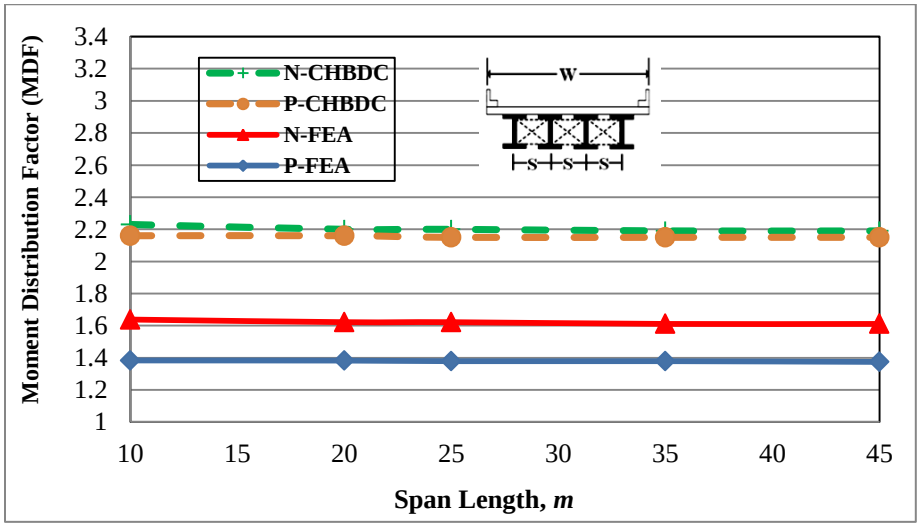

Figure 6.36: Effect of span length on exterior girder MDF for FLS design of steel bridges with width (W) 12 *m* and girder spacing (S) 2.4 *m*.

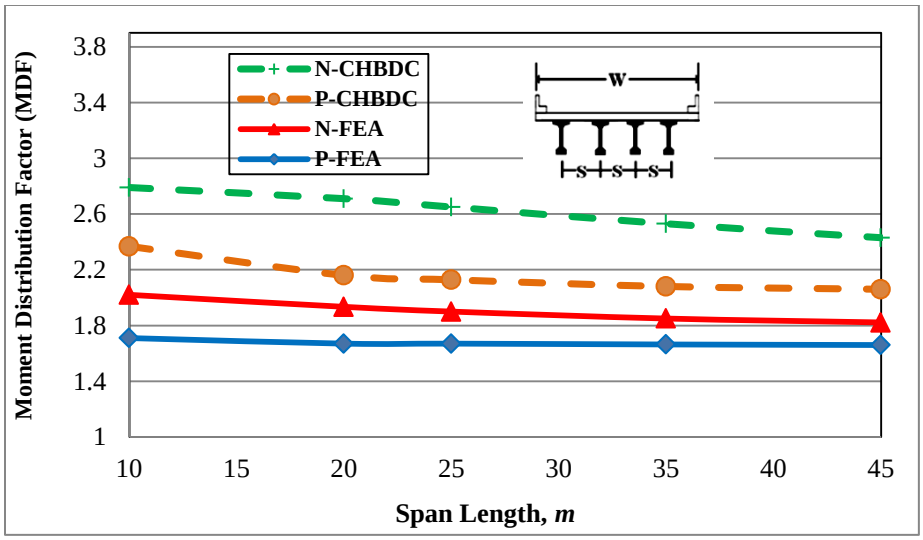

Figure 6.37: Effect of span length on interior girder MDF for ULS design of concrete bridges with width (W) 9.6 *m* and girder spacing (S) 2.4 *m*.

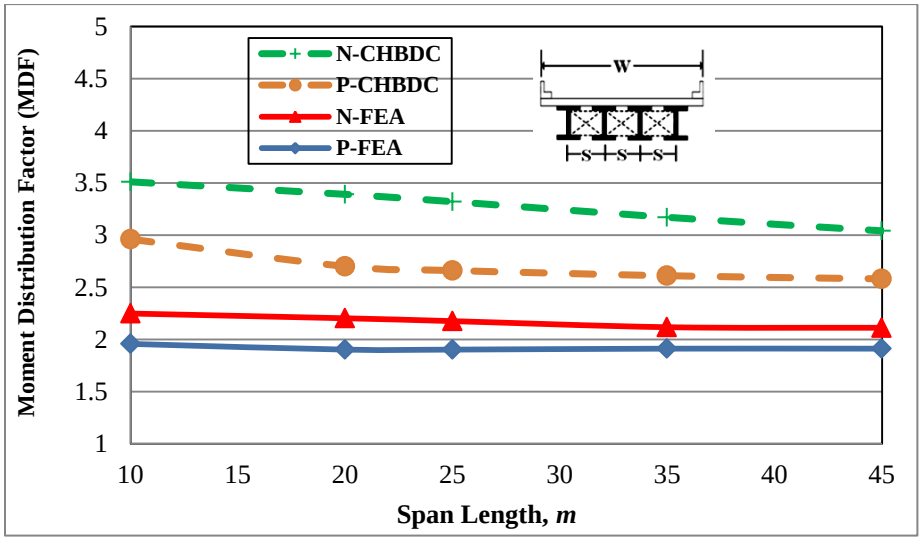

Figure 6.38: Effect of span length on interior girder MDF for FLS design of steel bridges with width (W) 12 *m* and girder spacing (S) 2.4 *m*.

6.1.2.3.2.2 EFFECT OF SPAN LENGTH ON SHEAR DISTRIBUTION FACTORS

Several bridge prototypes with different span lengths were analyzed and their responses were compared to investigate the effect of span length on shear distribution factor (SDF) of exterior girders at ULS design. As illustrated in Figure 6.39 and 6.40, CHBDC live load distribution equations generally yielded conservative estimates of exterior girder shear distribution factors at ULS design for integral abutment bridges with different span lengths. Further, those figures

show that the exterior girder shear distribution factor at ULS design in concrete and steel integral bridges derived from FEA decreased with an increase in the span length.

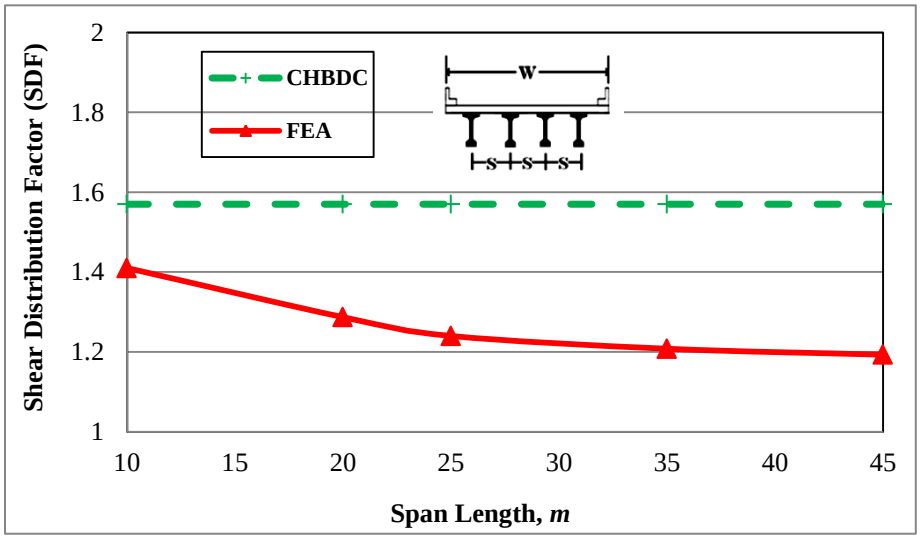

Figure 6.39: Effect of span length on exterior girder SDF for ULS design of concrete bridges with width (W) 9.6 *m* and girder spacing (S) 2.4 *m*.

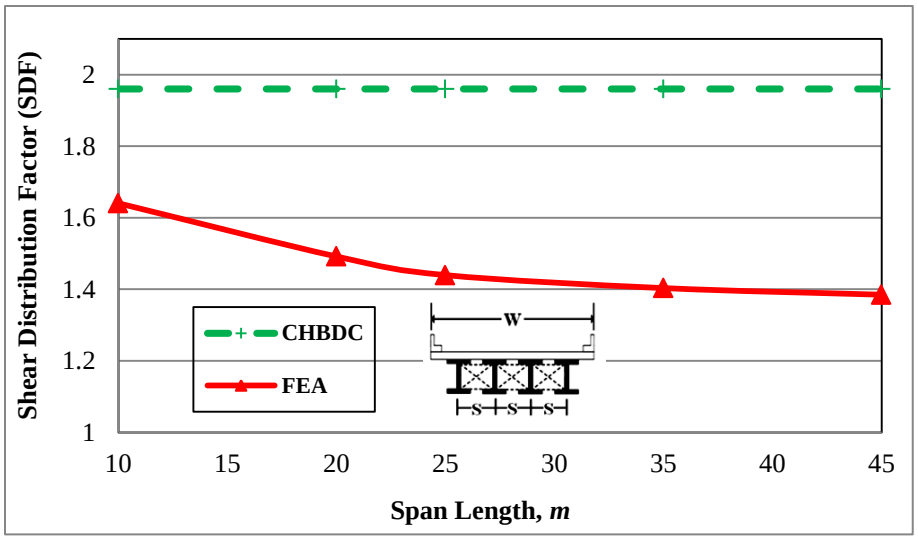

Figure 6.40: Effect of span length on exterior girder SDF for ULS design of steel bridges with width (W) 12 *m* and girder spacing (S) 2.4 *m*.

The sensitivity of the shear distribution factors (SDF) at ULS design for interior girders due to changes in span length has been shown in Figure 6.41 and 6.42. A typical comparison in Figure 6.41 indicates the good correspondence between the finite-element and CHBDC results for the

shear distribution factors (with maximum difference of around 7%). For instance, Figure 6.41 shows that shear distribution factor from FEA in concrete integral bridge was reduced only from 1.53 to 1.46 by increasing the span length from 10 to 45 *m* (a decrease of about 5%).

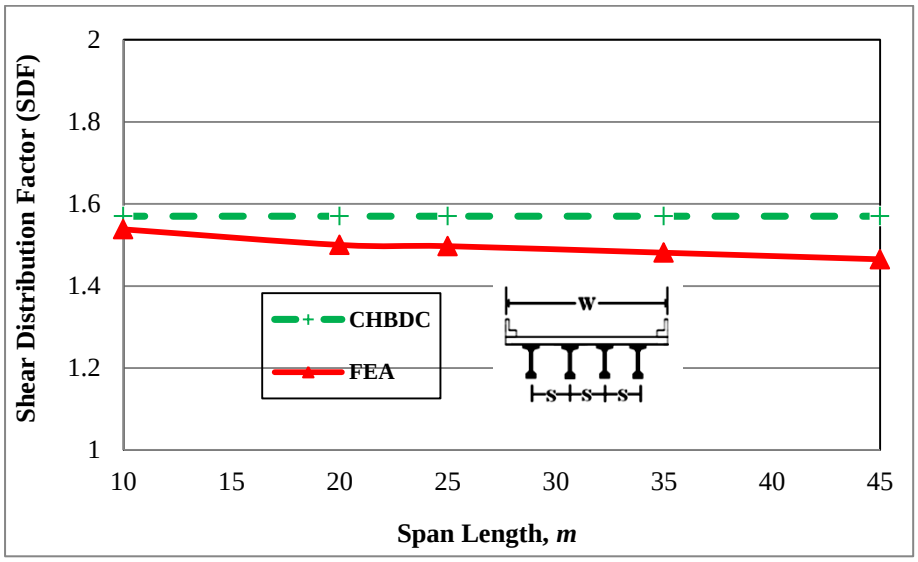

Figure 6.41: Effect of span length on interior girder SDF for ULS design of concrete bridges with width (W) 9.6 *m* and girder spacing (S) 2.4 *m*.

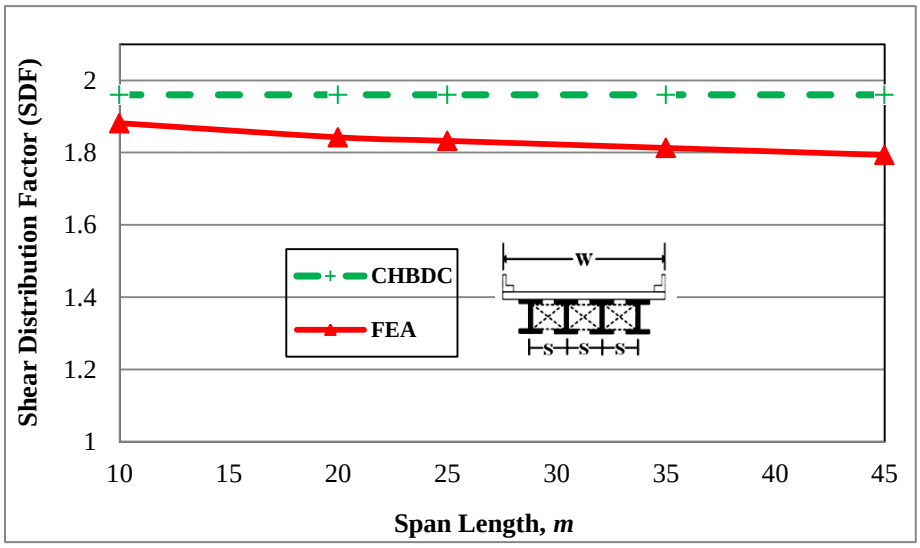

Figure 6.42: Effect of span length on interior girder SDF for ULS design of steel bridges with width (W) 12 *m* and girder spacing (S) 2.4 *m*.

Figure 6.43 and 6.44 present the comparison between moment distribution factors (MDF) calculated using CHBDC and FEA for exterior girders at ULS design. It can be observed from figures that CHBDC was extensively overestimating the MDF for concrete and composite bridges. In addition, as expected the largest shear distribution factor defined by FEA occurred at integral bridges with shortest length. As shown in Figure 6.44, the maximum shear distribution factor of 2.78 occurred for bridge span of 10 *m*, while it was 2.35 for span of 45 *m* (a reduction of 18%).

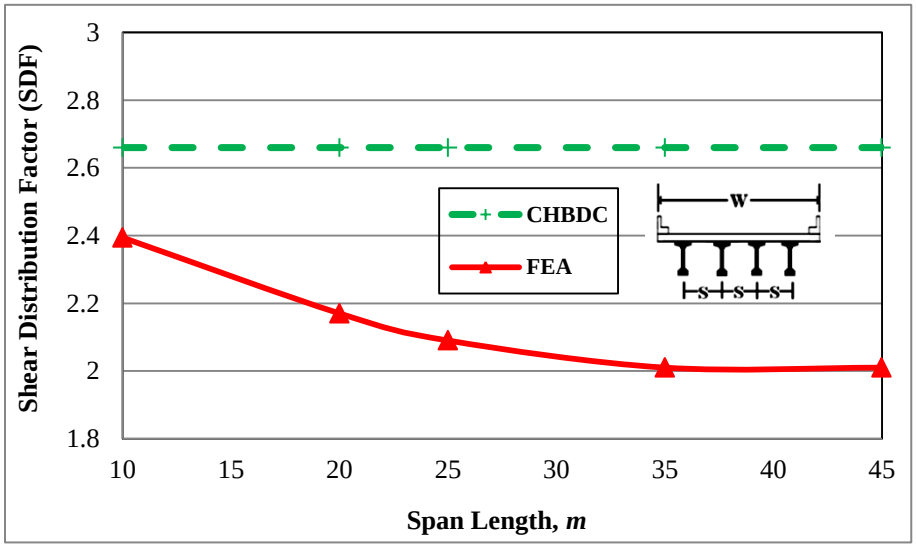

Figure 6.43: Effect of span length on exterior girder SDF for FLS design of concrete bridges with width (W) 9.6 *m* and girder spacing (S) 2.4 *m*.

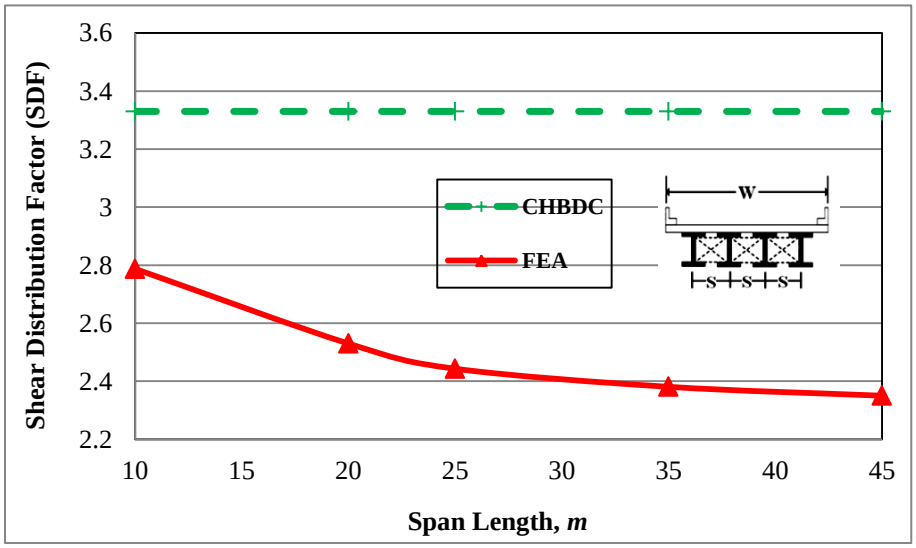

Figure 6.44: Effect of span length on exterior girder SDF for FLS design of steel bridges with width (W) 12 *m* and girder spacing (S) 2.4 *m*.

Figure 6.45 and 6.46 show variation of shear distribution factor (SDF) for interior girders of integral bridges at FLS design. The shear distribution factor was slightly reduced as the span length was increased. General trend of Figure 6.45 and 6.46 also depict that the span length had little effect on shear distribution factors at ULS design for interior girders compared to those for exterior girders.

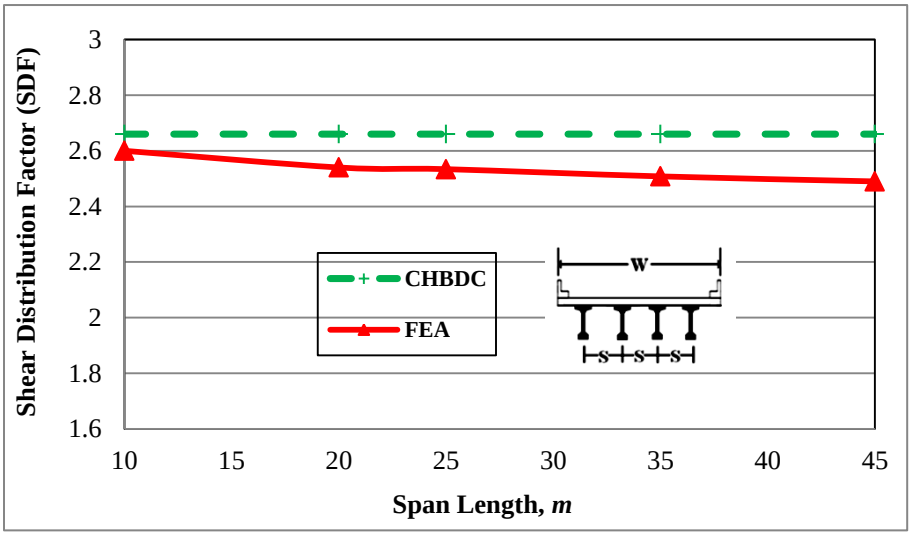

Figure 6.45: Effect of span length on interior girder SDF for ULS design of concrete bridges with width (W) 9.6 *m* and girder spacing (S) 2.4 *m*.

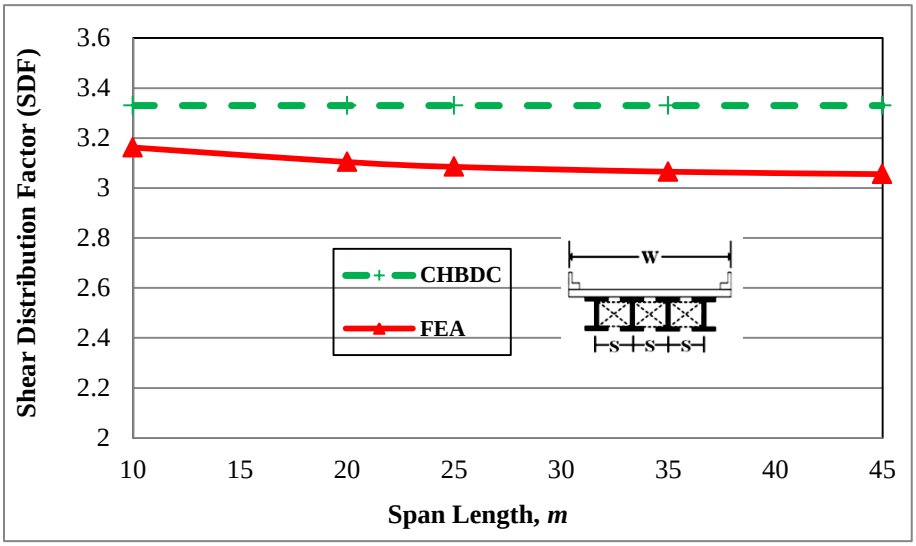

Figure 6.46: Effect of span length on interior girder SDF for FLS design of steel bridges with width (W) 12 *m* and girder spacing (S) 2.4 *m*.

6.1.2.3.3 EFFECT OF GIRDER SPACING AND COMPARISON WITH CHBDC

In order to investigate the effect of girder spacing, S, on girder distribution factor, four different girder spacing were considered, namely: 2, 2.4, 2.8 and 3.2 *m* as illustrated in Figure 6.47. For all bridge layouts, span length of 20 *m* was chosen. The concrete bridge width was 8 *m* in the case of 2 *m* girder spacing, 9.6 *m* in the case of 2.4 *m* girder spacing, 11.2 *m* in the case of 2.8 *m* girder spacing and 12.8 *m* in case of 3.2 *m* girder spacing, while the steel bridge width was 10 *m* in the case of 2 *m* girder spacing, 12 *m* in the case of 2.4 *m* girder spacing, 14 *m* in the case of 2.8 *m* girder spacing and 16 *m* in case of 3.2 *m* girder spacing.

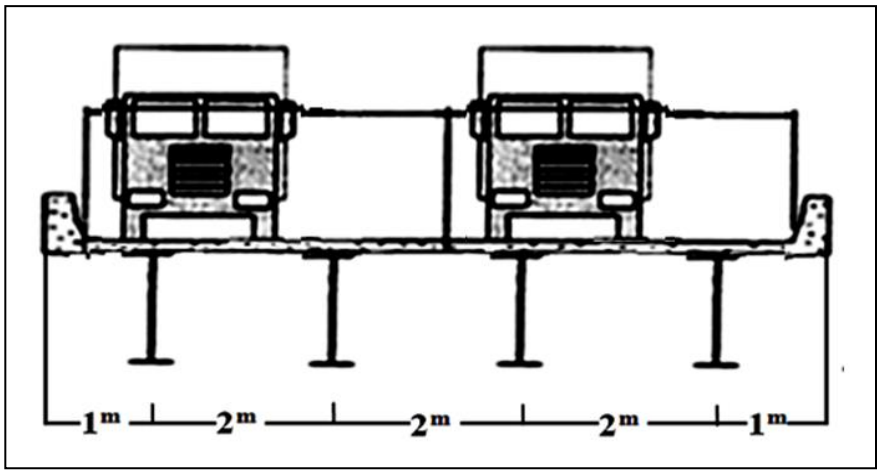

(a)

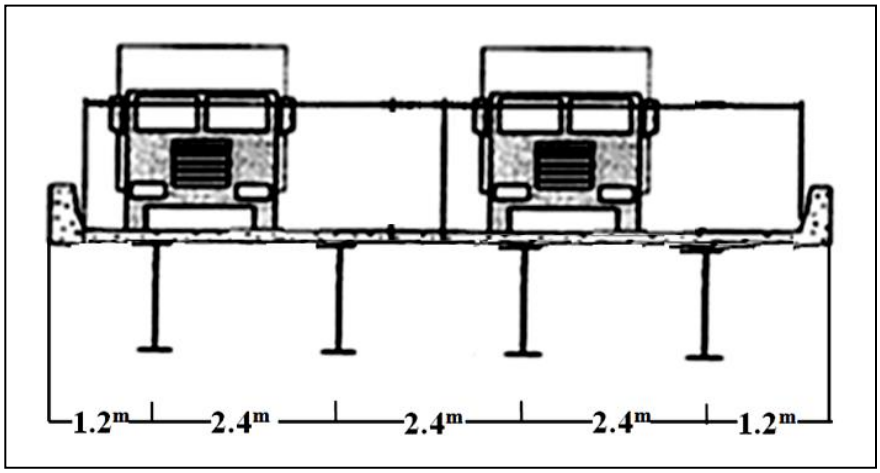

(b)

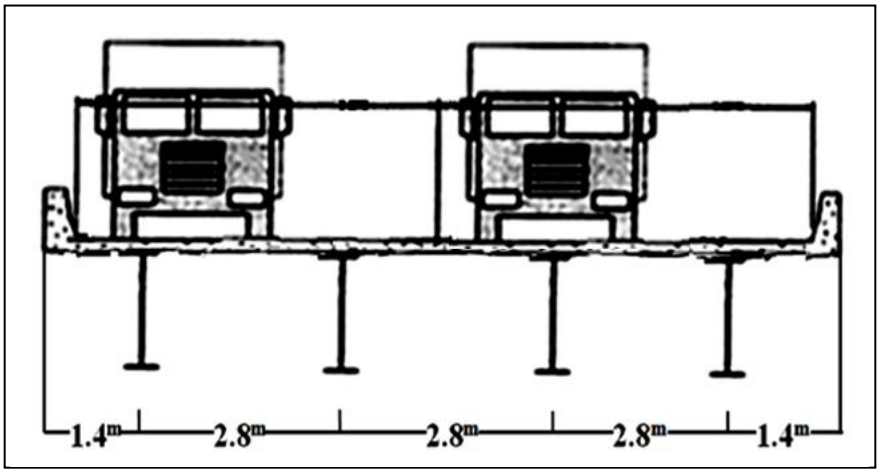

(c)

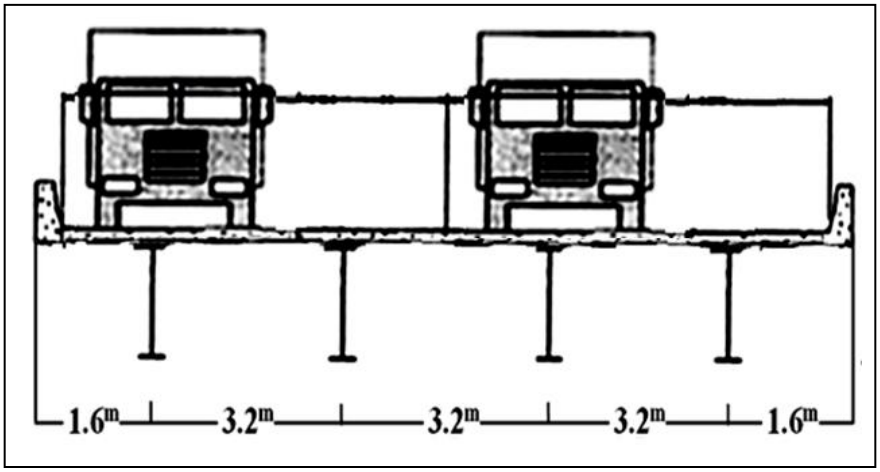

(d)

Figure 6.47: Different girder spacing considered for parametric study
(a) 2 *m*, (b) 2.4 *m*, (c) 2.8 *m*, (d) 3.2 *m*.

6.1.2.3.3.1 EFFECT OF GIRDER SPACING ON MOMENT DISTRIBUTION FACTORS

Figure 6.48 and 6.49 illustrates that moment distribution factor (MDF) for exterior girders of concrete and steel integral bridges at ULS design was greatly affected as girder spacing increases. Results shown in Figure 6.48 clearly indicate that larger girder spacing will lead to significantly larger moment distribution factors. For example, positive and negative moment distribution factor obtained from finite element analysis (P-FEA and N-FEA) for concrete

bridges with 2 *m* girder spacing were 1.01 and 1.06 while those factors for concrete bridges with 3.2 *m* girder spacing were 1.61 and 1.81 (an increase of about 59% and 71% respectively).

Figure 6.50 and 6.51 show the moment distribution factor girder for interior girders of integral bridges at ULS design. It can be seen from these figures that the general trend of moment distribution factor versus girder spacing for interior girder was very similar to that of the exterior girders.

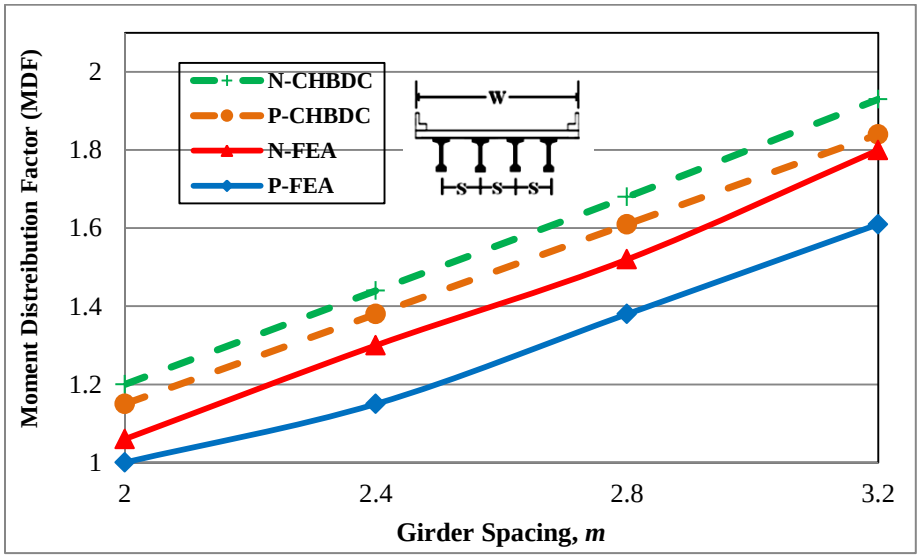

Figure 6.48: Effect of girder spacing on exterior girder MDF for ULS design of concrete bridges with span length of 20 *m*.

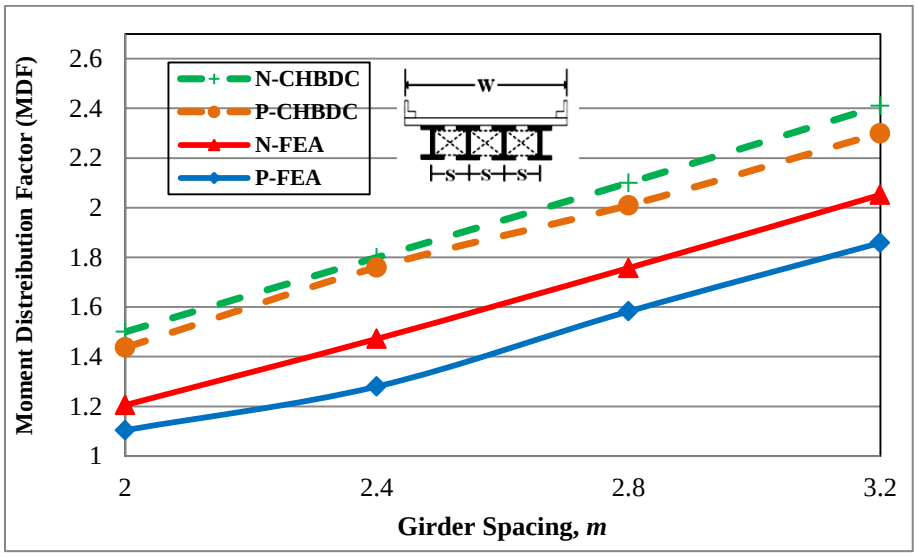

Figure 6.49: Effect of girder spacing on exterior girder MDF for ULS design of steel bridges with span length of 20 *m*.

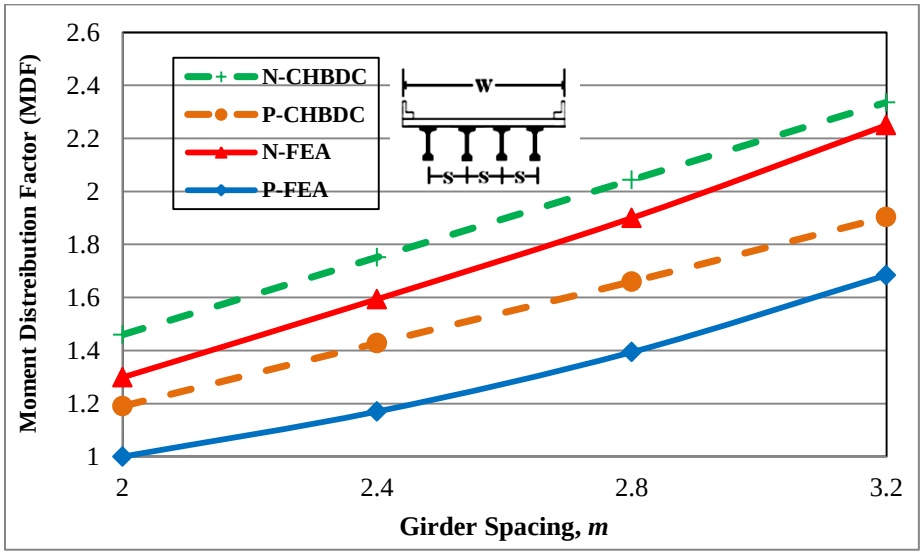

Figure 6.50: Effect of girder spacing on interior girder MDF for ULS design of concrete bridges with span length of 20 *m*.

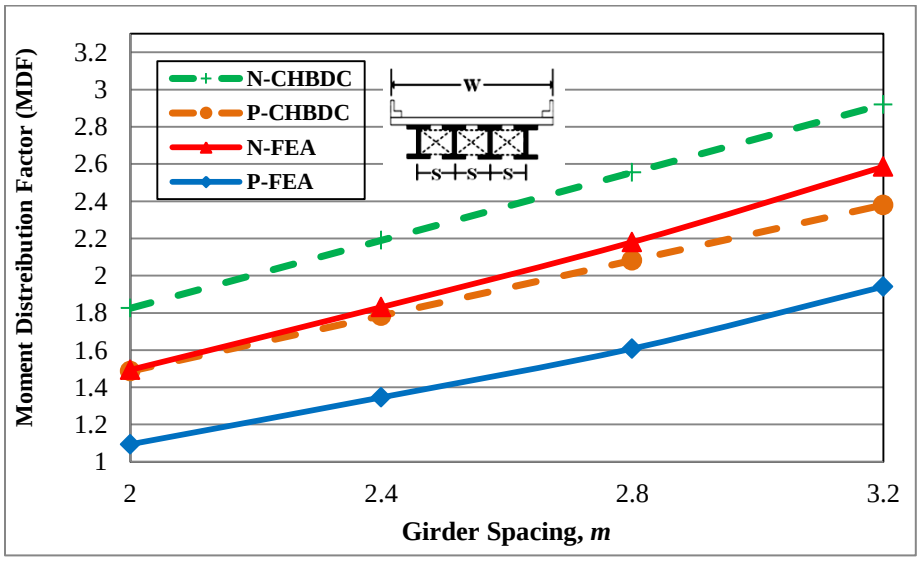

Figure 6.51: Effect of girder spacing on interior girder MDF for ULS design of steel bridges with span length of 20 *m*.

The effect of girder spacing on exterior girder moment distribution factor (MDF) at FLS design was also remarkable and girder spacing did affect moment distribution factor to a great extent. Figure 6.52 to 6.55 depict that CHBDC specifications obtain very conservative results for

exterior and interior distribution factor at FLS design. As an example, Figure 6.55 shows that the negative moment distribution factor was 2.3 for girder spacing of 2 *m*, while this value was 2.81 based on CHBDC expressions. This means that CHBDC expressions overestimate the response by 22%.

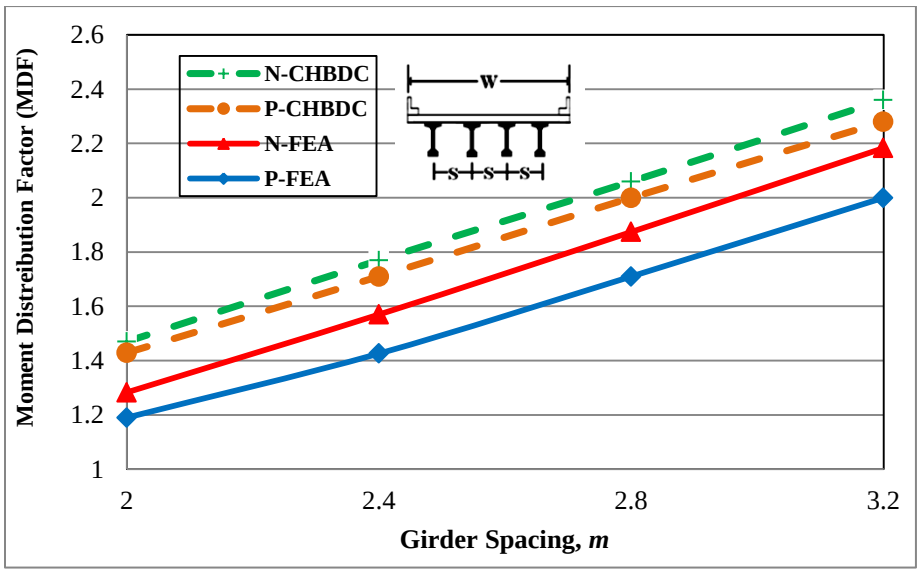

Figure 6.52: Effect of girder spacing on exterior girder MDF for FLS design of concrete bridges with span length of 20 *m*.

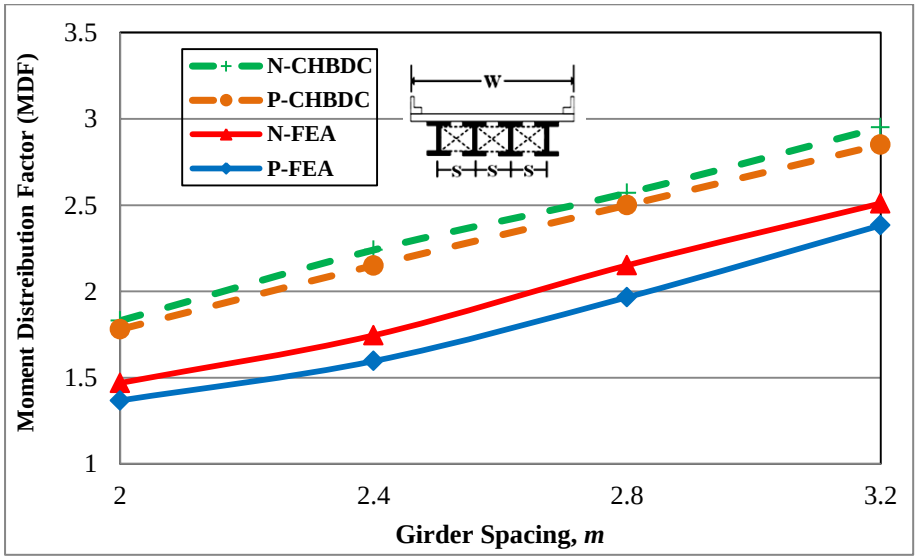

Figure 6.53: Effect of girder spacing on exterior girder MDF for FLS design of steel bridges with span length of 20 *m*.

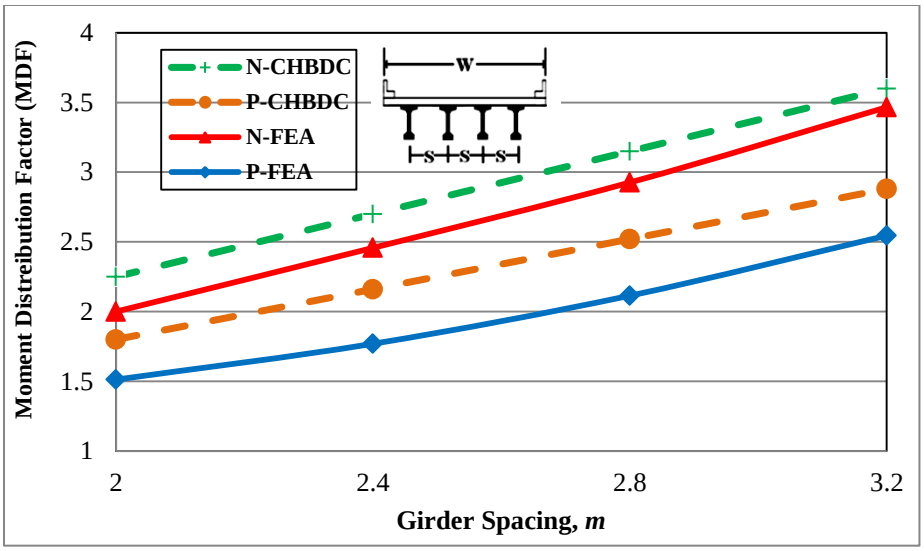

Figure 6.54: Effect of girder spacing on interior girder MDF for FLS design of concrete bridges with span length of 20 *m*.

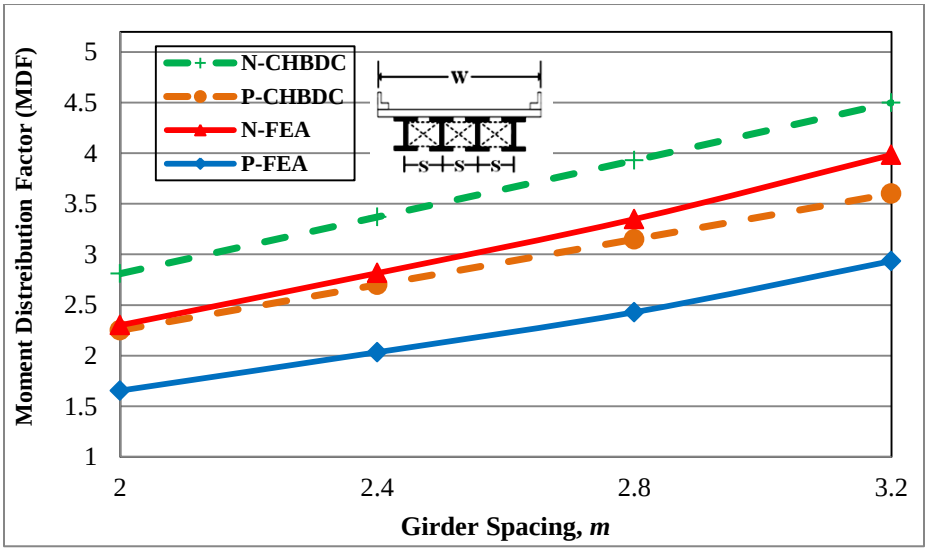

Figure 6.55: Effect of girder spacing on interior girder MDF for FLS design of steel bridges with span length of 20 *m*.

6.1.2.3.3.2 EFFECT OF GIRDER SPACING ON SHEAR DISTRIBUTION FACTORS

The effect of girder spacing on shear distribution factor (SDF) of exterior girders at ULS design are shown in Figure 6.56 and 6.57. It can be observed that the shear distribution factor is slightly affected by girder spacing. As an example, Figure 6.56 shows that the shear distribution factor

obtained from FEA was changed noticeably from 1.01 to 1.54 when the girder spacing changed from 2 to 3.2 *m*.

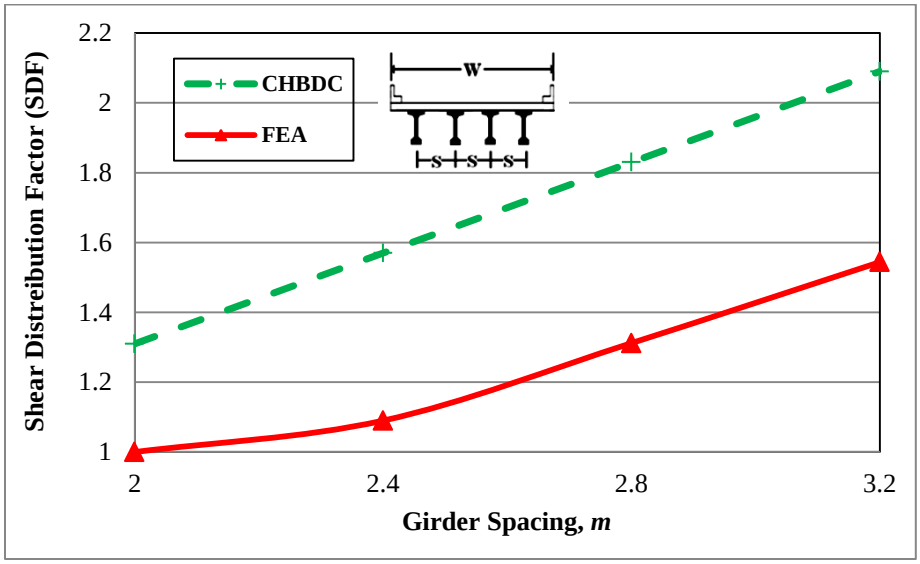

Figure 6.56: Effect of girder spacing on exterior girder SDF for ULS design of concrete bridges with span length of 20 *m*.

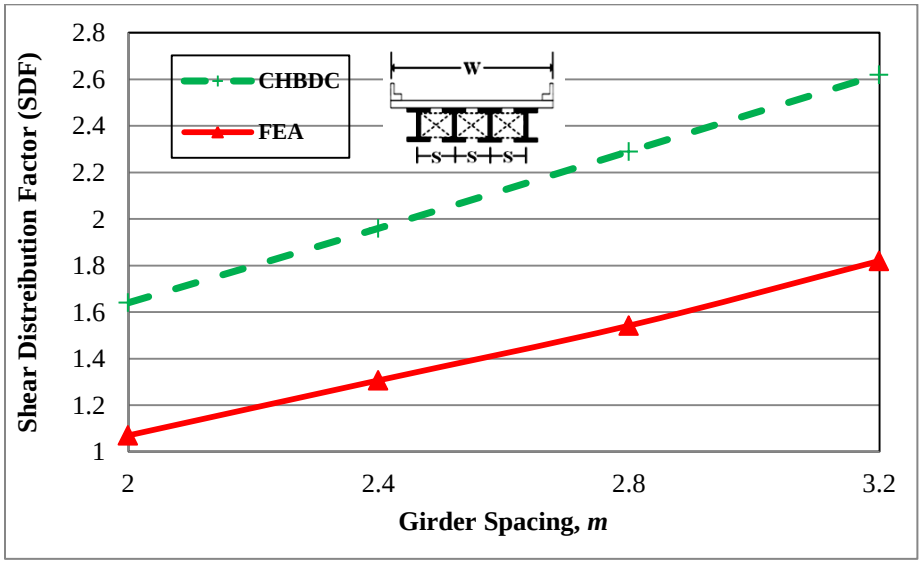

Figure 6.57: Effect of girder spacing on exterior girder SDF for ULS design of steel bridges with span length of 20 *m*.

The effect of girder spacing on shear distribution factor (SDF) of interior girder at ULS design for concrete and steel integral bridges was also investigated. As shown in Figure 6.58 and 6.59,

CHBDC simplified method estimated higher values of shear distribution factor for interior and exterior girders than FEA results. For different girder spacing, the difference between shear distribution factors obtained from FEA and CHBDC were less than 10 %.

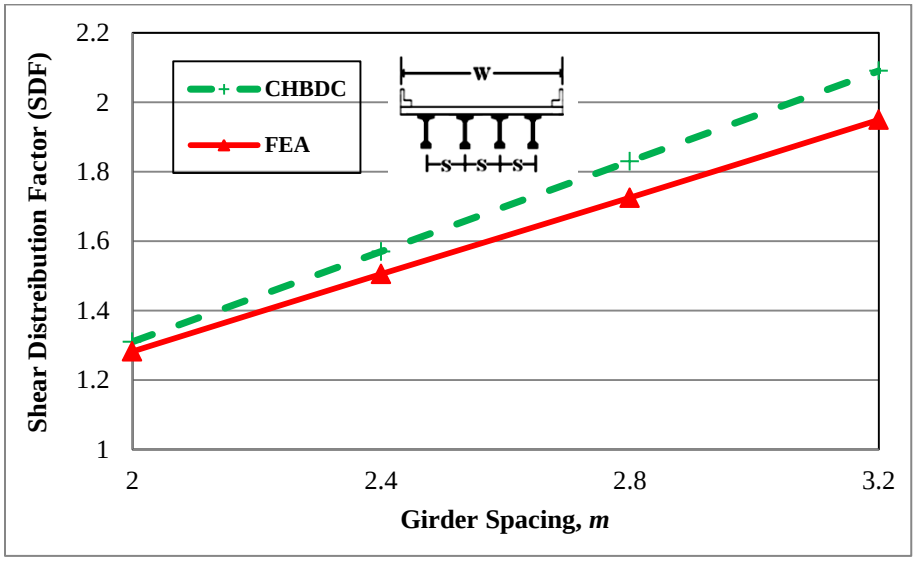

Figure 6.58: Effect of girder spacing on interior girder SDF for ULS design of concrete bridges with span length of 20 *m*.

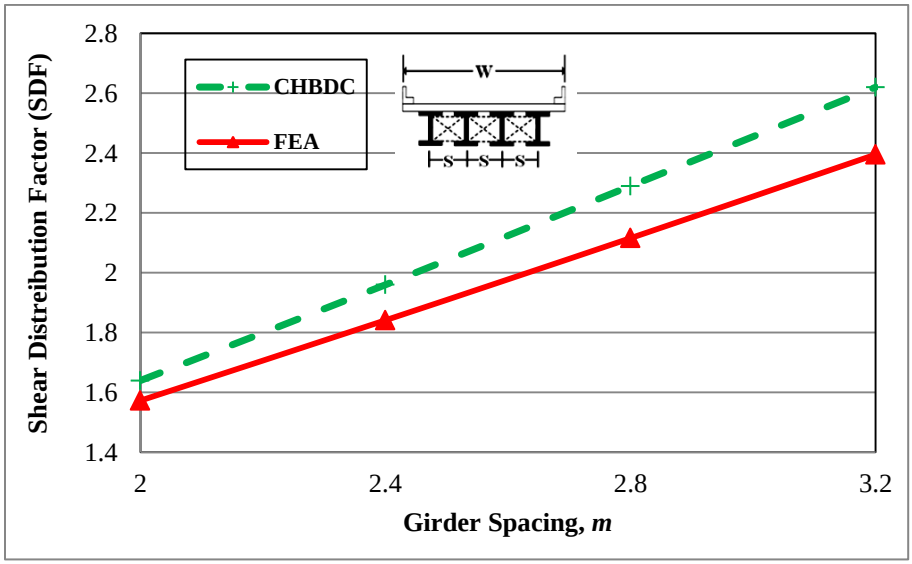

Figure 6.59: Effect of girder spacing on interior girder SDF for ULS design of steel bridges with span length of 20 *m*.

Figure 6.60 and 6.61 show that the effect of girder spacing on the shear distribution factor (SDF) of exterior girders at FLS design was significant. One would notice that the CHBDC expressions produce shear distribution factors greater than those obtained using FEA modelling. Also it should be noted that shear distribution factors increased with increase of girder spacing.

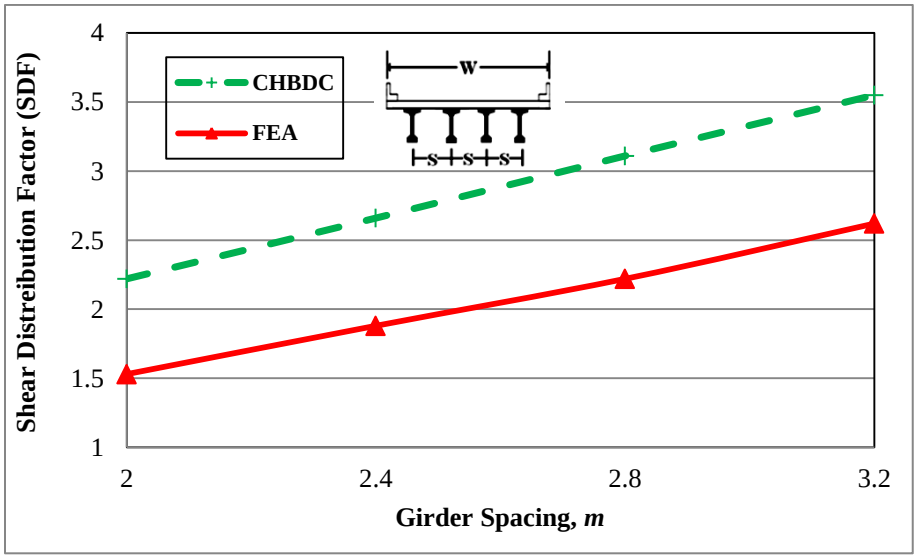

Figure 6.60: Effect of girder spacing on exterior girder SDF for FLS design of concrete bridges with span length of 20 *m*.

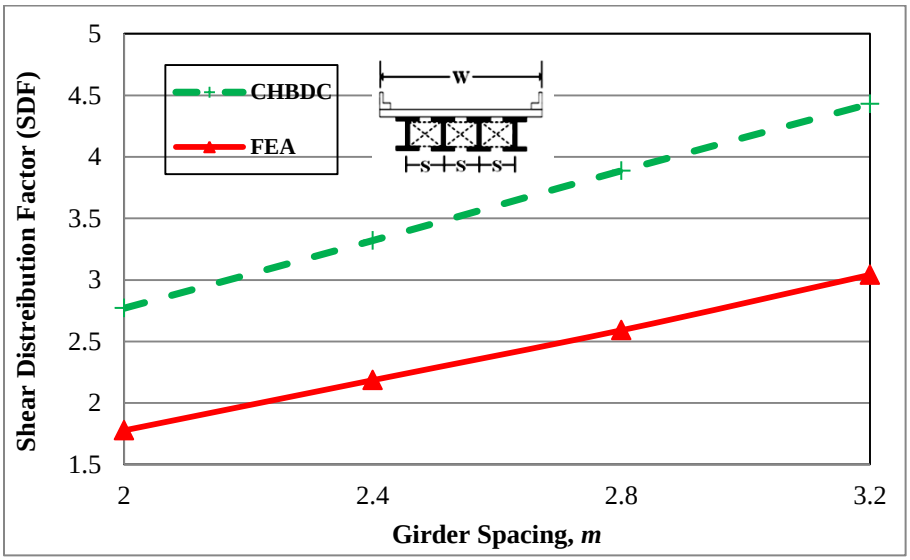

Figure 6.61: Effect of girder spacing on exterior girder SDF for FLS design of steel bridges with span length of 20 *m*.

From Figure 6.62 and 6.63, it can be noted that the magnitude of shear distribution factor (SDF) of interior girder for FLS using CHBDC expressions were slightly greater than those using FEA modelling. It can be seen in Figure 6.62, there was only about 5% difference between the shear distribution factors obtained from CHBDC equations and finite element analysis.

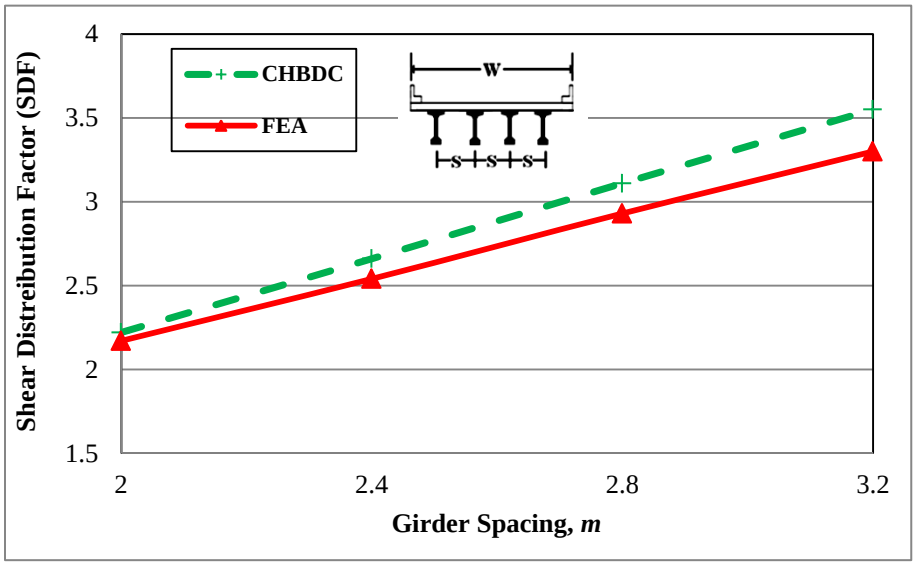

Figure 6.62: Effect of girder spacing on interior girder SDF for FLS design of concrete bridges with span length of 20 *m*.

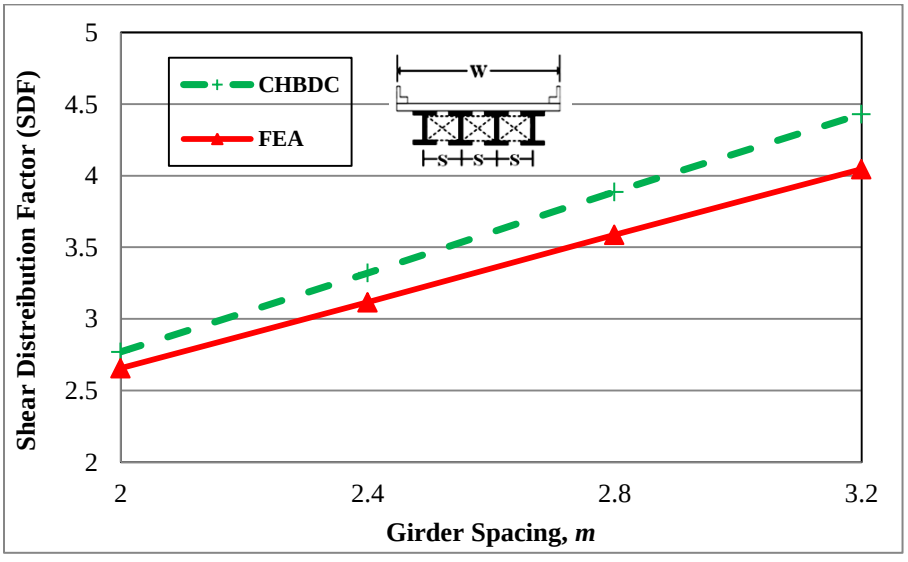

Figure 6.63: Effect of girder spacing on interior girder SDF for FLS design of span steel bridges with span length of 20 *m*.

6.1.2.3.4 EFFECT OF INTERMEDIATE DIAPHRAGMS/BRACINGS AND COMPARISON WITH CHBDC

CHBDC specifies load distribution factors for slab-on-girder bridges assuming that there are no intermediate diaphragms/cross bracings between ends diaphragms that exist only along the support lines. A sensitivity study was conducted herein to examine the effect of the presence of one, two and three intermediate diaphragms on load distribution factors among the girders. In case of concrete bridges, the effect of full-height intermediate diaphragm with 160 *mm* thickness on distribution factors was investigated. However, angle 150×100×125 *mm* cross-bracing was considered when examining the effect of the presence of bracing on the live load distribution factors. Figure 6.64 shows integral bridges with and without cross bracing between support lines.

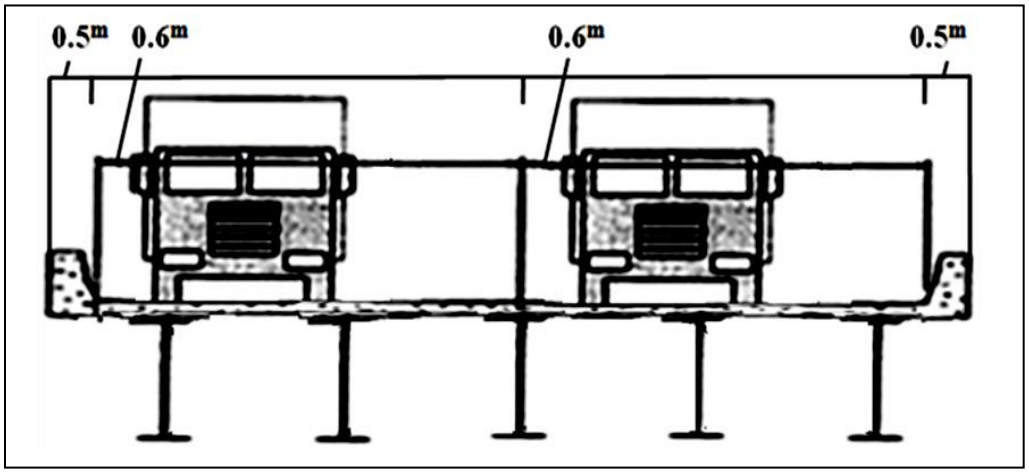

(a)

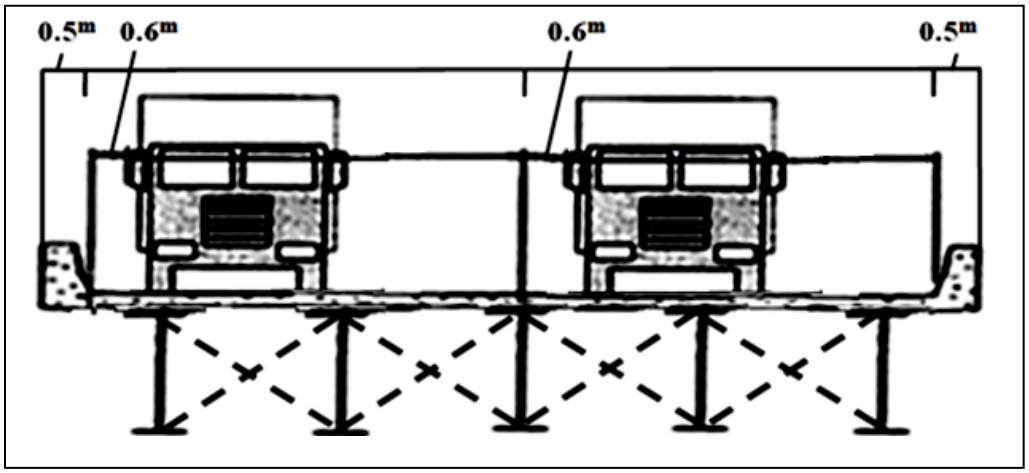

(b)

Figure 6.64: Integral abutment bridge cross-section
(a) Without cross-bracing, (b) With cross-bracing.

6.1.2.3.4.1 EFFECT OF INTERMEDIATE DIAPHRAGMS/BRACINGS ON MOMENT DISTRIBUTION FACTORS

Figure 6.65 to 6.68 show the effect of the number of diaphragms/bracings on moment distribution factor (MDF) at ULS design. It is observed in Figure 6.67 that negative moment distribution factor obtained from FEA decreased from 1.66 for a bridge with no cross bracing to 1.61 for a bridge with one cross bracing, representing a difference of only 4%. Similar trend was also observed for positive moment distribution factors. It can be concluded that intermediate diaphragms only cause marginal improvement in the moment distribution factors at ULS design.

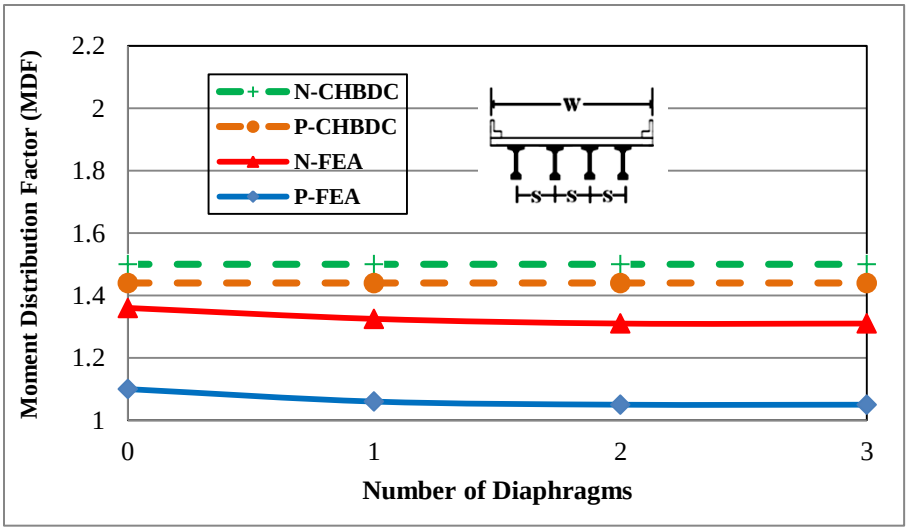

Figure 6.65: Effect of number of diaphragms on exterior girder MDF for ULS design of concrete bridges with width (W) 10 *m* and girder spacing (S) 2 *m*.

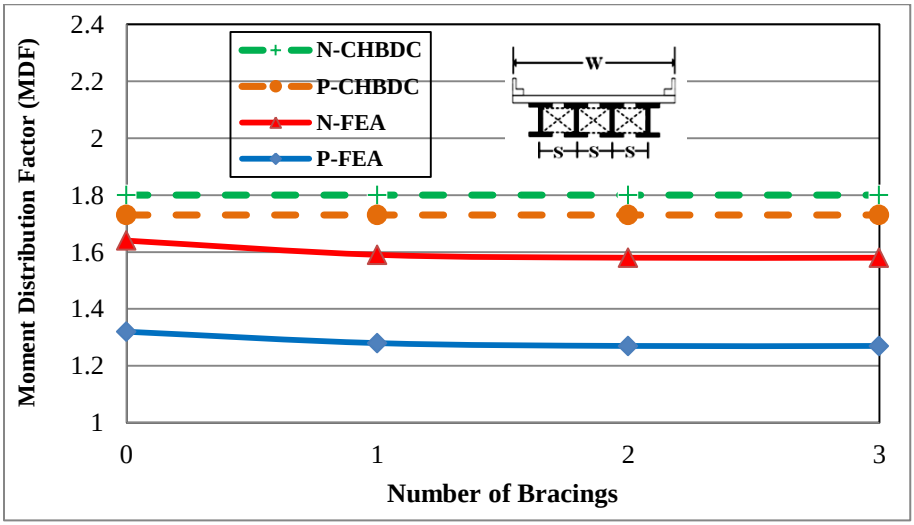

Figure 6.66: Effect of number of diaphragms on exterior girder MDF for ULS design of steel bridges with width (W) 12 *m* and girder spacing (S) 2.4 *m*.

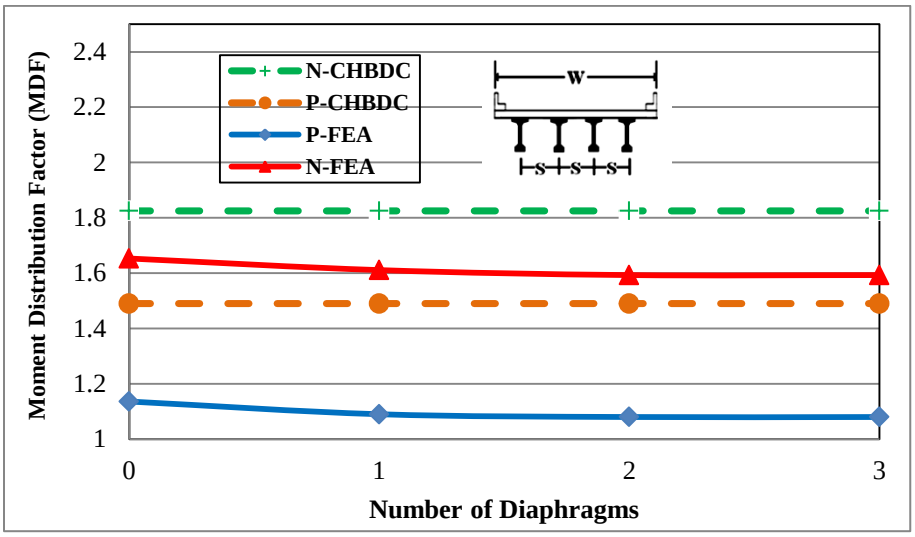

Figure 6.67: Effect of number of diaphragms on interior girder MDF for ULS design of concrete bridges with width (W) 10 *m* and girder spacing (S) 2 *m*.

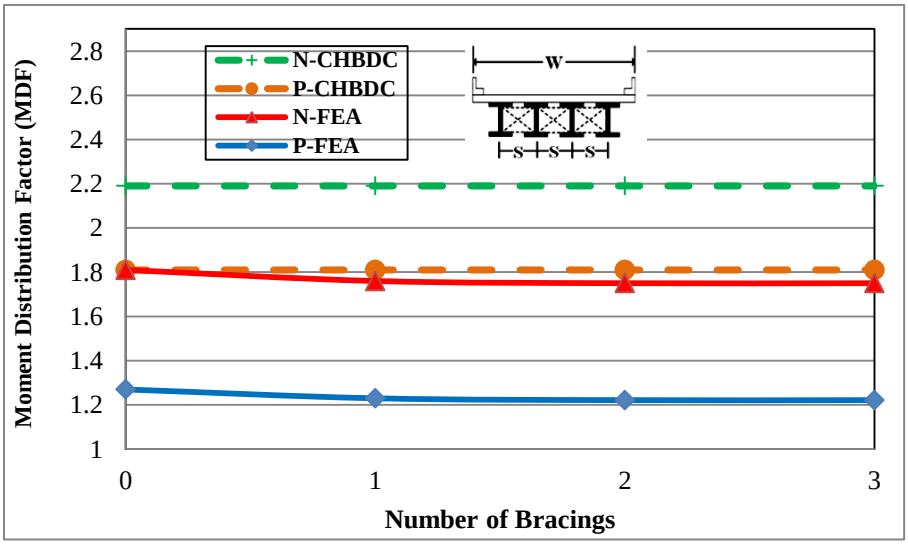

Figure 6.68: Effect of number of diaphragms on interior girder MDF for ULS design of steel bridges with width (W) 12 *m* and girder spacing (S) 2.4 *m*.

The sensitivity of the moment distribution factor (MDF) at FLS design for exterior and interior girders due to changes in number of intermediate diaphragms is shown in Figure 6.69 to 6.72. Slight improvement (similar to moment distribution factors at ULS design) was noted in the distribution factor for moment of exterior and interior girder at FLS.

The addition of braces between I-girders tended to slightly reduce the moment distribution factor. Therefore, it can be concluded that cross bracings with maximum spacing of 7.5 *m*, specified in CHBDC, was sufficient to produce fairly uniform moment distribution factors.

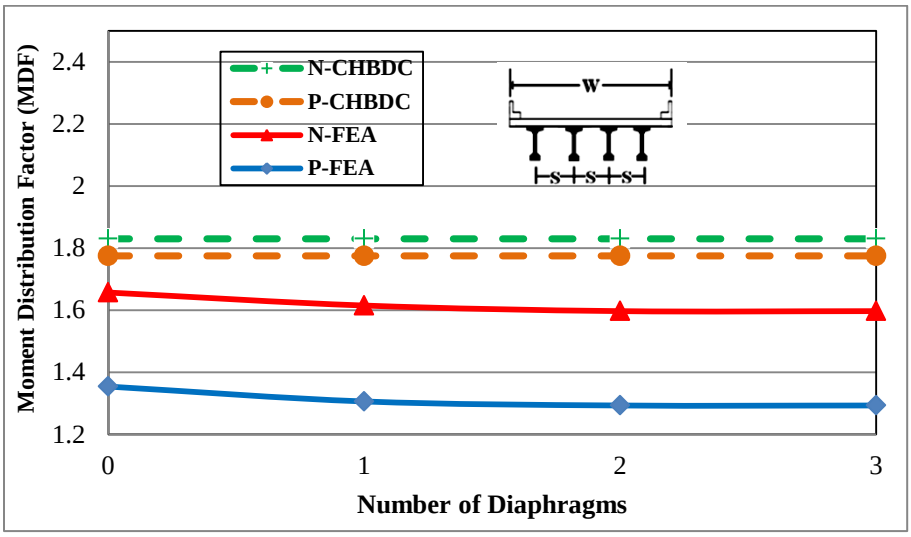

Figure 6.69: Effect of number of diaphragms on exterior girder MDF for FLS design of concrete bridges with width (W) 10 *m* and girder spacing (S) 2 *m*.

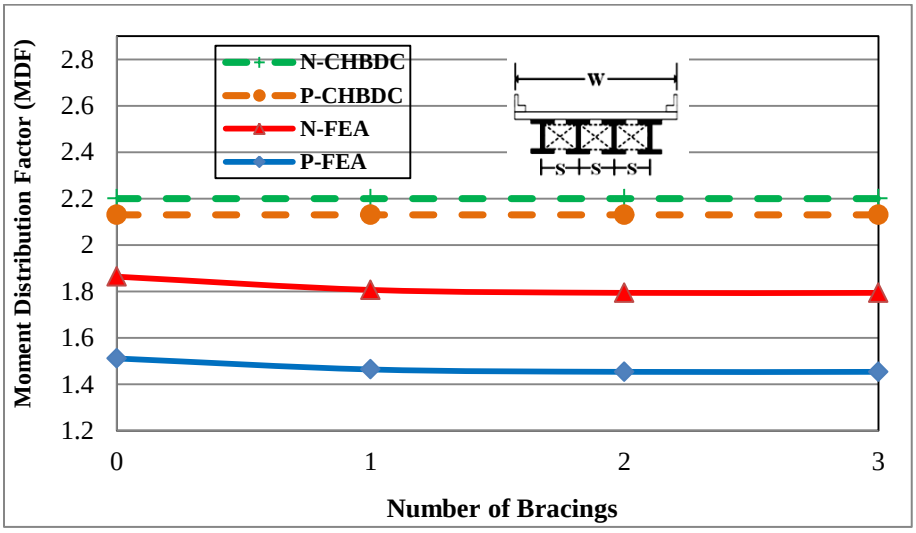

Figure 6.70: Effect of number of diaphragms on exterior girder MDF for FLS design of steel bridges with width (W) 12 *m* and girder spacing (S) 2.4 *m*.

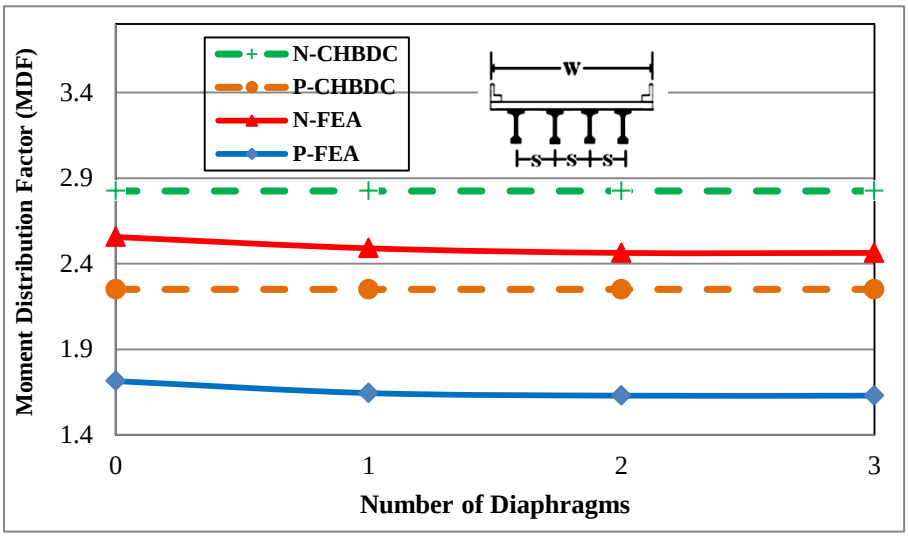

Figure 6.71: Effect of number of diaphragms on interior girder MDF for FLS design of concrete bridges with width (W) 10 *m* and girder spacing (S) 2 *m*.

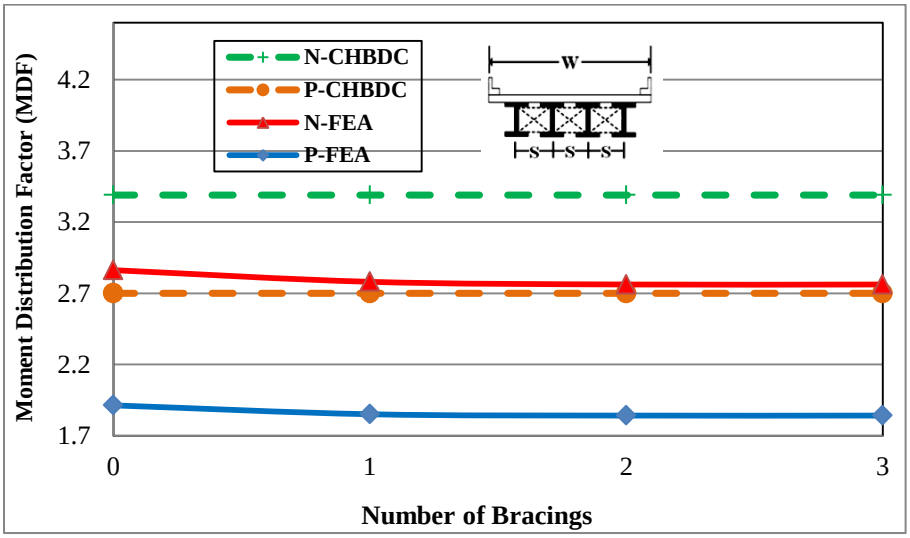

Figure 6.72: Effect of number of diaphragms on interior girder MDF for FLS design of steel bridges with width (W) 12 *m* and girder spacing (S) 2.4 *m*.

6.1.2.3.4.2 EFFECT OF INTERMEDIATE DIAPHRAGMS/BRACINGS ON SHEAR DISTRIBUTION FACTORS

Figure 6.73 to 6.76 illustrate the effect of the number of diaphragms or cross bracing on the shear distribution factor (SDF) at ULS design due to truck loading. It can be noted from Figure 6.75 that by increasing the number of cross bracing from zero to one for an integral bridge with fully

loaded lanes, the shear distribution factor of interior girder obtained from FEA decreased from 1.57 to 1.52, indicating a decrease of 3%. Although the moment distribution factor for interior girder was decreased by only 3% in integral bridges with fully load lanes, results of the FEA modelling showed that the moment distribution factor was decreased by more than 30% in integral bridges with partially loaded lanes. However, results from partially loaded lanes was not governing in the determining the shear distribution factor in this case.

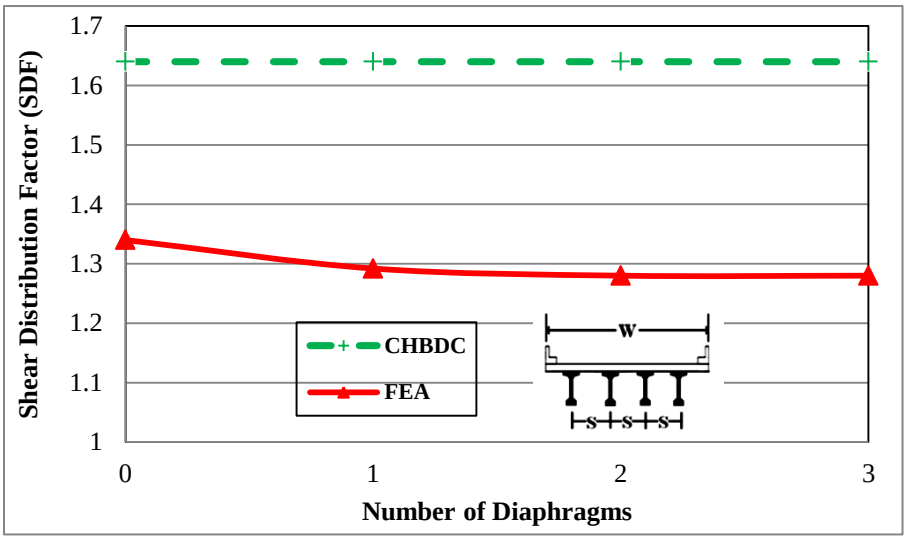

Figure 6.73: Effect of number of diaphragms on exterior girder SDF for ULS design of concrete bridges with width (W) 10 *m* and girder spacing (S) 2 *m*.

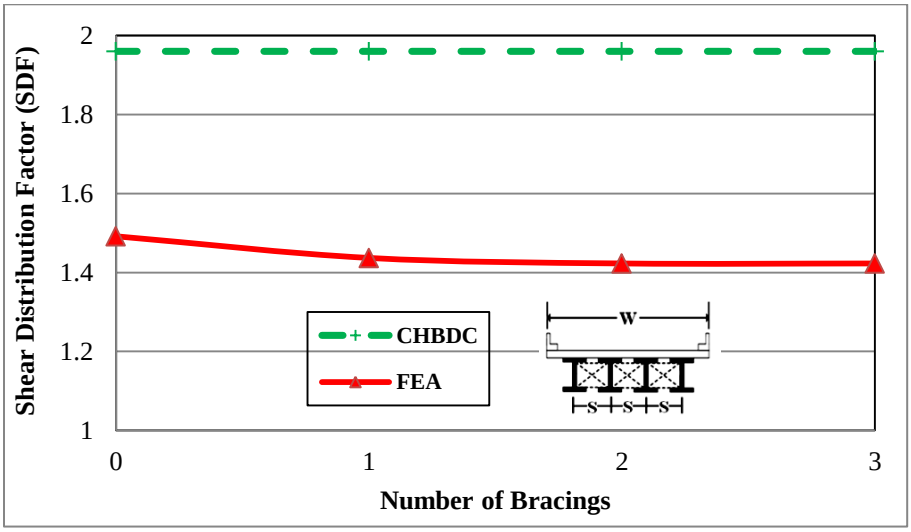

Figure 6.74: Effect of number of diaphragms on exterior girder SDF for ULS design of steel bridges with width (W) 12 *m* and girder spacing (S) 2.4 *m*.

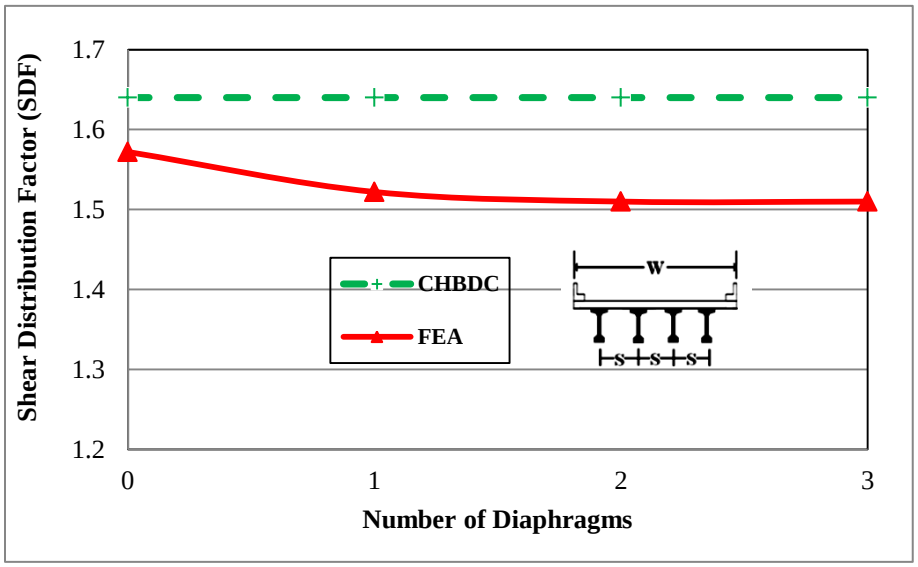

Figure 6.75: Effect of number of diaphragms on interior girder SDF for ULS design of concrete bridges with width (W) 10 *m* and girder spacing (S) 2 *m*.

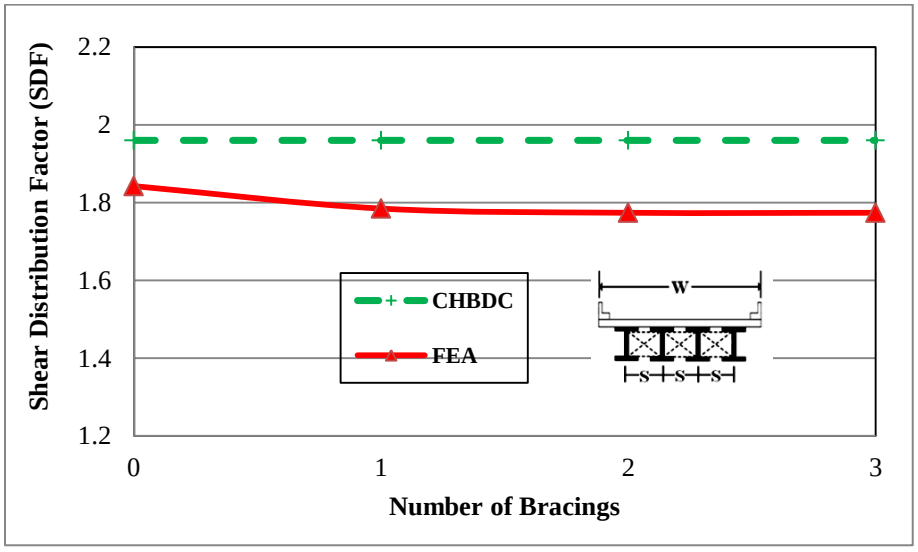

Figure 6.76: Effect of number of diaphragms on interior girder SDF for ULS design of steel bridges with width (W) 12 *m* and girder spacing (S) 2.4 *m*.

The relationships between the number of intermediate diaphragms (cross bracings) and the shear distribution factors (SDF) at FLS are presented in Figure 6.77 to 6.80. Once more, it can be seen from figures that cross bracing has insignificant effect on the shear distribution at FLS.

Notwithstanding the insignificant effect of cross bracing on the distribution factors noted above, cross bracings play an important role during the construction of the bridge as well as during its service. Cross bracings between girders increase the overall integrity of the bridge when subjected to partial loading, and therefore the CHBDC provision of cross bracing is a good design practice.

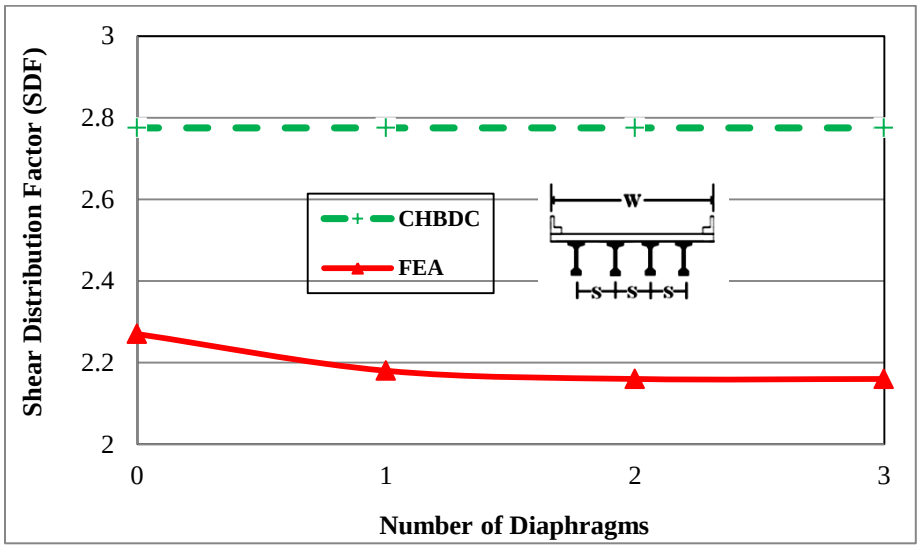

Figure 6.77: Effect of number of diaphragms on exterior girder SDF for FLS design of concrete bridges with width (W) 10 *m* and girder spacing (S) 2 *m*.

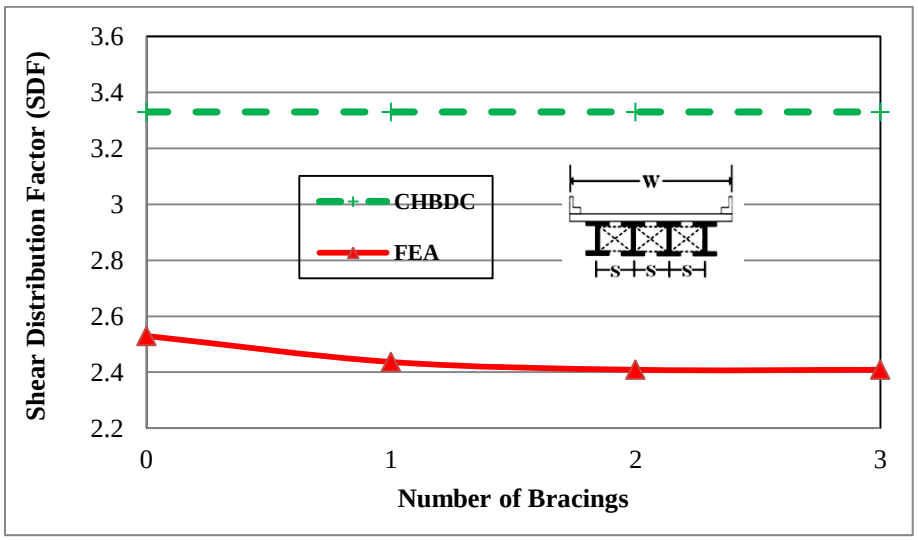

Figure 6.78: Effect of number of diaphragms on exterior girder SDF for FLS design of steel bridges with width (W) 12 *m* and girder spacing (S) 2.4 *m*.

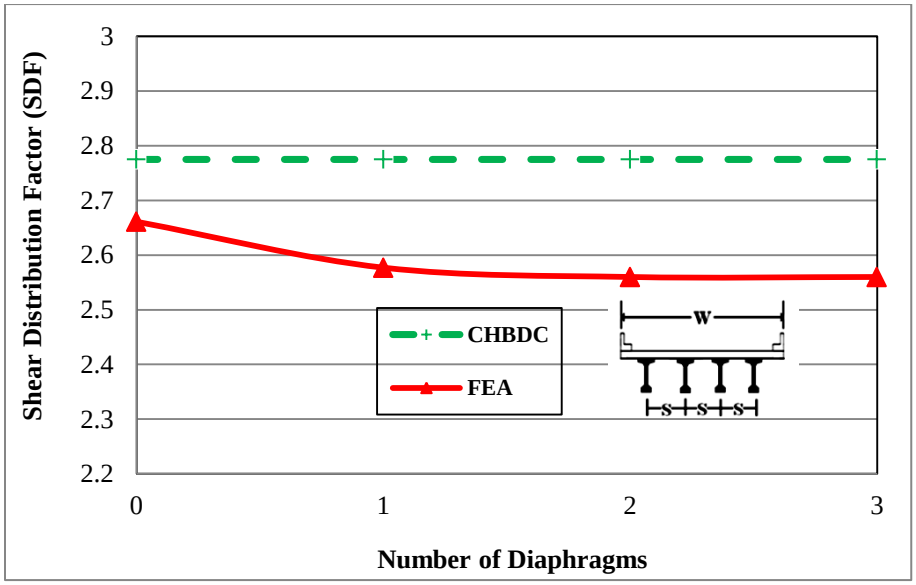

Figure 6.79: Effect of number of diaphragms on exterior girder SDF for ULS design of concrete bridges with width (W) 10 *m* and girder spacing (S) 2 *m*.

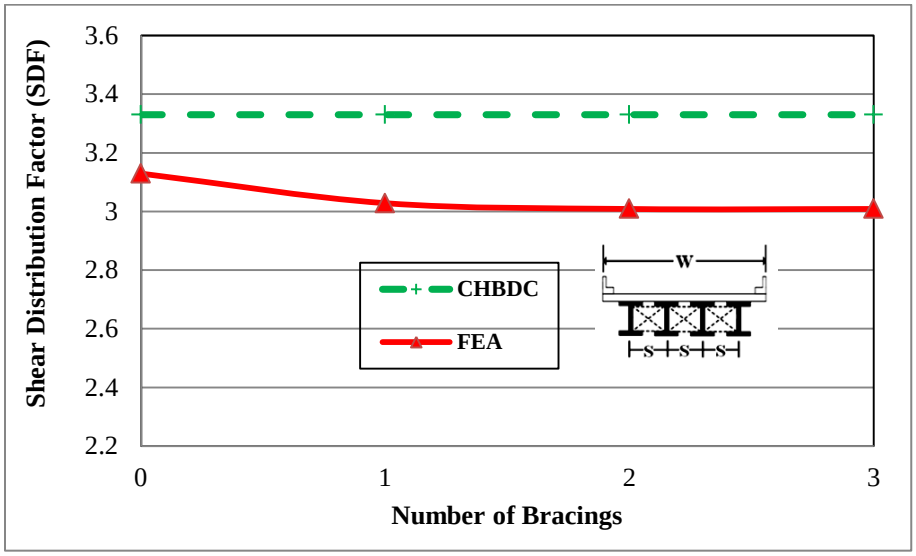

Figure 6.80: Effect of number of diaphragms on interior girder SDF for FLS design of steel bridges with width (W) 12 *m* and girder spacing (S) 2.4 *m*.

6.1.3 COMPARISON BETWEEN GIRDER DISTRIBUTION FACTORS OBTAINED FROM FEA AND CHBDC SIMPLIFIED METHOD

6.1.3.1 EFFECT OF NUMBER OF DESIGN LANES

The analysis results of the interior and exterior girders distribution factors for 20 *m* integral bridges are presented in Tables 6.2 to 6.5 for the case where one or more design lanes are loaded. In all the tables, the values of the parameters used, LLDFs obtained from FEAs and CHBDC as well as the ratio, *R*, of the LLDFs obtained from CHBDC to those obtained from FEA (*R*=CHBDC/FEA) are presented for the girder moment and shear. The data presented in the tables reveal that the difference between the FEA and CHBDC results for both interior and exterior girder moment was more for integral bridges with more number of design lanes. For the interior girders, the analyses results indicated that the ratio, *R*, for the girder shear ranged between 1.03 and 1.07. Thus, LLDFs obtained from FEA were generally in good agreement with those calculated using CHBDC LLDEs. However, for the exterior girder shear, the ratio, *R*, ranges between 1.12 and 1.25 where most of the *R* values were larger than 1.0 (i.e., CHBDC LLDEs generally yield conservative estimates of LLDFs for the girder shear).

Table 6.2: Comparison of MDFs from FEA results and CHBDC equations of concrete bridges for the cases where one or more design lanes are loaded.

Parameters			Positive moment distribution factor			Negative moment distribution factor		
Number of lanes	Limit state	Girder Type	CHBDC	FEA	R= CHBDC /FEA	CHBDC	FEA	R= CHBDC /FEA
1	ULS	Exterior	1.15	1	1.15	1.17	1.08	1.08
2	ULS	Exterior	1.17	1.02	1.14	1.2	1.1	1.09
3	ULS	Exterior	1.32	1.1	1.20	1.37	1.23	1.11
4	ULS	Exterior	1.54	1.22	1.26	1.6	1.36	1.17
1	ULS	Interior	1.05	1	1.05	1.08	1.02	1.08
2	ULS	Interior	1.19	1.07	1.11	1.45	1.33	1.09
3	ULS	Interior	1.31	1.12	1.16	1.6	1.43	1.11
4	ULS	Interior	1.47	1.16	1.26	1.8	1.56	1.15
1	FLS	Exterior	1.05	1.01	1.05	1.04	1	1.05
2	FLS	Exterior	1.47	1.32	1.11	1.42	1.30	1.09
3	FLS	Exterior	2.21	1.83	1.20	2.15	1.92	1.11
4	FLS	Exterior	2.84	2.24	1.26	2.79	2.37	1.17
1	FLS	Interior	1.05	1	1.05	1.08	1.01	1.07
2	FLS	Interior	1.79	1.6	1.11	2.25	2.08	1.08
3	FLS	Interior	2.75	2.35	1.17	3.46	3.08	1.12
4	FLS	Interior	3.62	2.86	1.26	4.6	3.98	1.15

Table 6.3: Comparison of MDFs from FEA results and CHBDC equations of steel bridges for the cases where one or more design lanes are loaded.

Parameters			Positive moment distribution factor			Negative moment distribution factor		
Number of lanes	Limit state	Girder Type	CHBDC	FEA	R= CHBDC /FEA	CHBDC	FEA	R= CHBDC /FEA
1	ULS	Exterior	1.38	1.00	1.38	1.41	1.13	1.25
2	ULS	Exterior	1.41	1.01	1.40	1.44	1.14	1.26
3	ULS	Exterior	1.59	1.04	1.53	1.65	1.25	1.32
4	ULS	Exterior	1.85	1.12	1.65	1.92	1.42	1.35
1	ULS	Interior	1.13	0.95	1.19	1.3	1.04	1.25
2	ULS	Interior	1.43	1.13	1.27	1.75	1.4	1.25
3	ULS	Interior	1.57	1.23	1.28	1.92	1.51	1.27
4	ULS	Interior	1.77	1.31	1.35	2.17	1.63	1.33
1	FLS	Exterior	1.05	0.9	1.17	1.05	0.9	1.17
2	FLS	Exterior	1.71	1.22	1.40	1.77	1.40	1.26
3	FLS	Exterior	2.59	1.69	1.53	2.66	2.01	1.32
4	FLS	Exterior	3.35	2.03	1.65	3.41	2.52	1.35
1	FLS	Interior	1.13	0.9	1.26	1.3	1.07	1.25
2	FLS	Interior	2.15	1.70	1.26	2.7	2.18	1.24
3	FLS	Interior	3.31	2.59	1.28	4.16	3.28	1.27
4	FLS	Interior	4.33	3.20	1.35	5.53	4.17	1.33

Table 6.4: Comparison of SDFs from FEA results and CHBDC equations of concrete bridges for the cases where one or more design lanes are loaded.

Parameters			Shear distribution factor		
Number of lanes	Limit state	Girder Type	CHBDC	FEA	R= CHBDC/FEA
1	ULS	Exterior	1.14	1.01	1.12
2	ULS	Exterior	1.3	1.07	1.21
3	ULS	Exterior	1.45	1.17	1.23
4	ULS	Exterior	1.68	1.34	1.25
1	ULS	Interior	1.14	1.10	1.03
2	ULS	Interior	1.3	1.23	1.05
3	ULS	Interior	1.45	1.36	1.06
4	ULS	Interior	1.68	1.56	1.07
1	FLS	Exterior	1.14	1	1.14
2	FLS	Exterior	2.21	1.80	1.22
3	FLS	Exterior	3.63	2.93	1.23
4	FLS	Exterior	4.84	3.87	1.25
1	FLS	Interior	1.14	1.1	1.03
2	FLS	Interior	2.21	2.09	1.05
3	FLS	Interior	3.63	3.41	1.06
4	FLS	Interior	4.84	4.49	1.07

Table 6.5: Comparison of SDFs from FEA results and CHBDC equations of steel bridges for the cases where one or more design lanes are loaded.

Parameters			Shear distribution factor		
Number of lanes	**Limit state**	**Girder Type**	**CHBDC**	**FEA**	**R= CHBDC/FEA**
1	ULS	Exterior	1.37	1.02	1.34
2	ULS	Exterior	1.57	1.15	1.37
3	ULS	Exterior	1.75	1.27	1.38
4	ULS	Exterior	2.02	1.45	1.39
1	ULS	Interior	1.37	1.27	1.08
2	ULS	Interior	1.57	1.43	1.10
3	ULS	Interior	1.75	1.57	1.11
4	ULS	Interior	2.02	1.80	1.12
1	FLS	Exterior	1.37	1.04	1.32
2	FLS	Exterior	2.66	1.99	1.34
3	FLS	Exterior	4.36	3.23	1.35
4	FLS	Exterior	5.81	4.27	1.36
1	FLS	Interior	1.37	1.28	1.07
2	FLS	Interior	2.66	2.44	1.09
3	FLS	Interior	4.36	3.96	1.10
4	FLS	Interior	5.81	5.22	1.11

6.1.3.2 EFFECT OF SPAN LENGTH

The results presented in Tables 6.6 to 6.9 indicate that the rate of difference between moment distribution factors obtained from FEA and CHBDC was decreased with increase of span length. Although CHBDC LLDEs were able to predict the shear distribution in interior girders of integral abutment bridges with reasonable accuracy (within 10%), they failed to do so in the case of exterior girder (as much as 31% difference). This mainly results from the better distribution of live load moment among the girders of integral abutment bridges and lesser variation of the LLDFs for integral abutment bridges. The better distribution of the live load moment in integral abutment bridges may be primarily due to the torsional rotational rigidity provided by the monolithic abutments to the girders and the slab, which was more predominant for shorter span bridges. Furthermore, the overhanging portion of the slab, which was free over the supports in jointed bridges, was fixed to the abutments in the case of integral abutment bridges. This could also enhance the distribution of live load moment among the girders of integral abutment bridges.

Table 6.6: Comparison of MDFs from FEA results and CHBDC equations of concrete bridges with different span lengths.

Parameters			Positive moment distribution factor			Negative moment distribution factor		
Span length (*m*)	Limit state	Girder Type	CHBDC	FEA	R= CHBDC /FEA	CHBDC	FEA	R= CHBDC /FEA
10	ULS	Exterior	1.42	1.08	1.31	1.47	1.16	1.26
20	ULS	Exterior	1.38	1.07	1.29	1.44	1.16	1.24
35	ULS	Exterior	1.36	1.06	1.29	1.43	1.15	1.24
45	ULS	Exterior	1.36	1.06	1.28	1.42	1.15	1.23
10	ULS	Interior	1.62	1.13	1.43	1.78	1.26	1.41
20	ULS	Interior	1.43	1.1	1.3	1.73	1.24	1.38
35	ULS	Interior	1.36	1.09	1.24	1.68	1.23	1.36
45	ULS	Interior	1.34	1.09	1.23	1.64	1.23	1.33
10	FLS	Exterior	1.74	1.33	1.30	1.78	1.42	1.25
20	FLS	Exterior	1.73	1.33	1.29	1.76	1.41	1.24
35	FLS	Exterior	1.72	1.33	1.29	1.75	1.40	1.24
45	FLS	Exterior	1.72	1.33	1.29	1.75	1.40	1.24
10	FLS	Interior	2.36	1.71	1.38	2.79	2.02	1.38
20	FLS	Interior	2.16	1.67	1.29	2.67	1.95	1.36
35	FLS	Interior	2.08	1.66	1.25	2.53	1.85	1.36
45	FLS	Interior	2.06	1.66	1.24	2.43	1.82	1.33

Table 6.7: Comparison of MDFs from FEA results and CHBDC equations of steel bridges with different span lengths.

Parameters			Positive moment distribution factor			Negative moment distribution factor		
Span length (*m*)	Limit state	Girder Type	CHBDC	FEA	R= CHBDC /FEA	CHBDC	FEA	R= CHBDC /FEA
10	ULS	Exterior	1.78	1.14	1.56	1.83	1.35	1.36
20	ULS	Exterior	1.73	1.11	1.56	1.8	1.33	1.35
35	ULS	Exterior	1.71	1.11	1.54	1.79	1.33	1.35
45	ULS	Exterior	1.7	1.11	1.53	1.78	1.33	1.34
10	ULS	Interior	2.03	1.29	1.57	2.24	1.45	1.54
20	ULS	Interior	1.79	1.26	1.42	2.19	1.42	1.54
35	ULS	Interior	1.7	1.24	1.37	2.11	1.41	1.50
45	ULS	Interior	1.68	1.24	1.35	2.05	1.41	1.45
10	FLS	Exterior	2.16	1.38	1.57	2.23	1.63	1.37
20	FLS	Exterior	2.16	1.38	1.57	2.2	1.62	1.36
35	FLS	Exterior	2.15	1.37	1.57	2.18	1.61	1.35
45	FLS	Exterior	2.15	1.37	1.57	2.18	1.61	1.35
10	FLS	Interior	2.96	1.95	1.52	3.51	2.24	1.57
20	FLS	Interior	2.7	1.90	1.42	3.39	2.20	1.54
35	FLS	Interior	2.61	1.91	1.37	3.17	2.11	1.50
45	FLS	Interior	2.58	1.91	1.35	3.04	2.11	1.44

Table 6.8: Comparison of SDFs from FEA results and CHBDC equations of concrete bridges with different span lengths.

Parameters			Shear distribution factor		
Span length (*m*)	**Limit state**	**Girder Type**	**CHBDC**	**FEA**	**R= CHBDC/FEA**
10	ULS	Exterior	1.57	1.41	1.11
20	ULS	Exterior	1.57	1.28	1.21
35	ULS	Exterior	1.57	1.20	1.29
45	ULS	Exterior	1.57	1.19	1.31
10	ULS	Interior	1.57	1.53	1.02
20	ULS	Interior	1.57	1.5	1.04
35	ULS	Interior	1.57	1.48	1.06
45	ULS	Interior	1.57	1.46	1.07
10	FLS	Exterior	2.66	2.39	1.11
20	FLS	Exterior	2.66	2.17	1.22
35	FLS	Exterior	2.66	2.01	1.32
45	FLS	Exterior	2.66	2.01	1.32
10	FLS	Interior	2.66	2.6	1.02
20	FLS	Interior	2.66	2.54	1.04
35	FLS	Interior	2.66	2.50	1.06
45	FLS	Interior	2.66	2.49	1.06

Table 6.9: Comparison of SDFs from FEA results and CHBDC equations of steel bridges with different span lengths.

Parameters			Shear distribution factor		
Span length (*m*)	**Limit state**	**Girder Type**	**CHBDC**	**FEA**	**R= CHBDC/FEA**
10	ULS	Exterior	1.96	1.64	1.20
20	ULS	Exterior	1.96	1.49	1.32
35	ULS	Exterior	1.96	1.40	1.40
45	ULS	Exterior	1.96	1.38	1.42
10	ULS	Interior	1.96	1.88	1.04
20	ULS	Interior	1.96	1.84	1.07
35	ULS	Interior	1.96	1.81	1.08
45	ULS	Interior	1.96	1.79	1.09
10	FLS	Exterior	3.33	2.78	1.20
20	FLS	Exterior	3.33	2.52	1.32
35	FLS	Exterior	3.33	2.38	1.40
45	FLS	Exterior	3.33	2.35	1.42
10	FLS	Interior	3.33	3.16	1.05
20	FLS	Interior	3.33	3.10	1.07
35	FLS	Interior	3.33	3.06	1.09
45	FLS	Interior	3.33	3.05	1.09

6.1.3.3 EFFECT OF GIRDER SPACING

Table 6.10 to 6.13 lists the analyses results for the case where the girder spacing, *S*, is taken as the main parameter. In order to properly include the effect of the girder spacing, *S*, in LLDEs for integral abutment bridges full range of girder spacing values such as 2, 2.4, 2.8 and 3.2 *m* were considered.

The results illustrates that CHBDC equations were highly overestimating the moment distribution factors for interior girders particularly for smaller girder spacing. For the exterior girders, the analyses results were similar to those of the interior girders for the girder moment. However, the large values of *R* for the exterior girder shear compared to those of the interior girder shear was mainly due to the fixity and vertical support provided by the abutments to the overhanging portion of the slab.

Table 6.10: Comparison of MDFs from FEA results and CHBDC equations of concrete bridges with different girder spacing.

Parameters			Positive moment distribution factor			Negative moment distribution factor		
Girder Spacing (*m*)	Limit state	Girder Type	CHBDC	FEA	R= CHBDC /FEA	CHBDC	FEA	R= CHBDC /FEA
2	ULS	Exterior	1.15	1	1.15	1.2	1.06	1.13
2.4	ULS	Exterior	1.38	1.15	1.2	1.44	1.3	1.10
2.8	ULS	Exterior	1.61	1.38	1.16	1.68	1.52	1.10
3.2	ULS	Exterior	1.84	1.61	1.14	1.93	1.8	1.07
2	ULS	Interior	1.19	1	1.19	1.46	1.29	1.12
2.4	ULS	Interior	1.42	1.17	1.22	1.752	1.59	1.09
2.8	ULS	Interior	1.66	1.39	1.19	2.044	1.9	1.07
3.2	ULS	Interior	1.90	1.68	1.13	2.336	2.25	1.03
2	FLS	Exterior	1.42	1.19	1.20	1.47	1.28	1.14
2.4	FLS	Exterior	1.71	1.42	1.19	1.77	1.57	1.12
2.8	FLS	Exterior	2	1.71	1.16	2.06	1.87	1.09
3.2	FLS	Exterior	2.28	2	1.14	2.36	2.18	1.08
2	FLS	Interior	1.8	1.51	1.19	2.25	2.04	1.12
2.4	FLS	Interior	2.16	1.76	1.22	2.7	2.45	1.09
2.8	FLS	Interior	2.52	2.11	1.19	3.15	2.92	1.07
3.2	FLS	Interior	2.88	2.54	1.13	3.6	3.46	1.03

Table 6.11: Comparison of MDFs from FEA results and CHBDC equations of steel bridges with different girder spacing.

Parameters			Positive distribution factor			Negative distribution factor		
Girder spacing (*m*)	Limit state	Girder Type	CHBDC	FEA	R=CHBDC /FEA	CHBDC	FEA	R=CHBDC /FEA
2	ULS	Exterior	1.43	1.10	1.30	1.5	1.20	1.25
2.4	ULS	Exterior	1.78	1.28	1.30	1.8	1.47	1.22
2.8	ULS	Exterior	2.01	1.58	1.27	2.1	1.75	1.20
3.2	ULS	Exterior	2.3	1.85	1.24	2.41	2.05	1.18
2	ULS	Interior	1.48	1.09	1.36	1.82	1.49	1.22
2.4	ULS	Interior	1.78	1.34	1.33	2.19	1.83	1.20
2.8	ULS	Interior	2.08	1.60	1.30	2.55	2.18	1.17
3.2	ULS	Interior	2.38	1.94	1.23	2.92	2.58	1.13
2	FLS	Exterior	1.78	1.36	1.31	1.83	1.46	1.25
2.4	FLS	Exterior	2.13	1.64	1.30	2.24	1.74	1.23
2.8	FLS	Exterior	2.5	1.96	1.28	2.57	2.15	1.20
3.2	FLS	Exterior	2.85	2.38	1.20	2.95	2.50	1.18
2	FLS	Interior	2.25	1.65	1.36	2.81	2.3	1.22
2.4	FLS	Interior	2.7	2.03	1.33	3.37	2.81	1.20
2.8	FLS	Interior	3.15	2.42	1.30	3.93	3.34	1.18
3.2	FLS	Interior	3.6	2.93	1.23	4.5	3.98	1.13

Table 6.12: Comparison of SDFs from FEA Results and CHBDC equations of concrete bridges with different girder spacing.

Parameters			Shear distribution factor		
Girder spacing (*m*)	Limit state	Girder Type	CHBDC	FEA	R= CHBDC/FEA
2	ULS	Exterior	1.31	1	1.31
2.4	ULS	Exterior	1.57	1.09	1.44
2.8	ULS	Exterior	1.83	1.31	1.39
3.2	ULS	Exterior	2.09	1.54	1.35
2	ULS	Interior	1.31	1.28	1.02
2.4	ULS	Interior	1.57	1.50	1.04
2.8	ULS	Interior	1.83	1.72	1.06
3.2	ULS	Interior	2.09	1.94	1.07
2	FLS	Exterior	2.22	1.53	1.45
2.4	FLS	Exterior	2.66	1.88	1.41
2.8	FLS	Exterior	3.11	2.22	1.40
3.2	FLS	Exterior	3.55	2.62	1.35
2	FLS	Interior	2.22	2.17	1.02
2.4	FLS	Interior	2.66	2.54	1.04
2.8	FLS	Interior	3.11	2.93	1.06
3.2	FLS	Interior	3.55	3.3	1.07

Table 6.13: Comparison of SDFs from FEA Results and CHBDC equations of steel bridges with different girder spacing.

Parameters			Shear distribution factor		
Girder spacing (*m*)	**Limit state**	**Girder Type**	**CHBDC**	**FEA**	**R= CHBDC/FEA**
2	ULS	Exterior	1.64	1.07	1.48
2.4	ULS	Exterior	1.96	1.30	1.51
2.8	ULS	Exterior	2.29	1.54	1.49
3.2	ULS	Exterior	2.62	1.81	1.45
2	ULS	Interior	1.64	1.57	1.04
2.4	ULS	Interior	1.96	1.84	1.07
2.8	ULS	Interior	2.29	2.11	1.09
3.2	ULS	Interior	2.62	2.39	1.10
2	FLS	Exterior	2.77	1.77	1.56
2.4	FLS	Exterior	3.32	2.18	1.52
2.8	FLS	Exterior	3.88	2.59	1.50
3.2	FLS	Exterior	4.43	3.04	1.46
2	FLS	Interior	2.77	2.65	1.05
2.4	FLS	Interior	3.32	3.11	1.07
2.8	FLS	Interior	3.88	3.58	1.08
3.2	FLS	Interior	4.43	4.045	1.10

6.1.3.4 EFFECT OF INTERMEDIATE DIAPHRAGMS

The analysis results from finite element analysis and CHBDC equations for girder distribution factors of integral abutment bridges with or without intermediate diaphragms are presented in Table 6.14 to 6.17.

Results indicate that presence of intermediate diaphragms (cross bracings) at equal intervals between support lines produce consistent reactions on the substructure. However, due to presence of one or more intermediate diaphragms (cross bracing) in integral abutment bridge, the ratio of the LLDFs obtained from CHBDC to those obtained from FEA was only changed by maximum 5%. Therefore in the development of new live load distribution factor equations, effect of intermediate diaphragms on distribution factors was ignored.

Table 6.14: Comparison of MDFs from FEA Results and CHBDC equations of concrete bridges with different number of bracings.

Parameters			Positive moment distribution factor			Negative moment distribution factor		
Number of diaphragm	Limit state	Girder Type	CHBDC	FEA	R= CHBDC /FEA	CHBDC	FEA	R= CHBDC /FEA
1	ULS	Exterior	1.44	1.06	1.35	1.5	1.32	1.13
2	ULS	Exterior	1.44	1.05	1.37	1.5	1.31	1.14
3	ULS	Exterior	1.44	1.05	1.37	1.5	1.31	1.14
1	ULS	Interior	1.49	1.09	1.36	1.82	1.61	1.13
2	ULS	Interior	1.49	1.08	1.37	1.82	1.59	1.14
3	ULS	Interior	1.49	1.08	1.37	1.82	1.59	1.14
1	FLS	Exterior	1.77	1.30	1.35	1.83	1.61	1.13
2	FLS	Exterior	1.77	1.29	1.37	1.83	1.59	1.14
3	FLS	Exterior	1.77	1.29	1.37	1.83	1.59	1.14
1	FLS	Interior	2.25	1.64	1.36	2.82	2.49	1.13
2	FLS	Interior	2.25	1.62	1.38	2.82	2.46	1.14
3	FLS	Interior	2.25	1.62	1.38	2.82	2.46	1.14

Table 6.15: Comparison of MDFs from FEA Results and CHBDC equations of steel bridges with different number of bracings.

Parameters			Positive moment distribution factor			Negative moment distribution factor		
Number of bracing	Limit state	Girder Type	CHBDC	FEA	R= CHBDC /FEA	CHBDC	FEA	R= CHBDC /FEA
1	ULS	Exterior	1.73	1.19	1.45	1.8	1.47	1.22
2	ULS	Exterior	1.73	1.18	1.47	1.8	1.46	1.23
3	ULS	Exterior	1.73	1.18	1.47	1.8	1.46	1.23
1	ULS	Interior	1.79	1.22	1.47	2.19	1.76	1.24
2	ULS	Interior	1.79	1.22	1.47	2.19	1.75	1.25
3	ULS	Interior	1.79	1.22	1.47	2.19	1.75	1.25
1	FLS	Exterior	2.13	1.46	1.46	2.2	1.80	1.22
2	FLS	Exterior	2.13	1.45	1.47	2.2	1.79	1.23
3	FLS	Exterior	2.13	1.45	1.47	2.2	1.79	1.23
1	FLS	Interior	2.7	1.85	1.46	3.39	2.78	1.22
2	FLS	Interior	2.7	1.84	1.47	3.39	2.76	1.23
3	FLS	Interior	2.7	1.84	1.47	3.39	2.76	1.23

Table 6.16: Comparison of SDFs from FEA Results and CHBDC equations of concrete bridges with different number of bracings.

Parameters			Shear distribution factor		
Number of diaphragm	**Limit state**	**Girder Type**	**CHBDC**	**FEA**	**R= CHBDC/FEA**
1	ULS	Exterior	1.64	1.29	1.26
2	ULS	Exterior	1.64	1.28	1.28
3	ULS	Exterior	1.64	1.28	1.28
1	ULS	Interior	1.64	1.52	1.07
2	ULS	Interior	1.64	1.51	1.08
3	ULS	Interior	1.64	1.51	1.08
1	FLS	Exterior	2.77	2.18	1.27
2	FLS	Exterior	2.77	2.16	1.28
3	FLS	Exterior	2.77	2.16	1.28
1	FLS	Interior	2.77	2.57	1.07
2	FLS	Interior	2.77	2.56	1.08
3	FLS	Interior	2.77	2.56	1.08

Table 6.17: Comparison of SDFs from FEA Results and CHBDC equations of steel bridges with different number of bracings.

Parameters			Shear distribution factor		
Number of Bracing	**Limit state**	**Girder Type**	**CHBDC**	**FEA**	**R= CHBDC/FEA**
1	ULS	Exterior	1.96	1.43	1.37
2	ULS	Exterior	1.96	1.42	1.38
3	ULS	Exterior	1.96	1.42	1.38
1	ULS	Interior	1.96	1.78	1.10
2	ULS	Interior	1.96	1.77	1.11
3	ULS	Interior	1.96	1.77	1.11
1	FLS	Exterior	3.33	2.43	1.37
2	FLS	Exterior	3.33	2.40	1.39
3	FLS	Exterior	3.33	2.40	1.39
1	FLS	Interior	3.33	3.02	1.10
2	FLS	Interior	3.33	3.00	1.11
3	FLS	Interior	3.33	3.00	1.11

6.1.4 DEVELOPMENT OF NEW DISTRIBUTION FACTOR EQUATIONS FOR INTEGRAL ABUTMENT BRIDGES

As stated earlier in chapter 1, one of the objectives of this study was to develop empirical expressions to evaluate moment and shear distribution factors.

The finite element analysis results presented in Tables 6.14 to 6.17 reveal that the variation of the LLDFs for the exterior and interior girders of integral abutment bridges as a function of the number of bracing or diaphragm was modest. Accordingly, live load distribution equations (LLDEs) for girders of integral abutment bridges were developed considering the span length, *L*, girder spacing, *S*, and number of design lanes, *n*. Based on the data generated from parametric study on integral bridges and using regression analysis techniques, first in section 6.1.4.1 sets of live load distribution equations (LLDEs) were developed in the form of correction factors to multiplied by to the available CHBDC values for conventional slab-on-girder bridges supported over isolated bearings. Then in section 6.1.4.2, new empirical equations for distribution factors were proposed in the same form as CHBDC. These factors were given to estimate live load moments and shears for interior and exterior of integral bridges at ultimate, serviceability and fatigue limit state designs.

6.1.4.1 CORRECTION FACTORS TO ESTIMATE LIVE LOAD DISTRIBUTION FACTORS FOR ITEGRAL ABUTMENT BRIDGE GIRDERS

A set of equations in the form of correction factors were presented to obtain the LLDFs for the exterior and interior of integral abutment bridges at ultimate and fatigue limit state. To calculate the LLDF for the girder moment of girders in integral bridges at ULS design, the CHBDC LLDF obtained from Equation (2.22) was simply multiplied by a correction factor, C_f. Accordingly, the LLDE for the girder moment of exterior girder of concrete bridges was expressed as:

$$F_{m,IAB} = C_f \times F_{m,CHBDC} = C_f \times \frac{SN}{F(1+\frac{\mu C_f}{100})} \tag{6.6}$$

The correction factor, C_f, was assumed to have the following form:

$$C_f = a \times L^b \times S^c \times n^d \tag{6.7}$$

Where a, b and c constants to be determined via regression analyses, based on the least square method, using the data presented in Tables 6.2 to Table 6.13. Tables 6.18 to 6.21 summarize correction factor equations that can be used to estimate live load distribution factors for steel and concrete I-girder bridges. CHBDC equations are able to predict the shear distribution factors for interior girders with reasonable accuracy (within 7 to 8%). Therefore, CHBDC live load distribution equations can be conservatively used to calculate the live load shear forces in the interior girders of integral bridges.

Table 6.18: Correction factor equations for moment of concrete integral abutment bridge.

Girder	Proposed Correction Factor for Moment Distribution Factor (C_f)			
	ULS and SLS		FLS	
	Positive Moment	Negative Moment	Positive Moment	Negative Moment
Exterior	$C_f = 0.786 \times L^{0.015} \times S^{0.105} \times n^{-0.06}$	$C_f = 0.838 \times L^{0.011} \times S^{0.104} \times n^{-0.05}$	$C_f = 0.847 \times L^{0.011} \times S^{0.104} \times n^{-0.05}$	$C_f = 0.791 \times L^{0.011} \times S^{0.104} \times n^{-0.05}$
Interior	$C_f = 0.869 \times L^{0.011} \times S^{0.105} \times n^{-0.12}$	$C_f = 0.757 \times L^{0.032} \times S^{0.163} \times n^{-0.04}$	$C_f = 0.593 \times L^{0.074} \times S^{0.38} \times n^{-0.12}$	$C_f = 0.837 \times L^{0.015} \times S^{0.164} \times n^{-0.04}$

Table 6.19: Correction factor equations for shear of concrete integral abutment bridge.

Girder	Proposed Correction Factor for Shear Distribution Factor (C_f)	
	ULS and SLS	FLS
Exterior	$C_f = 0.986 \times L^{-0.1} \times S^{0.157} \times n^{-0.06}$	$C_f = 1.103 \times L^{-0.11} \times S^{0.136} \times n^{-0.06}$
Interior	$C_f = 1$	$C_f = 1$

Table 6.20: Correction factor equations for moment of steel integral abutment bridge.

Girder	Proposed Correction Factor for Moment Distribution Factor (C_f)			
	ULS and SLS		FLS	
	Positive Moment	Negative Moment	Positive Moment	Negative Moment
Exterior	$C_f = 0.665 \times L^{0.012} \times S^{0.109} \times n^{-0.12}$	$C_f = 0.71 \times L^{0.008} \times S^{0.125} \times n^{-0.06}$	$C_f = 0.736 \times L^{0.001} \times S^{0.112} \times n^{-0.24}$	$C_f = 0.764 \times L^{0.0009} \times S^{0.126} \times n^{-0.1}$
Interior	$C_f = 0.515 \times L^{0.103} \times S^{0.209} \times n^{-0.08}$	$C_f = 0.636 \times L^{0.034} \times S^{0.161} \times n^{-0.03}$	$C_f = 0.534 \times L^{0.076} \times S^{0.21} \times n^{-0.04}$	$C_f = 0.626 \times L^{0.048} \times S^{0.16} \times n^{-0.05}$

Table 6.21: Correction factor equation for shear of steel integral abutment bridge.

Girder	Proposed Correction Factor for Shear Distribution Factor (C_f)	
	ULS and SLS	FLS
Exterior	$C_f = 0.933 \times L^{-0.11} \times S^{0.124} \times n^{-0.02}$	$C_f = 0.944 \times L^{-0.11} \times S^{0.136} \times n^{-0.02}$
Interior	$C_f = 1$	$C_f = 1$

6.1.4.1.1 VERIFICATION OF CORRECTION FACTORS AND LIVE LOAD DISTRIBUTION EQUATIONS FOR INTEGRAL BRIDGES

The live load distribution equations (LLDEs) derived for girder moments and shears of integral abutment bridges were verified against available FEA results. For this purpose, live load distribution factors (LLDFs) for the girder moment and shear of integral abutment bridges were calculated using CHBDC LLDEs, CHBDC LLDEs multiplied by the reduction correction factors (new formula) and finite element analysis (FEA).

The LLDFs obtained from CHBDC equations, proposed equations (New Formula) and FEA results are presented in Table 6.22 and 6.23 for 2 design lanes concrete and steel integral bridge with 2 *m* girder spacing and 20 *m* span length. As observed from Table 6.22, CHBDC live load distribution equations generally produce conservative estimates of live load girder moments and shear for exterior and interior girder in integral abutment bridges for the range of values of span length, girder spacing and number of design lanes considered in this study. However, the proposed correction factors multiplied by the CHBDC live load distribution equations (New Formula) produce reasonable estimates of live load moments in the girders of single-span short to medium length integral abutment bridges. To further verify the applicability of the proposed equations to integral abutment bridges, the difference in percentage of the LLDFs obtained from the proposed and CHBDC live load distribution equations to FEA results are presented in Table 6.22 for the entire data obtained from the analyses. The proposed correction factors produce averages ranging between 1.01 and 1.05. Nevertheless, CHBDC live load distribution equations produce averages ranging between 1.13 and 1.47. This clearly indicates that the proposed correction factors produce more reasonable and less scattered estimates of live load effects in integral abutment bridge girders compared to CHBDC live load distribution equations.

Table 6.22: LLDFs obtained from the proposed LLDEs, CHBDC LLDEs and FEA for concrete bridges.

Moment (M) and Shear (V)	Limit State	Distribution Factor			Difference %	
		CHBDC	New Formula	FEA	CHBDC and FEA	New Formula and FEA
$M_{Exterior\text{-}Positive}$	ULS	1.15	0.98	1	15	2
$M_{Exterior\text{-}Negative}$	ULS	1.2	1.07	1.06	13	1
$M_{Exterior\text{-}Positive}$	FLS	1.42	1.2	1.19	19	1
$M_{Exterior\text{-}Negative}$	FLS	1.47	1.23	1.28	15	4
$M_{Interior\text{-}Positive}$	ULS	1.19	1.05	1	19	5
$M_{Interior\text{-}Negative}$	ULS	1.46	1.31	1.29	13	1
$M_{Interior\text{-}Positive}$	FLS	1.8	1.58	1.51	19	4
$M_{Interior\text{-}Negative}$	FLS	2.25	2.14	2.04	10	5
$V_{Exterior}$	FLS	1.31	0.95	1	35	5
$V_{Interior}$	FLS	2.22	1.62	1.53	45	5

Table 6.23: LLDFs obtained from the proposed LLDEs, CHBDC LLDEs and FEA for steel bridges.

Moment (M) and Shear (V)	Limit State	Distribution Factor			Difference %	
		CHBDC	New Formula	FEA	CHBDC and FEA	New Formula and FEA
$M_{Exterior\text{-}Positive}$	ULS	1.76	1.24	1.28	37	3
$M_{Exterior\text{-}Negative}$	ULS	1.8	1.4	1.47	22	5
$M_{Exterior\text{-}Positive}$	FLS	2.15	1.51	1.58	36	4
$M_{Exterior\text{-}Negative}$	FLS	2.24	1.64	1.74	28	5
$M_{Interior\text{-}Positive}$	ULS	1.78	1.41	1.34	32	5
$M_{Interior\text{-}Negative}$	ULS	2.19	1.73	1.83	19	5
$M_{Interior\text{-}Positive}$	FLS	2.7	2.1	2.03	33	3
$M_{Interior\text{-}Negative}$	FLS	3.37	2.76	2.81	19	2
$V_{Exterior}$	FLS	1.96	1.41	1.35	45	4
$V_{Interior}$	FLS	3.32	2.25	2.34	47	4

6.1.4.2 EMPERICAL EQUATIONS FOR THE LOAD DISTRIBUTION FACTORS IN THE SAME FORM AS CHBDC EXPRESSIONS

Based on results obtained from the parametric study on selected bridge configurations, empirical expressions similar to format of CHBDC expressions were developed for positive moment, negative moment and shear distribution factors (F_m^+, F_m^- and F_v) of single-span integral bridges at ultimate and fatigue limit states. The developed empirical formulas for CHBDC truck load include the following parameters:

1- Span length of the bridge (L)

2- Girder spacing (S)

3- Number of lanes (n)

Using a statistical computer package for best fit based on the method of least squares, the empirical formulas for distribution factors were developed with minimum error. It should be noted that the highest values for a specific girder from all the loading cases were considered in the creation of the empirical equations.

The following expressions were derived in the same format, as those originally exist in CHBDC for integral bridge girders.

6.1.4.2.1 EMPERICAL EQUATIONS FOR MOMENT DISTRIBUTION FACTORS

For positive and negative moment distribution factors due to CHBDC live loading for ultimate and fatigue limit states design:

$$F_{m,IAB} = \frac{SN}{F(1+\frac{\mu C_f}{100})} \tag{6.8}$$

It should be noted that the values of F and C_f in CHBDC equations are a linear function of span length (L) in case of ultimate and fatigue limit state designs for longitudinal moments.

Based on the data generated from the parametric study, it was observed that the span length, girder spacing and number of design lanes have an effect on the response and they should be included in the developed expressions. As such, it was decided to use F and C_f in the following forms.

$$F = (a + bL)S^c \tag{6.9}$$

$$C_f = d + eL \quad (6.10)$$

Where, a, b, c, d and e are new constants in the proposed empirical equation. Typical samples of the results from CHBDC and parameters of empirical equations are given in Appendix A.1 to Appendix B.10.

In this study, new empirical expressions were developed for the positive and negative moment distribution factors for ULS, SLS and FLS. Data generated from the parametric study was used to develop the new parameters (F, C_f) and their constants (a, b, c, d and e). Tables 6.24 and 6.27 present developed parameters of empirical equations of positive and negative moment distribution factors at ultimate limit state (ULS) for concrete and steel integral bridges, respectively. While Tables 6.28 and 6.31 present the developed parameters of the empirical equations of positive and negative moment distribution factors for concrete and steel integral bridges at fatigue limit state (FLS), respectively. These parameters were developed to be in a similar format to that used in CHDBC simplified method of analysis.

Table 6.24: Equation parameters for positive moment distribution factor of concrete bridges at ULS.

No of Design lanes	Girder Position	Value of F	Value of C_f
1	External	$(14.69+0.38L)\ S^{-0.10}$	$-78.42-0.12L$
	Internal	$(15.59+0.18L)\ S^{-0.10}$	$-77.78-0.01L$
2	External	$(23.87+0.52L)\ S^{-0.10}$	$-71.80-0.12L$
	Internal	$(23.72+0.28L)\ S^{-0.10}$	$-72.08-0.01L$
3	External	$(29.97+0.38L)\ S^{-0.10}$	$-67.32-0.04L$
	Internal	$(29.72+0.34L)\ S^{-0.10}$	$-67.98-0.01L$
4	External	$(33.15+0.39L)\ S^{-0.10}$	$-65.60-0.02L$
	Internal	$(33.48+0.49L)\ S^{-0.10}$	$-65.43-0.07L$

Table 6.25: Equation parameters for negative moment distribution factor of concrete bridges at ULS.

No of Design lanes	Girder Position	Value of F	Value of C_f
1	External	$(16.35+0.10L)\ S^{-0.10}$	-77.24-0.06*L*
	Internal	$(17.21+0.18L)\ S^{-0.16}$	-76.65-0.10*L*
2	External	$(25.50+0.11L)\ S^{-0.10}$	-70.81-0.02*L*
	Internal	$(23.01+0.17L)\ S^{-0.16}$	-72.49-0.10*L*
3	External	$(30.85+0.11L)\ S^{-0.10}$	-67.12-0.02*L*
	Internal	$(27.79+0.24L)\ S^{-0.16}$	-68.51-0.13*L*
4	External	$(33.96+0.09L)\ S^{-0.10}$	-64.96-0.01*L*
	Internal	$(31.88+0.11L)\ S^{-0.16}$	-66.21-0.03*L*

Table 6.26: Equation parameters for positive moment distribution factor of steel bridges at ULS.

No of Design lanes	Girder Position	Value of F	Value of C_f
1	External	$(16.50+0.44L)\ S^{-0.11}$	-77.22-0.12*L*
	Internal	$(19.53+0.05L)\ S^{-0.21}$	-75.05+0.07*L*
2	External	$(27.03+0.59L)\ S^{-0.11}$	-69.16-0.13*L*
	Internal	$(28.18+0.09L)\ S^{-0.21}$	-68.33+0.07*L*
3	External	$(33.11+0.67L)\ S^{-0.11}$	-64.40-0.14*L*
	Internal	$(34.42+0.12L)\ S^{-0.21}$	-63.66+0.07*L*
4	External	$(40.79+0.73L)\ S^{-0.11}$	-65.20-0.10*L*
	Internal	$(38.55+0.12L)\ S^{-0.21}$	-60.57-0.08*L*

Table 6.27: Equation parameters for negative moment distribution factor of steel bridges at ULS.

No of Design lanes	Girder Position	Value of F	Value of C_f
1	External	$(19.14+0.01L)\ S^{-0.12}$	-75.27-0.02L
	Internal	$(19.85+0.15L)\ S^{-0.16}$	-74.73-0.11L
2	External	$(29.26+0.10L)\ S^{-0.10}$	-67.56-0.10L
	Internal	$(25.43+0.18L)\ S^{-0.16}$	-70.31-0.12L
3	External	$(35.12+0.09L)\ S^{-0.10}$	-63.16-0.09L
	Internal	$(30.70+0.24L)\ S^{-0.16}$	-65.96-0.16L
4	External	$(38.25+0.11L)\ S^{-0.10}$	-60.83-0.10L
	Internal	$(34.75+0.19L)\ S^{-0.16}$	-63.54-0.12L

Table 6.28: Equation parameters for positive moment distribution factor of concrete bridges at FLS.

No of Design lanes	Girder Position	Value of F	Value of C_f
1	External	$(18.78+0.13L)\ S^{-0.10}$	-75.54-0.07L
	Internal	$(21.86-0.01L)\ S^{-0.38}$	-73.24-0.01L
2	External	$(23.30+0.06L)\ S^{-0.10}$	-72.27-0.03L
	Internal	$(23.92-0.01L)\ S^{-0.38}$	-71.95-0.02L
3	External	$(23.57+0.08L)\ S^{-0.10}$	-72.04-0.06L
	Internal	$(24.16-0.01L)\ S^{-0.38}$	-71.74-0.01L
4	External	$(24.11+0.09L)\ S^{-0.10}$	-71.67-0.06L
	Internal	$(25.05-0.01L)\ S^{-0.38}$	-71.14-0.02L

Table 6.29: Equation parameters for negative moment distribution factor of concrete bridges at FLS.

No of Design lanes	Girder Position	Value of F	Value of C_f
1	External	$(22.05+0.10L)\ S^{-0.10}$	-73.18-0.07L
	Internal	$(20.05+0.01L)\ S^{-0.16}$	-76.21+0.01L
2	External	$(24.13+0.02L)\ S^{-0.10}$	-71.75-0.01L
	Internal	$(20.21+0.01L)\ S^{-0.16}$	-74.53+0.01L
3	External	$(24.03+0.02L)\ S^{-0.10}$	-71.56+0.01L
	Internal	$(20.16+0.01L)\ S^{-0.16}$	-74.64+0.01L
4	External	$(25.24+0.02L)\ S^{-0.1}$	-70.98-0.01L
	Internal	$(20.75+0.05L)\ S^{-0.16}$	-74.14-0.04L

Table 6.30: Equation parameters for positive moment distribution factor of steel bridges at FLS.

No of Design lanes	Girder Position	Value of F	Value of C_f
1	External	$(20.70+0.17L)\ S^{-0.11}$	-74.08-0.09L
	Internal	$(23.21-0.01L)\ S^{-0.21}$	-72.14-0.02L
2	External	$(27.41+0.16L)\ S^{-0.11}$	-68.85-0.10L
	Internal	$(28.30-0.02L)\ S^{-0.21}$	-68.21-0.02L
3	External	$(29.17+0.13L)\ S^{-0.11}$	-67.36-0.08L
	Internal	$(24.33-0.01L)\ S^{-0.21}$	-71.60-0.02L
4	External	$(30.74+0.15L)\ S^{-0.11}$	-66.08-0.09L
	Internal	$(24.90-0.02L)\ S^{-0.21}$	-71.27-0.02L

Table 6.31: Equation parameters for negative moment distribution factor of steel bridges at FLS.

No of Design lanes	Girder Position	Value of F	Value of C_f
1	External	$(22.76+0.12L)\ S^{-0.12}$	-72.60-0.08*L*
	Internal	$(23.21-0.01L)\ S^{-0.16}$	-73.85-0.01*L*
2	External	$(25.41+0.06L)\ S^{-0.12}$	-70.66-0.04*L*
	Internal	$(23.37-0.01L)\ S^{-0.16}$	-71.98-0.01*L*
3	External	$(25.80+0.05L)\ S^{-0.12}$	-70.05-0.03*L*
	Internal	$(23.42-0.01L)\ S^{-0.16}$	-72.06-0.01*L*
4	External	$(26.98+0.10L)\ S^{-0.12}$	-69.47-0.08*L*
	Internal	$(23.99-0.01L)\ S^{-0.16}$	-71.54-0.01*L*

6.1.4.2.2 EMPERICAL EQUATIONS FOR SHEAR DISTRIBUTION FACTORS

For the developed shear distribution factor equation, the following equation was proposed

$$F_{v,IAB} = \frac{SN}{F} \tag{6.11}$$

The parameter considered in this study for F is a multiplier of a linear function of span length (L) and exponential function of the girder spacing in a bridge cross-section as follows:

$$F = (a + bL)S^c \tag{6.12}$$

Tables 6.32 through 6.35 present developed parameters of the empirical equation for shear distribution factors of concrete and steel integral abutment bridges at ULS and FLS for exterior girder. It can be observed that in the new parameter empirical equation, values of a and b are different for different number of lanes, but the value of c is constant for different number of lanes.

Table 6.32: Equation parameters shear distribution factor of concrete bridges at ULS.

No of Design lanes	Girder Position	Value of F
1	External	$(3.53+0.02L)\ S^{-0.16}$
2	External	$(8.20+0.03L)\ S^{-0.16}$
3	External	$(11.29+0.04L)\ S^{-0.16}$
4	External	$(13.22+0.05L)\ S^{-0.16}$

Table 6.33: Equation parameters shear distribution factor of steel bridges at ULS.

No of Design lanes	Girder Position	Value of F
1	External	$(3.80+0.03L)\ S^{-0.13}$
2	External	$(8.61+0.04L)\ S^{-0.13}$
3	External	$(11.67+0.05L)\ S^{-0.13}$
4	External	$(13.51+0.06L)\ S^{-0.13}$

Table 6.34: Equation parameters shear distribution factor of concrete bridges at FLS.

No of Design lanes	Girder Position	Value of F
1	External	$(3.99+0.02L)\ S^{-0.14}$
2	External	$(8.56+0.04L)\ S^{-0.14}$
3	External	$(13.85+0.08L)\ S^{-0.14}$
4	External	$(19.23+0.11L)\ S^{-0.14}$

Table 6.35: Equation parameters shear distribution factor of steel bridges at FLS.

No of Design lanes	Girder Position	Value of F
1	External	$(3.80+0.03L)\ S^{-0.13}$
2	External	$(8.61+0.04L)\ S^{-0.13}$
3	External	$(11.67+0.05L)\ S^{-0.13}$
4	External	$(13.51+0.06L)\ S^{-0.13}$

6.1.4.2.3 CORRELATION BETWEEN LOAD DISTRIBUTION FACTORS FROM FEA RESULTS AND PROPOSED EQUATIONS INDEPENDENT OF CHBDC

The correlation between the developed formulas for positive moment and negative moment distribution factors and the values obtained from the finite-element analysis for ultimate and fatigue limit state designs are shown in Figures 6.81 through 6.84.

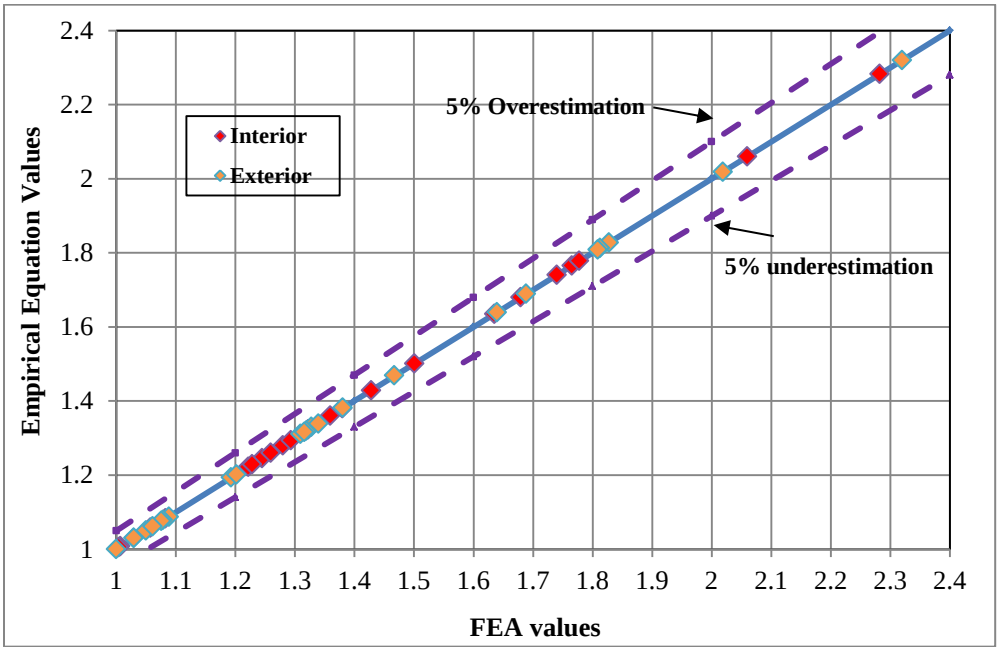

Figure 6.81: Comparison between moment distribution factors from the empirical equation and FEA for concrete bridges at ULS.

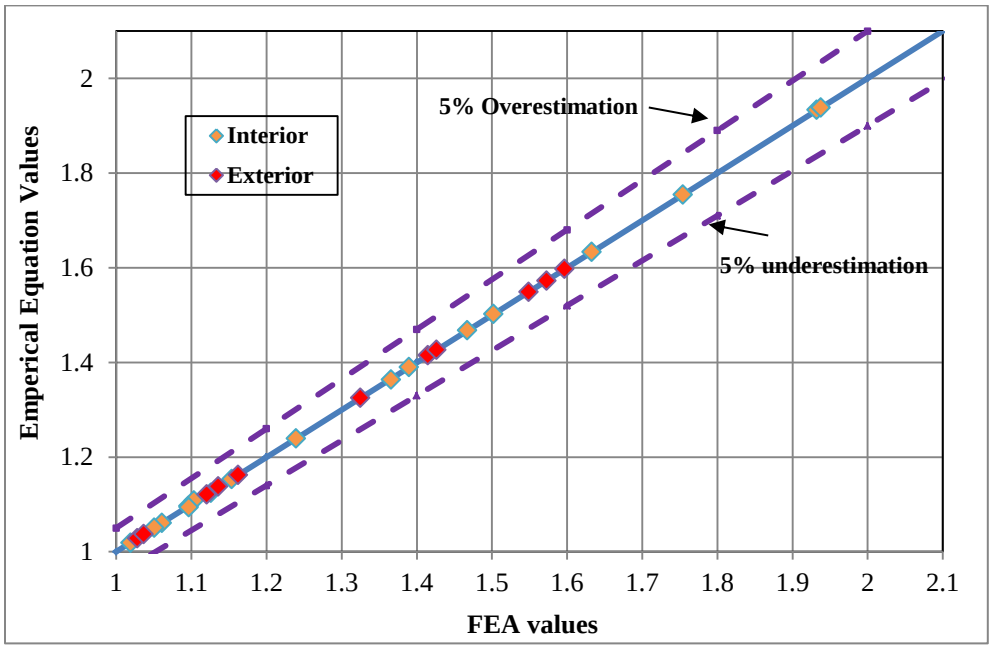

Figure 6.82: Comparison between moment distribution factors from the empirical equation and FEA for steel bridges at ULS.

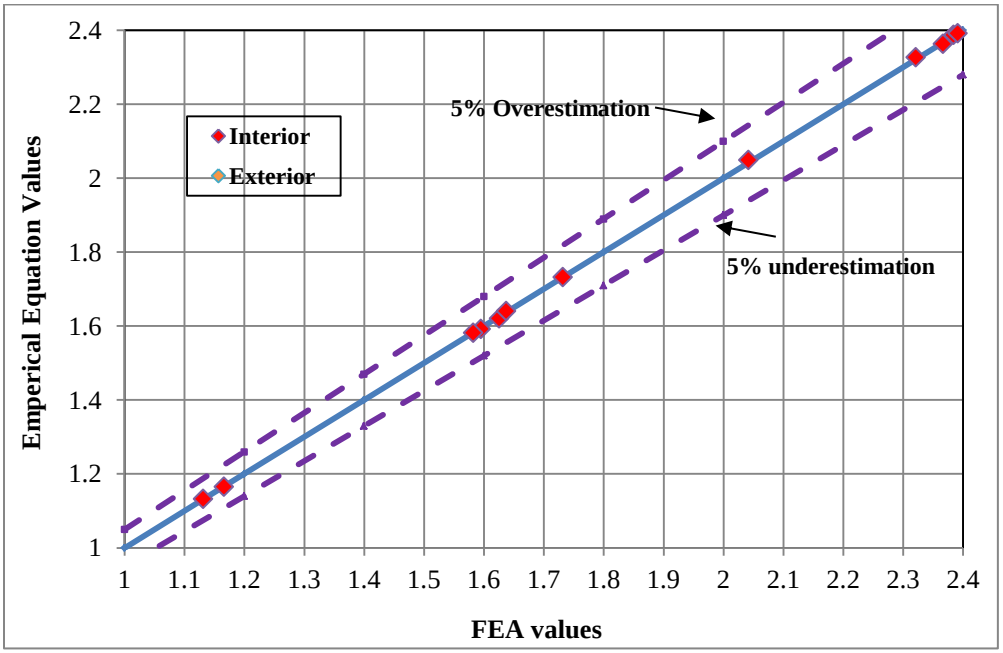

Figure 6.83: Comparison between moment distribution factors from the empirical equation and FEA for concrete bridges at FLS.

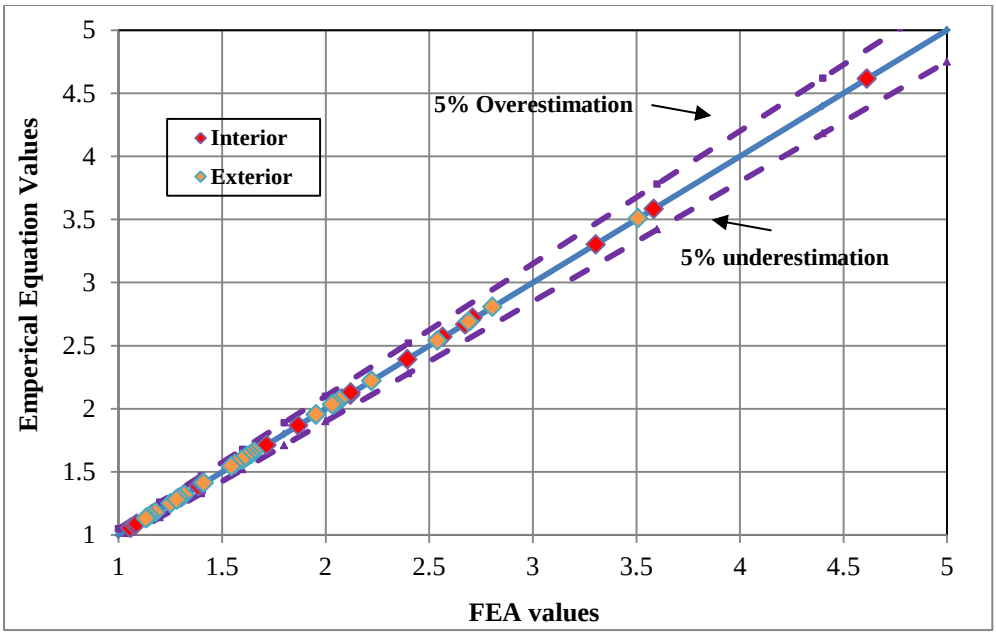

Figure 6.84: Comparison between moment distribution factors from the empirical equation and FEA for steel bridges at FLS.

Figures 6.85 through 6.88 show the correlation between shear distribution factors for exterior girders obtained from proposed empirical equations and FEA at ULS and FLS design.

It is obvious that all graphs show very good correlation between values obtained from developed formulas and those calculated results from FEA.

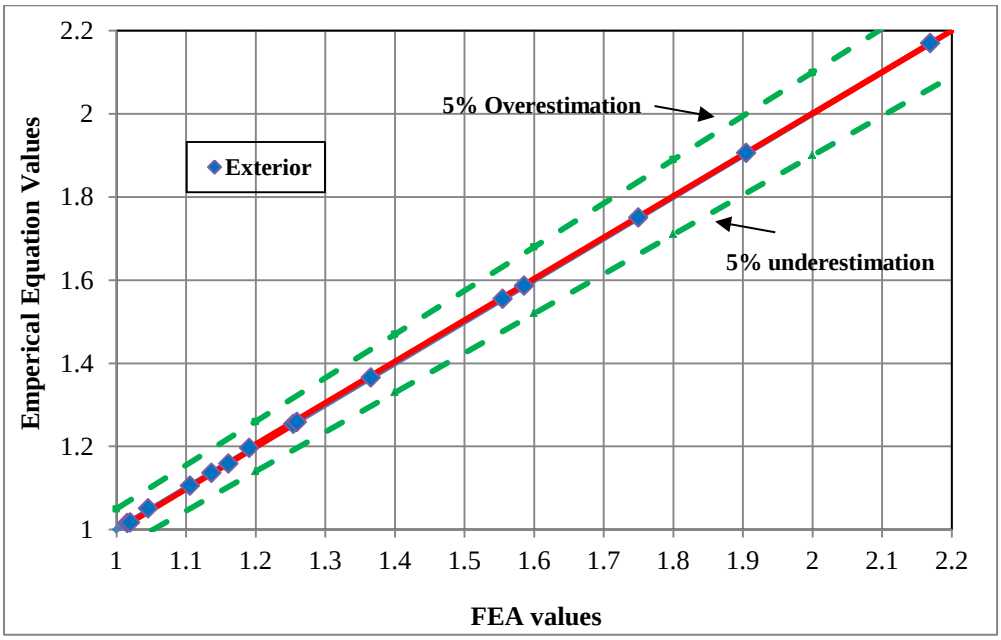

Figure 6.85: Comparison between shear distribution factors from the empirical equation and FEA for concrete bridges at ULS.

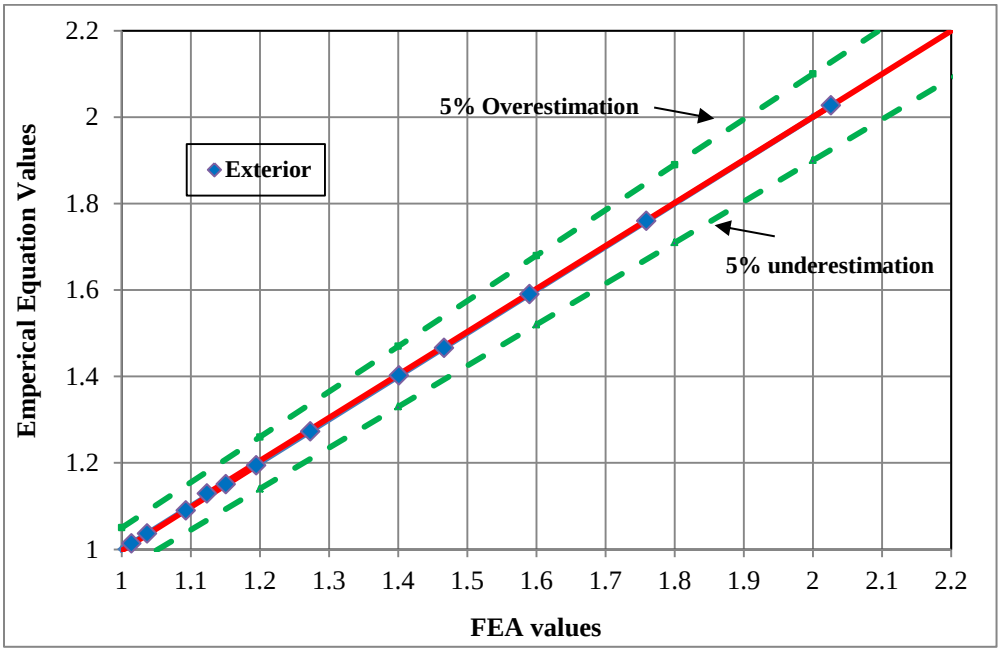

Figure 6.86: Comparison between shear distribution factors from the empirical equation and FEA for steel bridges at ULS.

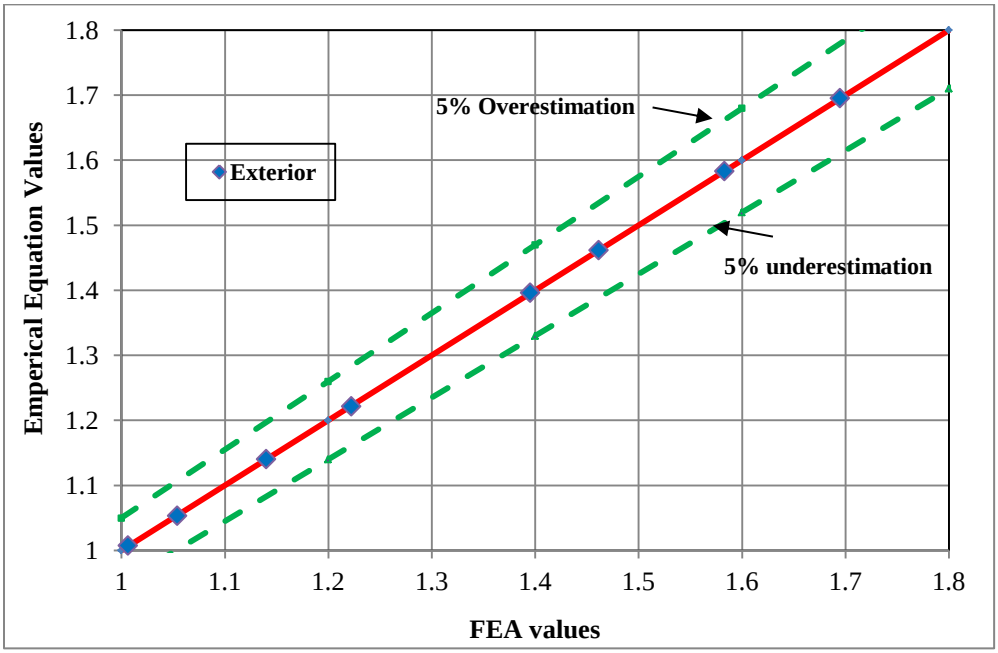

Figure 6.87: Comparison between shear distribution factors from the empirical equation and FEA for concrete bridges at FLS.

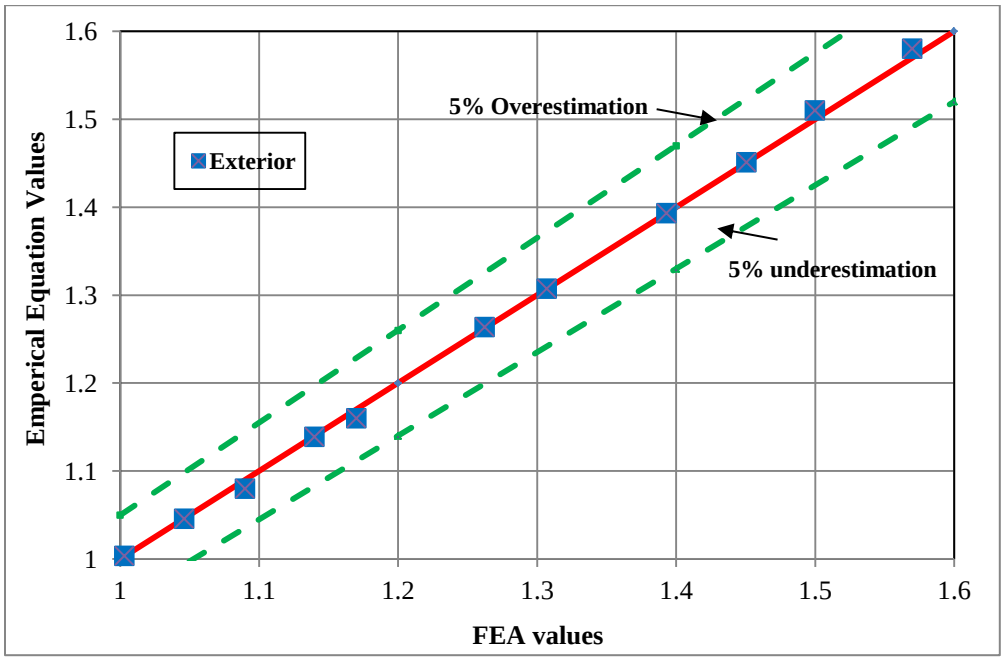

Figure 6.88: Comparison between shear distribution factors from the empirical equation and FEA for steel bridges at FLS.

CHAPTER 7: CONCLUSIONS AND RECOMMENDATIONS FOR FUTURE RESEARCH

7.1 SUMMARY

Many integral abutment bridges were increasingly built in North America during past few decades due to their many advantages in economy and safety. However, a rational guideline to determine the maximum length and skew angle limits for integral bridges due to seasonal temperature variations do not exist in bridge codes. Literature review also revealed that live load distribution among girders in integral abutment bridges due to truck loading conditions is as yet unavailable.

In order to address those situations and possibly expand the use of integral abutment bridges, first, recent literature regarding integral abutment bridge use and performance were reviewed. Next, 3-D finite element models of selected integral bridges were developed. The finite element models were calibrated using data available from filed tests on integral bridges subjected to the seasonal temperature variations and truck loading. Then, a series of practical-design-oriented parametric studies were carried out on integral bridges subjected to temperature variations and CHBDC truck loading conditions. Finally, results obtained from parametric studies were used to deduce new empirical expressions for length limits and girder live load distribution factors.

7.2 CONCLUSIONS

Based on the results obtained from the parametric study conducted on selected integral abutment bridge configurations subjected to seasonal temperature variations and CHBDC truck loading, the following conclusions can be drawn:

1- The effect of the orientation of the steel H-piles on the pile displacement of integral bridges with stub abutments is negligible.

2- A concrete bridge has longer allowable total length than that for a steel bridge as the former is less sensitive to seasonal temperature variations.

3- Abutments height has a significant influence on pile displacement. Accordingly, taller abutment is recommended to be built to increase the length limits of integral bridges based on the ability of piles to sustain thermal displacements.

4- Variations in the abutment thickness within the practical range have only a minor effect on the pile deformation and pile bending moment.

5- With increase in skew angle more than 20^o (representing a reasonable upper limit for skewed integral bridge in this study), integral abutment bridges experience transverse movement due to skewness. Skewed bridges with skew angles less than 20^o exhibited insignificant transverse movement under seasonal temperature variations.

6- Larger pile sizes in integral abutment bridges cause noticeably smaller pile-head displacement and smaller pile-head moment.

7- Different soil types (i.e., soft to stiff clay or loose to dense sand) have very little effect on substructure deformation and pile bending moments.

8- With an increase in total bridge length, substructure deformation, pile deformations and pile stresses increase correspondingly.

9- Wingwall lengths (i.e. 3, 4 and 5 *m*) and wingwall orientations (perpendicular, 45^o and parallel to traffic direction) has insignificant impact on the behaviour of integral abutment bridges.

10- The performance of integral abutment bridges with the same total length is not affected by different girder depths (shallow and deep girders).

11- Different girder types including steel I-girders and box-girders have a secondary influence on the pile performance that can be ignored on defining maximum length limits.

12- A change in the number of design lanes, and consequently the bridge width, significantly affects the transverse displacements of an integral abutment when the bridge-skew angle, θ, exceeds about 20^o.

13- Straight integral abutment bridges with the same length have similar longitudinal pile displacements irrespective of different number of design lanes or bridge width.

14- Sets of empirical equations of the bridge limiting length to ignore effects of temperature variations on integral abutment bridges were developed for concrete and steel bridges in the form of steel pile size, abutment height, abutment pile connection type, skew angle and number of design lanes. This set of empirical equations has the following scope and limitations of use: (i) number of design lanes ranges from 1 to 8; (ii) the abutment-pile joint can be hinged or fixed; (iii) the developed equations are applicable to slab-on-girder bridges and multi-box girder bridges, both make of concrete or steel materials; (iv) the developed equations are applicable to three H-pile sizes, namely: HP200 ×53, HP 250 ×85, and HP 310 ×110; (v) the bridge skew angle does not exceed 60°; and (vi) abutment height ranges from 1 to 6 *m*.

15- Variations in the abutment height and thickness within the practical range have insignificant effect on the girder live load distribution.

16- Changes in wingwall length and orientations (perpendicular and parallel to direction of traffic) have very slight impact on the girder distribution factors.

17- Number of design lanes, girders spacing and bridge length proved to have significant influence on live load distribution factors.

18- The presence and change in numbers of intermediate diaphragms or cross bracings have very little effect on live load distribution factors.

19- Live load distribution equations for slab-on-girder bridges specified in CHBDC predict the shear distribution factors for interior girders of integral abutment bridges with reasonable accuracy provided that the span length, L, in this equation is obtained based on 2D frame analysis of the integral bridge under uniformly distributed dead load.

20- Live load distribution equations specified in CHBDC for slab-on-girder bridges lead to significant overestimation for the interior and exterior girder moments and exterior girder shear force when compared to the results obtained from finite-element analyses.

21- First set of empirical expressions were developed in the form of correction factors which can be apply to the CHBDC live load distribution equations for slab-on-girder bridges to obtain a reliable and better estimation of the girder moments and exterior girder shear force of single-span integral abutment bridges.

22- Second set of empirical expressions were developed for the girder moment and exterior girder shear of integral abutment bridges in the same form as those specified in CHBDC for possible inclusion in CHBDC for integral abutment bridges. These empirical expressions can be applied to integral abutment bridges provided that: (i) the integral abutment bridges is of single span with length ranging from 10 to 45 *m*; (ii) the number of design lanes ranges from 1 to 4; (iii) the bridge is made of slab-on-girders with girders made of steel or concrete I shapes; (vi) the skew angle is 0; the applied load is CHBDC truck loading; the span length, L, in the expression is based on 2D frame analysis of the integral abutment bridge subjected to uniform dead load.

7.3 RECOMMENDATIONS FOR FUTURE RESEARCH

It is recommended that further research efforts be directed to address the following:

1- Investigate the effect of skewness of bridge superstructure on the live load distribution of integral abutment bridges.

2- Study the load distribution in curved integral bridges.

3- Extension of the developed load distribution factors to rigid frame bridges.

4- Extending integral concepts to curved bridges by investigating their live distribution factors and bridge span limitations for seasonal temperature variations.

5- As some curved bridges are skewed at the ends, skewness is another topic that should be incorporated into the effects of curvature on the performance of integral abutment bridges.

6- Development of live load distribution factors for axial load, bending moment and shear force of piles in integral bridges.

7- Prestressed concrete piles can be viable alternative to steel H-piles for short bridges. Correlation between the prestressed concrete piles and the steel H-piles with respect to bridge span limitation and skew angles due to temperature variations, along with the bridge structural performance under live load, needs to be investigated.

8- Study the dynamic response of straight and skewed integral abutment bridge under the paasge of truck loading.

9- Study the seismic response of skewed integral abutment bridges.

10- Develop expressions for pile moment and shear resulting from seasonal temperature variations and live load on the bridge superstructure.

APPENDIX A

Table A.1: Empirical equation parameters for moment distribution factors of concrete interior girders at ULS.

Bridge Length, (m)	# of lanes (n)	Girder Spacing, (m)	Results from CHBDC	Parameters of Empirical Equations					Empirical Equation
			F_m^+	a	b	c	d	e	F_m^+
20	1	2	1.05	15.59	0.18	0.10	-77.78	-0.01	1.01
20	1	2.4	1.26	15.59	0.18	0.10	-77.78	-0.01	1.24
20	1	3.2	1.68	15.59	0.18	0.10	-77.78	-0.01	1.65
35	1	2	0.92	15.59	0.18	0.10	-77.78	-0.01	0.89
45	1	2	0.85	15.59	0.18	0.10	-77.78	-0.01	0.83
20	2	2	1.19	23.72	0.28	0.10	-72.08	-0.01	1.05
20	2	2.4	1.43	23.72	0.28	0.10	-72.08	-0.01	1.29
20	2	3.2	1.90	23.72	0.28	0.10	-72.08	-0.01	1.77
35	2	2	1.04	23.72	0.28	0.10	-72.08	-0.01	0.93
45	2	2	0.96	23.72	0.28	0.10	-72.08	-0.01	0.86
20	3	2	1.31	29.72	0.34	0.10	-67.98	-0.01	1.11
20	3	2.4	1.57	29.72	0.34	0.10	-67.98	-0.01	1.36
20	3	3.2	2.10	29.72	0.34	0.10	-67.98	-0.01	1.86
35	3	2	1.15	29.72	0.34	0.10	-67.98	-0.01	0.98
45	3	2	1.06	29.72	0.34	0.10	-67.98	-0.01	0.90
20	4	2	1.47	33.48	0.49	0.10	-65.43	-0.07	1.20
20	4	2.4	1.76	33.48	0.49	0.10	-65.43	-0.07	1.47
20	4	3.2	2.35	33.48	0.49	0.10	-65.43	-0.07	2.02
35	4	2	1.29	33.48	0.49	0.10	-65.43	-0.07	1.06
45	4	2	1.20	33.48	0.49	0.10	-65.43	-0.07	0.99

Table A.2: Empirical equation parameters for moment distribution factors of concrete interior girders at ULS.

Bridge Length, (m)	**# of lanes (n)**	**Girder Spacing, (m)**	**Results from CHBDC**	**Parameters of Empirical Equations**					**Empirical Equation**
			F_m^-	a	b	c	d	e	F_m^-
20	1	2	1.08	17.21	0.18	0.16	-76.65	-0.10	1.01
20	1	2.4	1.30	17.21	0.18	0.16	-76.65	-0.10	1.24
20	1	3.2	1.76	17.21	0.18	0.16	-76.65	-0.10	1.72
35	1	2	1.04	17.21	0.18	0.16	-76.65	-0.10	0.96
45	1	2	1.03	17.21	0.18	0.16	-76.65	-0.10	0.94
20	2	2	1.46	23.01	0.17	0.16	-72.49	-0.10	1.32
20	2	2.4	1.75	23.01	0.17	0.16	-72.49	-0.10	1.63
20	2	3.2	2.33	23.01	0.17	0.16	-72.49	-0.10	2.28
35	2	2	1.41	23.01	0.17	0.16	-72.49	-0.10	1.28
45	2	2	1.38	23.01	0.17	0.16	-72.49	-0.10	1.26
20	3	2	1.60	27.79	0.24	0.16	-68.51	-0.13	1.43
20	3	2.4	1.92	27.79	0.24	0.16	-68.51	-0.13	1.76
20	3	3.2	2.56	27.79	0.24	0.16	-68.51	-0.13	2.47
35	3	2	1.54	27.79	0.24	0.16	-68.51	-0.13	1.38
45	3	2	1.52	27.79	0.24	0.16	-68.51	-0.13	1.36
20	4	2	1.80	31.88	0.11	0.16	--66.21	-0.03	1.59
20	4	2.4	2.16	31.88	0.11	0.16	--66.21	-0.03	1.96
20	4	3.2	2.88	31.88	0.11	0.16	--66.21	-0.03	2.74
35	4	2	1.74	31.88	0.11	0.16	--66.21	-0.03	1.54
45	4	2	1.71	31.88	0.11	0.16	--66.21	-0.03	1.51

Table A.3: Empirical equation parameters for moment distribution factors of concrete exterior girders at ULS.

Bridge Length, (*m*)	**# of lanes (n)**	**Girder Spacing, (*m*)**	**Results from CHBDC**	**Parameters of Empirical Equations**					**Empirical Equation**
			F_m^+	***a***	***b***	***c***	***d***	***e***	F_m^+
20	1	2	1.13	14.69	0.38	0.10	-78.42	-0.12	1.00
20	1	2.4	1.36	14.69	0.38	0.10	-78.42	-0.12	1.22
20	1	3.2	1.81	14.69	0.38	0.10	-78.42	-0.12	1.68
35	1	2	0.98	14.69	0.38	0.10	-78.42	-0.12	0.87
45	1	2	0.92	14.69	0.38	0.10	-78.42	-0.12	0.82
20	2	2	1.15	23.87	0.52	0.10	-71.80	-0.12	0.97
20	2	2.4	1.38	23.87	0.52	0.10	-71.80	-0.12	1.19
20	2	3.2	1.84	23.87	0.52	0.10	-71.80	-0.12	1.64
35	2	2	1.00	23.87	0.52	0.10	-71.80	-0.12	0.85
45	2	2	0.93	23.87	0.52	0.10	-71.80	-0.12	0.80
20	3	2	1.30	29.97	0.38	0.10	-67.32	-0.04	1.07
20	3	2.4	1.56	29.97	0.38	0.10	-67.32	-0.04	1.32
20	3	3.2	2.08	29.97	0.38	0.10	-67.32	-0.04	1.81
35	3	2	1.14	29.97	0.38	0.10	-67.32	-0.04	0.95
45	3	2	1.06	29.97	0.38	0.10	-67.32	-0.04	0.88
20	4	2	1.51	33.15	0.39	0.10	-65.60	-0.02	1.23
20	4	2.4	1.81	33.15	0.39	0.10	-65.60	-0.02	1.50
20	4	3.2	2.41	33.15	0.39	0.10	-65.60	-0.02	2.06
35	4	2	1.32	33.15	0.39	0.10	-65.60	-0.02	1.08
45	4	2	1.22	33.15	0.39	0.10	-65.60	-0.02	1.00

Table A.4: Empirical equation parameters for moment distribution factors of concrete exterior girders at ULS.

Bridge Length, (m)	# of lanes (n)	Girder Spacing, (m)	Results from CHBDC	Parameters of Empirical Equations					Empirical Equation
			F_m^-	a	b	c	d	e	F_m^-
20	1	2	1.17	16.35	0.10	0.10	-77.24	-0.06	1.09
20	1	2.4	1.40	16.35	0.10	0.10	-77.24	-0.06	1.33
20	1	3.2	1.87	16.35	0.10	0.10	-77.24	-0.06	1.83
35	1	2	1.17	16.35	0.10	0.10	-77.24	-0.06	1.05
45	1	2	1.17	16.35	0.10	0.10	-77.24	-0.06	1.03
20	2	2	1.20	25.50	0.11	0.10	-70.81	-0.02	1.08
20	2	2.4	1.44	25.50	0.11	0.10	-70.81	-0.02	1.32
20	2	3.2	1.92	25.50	0.11	0.10	-70.81	-0.02	1.81
35	2	2	1.20	25.50	0.11	0.10	-70.81	-0.02	1.03
45	2	2	1.20	25.50	0.11	0.10	-70.81	-0.02	1.00
20	3	2	1.36	30.85	0.11	0.10	-67.12	-0.02	1.20
20	3	2.4	1.63	30.85	0.11	0.10	-67.12	-0.02	1.46
20	3	3.2	2.18	30.85	0.11	0.10	-67.12	-0.02	2.01
35	3	2	1.36	30.85	0.11	0.10	-67.12	-0.02	1.15
45	3	2	1.36	30.85	0.11	0.10	-67.12	-0.02	1.12
20	4	2	1.59	33.96	0.09	0.10	-64.96	-0.01	1.38
20	4	2.4	1.91	33.96	0.09	0.10	-64.96	-0.01	1.69
20	4	3.2	2.54	33.96	0.09	0.10	-64.96	-0.01	2.32
35	4	2	1.59	33.96	0.09	0.10	-64.96	-0.01	1.34
45	4	2	1.59	33.96	0.09	0.10	-64.96	-0.01	1.31

Table A.5: Empirical equation parameters for shear distribution factors of concrete exterior girders at ULS.

Bridge Length, (m)	**# of lanes (n)**	**Girder Spacing, (m)**	**Results from CHBDC**	**Parameters of Empirical Equations**			**Empirical Equation**
			F_v	a	b	c	F_v
20	1	2	1.13	3.53	0.02	0.16	0.92
20	1	2.4	1.36	3.53	0.02	0.16	1.14
20	1	3.2	1.81	3.53	0.02	0.16	1.59
35	1	2	0.98	3.53	0.02	0.16	0.76
45	1	2	0.92	3.53	0.02	0.16	0.68
20	2	2	1.30	8.20	0.03	0.16	1.01
20	2	2.4	1.56	8.20	0.03	0.16	1.25
20	2	3.2	2.08	8.20	0.03	0.16	1.75
35	2	2	1.30	8.20	0.03	0.16	0.96
45	2	2	1.30	8.20	0.03	0.16	0.93
20	3	2	1.45	11.29	0.04	0.16	1.10
20	3	2.4	1.74	11.29	0.04	0.16	1.36
20	3	3.2	2.32	11.29	0.04	0.16	1.90
35	3	2	1.45	11.29	0.04	0.16	1.05
45	3	2	1.45	11.29	0.04	0.16	1.02
20	4	2	1.68	13.22	0.05	0.16	1.26
20	4	2.4	2.02	13.22	0.05	0.16	1.55
20	4	3.2	2.69	13.22	0.05	0.16	2.17
35	4	2	1.68	13.22	0.05	0.16	1.20
45	4	2	1.68	13.22	0.05	0.16	1.16

Table A.6: Empirical equation parameters for moment distribution factors of concrete interior girders at FLS.

Bridge Length, (m)	# of lanes (n)	Girder Spacing, (m)	Results from CHBDC	Parameters of Empirical Equations					Empirical Equation
			F_m^+	a	b	c	d	e	F_m^+
20	1	2	0.94	21.86	-0.01	0.38	-73.24	-0.01	0.90
20	1	2.4	1.21	21.86	-0.01	0.38	-73.24	-0.01	1.17
20	1	3.2	1.77	21.86	-0.01	0.38	-73.24	-0.01	1.73
35	1	2	0.95	21.86	-0.01	0.38	-73.24	-0.01	0.92
45	1	2	0.94	21.86	-0.01	0.38	-73.24	-0.01	0.92
20	2	2	1.80	23.92	-0.01	0.38	-71.95	-0.02	1.59
20	2	2.4	2.15	23.92	-0.01	0.38	-71.95	-0.02	2.05
20	2	3.2	3.15	23.92	-0.01	0.38	-71.95	-0.02	3.05
35	2	2	1.76	23.92	-0.01	0.38	-71.95	-0.02	1.62
45	2	2	1.74	23.92	-0.01	0.38	-71.95	-0.02	1.61
20	3	2	2.75	24.16	-0.01	0.38	-71.74	-0.01	2.33
20	3	2.4	3.31	24.16	-0.01	0.38	-71.74	-0.01	2.99
20	3	3.2	4.54	24.16	-0.01	0.38	-71.74	-0.01	4.44
35	3	2	2.69	24.16	-0.01	0.38	-71.74	-0.01	2.37
45	3	2	2.66	24.16	-0.01	0.38	-71.74	-0.01	2.36
20	4	2	3.60	25.05	-0.01	0.38	-74.14	-0.02	2.94
20	4	2.4	4.33	25.05	-0.01	0.38	-74.14	-0.02	3.78
20	4	3.2	5.76	25.05	-0.01	0.38	-74.14	-0.02	5.61
35	4	2	3.54	25.05	-0.01	0.38	-74.14	-0.02	3.00
45	4	2	3.50	25.05	-0.01	0.38	-74.14	-0.02	3.00

Table A.7: Empirical equation parameters for moment distribution factors of concrete interior girders at FLS.

Bridge Length, (m)	**# of lanes (n)**	**Girder Spacing, (m)**	**Results from FEA**	**Parameters of Empirical Equations**					**Empirical Equation**
			F_m^-	a	b	c	d	e	F_m^-
20	1	2	0.93	20.05	0.01	0.16	-76.21	0.01	0.92
20	1	2.4	1.12	20.05	0.01	0.16	-76.21	0.01	1.12
20	1	3.2	1.60	20.05	0.01	0.16	-76.21	0.01	1.58
35	1	2	0.91	20.05	0.01	0.16	-76.21	0.01	0.90
45	1	2	0.90	20.05	0.01	0.16	-76.21	0.01	0.89
20	2	2	1.78	20.21	0.01	0.16	-74.53	0.01	1.70
20	2	2.4	2.14	20.21	0.01	0.16	-74.53	0.01	2.10
20	2	3.2	2.95	20.21	0.01	0.16	-74.53	0.01	2.93
35	2	2	1.75	20.21	0.01	0.16	-74.53	0.01	1.68
45	2	2	1.73	20.21	0.01	0.16	-74.53	0.01	1.66
20	3	2	2.72	20.16	0.01	0.16	-74.64	0.01	2.56
20	3	2.4	3.26	20.16	0.01	0.16	-74.64	0.01	3.17
20	3	3.2	4.45	20.16	0.01	0.16	-74.64	0.01	4.42
35	3	2	2.70	20.16	0.01	0.16	-74.64	0.01	2.53
45	3	2	2.67	20.16	0.01	0.16	-74.64	0.01	2.51
20	4	2	3.55	20.75	0.05	0.16	-74.14	-0.04	3.29
20	4	2.4	4.26	20.75	0.05	0.16	-74.14	-0.04	4.07
20	4	3.2	5.78	20.75	0.05	0.16	-74.14	-0.04	5.69
35	4	2	3.49	20.75	0.05	0.16	-74.14	-0.04	3.27
45	4	2	3.46	20.75	0.05	0.16	-74.14	-0.04	3.25

Table A.8: Empirical equation parameters for moment distribution factors of concrete exterior girders at FLS.

Bridge Length, (m)	**# of lanes (n)**	**Girder Spacing, (m)**	**Results from CHBDC**	**Parameters of Empirical Equations**					**Empirical Equation**
			F_m^+	a	b	c	d	e	F_m^+
20	1	2	0.93	18.78	0.13	0.10	-75.54	-0.07	0.87
20	1	2.4	1.12	18.78	0.13	0.10	-75.54	-0.07	1.07
20	1	3.2	1.49	18.78	0.13	0.10	-75.54	-0.07	1.47
35	1	2	0.89	18.78	0.13	0.10	-75.54	-0.07	0.84
45	1	2	0.87	18.78	0.13	0.10	-75.54	-0.07	0.83
20	2	2	1.29	23.30	0.06	0.10	-72.27	-0.03	1.29
20	2	2.4	1.59	23.30	0.06	0.10	-72.27	-0.03	1.58
20	2	3.2	2.20	23.30	0.06	0.10	-72.27	-0.03	2.18
35	2	2	1.27	23.30	0.06	0.10	-72.27	-0.03	1.27
45	2	2	1.26	23.30	0.06	0.10	-72.27	-0.03	1.26
20	3	2	2.15	23.57	0.08	0.10	-72.04	-0.06	1.91
20	3	2.4	2.58	23.57	0.08	0.10	-72.04	-0.06	2.34
20	3	3.2	3.44	23.57	0.08	0.10	-72.04	-0.06	3.22
35	3	2	2.11	23.57	0.08	0.10	-72.04	-0.06	1.89
45	3	2	2.09	23.57	0.08	0.10	-72.04	-0.06	1.88
20	4	2	2.79	24.11	0.09	0.10	-71.67	-0.06	2.45
20	4	2.4	3.35	24.11	0.09	0.10	-71.67	-0.06	2.99
20	4	3.2	4.46	24.11	0.09	0.10	-71.67	-0.06	4.11
35	4	2	2.73	24.11	0.09	0.10	-71.67	-0.06	2.41
45	4	2	2.70	24.11	0.09	0.10	-71.67	-0.06	2.39

Table A.9: Empirical equation parameters for moment distribution factors of concrete exterior girders at FLS.

Bridge Length, (m)	**# of lanes (n)**	**Girder Spacing, (m)**	**Results from CHBDC**	**Parameters of Empirical Equations**					**Empirical Equation**
			F_m^-	a	b	c	d	e	F_m^-
20	1	2	0.80	22.05	0.10	0.10	-73.18	-0.07	0.70
20	1	2.4	0.96	22.05	0.10	0.10	-73.18	-0.07	0.86
20	1	3.2	1.28	22.05	0.10	0.10	-73.18	-0.07	1.18
35	1	2	0.78	22.05	0.10	0.10	-73.18	-0.07	0.69
45	1	2	0.77	22.05	0.10	0.10	-73.18	-0.07	0.68
20	2	2	1.48	24.13	0.02	0.10	-71.75	-0.01	1.25
20	2	2.4	1.77	24.13	0.02	0.10	-71.75	-0.01	1.53
20	2	3.2	2.36	24.13	0.02	0.10	-71.75	-0.01	2.10
35	2	2	1.46	24.13	0.02	0.10	-71.75	-0.01	1.25
45	2	2	1.45	24.13	0.02	0.10	-71.75	-0.01	1.24
20	3	2	2.21	24.03	0.01	0.10	-71.56	0.01	1.85
20	3	2.4	2.66	24.03	0.01	0.10	-71.56	0.01	2.25
20	3	3.2	3.53	24.03	0.01	0.10	-71.56	0.01	3.09
35	3	2	2.19	24.03	0.01	0.10	-71.56	0.01	1.82
45	3	2	2.17	24.03	0.01	0.10	-71.56	0.01	1.81
20	4	2	2.84	25.24	0.02	0.10	-70.98	-0.01	2.33
20	4	2.4	3.41	25.24	0.02	0.10	-70.98	-0.01	2.85
20	4	3.2	4.54	25.24	0.02	0.10	-70.98	-0.01	3.91
35	4	2	2.81	25.24	0.02	0.10	-70.98	-0.01	2.32
45	4	2	2.79	25.24	0.02	0.10	-70.98	-0.01	2.30

Table A.10: Empirical equation parameters for shear distribution factors of concrete exterior girders at FLS.

Bridge Length, (m)	# of lanes (n)	Girder Spacing, (m)	Results from CHBDC	Parameters of Empirical Equations			Empirical Equation
			F_v	a	b	c	F_v
20	1	2	1.14	3.99	0.02	0.14	0.99
20	1	2.4	1.37	3.99	0.02	0.14	1.22
20	1	3.2	1.82	3.99	0.02	0.14	1.69
35	1	2	1.12	3.99	0.02	0.14	0.92
45	1	2	1.11	3.99	0.02	0.14	0.88
20	2	2	1.11	8.56	0.04	0.14	0.93
20	2	2.4	1.33	8.56	0.04	0.14	1.14
20	2	3.2	1.78	8.56	0.04	0.14	1.58
35	2	2	1.09	8.56	0.04	0.14	0.86
45	2	2	1.08	8.56	0.04	0.14	0.83
20	3	2	1.05	13.85	0.08	0.14	0.86
20	3	2.4	1.26	13.85	0.08	0.14	1.05
20	3	3.2	1.68	13.85	0.08	0.14	1.46
35	3	2	1.03	13.85	0.08	0.14	0.79
45	3	2	1.02	13.85	0.08	0.14	0.79
20	4	2	1.02	19.23	0.11	0.14	0.82
20	4	2.4	1.22	19.23	0.11	0.14	1.00
20	4	3.2	1.63	19.23	0.11	0.14	1.40
35	4	2	1.02	19.23	0.11	0.14	0.77
45	4	2	0.98	19.23	0.11	0.14	0.72

APPENDIX B

Table B.1: Empirical equation parameters for moment distribution factors of steel interior girders at ULS.

Bridge Length, (m)	# of lanes (n)	Girder Spacing, (m)	Results from CHBDC	Parameters of Empirical Equations					Empirical Equation
			F_m^+	a	b	c	d	e	F_m^+
20	1	2	1.05	19.53	0.05	0.21	-75.05	0.07	0.85
20	1	2.4	1.26	19.53	0.05	0.21	-75.05	0.07	1.06
20	1	3.2	1.68	19.53	0.05	0.21	-75.05	0.07	1.50
35	1	2	0.92	19.53	0.05	0.21	-75.05	0.07	0.79
45	1	2	0.85	19.53	0.05	0.21	-75.05	0.07	0.75
20	2	2	1.19	28.18	0.09	0.21	-68.36	0.07	0.93
20	2	2.4	1.43	28.18	0.09	0.21	-68.37	0.07	1.15
20	2	3.2	1.90	28.18	0.09	0.21	-68.33	0.07	1.63
35	2	2	1.04	28.18	0.09	0.21	-68.33	0.07	0.85
45	2	2	0.96	28.18	0.09	0.21	-68.33	0.07	0.81
20	3	2	1.31	34.42	0.12	0.21	-63.66	0.07	0.99
20	3	2.4	1.57	34.42	0.12	0.21	-63.66	0.07	1.24
20	3	3.2	2.10	34.42	0.12	0.21	-63.66	0.07	1.75
35	3	2	1.15	34.42	0.12	0.21	-63.66	0.07	0.92
45	3	2	1.06	34.42	0.12	0.21	-63.66	0.07	0.88
20	4	2	1.47	38.55	0.12	0.21	-60.57	0.08	1.09
20	4	2.4	1.76	38.55	0.12	0.21	-60.57	0.08	1.36
20	4	3.2	2.35	38.55	0.12	0.21	-60.57	0.08	1.93
35	4	2	1.29	38.55	0.12	0.21	-60.57	0.08	1.02
45	4	2	1.20	38.55	0.12	0.21	-60.57	0.08	0.97

Table B.2: Empirical equation parameters for moment distribution factors of steel interior girders at ULS.

Bridge Length, (m)	**# of lanes (n)**	**Girder Spacing, (m)**	**Results from CHBDC**	**Parameters of Empirical Equations**					**Empirical Equation**
			F_m^-	a	b	c	d	e	F_m^-
20	1	2	1.08	19.85	0.15	0.16	-74.73	-0.11	0.85
20	1	2.4	1.30	19.85	0.15	0.16	-74.73	-0.11	1.05
20	1	3.2	1.73	19.85	0.15	0.16	-74.73	-0.11	1.47
35	1	2	1.04	19.85	0.15	0.16	-74.73	-0.11	0.83
45	1	2	1.03	19.85	0.15	0.16	-74.73	-0.11	0.83
20	2	2	1.12	25.43	0.18	0.16	-70.32	-0.12	1.12
20	2	2.4	1.39	25.43	0.18	0.16	-70.32	-0.12	1.39
20	2	3.2	1.94	25.43	0.18	0.16	-70.32	-0.12	1.94
35	2	2	1.11	25.43	0.18	0.16	-70.32	-0.12	1.11
45	2	2	1.09	25.43	0.18	0.16	-70.32	-0.12	1.09
20	3	2	1.60	30.70	0.24	0.16	-65.96	-0.16	1.22
20	3	2.4	1.92	30.70	0.24	0.16	-65.96	-0.16	1.51
20	3	3.2	2.56	30.70	0.24	0.16	-65.96	-0.16	2.10
35	3	2	1.54	30.70	0.24	0.16	-65.96	-0.16	1.19
45	3	2	1.52	30.70	0.24	0.16	-65.96	-0.16	1.19
20	4	2	1.80	34.75	0.19	0.16	-63.54	-0.12	1.36
20	4	2.4	2.16	34.75	0.19	0.16	-63.54	-0.12	1.68
20	4	3.2	2.88	34.75	0.19	0.16	-63.54	-0.12	2.35
35	4	2	1.74	34.75	0.19	0.16	-63.54	-0.12	1.34
45	4	2	1.71	34.75	0.19	0.16	-63.54	-0.12	1.33

Table B.3: Empirical equation parameters for moment distribution factors of steel exterior girders at ULS.

Bridge Length, (m)	**# of lanes (n)**	**Girder Spacing, (m)**	**Results from CHBDC**	**Parameters of Empirical Equations**					**Empirical Equation**
			F_m^+	a	b	c	d	e	F_m^+
20	1	2	1.13	16.50	0.44	0.11	-77.22	-0.12	0.84
20	1	2.4	1.36	16.50	0.44	0.11	-77.22	-0.12	1.02
20	1	3.2	1.81	16.50	0.44	0.11	-77.22	-0.12	1.41
35	1	2	0.98	16.50	0.44	0.11	-77.22	-0.12	0.73
45	1	2	0.92	16.50	0.44	0.11	-77.22	-0.12	0.69
20	2	2	1.15	27.03	0.59	0.11	-69.16	-0.13	0.79
20	2	2.4	1.38	27.03	0.59	0.11	-69.16	-0.13	0.96
20	2	3.2	1.84	27.03	0.59	0.11	-69.16	-0.13	1.32
35	2	2	1.01	27.03	0.59	0.11	-69.16	-0.13	0.69
45	2	2	0.93	27.03	0.59	0.11	-69.16	-0.13	0.64
20	3	2	1.30	33.11	0.67	0.11	-64.40	-0.14	0.85
20	3	2.4	1.56	33.11	0.67	0.11	-64.40	-0.14	1.04
20	3	3.2	2.08	33.11	0.67	0.11	-64.40	-0.14	1.43
35	3	2	1.14	33.11	0.67	0.11	-64.40	-0.14	0.75
45	3	2	1.06	33.11	0.67	0.11	-64.40	-0.14	0.70
20	4	2	1.51	40.79	0.73	0.11	-65.20	-0.10	0.95
20	4	2.4	1.81	40.79	0.73	0.11	-65.20	-0.10	1.16
20	4	3.2	2.41	40.79	0.73	0.11	-65.20	-0.10	1.60
35	4	2	1.32	40.79	0.73	0.11	-65.20	-0.10	0.84
45	4	2	1.22	40.79	0.73	0.11	-65.20	-0.10	0.75

Table B.4: Empirical equation parameters for moment distribution factors of steel exterior girders at ULS.

Bridge Length, (m)	# of lanes (n)	Girder Spacing, (m)	Results from CHBDC	Parameters of Empirical Equations					Empirical Equation
			F_m^-	a	b	c	d	e	F_m^-
20	1	2	1.17	19.14	0.01	0.12	-75.27	-0.02	0.93
20	1	2.4	1.40	19.14	0.01	0.12	-75.27	-0.02	1.14
20	1	3.2	1.87	19.14	0.01	0.12	-75.27	-0.02	1.57
35	1	2	1.17	19.14	0.01	0.12	-75.27	-0.02	0.93
45	1	2	1.17	19.14	0.01	0.12	-75.27	-0.02	0.93
20	2	2	1.20	29.26	0.10	0.12	-67.56	-0.10	0.91
20	2	2.4	1.44	29.26	0.10	0.12	-67.56	-0.10	1.12
20	2	3.2	1.92	29.26	0.10	0.12	-67.56	-0.10	1.55
35	2	2	1.20	29.26	0.10	0.12	-67.56	-0.10	0.92
45	2	2	1.20	29.26	0.10	0.12	-67.56	-0.10	0.92
20	3	2	1.36	35.12	0.09	0.12	-63.16	-0.09	1.01
20	3	2.4	1.63	35.12	0.09	0.12	-63.16	-0.09	1.24
20	3	3.2	2.18	35.12	0.09	0.12	-63.16	-0.09	1.71
35	3	2	1.36	35.12	0.09	0.12	-63.16	-0.09	1.01
45	3	2	1.36	35.12	0.09	0.12	-63.16	-0.09	1.01
20	4	2	1.59	38.25	0.11	0.12	-60.83	-0.10	1.16
20	4	2.4	1.91	38.25	0.11	0.12	-60.83	-0.10	1.42
20	4	3.2	2.54	38.25	0.11	0.12	-60.83	-0.10	1.97
35	4	2	1.59	38.25	0.11	0.12	-60.83	-0.10	1.16
45	4	2	1.59	38.25	0.11	0.12	-60.83	-0.10	1.16

Table B.5: Empirical equation parameters for shear distribution factors of steel exterior girders at ULS.

Bridge Length, (m)	**# of lanes (n)**	**Girder Spacing, (m)**	**Results from CHBDC**	**Parameters of Empirical Equations**			**Empirical Equation**
			F_v	a	b	c	F_v
20	1	2	1.13	3.80	0.03	0.13	0.83
20	1	2.4	1.36	3.80	0.03	0.13	1.01
20	1	3.2	1.81	3.80	0.03	0.13	1.40
35	1	2	0.98	3.80	0.03	0.13	0.67
45	1	2	0.92	3.80	0.03	0.13	0.61
20	2	2	1.30	8.61	0.04	0.13	0.94
20	2	2.4	1.56	8.61	0.04	0.13	1.15
20	2	3.2	2.08	8.61	0.04	0.13	1.59
35	2	2	1.30	8.61	0.04	0.13	0.88
45	2	2	1.30	8.61	0.04	0.13	0.86
20	3	2	1.45	11.67	0.05	0.13	1.04
20	3	2.4	1.74	11.67	0.05	0.13	1.27
20	3	3.2	2.32	11.67	0.05	0.13	1.76
35	3	2	1.45	11.67	0.05	0.13	0.96
45	3	2	1.45	11.67	0.05	0.13	0.95
20	4	2	1.68	13.51	0.06	0.13	1.19
20	4	2.4	2.01	13.51	0.06	0.13	1.47
20	4	3.2	2.69	13.51	0.06	0.13	2.02
35	4	2	1.68	13.51	0.06	0.13	1.12
45	4	2	1.68	13.51	0.06	0.13	1.09

Table B.6: Empirical equation parameters for moment distribution factors of steel interior girders at FLS.

Bridge Length, (m)	# of lanes (n)	Girder Spacing, (m)	Results from CHBDC	Parameters of Empirical Equations					Empirical Equation
			F_m^+	a	b	c	d	e	F_m^+
20	1	2	0.94	23.21	-0.01	0.21	-72.14	-0.02	0.73
20	1	2.4	1.13	23.21	-0.01	0.21	-72.14	-0.02	0.91
20	1	3.2	1.50	23.21	-0.01	0.21	-72.14	-0.02	1.29
35	1	2	0.92	23.21	-0.01	0.21	-72.14	-0.02	0.74
45	1	2	0.91	23.21	-0.01	0.21	-72.14	-0.02	0.75
20	2	2	1.80	28.30	-0.02	0.21	-68.21	-0.02	1.06
20	2	2.4	2.15	28.30	-0.02	0.21	-68.21	-0.02	1.31
20	2	3.2	2.88	28.30	-0.02	0.21	-68.21	-0.02	1.87
35	2	2	1.76	28.30	-0.02	0.21	-68.21	-0.02	1.08
45	2	2	1.74	28.30	-0.02	0.21	-68.21	-0.02	1.08
20	3	2	2.75	24.33	-0.01	0.21	-71.60	-0.02	2.04
20	3	2.4	3.31	24.33	-0.01	0.21	-71.60	-0.02	2.55
20	3	3.2	4.40	24.33	-0.01	0.21	-71.60	-0.02	3.60
35	3	2	2.69	24.33	-0.01	0.21	-71.60	-0.02	2.08
45	3	2	2.66	24.33	-0.01	0.21	-71.60	-0.02	2.08
20	4	2	3.6	24.90	-0.02	0.21	-71.27	-0.02	2.64
20	4	2.4	4.33	24.90	-0.02	0.21	-71.27	-0.02	3.30
20	4	3.2	5.76	24.90	-0.02	0.21	-71.27	-0.02	4.66
35	4	2	3.54	24.90	-0.02	0.21	-71.27	-0.02	2.71
45	4	2	3.50	24.90	-0.02	0.21	-71.27	-0.02	2.71

Table B.7: Empirical equation parameters for moment distribution factors of steel interior girders at FLS.

Bridge Length, (m)	# of lanes (n)	Girder Spacing, (m)	Results from CHBDC	Parameters of Empirical Equations					Empirical Equation
			F_m^-	a	b	c	d	e	F_m^-
20	1	2	0.93	23.21	-0.01	0.16	-73.85	-0.01	0.75
20	1	2.4	1.12	23.21	-0.01	0.16	-73.85	-0.01	0.93
20	1	3.2	1.50	23.21	-0.01	0.16	-73.85	-0.01	1.30
35	1	2	0.91	23.21	-0.01	0.16	-73.85	-0.01	0.75
45	1	2	0.90	23.21	-0.01	0.16	-73.85	-0.01	0.75
20	2	2	1.78	23.37	-0.01	0.16	-71.98	-0.01	1.39
20	2	2.4	2.14	23.37	-0.01	0.16	-71.98	-0.01	1.71
20	2	3.2	2.85	23.37	-0.01	0.16	-71.98	-0.01	2.39
35	2	2	1.75	23.37	-0.01	0.16	-71.98	-0.01	1.40
45	2	2	1.73	23.37	-0.01	0.16	-71.98	-0.01	1.40
20	3	2	2.08	23.42	-0.01	0.16	-72.06	-0.01	2.08
20	3	2.4	2.57	23.42	-0.01	0.16	-72.06	-0.01	2.56
20	3	3.2	3.58	23.42	-0.01	0.16	-72.06	-0.01	3.58
35	3	2	2.12	23.42	-0.01	0.16	-72.06	-0.01	2.12
45	3	2	2.12	23.42	-0.01	0.16	-72.06	-0.01	2.12
20	4	2	3.55	23.99	-0.01	0.16	-71.54	-0.01	2.67
20	4	2.4	4.26	23.99	-0.01	0.16	-71.54	-0.01	3.30
20	4	3.2	5.68	23.99	-0.01	0.16	-71.54	-0.01	4.61
35	4	2	3.49	23.99	-0.01	0.16	-71.54	-0.01	2.71
45	4	2	3.46	23.99	-0.01	0.16	-71.54	-0.01	2.71

Table B.8: Empirical equation parameters for moment distribution factors of steel exterior girders at FLS.

Bridge Length, (m)	**# of lanes (n)**	**Girder Spacing, (m)**	**Results from CHBDC**	**Parameters of Empirical Equations**					**Empirical Equation**
			F_m^+	a	b	c	d	e	F_m^+
20	1	2	0.93	20.70	0.17	0.11	-74.08	-0.09	0.74
20	1	2.4	1.12	20.70	0.17	0.11	-74.08	-0.09	0.91
20	1	3.2	1.49	20.70	0.17	0.11	-74.08	-0.09	1.25
35	1	2	0.89	20.70	0.17	0.11	-74.08	-0.09	0.71
45	1	2	0.87	20.70	0.17	0.11	-74.08	-0.09	0.69
20	2	2	1.42	27.41	0.16	0.11	-68.85	-0.10	0.96
20	2	2.4	1.71	27.41	0.16	0.11	-68.85	-0.10	1.18
20	2	3.2	2.28	27.41	0.16	0.11	-68.85	-0.10	1.62
35	2	2	1.39	27.41	0.16	0.11	-68.85	-0.10	0.94
45	2	2	1.37	27.41	0.16	0.11	-68.85	-0.10	0.93
20	3	2	2.15	29.17	0.13	0.11	-67.36	-0.08	1.32
20	3	2.4	2.58	29.17	0.13	0.11	-67.36	-0.08	1.61
20	3	3.2	3.44	29.17	0.13	0.11	-67.36	-0.08	2.22
35	3	2	2.11	29.17	0.13	0.11	-67.36	-0.08	1.29
45	3	2	2.09	29.17	0.13	0.11	-67.36	-0.08	1.28
20	4	2	2.79	30.74	0.15	0.11	-66.08	-0.09	1.60
20	4	2.4	3.35	30.74	0.15	0.11	-66.08	-0.09	1.95
20	4	3.2	4.46	30.74	0.15	0.11	-66.08	-0.09	2.69
35	4	2	2.73	30.74	0.15	0.11	-66.08	-0.09	1.56
45	4	2	2.70	30.74	0.15	0.11	-66.08	-0.09	1.54

Table B.9: Empirical equation parameters for moment distribution factors of steel exterior girders at FLS.

Bridge Length, (m)	# of lanes (n)	Girder Spacing, (m)	Results from CHBDC	Parameters of Empirical Equations					Empirical Equation
			F_m^-	a	b	c	d	e	F_m^-
20	1	2	0.8	22.76	0.12	0.13	-72.60	-0.08	0.67
20	1	2.4	0.96	22.76	0.12	0.13	-72.60	-0.08	0.82
20	1	3.2	1.28	22.76	0.12	0.13	-72.60	-0.08	1.13
35	1	2	0.78	22.76	0.12	0.13	-72.60	-0.08	0.65
45	1	2	0.77	22.76	0.12	0.13	-72.60	-0.08	0.64
20	2	2	1.47	25.41	0.06	0.13	-70.66	-0.04	1.15
20	2	2.4	1.77	25.41	0.06	0.13	-70.66	-0.04	1.77
20	2	3.2	2.36	25.41	0.06	0.13	-70.66	-0.04	2.36
35	2	2	1.46	25.41	0.06	0.13	-70.66	-0.04	1.46
45	2	2	1.45	25.41	0.06	0.13	-70.66	-0.04	1.45
20	3	2	2.21	25.80	0.05	0.12	-70.05	-0.03	1.65
20	3	2.4	2.66	25.80	0.05	0.12	-70.05	-0.03	2.04
20	3	3.2	3.53	25.80	0.05	0.12	-70.05	-0.03	2.80
35	3	2	2.19	25.80	0.05	0.12	-70.05	-0.03	1.64
45	3	2	2.17	25.80	0.05	0.12	-70.05	-0.03	1.63
20	4	2	2.84	26.98	0.10	0.12	-69.47	-0.08	2.06
20	4	2.4	3.41	26.98	0.10	0.12	-69.47	-0.08	2.54
20	4	3.2	4.54	26.98	0.10	0.12	-69.47	-0.08	3.51
35	4	2	2.81	26.98	0.10	0.12	-69.47	-0.08	2.05
45	4	2	2.79	26.98	0.10	0.12	-69.47	-0.08	2.03

Table B.10: Empirical equation parameters for shear distribution factors of concrete exterior girders at FLS.

Bridge Length, (m)	# of lanes (n)	Girder Spacing, (m)	Results from CHBDC	Parameters of Empirical Equations			Empirical Equation
			F_v	a	b	c	F_v
20	1	2	1.14	4.66	0.03	0.14	0.85
20	1	2.4	1.37	4.66	0.03	0.14	1.04
20	1	3.2	1.82	4.66	0.03	0.14	1.45
35	1	2	1.12	4.66	0.03	0.14	0.79
45	1	2	1.11	4.66	0.03	0.14	0.76
20	2	2	1.11	9.73	0.05	0.14	0.82
20	2	2.4	1.33	9.73	0.05	0.14	1.00
20	2	3.2	1.78	9.73	0.05	0.14	1.39
35	2	2	1.09	9.73	0.05	0.14	0.75
45	2	2	1.08	9.73	0.05	0.14	0.73
20	3	2	1.05	15.48	0.09	0.14	0.77
20	3	2.4	1.26	15.48	0.09	0.14	0.94
20	3	3.2	1.68	15.48	0.09	0.14	1.31
35	3	2	1.03	15.48	0.09	0.14	0.71
45	3	2	1.02	15.48	0.09	0.14	0.68
20	4	2	1.02	21.31	0.12	0.14	0.74
20	4	2.4	1.22	21.31	0.12	0.14	0.91
20	4	3.2	1.63	21.31	0.12	0.14	1.26
35	4	2	1.02	21.31	0.12	0.14	0.70
45	4	2	0.98	21.31	0.12	0.14	0.65

APPENDIX C

SAP2000 Input File for Non-Skewed 20-*m* Single-Span Steel Integral Bridge Subjected to Temperature Decrease of -48^{o}C

```
File C:\Users\Navid\Desktop\Input 1\1Span20-0.s2k was saved on 7/24/13 at
16:55:12

TABLE:  "PROGRAM CONTROL"
   ProgramName=SAP2000   Version=14.1.0   ProgLevel=Advanced   LicenseOS=Yes
LicenseSC=Yes   LicenseBR=Yes   LicenseHT=No   CurrUnits="KN, m, C"

TABLE:  "ACTIVE DEGREES OF FREEDOM"
   UX=Yes   UY=Yes   UZ=Yes   RX=Yes   RY=Yes   RZ=Yes

TABLE:  "ANALYSIS OPTIONS"
   Solver=Advanced   SolverProc=Auto   Force32Bit=No   StiffCase=None
GeomMod=No

TABLE:  "COORDINATE SYSTEMS"
   Name=GLOBAL   Type=Cartesian   X=0   Y=0   Z=0   AboutZ=0   AboutY=0
AboutX=0

TABLE:  "GRID LINES"
   CoordSys=GLOBAL   AxisDir=X   GridID=A   XRYZCoord=0   LineType=Primary
LineColor=Gray8Dark   Visible=Yes   BubbleLoc=End   AllVisible=Yes
BubbleSize=1.25
   CoordSys=GLOBAL   AxisDir=X   GridID=B   XRYZCoord=6   LineType=Primary
LineColor=Gray8Dark   Visible=Yes   BubbleLoc=End
   CoordSys=GLOBAL   AxisDir=X   GridID=C   XRYZCoord=12   LineType=Primary
LineColor=Gray8Dark   Visible=Yes   BubbleLoc=End
-------------------------------------------------------------------------------
Rest of the "GRID LINES" were deleted
-------------------------------------------------------------------------------

TABLE:  "MATERIAL PROPERTIES 01 - GENERAL"
   Material=4000Psi   Type=Concrete   SymType=Isotropic   TempDepend=No
Color=Red   Notes="Normalweight f'c = 4 ksi added 2/15/2010 4:18:12 PM"
   Material=A992Fy50   Type=Steel   SymType=Isotropic   TempDepend=No
Color=Cyan   Notes="ASTM A992 Fy=50 ksi added 2/15/2010 4:18:12 PM"
   Material=Con_30   Type=Concrete   SymType=Isotropic   TempDepend=No
Color=Red   Notes="Normalweight f'c = 4 ksi added 2/15/2010 4:18:12 PM"
   Material=Steel   Type=Steel   SymType=Isotropic   TempDepend=No
Color=Cyan   Notes="ASTM A992 Fy=50 ksi added 2/15/2010 4:18:12 PM"
-------------------------------------------------------------------------------
Rest of the "MATERIAL PROPERTIES 01 - GENERAL" were deleted
-------------------------------------------------------------------------------

TABLE:  "MATERIAL PROPERTIES 02 - BASIC MECHANICAL PROPERTIES"
   Material=4000Psi   UnitWeight=23.563121614979   UnitMass=2.40276960611018
E1=24855578.2847654   G12=10356490.9519856   U12=0.2   A1=0.0000099
   Material=A992Fy50   UnitWeight=76.9728639422648
UnitMass=7.84904737995992   E1=199947978.795958   G12=76903068.767676
U12=0.3   A1=0.0000117
   Material=Con_30   UnitWeight=23.563121614979   UnitMass=2.40276960611018
E1=26000000   G12=10833333.3333333   U12=0.2   A1=0.0000099
```

```
   Material=Steel   UnitWeight=76.9728639422648   UnitMass=7.84904737995992
E1=199947978.795958   G12=76903068.767676   U12=0.3   A1=0.0000117
-----------------------------------------------------------------------------------------
Rest of the "MATERIAL PROPERTIES 02" were deleted
-----------------------------------------------------------------------------------------


TABLE:  "FRAME SECTION PROPERTIES 01 - GENERAL"

   SectionName=Pile   Material=Steel   Shape="I/Wide Flange"   t3=0.3048
t2=0.127   tf=0.009652   tw=0.00635   t2b=0.127   tfb=0.009652
Area=0.0042645076   TorsConst=9.65117678053953E-08   I33=6.5724174702235E-05
_
        I22=3.30125717301008E-06   AS2=0.00193548   AS3=2.04300666666667E-03
S33=4.3126098885981E-04   S22=5.19883019371667E-05   Z33=4.911874950424E-04
Z22=0.000080716532115   R33=0.124144683132414   R22=2.78230817990979E-02 _
        ConcCol=No   ConcBeam=No   Color=White   TotalWt=246.188522456661
TotalMass=25.1042416534491   FromFile=No   AMod=1   A2Mod=1   A3Mod=1
JMod=1   I2Mod=1   I3Mod=1   MMod=1   WMod=1   Notes="Added 2/15/2010 6:51:51
PM"
-----------------------------------------------------------------------------------------
Rest of the "FRAME SECTION PROPERTIES 01 - GENERAL" were deleted
-----------------------------------------------------------------------------------------
TABLE:  "LOAD PATTERN DEFINITIONS"
   LoadPat=DEAD   DesignType=DEAD   SelfWtMult=1
   LoadPat=TempF   DesignType=TEMPERATURE   SelfWtMult=0
   LoadPat=K0   DesignType=OTHER   SelfWtMult=0

TABLE:  "COMBINATION DEFINITIONS"
   ComboName=against   ComboType="Linear Add"   AutoDesign=No
CaseType="NonLin Static"   CaseName=K0   ScaleFactor=1   SteelDesign=No
ConcDesign=No   AlumDesign=No   ColdDesign=No
   ComboName=away   ComboType="Linear Add"   AutoDesign=No   CaseType="NonLin
Static"   CaseName=K0   ScaleFactor=0.62   SteelDesign=No   ConcDesign=No
AlumDesign=No   ColdDesign=No
   ComboName=away   CaseType="NonLin Static"   CaseName=TempF   ScaleFactor=1

TABLE:  "GROUPS 1 - DEFINITIONS"
   GroupName=ALL   Selection=Yes   SectionCut=Yes   Steel=Yes   Concrete=Yes
Aluminum=Yes   ColdFormed=Yes   Stage=Yes   Bridge=Yes   AutoSeismic=No
AutoWind=No   SelDesSteel=No   SelDesAlum=No   SelDesCold=No   MassWeight=Yes
Color=Red
-----------------------------------------------------------------------------------------
Rest of the "GROUPS 1 - DEFINITIONS" were deleted
-----------------------------------------------------------------------------------------
 TABLE:  "GROUPS 2 - ASSIGNMENTS"
   GroupName=Superstr   ObjectType=Joint   ObjectLabel=1
   GroupName=Superstr   ObjectType=Joint   ObjectLabel=2
   GroupName=Superstr   ObjectType=Joint   ObjectLabel=3631
   GroupName=No-spring   ObjectType=Joint   ObjectLabel=1
   GroupName=No-spring   ObjectType=Joint   ObjectLabel=2
   GroupName=No-spring   ObjectType=Joint   ObjectLabel=24
-----------------------------------------------------------------------------------------
Rest of the "GROUPS 2 - ASSIGNMENTS" were deleted
-----------------------------------------------------------------------------------------
TABLE:  "JOINT PATTERN DEFINITIONS"
   Pattern=Default
   Pattern=At-rest
```

```
TABLE:  "LOAD CASE DEFINITIONS"
   Case=DEAD   Type=LinStatic   InitialCond=Zero   DesTypeOpt="Prog Det"
DesignType=DEAD   AutoType=None   RunCase=No   CaseStatus="Not Run"
   Case=MODAL   Type=LinModal   InitialCond=Zero   DesTypeOpt="Prog Det"
DesignType=OTHER   AutoType=None   RunCase=No   CaseStatus="Not Run"
   Case=TempF   Type=NonStatic   InitialCond=Zero   DesTypeOpt="Prog Det"
DesignType=TEMPERATURE   AutoType=None   RunCase=Yes   CaseStatus="Not Run"
   Case=K0   Type=NonStatic   InitialCond=Zero   DesTypeOpt="Prog Det"
DesignType=OTHER   AutoType=None   RunCase=Yes   CaseStatus="Not Run"
   Case=N0-spring   Type=NonStatic   InitialCond=Zero   DesTypeOpt="Prog Det"
DesignType=OTHER   AutoType=None   RunCase=Yes   CaseStatus="Not Run"

TABLE:  "CASE - STATIC 1 - LOAD ASSIGNMENTS"
   Case=DEAD   LoadType="Load pattern"   LoadName=DEAD   LoadSF=1
   Case=TempF   LoadType="Load pattern"   LoadName=TempF   LoadSF=1
   Case=K0   LoadType="Load pattern"   LoadName=K0   LoadSF=1

TABLE:  "CASE - STATIC 2 - NONLINEAR LOAD APPLICATION"
   Case=TempF   LoadApp="Full Load"   MonitorDOF=U1   MonitorJt=1
   Case=K0   LoadApp="Full Load"   MonitorDOF=U1   MonitorJt=1
   Case=N0-spring   LoadApp="Full Load"   MonitorDOF=U1   MonitorJt=1

TABLE:  "CASE - STATIC 4 - NONLINEAR PARAMETERS"
   Case=TempF   Unloading="Unload Entire"   GeoNonLin=None
ResultsSave="Final State"   MaxTotal=200   MaxNull=50   MaxIterCS=10
MaxIterNR=40   ItConvTol=0.0001   UseEvStep=Yes   EvLumpTol=0.01
LSPerIter=20   LSTol=0.1 _
       LSStepFact=1.618   FrameTC=Yes   FrameHinge=Yes   CableTC=Yes
LinkTC=Yes   LinkOther=Yes   TFMaxIter=10   TFTol=0.01   TFAccelFact=1
TFNoStop=No
   Case=K0   Unloading="Unload Entire"   GeoNonLin=None   ResultsSave="Final
State"   MaxTotal=200   MaxNull=50   MaxIterCS=10   MaxIterNR=40
ItConvTol=0.0001   UseEvStep=Yes   EvLumpTol=0.01   LSPerIter=20   LSTol=0.1
LSStepFact=1.618 _
       FrameTC=Yes   FrameHinge=Yes   CableTC=Yes   LinkTC=Yes
LinkOther=Yes   TFMaxIter=10   TFTol=0.01   TFAccelFact=1   TFNoStop=No
   Case=N0-spring   Unloading="Unload Entire"   GeoNonLin=None   MaxTotal=200
MaxNull=50   MaxIterCS=10   MaxIterNR=40   ItConvTol=0.0001   UseEvStep=Yes
EvLumpTol=0.01   LSPerIter=20   LSTol=0.1   LSStepFact=1.618 _
       StageSave="End of Final Stage"   StageMinIns=1   StageMinTD=1
FrameTC=Yes   FrameHinge=Yes   CableTC=Yes   LinkTC=Yes   LinkOther=Yes
TimeDepMat=No   TFMaxIter=10   TFTol=0.01   TFAccelFact=1   TFNoStop=No

TABLE:  "CASE - STATIC 5 - NONLINEAR STAGE DEFINITIONS"
   Case=N0-spring   Stage=1   Duration=0   Output=No

TABLE:  "CASE - STATIC 6 - NONLINEAR STAGE DATA"
   Case=N0-spring   Stage=1   Operation="Add Structure"   ObjType=Group
ObjName=No-spring   Age=0

TABLE:  "CASE - MODAL 1 - GENERAL"
   Case=MODAL   ModeType=Eigen   MaxNumModes=12   MinNumModes=1
EigenShift=0   EigenCutoff=0   EigenTol=0.000000001   AutoShift=Yes

TABLE:  "BRIDGE PREFERENCES"
   NorthAngle=90   MaxDiscCurv=1
```

```
TABLE:  "BRIDGE DESIGN PREFERENCES - AASHTOLRFD07"
   HingeOpt="Auto: AASHTO/Caltrans Hinge"

TABLE:  "JOINT COORDINATES"
   Joint=1   CoordSys=GLOBAL   CoordType=Cartesian   XorR=20   Y=0   Z=0
SpecialJt=Yes   GlobalX=20   GlobalY=0   GlobalZ=0
   Joint=2   CoordSys=GLOBAL   CoordType=Cartesian   XorR=0   Y=0   Z=0
SpecialJt=Yes   GlobalX=0   GlobalY=0   GlobalZ=0
   Joint=24   CoordSys=GLOBAL   CoordType=Cartesian   XorR=0   Y=0   Z=-6
SpecialJt=Yes   GlobalX=0   GlobalY=0   GlobalZ=-6
   Joint=31   CoordSys=GLOBAL   CoordType=Cartesian   XorR=-3.5   Y=0   Z=0
SpecialJt=Yes   GlobalX=-3.5   GlobalY=0   GlobalZ=0
   Joint=32   CoordSys=GLOBAL   CoordType=Cartesian   XorR=-3.5   Y=0   Z=-
1.5   SpecialJt=Yes   GlobalX=-3.5   GlobalY=0   GlobalZ=-1.5
-------------------------------------------------------------------------------------
Rest of the "JOINT COORDINATES" were deleted
-------------------------------------------------------------------------------------

TABLE:  "CONNECTIVITY - FRAME"
   Frame=1880   JointI=3643   JointJ=3760   IsCurved=No   Length=1
CentroidX=-3.88144377749811E-17   CentroidY=0.75   CentroidZ=-6.5
   Frame=1881   JointI=3760   JointJ=3761   IsCurved=No   Length=1
CentroidX=2.91243808583919E-17   CentroidY=0.75   CentroidZ=-7.5
   Frame=1882   JointI=3761   JointJ=3762   IsCurved=No   Length=1
CentroidX=4.99275100429575E-17   CentroidY=0.75   CentroidZ=-8.5
   Frame=1883   JointI=3762   JointJ=3763   IsCurved=No   Length=1
CentroidX=-3.6036169707987E-17   CentroidY=0.75   CentroidZ=-9.5
   Frame=1884   JointI=3763   JointJ=3764   IsCurved=No   Length=1
CentroidX=20   CentroidY=4.75   CentroidZ=-21.5
-------------------------------------------------------------------------------------
Rest of the "CONNECTIVITY - FRAME" were deleted
-------------------------------------------------------------------------------------

 TABLE:  "CONNECTIVITY - AREA"
   Area=51   NumJoints=4   Joint1=3640   Joint2=3756   Joint3=72   Joint4=71
Perimeter=3.74638688690176   AreaArea=0.650999999999999   CentroidX=-
0.341218637992832   CentroidY=16   CentroidZ=-4.19290322580645
   Area=52   NumJoints=4   Joint1=3756   Joint2=3757   Joint3=73   Joint4=72
Perimeter=3.57277065851894   AreaArea=0.651   CentroidX=-0.341218637992832
CentroidY=16   CentroidZ=-3.26114695340502
   Area=53   NumJoints=4   Joint1=3757   Joint2=3758   Joint3=74   Joint4=73
Perimeter=3.43025633827717   AreaArea=0.651000000000001   CentroidX=-
0.341218637992831   CentroidY=16   CentroidZ=-2.32939068100358
   Area=54   NumJoints=4   Joint1=3758   Joint2=3759   Joint3=75   Joint4=74
Perimeter=3.32778580490182   AreaArea=0.651   CentroidX=-0.341218637992831
CentroidY=16   CentroidZ=-1.39763440860215
   Area=55   NumJoints=4   Joint1=3759   Joint2=3631   Joint3=76   Joint4=75
Perimeter=3.27386273190299   AreaArea=0.651   CentroidX=-0.341218637992831
CentroidY=16   CentroidZ=-0.465878136200717
   Area=56   NumJoints=4   Joint1=71   Joint2=72   Joint3=78   Joint4=77
Perimeter=3.46638688690177   AreaArea=0.553   CentroidX=-1.03966244725738
CentroidY=16   CentroidZ=-3.56430379746835
-------------------------------------------------------------------------------------
Rest of the "CONNECTIVITY - AREA" were deleted
-------------------------------------------------------------------------------------

TABLE:  "CONNECTIVITY - LINK"
   Link=L-1   JointI=3643   JointJ=3643   Length=0   CentroidX=-
1.38506827535023E-17   CentroidY=0.75   CentroidZ=-6
```

```
   Link=L-2   JointI=3638   JointJ=3638   Length=0   CentroidX=-
2.77013655070046E-17   CentroidY=1.5   CentroidZ=-6
   Link=L-3   JointI=3648   JointJ=3648   Length=0   CentroidX=-
2.42969706854002E-16   CentroidY=2.58333333333333   CentroidZ=-6
   Link=L-4   JointI=3650   JointJ=3650   Length=0   CentroidX=-
3.70797142990043E-17   CentroidY=3.66666666666667   CentroidZ=-6
-------------------------------------------------------------------------------------------
Rest of the "CONNECTIVITY - AREA" were deleted
-------------------------------------------------------------------------------------------

TABLE:  "JOINT RESTRAINT ASSIGNMENTS"
   Joint=3664   U1=No   U2=No   U3=Yes   R1=No   R2=No   R3=No
   Joint=3665   U1=No   U2=No   U3=Yes   R1=No   R2=No   R3=No
   Joint=3666   U1=No   U2=No   U3=Yes   R1=No   R2=No   R3=No
   Joint=3667   U1=No   U2=No   U3=Yes   R1=No   R2=No   R3=No
-------------------------------------------------------------------------------------------
Rest of the "JOINT RESTRAINT ASSIGNMENTS" were deleted
-------------------------------------------------------------------------------------------

TABLE:  "JOINT LOCAL AXES ASSIGNMENTS 1 - TYPICAL"
   Joint=3631   AngleA=4.2552342906299E-16   AngleB=0   AngleC=0
AdvanceAxes=Yes
   Joint=3632   AngleA=4.2552342906299E-16   AngleB=0   AngleC=0
AdvanceAxes=Yes
   Joint=3633   AngleA=4.2552342906299E-16   AngleB=0   AngleC=0
AdvanceAxes=Yes
   Joint=3634   AngleA=4.2552342906299E-16   AngleB=0   AngleC=0
AdvanceAxes=Yes
   Joint=3635   AngleA=4.2552342906299E-16   AngleB=0   AngleC=0
AdvanceAxes=Yes
   Joint=3636   AngleA=4.2552342906299E-16   AngleB=0   AngleC=0
-------------------------------------------------------------------------------------------
Rest of the "JOINT LOCAL AXES ASSIGNMENTS 1-TYPCAL" were deleted
-------------------------------------------------------------------------------------------

TABLE:  "JOINT LOCAL AXES ASSIGNMENTS 2 - ADVANCED"
   Joint=3631   LocalPlane=31   AxOption1="Coord Dir"   AxCoordSys=GLOBAL
AxCoordDir=Z   AxVecJt1=None   AxVecJt2=None   PlOption1="Coord Dir"
PlCoordSys=GLOBAL   CoordDir1=X   CoordDir2=Y   PlVecJt1=None   PlVecJt2=None
AxVecX=0 _
        AxVecY=0   AxVecZ=1   PlVecX=1   PlVecY=0   PlVecZ=0
   Joint=3632   LocalPlane=31   AxOption1="Coord Dir"   AxCoordSys=GLOBAL
AxCoordDir=Z   AxVecJt1=None   AxVecJt2=None   PlOption1="Coord Dir"
PlCoordSys=GLOBAL   CoordDir1=X   CoordDir2=Y   PlVecJt1=None   PlVecJt2=None
AxVecX=0 _
-------------------------------------------------------------------------------------------
Rest of the "JOINT LOCAL AXES ASSIGNMENTS 2 - ADVANCED" were deleted
-------------------------------------------------------------------------------------------

TABLE:  "JOINT PATTERN ASSIGNMENTS"
   Joint=1   Pattern=Default   Value=0
   Joint=2   Pattern=Default   Value=0
   Joint=24   Pattern=Default   Value=60
   Joint=33   Pattern=Default   Value=50
-------------------------------------------------------------------------------------------
Rest of the "JOINT PATTERN ASSIGNMENTS" were deleted
-------------------------------------------------------------------------------------------

 TABLE:  "FRAME SECTION ASSIGNMENTS"
```

```
   Frame=1880   SectionType="I/Wide Flange"   AutoSelect=N.A.   AnalSect=Pile
DesignSect=Pile   MatProp=Default
   Frame=1881   SectionType="I/Wide Flange"   AutoSelect=N.A.   AnalSect=Pile
DesignSect=Pile   MatProp=Default
   Frame=1882   SectionType="I/Wide Flange"   AutoSelect=N.A.   AnalSect=Pile
DesignSect=Pile   MatProp=Default
   Frame=1883   SectionType="I/Wide Flange"   AutoSelect=N.A.   AnalSect=Pile
DesignSect=Pile   MatProp=Default
-----------------------------------------------------------------------------------------
Rest of the "FRAME SECTION ASSIGNMENTS" were deleted
-----------------------------------------------------------------------------------------

TABLE:  "FRAME INSERTION POINT ASSIGNMENTS"
   Frame=1880   CardinalPt="10 (centroid)"   Mirror2=No   Transform=Yes
   Frame=1881   CardinalPt="10 (centroid)"   Mirror2=No   Transform=Yes
   Frame=1882   CardinalPt="10 (centroid)"   Mirror2=No   Transform=Yes
   Frame=1883   CardinalPt="10 (centroid)"   Mirror2=No   Transform=Yes
   Frame=1884   CardinalPt="10 (centroid)"   Mirror2=No   Transform=Yes
-----------------------------------------------------------------------------------------
Rest of the "FRAME INSERTION POINT ASSIGNMENTS" were deleted
-----------------------------------------------------------------------------------------

TABLE:  "FRAME OUTPUT STATION ASSIGNMENTS"
   Frame=1880   StationType=MinNumSta   MinNumSta=3   AddAtElmInt=Yes
AddAtPtLoad=Yes
   Frame=1881   StationType=MinNumSta   MinNumSta=3   AddAtElmInt=Yes
AddAtPtLoad=Yes
   Frame=1882   StationType=MinNumSta   MinNumSta=3   AddAtElmInt=Yes
AddAtPtLoad=Yes
   Frame=1883   StationType=MinNumSta   MinNumSta=3   AddAtElmInt=Yes
AddAtPtLoad=Yes
   Frame=1884   StationType=MinNumSta   MinNumSta=3   AddAtElmInt=Yes
AddAtPtLoad=Yes
-----------------------------------------------------------------------------------------
Rest of the "FRAME OUTPUT STATION ASSIGNMENTS" were deleted
-----------------------------------------------------------------------------------------

TABLE:  "FRAME AUTO MESH ASSIGNMENTS"
   Frame=1880   AutoMesh=Yes   AtJoints=Yes   AtFrames=No   NumSegments=0
MaxLength=0   MaxDegrees=0
   Frame=1881   AutoMesh=Yes   AtJoints=Yes   AtFrames=No   NumSegments=0
MaxLength=0   MaxDegrees=0
   Frame=1882   AutoMesh=Yes   AtJoints=Yes   AtFrames=No   NumSegments=0
MaxLength=0   MaxDegrees=0
   Frame=1883   AutoMesh=Yes   AtJoints=Yes   AtFrames=No   NumSegments=0
MaxLength=0   MaxDegrees=0
   Frame=1884   AutoMesh=Yes   AtJoints=Yes   AtFrames=No   NumSegments=0
-----------------------------------------------------------------------------------------
Rest of the "FRAME AUTO MESH ASSIGNMENTS" were deleted
-----------------------------------------------------------------------------------------

 TABLE:  "FRAME LOADS - TEMPERATURE"
   Frame=2643   LoadPat=TempF   Type=Temperature   Temp=-50   JtPattern=None
   Frame=2644   LoadPat=TempF   Type=Temperature   Temp=-50   JtPattern=None
   Frame=2645   LoadPat=TempF   Type=Temperature   Temp=-50   JtPattern=None
   Frame=2646   LoadPat=TempF   Type=Temperature   Temp=-50   JtPattern=None
   Frame=2647   LoadPat=TempF   Type=Temperature   Temp=-50   JtPattern=None
   Frame=2648   LoadPat=TempF   Type=Temperature   Temp=-50   JtPattern=None
-----------------------------------------------------------------------------------------
Rest of the "FRAME LOADS - TEMPERATURE" were deleted
-----------------------------------------------------------------------------------------
```

```
TABLE:  "FRAME DESIGN PROCEDURES"
   Frame=1880   DesignProc="From Material"
   Frame=1881   DesignProc="From Material"
   Frame=1882   DesignProc="From Material"
   Frame=1883   DesignProc="From Material"
-------------------------------------------------------------------------------------------
 Rest of the "FRAME DESIGN PROCEDURES" were deleted
-------------------------------------------------------------------------------------------

TABLE:  "OVERWRITES - STEEL DESIGN - AISC-LRFD93"
   Frame=1880   DesignSect="Program Determined"   FrameType="Program
Determined"   Fy=0   RLLF=0   AreaRatio=0   XLMajor=0   XLMinor=0   XKMajor=0
XKMinor=0   CmMajor=0   CmMinor=0   Cb=0   B1Major=0   B1Minor=0   B2Major=0
B2Minor=0
        PhiPnc=0   PhiPnt=0   PhiMn3=0   PhiMn2=0   PhiVn2=0   PhiVn3=0
CheckDefl="Program Determined"   DeflType="Program Determined"   DLRat=0
SDLAndLLRat=0   LLRat=0   TotalRat=0   NetRat=0   DLAbs=0   SDLAndLLAbs=0
LLAbs=0
        TotalAbs=0   NetAbs=0   SpecCamber=0
-------------------------------------------------------------------------------------------
Rest of the "OVERWRITES - STEEL DESIGN - AISC-LRFD93" were deleted
-------------------------------------------------------------------------------------------

TABLE:  "AREA SECTION ASSIGNMENTS"
   Area=51   Section=Wingwall   MatProp=Default
   Area=52   Section=Wingwall   MatProp=Default
   Area=53   Section=Wingwall   MatProp=Default
   Area=54   Section=Wingwall   MatProp=Default
   Area=55   Section=Wingwall   MatProp=Default
   Area=1752   Section=Abut   MatProp=Default
   Area=1753   Section=Abut   MatProp=Default
   Area=1754   Section=Abut   MatProp=Default
   Area=1755   Section=Abut   MatProp=Default
   Area=1756   Section=Abut   MatProp=Default
   Area=1951   Section=Slab   MatProp=Default
   Area=1952   Section=Slab   MatProp=Default
   Area=1953   Section=Slab   MatProp=Default
   Area=1954   Section=Slab   MatProp=Default
   Area=1955   Section=Slab   MatProp=Default
   Area=1956   Section=Slab   MatProp=Default
   Area=1957   Section=Slab   MatProp=Default
-------------------------------------------------------------------------------------------
Rest of the "AREA SECTION ASSIGNMENTS" were deleted
-------------------------------------------------------------------------------------------

TABLE:  "AREA OVERWRITES - JOINT OFFSETS"
   Area=51   OffsetOver=Object   Offset1=0   Offset2=0   Offset3=0
Offset4=0
   Area=52   OffsetOver=Object   Offset1=0   Offset2=0   Offset3=0
Offset4=0
   Area=53   OffsetOver=Object   Offset1=0   Offset2=0   Offset3=0
Offset4=0
-------------------------------------------------------------------------------------------
 Rest of the "AREA SECTION ASSIGNMENTS" were deleted
-------------------------------------------------------------------------------------------

TABLE:  "AREA LOADS - SURFACE PRESSURE"
   Area=1752   LoadPat=K0   Face=Top   Pressure=1   JtPattern=Default
   Area=1753   LoadPat=K0   Face=Top   Pressure=1   JtPattern=Default
   Area=1754   LoadPat=K0   Face=Top   Pressure=1   JtPattern=Default
   Area=1755   LoadPat=K0   Face=Top   Pressure=1   JtPattern=Default
```

```
   Area=1756   LoadPat=K0   Face=Top   Pressure=1   JtPattern=Default
   Area=1757   LoadPat=K0   Face=Top   Pressure=1   JtPattern=Default
   Area=1758   LoadPat=K0   Face=Top   Pressure=1   JtPattern=Default
------------------------------------------------------------------------------------------
 Rest of the "AREA LOADS - SURFACE PRESSURE" were deleted
------------------------------------------------------------------------------------------

 TABLE:  "AREA LOADS - TEMPERATURE"
   Area=1951   LoadPat=TempF   Type=Temperature   Temp=-48   JtPattern=None
   Area=1952   LoadPat=TempF   Type=Temperature   Temp=-48   JtPattern=None
   Area=1953   LoadPat=TempF   Type=Temperature   Temp=-48   JtPattern=None
   Area=1954   LoadPat=TempF   Type=Temperature   Temp=-48   JtPattern=None
   Area=1955   LoadPat=TempF   Type=Temperature   Temp=-48   JtPattern=None
   Area=1956   LoadPat=TempF   Type=Temperature   Temp=-48   JtPattern=None
   Area=1957   LoadPat=TempF   Type=Temperature   Temp=-48   JtPattern=None
------------------------------------------------------------------------------------------
 Rest of the "AREA LOADS - TEMPERATURE" were deleted
------------------------------------------------------------------------------------------

 TABLE:  "LINK PROPERTY ASSIGNMENTS"
   Link=L-1   LinkType="MultiLinear Elastic"   LinkJoints=SingleJoint
 LinkProp=Abut-L7   LinkFDProp=None
   Link=L-2   LinkType="MultiLinear Elastic"   LinkJoints=SingleJoint
 LinkProp=Abut-L7   LinkFDProp=None
   Link=L-3   LinkType="MultiLinear Elastic"   LinkJoints=SingleJoint
 LinkProp=Abut-L7   LinkFDProp=None
   Link=L-4   LinkType="MultiLinear Elastic"   LinkJoints=SingleJoint
 LinkProp=Abut-L7   LinkFDProp=None
   Link=L-5   LinkType="MultiLinear Elastic"   LinkJoints=SingleJoint
 LinkProp=Abut-L7   LinkFDProp=None
   Link=L-6   LinkType="MultiLinear Elastic"   LinkJoints=SingleJoint
 LinkProp=Abut-L7   LinkFDProp=None
------------------------------------------------------------------------------------------
 Rest of the "LINK PROPERTY ASSIGNMENTS" were deleted
------------------------------------------------------------------------------------------

 TABLE:  "LINK LOCAL AXES ASSIGNMENTS 1 - TYPICAL"
   Link=R-1   Angle=180   AdvanceAxes=No
   Link=R-2   Angle=180   AdvanceAxes=No
   Link=R-3   Angle=180   AdvanceAxes=No
   Link=R-4   Angle=180   AdvanceAxes=No
------------------------------------------------------------------------------------------
 Rest of the "LINK PROPERTY ASSIGNMENTS" were deleted
------------------------------------------------------------------------------------------

 TABLE:  "PREFERENCES - DIMENSIONAL"
   MergeTol=0.001   FineGrid=0.25   Nudge=0.25   SelectTol=3   SnapTol=12
 SLineThick=1   PLineThick=4   MaxFont=8   MinFont=3   AutoZoom=10
 ShrinkFact=70   TextFileLen=240

 TABLE:  "PREFERENCES - STEEL DESIGN - AISC-LRFD93"
   THDesign=Envelopes   FrameType="Moment Frame"   PatLLF=0.75
 SRatioLimit=0.95   MaxIter=1   PhiB=0.9   PhiC=0.85   PhiT=0.9   PhiV=0.9
 PhiCA=0.9   CheckDefl=Yes   DLRat=120   SDLAndLLRat=120   LLRat=360
 TotalRat=240   NetRat=240

 TABLE:  "PREFERENCES - CONCRETE DESIGN - ACI 318-05/IBC2003"
   THDesign=Envelopes   NumCurves=24   NumPoints=11   MinEccen=No
 PatLLF=0.75   UFLimit=0.95   SeisCat=D   PhiT=0.9   PhiCTied=0.65
 PhiCSpiral=0.7   PhiV=0.75   PhiVSeismic=0.6   PhiVJoint=0.85
```

```
TABLE:  "PREFERENCES - COLD FORMED DESIGN - AISI-ASD96"
   THDesign=Envelopes   FrameType="Braced Frame"   SRatioLimit=1   MaxIter=1
OmegaBS=1.67   OmegaBUS=1.67   OmegaBLTB=1.67   OmegaVS=1.67   OmegaVNS=1.5
OmegaT=1.67   OmegaC=1.8

TABLE:  "OPTIONS - COLORS - OUTPUT"
   DeviceType=Screen   Contour1=13107400   Contour2=6553828   Contour3=Red
Contour4=16639   Contour5=Orange   Contour6=43775   Contour7=54527
Contour8=Yellow   Contour9=65408   Contour10=Green   Contour11=8453888
Contour12=Cyan _
       Contour13=16755200   Contour14=16733440   Contour15=Blue
Transpare=0.5   Ratio1=Cyan   Ratio2=Green   Ratio3=Yellow   Ratio4=Orange
Ratio5=Red   RatioNotD=Gray4   RatioNotC=Red   RatioVal1=0.5   RatioVal2=0.7
RatioVal3=0.9 _
       RatioVal4=1   DFillPos=Yellow   DFillNeg=Red   DFillRPos=Blue
DFillRNeg=Cyan
   DeviceType=Printer   Contour1=Black   Contour2=3158064   Contour3=4210752
Contour4=5263440   Contour5=6316128   Contour6=7368816   Contour7=Gray8Dark
Contour8=Gray7   Contour9=Gray6   Contour10=Gray5   Contour11=Gray4 _
       Contour12=Gray3   Contour13=Gray2   Contour14=Gray1Light
Contour15=White   Transpare=0   Ratio1=Gray2   Ratio2=Gray4
Ratio3=Gray8Dark   Ratio4=4210752   Ratio5=Black   RatioNotD=Gray4
RatioNotC=Black   RatioVal1=0.5 _
       RatioVal2=0.7   RatioVal3=0.9   RatioVal4=1   DFillPos=Gray8Dark
DFillNeg=Gray8Dark   DFillRPos=4210752   DFillRNeg=4210752
   DeviceType="Color Printer"   Contour1=13107400   Contour2=6553828
Contour3=Red   Contour4=16639   Contour5=Orange   Contour6=43775
Contour7=54527   Contour8=Yellow   Contour9=65408   Contour10=Green
Contour11=8453888 _
      RatioVal3=0.9   RatioVal4=1   DFillPos=Red   DFillNeg=Red
DFillRPos=Blue   DFillRNeg=Blue
```

Rest of the "OPTIONS - COLORS - OUTPUT" were deleted

Output

```
ELEM=JOINT    TYPE=DISP, REAC LOAD=*
ELEM=SHELL    TYPE=FORCE  LOAD=*
ELEM=SHELL    TYPE=STRESS  LOAD=*
ELEM=FRAME    TYPE=JOITF LOAD=*


END TABLE DATA
```

APPENDIX D

SAP2000 Input File for 20-*m* Single-Span Steel Integral Bridge with 60^{o} Skew Angle Subjected to Temperature Increase of $+40^{o}C$

```
File C:\Users\Navid\Desktop\Input 2\1Span20-60.s2k was saved on 7/24/13 at
18:55:08

TABLE:  "PROGRAM CONTROL"
   ProgramName=SAP2000   Version=14.1.0   ProgLevel=Advanced   LicenseOS=Yes
LicenseSC=Yes   LicenseBR=Yes   LicenseHT=No   CurrUnits="KN, m, C"

TABLE:  "ACTIVE DEGREES OF FREEDOM"
   UX=Yes   UY=Yes   UZ=Yes   RX=Yes   RY=Yes   RZ=Yes

TABLE:  "ANALYSIS OPTIONS"
   Solver=Advanced   SolverProc=Auto   Force32Bit=No   StiffCase=None
GeomMod=No

TABLE:  "COORDINATE SYSTEMS"
   Name=GLOBAL   Type=Cartesian   X=0   Y=0   Z=0   AboutZ=0   AboutY=0
AboutX=0

TABLE:  "GRID LINES"
   CoordSys=GLOBAL   AxisDir=X   GridID=A   XRYZCoord=0   LineType=Primary
LineColor=Gray8Dark   Visible=Yes   BubbleLoc=End   AllVisible=Yes
BubbleSize=1.25
   CoordSys=GLOBAL   AxisDir=X   GridID=B   XRYZCoord=6   LineType=Primary
LineColor=Gray8Dark   Visible=Yes   BubbleLoc=End
   CoordSys=GLOBAL   AxisDir=X   GridID=C   XRYZCoord=12   LineType=Primary
LineColor=Gray8Dark   Visible=Yes   BubbleLoc=End
-------------------------------------------------------------------------------------
Rest of the "GRID LINES" were deleted
-------------------------------------------------------------------------------------

TABLE:  "MATERIAL PROPERTIES 01 - GENERAL"
   Material=4000Psi   Type=Concrete   SymType=Isotropic   TempDepend=No
Color=Red   Notes="Normalweight f'c = 4 ksi added 2/15/2010 4:18:12 PM"
   Material=A992Fy50   Type=Steel   SymType=Isotropic   TempDepend=No
Color=Cyan   Notes="ASTM A992 Fy=50 ksi added 2/15/2010 4:18:12 PM"
   Material=Con_30   Type=Concrete   SymType=Isotropic   TempDepend=No
Color=Red   Notes="Normalweight f'c = 4 ksi added 2/15/2010 4:18:12 PM"
   Material=Steel   Type=Steel   SymType=Isotropic   TempDepend=No
Color=Cyan   Notes="ASTM A992 Fy=50 ksi added 2/15/2010 4:18:12 PM"
-------------------------------------------------------------------------------------
Rest of the "MATERIAL PROPERTIES 01 - GENERAL" were deleted
-------------------------------------------------------------------------------------

TABLE:  "MATERIAL PROPERTIES 02 - BASIC MECHANICAL PROPERTIES"
   Material=4000Psi   UnitWeight=23.563121614979   UnitMass=2.40276960611018
E1=24855578.2847654   G12=10356490.9519856   U12=0.2   A1=0.0000099
   Material=A992Fy50   UnitWeight=76.9728639422648
UnitMass=7.84904737995992   E1=199947978.795958   G12=76903068.767676
U12=0.3   A1=0.0000117
```

```
   Material=Con_30   UnitWeight=23.563121614979   UnitMass=2.40276960611018
E1=26000000   G12=10833333.3333333   U12=0.2   A1=0.0000099
   Material=Steel   UnitWeight=76.9728639422648   UnitMass=7.84904737995992
E1=199947978.795958   G12=76903068.767676   U12=0.3   A1=0.0000117

TABLE:  "MATERIAL PROPERTIES 03A - STEEL DATA"
   Material=A992Fy50   Fy=344737.894475789   Fu=448159.262818526
EffFy=379211.683923368   EffFu=492975.189100378   SSCurveOpt=Simple
SSHysType=Kinematic   SHard=0.015   SMax=0.11   SRup=0.17   FinalSlope=-0.1
   Material=Steel   Fy=350000   Fu=450000   EffFy=380000   EffFu=500000
SSCurveOpt=Simple   SSHysType=Kinematic   SHard=0.015   SMax=0.11   SRup=0.17
FinalSlope=-0.1

TABLE:  "MATERIAL PROPERTIES 03B - CONCRETE DATA"
   Material=4000Psi   Fc=27579.0315580631   LtWtConc=No   SSCurveOpt=Mander
SSHysType=Takeda   SFc=2.21914221766202E-03   SCap=0.005   FinalSlope=-0.1
FAngle=0   DAngle=0
   Material=Con_30   Fc=30000   LtWtConc=No   SSCurveOpt=Mander
SSHysType=Takeda   SFc=2.21914221766202E-03   SCap=0.005   FinalSlope=-0.1
FAngle=0   DAngle=0

TABLE:  "FRAME SECTION PROPERTIES 01 - GENERAL"

   SectionName=Pile   Material=Steel   Shape="I/Wide Flange"   t3=0.3048
t2=0.127   tf=0.009652   tw=0.00635   t2b=0.127   tfb=0.009652
Area=0.0042645076   TorsConst=9.65117678053953E-08   I33=6.5724174702235E-05
_
       I22=3.30125717301008E-06   AS2=0.00193548   AS3=2.04300666666667E-03
S33=4.3126098885981E-04   S22=5.19883019371667E-05   Z33=4.911874950424E-04
Z22=0.000080716532115   R33=0.124144683132414   R22=2.78230817990979E-02 _
       ConcCol=No   ConcBeam=No   Color=White   TotalWt=246.188522456661
TotalMass=25.1042416534491   FromFile=No   AMod=1   A2Mod=1   A3Mod=1
JMod=1   I2Mod=1   I3Mod=1   MMod=1   WMod=1   Notes="Added 2/15/2010 6:51:51
PM"
-------------------------------------------------------------------------------------------
Rest of the "FRAME SECTION PROPERTIES 01 - GENERAL" were deleted
-------------------------------------------------------------------------------------------

TABLE:  "AREA SECTION PROPERTIES"
   Section=Abut   Material=Con_30   MatAngle=0   AreaType=Shell   Type=Shell-
Thick   DrillDOF=Yes   Thickness=1.2   BendThick=1.2   Color=Green   F11Mod=1
F22Mod=1   F12Mod=1   M11Mod=1   M22Mod=1   M12Mod=1   V13Mod=1   V23Mod=1
MMod=1 _
       WMod=1   Notes="Added 2/15/2010 6:57:26 PM"
   Section=ASEC1   Material=A992Fy50   MatAngle=0   AreaType=Shell
Type=Shell-Thin   DrillDOF=Yes   Thickness=0.25   BendThick=0.25   Color=Blue
F11Mod=1   F22Mod=1   F12Mod=1   M11Mod=1   M22Mod=1   M12Mod=1   V13Mod=1
V23Mod=1 _
       MMod=1   WMod=1   Notes="Added 2/15/2010 4:18:41 PM"
-------------------------------------------------------------------------------------------
Rest of the "AREA SECTION PROPERTIES" were deleted
-------------------------------------------------------------------------------------------

TABLE:  "AREA SECTION PROPERTY DESIGN PARAMETERS"
   Section=Abut   RebarMat=None   RebarOpt=Default
   Section=ASEC1   RebarMat=None   RebarOpt=Default
   Section=Slab   RebarMat=None   RebarOpt=Default
   Section=Wingwall   RebarMat=None   RebarOpt=Default
```

```
------------------------------------------------------------------------------------------
Rest of the "AREA SECTION PROPERTY DESIGN PARAMETERS" were deleted
------------------------------------------------------------------------------------------

TABLE:  "LINK PROPERTY DEFINITIONS 01 - GENERAL"
   Link=Abut-L1   LinkType="MultiLinear Elastic"   Mass=0   Weight=0
RotInert1=0   RotInert2=0   RotInert3=0   DefLength=1   DefArea=1   PDM2I=0
PDM2J=0   PDM3I=0   PDM3J=0   Color=Yellow   Notes="Added 2/15/2010 7:15:13
PM"
   Link=Abut-L2   LinkType="MultiLinear Elastic"   Mass=0   Weight=0
RotInert1=0   RotInert2=0   RotInert3=0   DefLength=1   DefArea=1   PDM2I=0
PDM2J=0   PDM3I=0   PDM3J=0   Color=White   Notes="Added 2/15/2010 7:16:37
PM"
   Link=Abut-L3   LinkType="MultiLinear Elastic"   Mass=0   Weight=0
RotInert1=0   RotInert2=0   RotInert3=0   DefLength=1   DefArea=1   PDM2I=0
PDM2J=0   PDM3I=0   PDM3J=0   Color=Gray8Dark   Notes="Added 2/15/2010
7:16:46 PM"
------------------------------------------------------------------------------------------
Rest of the "LINK PROPERTY DEFINITIONS 01 - GENERAL" were deleted
------------------------------------------------------------------------------------------
TABLE:  "LINK PROPERTY DEFINITIONS 03 - MULTILINEAR"
   Link=Abut-L1   DOF=U2   Fixed=No   NonLinear=No   TransKE=40   TransCE=0
DJ=0
   Link=Abut-L2   DOF=U2   Fixed=No   NonLinear=Yes   TransKE=750   TransCE=0
DJ=0   Point=1   Force=-72   Displ=-0.29
   Link=Abut-L2   DOF=U2   Point=2   Force=-68   Displ=-0.054
   Link=Abut-L2   DOF=U2   Point=3   Force=-36   Displ=-0.018
   Link=Abut-L2   DOF=U2   Point=4   Force=0   Displ=0
   Link=Abut-L2   DOF=U2   Point=5   Force=0.1   Displ=0.1
   Link=Abut-L3   DOF=U2   Fixed=No   NonLinear=Yes   TransKE=1500
TransCE=0   DJ=0   Point=1   Force=-144   Displ=-0.29
   Link=Abut-L3   DOF=U2   Point=2   Force=-136   Displ=-0.054
   Link=Abut-L3   DOF=U2   Point=3   Force=-72   Displ=-0.018
   Link=Abut-L3   DOF=U2   Point=4   Force=0   Displ=0
   Link=Abut-L3   DOF=U2   Point=5   Force=0.1   Displ=0.1
   Link=Abut-L4   DOF=U2   Fixed=No   NonLinear=Yes   TransKE=2250
------------------------------------------------------------------------------------------
Rest of the "LINK PROPERTY DEFINITIONS 03 - MULTILINEAR" were deleted
------------------------------------------------------------------------------------------
TABLE:  "LOAD PATTERN DEFINITIONS"
   LoadPat=DEAD   DesignType=DEAD   SelfWtMult=1
   LoadPat=TempR   DesignType=TEMPERATURE   SelfWtMult=0
   LoadPat=K0   DesignType=OTHER   SelfWtMult=0

TABLE:  "AUTO WAVE 3 - WAVE CHARACTERISTICS - GENERAL"
   WaveChar=Default   WaveType="From Theory"   KinFactor=1   SWaterDepth=45
WaveHeight=18   WavePeriod=12   WaveTheory=Linear

TABLE:  "COMBINATION DEFINITIONS"
   ComboName=against   ComboType="Linear Add"   AutoDesign=No
CaseType="NonLin Static"   CaseName=K0   ScaleFactor=1   SteelDesign=No
ConcDesign=No   AlumDesign=No   ColdDesign=No
   ComboName=against   CaseType="NonLin Static"   CaseName=TempR
ScaleFactor=1
   ComboName=away   ComboType="Linear Add"   AutoDesign=No   CaseType="NonLin
Static"   CaseName=K0   ScaleFactor=0.62   SteelDesign=No   ConcDesign=No
AlumDesign=No   ColdDesign=No
```

```
TABLE:  "FUNCTION - RESPONSE SPECTRUM - USER"
   Name=UNIFRS   Period=0   Accel=1   FuncDamp=0.05
   Name=UNIFRS   Period=1   Accel=1

TABLE:  "FUNCTION - TIME HISTORY - USER"
   Name=RAMPTH   Time=0   Value=0
   Name=RAMPTH   Time=1   Value=1
   Name=RAMPTH   Time=4   Value=1
   Name=UNIFTH   Time=0   Value=1
   Name=UNIFTH   Time=1   Value=1

TABLE:  "FUNCTION - POWER SPECTRAL DENSITY - USER"
   Name=UNIFPSD   Frequency=0   Value=1
   Name=UNIFPSD   Frequency=1   Value=1

TABLE:  "FUNCTION - STEADY STATE - USER"
   Name=UNIFSS   Frequency=0   Value=1
   Name=UNIFSS   Frequency=1   Value=1

TABLE:  "GROUPS 1 - DEFINITIONS"
   GroupName=ALL   Selection=Yes   SectionCut=Yes   Steel=Yes   Concrete=Yes
Aluminum=Yes   ColdFormed=Yes   Stage=Yes   Bridge=Yes   AutoSeismic=No
AutoWind=No   SelDesSteel=No   SelDesAlum=No   SelDesCold=No   MassWeight=Yes
Color=Red

TABLE:  "GROUPS 2 - ASSIGNMENTS"
   GroupName=Superstr   ObjectType=Joint   ObjectLabel=1
   GroupName=Superstr   ObjectType=Joint   ObjectLabel=2
   GroupName=Superstr   ObjectType=Joint   ObjectLabel=958
   GroupName=Superstr   ObjectType=Joint   ObjectLabel=959
   GroupName=Superstr   ObjectType=Joint   ObjectLabel=960
-------------------------------------------------------------------------------------------
Rest of the "GROUPS 2 - ASSIGNMENTS" were deleted
-------------------------------------------------------------------------------------------
  TABLE:  "JOINT PATTERN DEFINITIONS"
   Pattern=Default
   Pattern=K0

TABLE:  "MASSES 1 - MASS SOURCE"
   MassFrom=Elements

TABLE:  "FUNCTION - PLOT FUNCTIONS"
   PlotFunc="Input Energy"   Type=Energy   Component=Input   Mode=All

TABLE:  "LOAD CASE DEFINITIONS"
   Case=DEAD   Type=LinStatic   InitialCond=Zero   DesTypeOpt="Prog Det"
DesignType=DEAD   AutoType=None   RunCase=No   CaseStatus="Not Run"
   Case=MODAL   Type=LinModal   InitialCond=Zero   DesTypeOpt="Prog Det"
DesignType=OTHER   AutoType=None   RunCase=No   CaseStatus="Not Run"
   Case=TempR   Type=NonStatic   InitialCond=Zero   DesTypeOpt="Prog Det"
DesignType=TEMPERATURE   AutoType=None   RunCase=No   CaseStatus="Not Run"
   Case=K0   Type=NonStatic   InitialCond=Zero   DesTypeOpt="Prog Det"
DesignType=OTHER   AutoType=None   RunCase=Yes   CaseStatus="Not Run"
   Case=No-spring   Type=NonStatic   InitialCond=Zero   DesTypeOpt="Prog Det"
DesignType=OTHER   AutoType=None   RunCase=Yes   CaseStatus="Not Run"

TABLE:  "CASE - STATIC 1 - LOAD ASSIGNMENTS"
```

```
   Case=DEAD   LoadType="Load pattern"   LoadName=DEAD   LoadSF=1
   Case=TempR   LoadType="Load pattern"   LoadName=TempR   LoadSF=1
   Case=K0   LoadType="Load pattern"   LoadName=K0   LoadSF=1

TABLE:  "CASE - STATIC 2 - NONLINEAR LOAD APPLICATION"
   Case=TempR   LoadApp="Full Load"   MonitorDOF=U1   MonitorJt=1
   Case=K0   LoadApp="Full Load"   MonitorDOF=U1   MonitorJt=1
   Case=No-spring   LoadApp="Full Load"   MonitorDOF=U1   MonitorJt=1

TABLE:  "CASE - STATIC 4 - NONLINEAR PARAMETERS"
   Case=TempR   Unloading="Unload Entire"   GeoNonLin=None
ResultsSave="Final State"   MaxTotal=200   MaxNull=50   MaxIterCS=10
MaxIterNR=40   ItConvTol=0.0001   UseEvStep=Yes   EvLumpTol=0.01
LSPerIter=20   LSTol=0.1 _
        LSStepFact=1.618   FrameTC=Yes   FrameHinge=Yes   CableTC=Yes
LinkTC=Yes   LinkOther=Yes   TFMaxIter=10   TFTol=0.01   TFAccelFact=1
TFNoStop=No
   Case=K0   Unloading="Unload Entire"   GeoNonLin=None   ResultsSave="Final
State"   MaxTotal=200   MaxNull=50   MaxIterCS=10   MaxIterNR=40
ItConvTol=0.0001   UseEvStep=Yes   EvLumpTol=0.01   LSPerIter=20   LSTol=0.1
LSStepFact=1.618 _
        FrameTC=Yes   FrameHinge=Yes   CableTC=Yes   LinkTC=Yes
LinkOther=Yes   TFMaxIter=10   TFTol=0.01   TFAccelFact=1   TFNoStop=No
   Case=No-spring   Unloading="Unload Entire"   GeoNonLin=None   MaxTotal=200
MaxNull=50   MaxIterCS=10   MaxIterNR=40   ItConvTol=0.0001   UseEvStep=Yes
EvLumpTol=0.01   LSPerIter=20   LSTol=0.1   LSStepFact=1.618 _
        StageSave="End of Final Stage"   StageMinIns=1   StageMinTD=1
FrameTC=Yes   FrameHinge=Yes   CableTC=Yes   LinkTC=Yes   LinkOther=Yes
TimeDepMat=No   TFMaxIter=10   TFTol=0.01   TFAccelFact=1   TFNoStop=No

TABLE:  "CASE - STATIC 5 - NONLINEAR STAGE DEFINITIONS"
   Case=No-spring   Stage=1   Duration=0   Output=No

TABLE:  "CASE - STATIC 6 - NONLINEAR STAGE DATA"
   Case=No-spring   Stage=1   Operation="Add Structure"   ObjType=Group
ObjName=No-spring   Age=0

TABLE:  "CASE - MODAL 1 - GENERAL"
   Case=MODAL   ModeType=Eigen   MaxNumModes=12   MinNumModes=1
EigenShift=0   EigenCutoff=0   EigenTol=0.000000001   AutoShift=Yes

TABLE:  "BRIDGE PREFERENCES"
   NorthAngle=90   MaxDiscCurv=1

TABLE:  "BRIDGE DESIGN PREFERENCES - AASHTOLRFD07"
   HingeOpt="Auto: AASHTO/Caltrans Hinge"

TABLE:  "JOINT COORDINATES"
   Joint=1   CoordSys=GLOBAL   CoordType=Cartesian   XorR=20   Y=0   Z=0
SpecialJt=Yes   GlobalX=20   GlobalY=0   GlobalZ=0
   Joint=2   CoordSys=GLOBAL   CoordType=Cartesian   XorR=0   Y=0   Z=0
SpecialJt=Yes   GlobalX=0   GlobalY=0   GlobalZ=0
   Joint=3   CoordSys=GLOBAL   CoordType=Cartesian   XorR=13.1564051684408
Y=8   Z=-4.3   SpecialJt=No   GlobalX=13.1564051684408   GlobalY=8
GlobalZ=-4.3
```

```
------------------------------------------------------------------------------------------
   Rest of the "JOINT COORDINATES" were deleted
------------------------------------------------------------------------------------------

TABLE:  "CONNECTIVITY - FRAME"
   Frame=247   JointI=970   JointJ=1216   IsCurved=No   Length=1
CentroidX=0.649519052838329   CentroidY=0.375   CentroidZ=-6.5
   Frame=248   JointI=1216   JointJ=1217   IsCurved=No   Length=1
CentroidX=0.649519052838329   CentroidY=0.375   CentroidZ=-7.5
   Frame=249   JointI=1217   JointJ=1218   IsCurved=No   Length=1
CentroidX=0.649519052838329   CentroidY=0.375   CentroidZ=-8.5
------------------------------------------------------------------------------------------
Rest of the "CONNECTIVITY - FRAME" were deleted
------------------------------------------------------------------------------------------

TABLE:  "CONNECTIVITY - AREA"
   Area=1   NumJoints=4   Joint1=967   Joint2=1083   Joint3=4   Joint4=3
Perimeter=3.74638880953099   AreaArea=0.651001201662488
CentroidX=13.5151871927124   CentroidY=8   CentroidZ=-4.19290322580645
   Area=2   NumJoints=4   Joint1=1083   Joint2=1084   Joint3=5   Joint4=4
Perimeter=3.57277277546349   AreaArea=0.65100120166249
CentroidX=13.5151871927124   CentroidY=8   CentroidZ=-3.26114695340502
------------------------------------------------------------------------------------------
Rest of the "CONNECTIVITY - AREA" were deleted
------------------------------------------------------------------------------------------

TABLE:  "CONNECTIVITY - LINK"
   Link=L-1   JointI=970   JointJ=970   Length=0
CentroidX=0.649519052838329   CentroidY=0.375   CentroidZ=-6
   Link=L-2   JointI=965   JointJ=965   Length=0   CentroidX=1.29903810567666
CentroidY=0.75   CentroidZ=-6
   Link=L-3   JointI=975   JointJ=975   Length=0   CentroidX=2.2372322931098
------------------------------------------------------------------------------------------
Rest of the "CONNECTIVITY - LINK" were deleted
------------------------------------------------------------------------------------------

TABLE:  "JOINT RESTRAINT ASSIGNMENTS"
   Joint=991   U1=No   U2=No   U3=Yes   R1=No   R2=No   R3=No
   Joint=992   U1=No   U2=No   U3=Yes   R1=No   R2=No   R3=No
   Joint=993   U1=No   U2=No   U3=Yes   R1=No   R2=No   R3=No
   Joint=994   U1=No   U2=No   U3=Yes   R1=No   R2=No   R3=No
------------------------------------------------------------------------------------------
Rest of the "JOINT RESTRAINT ASSIGNMENTS" were deleted
------------------------------------------------------------------------------------------

TABLE:  "JOINT LOCAL AXES ASSIGNMENTS 1 - TYPICAL"
   Joint=959   AngleA=-60   AngleB=0   AngleC=0   AdvanceAxes=Yes
   Joint=960   AngleA=-60   AngleB=0   AngleC=0   AdvanceAxes=Yes
   Joint=961   AngleA=-60   AngleB=0   AngleC=0   AdvanceAxes=Yes
------------------------------------------------------------------------------------------
Rest of the "JOINT LOCAL AXES ASSIGNMENTS 1 - TYPICAL" were deleted
------------------------------------------------------------------------------------------

TABLE:  "JOINT LOCAL AXES ASSIGNMENTS 2 - ADVANCED"
   Joint=959   LocalPlane=31   AxOption1="Coord Dir"   AxCoordSys=GLOBAL
AxCoordDir=Z   AxVecJt1=None   AxVecJt2=None   PlOption1="Coord Dir"
PlCoordSys=GLOBAL   CoordDir1=X   CoordDir2=Y   PlVecJt1=None   PlVecJt2=None
AxVecX=0 _
        AxVecY=0   AxVecZ=1   PlVecX=1   PlVecY=0   PlVecZ=0
   Joint=960   LocalPlane=31   AxOption1="Coord Dir"   AxCoordSys=GLOBAL
AxCoordDir=Z   AxVecJt1=None   AxVecJt2=None   PlOption1="Coord Dir"
PlCoordSys=GLOBAL   CoordDir1=X   CoordDir2=Y   PlVecJt1=None   PlVecJt2=None
AxVecX=0 _
        AxVecY=0   AxVecZ=1   PlVecX=1   PlVecY=0   PlVecZ=0
```

```
------------------------------------------------------------------------------------------
 Rest of the "JOINT LOCAL AXES ASSIGNMENTS 2 - ADVANCED" were deleted
------------------------------------------------------------------------------------------

TABLE:  "JOINT PATTERN ASSIGNMENTS"
   Joint=1   Pattern=K0   Value=0
   Joint=2   Pattern=K0   Value=0
   Joint=24   Pattern=K0   Value=60
   Joint=33   Pattern=K0   Value=50
------------------------------------------------------------------------------------------
Rest of the "JOINT PATTERN ASSIGNMENTS" were deleted
------------------------------------------------------------------------------------------

TABLE:  "FRAME SECTION ASSIGNMENTS"
   Frame=247   SectionType="I/Wide Flange"   AutoSelect=N.A.   AnalSect=Pile
DesignSect=Pile   MatProp=Default
   Frame=248   SectionType="I/Wide Flange"   AutoSelect=N.A.   AnalSect=Pile
DesignSect=Pile   MatProp=Default
   Frame=249   SectionType="I/Wide Flange"   AutoSelect=N.A.   AnalSect=Pile
DesignSect=Pile   MatProp=Default
   Frame=250   SectionType="I/Wide Flange"   AutoSelect=N.A.   AnalSect=Pile
DesignSect=Pile   MatProp=Default
------------------------------------------------------------------------------------------
Rest of the "FRAME SECTION ASSIGNMENTS" were deleted
------------------------------------------------------------------------------------------

TABLE:  "FRAME LOCAL AXES ASSIGNMENTS 1 - TYPICAL"
   Frame=247   Angle=60   MirrorAbt2=No   MirrorAbt3=No   AdvanceAxes=No
   Frame=248   Angle=60   MirrorAbt2=No   MirrorAbt3=No   AdvanceAxes=No
   Frame=249   Angle=60   MirrorAbt2=No   MirrorAbt3=No   AdvanceAxes=No
   Frame=250   Angle=60   MirrorAbt2=No   MirrorAbt3=No   AdvanceAxes=No
------------------------------------------------------------------------------------------
Rest of the "FRAME LOCAL AXES ASSIGNMENTS 1 - TYPICAL" were deleted
------------------------------------------------------------------------------------------

TABLE:  "FRAME INSERTION POINT ASSIGNMENTS"
   Frame=247   CardinalPt="10 (centroid)"   Mirror2=No   Transform=Yes
   Frame=248   CardinalPt="10 (centroid)"   Mirror2=No   Transform=Yes
   Frame=249   CardinalPt="10 (centroid)"   Mirror2=No   Transform=Yes
   Frame=250   CardinalPt="10 (centroid)"   Mirror2=No   Transform=Yes
------------------------------------------------------------------------------------------
Rest of the "FRAME INSERTION POINT ASSIGNMENTS" were deleted
------------------------------------------------------------------------------------------


TABLE:  "FRAME OUTPUT STATION ASSIGNMENTS"
   Frame=247   StationType=MinNumSta   MinNumSta=3   AddAtElmInt=Yes
AddAtPtLoad=Yes
   Frame=248   StationType=MinNumSta   MinNumSta=3   AddAtElmInt=Yes
AddAtPtLoad=Yes
   Frame=249   StationType=MinNumSta   MinNumSta=3   AddAtElmInt=Yes
AddAtPtLoad=Yes
------------------------------------------------------------------------------------------
 Rest of the "FRAME OUTPUT STATION ASSIGNMENTS" were deleted
------------------------------------------------------------------------------------------

TABLE:  "FRAME AUTO MESH ASSIGNMENTS"
   Frame=247   AutoMesh=Yes   AtJoints=Yes   AtFrames=No   NumSegments=0
MaxLength=0   MaxDegrees=0
   Frame=248   AutoMesh=Yes   AtJoints=Yes   AtFrames=No   NumSegments=0
MaxLength=0   MaxDegrees=0
```

```
------------------------------------------------------------------------------------------
Rest of the "FRAME AUTO MESH ASSIGNMENTS" were deleted
------------------------------------------------------------------------------------------

 TABLE:  "FRAME LOADS - TEMPERATURE"
   Frame=1002   LoadPat=TempR   Type=Temperature   Temp=40   JtPattern=None
   Frame=1003   LoadPat=TempR   Type=Temperature   Temp=40   JtPattern=None
   Frame=1004   LoadPat=TempR   Type=Temperature   Temp=40   JtPattern=None
   Frame=1005   LoadPat=TempR   Type=Temperature   Temp=40   JtPattern=None
   Frame=1006   LoadPat=TempR   Type=Temperature   Temp=40   JtPattern=None
------------------------------------------------------------------------------------------
Rest of the "FRAME LOADS - TEMPERATURE" were deleted
------------------------------------------------------------------------------------------

TABLE:  "FRAME DESIGN PROCEDURES"
   Frame=247   DesignProc="From Material"
   Frame=248   DesignProc="From Material"
   Frame=249   DesignProc="From Material"
   Frame=250   DesignProc="From Material"
------------------------------------------------------------------------------------------
Rest of the "FRAME DESIGN PROCEDURES" were deleted
------------------------------------------------------------------------------------------

TABLE:  "OVERWRITES - STEEL DESIGN - AISC-LRFD93"
   Frame=247   DesignSect="Program Determined"   FrameType="Program
Determined"   Fy=0   RLLF=0   AreaRatio=0   XLMajor=0   XLMinor=0   XKMajor=0
XKMinor=0   CmMajor=0   CmMinor=0   Cb=0   B1Major=0   B1Minor=0   B2Major=0
B2Minor=0 _
        PhiPnc=0   PhiPnt=0   PhiMn3=0   PhiMn2=0   PhiVn2=0   PhiVn3=0
CheckDefl="Program Determined"   DeflType="Program Determined"   DLRat=0
SDLAndLLRat=0   LLRat=0   TotalRat=0   NetRat=0   DLAbs=0   SDLAndLLAbs=0
LLAbs=0 _
        TotalAbs=0   NetAbs=0   SpecCamber=0
   Frame=248   DesignSect="Program Determined"   FrameType="Program
Determined"   Fy=0   RLLF=0   AreaRatio=0   XLMajor=0   XLMinor=0   XKMajor=0
XKMinor=0   CmMajor=0   CmMinor=0   Cb=0   B1Major=0   B1Minor=0   B2Major=0
B2Minor=0 _
        PhiPnc=0   PhiPnt=0   PhiMn3=0   PhiMn2=0   PhiVn2=0   PhiVn3=0
CheckDefl="Program Determined"   DeflType="Program Determined"   DLRat=0
SDLAndLLRat=0   LLRat=0   TotalRat=0   NetRat=0   DLAbs=0   SDLAndLLAbs=0
LLAbs=0 _
        TotalAbs=0   NetAbs=0   SpecCamber=0
   Frame=249   DesignSect="Program Determined"   FrameType="Program
Determined"   Fy=0   RLLF=0   AreaRatio=0   XLMajor=0   XLMinor=0   XKMajor=0
XKMinor=0   CmMajor=0   CmMinor=0   Cb=0   B1Major=0   B1Minor=0   B2Major=0
B2Minor=0 _
        PhiPnc=0   PhiPnt=0   PhiMn3=0   PhiMn2=0   PhiVn2=0   PhiVn3=0
CheckDefl="Program Determined"   DeflType="Program Determined"   DLRat=0
SDLAndLLRat=0   LLRat=0   TotalRat=0   NetRat=0   DLAbs=0   SDLAndLLAbs=0
LLAbs=0 _
        TotalAbs=0   NetAbs=0   SpecCamber=0
------------------------------------------------------------------------------------------
Rest of the "OVERWRITES - STEEL DESIGN - AISC-LRFD93" were deleted
------------------------------------------------------------------------------------------

TABLE:  "AREA SECTION ASSIGNMENTS"
   Area=1   Section=Wingwall   MatProp=Default
   Area=2   Section=Wingwall   MatProp=Default
   Area=3   Section=Wingwall   MatProp=Default
   Area=1172   Section=Slab   MatProp=Default
   Area=1173   Section=Slab   MatProp=Default
```

```
   Area=1174   Section=Slab   MatProp=Default
-------------------------------------------------------------------------------------------
Rest of the "AREA SECTION ASSIGNMENTS" were deleted
-------------------------------------------------------------------------------------------

TABLE:  "AREA OVERWRITES - JOINT OFFSETS"
   Area=1   OffsetOver=Object   Offset1=0   Offset2=0   Offset3=0   Offset4=0
   Area=2   OffsetOver=Object   Offset1=0   Offset2=0   Offset3=0   Offset4=0
   Area=3   OffsetOver=Object   Offset1=0   Offset2=0   Offset3=0   Offset4=0
   Area=4   OffsetOver=Object   Offset1=0   Offset2=0   Offset3=0   Offset4=0
   Area=5   OffsetOver=Object   Offset1=0   Offset2=0   Offset3=0   Offset4=0
-------------------------------------------------------------------------------------------
Rest of the "AREA OVERWRITES - JOINT OFFSETS" were deleted
-------------------------------------------------------------------------------------------

TABLE:  "AREA LOADS - SURFACE PRESSURE"
   Area=728   LoadPat=K0   Face=Top   Pressure=1   JtPattern=K0
   Area=729   LoadPat=K0   Face=Top   Pressure=1   JtPattern=K0
   Area=730   LoadPat=K0   Face=Top   Pressure=1   JtPattern=K0
   Area=731   LoadPat=K0   Face=Top   Pressure=1   JtPattern=K0
-------------------------------------------------------------------------------------------
Rest of the "AREA LOADS - SURFACE PRESSURE" were deleted
-------------------------------------------------------------------------------------------


TABLE:  "AREA LOADS - TEMPERATURE"
   Area=1167   LoadPat=TempR   Type=Temperature   Temp=40   JtPattern=None
   Area=1168   LoadPat=TempR   Type=Temperature   Temp=40   JtPattern=None
   Area=1169   LoadPat=TempR   Type=Temperature   Temp=40   JtPattern=None
   Area=1170   LoadPat=TempR   Type=Temperature   Temp=40   JtPattern=None
   Area=1171   LoadPat=TempR   Type=Temperature   Temp=40   JtPattern=None
-------------------------------------------------------------------------------------------
Rest of the "AREA LOADS - TEMPERATURE" were deleted
-------------------------------------------------------------------------------------------

TABLE:  "LINK PROPERTY ASSIGNMENTS"
   Link=L-1   LinkType="MultiLinear Elastic"   LinkJoints=SingleJoint
LinkProp=Abut-L7   LinkFDProp=None
   Link=L-2   LinkType="MultiLinear Elastic"   LinkJoints=SingleJoint
LinkProp=Abut-L7   LinkFDProp=None
   Link=L-3   LinkType="MultiLinear Elastic"   LinkJoints=SingleJoint
LinkProp=Abut-L7   LinkFDProp=None
   Link=L-4   LinkType="MultiLinear Elastic"   LinkJoints=SingleJoint
LinkProp=Abut-L7   LinkFDProp=None
-------------------------------------------------------------------------------------------
Rest of the "LINK PROPERTY ASSIGNMENTS" were deleted
-------------------------------------------------------------------------------------------

TABLE:  "LINK LOCAL AXES ASSIGNMENTS 1 - TYPICAL"
   Link=L-1   Angle=210   AdvanceAxes=No
   Link=L-2   Angle=210   AdvanceAxes=No
   Link=L-3   Angle=210   AdvanceAxes=No
   Link=L-4   Angle=210   AdvanceAxes=No
   Link=L-5   Angle=210   AdvanceAxes=No
-------------------------------------------------------------------------------------------
Rest of the "LINK LOCAL AXES ASSIGNMENTS 1 - TYPICAL" were deleted
-------------------------------------------------------------------------------------------

TABLE:  "PREFERENCES - DIMENSIONAL"
   MergeTol=0.001   FineGrid=0.25   Nudge=0.25   SelectTol=3   SnapTol=12
SLineThick=1   PLineThick=4   MaxFont=8   MinFont=3   AutoZoom=10
ShrinkFact=70   TextFileLen=240
```

```
TABLE:  "PREFERENCES - STEEL DESIGN - AISC-LRFD93"
   THDesign=Envelopes   FrameType="Moment Frame"   PatLLF=0.75
SRatioLimit=0.95   MaxIter=1   PhiB=0.9   PhiC=0.85   PhiT=0.9   PhiV=0.9
PhiCA=0.9   CheckDefl=Yes   DLRat=120   SDLAndLLRat=120   LLRat=360
TotalRat=240   NetRat=240

TABLE:  "PREFERENCES - CONCRETE DESIGN - ACI 318-05/IBC2003"
   THDesign=Envelopes   NumCurves=24   NumPoints=11   MinEccen=No
PatLLF=0.75   UFLimit=0.95   SeisCat=D   PhiT=0.9   PhiCTied=0.65
PhiCSpiral=0.7   PhiV=0.75   PhiVSeismic=0.6   PhiVJoint=0.85

TABLE:  "PREFERENCES - ALUMINUM DESIGN - AA-ASD 2000"
   THDesign=Envelopes   FrameType="Moment Frame"   SRatioLimit=1   MaxIter=1
LatFact=1.33333333333333   UseLatFact=No   Bridge=No

TABLE:  "PREFERENCES - COLD FORMED DESIGN - AISI-ASD96"
   THDesign=Envelopes   FrameType="Braced Frame"   SRatioLimit=1   MaxIter=1
OmegaBS=1.67   OmegaBUS=1.67   OmegaBLTB=1.67   OmegaVS=1.67   OmegaVNS=1.5
OmegaT=1.67   OmegaC=1.8


TABLE:  "OPTIONS - COLORS - OUTPUT"
   DeviceType=Screen   Contour1=13107400   Contour2=6553828   Contour3=Red
Contour4=16639   Contour5=Orange   Contour6=43775   Contour7=54527
Contour8=Yellow   Contour9=65408   Contour10=Green   Contour11=8453888
Contour12=Cyan _
        Contour13=16755200   Contour14=16733440   Contour15=Blue
Transpare=0.5   Ratio1=Cyan   Ratio2=Green   Ratio3=Yellow   Ratio4=Orange
Ratio5=Red   RatioNotD=Gray4   RatioNotC=Red   RatioVal1=0.5   RatioVal2=0.7
RatioVal3=0.9 _
        RatioVal4=1   DFillPos=Yellow   DFillNeg=Red   DFillRPos=Blue
DFillRNeg=Cyan

DFillRPos=Blue   DFillRNeg=Blue
```

Rest of the "OPTIONS - COLORS - OUTPUT" were deleted

Output

```
ELEM=JOINT    TYPE=DISP, REAC LOAD=*
ELEM=SHELL    TYPE=FORCE  LOAD=*
ELEM=SHELL    TYPE=STRESS  LOAD=*
ELEM=FRAME    TYPE=JOITF LOAD=*


END TABLE DATA
```

REFERENCES

[1] Abendroth, R. E., and Greimann, L. F. (2005). Field Testing of Integral Abutments. Iowa Department of Transportation, Report No. HR-399, Ames, IA.

[2] Abendroth, R. E., Greimann, L., and LaViolette, M. D. (2007). An Integral Abutment Bridge with Precast Concrete Piles. Center for Transportation Research and Education Iowa State University, Final Report, Report No. IHRB Project TR-438, Ames, IA.

[3] American Association of State Highway and Transportation Officials. (1994). AASHTO LRFD Bridge Design Specifications. First Edition. Washington, D.C.

[4] American Association of State Highway and Transportation Officials. (2000). AASHTO LRFD Bridge Design Specifications. Second Edition. Washington, D.C.

[5] American Association of State Highway and Transportation Officials. (2004). AASHTO LRFD Bridge Design Specifications.Third Edition. Washington, D.C.

[6] American Association of State Highway and Transportation Officials. (1996). Standard Specifications for Highway Bridges. Washington, D.C.

[7] Bakht, B., Cheung, M.S., and Aziz, T. S. (1979). Application of Simplified Method of Calculating Longitudinal Moments to the Ontario Highway Bridge design Code. Canadian Journal of Civil Engineering, 19 (4): 551-559.

[8] Barker, R. M., Duncan, J., Rojiani, K. B., Ooi, P. S., Tan, C. K., and Kim, S. G. (1991). Manuals for The Design of Bridge Foundations, Transportation Research Board: NCHRP Report 343. Washington, D.C.

[9] Barr, P. J., Eberhard, M. O., and Stanton, J. F. (2001). Live-Load Distribution Factors in Prestressed Concrete Girder Bridges. ASCE Journal of Bridge Engineering, 6(5): 298-306.

[10] Bonczar, C., F Breña, S., Civjan, S., DeJong, J., Crellin, B., and Crovo, D. (2005). Field Data and FEM Modeling of the Orange-Wendell Bridge. Integral Abutment and Jointless Bridges, (pp. 163-173), Baltimore, MD.

[11] Bowles, J. (1996). Foundation Analysis and Design. 5th ed. McGraw-Hill, New York, NY.

[12] Canadian Geothechnical Society, (1992). Canadian Foundation Engineering Manual. 3rd Edition, Toronto, ON.

[13] Canadian Standard Association, CSA. (2000). Canadian Highway Bridge Design Code, CHBDC. Etobicoke, ON.

[14] Canadian Standard Association, CSA. (2006). Canadian Highway Bridge Design Code, CHBDC. Etobicoke, ON.

[15] Civjan, S. A., Brena, S. F., Butler D. A., and Crovo D. S. (2004). Field Monitoring of an Integral Abutment Bridge in Massachusetts, Transportation Research Record: Journal of the Transportation Research Board. No. 1892, TRB, National Research Council, Washington, D.C., 160–169.

[16] Clough, G. W., and Duncan, J. M. (1991). Earth Pressures. Chapter 6. In H. Y. Fang, Foundation Engineering Manual, 2nd Ed. (pp. 223–235). New York: Van NostrandReinhold.

[17] Deatherage, J. H., Burdette, E. G., Howard, S. C., Ingram, E. E., and Goodpasture, D. W. (2005). Behavior of Pile Supported Integral Abutments. Integral Abutment and Jointless Bridges, (pp. 222-233). Baltimore, MD.

[18] Dicleli, M., and Albhaisi, S. M. (2003). Effect of Cyclic Thermal Loading on the Performance of Steel H-Pile in Integral Bridges with Stub-Abutments. Journal of Const. Steel Research, 60: 161–182.

[19] Dicleli, M., and Albhaisi, S. M. (2005). Analytical Formulation of Maximum Lenght limits of Integral Bridges on Cohesive Soils. Canadian Journal of Civil Engineering, 32: 726–738.

[20] Dicleli, M., and Erhan, S. (2008). Effect of Soil and Substructure Properties on Live Load Distribution in Integral Abutment Bridges. ASCE Journal of Bridge Engineering, 13(5): 527-539.

[21] Dicleli, M., and Erhan, S. (2009). Live Load Distribution Formulas for Single-Span Prestressed Concrete Integral Abutment Bridge Girders. ASCE Journal of Bridge Engineering, 14(6): 472-487.

[22] Emanuel, J. H., and Hulsey, J. L. (1978). Temperature in Composite Bridges. ASCE Journal of the Structural Division, 104(1): 65-78.

[23] Erhan, S., and Dicleli, M, (2011). Effect of Foundation Soil Stiffness on the Seismic Performance of Integral Bridges. "Structural Engineering International", 21, 162-168.

[24] Faraji, S., Ernst, H., Ting, J. M., and Crovo, D. S. (2001). Nonlinear Analysis of Integral Bridges: Finite-Element Model. Journal of Geotechnical and Geoenvironmental Engineering, 127(5) : 454–461.

[25] Frosch, R. J., Wenning M., and Chovichien V. (2005). The In-Service Behavior of Integral Bridges: Abutment-pile Response, 2005 FHWA Conference on Integral Abutments and Jointless Bridges, pp. 30-40.

[26] Gangone, M. V., Whelan, M. J., Fuchs, M. P., and Janoyan, K. D. (2007). Performance Monitoring of a Short-Span Integral-Abutment Bridge Using Wireless Sensor Technology. Sensor Systems and Networks: Phenomena, Technology, and Applications for NDE and Health Monitoring 2007. San Diego, CA: The International Society for Optical Engineering.

[27] Girton, D. D., Hawkinson, T. R., and Greimann, L. F. (1989). Validation of Design Recommendations for Integral-Abutment Piles. Final Report, Iowa DOT Project No. HR-292, Iowa Department of Transportation, Ames, IA.

[28] Greimann, L. F., Yang, P. S., Edmunds, S. K., and Wolde-Tinsae, A. M. (1984). Design of Piles for Integral Abutment Bridges. Final Report, Iowa DOT Project No. HR-252, Iowa Department of Transportation, Ames, IA.

[29] Greimann, L. , Phares , B., Faris, A., and Bigelow, J. (2008). Integral Bridge Abutment-to-Approach Slab Connection. Final Report, Iowa DOT Project No. TR-530 & TR-539, Iowa Department of Transportation, Ames, IA.

[30] Haliburton, T. (1971). Soil Structure Interaction; Numerical Analysis of Beams and Beam Columns. Stillwater, Oklahoma: Technical Publication No. 14, School of Civil Engineering, Oklahoma State University.

[31] Hartt, S. L., Sandford, T. C., and Davids, W. G. (2006). Monitoring a Pile-Supported Integral Abutment. Bridge at a Site with Shallow Bedrock. Phase II. Maine Department of Transportation, Report No.ME 01-7, Augusta, ME.

[32] Hassiotis, S., Khodair Y., Roman E., and Dehne Y. (2006), Evaluation of Integral Abutments, Final Report, FHWA-NJ-2005-025, Federal Highway Administration, Washington, D.C.

[33] Hassiotis, S. and Roman, E. (2005). A Survey of Current Issues on the Use of Integral Abutment Bridges. Journal of Bridge Structures, Taylor & Francis Group Ltd., 1 (2): 81-101T.

[34] Huang, J., French, C., and Shield, C. (2004). Behavior of Concrete Integral Abutment Bridges. St. Paul, Minnesota: Minnesota Department of Transportation, Report No. MN/RC - 2004-43.

[35] Hussain, I., and Bagnariol, D. (1996). Integral Abutment Bridges. Ontario Ministry of Transportation, Report No. SO-96-01, St. Catharines, ON.

[36] Ibrahim, M., Sennah, K., and Samaan, M. (2010). Structural Design Issues for Integral Abutment Bridges. Proceedings of 8th International Conference on Short and Medium Span Bridges, Canadian Society for Civil Engineering, (pp. 310: 1-10). Niagara Falls, ON.

[37] Jaeger, L., and Bakht, B. (1982). The Grillage Analogy in Bridge Analysis. Canadian Journal of Civil Engineering: 224-235.

[38] Jorgenson, J.L. (1983). Behaviour of Abutment Piles in an Integral Abutment in Response to Transportation, Report No. SO-96-01, St.Catharines, ON.

[39] Khan, W. (2010). Load distribution in Adjacent Precast Deck Free Concrete Box-Girder Bridges. M.Eng thesis, Department of Civil Engineering, Ryerson University ,Toronto, Ontario, Canada.

[40] Kim, W., and Laman, J. A. (2012). Seven Year Field Monitoring of Four Integral Abutment Bridges. Journal of Performance of Constructed Facilities, 26(1): 54-64.

[41] Knickerbocker, D., and Basu, P. (2004). Behavior of Jointless High Performance Concrete Bridges. Tennessee Department o f Transportation, Report# TNSPR-RES1162, Nashville.

[42] Kunin, J., and Alampalli, S. (2000). Integral abutment bridges:Current Practice in United States and Canada. ASCE Journal of Perfgormance of Constructed Facilities, 14(3): 104-111.

[43] Kuppa, S., and Roeder, C. (1991). Thermal Movements in Bridges. University of Washington, Final Report-National Science Foundation, Grant CES-8714894, Washington, D.C.

[44] Laman, J. A., and Kim, W. (2009). Monitoring of integral abutment bridges and design criteria development. Rep. No. FHWA-PA- 2009-005-PSU002, Pennsylvania Transportation Research Council, Harrisburg, PA.

[45] Lan, C. (2012). On the Performance of Super-Long Integral Abutment Bridges. Ph.D. Dissertation, Department of Civil Mechanical Structural Systems, University of Trento, Trento, Italy.

[46] Maleki, S. (2002). Free-vibration of Continuous Slab-Beam Skewed Bridges. Journal of Sound and Vibration, 255 (4): 793-903.

[47] Meng, J., and Lui, E. (2002). Refined Stick Model for Dynamic Analysis of Skew Highway Bridges. ASCE Journal of Bridge Engineering, 7 (3): 184-194.

[48] Ministry of Transportation and Communications. (1983). Ontario Highway Bridge Design Code, OHBDC, Second Edition. Downsview, ON.

[49] Ministry of Transportation Ontario. (1991). Ontario Highway Bridge Design Code, OHBDC. Third Edition. Downsview, ON.

[50] Moorty, S., and Roeder, C. (1991). Thermal Movements in Bridges. Transportation Research Record, 1290(1): 135-143.

[51] Newmark, N., Siess, C., and Penman, R. (1948). Studies of Slab and Beam Highway Bridges. Part I: Tests of Simple-Span Right I-Beam Bridges. Engineering Experiment Station, University of Illinois, Urbana III, Buletin Series No. 375.

[52] Nikravan, N., and Sennah, K., (2012). Extending Limits of Applicability for Integral Abutment Bridges. Proceeding of the CSCE 3rd International Structural Specialty Conference, Canadian Society for Civil Engineering (CSCE), STR-R5-1005, Edmonton, Canada, pp. 1-10.

[53] Nikravan, N., and Sennah, K., (2013). Parametric Study on the Effect of Temperature Variation in Integral Abutment Bridges, Proceeding of the CSCE General Conference, Canadian Society for Civil Engineering (CSCE), GEN-97, Montreal, Canada, pp. 1-10.

[54] Nikravan, N., and Sennah, K., (2013). Parametric Model on the CHBDC Truck Load Distribution among Girders in Single-Span Integral Abutment Bridges, Proceeding of the CSCE General Conference, Canadian Society for Civil Engineering (CSCE), GEN-98, Montreal, Canada, pp. 1-10.

[55] Potgieter, I., and Gamble, W. (1983). Nonlinear Temperature Distributions in Bridges at Different Locations in the United States. PCI Journal, Precast/Prestressed Concrete Institute , 80-103.

[56] Precast/Prestressed Concrete Institute, (2001). The State of the Art of Precast/Prestressed Integral Bridges. Report by PCI Subcommittee on Integral Bridge, PCI Publication Number IB-01, Chicago.

[57] Purvis, P. (2003). Bridge Deck Joint Performance, NCHRP Synthesis 319. Washington, D.C.: National Cooperative Highway Research Program.

[58] Reese, L. C., and Impe, W. F. (2001). Single Piles and Pile Groups Under Lateral Loading. Taylor & Francis Group, London, UK.

[59] Roberts-Wollman, C. L., Breen, J. E., and Cawrse, J. (2002). Measurements of Thermal Gradients and their Effects on Segmental Concrete Bridge. ASCE Journal of Bridge Engineering, 7(3): 166–174.

[60] Roeder, C. W. (2003). Proposed Design Method for Thermal Bridge Movements. ASCE Journal of Bridge Engineering, 8(1):12-19.

[61] SAP2000, (2010). Integrated Finite Element Analysis and Design of Structures, Computer and Structure Inc. Berkely, CA.

[62] Sandford, T. C., Davids, W. G., Hartt, S. L., and Delano, J. G. (2006). Construction-induced stresses in H-piles supporting an integral abutment bridge. Transportation Research Record, Transportation Research Board, 39–48.

[63] Shahawy, M., and Huang, D. (2001). Analytical and Field Investigation of Lateral Load Distribution in Concrete Slab-on-Girder Bridges. ACI Structural Journal: 590-599.

[64] Siddique, A., Sparling, B., and Wegner, L. (2007). Assessment of Vibration-Based Damage Detection for an Integral Abutment Bridge. Canadian Journal of Civil Engineering, 34: 438-452.

[65] Skempton, A. (1951). The Bearing Capacity of Clays. Building Research Congress, Division I, Part 3, (pp. 180–189). London.

[66] Tabsh, S., and Mourad, S. (2003). Structural Design Issues For Jointless Bridges. Proceeding of the 9th Structural Engineering Confrence. Abu Dhabi: Emerging Technologies in Structural Engineering, pp. 277-284.

[67] Terzaghi, K. V. (1955). Evaluation of Coefficient of Subgrade Reaction, Geotechnique, 5(4): 297-32.

[68] Yannotti, A. P., Alampalli, S., and White 2nd, H. L. (2005). New York State Department of Transportation's Experience with Integral Abutment Bridges. Integral Abutment and Jointless Bridges, (pp. 41-49), Baltimore, MD.

[69] Zokaie, T. (2000). AASHTO-LRFD Live Load Distribution Specifications. ASCE Journal of Bridge Engineering, 5(2): 131-138.